PB87-147633

Proceedings: Symposium on the Transfer and Utilization of Particulate Control Technology (6th). Volume 3

Radian Corp., Research Triangle Park, NC

Prepared for

Environmental Protection Agency
Research Triangle Park, NC

Dec 86

U.S. Department of Commerce
National Technical Information Service
NTIS

PB87-147633

EPA/600/9-86/031c
December 1986

Proceedings: Sixth Symposium on the Transfer and Utilization of Particulate Control Technology

Volume 3

Holly Re[illegible] Compiler

Radian [illegible]ation
P.O. B[illegible]00
Research Triangle Park, North Carolina 27709

EPA Contract 68-02-3994, Task 46

EPA Project Officer:
Dale L. Harmon
Air and Energy Engineering Research Laboratory
Research Triangle Park, NC 27711

EPRI Project Manager:
R.F. Altman
Air Quality Control Program
Coal Combustion Systems Division
Palo Alto, California 94304

AIR AND ENERGY ENGINEERING RESEARCH LABORATORY
OFFICE OF RESEARCH AND DEVELOPMENT
U.S. ENVIRONMENTAL PROTECTION AGENCY
RESEARCH TRIANGLE PARK, NC 27711

REPRODUCED BY
U.S. DEPARTMENT OF COMMERCE
NATIONAL TECHNICAL
INFORMATION SERVICE
SPRINGFIELD, VA. 22161

TECHNICAL REPORT DATA

(Please read Instructions on the reverse before completing)

1. REPORT NO. EPA/600/9-86/031c	2.	3. RECIPIENT'S ACCESSION NO. PB87-147633/AS
4. TITLE AND SUBTITLE Proceedings: Sixth Symposium on the Transfer and Utilization of Particulate Control Technology; Volume 3		5. REPORT DATE December 1986
		6. PERFORMING ORGANIZATION CODE
7. AUTHOR(S) Holly Rossi, Compiler		8. PERFORMING ORGANIZATION REPORT NO. EPRI CS-4918
9. PERFORMING ORGANIZATION NAME AND ADDRESS Radian Corporation P.O. Box 13000 Research Triangle Park, North Carolina 27709		10. PROGRAM ELEMENT NO.
		11. CONTRACT/GRANT NO. 68-02-3994, Task 46
12. SPONSORING AGENCY NAME AND ADDRESS EPA, Office of Research and Development Air and Energy Engineering Research Laboratory Research Triangle Park, NC 27711		13. TYPE OF REPORT AND PERIOD COVERED Proceedings; February 1986
		14. SPONSORING AGENCY CODE EPA/600/13

15. SUPPLEMENTARY NOTES AEERL project officer is Dale L. Harmon, Mail Drop 61, 919/541-2429.

16. ABSTRACT These proceedings document the Sixth Symposium on the Transfer and Utilization of Particulate Control Technology, in New Orleans, LA, February 25-28, 1986. The symposium, the second of its kind to be sponsored jointly by EPA and EPRI, was devoted to discussions of particulate emissions control. Its objectives were to promote the transfer of results of particulate control research to potential users of technologies, and to provide a medium for exchange of ideas between researchers in the fields of particulate control development and application. The proceedings contain 84 papers presented by EPA and other federal and state agency representatives, EPRI staff members, representatives of utility companies, equipment and process suppliers, university representatives, and research and development companies. Additionally, individuals from Australia, Canada, Denmark, Great Britain, Italy, Japan, and South Africa presented information on worldwide technological developments. Electrostatic precipitators and fabric filters were the major topics discussed. Other topics of interest included system operation and maintenance, fugitive emission control, integrated control processes (e.g., SO2 and particulate control), and advanced energy applications (e.g., high temperature applications).

17. KEY WORDS AND DOCUMENT ANALYSIS

a. DESCRIPTORS		b. IDENTIFIERS/OPEN ENDED TERMS	c. COSATI Field/Group	
Pollution	Processing	Pollution Control	13B	13H
Particles	Leakage	Stationary Sources	14G	
Electrostatic Precipitators		Particulate	13I	
Filters	Sulfur Dioxide	Fabric Filters		07B
Fabrics	Nitrogen Oxides	Fugitive Emissions	11E	
Maintenance			15E	

18. DISTRIBUTION STATEMENT Release to Public	19. SECURITY CLASS *(This Report)* Unclassified	21. NO. OF PAGES 401
	20. SECURITY CLASS *(This page)* Unclassified	22. PRICE

EPA Form 2220-1 (9-73)

ABSTRACT

These Proceedings document the Sixth Symposium on the Transfer and Utilization of Particulate Control Technology, held February 25 through 28, 1986, in New Orleans, Louisiana. The Symposium was sponsored by the U. S. EPA's Air and Energy Engineering Research Laboratory in Research Triangle Park, North Carolina, and EPRI's Coal Combustion Systems Division, in Palo Alto, California.

The objectives of the Symposium were to provide an opportunity for the exchange of knowledge and to stimulate new ideas in the field of particulate control research with the goal of extending the technology and aiding its diffusion among designers, users, and educators. Fabric filters and electrostatic precipitators were the major topics, but novel concepts and advanced technologies were also explored. Topics discussed in each day's sessions are listed below:

Tuesday, February 25

- Plenary Session
- ESP: Hot-Side Precipitator
- FF: Advanced Concepts I
- Scrubbers
- ESP: Performance Enhancement I
- FF: Advanced Concepts II
- Opacity/Measurements

Wednesday, February 26

- ESP: Performance Enhancement II
- FF: Practical Considerations
- Advanced Energy Applications I
- ESP: Performance Estimating (Modeling)
- FF: Pilot-Scale Studies
- Advanced Energy Applications II

Thursday, February 27

- ESP: Advanced Technology
- Operation and Maintenance

ACKNOWLEDGEMENT

The assistance of Holly Rossi, Radian Corporation, in compiling these Proceedings is gratefully acknowledged.

TABLE OF CONTENTS

VOLUME 1, PLENARY, SCRUBBERS, OPACITY/MEASUREMENTS, ADVANCED ENERGY APPLICATIONS I, ADVANCED ENERGY APPLICATIONS II, INTEGRATED CONTROL PROCESSES I, AND INTEGRATED CONTROL PROCESSES II

VOLUME 2, ELECTROSTATIC PRECIPITATOR TECHNOLOGY: HOT-SIDE PRECIPITATOR STUDIES, PERFORMANCE ENHANCEMENT I, PERFORMANCE ENHANCEMENT II, PERFORMANCE ESTIMATING (MODELING), ADVANCED TECHNOLOGY, FUNDAMENTALS I, CONTROLS AND ENERGY CONSUMPTION, FUNDAMENTALS II, AND DESIGN CONSIDERATIONS,

VOLUME 3, FF: ADVANCED CONCEPTS I, FF: ADVANCED CONCEPTS II, FF: PRACTICAL CONSIDERATIONS, FF: PILOT SCALE STUDIES, OPERATION AND MAINTENANCE, FUGITIVE EMISSIONS

VOLUME 1

PLENARY, SCRUBBERS, OPACITY/MEASUREMENTS, ADVANCED ENERGY APPLICATIONS I, ADVANCED ENERGY APPLICATIONS II, INTEGRATED CONTROL PROCESSES I, AND INTEGRATED CONTROL PROCESSES II

Section Page

PLENARY SESSION
Ralph F. Altman, Chairman

Keynote Address: Particulate Matter Control - The Rapidly Advancing Technology P-1
Grady B. Nichols*

Session C-1: SCRUBBERS
Dale L. Harmon, Chairman

Development of Improved Single Drop Collection Efficiency Correlations for Microcomputer Modeling of Venturi Scrubber Performance 1-1
K. Ellwood, A. W. Gnyp, C. C. St. Pierre, and S. Viswanathan*

Fume Filtration Through a Dynamic Liquid Spray Curtain 2-1
H. H. Elliott*, H. L. Marschall, and D. G. Jones

Session C-2: OPACITY/MEASUREMENTS
Phil A. Lawless, Chairman

Options to Alleviate Plume Opacity Problems Caused by Condensation Aerosols 3-1
A. S. Damle*, D. S. Ensor, and L. E. Sparks

Relationship of Opacity to the Loss Mechanisms in ESP's 4-1
D. S. Ensor, P. A. Lawless*, and L. E. Sparks

*Denotes speaker.

Section

Page

Stack Opacity Model 5-1
D. J. Mormile, G. C. Stegmann, and B. F. Piper*

The Collection of Fine Particulate in Power Plant Electrostatic Precipitators 6-1
L. T. McEvoy, K. R. Parker, and A. Russell-Jones*

Predicting the Particle Size Distribution of Fly Ash 7-1
R. S. Dahlin*, J. P. Gooch, and L. Y. Sadler, III

Quality Assurance Considerations for Particle Sizing Measurements 8-1
G. L. Johnson* and C. E. Tatsch

Session C-3: ADVANCED ENERGY APPLICATIONS I
John S. Maulbetsch, Chairman

Technical and Economic Evaluation of High Temperature and High Pressure Particulate Cleanup Systems 9-1
R. Zaharchuk* and L. N. Rubow

Particulate Control at High Temperature and Pressure for Emerging Electric Power Generation Technologies 10-1
R. C. Bedick and R. J. Dellefield*

The Testing and Evaluation of Ceramic Filter Fabrics 11-1
R. Chang*, J. Sawyer, H. Lips, R. C. Bedick, and R. J. Dellefield

Hot Gas Clean-Up by Means of Porous Ceramic Filter Elements 12-1
P. Eggerstedt* and J. F. Zievers

Test and Development of Woven Ceramic Bag and Porous Ceramic Candle Filters for HTHP Application .... **
T. E. Lippert*, D. F. Ciliberti, O. J. Tassicker, and S. G. Drenker

Session C-4: ADVANCED ENERGY APPLICATIONS II
George A. Rinard, Chairman

Results of Parametric Tests on an Electrostatic Precipitator Operating at High Temperature and High Pressure Conditions 13-1
G. A. Rinard, D. E. Rugg*, M. Durham, and J. Armstrong

Design of Baghouse and Electrostatic Precipitator for the Coal-Fired Flow Facility 14-1
J. P. Foote*

---

*Denotes speaker.

**This paper was presented, but a manuscript was not submitted.

Section Page

Granular Bed Filter Component Design for High Temperature and High Pressure 15-1
K. B. Wilson*

The Interaction of a Gas with Solid and Liquid Particles in a Rotating System 16-1
H. Heshmat* and O. Pinkus

The Development and Testing of a Compact Cross Flow Filter for High Temperature Applications in Advanced Energy Systems .. **
D. F. Ciliberti and T. E. Lippert

Session C-5: INTEGRATED CONTROL PROCESSES I
J. Edward Cichanowicz, Chairman

Particulate Control Integration with Wet Scrubber SO_2 Removal and Waste Generation 17-1
P. M. Maroney*, S. A. Davidson, S. M. Katzberger, and J. E. Cichanowicz

Kinetics of Reaction Between Hydrated Lime and Sulfur Dioxide 18-1
A. S. Damle*, K. Ramanathan, and D. L. Harmon

Mini Spray Dryers for Low-Cost SO_2 Control 19-1
C. B. Sedman and L. E. Sparks*

Electrostatic Precipitator Performance Characterization in Spray Dryer Flue Gas Desulfurization Systems 20-1
G. E. Bresowar*, R. F. Robards, and R. A. Runyan

Fabric Filter Operating Experience on a Dry FGD System at Austell Box Board Corporation 21-1
W. H. Bradley*

Session C-6: INTEGRATED CONTROL PROCESSES II
G. E. Bresowar, Chairman

Results of Pilot-Scale Tests of E-SO_x 22-1
L. E. Sparks*, G. H. Ramsey, R. E. Valentine, and N. Plaks

Researches for Optimal Integrated Flue Gas Treatment 23-1
G. Dinelli and M. Rea*

Utility Case History on Firing Enhanced Emulsified Fuel Oil to Reduce Particulate and NO_x Emissions 24-1
E. S. Behrens*

---

*Denotes speaker.

**This paper was presented, but a manuscript was not submitted.

Section Page

Particulate Control Devices for Municipal Refuse-to-Energy Plants 25-1
M. Kapner*

Integrated Control Device for Micronic and Submicronic Particulate and Acidic Gas Control 26-1
T. K. Ewan* and O. L. Holland

Appendix:Attendees A-1

VOLUME 2

ELECTROSTATIC PRECIPITATOR TECHNOLOGY:
HOT-SIDE PRECIPITATOR STUDIES, PERFORMANCE ENHANCEMENT I, PERFORMANCE ENHANCEMENT II, PERFORMANCE ESTIMATING (MODELING), ADVANCED TECHNOLOGY, FUNDAMENTALS I, CONTROLS AND ENERGY CONSUMPTION, FUNDAMENTALS II, AND DESIGN CONSIDERATIONS,

Session A-1: HOT-SIDE PRECIPITATOR STUDIES
Wallis A. Harrison, Chairman

Hot Precipitators and Duct Design Considerations 1-1
J. A. Werhane*, W. G. Doran, and O. Zaben

Considerations for the Cyclic Operation of Hot-Side Electrostatic Precipitators 2-1
F. C. Southworth*, R. K. Miller, and C. A. Altin

Structural Investigation of Large Hot-Side Electrostatic Precipitators .... **
C. A. Altin*

Session A-2: PERFORMANCE ENHANCEMENT I
B. G. McKinney, Chairman

A Comparison of Electrostatic Precipitator Performance Enhancement Technologies 3-1
J. Dalmon, G. L. Dalton*, and R. S. Hansen

Baltimore Gas and Electric Experience with Combined SO_3/NH_3 Injection for Precipitator Performance Improvement 4-1
W. E. Cummings, Jr.* and W. H. Reamy

A Design Methodology for Optimized Water Conditioning of High Resistivity Fly Ash 5-1
N. W. Frisch* and W. T. Hartshorn

A New Chemical Conditioner Together with Good Operations and Maintenance Program Management Helps Meet Emissions Objectives 6-1
R. K. Sinha*

*Denotes speaker.

**This paper was presented, but a manuscript was not submitted.

Section Page

Session A-3: PERFORMANCE ENHANCEMENT II
Ralph F. Altman, Chairman

Evaluation of Broad and Narrow Pulse Energization of a Cold-Side Electrostatic Precipitator 7-1
H. R. Osmers* and D. J. Sugumele

Full Scale Demonstration Results of Electrostatic Precipitator Pulse Energization 8-1
T. W. Lugar* and J. M. Friday

Field Evaluation of Pulse Energization under Different Operating Conditions 9-1
S. Masuda* and S. Hosokawa

Long-Term Experience with Pulsed Energization of ESP's at a Danish Power Station 10-1
K. Porle*, R. Karlsson, and B. Kirkegaard

Session A-4: PERFORMANCE ESTIMATING (MODELING)
Ronald B. Mosley, Chairman

An Improved Model for Predicting Fly Ash Resistivity 11-1
R. E. Bickelhaupt* and L. E. Sparks

A Selected Review of Critical Parameters and Formulae for Design and Performance Evaluation of Electrostatic Precipitators 12-1
H. J. Hall*

Predicting Cold-Side Precipitator Performance Based Upon Coal and Ash Chemistry 13-1
F. A. Horney and V. H. Belba*

Evolution of an Interactive Model for Predicting Voltage-Current Curves in ESP's with Novel Electrodes .... **
P. A. Lawless* and L. E. Sparks

Approximate Method to Calculate Characteristics of Contaminated-Wire and Strip-Discharge Electrodes 14-1
K. J. McLean*, L. E. Sparks, and G. H. Ramsey

Session A-5: ADVANCED TECHNOLOGY
Leslie E. Sparks, Chairman

Pilot Plant Evaluation of the Cooled-Electrode Precharger as an ESP Retrofit Device .... **
M. Durham*, G. A. Rinard, and D. E. Rugg

*Denotes speaker.

**This paper was presented, but a manuscript was not submitted.

Section Page

Pilot-Scale Evaluation of ESP Wide Plate Spacing 15-1
R. F. Altman*, E. C. Landham, Jr., J. L. DuBard, and H. L. Wheeler

Pilot-Scale Evaluation of ESP Intermittent Energization 16-1
E. C. Landham, Jr.*, J. L. DuBard, W. E. Piulle, and L. F. Rettenmaier

Operating Results of Moving Electrode Type Electrostatic Precipitators for Coal-Fired Boilers 17-1
H. Asano*, H. Yabuta, and M. Ohtsuka

Pilot-Scale Evaluation of Multi-Stage Electrostatic Precipitator .... **
L. E. Sparks*, G. M. Ramsey, and N. Plaks

Session A-6: FUNDAMENTALS I
Sidney A. Self, Chairman

Medium-Sulfur Coal and Fly Ash Resistivity 18-1
W. A. Harrison*, J. K. Nicholson, J. L. DuBard, and L. E. Sparks

The Effect of High Mass Loading on Fly Ash Precipitators 19-1
M. G. Faulkner*, J. L. DuBard, and L. E. Sparks

The Effective Dielectric Constant of Fly Ash 20-1
R. P. Young*, J. L. DuBard, and L. E. Sparks

Diagnostic Technology of Precipitator Operation 21-1
S. Masuda*, T. Itagaki, and S. Hosokawa

Session B-6: CONTROLS AND ENERGY CONSUMPTION
James L. DuBard, Chairman

Electrostatic Precipitator Power Measurements 22-1
P. Gelfand*, E. C. Landham, Jr., and L. F. Rettenmaier

ESP Energy Management and Optimization of Collection Efficiency 23-1
B. Borowy*, M. McLauchlin, and W. F. Frazier

The Evaluation of Tests and the Economic Implications of Power Reduction on Electrostatic Precipitators 24-1
D. L. Lueckenotte* and V. L. Kunzweiler

First Utility Application of a New Microprocessor-Based Distributed Control System for Electrostatic Precipitators 25-1
G. R. Gawreluk*, M. Barav, and S. R. Coco

---

*Denotes speaker.

**This paper was presented, but a manuscript was not submitted.

Section Page

Power Consumption of Opacity Feedback Controlled Electrostatic Precipitator Transformer-Rectifiers 26-1
J. J. Roosma* and J. B. Howard

Interactive Electrostatic Precipitator Controls .... **
C. A. Altin*, R. E. Comer, P. T. Nielsen, and R. J. Burgess

Session A-7: FUNDAMENTALS II
Owen Tassiker, Chairman

Electric Field Measurements in an Operating Precipitator 27-1
J. L. DuBard*, E. C. Landham, Jr., and R. F. Altman

Finite-Diffusivity Effects in Single-Stage Precipitators - Theory and Experiment 28-1
S. A. Self*, M. Mitchner, D. H. Choi, K. D. Kihm, and R. Leach

Three-Dimensional Calculations of Negative Tuft Corona 29-1
M. K. Owen*, T. Yamamoto, P. A. Lawless, and L. E. Sparks

The Simulation of Corona Discharges under Practical Precipitator Conditions 30-1
I. Gallimberti*

Some Electrical Characteristics of Back Corona 31-1
K. J. McLean*, L. E. Sparks, and G. H. Ramsey

Session B-7: DESIGN CONSIDERATIONS
Sidney R. Orem, Chairman

Laboratory Measurements of Some Electrical Parameters in Conventional and Wide Duct Precipitators 32-1
A. A. Elmoursi and G. S. P. Castle*

Influence of Gas Distribution on Precipitator Performance 33-1
L. Lind*

Development and Testing of a Collecting Curtain for an Electrostatic Precipitator 34-1
H. L. Engelbrecht* and R. J. McMullan

Characterization of Discharge Electrode Performance: Results of Laboratory and Pilot Plant Experiments 35-1
L. A. Hawkins* and H. L. Wheeler

*Denotes speaker.

**This paper was presented, but a manuscript was not submitted.

Section Page

VOLUME 3

FF: ADVANCED CONCEPTS I, FF: ADVANCED CONCEPTS II, FF: PRACTICAL CONSIDERATIONS, FF: PILOT SCALE STUDIES, OPERATION AND MAINTENANCE, FUGITIVE EMISSIONS

Session B-1: FF: ADVANCED CONCEPTS I
Louis S. Hovis, Chairman

Distribution of Fly Ash in a Filter Bag Operating with a Charged Axial Electrode 1-1
G. E. R. Lamb* and K. T. Duffy

Study of Electrostatically Stimulated Filtration Fundamentals 2-1
D. W. VanOsdell, A. S. Viner*, K. D. Carter, and L. S. Hovis

Session B-2: FF: ADVANCED CONCEPTS II
Norman Plaks, Chairman

Mathematical Model for Advanced Electrically Stimulated Fabric Filtration 3-1
T. Yamamoto*, D. S. Ensor, R. B. Mosley, L. S. Hovis, and N. Plaks

Advanced ESFF Laboratory Test Results 4-1
R. B. Mosley*, L. S. Hovis, and B. E. Daniel

Advanced ESFF Applied to a Stoker Coal-Fired Boiler 5-1
G. P. Greiner*, A. S. Viner, L. S. Hovis, and R. Gibbs

Advanced Electrostatic Fabric Filtration Experience at Southwestern Public Service Company 6-1
R. Serrurier*

Economics of Advanced Electrostatic Stimulation of Fabric Filtration 7-1
L. S. Hovis* and A. S. Viner

Session B-3: FF: PRACTICAL CONSIDERATIONS
John D. McKenna, Chairman

Evaluation of Acid-Resistant Synthetic Needled Felt Filter Media in Coal-Fired Boiler Pulse-Jet Baghouses 8-1
W. T. Grubb*

Laboratory Studies of the Filtration Performance of Various Filter Media under Simulated Field Conditions 9-1
P. E. Frankenburg*

---

* Denotes speaker.

** This paper was presented, but a manuscript was not submitted.

Section Page

Evaluation of a Specific Type of Filter Bag Supplied by Various Vendors 10-1
Y. J. Chen*, P. N. Roberts, and T. D. Tarnok

Catenary Analysis of a Fabric Filter Bag During Reverse-Gas Cleaning 11-1
E. A. Samuel* and J. G. Musgrove

Aerosol Deposition in Fabric Filters 12-1
D. S. Ensor*, T. Yamamoto, and A. S. Viner

Session B-4: FF: PILOT SCALE STUDIES
John Maulbetsch, Chairman

Performance of a High-Sulfur-Coal, Pilot-Scale Fabric Filter 13-1
R. F. Heaphy*, R. P. Wilson, and W. E. Piulle

Flue Gas Conditioning for Improved Baghouse Performance 14-1
D. L. Laudal* and S. J. Miller

Session B-5: OPERATION AND MAINTENANCE
Robert P. Gehri, Chairman

Operation and Maintenance Experience at Harrington Station 15-1
W. Hooks, O. Plunk*, and D. L. Harmon

Computer Monitoring of Pilot Plant Baghouse Performance 16-1
A. S. Viner*, L. M. Fickel, and L. S. Hovis

The Design of Repairs to Upgrade 10-Year-Old Industrial Precipitators 17-1
V. L. Kunzweiler* and J. B. Landwehr

Performance Improvement History of Inadequately Performing Precipitators 18-1
J. G. Musgrove*, W. R. Lane, and M. W. Wei

Performance Improvement and Fire Prevention in Fly Ash Collection System at a 50MW Wood-Fired Power Plant 19-1
E. Gal* and M. Murphy

Session C-7: FUGITIVE EMISSIONS
Dale L. Harmon, Chairman

Identification, Assessment, and Control of Fugitive Particulate Emissions 20-1
C. Cowherd, Jr.*, J. S. Kinsey, and D. L. Harmon

*Denotes speaker.

**This paper was presented, but a manuscript was not submitted.

Section Page

Process Fugitive Particulates - Design Methods for Enclosures 21-1
H. D. Goodfellow*, T. Cesta, E. R. Kashdan, D. W. Coy, and J. J. Spivey

Field Evaluation of Windscreens as a Fugitive Dust Control Measure for Materials Storage Piles 22-1
R. A. Zimmer*, K. Axetell, Jr., and T. C. Ponder, Jr.

Measurement of Fugitive Emissions in a Coal-Fired Power Plant 23-1
G. E. Muleski*, F. J. Pendleton, and W. A. Rugenstein

---

*Denotes speaker.

**This paper was presented, but a manuscript was not submitted.

Session A-1: HOT-SIDE PRECIPITATOR STUDIES

Wallis A. Harrison, Chairman
Southern Company Services
Birmingham, AL

HOT PRECIPITATORS AND DUCT DESIGN CONSIDERATIONS

by: J. A. Werhane
W. G. Doran
O. Zaben
Sargent & Lundy
Chicago, Illinois 60603

ABSTRACT

Many utilities have experienced operating and structural problems with hot precipitators installed on units firing western coals. This paper will discuss the remedies available and their effectiveness. Emphasis will be placed on design considerations and the costs associated with the more effective remedies. Remedies discussed will include repairs and modifications to the existing precipitator/ductwork, conversion of the existing collection equipment from hot to cold side operation, and abandonment of existing equipment in favor of new precipitators or baghouses.

INTRODUCTION

During the late 1960s and early 1970s, state-of-the-art technical information and overall economics supported the selection of hot-side precipitators as the proper particulate control strategy for plants designed to fire low-sulfur coals. Several utilities that selected this seemingly logical option are now experiencing unanticipated operational and structural problems with the precipitators. Surveys conducted by the utility industry along with Sargent & Lundy's (S&L) direct experience indicate that hot-side operating problems can be attributed to one or more of the following: (1) coal and ash properties, (2) inadequate mechanical cleaning and control methods, and (3) unanticipated structural loads. The same surveys indicate that conservatively sized cold-side precipitators are operating with fewer problems on units firing similar fuels. The problems that occur in cold-side systems are usually not as frequent or severe because of their lower operating temperatures.

HISTORICAL PERSPECTIVE AND DESIGN CONSIDERATIONS

The enactment of federal regulations in the early 1970s that required new coal-fired power plants to control particulate and sulfur dioxide emissions spurred the interest in and development of hot-side precipitators. The New Source Performance Standards (NSPS) were enacted on December 23, 1971, and apply to units started after August 17, 1971. The NSPS established particulate emission levels of 0.1 $lb/10^6$ Btu, sulfur dioxide emission levels of 1.2 $lb/10^6$ Btu, and a maximum opacity level of 20%. To meet these stringent levels of control, utilities had to choose between the following fuel-related emission control strategies: (1) burn a high-sulfur fuel and install a precipitator to control particulate emissions and a flue gas desulfurization (FGD) system to control SO_2 emissions, or (2) burn a low-sulfur western fuel that met the SO_2 emission limitations without FGD and install precipitators to control particulate emissions.

Baghouse technology for large central stations was in its infancy in the early 1970s. As a result, baghouses were considered an acceptable particulate control strategy for only a few large central stations.

Many utilities chose the low-sulfur coal emission control strategy because a ready supply of low-cost, low-sulfur compliance fuels was available from western states and because FGD systems were complicated, costly, and not fully developed. The low-sulfur coal strategy was also attractive because it minimized the cost of new generating capacity; it required no initial investment in an FGD system and no maintenance costs for FGD reactants and waste disposal. The decision to use hot-side precipitators followed from the decision to use low-sulfur coal to meet the NSPS. Hot precipitator technology developed as a result of the problems anticipated in cold-side collection of high-resistivity ash from low-sulfur western fuels. The following tended to favor hot-side equipment: (1) From a performance standpoint, hot-side precipitators are highly reliable and can be designed with a much higher degree of certainty. (2) Hot-side units are less expensive than cold-side on low-sulfur coals. (3) Hot precipitators perform more reliably than cold units operating in high resistivity situations.

There were other advantages that tended to support the selection of a hot precipitator. At temperatures above 600°F, the precipitator was well above the acid and water dew point, and thus less corrosion was expected. With moisture not being as much of a concern, ash hopper pluggage was believed to be reduced, along with easier hopper emptying and easier dust transport. Hot-side operation also afforded better electrical stability and higher corona current densities than in cold-side operations. Cold-side precipitators represented a higher initial investment cost because of the additional collection area required. Therefore, at that time the industry believed hot-side precipitators had an economic and operational advantage over cold-side precipitators for collecting highly resistive ash.

Cold-Side Precipitators

At flue gas temperatures typically experienced on the cold side (250° to 350°F), the primary determinant of collected fly ash resistivity is the ash particle's surface conductivity. Sulfur trioxide and moisture in the flue gas form a conductive film on the particles. With high-sulfur coals, the resistivity is less than 10^{10} ohm-cm and the fly ash is easily precipitated. With decreasing sulfur content, the resistivity increases well above the critical 10^{10}-ohm-cm value as shown on Figure 1. With the low-sulfur highly resistive fly ashes, the migration of ash particles to the collector plates is reduced, and a larger precipitator SCA is needed to overcome the reduced migration velocity. SCAs in the range of 600 to 800 ft^2/1000 acfm are common for cold-side high-efficiency precipitators that successfully collect fly ash from boilers firing a low-sulfur fuel.

Hot-Side Precipitators

The theoretical effect of temperature on resistivity can be seen in Figure 1 for a high-resistivity low-sulfur coal ash. For hot-side temperatures (greater than 630°F) the resistivity is well below the critical value. As temperatures increase, the surface conductive constituents (water and sulfur trioxide) are vaporized and bulk or volume conductivity (through the bulk of the ash) increases. The figure also illustrates that resistivity is relatively insensitive to temperature fluctuations on the hot side. Conversely, on the cold side, a 50°F temperature fluctuation can affect resistivity by an order of magnitude. Theoretically equivalent collection efficiency can be obtained with a 200- to 400-SCA on the hot side or a 600- to 800-SCA cold-side precipitator for a high-resistivity low-sulfur coal ash.

In the early 1970s, only a small amount of data was available for all sizing decisions regarding hot-side precipitators. As shown in Figure 2, only 30 units were in the data base before 1972. Of these, all but three were firing eastern low-sulfur coals. Resistivity and performance data based on eastern coals were also used to size precipitators on units firing western coals. In the few years that followed, 70 new hot precipitators were authorized, with about 50% for units firing Powder River Basin coals. The resistivity approach proved adequate for units firing eastern low-sulfur coals and most of the coals from Colorado, Utah, and New Mexico. However, the ash properties of coals from the Powder River basin were significantly different even though the ash resistivities were similar. As more operating experience was collected and analyzed, certain ash properties correlated directly with these collection difficulties. Comparisons were inevitably made to the more successful hot precipitator installations to determine which characteristics led to good performance. One of the results of these comparisons was a guideline of coal characteristics that should result in good hot precipitator performance:

- Coal moisture should be between 5% and 15%.
- The sum of CaO and MgO should be less than 20%.
- The ratio SiO_2 to CaO should be between 3 and 12.
- The amount of Na_2O should be between 1% and 3%.
- The ratio of total base to Na_2O should be less than 12.

Comparing these performance characteristics to regional coal analyses (see Table 1) suggests why Powder River Basin coals may be difficult to collect. As shown, the Powder River Basin coals exhibit none or only one of the desirable characteristics.

Tenacious ash, commonly called sticky ash because of its behavior on precipitator components, is the most common complaint with Powder River basin coals. High sodium, magnesium, calcium, and sulfate content have been identified as the chemical parameters leading to stickiness. Moisture may also be involved causing the buildup, since hot precipitators with good operational characteristics have had lower coal moisture content. This sticky ash is typically removed by mechanical systems installed on the precipitator.

One theory proposed to account for precipitator performance deterioration caused by dust buildup is the sodium depletion or sodium migration theory. As fly ash builds up on the plates and wires in a precipitator, the electrical field strength causes sodium ions to migrate outward through the ash layer on the plates resulting in sodium depletion in the inner ash layers. The inner layer becomes very resistive, degrading precipitator performance. Figure 3 illustrates the sodium depletion phenomena. The opposite effect takes place on the precipitator wire; i.e., sodium ions migrate to the wire surface and suppress the corona generation. All that is needed to start the process is a layer of ash buildup that is not rapped off the electrode surfaces. Low ash density, low ash cohesion, high electrical attraction, and chemical or physical adhesion (to precipitator surfaces) will compound the problem.

In addition to problems with sticky ash, some hot-side precipitator systems experience structural problems. The structural problems most frequently observed are: (1) buckling of internal and external beams, struts,

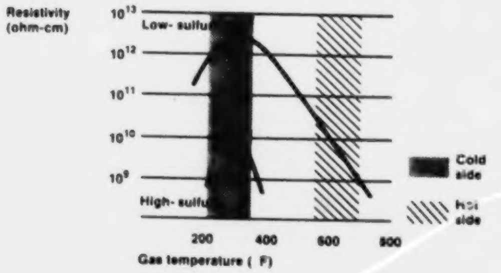

Figure 1. Fly ash resistivity relationships to gas temperatures and sulfur content.

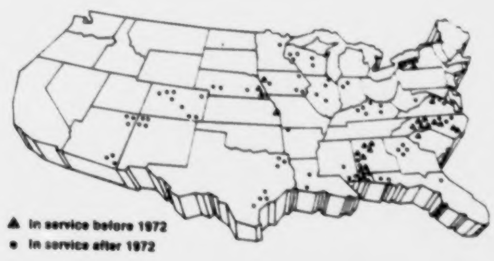

Figure 2. Hot precipitators in service (100 MW and larger).

and diagonals; (2) failures of internal and external connections; (3) buckling, cracking, and tearing of the precipitator and ductwork skin plate; (4) uplift of the supports; (5) failures of the anchor and guide details; and (6) deterioration of the slide bearing plates.

Designers now recognize that actual thermal gradients in hot precipitators may be on the order of 300° to 350°F or even higher. Thermal gradients of this magnitude can cause a structure to self-destruct if it is not flexible enough to accommodate the differential growth patterns produced. In fact, these thermal gradients are primarily responsible for the member buckling and connection failures at hot-side installations. Structural deficiencies like these can jeopardize the stability of the system and produce unpredictable thermal movements. Unpredictable movements, in turn, can damage the expansion joints and cause eccentricities much larger than those assumed in the design. The deficiencies can also affect the performance of the precipitator by causing or aggravating collector plate misalignment, the shorting out of electrical fields, and air inleakage.

REMEDIES

A large number of potential remedies are available to a utility faced with hot-side precipitator performance, structural, or operating problems. These remedies can generally be classified as major cost expenditures that eliminate the root cause of the problem or as low-cost steps that may solve a part of the problem or alleviate a symptom. To date, most utilities have opted for low-cost solutions to cure all or as many of the problems as possible. This strategy has had only limited success. Other utilities have made or are making major cost modifications to resolve the root cause of their operating problems. The completed projects have been successful.

An important step in solving precipitator problems is the laboratory flow testing of scale models of precipitators, baghouses, and the connecting ductwork, both for evaluating new and retrofit designs and for solving

TABLE 1. REGIONAL COMPARISON OF LOW-SULFUR COAL ASH

Coal Source	Moisture (%)	CaO+ MgO (%)	SiO_2/ CaO	Na_2O (%)	Base/ Na_2O
Powder River "Decker"	24.5	34.8	1.3	$\boxed{1.6}$	22.0
Powder River "Jacobs Ranch"	28.9	28.5	1.2	$\boxed{1.5}$	19.0
Powder River "Spring Creek"	24.5	22.6	1.4	8.4	$\boxed{2.7}$
Performance Guideline	5-15	≤<20	3-12	1-3	<12
Kentucky	$\boxed{6.1}$	$\boxed{3.0}$	25.0	0.8	$\boxed{3.0}$
Colorado	$\boxed{14.3}$	$\boxed{11.0}$	$\boxed{4.6}$	$\boxed{3.0}$	$\boxed{3.6}$
New Mexico(1)	$\boxed{14.5}$	$\boxed{6.0}$	$\boxed{11.6}$	$\boxed{1.8}$	$\boxed{3.4}$
New Mexico(2)	17.80	$\boxed{5.0}$	13.8	$\boxed{1.4}$	$\boxed{8.0}$
Utah	$\boxed{6.4}$	$\boxed{8.5}$	$\boxed{6.0}$	4.5	$\boxed{2.0}$

☐ Characteristics that meet guideline

▨ Characteristics that exceed guideline

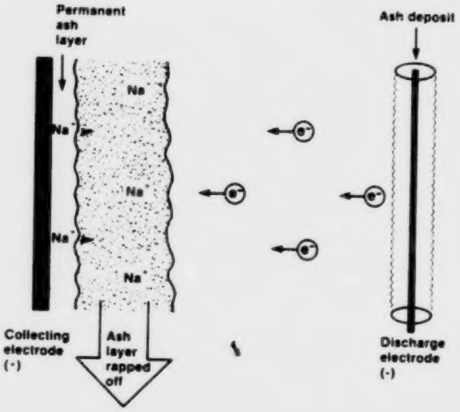

Figure 3. Representation of sodium depletion phenomenon.

problems with existing installations. Proposed modifications to improve distribution can be economically modeled and tested before being implemented.

Most of the structural problems experienced at hot-side precipitator installations can be attributed to three major causes: (1) a layout that does not properly consider the interaction of the components under thermal loads, (2) thermal effects that differ markedly from those considered in the design, and (3) the selection of materials without proper consideration of their behavior at high temperatures. To a lesser extent, the problems can also be aggravated by errors in construction and poor thermal insulation.

New and existing precipitator systems can be designed and modified to minimize structural problems by thoroughly considering structural behavior at elevated temperatures and the effects of thermal gradients. The engineering process needs to account for these effects in conjunction with normal loads, that is, those loads imposed on any large outdoor structure. The discussion of structural considerations in this paper is limited to thermal effects and physical arrangement considerations in hot precipitator design. Furthermore, the discussion focuses on providing a new design, and as such concentrates on root-cause solutions to hot precipitator problems, but the same principles could be advantageously applied to the backfit of a problem installation.

LOW-COST CORRECTIVE ALTERNATIVES

This section evaluates twelve low-cost means of improving precipitator performance. Some involve the upgrading of existing equipment, while others require the installation of new equipment. Their effectiveness varies depending on coal and precipitator characteristics.

Rapping System

The ability to remove collected or accumulated ash from the electrode surfaces relies primarily on brute force methods. The most common of these are rapping systems. The effectiveness of the rapping system depends on the rappers, the rapper controls, and the ability of the plate and electrode suspension systems to transmit the rapping forces. When effectively transmitted, a shear force is developed between the ash and its bond to the surface rapped, and the ash is dislodged. For new units, rigid-frame precipitator designs are considered more effective transmitters of rapping forces to the plates and electrodes. Weighted-wire designs, the type used extensively in the early 1970s, are the least effective in transmitting the rapping forces to wires. For existing precipitators with plate and wire buildup, upgrading the rapping system should be considered if the rapping system is ineffective. This may help improve performance provided the ash is not extremely tenacious.

Rapper Controls

The control of upgraded rappers is important to minimize reentrainment. A digital microprocessor-based control system is required to optimize rapping effectiveness for expected variations in fuel and ash characteristics. The digital control system would allow operation with reduced frequency rapping.

Automatic Voltage Controls

In theory, a digital automatic voltage control (AVC) system maintains usable precipitator power at the highest level possible for the specific, existing gas-side conditions within the precipitator. In the digital system, microprocessors are used to sense the onset of sparking and take corrective action before a spark occurs. Realistically, while sparking cannot be completely eliminated, it can be reduced significantly by monitoring conditions on the primary and secondary side of the transformer rectifier (TR) set, recalling the voltage and current characteristics that existed at the last sparking incident, and taking corrective action as these reoccur. Microprocessors provide the speed and memory necessary for this control.

Precharging

Precharging, sometimes referred to as high intensity ionization or two-stage precipitation, is used to charge fly ash particles before they enter the precipitator. The precharger, or first stage, is located in the flue gas ductwork upstream of the precipitator and creates a highly charged field through which the fly ash particles travel. Precharging has been tried on numerous units on a trial basis. Test results indicate a decrease in emissions in some cases, but many problems still exist. Developmental work is still continuing, and the technology is not considered commercially available.

Reverse Polarity

Reverse polarity or positive corona operation has been considered a means of combating the sodium depletion discussed earlier in this paper. The polarity of the transformer rectifier sets is periodically reversed so that the corona generated is positive and the electric field force within the precipitator is reversed. Theoretically, this reversal should cause the sodium ions, which have migrated to the outer ash layers on the plates, to migrate back to the inner layer and restore the ash resistivity to acceptable levels. Unfortunately, reverse polarity or positive corona operation appears to be technically unsound.

Plate Doping

Plate doping, like reverse polarity, is another potential remedy for combating sodium depletion. The plates are coated with a sodium-based material that when influenced by the electric field "donates" sodium ions to the ash buildup layer to replace those migrating away from the plate surface. In theory, the additional sodium ions preclude the development of the highly resistive inner layer of ash, which is the root of the problem in the sodium depletion theory. Presumably, the plates have to be coated, or doped, at specific time intervals to avoid their sodium ions being entirely depleted. Thus, plate doping appears to be only a temporary remedy.

Ammonia Conditioning

Ammonia conditioning has been used primarily with cold-side precipitators to alter the electrical properties of the flue gas through a space-charge effect and to increase the cohesiveness of the fly ash particles, thereby lowering reentrainment losses. It can be used on hot-side applications to increase or improve the space-charge effect, thereby suppressing back corona and substantially increasing the precipitator operating voltage. The resulting higher field strength enhances particle charging and improves collection efficiency. Ammonia conditioning has not been shown to alter the resistivity of the fly ash but has been reported to reduce or inhibit the formation of calcium sulfate in the fly ash.

Sodium Conditioning

Flue gas conditioning modifies coal ash characteristics in an attempt to alleviate a specific fireside problem. To improve precipitator performance, conditioning is used primarily, but not always, to modify the electrical characteristics of the fly ash or flue gas, thereby facilitating the charging and collection of the ash particles. For hot-side precipitator applications, the bulk or volume electrical properties of the fly ash affect the fly ash resistivity. The most common flue gas additives for modifying volume properties are sodium-based materials, which can be injected "wet" or "dry."

Because sodium can reduce the ash fusion temperature of the coal ash and result in upper furnace slagging and convective pass fouling, only a limited amount can be added to the coal feed. Generally, sodium levels below 3% (Na_2O in ash) should not cause boiler fouling problems. To prevent sodium-caused boiler fouling altogether, the sodium can be injected downstream of the economizer in wet or dry form. Downstream injection can be used either alone or in conjunction with sodium addition to the coal feed. Injecting sodium downstream of the economizer, however, can result in additive buildup in the ducts if not properly injected or in low-temperature fouling deposits if the flue gas temperature is too low. Adding sodium in dry form downstream of the economizer, or "coprecipitation," is ineffective if the additive is not completely mixed with the fly ash in the flue gas stream. Based on the foregoing discussion, sodium conditioning by itself is not considered to be a practical solution for precipitator performance problems for units firing Powder River Basin coals. Although sodium conditioning does offer some improvement on units that fire coal with low-sodium ash, it does not alleviate the fly ash buildup problem. Furthermore, no improvement would be expected with sodium conditioning units firing coal with high-sodium ash.

Particle Growth Conditioning

Particle growth conditioning involves the injection of a special dry refractory material into the boiler's burner coal/air pipes. The additive "seeds" the flue gas and provides nucleation sites on which volatilized ash components can condense rather than forming submicron fume particles as they otherwise would. The only particle growth conditioning process currently on the market takes its name from its manufacturer, the Dearborn Utility Services Company. This process is offered by its manufacturer only to extend precipitator operating times between outages, not to cure the ash buildup problem.

Sonic Horns

Sonic horns produce very-low-frequency sound energy to create aerodynamic forces that loosen the ash, allowing it to fall into the precipitator hoppers. The sound waves generated have excellent rebound characteristics and, in theory, can easily penetrate the rather congested internal spaces of the precipitator and reach all surfaces within the horn's sphere influence. Because the sound power emitted follows the inverse square law, rapidly diminishing with distance, several horns would be required to effectively cover the entire precipitator. Test results have shown a slight reduction in the buildup on the wires, but the plates were unaffected. Ash buildup continued to occur even with the sonic horn in place.

Pulsed Energization

Pulsed energization is a method of coping with the adverse effects of high-resistivity fly ash by modifying the waveform of the power supplied to the precipitator. Pulsed energization involves the superposition of a high voltage pulse over the normal voltage waveform from the secondary of the TR set. The precipitator's automatic voltage control system maintains the normal secondary voltage below the sparking and back corona thresholds. The pulser unit superimposes a voltage pulse that exceeds the sparking and back corona threshold. Pulsed energization theoretically can improve precipitator performance by increasing peak voltage on the secondary of the TR sets, thereby improving particle charging; providing a more uniform corona along the entire length of the wires; increasing particle migration velocity, thereby improving efficiency; and improving the electrostatic component of the forces holding the dust to the plates.

In a study of the Buell and Research-Cottrell pulser systems at Lansing Smith 2, conducted by Southern Research Institute for the Electric Power Research Institute (EPRI), two salient points can be extracted from the many conclusions drawn: (1) there was some improvement in precipitator performance with both systems, but not enough to allow the precipitator to operate in compliance; and (2) there is no reliable method for predicting the degree of performance improvement with pulsed energization at this time. Recent tests indicate that performance improves less with pulsed energization in full-size, actual installations than it does in pilot-sized plants. There is also some uncertainty about the feasibility of applying high-speed, high-voltage pulsing technology to utility precipitator service at this time without further development work.

Coal Washing

Coal washing or beneficiation involves the physical separation of refuse material, namely pyritic sulfur and extraneous ash, from the coal. Specific gravity or density separation is the most common method used. While more sophisticated methods are under development, none are yet commercially available. For the power industry today, the major incentive for coal washing is the reduction of sulfur content in noncompliance coals to eliminate the need for FGD systems or at least reduce their operating costs. Reducing the sulfur in presently fired low-sulfur coals by washing would not be of any benefit since they are typically already compliance coals. The removal of ash by washing, however, could improve precipitator performance if the composition of the ash were modified in the right direction. However, only the extraneous ash in the raw coal is removed during washing. The little ash that low-rank western coals do have is usually inherent rather than extraneous and is not likely to be removed or modified by washing.

ROOT-CAUSE CORRECTION ALTERNATIVES

Depending on the situation, mechanical or structural modifications may be necessary to solve the root cause of a precipitator problem. This section examines over a dozen alternatives aimed at correcting the root causes of hot-side precipitator performance problems. The mechanical solutions to poor precipitator performance depend on having solved the potentially significant structural problems.

The best place to begin understanding and resolving or preventing structural problems is to look at the overall arrangement of the precipitator system and the interaction between individual components. For example, segmenting the precipitator inlet and outlet ductwork into nozzles, each independently cantilevered off the precipitator, can reduce the potential for large thermal gradients across the ductwork. An independent cantilevered support arrangement also reduces the potential for damage should large gradients occur, since the nozzles are physically separated and thus cannot transfer loads directly to each other or to the support structure. Likewise, if expansion joints are provided between the nozzles and the connecting ductwork, they isolate the precipitator from the ductwork and simplify the design of the supporting structures (Figure 4).

Stub Column Design

Precipitators are typically supported by a series of stub columns that are extensions of the internal structural columns. These stub columns rest on lubricated bearing plate assemblies designed to allow thermal movements while minimizing frictional forces. To control the thermal expansion and contraction and to resist externally applied loads such as wind without restraining expansion, two orthogonal column lines are usually chosen to be the "anchor" or "guide" lines. The stub column at the intersection of both anchor lines is known as the "anchor point" and is firmly attached to the support structure. The other stub columns on the anchor lines are provided with guides to allow movement only along the anchor lines. All thermal expansion is thus limited to be radially outward from the anchor point. Good practice dictates locating the anchor point as close to the mass center of the precipitator as practical. When it is, the frictional forces on either side of the anchor lines will cancel each other out, and a minimum of unbalanced frictional force will have to be resisted by the guide details (Figure 5).

It is also advantageous to locate stub columns only at the hopper corners. This location allows each stub column to be supported directly above a support structure column, with no stub columns supported by beams in flexure. If the precipitator is supported in this way, there is no appreciable difference in stiffness between any of the support points, which simplifies the design of the system and allows fairly accurate predictions of load transfer paths.

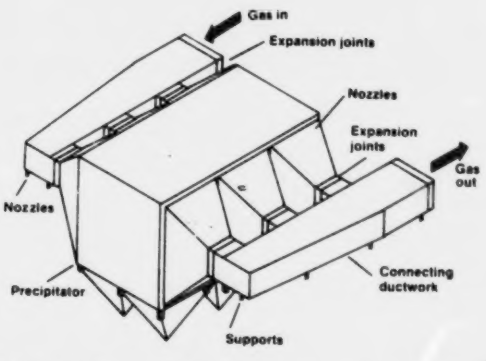

Figure 4. Precipitator arrangement.

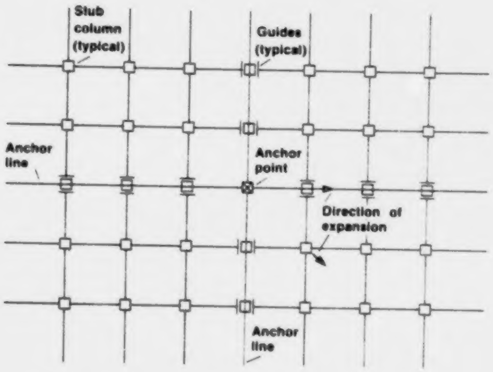

Figure 5. Plan of precipitator support system.

Spherical slide bearing assemblies have distinct advantages over flat slide bearing assemblies. Spherical assemblies (1) have two lubricated sliding surfaces to allow the stub columns to rotate as well as move laterally, and (2) eliminate edge loading of the baseplates, which can be detrimental to the lubricating material.

Another consideration is that precipitator stub columns should be long enough to provide for adequate heat transfer to the environment. The design, therefore, must take into account the space necessary to properly install insulation in the hopper crotches while not restricting air circulation around the column. The governing factor is the clearance between the hopper lagging and the support steel, which is influenced by the location of the hopper stiffeners. When the stub columns are short, they can cool only by thermal conduction through the slide bearing assemblies and into the support steel. The support steel then acts as a radiator to release the heat to the atmosphere. Cooling by convection is restricted because the stub columns are located in a stagnant air layer. Lengthening the stub columns improves the rate of cooling by exposing more of the column to air outside of the stagnant zone. This improved cooling causes a reduction in the temperature of the slide bearing assemblies and the support steel, with a corresponding reduction in the negative thermal effects.

Bracing Arrangements

Another consideration concerning the layout of the structural components of a hot-side precipitator system is to make the internal and external bracing arrangements as statically determinate as possible. Highly braced indeterminate structures exert more resistance to thermal gradients and changes in temperature. This resistance can cause self-destruction. Therefore, the vertical bracing, both internal and external, should only be used in the bays adjacent to anchor lines. Other schemes to reduce the stiffness of the structure, such as providing slotted connections at strategic locations, can sometimes be used to advantage when modifying existing systems.

Materials Selection and High-Temperature Behavior

All of the preceding suggestions for improving the physical configuration of a hot-side precipitator system are intended to reduce the effects of thermal gradients and increase the predictability of the structural behavior. Even when all of these guidelines are followed, however, it is still necessary to understand the nature and magnitude of the gradients. Proper material selection and an understanding of structural behavior at high temperatures are important when designing hot-side systems. Research has shown that structural steels behave quite differently at high temperatures than at room temperature. In addition, steels with certain critical alloying elements in the right proportions will behave much more satisfactorily than other steels. Five phenomena are significant to the structural designer: (1) yield strength variations; (2) modulus of elasticity variations; (3) coefficient of thermal expansion; (4) creep rupture; and (5) graphitization. Table 2 summarizes the conclusions that can be drawn from studies of variations of material properties with temperature. Guidelines are offered for the selection of materials under elevated temperature service conditions. These guidelines are based on Sargent & Lundy's experience and represent a balance between material costs and expected serviceability.

Addition of a Particulate Scrubber

A wet particulate scrubber removes fly ash from the flue gas mechanically. Typical scrubber design includes scrubber equipment consisting of vertical cylindrical venturi scrubber towers and vertical cylindrical mist eliminator towers located downstream of the induced-draft (ID) fans. Although the technology for wet particulate scrubbing is available, the use of a particulate scrubber has several major drawbacks. Among them are abrasion, corrosion, blowdown requirements, and loss of plume rise.

Switching Fuels

Changing fuels does offer a possible solution to a hot precipitator performance problem but might cause problems with the boiler and its auxiliaries. Also, changing fuels and canceling existing long-term coal contracts would probably result in a protracted and costly litigation. Changing fuels provides no guarantee of continued compliance with mandated air quality requirements and does not alleviate structural problems. Because of these difficulties, changing fuels is not considered a practical economic solution for many hot precipitator problems.

Additional Hot-Side Collecting Plate Area

The use of additional collecting plate area on the hot side, either by increasing the size of the existing precipitator or by adding a new hot-side unit in series with the old one, would not solve the performance problem unless the existing precipitator was made to perform properly. Since most hot-side units collecting fly ash from low-sulfur western coal are having operating problems, even those with rigid frame designs, additional hot-side collecting plate area will not completely cure the problem. Increasing the size of the existing hot-side precipitator or adding a series precipitator, however, would be no more cost effective than simply adding a new cold-side unit and could possibly be less cost effective. The ductwork requirements would be extensive, additional ash handling equipment would be required, and boiler efficiency would be reduced by the heat loss in the new equipment.

TABLE 2. PREFERRED MATERIALS BY TEMPERATURE RANGE

Item	Temperature Range	Preferred Material
Structural steel	Below 700°F	ASTM A36
	700°F-1000°F	ASTM A242*
Slide bearing plates	Below 450°F	Lubrite or American Bearing Co. bronze
	Above 450°F	Lubrite or American Bearing Co. manganese, bronze, or Meehanite
Welding electrodes	Below 700°F (with ASTM A36 steel)	AWS E70XX
	Above 700°F (with ASTM A242 steel)	AWS E80XX-B2L

*A242 with controlled chemistry as follows (values in weight percent):

C - 0.12 max
Mn - 0.20 to 0.50
P - 0.07 to 0.15
S - 0.05 max.
Si - 0.25 to 0.75
Cu - 0.25 to 0.55
Cr - 0.75 to 1.25
Ni - 0.4 max.
V - 0.02 min
Fe - balance

Cold-Side Helper Precipitator

A new cold-side "helper" precipitator could be added downstream of an existing hot precipitator so that the hot and cold units would work together in series. The dust buildup and performance degradation of the existing hot precipitator would undoubtedly continue, placing most of the work on the new cold precipitator. The cold precipitator would have to be sized for the "worst-case" performance degradation of the hot precipitator. Even in its worst-case condition, the hot precipitator would remove some of the fly ash from the flue gas stream, particularly the larger sized particles. Performance is reduced because migration velocity increases with particle diameter and decreases for finer particle sizes. To compensate for prescreening the larger particles by the hot precipitator, the design migration velocity for the new cold-side unit would have to be lower than the value used for a full-sized cold-side unit because the mass mean particle diameter is lower.

Helper Baghouse

A baghouse in either helper or sidestream configuration could be considered to help relieve hot-side precipitator problems. Such a helper baghouse would be located on the cold side, downstream of the existing precipitator. The precipitator would be energized and provide some degree of particulate collection. On the surface, it would seem that energizing the precipitator would decrease the efficiency requirements (and the size) of the helper baghouse. This is not the case, however, as the collection efficiency of the baghouse is relatively insensitive to inlet grain loading. Baghouses are designed by flow, so that the air-to-cloth ratio for a helper unit would be the same as, or possibly slightly higher than, for a baghouse if the precipitator were not present. In fact, the presence of the energized precipitator might hinder baghouse operation by prescreening larger particles, which normally help the bags collect finer ash particles. Again the loss in boiler efficiency caused by heat losses in the hot ductwork is a disadvantage.

Hot-to-Cold Conversion

The conversion of a hot-side precipitator to cold-side operation may be accomplished by rerouting the inlet and outlet ductwork to place the air heater upstream of the precipitator. An existing hot-side precipitator converted to cold-side operation would have an increased SCA by virtue of the reduction in gas volume due to the lower cold-side gas temperature. Unfortunately, this increase in SCA is typically not large enough to counteract the increased fly ash resistivity. Either added plate area or SO_3 conditioning is usually needed to achieve compliance.

Hot-to-Cold Conversion with Sulfur Trioxide Conditioning

Sulfur trioxide conditioning increases precipitator efficiency by reducing fly ash resistivity on the cold side. A flow diagram of the SO_3 gas conditioning process is shown in Figure 6. SO_3 conditioning has been used successfully to improve cold-side efficiency on western low-sulfur coals, including numerous applications with Powder River Basin coals. The Pleasant Prairie Station of Wisconsin Electric Power Company is a specific application of SO_3 conditioning on Exxon's Rawhide coal. The Pleasant Prairie precipitator is a weighted wire design with 9-inch plate spacing. The Pleasant

Prairie Station is unique in that the precipitator was originally designed for hot-side operation. A decision was made to switch to the cold side with SO_3 conditioning during construction of the unit.

The SO_3 conditioning process involves truck or rail deliveries of molten sulfur. The sulfur is stored in heated tanks to maintain its molten state. The molten sulfur is fed to a combustor where it combines with oxygen from feed air to form SO_2. The SO_2 stream from the combustor is passed through a vanadium pentoxide catalyst where it is oxidized further, and SO_3 is then injected into the ductwork at a location where it is possible to get uniform coverage of the particulates. There are several other items to consider as well. The steam used by the SO_3 conditioning system represents a decrease in the gross generator output of the unit. The catalyst used to form the SO_3 needs replacement after 8 years of continuous service. The maintenance, however, is low, possibly one man per week for one shift.

Hot-to-Cold Conversion with New Sidestream Precipitator

Hot-to-cold conversion with a new sidestream precipitator involves redirecting the gas flow such that the existing precipitator is downstream of the air heater and constructing a new auxiliary sidestream precipitator to operate in parallel with the existing precipitator boxes. Figure 7 is a process flow diagram of this alternative arrangement. The hot-to-cold conversion portion of this alternative would be essentially the same as described previously for hot-to-cold conversion.

Additional collecting plate area is required when collecting the fly ash particulate on the cold side. The total SCA needed is the same as for a new full-sized precipitator. The sidestream precipitator is added for this purpose. New ductwork is usually required from upstream of the existing ID fans to the new sidestream precipitator and from the new sidestream precipitator to the stack. The existing ID fans are used for the draft system and the converted existing precipitators. New ID fans are added to support the new sidestream precipitators.

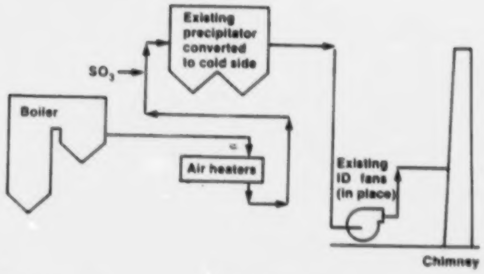
Existing precipitator converted to cold side
SO_3
Boiler
Air heaters
Existing ID fans (in place)
Chimney

Figure 6. Flow diagram of existing hot-side precipitator converted to cold side with SO_3 conditioning.

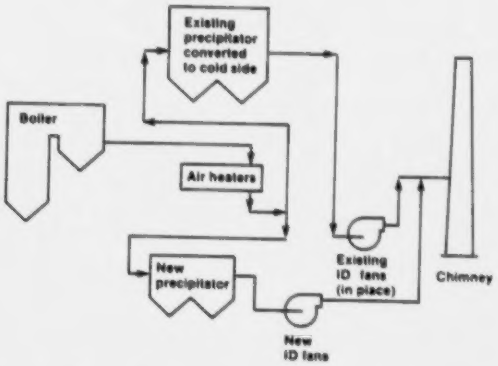
Existing precipitator converted to cold side
Boiler
Air heaters
New precipitator
Existing ID fans (in place)
Chimney
New ID fans

Figure 7. Flow diagram of existing hot-side precipitator converted to cold side with sidestream precipitator.

New Cold-Side Precipitator

For stations with hot-side ash handling problems, the addition of a new cold-side precipitator could provide compliance with particulate emission and opacity limits. This alternative (Figure 8) and the baghouse alternative have the shortest duration between authorization and initial operation. Several cold-side precipitators are currently operating successfully on the Powder River Basin coals.

The ductwork design to interconnect a new precipitator usually makes use of existing ductruns where practical. All existing ductwork that is reused is reinsulated. In this design, new ductwork is tied in just upstream of the existing ID fans. New ductwork is installed to and from the new precipitator. The ductwork from the new precipitator ties into the ductwork outside of the stack, thereby avoiding stack modifications. Ductwork modifications at the air heater to convert from hot to cold are also necessary. The existing precipitators would be abandoned or repaired as necessary to ensure stability, or they could be demolished for scrap.

Unit outages are required when changing the physical connection of the existing ductwork from hot to cold side by revising the existing ducts into and out of the air preheaters. Therefore, those construction activities must be performed in a minimum amount of time.

New Cold-Side Baghouse

Baghouses are now considered a proven technology capable of providing a constant outlet loading regardless of the fuel being fired. Baghouses are designed to capture ash of all particle sizes at constant efficiency. A baghouse collects particles on the inside surfaces of the bags. To clean the bags, compartments in the baghouse are individually isolated, and clean flue gas is blown through the bags in the compartment, collapsing the bags and dislodging the collected ash. Cleaning is usually initiated when a high-pressure drop is detected. Cleaning can be done as frequently as every 2 hours, or only once per shift. On units firing coal with fine fly ash, cleaning is typically initiated by a timer. The bag material must withstand the air heater outlet temperature under normal operations and therefore is usually constructed from a woven fiberglass. This material has been successfully demonstrated in utility baghouses with air-to-cloth ratios of 2.0 or less and has an average expected life of 3 years or more.

CASE STUDIES

The problems experienced with operating units indicate that hot-side precipitators are rapidly reaching the end of their useful lives. The following case studies were developed for a 600-MW unit. Several alternatives were evaluated to remedy three problems: (1) ash accumulation on plates and wires; (2) collection deficiencies; and (3) structural integrity. In addition to evaluating the effectiveness of the alternatives in solving these problems, this section considers how sensitive the selection of a potential fix is to variations in three factors: (1) the severity of the accumulations; (2) the available collection area of the precipitator; and (3) the structural condition of the precipitator and support steel.

CASE A examines a precipitator in poor structural condition but with acceptable operating performance because of continuous and costly maintenance effort. Costs have been evaluated for three potential remedies: (1) lengthening the stub columns; (2) replacing the existing flat slide plates with spherical slide plates; and (3) eliminating redundant members to reduce structural stiffness. The costs associated with each fix are shown in Table 3. As will become clear when the other cases are examined, these costs are relatively small.

CASE B is based on the assumptions that (1) the precipitator is large and the on-line rapper system is not effective, and (2) unit loading does not permit offline rapping on weekends and the ash accumulations are more severe, which requires offline washing (or sand blasting) of the precipitators at intervals of every 3 to 4 months. With the exception of plate wear, however, the unit is in good structural condition. Remedies for this condition are major. They include the following possibilities:

- sodium conditioning where ash sodium levels are low,
- several hot-to-cold conversion alternatives, or
- abandonment of the existing precipitators with replacement by new cold-side baghouses or electrostatic precipitators.

The conversion and replacement alternatives have major impacts on the system because of scheduling and cost considerations. It is typical for 30 to 60 months to elapse from the decision to proceed until the initial startup. In addition, an outage of 3 to 4 months is required. The capital costs for these remedies, as shown on Table 4, range from 2 to 60 million dollars. Among the factors influencing these costs, the amount of plate wear is important. If plate wear has been high, the collector plates may need to be replaced. Operating or system cost variations also depend on the risk of success. Obviously, risk consideration tends to favor conversions that can use an existing large precipitator and alternatives that abandon and replace the existing structures.

CASE C involves units troubled by most of the operating problems discussed and whose structure is in poor condition. Problems include severe plate and wire accumulations and heavy wear on plates. Furthermore, washing must be performed off line. Complications also result because the unit is base loaded and the existing precipitators are small. For these units, any continued use of the existing precipitators may require plate replacement and structural repairs along with the hot-to-cold conversion alternatives. The small initial size also eliminates any chance of operating converted units without gas conditioning or additional sidestream surface. The abandon and

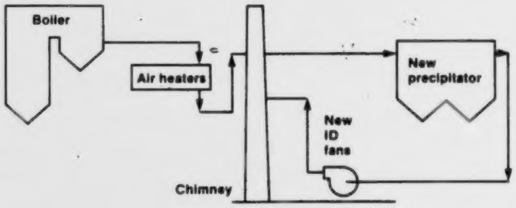

Figure 8. Flow diagram of new cold-side precipitator addition.

TABLE 3. CASE A COSTS

Potential Remedy	Estimated Cost
Replace stub columns	
Lengthen stub columns	$1.3 million
Install spherical slide plates	$0.4 million
Reduce structural stiffness	$0.7 million

TABLE 4. CASE B COSTS

Potential Remedy	Estimated Cost
Install sodium conditioning	$2.0 million
Convert from hot to cold	
No SO_3 conditioning	$24 million
With SO_3 conditioning	$30 million
Added surface (sidestream precipitator)	$50 million
Abandon and replace	$50 to 60 million

TABLE 5. CASE C COSTS

Potential Remedy	Estimated Cost
Convert from hot to cold	
With SO_3 conditioning	$35 million
Added surface (sidestream precipitator)	$60 million
Abandon and replace	$50 to 60 million

replace alternatives are strongly influenced by risk considerations, and slight differences in costs between conversion and replacement alternatives become inconsequential. The capital costs for these alternatives are shown in Table 5. The differential between conversion and replacement, about 20 million dollars, can also be reduced by an evaluation of overall system costs. In a recently completed study, the capital cost differential was completely eliminated when auxiliary power, operating and maintenance, downtime, and replacement power differentials were taken into account.

CONCLUSIONS

The preceding discussions focused on a technology, the use of hot-side precipitators, that will probably never be applied to new units again. Even so, that hot-side precipitators should not be used is not the only conclusion from the material presented. Instead the reader should conclude, as Sargent & Lundy has, that problems encountered with hot precipitators depend on specific parameters related to each installation. The coal characteristics, precipitator size, structural condition of the precipitator, and status of the design of the duct work and supports all affect the types of modifications that would resolve the problems of an existing installation. Each installation requires an individual and comprehensive study to determine the best course of action. Sargent & Lundy believes that solutions are available to relieve many of the problems discussed because it is now possible to identify the root causes of the problems in older installations.

In addition, changing technology has advanced the state of the art in precipitator and duct design and can be used to solve the problems becoming evident in the precipitators and ductwork designed in the 1970s. To avoid the problems discussed, the application principles reviewed in the paper for hot-side precipitators can and should be applied to new cold-side precipitators and baghouses. Sargent & Lundy can recommend this application with a high degree of confidence because the industry has matured and now understands the collection difficulties inherent with differences between various coal ashes and knows how to properly predict and design for thermal gradients.

The work described in this paper was not funded by the U.S. Environmental Protection Agency, thus the contents do not necessarily reflect the views of the Agency and no official endorsement should be inferred.

CONSIDERATIONS FOR THE CYCLIC OPERATION OF HOT-SIDE ELECTROSTATIC PRECIPITATORS

Fred C. Southworth
Plant Manager

Richard K. Miller
Project Engineer
Dayton Power & Light Company

Charles A. Altin
Project Manager
Ebasco Services Incorporated

PRESENTED AT
THE EPA/EPRI SIXTH SYMPOSIUM ON
THE TRANSFER AND UTILIZATION OF
PARTICULATE CONTROL TECHNOLOGY

FEBRUARY 1986

CONSIDERATIONS FOR THE CYCLIC OPERATION OF HOT-SIDE ELECTROSTATIC PRECIPITATORS

By: Fred C. Southworth
Richard K. Miller
Dayton Power & Light Company
Dayton, Ohio 45401

Charles A. Altin
Ebasco Services Incorporated
Norcross, Georgia 30092

ABSTRACT

Changing and shifting load demands have required electric utilities to reevaluate the mix of base-loaded, cycling and peaking units within their systems. This reevaluation can result in converting base-loaded units into cyclic operation and has resulted in the design of new units specifically for cyclic duty. Cyclic operation requires that special attention be given to the design and operational aspects of electrostatic precipitators in order to achieve compliance with environmental regulations.

This paper discusses those design and operational aspects which must be considered for hot-side electrostatic precipitators. Specifically, start-up and shutdown procedures, structural features, cyclic automatic voltage controllers, and rapper flexibility are addressed.

CONSIDERATIONS FOR THE CYCLIC OPERATION OF HOT-SIDE ELECTROSTATIC PRECIPITATORS

Changing and shifting load demands have required electric utilities to reevaluate the mix of base-loaded, cyclic and peaking units within their systems. In recent years, these demand changes have occurred for several reasons: (1) Over the last twenty years, new large units, many of which were nuclear, have been placed into base-loaded service and (2) reduced demand caused by economic recession, oil embargo, inflated/deflated energy costs, and conservation have altered load characteristics which, in terms of the reassessment, will have an effect on the degree and description of capacity reserves. In addition, unit life extension programs along with cogeneration facilities will have a significant impact on the short-range operation and long-range utility generation planning.

In addition to the load demand changes, increasing unit operating and maintenance costs have resulted in an evolution in operating philosophies. Generating units are generally designed for a useful life of 30 to 40 years and when new, are considered to be base-loaded units. As units age, operation and maintenance costs increases make it attractive to operate more cost-effective, newer units. Traditionally, the first third of the unit's life cycle would be as a base-loaded unit. During the second third, the unit would be used for intermediate service providing low load operation and load swinging, followed by use as a peaking or cyclic unit for its remaining years.

Many of the larger base-loaded units placed into service in the mid-to-late 1960s and early 1970s were designed with hot-side electrostatic precipitators. Initial experience with hot-side ESPs was generally good with those utilizing low sulfur Eastern coals.

Conversion of units with hot-side ESPs from base-loaded operation to cyclic operation requires that specific attention be given to certain design and operational items, specifically start-up and shutdown procedures, structural concerns, cyclic automatic voltage controls, and reliable, flexible rapper controls.

HISTORICAL DEVELOPMENT OF THE STATION

The Killen Electric Generating Station consists of one 600-megawatt unit placed in service in June of 1982. This unit was designed to operate on low sulfur Eastern coal and to utilize a two-shift cyclic operational regime. The decision to design the unit for two-shift cyclic operation was based on load forecasts into the 1990s coupled with considerations for the age and reliability of the base-loaded units in the system.

Over the years, the term "cyclic" has been used to describe a number of operational regimes. The DP&L Company elected to define "cyclic operation" as daily off/on operation. The unit was designed to be started up each morning and shutdown and bottled-up each evening. It was thought that designing to this severe application would provide the assurance that the unit would be able to maintain the high standards of reliability and availability required by DP&L. Further, the design included all those features relative to heat rate improvement and reliability exhibited by the most modern base-loaded units.

The decision to install hot-side ESPs was based on DP&L's previous experience with hot-side precipitators on small cyclic units as well as general industry experience on larger base-loaded units. When this unit was designed in the mid-1970s, hot-side precipitators had performed well on low sulfur Eastern coals. DP&L had just completed the retrofit installation of hot-side ESPs on two 150-megawatt units at the F. M. Tait Station in 1976 and six 60-megawatt units at the O. H. Hutchings Station in 1974. The six units at Hutchings were operated on a daily off/on cyclic regime similar to that to be employed at the Killen Station. Although the scale-up factor was substantial, the precipitator suppliers saw, in general, no major obstacles with implementing such a design at Killen.

PRECIPITATOR DESIGN FEATURES

The Killen electrostatic precipitator system consists of two precipitator casings located between the steam generator's economizer exit and air heater inlet. Each casing is approximately 186 feet in length, 49 feet in depth, and 77 feet in height. A plan view of the precipitator arrangement is depicted by Figure 1. The precipitators are arranged in an "in-line-parallel" configuration. In this configuration, the flue gas exits the economizer making a 90-degree downward turn into a vertical duct which then makes another 90-degree turn so that the ductwork and flue gas travel along the north-south plant axis. As the flue gas approaches the precipitator, a large plenum chamber is used to turn the gas 90 degrees so that it travels in the east-west directions through the precipitators. The flue gas is distributed across the precipitator face through the use of two perforated baffle plates. The flue gas then travels through the precipitators and exits into outlet plenum chamber. The gas turns 90 degrees with the use of turning vanes and travels onward to the air heaters.

In consideration of Killen's cyclic design, a conservative approach was set forth in the precipitator specification. This approach entailed establishing a worst-case design condition which was not expected to be experienced in the foreseeable operational future of the unit. The selection of the worst-case design condition was intended to provide significant safety factors or margins and/or improved performance levels when functioning under typical conditions. The worst-case design approach (maximum coal ash, minimum coal heating value, maximum gas flow representing induced draft fan test block conditions, gas temperature margins, and operation with 10 percent of the electrical bus sections out of service) was utilized in order to assure that Killen's precipitator emissions would be significantly below that required by the Federal New Source Performance Standards on a continuous basis. This design approach was intended to overcome any uncertainty associated with precipitator performance under cyclic loading conditions.

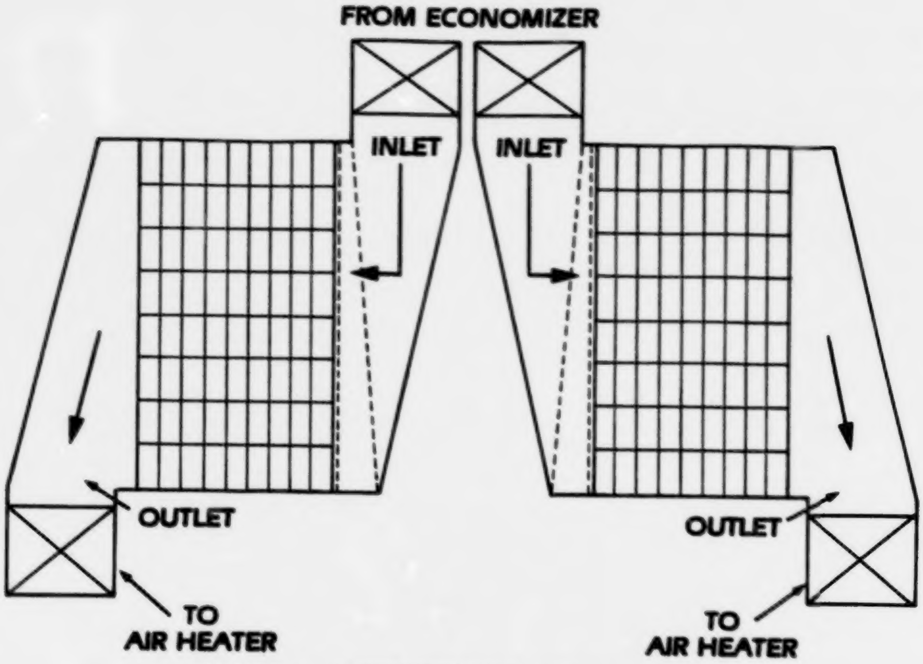

FIGURE 1 - PRECIPITATOR ARRANGEMENT

The Killen precipitators' design parameters can be summarized by the following:

Collection efficiency	99.552 percent	
Gas temperature	560 to 725°F	
Maximum gas flow	3.7×10^6 ACFM	
Maximum ESP inlet gas velocity	5.2 fps	
Treatment time	7.8 seconds	
Number of fields/precipitator	9	
Number of cells	8 wide/precipitator	
Collection plate area	1,283,040 sq. feet	
Specific Collecting Area (SCA)	347 sq. feet/1000 ACFM	
Aspect ratio	1.23	
Number of transformer-rectifier sets	72	
Number of electrical bus sections	144	
Number of collecting plate rappers	1008	
Number of discharge electrode rappers	288	
	Rated	Expected
Current density - microamps/sq. feet	63.55	47.70
Corona power - watts/1000 ACFM	1131	848
Corona power density - watts/sq. feet	3.26	2.44

OPERATIONAL EXPERIENCE

During the first 42 months of operation from June 1982 through December 1985, the Killen unit experienced 730 starts as depicted by Figure 2. In addition to frequent starts, the precipitators were required to respond adequately to rapid changes in system load demand and maintain compliance with New Source Performance Standards. During start-up conditions and load changes, this hot-side ESP is exposed to a wide range of flue gas temperatures and conditions. Essentially this precipitator is expected to perform as a cold-side ESP, a warm cold-side ESP, a cool hot-side ESP and a true hot-side ESP in its day-to-day operation. Precipitator performance was generally adequate under steady state conditions but failed to perform satisfactorily under rapid load changes and unit start-up conditions.

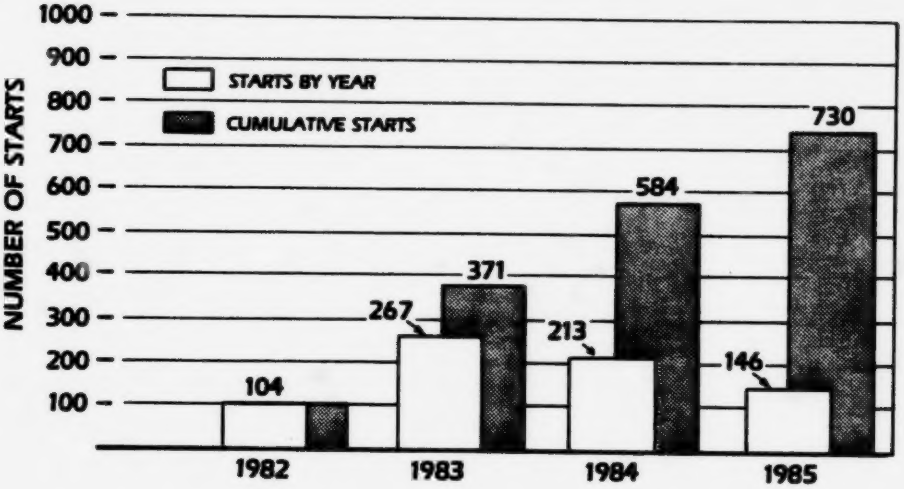

FIGURE 2 - YEARLY START-UPS

This unsatisfactory performance level prompted DP&L to not only closely examine the precipitator itself but thoroughly evaluate the process conditions being imposed on the precipitator system by the nature of cyclic operation.

Periods of poor precipitator performance were characterized by widespread low transformer-rectifier power levels, high frequency of bus section trips, significant wire breakage, poor spark response of the AVCs, and excessive rapper failures. Compounding these performance problems were indications of wire-to-plate misalignment, air infiltration, and bowed internal members. It was not until a systematic and thorough internal inspection was conducted that the entire process could be accurately characterized.

It should be noted that when performing an inspection of this type, careful notes should be taken documenting all problem areas so that a comparison can be made in the future. Original erection notes including measurements, sign-off sheets, and wire-to-plate alignment checks are all beneficial in determining the cause of failures and possible corrective action. Several internal problems were noted during these inspections, many of which appeared to be directly related to the cyclic nature of the unit.

There were significant wire deposits, ranging from 1/4 to 2 inches in diameter and generally associated with those bus sections experiencing rapper failure. Rapper reliability and sequencing are crucial in order to maintain wire cleanliness, especially during start-up and low temperature operation when the ash may have a greater tendency to be cementitious or exhibit higher electrical resistivity.

The structural investigation revealed many instances of bowed internal bracing. These members were relatively small horizontal beams (6-inch WF) when compared to main structural elements, i.e. columns. These wind bracing members experience rapid increase in temperature relative to the surrounding structure during start-up conditions. Contact with collecting plates was verified in several locations which may have resulted in temporary distortion causing low power levels. Permanent damage to the collecting plates was not observed.

A complete alignment check was made measuring the wire-to-plate spacing throughout the precipitator. Although massive misalignment was not found, some reduced power levels can be attributed to a general misalignment which was present. Having the original construction alignment documentation to compare to the actual measurements after years of operation is helpful in evaluating the effects of cyclic operation.

Several instances of tears in ductwork floor plate and distortion on vertical sidewalls were found. Evidence was found of uplift of the precipitator support legs and failure of several slide bearings. Each of the 124 bearings was physically examined to determine the condition of the bearing. In addition, data were gathered noting all critical dimensions, movements, and general condition of the teflon bearing pads.

Many of these structural problems have been experienced in other hot-side ESPs, however, the point in time that they appear is accelerated by cyclic operation. Cyclic operation in conjunction with air infiltration creates additional precipitator performance problems. These circumstances create a localized condition of changing gas properties and internal alignment both of which adversely affect performance.

These symptoms made it necessary to develop a testing program to analyze the performance of the precipitator system under a wide range of operating conditions.

FUEL QUALITY

The quality of the coal being burned and the variation in coal from that originally specified have a significant impact on the performance of the precipitator. In order to provide the Killen Station with the greatest amount of flexibility in fuel procurement and still insure adequate performance of the precipitator, the specification included a fuel and ash analysis presenting a range and performance value for each parameter. It should be noted that the performance coal may represent a specific analysis whereas the range of fuel characteristics represent many samples which do not add up to 100 percent. The following represent the coal quality specification range in the Killen precipitator specification:

	Performance	Miminum	Maximum
Proximate Analysis Percent by weight			
Fixed Carbon	44.0	37.0	57.0
Volatile Matter	29.0	29.0	40.0
Moisture	6.0	3.0	15.0
Ash	21.0	10.0	23.0
Heating Value, Btu/lb.	11,000	10,500	12,000
Sulfur	0.6	0.6	4.0
Ultimate Analysis Percent by weight (dry)			
Carbon	64.9	58.0	81.0
Hydrogen	4.2	4.0	6.0
Oxygen (by difference)	6.3	4.0	10.0
Nitrogen	1.7	1.0	2.0
Sulfur	0.6	0.6	4.0
Ash	22.3	10.0	23.0
Ash Mineral Analysis Percent by weight on an ignited basis			
Phosphorous Pentoxide - P_2O_5	1.01	0.04	3.00
Silica - SiO_2	57.44	30.00	58.00
Ferric Oxide - Fe_2O_3	2.94	2.90	36.00
Alumina - Al_2O_3	32.62	18.00	36.00
Titania - TiO_2	0.34	0.30	3.00
Lime - CaO	0.91	0.90	9.00
Magnesia - MgO	0.90	0.20	2.00
Sulfur Trioxide - SO_3	0.19	0.10	7.00
Potassium Oxide - K_2O	2.74	0.40	4.00
Sodium Oxide - Na_2O	0.55	0.20	2.00

An evaluation of the coal received at the Killen Station since start-up in 1982 and samples of the specific coal used during the precipitator testing program indicate that all the coal burned at the Station is of significantly better quality than that outlined in the precipitator specification.

Ash samples obtained at the economizer outlet were analyzed for electrical resistivity and chemical composition. The ash mineral analyses showed that generally the quantities of all components were within the ranges in the specification. Resistivity data indicated that the Killen precipitator could be operating in light, moderate, or heavy back ionization depending on the operating temperature range. This, of course, is even more critical when considering cyclic operation when at low loads, the operating temperatures result in unfavorable resistivity levels. In essence, the severity of the back ionization decreases as flue gas temperatures increase. With every start-up and shutdown of the Killen unit, the precipitator is subjected to high ash resistivity conditions.

TEST PROGRAM

To accurately characterize the performance of this precipitator and to analyze its response to process change, a detailed testing program was developed.

During the test period, the unit was operated in accordance with a specific load schedule. Deviation from the schedule as required by system demand was not a major problem inasmuch as the deviation was within the normal operating parameters of the unit. The test regime was specifically designed to expose the unit to a wide range of ramp rates, load levels, and operating conditions which could result in performance problems. The test period consisted of a three-week period of restricted load regime followed by a five-week period during which the unit operated as system load required with data being collected during the entire period.

Since the process conditions were constantly and rapidly changing and many of the opacity spikes were of short duration, an automated data collection system was designed and installed to "capture the event." This automated data acquisition system collected 40 operating parameters from the station computer as well as temperature measurements from 160 thermocouple points both on selected structural members and in the gas stream. This data was collected to develop a basic understanding of the events surrounding precipitator performance problems associated with load changes and steady state operation.

Prior to the commencement of the test program, the precipitators were mechanically cleaned to remove the ash deposits from the wires and plates. In addition, the inlet and outlet plenums were vacuumed clean. This cleaning was necessary for two reasons; first, to facilitate a thorough internal structural inspection and second, to begin the test period with reasonably clean precipitators so as to monitor performance degradation. Thermocouples were installed inside the precipitators to measure gas and steel temperatures. Thermocouples were installed on each of the precipitator support sliding bearings. Movement detectors were installed at locations on precipitator internal wind bracing which had bowed and appeared to have contacted collection plates.

Inasmuch as rapper failures were a problem and since rapper reliability does have a significant impact on precipitator performance, five new test discharge electrode rapping systems were installed. The rappers were evaluated not only from a reliability and cleaning effectiveness standpoint, but also would the rapper and its control have the flexibility to cope with changing rapping requirements as a result of cyclic operations. Three of the test rapper types were of the electromagnetic lift, gravity drop design. The other test rapper types were of pneumatic and mechanical drop rod designs. The location of these test rappers was coordinated with the placement of the test AVCs as depicted in Figure 3.

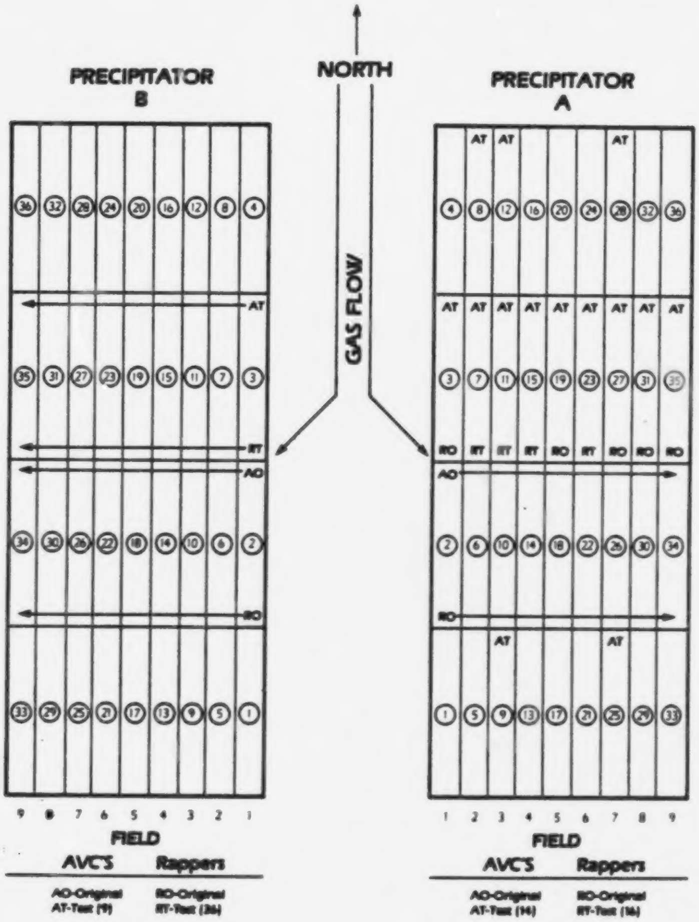

FIGURE 3 - LOCATION OF TEST EQUIPMENT

With the less-than-optimal performance by the original analog automatic voltage controls under the cyclic operation, test AVC units were donated from seven manufacturers and strategically placed on each precipitator as depicted by Figure 3. The test units were of analog and microprocessor-based designs. It should be noted that the selection of the location of the test AVCs and rappers was the sole responsibility of the project team. Efforts were made to distribute the test equipment throughout the precipitator to provide the best indication of expected performance. To assure a good basis for comparison to existing units and hopefully to allow for meaningful results, the original AVCs were recalibrated and all nonfunctioning rappers repaired and placed in good operating condition.

RECOMMENDED ACTION PLANS

The results of the field inspections and the data collected during the test program were thoroughly analyzed. Based on this information, the following five specific action items were recommended for implementation:

- Replace the existing analog automatic voltage controllers with state-of-the-art, microprocessor-based controls capable of dealing with back ionization and highly resistive ash conditions. In addition, a supervisory computer system should be installed to provide for the coordinated control of all AVCs while monitoring the changing process conditions, opacity, and energy consumption.

- Replace the existing rapping system with new more effective, reliable rappers. The new rapping system should be controlled by its own microprocessor which will be coordinated with the supervisory system to provide maximum rapping sequencing and timing flexibility.

- Conduct full-scale air flow and model studies to determine the modifications necessary to assure adequate gas flow distribution at all load levels, ramping rates, and fuel characteristics.

- Perform detailed structural analysis of the precipitators' sliding bearings, replacing those which have failed and others, as necessary, with new bearings capable of withstanding all imposed loads and movements.

- Perform a detailed structural analysis of the entire precipitator system to determine what forces and movements have actually occurred in the unit to have caused bowed beams and buckled plate work. Following the analysis make the necessary field modifications to the precipitator internals to insure correct alignment and long-term structural integrity.

These action items were designed to offer the Killen precipitator system the best opportunity of achieving intended performance levels and complying with emission regulations while maintaining its internal alignment and structural integrity.

CONCLUSIONS

- Prior to committing to the conversion from base-loaded to cyclic operation, a thorough testing program should be performed to determine the effects of cyclic operation on the entire unit. Detailed testing programs and evaluation of the hot-side precipitator system should be performed prior to commitment to determine any modifications which would be necessary to maintain compliance with admission regulations.
- State-of-the-art, microprocessor-based automatic voltage controllers capable of dealing with back ionization, highly resistive ash conditions, and constantly changing process conditions are necessary for cyclic operation.
- Structural problems are aggravated by cyclic operation with the repeated start-ups and shutdowns. The precipitator is a very complex structure which requires three dimensional analysis for correction of problem areas.
- Rapper reliability and sequencing flexibility are necessary to adjust rapping frequencies with respect to load conditions to provide optimal rapping efficiencies and avoid rapping reentrainment.

The problems experienced at the Killen Station may not be uncommon to the industry especially when looking at cyclic units; however, the testing program described here was specifically set up for this unit. Although the results are not necessarily applicable to other units, this case history may provide information to other utilities to prevent severe operational and structural problems.

The Killen experience should be viewed from the standpoint of a case study in terms of methodology. It is felt that each precipitator and its operating conditions are unique, hence each system must be appropriately studied.

The work described in this paper was not funded by the U.S. Environmental Protection Agency and therefore the contents do not necessarily reflect the views of the Agency and no official endorsement should be inferred.

Session A-2: PERFORMANCE ENHANCEMENT I

B. G. McKinney, Chairman
Electric Power Research Institute
Chattanooga, TN

A COMPARISON OF ELECTROSTATIC PRECIPITATOR PERFORMANCE ENHANCEMENT TECHNOLOGIES

BY

J. DALMON, G. L. DALTON & R. S. HANSEN

Electricity Supply
Commission
P. O. Box 1091
JOHANNESBURG
2000
R.S.A.

ABSTRACT

Extensive trials into electrostatic precipitator performance enhancement methods have been conducted on the highly resistive ashes resulting from the low sulphur, high ash coals burned in South African power stations.

Gas conditioning with sulphur trioxide, ammonia and triethylamine, as well as high voltage pulsing and microprocessor control have been examined.

It is concluded that gas conditioning is capable of reducing emissions by more than 80%, high voltage pulsing by between 25% and 52% and microprocessors by up to 26%.

In terms of migration velocity enhancement it was found that with gas conditioning and high voltage pulsing the lower the baseline efficiency the greater the enhancement, while no such dependency was apparent with microprocessors.

INTRODUCTION

The particulate emissions from the electrostatic precipitators on some of Escom's power stations exceed the levels currently required by the Chief Air Pollution Control Officer. The reasons include low original efficiency specifications, gas flow rates that are considerably in excess of design, very high ash coals with low sulphur contents, which, coupled with low sodium in ash give highly resistive, difficult to precipitate ashes.

As a consequence an investigational program has been conducted with the object of seeking the best technological and economical solution for upgrading these precipitators. This has involved trials on operational units at Escom's Hendrina, Kriel and Duvha Power Stations and at the Rooiwal Power Station of the Pretoria Municipality. In addition, results are available from tests at the Johannesburg Kelvin Power Station (1) and from Steam

Generating Plant at Sasol (2).

The trials, which have spanned the past three years, are listed in Table 1. The techniques used have been flue gas conditioning, high voltage pulsing and microprocessor control. This paper summarizes and compares the results obtained and gives an overall perspective, but does not address the economic implications.

TECHNOLOGIES INVESTIGATED

FLUE GAS CONDITIONING

Flue gas conditioning is the process of injecting chemicals into the gas prior to the precipitator in order to modify ash particle properties, such as resistivity and cohesiveness. This makes the particles more amenable to collection.

The chemicals used were sulphur trioxide, ammonia, and triethylamine the latter known colloquially as TEA.

The ideal additive should not have any adverse effect on the plant or the environment and it should not be a hazard to personnel.

SULPHUR TRIOXIDE (SO_3)

This chemical is in commercial power station use, notably in the USA. It acts by reducing ash resistivity and, thus, improving electrical conditions within the precipitator.

In all the trials reported here the SO_3 was produced by vapourising liquid SO_2 and passing the gas, mixed with heated filtered air, over a vanadium pentoxide catalyst. The resulting SO_3 gas, at a temperature of approximately 300°C which is well above the acid dewpoint, was fed via heat-insulated ducting to a distribution manifold and injected into the flue gas at the airheater outlet through a grid of nozzles located over the flue duct cross section. A Wahlco transportable system was used throughout the Escom trials and a Lurgi unit at the non-Escom power station at Sasol.

AMMONIA (NH_3)

Ammonia has been the subject of many trials worldwide and has been used operationally in the USA and, more extensively, in Australia. It is not entirely clear how it affects ESP performance but resistivity modification, space charge enhancement and increased particle cohesiveness, together or separately, all appear to contribute. It seems to be plant specific and may cause precipitator electrode fouling, or if injected before the airheater, can promote element blockage.

The NH_3 gas in the Escom tests was derived from liquid ammonia and the Wahlco SO_3 injection equipment, which was already installed on Kriel No. 6 ESP, was purged and suitably modified to control and inject the gas. Injection took place at the airheater outlet using the same nozzles as for the SO_3 trial.

Reproduced from best available copy.

TRIETHYLAMINE (TEA)

Triethylamine reduces ash resistivity and, it is claimed (3) causes gas phase particle agglomeration thus producing larger, more easily precipitated particles.

TEA has been investigated in several countries with variable results and was used operationally for a period at one power station in Australia (4). It is still used on one ESP at the Johannesburg's Kelvin Power Station (1), but was not successful there on other similar units. In the trial at Hendrina it was pumped in liquid form to compressed air assisted injection nozzles at the airheater outlet.

HIGH VOLTAGE PULSING

Pulse energisation consists, in principle, of short duration, high voltage pulses superimposed on a base DC voltage ; the duration being long enough to charge the ash particles but too short to initiate flashovers between the ESP electrodes. Pulse duration is typically within the range 50 to 200 µs and the repetition rate 25 to 400 per second.

It is claimed by the manufactures that pulsing gives the best results with highly resistive ash and that power savings, compared with conventional energisation, are possible. There are few operational installations and definitive trial data is scarce.

Two systems were evaluated, refered to here as Type A and Type B.

Type A was used at Rooiwal and Hendrina and consisted of 4 prototype units mounted on a trailer and the pulse and base voltage sets were separate. Each base-pulse combination was coupled to a precipitator field by a temporary dry high voltage cable. Individual pulses are generated with fully controllable width, amplitude and repetition rate.

Type B differed by having the base and pulse voltage supply in one common unit and a pair of these were mounted on the ESP roof at Hendrina and connected to the HV electrodes by a solid bus system. As the plate area supplied by each pulser was limited in these trial units, each ESP field was temporarily split into two parallel halves (one for each pulser) and it was only possible to pulse one field at a time. These units rely on the L-C constants of the circuit, including the precipitator, to produce resonant bursts of damped pulses. The number of pulses per burst and the burst repetition rate can be adjusted.

MICROPROCESSOR CONTROLLERS

The advantages claimed for microprocessors are a faster reaction time, compared with analog controllers, to flashovers in the ESP and a more rapid adjustment to process changes, taking cognisance of the preceeding events leading to flashovers.

Three Commercial microprocessors were tested, called here Type X, Type Y and Type Z. Types X and Y attempt to maximise the area under the high voltage-time curve for the prevailing conditions, thus providing maximum useful power for precipitation. Type Z in addition, has a semi-pulsing function. In this mode, HV rectification is inhibited during a pre-set number of mains half cycles, up to 15. This is designated current ratio 1:15. Full pulsing, current ratio 1:1, is equivalent to analog operation. In the semi-pulsing mode the current density is effectively decreased, hence the charge accumulation on the surface of highly resistive dust on the collecting plates is lessened, back ionisation is suppressed and dust is more easily removed during rapping. Additionally, any decrease in current density will result in a corresponding decrease in power consumption.

SELECTION OF STATIONS AND OPERATIONAL CONSTRAINTS

The stations involved in the trials and the technologies used are given in Table 1 and the precipitator specifications in Table 2. The trials were carried out on operational units and power generation had priority over test requirements. All tests were at full, or near full, boiler load and some 160 separate tests were conducted.

It was not always possible to inspect the interior of the precipitator for mechanical and electrical integrity, nor to note the state of dust accumulations on electrodes either before, during or after a test series. Every effort was made, from external examination, to ensure that the units were in the best condition possible for testing, i.e. rappers working, hoppers emptied and all electrical fields working satisfactorily. Where it was known that rapping failures had occured a period of power-off rapping was instituted prior to testing in an attempt to bring the electrodes to a reasonable state of cleanliness. This applied particularly to the pulser tests on No. 5 unit at Hendrina. This precipitator had been washed down and overhauled before the 1982 SO_3 trials, but was in the "as found" condition for the TEA and Type A pulser trials. It was washed and certain repairs were undertaken before commencement of Type B pulser tests. Unit No. 7 at this station was not specially prepared for testing, nor was No. 2 unit which the tests revealed to be in a poor state.

Kriel No. 3 was in an "as found" condition but No. 6 had been subjected to a general overhaul before the various trials on this unit began with the Type Z microprocessor in November 1983. The Rooiwal precipitators were washed and repaired before testing commenced. All other precipitators were in a normal operational condition.

One problem, common to testing at Duvha, Kriel and Hendrina 5, except for the SO_3 trial on the latter unit, was boiler tube leaks. These had the general effect of depressing efficiency by, presumably, causing accumulation of sticky deposits of dust on the electrodes. Because of the uncertainties associated with test results obtained when major tube leaks were present, such tests have been excluded from the comparisons in this paper, as have all tests where known faults occured.

BASIS FOR COMPARING RESULTS

Although the tests on each unit were carried out as far as possible at constant conditions, variations in coal quality and gas flow rates inevitably occured.

Electrostatic precipitator efficiency is dependent on gas flow rate, as shown in the well known Deutsch equation :-

$$\text{Efficiency} = 1 - \exp(-Ac/Q)$$

Where :- A = Total collecting plate area

Q = Gas flow rate

c = Particle effective migration velocity (emv)

This expression has been used to normalize the efficiencies from all trials on a particular unit to the average value of Q for all the acceptable tests on that unit using the measured value for 'c'. The Q values are given in Table 3. Flow rates for individual tests do not deviate from the average by more than ± 13 % in the worst case. It is assumed, as is implicit in the Deutsch expression, that emv is independent of changes in gas velocity through the precipitator. This is not strictly true but the variation is small over the range considered.

The ash content of the coals and, consequently the inlet burdens, also varied during each trial. Thus, even if the precipitator collection efficiency were constant the emissions would change. The inlet burdens for all the tests on a given unit have, therefore, been averaged (See Table 3) and with the optimum efficiency for a particular trial have been used to calculate a normalized emission as given in Table 3. It must be pointed out, however, that the programme was spread out over three years and when comparing results from precipitators used in more than one trial series, variations in the baseline efficiency due to changes in the condition of the precipitator, as well as the enhancement process, have affected the emission.

Gas temperature, sulphur in coal and the chemical composition of the ash were reasonably constant for a given unit and no adjustments to efficiencies have been made for these parameters. The important coal and ash properties have been averaged for each trial and are given in Table 4.

Baseline performance results quoted in figures and tables represent the averages of many individual tests and similarly optimum values for pulser and microprocessor trials are averages of the best condition.

COMPARISON OF RESULTS

PERFORMANCE

The normalized efficiencies for all gas conditioning trials are plotted in

Figure 1 against injection rates. It is apparent that there is an optimum rate in each case and that excessive dosage causes a fall in efficiency. This would be due to the ash becoming too conducting and behaving like carbonized coal particles which, as is well known, loose charge very rapidly on contact with the collecting electrode and are repelled back into the gas stream. This collection and repulsion process would be repeated many times until some particles escape to the stack.

The optimum efficiencies and dosage rates are listed in Table 3 from which it is clear that SO$_3$, for which there is most data, has an optimum rate varying from 20 to 35 ppm by volume vpm. This may not be the most economic rate as is shown by Kriel 6 (Figure 1) which achieves most of its improvement at 9 vpm. It may also be noted from Figure 1 that there was no extra efficiency improvement when the Type Z microprocessor was used concurrently with SO$_3$.

Ammonia had an optimum dosing rate of 40 vpm and TEA a very low value of 3 vpm. Table 3 shows that SO$_3$ is more effective than NH$_3$ at Kriel 6 and that SO$_3$ and TEA are about equally effective on Hendrina 5. It is apparent from Figure 1 and Table 3 that gas conditioning has raised efficiencies in some cases to well over 99 %.

The rapidity with which an additive reacts is typified by the opacity monitor chart for a TEA test as reproduced in Figure 2.

All results are compared in Figure 3 in terms of the percentage reduction in slip versus baseline slip. Slip is defined as 100 % minus efficiency and represents the dust escaping to the atmosphere. It is a more sensitive measure of performance than efficiency. From Figure 3 it may be seen that gas conditioning is capable of reducing slip by more than 80 % and in the case of SO$_3$ on Kriel 6 by over 98 %. No efficiency data is available for TEA at Kelvin, but a 38 % reduction in emission was achieved with a remarkably low dosing rate of 0,2 vpm.

The reduction in slip is not so great with HV pulsing, being in the region of 25 % to 52 % (Figure 3). At Rooiwal, optimum efficiency was achieved with both fields pulsed using the Type A equipment and at Hendrina by pulsing the centre and outlet fields. These results have been discussed in detail by Lugar et al (5). Type B pulsers at Hendrina gave the best performance on the outlet field. It must be remembered that whereas one Type A pulser treated a complete field and there was the capability of pulsing all 3 fields simultaneously, the two Type B pulsers could only pulse one field at a time. The latter arrangement had some advantages in so far as smaller sub-sections allow a better electrical performance and, hence, an improved collection efficiency (6). It should be borne in mind that the results quoted here are subject to the constraints of the number of pulsers available for trial and on the degree of field sub-division. Further performance improvement by pulsing should be possible by optimising the number of fields pulsed, and by field sub-division.

It should be mentioned that a power-off rapping technique used prior to certain tests with both types of pulser at Hendrina reduced baseline

Reproduced from best available copy.

emissions initially but opacity monitor charts indicated that these increased gradually within a few hours of the restoration of power. This deterioration did not occur with pulsing (See Figure 4). Calculations based on opacity monitor correlations for steady conditions indicated a slip reduction of approximately 44 % for the Type A pulsers which is comparable to the Rooiwal results (Figure 3).

The three micro-processors gave slip reduction of between 5 % and 26 % (Figure 3) and the improvement does not seem to be related to baseline slip. This is probably because they do not alter basic conditions within the ESP but simply optimise performance for the given dust and gas. The Type Z gave its best results at a current ratio of 1:7.

The normalized slip, in conjunction with the averaged inlet burden has been used to calculate a normalized emission for each trial (Table 3). The emission value, is of course, related to the baseline efficiency for that particular trial which in turn is dependent on the condition of the precipitator at the time. Nevertheless, this approach illustrates the general levels of emission that may realistically be achieved.

An alternative method of comparing the technologies is to plot emv enhancement, that is, the ratio of emv with treatment to baseline emv, against baseline slip. This indicates, Figure 5, that for gas conditioning and high voltage pulsing the enhancement is, in general, related to baseline conditions and the higher the slip (the lower the efficiency) the greater is the enhancement. Improvements with microprocessors are not related to basline slip, for reasons advanced earlier, and their enhancement ratio is less than 1:1. On this basis gas conditioning is clearly seen to be superior to HV pulsing which in turn is better than microprocessors. On Kriel 6 the enhancement ratio for SO_3 at over 2,5 is much above the empirical curve drawn for gas conditioning, otherwise, the treatment gas does not seem to be important.

RESISTIVITY AND ELECTRICAL ENERGISATION

It is quite clear from Table 4 that South African coals give rise to highly resistive ashes (generally 10^{12} to 10^{13} ohm cm). This is to be expected as the coal sulphurs are low (mostly between 0,5 and 1,1 %). Duvha has the marginally highest sulphur of 1,17 %, the highest ash iron content (5,8 %) and the lowest resistivity ($8,4 \times 10^{11}$ ohm cm). The high calcium in the ashes probably contributes to the high resistivities and the low sodium content (0,03 % to 0,36 %) does not mitigate the effect.

Table 4 shows that all the gaseous additives reduced ash resistivity, but by differing amounts. NH_3 had the least effect, less than one order of magnitude and it was found that this did not vary significantly or consistently with injection rate. With SO_3 the resistivity reduction was related to dosage and the optimum reduction was between 2 and 3 orders of magnitude. The biggest reduction, of about 4 orders of magnitude, was with TEA, but like NH_3 the resistivity did not vary much with dose rate.

The high resistivity ashes gave rise to back-ionisation and this is illustrated by representative voltage - current characteristics taken on Kriel 3 with zero conditioning (Figure 6). These exhibit typical back-ionisation fold-over curves on inlet and outlet fields and reveal the inability of the analog controller on the inlet field to select the optimum operating voltage under back ionisation conditions. A significant rise in voltage is apparent with conditioning and this response is representative of all the additives tested. No back ionisation was apparant at Duvha, with ash of slightly lower resistivity.

In Figure 7 the effect of NH_3 dose rate in suppressing back ionisation current on the RH casing at Kriel Unit 6 is compared with simultaneous measurements on the untreated LH casing where the current remained uniformly high. Figure 8 demonstrates unequivocally that under baseline conditions with back ionisation, high power inputs are not synonymous with high performance. The magnitude and importance of the increased voltage obtained with pulsing is well illustrated (for the Type A pulser) in Figure 9.

It is claimed that HV pulsing and microprocessor control can, in some circumstances, give rise to a power saving. At Rooiwal there was no saving, but at Hendrina with both pulsers types the maximum power reduction would be 80 % assuming all fields pulsed. The Type Z microprocessor gave a 90 % reduction in power and the Type Y a small reduction, both with moderate efficiency increases. The Type X also gave a marginal efficiency increase (from a high baseline, Table 3) but with an increased power input. The higher power consumption could be attributed to the less resistive ash which did not give back ionisation. Tests with the Type Z controller, over a range of current ratios, in conjunction with SO_3 injection also indicated that with a moderate ash resistivity the best performance was obtained with the highest power input, i.e. with a current ratio of 1:1.

PARTICLE SIZE EFFECTS

It was possible to analyse the performance of certain tests in terms of particle size. With SO_3 injection on Kriel units 3 and 6, the greatest effect was on the smaller particles (Figure 10). The emv of 20 µm particles, for example, in both cases more than doubled at about 10 vpm injection and on Kriel 6 at 30 vpm the emv of these particles almost tripled. Particles less than 20 µm account for some 30 % of the inlet ash. It may be observed from Figure 10 that the emv of particles above 70 µm has decreased with injection. This could be due to the preferential adsorption of SO_3 on larger particles making them very conductive and causing particle "bounce" as described previously.

In contrast to SO_3, the effect of TEA was to spread the emv improvement more or less equally over the particle size spectrum. This was also apparent with HV pulsing at Rooiwal where pulsing did not seem to act selectively on any particular size range.

AGGLOMERATION

A possible mechanism for ESP performance enhancement with gas conditioning could be due to increased particle cohesion. This would tend to increase the effective particle diameter by agglomeration if gas phase collisions occurred and would make them easier to precipitate, or if agglomeration occurred on the electrodes it could reduce re-entrainment. Alternatively, additives could make the ash sticky and difficult to remove from electrodes and hoppers.

Tests for agglomerates were carried out by traversing sticky target plates across the gas stream in the inlet and outlet flue ducts in the NH_3 and TEA trials. No change in agglomeration was found at the inlet but at the outlet maximum agglomerate diameter had increased from 100 µm with no conditioning to 500 µm at the maximum dosage rates with both chemicals. These tests were not conducted for SO_3 but on Kriel 3 an extremely sticky deposit of fly ash built up on the sampling probes in the presence of a boiler tube leak. There was no opportunity to examine the electrodes following these trials but no problems occured with hopper de-dusting for any of the chemicals.

It should be borne in mind when contemplating the use of additives that tube leaks are not an infrequent occurance.

FATE OF INJECTED CHEMICALS

It has been reported elsewhere (4) that a considerable proportion of the injected additives can escape to atmosphere. Figures of up to 25% and 54% being quoted for NH_3 and TEA respectively.

In the present trials up to 50% of the NH_3 at Kriel and between 4% and 89% of the TEA injected at Hendrina was detected on ash leaving the precipitator.

Analysis of inlet, hopper and outlet ash showed that adsorption of NH_3 increased with residence time. This is due, in part, to the ash becoming finer towards the ESP outlet, thus providing a larger specific surface for adsorption. An internal inspection of the ESP after a washdown, some 2 months after NH_3 injection terminated, revealed a strong smell of ammonia, especially at the top of the treatment chamber.

TEA showed a low adsorption on hopper ash compared with outlet samples. (0,01% compared with 2% at maximum dosage rate). This has also been observed in CEGB trials (7) where there was some evidence that a triethylamine sulphate compound had been deposited on the ash surface. This deposit apparently decomposed by reaction with the ash leaving the sulphate on the surface and releasing the free amine for further gas phase contact with the fly ash. This mechanism could account for the effectiveness of very small amounts of the chemical observed at Kelvin and Hendrina.

Other than establishing that there was no discernable decrease in the pH of the ash slurry leaving the ESP at maximum SO_3 dosage rates, the fate of SO_3 was not studied as it has been established elsewhere that, provided there is no overdosing, it is almost entirely adsorbed on the ash (8 & 9) and is eventually neutralized by reaction with surface calcium. Overdosing can cause acid agglomerates and visible plumes. On Hendrina 5 injection of 20 vpm SO_3 resulted in 5 vpm at the ESP outlet.

CONCLUSIONS

The flue gas additives, sulphur trioxide, ammonia and triethylamine all reduced particle emission by more than 80 %. The best result was with SO_3 on Kriel 6 which gave a 99 % reduction. Ammonia on the same unit achieved 90 % reduction, while SO_3 and triethylamine had an equal effect on Hendrina 5, reducing emission by 86 %.

Optimum dosing rates for SO_3 varied between 20 and 35 vpm while for NH_3 and triethylamine the rates were 40 vpm and 3 vpm respectively.

With SO_3 the greatest performance enhancement was on the finer particles whilst with triethylamine and HV pulsing the improvement was spread over the whole size spectrum.

High voltage pulsing achieved reductions in emission of between 25 % and 50 %, but there is scope for greater improvement by sub-dividing precipitator fields and optimising the number of fields pulsed.

There was limited evidence that HV pulsing could maintain an increased performance following electrode cleaning but with normal energisation performance deteriorated fairly rapidly.

There was a considerable power saving with high voltage pulsing and with microprocessors when highly resistive ash was being treated. With ashes of optimum resistivity best results with microprocessors were at maximum power.

Microprocessors reduced emission by up to 26 %. However, their chief benefits would be in terms of power saving and improving day-to-day operation of ESP's presently equipped with analog controllers.

Particle migration velocity enhancement was, in general, dependent on baseline efficiency, the lower the efficiency the greater the enhancement.

ACKNOWLEDGEMENTS

The co-operation of the various power station staff during the trials and the assistance of the various manufacturers is greatly appreciated.

This paper is published by permission of Escom. The work described in this paper was not funded by the US Environmental Protection Agency and therefore the contents do not necessarily reflect the views of the Agency and no official endorsement should be inferred.

REFERENCES

1. HEINICHEN, D. and POTGIETER, I.P., 1983
   Reducing the Particulate Emissions of Coal-Fired Power Stations, Second C.S.I.R.O. Conference on Electrostatic Precipitators, Aug., Bowral, Australia.

2. LURGI SOUTH AFRICA LTD. 1984 - Private Communication.

Reproduced from
best available copy.

3. PAULSON, C.A.J. and POTTER, E.C., 1983
Flue Gas Additives for Better Electrostatic Precipitation of Fly Ash, 2nd CSIRO Conference on Electrostatic Precipitation, Aug., Bowral, Australia.

4. WALKER, F.H., 1983
A Review of Recent Experience with Flue gas Conditioning in N.S.W. Power Stations and the Fate of the Conditioning Agents, Ibid.

5. LUGAR, T.W., BRUMMER, J.H., ROSCH, T.W. and DALMON, J. 1985,
The Dynamic Response of Precipitator Performance to Pulse Powering, ASME Paper 85 - JPGC - Pwr - 19. Power Generation Conference, Milwaukee, Oct. 20 - 24.

6. DALMON, J., 1980,
Electrostatic Precipitator for Large Power Station Boilers, Journal of Electrostatics, 8, 309 - 324.

7. DALMON, J., 1978
Private Communication

TABLE #1

ELECTROSTATIC PRECIPITATOR PERFORMANCE ENHANCEMENT TRIALS

STATION	UNIT	DATE	EQUIPMENT
FLUE GAS CONDITIONING			
SO_3			
HENDRINA	5 RH	04/11/82-29/12/82	WAHLCO
HENDRINA	7 RH	27/01/83-24/02/83	WAHLCO
KRIEL	3 LH/RH	30/03/83-05/08/83	WAHLCO
KRIEL	6 RH/RH	18/01/84-17/04/84 *	WAHLCO
SASOL I	3	10/04/84-17/04/84	LURGI
NH_3			
KRIEL	6 RH/RH	24/04/84-05/06/84	MODIFIED WAHLCO
TEA			
HENDRINA	5 RH	12/12/84-16/01/85	ESCOM
KELVIN	14	18/08/81-25/08/81	STATION
MICROPROCESSORS			
DUVHA	3 LH	15/08/83-22/09/83	TYPE 'X'
HENDRINA	2 RH	03/04/84-05/04/84	TYPE 'Y'
KRIEL	6 RH/RH	29/11/83-26/04/84 *	TYPE 'Z'
HIGH VOLTAGE PULSERS			
ROOIWAL	5 LH&RH	22/03/85-28/03/85	TYPE 'A'
HENDRINA	5 RH	18/04/85-23/05/85	TYPE 'A'
HENDRINA	5 RH	22/10/85-05/11/85	TYPE 'B'

* SOME TESTS WITH SO_3 AND TYPE 'Z' MICROPROCESSOR COMBINED

TABLE #2

ELECTROSTATIC PRECIPITATOR SPECIFICATIONS

STATION	HENDRINA	HENDRINA	KRIEL	KRIEL	DUVHA	KELVIN	ROOIWAL	SASOL
UNIT	2&5	7	3	6	3	14	5	3
PARALLEL CASINGS	2	2	2	2	2	2	2	1
PARALLEL FIELDS	1	1	1	2	2	1	1	1
SERIES FIELDS	3	2	3	4	7	2	2	2
TOTAL FIELDS	6	4	6	16	28	4	4	2
FIELD LENGTH (m)	3.84	5.5	5	5	3	4.09 *	-	3.5
FIELD HEIGHT (m)	10.5	12	12	13	13.5	7.2	-	11.25
PLATE SPACING (mm)	250	250	300	300	300	254	254	250
TOTAL PLATE AREA (m^2)	29722	24288	57600	93600	104328	6852	9072	7230
NUMBER OF TR SETS	6	4	6	16	20	2	4	2
COAL ASH (%)	26.2	26.0	19.7	29.6	28.85	16.0	10-20	-
COAL SULPHUR (%)	0.8	0.8	1.11	1.05	1.0	0.7	0.7-1.2	0.6
CARBON IN ASH (%)	-	2	3.2	2	2.3	-	-	1.0
GAS FLOW RATE (Am^3/s)	384	380	826	910.5	913.4	131	112.8	107.6
GAS TEMPERATURE (°C)	138	136	135	135	130	135	139	180
GAS VELOCITY (m/s)	1.37	1.38	1.43	1.3	1.24	1.17	-	0.82
INLET BURDEN (g/Am^3)	-	17.0	12.8	20	18.3	26.24	-	-
INLET BURDEN (g/Nm^3)	30.9	30.9	-	-	-	11.49	18.0	30.3
EFFICIENCY (%)	98	96	98	98.72	99.59	97.5	96.7	98.7
EMV (cm/s)	5.06	5.03	5.6	4.25	4.8	7.05	4.24	6.47
W_k (cm/s)	19.82	16.17	21.87	18.57	26.32	26.02	14.47	28.07

* KELVIN PLATES VARY IN LENGTH (52 AS ABOVE BUT 10 SHORTER) AFTER RETROFIT EARLY 1970's

TABLE #3

OPTIMUM PERFORMANCE BASED ON NORMALISED INLET CONDITIONS

STATION	UNIT	TREATMENT	OPTIMUM CONDITION	AVERAGE GAS FLOW RATE	NORMALISED EFFICIENCY		AVERAGE INLET BURDEN	NORMALISED EMISSION
					BASELINE	OPTIMUM		
				Am^3/s	%	%	g/Sm^3	mg/Sm^3
HENDRINA	5	SO_3	25 vpm	200	98.19	99.76	27.50	66
HENDRINA	7	SO_3	30 vpm	210	86.54	97.32	20.74	556
KRIEL	3	SO_3	20 vpm	250	88.06	98.49	23.80	359
KRIEL	6	SO_3	30 vpm	239	94.67	99.94	27.93	17
SASOL	3	SO_3	35 vpm	126	95.56	99.34	24.80	164
KRIEL	6	NH_3	40 vpm	239	95.11	99.49	27.93	142
HENDRINA	5	$(C_2H_5)_3N$	3 vpm	200	97.17	99.62	27.50	105
KELVIN	14	$(C_2H_5)_3N$	0.2 vpm	144	-	-	-	830
DUVHA	3	M'PROC. X	-	260	99.18	99.40	22.80	138
HENDRINA	2	M'PROC. Y	-	210	91.68	92.95	29.20	2059
KRIEL	6	M'PROC. Z	Ratio 1:7	239	97.28	97.41	27.93	724
ROOIWAL	5	HV PULSER 'A'	All fields	50.8	92.98	96.62	19.14	647
HENDRINA	5	HV PULSER 'A'	Centre & Out	200	96.83	97.64	27.50	650
HENDRINA	5	HV PULSER 'B'	Outlet	200	94.37	96.93	27.50	847

TABLE #4

COAL AND ASH PROPERTIES

STATION	UNIT	TREATMENT	COAL		ASH				RESISTIVITY	
			ASH	S	C	Na_2O	Fe_2O_3	CaO	BASELINE	CONDITIONED
			%	%	%	%	%	%	Ohm/cm	Ohm/cm
HENDRINA	5	SO_3	25.3	0.70	5.4	-	-	-	1.7 E13	2.1 E11
HENDRINA	7	SO_3	22.2	0.87	-	-	-	-	4.0 E12	2.0 E10
KRIEL	3	SO_3	24.5	0.76	1.1	0.36	2.7	10.4	3.0 E12	1.0 E09
KRIEL	6	SO_3	28.8	0.80	0.8	0.09	3.1	8.7	-	-
SASOL	3	SO_3	27.5	0.48	2.2	-	-	-	-	-
KRIEL	6	NH_3	28.7	0.76	0.6	0.04	3.1	7.5	1.6 E12	5.7 E11
HENDRINA	5	$(C_2H_5)_3N$	23.7	1.03	3.9	0.14	4.0	3.6	1.9 E12	2.0 E08
KELVIN	14	$(C_2H_5)_3N$	20.3	1.01	16.7	-	-	-	2.0 E12	1.1 E08
DUVHA	3	M'PROC 'X'	23.8	1.17	1.2	0.17	5.8	4.9	8.4 E11	-
HENDRINA	2	M'PROC 'Y'	-	-	-	-	-	-	-	-
KRIEL	6	M'PROC 'Z'	28.3	0.88	1.2	0.24	2.9	7.7	-	-
ROOIWAL	5	PULSER 'A'	20.9	1.09	3.7	0.15	4.5	5.1	6.3 E12	-
HENDRINA	5	PULSER 'A'	25.5	1.11	5.8	0.03	3.7	3.3	2.2 E12	-
HENDRINA	5	PULSER 'B'	24.2	0.77	4.1	0.10	3.8	4.8	2.3 E12	-

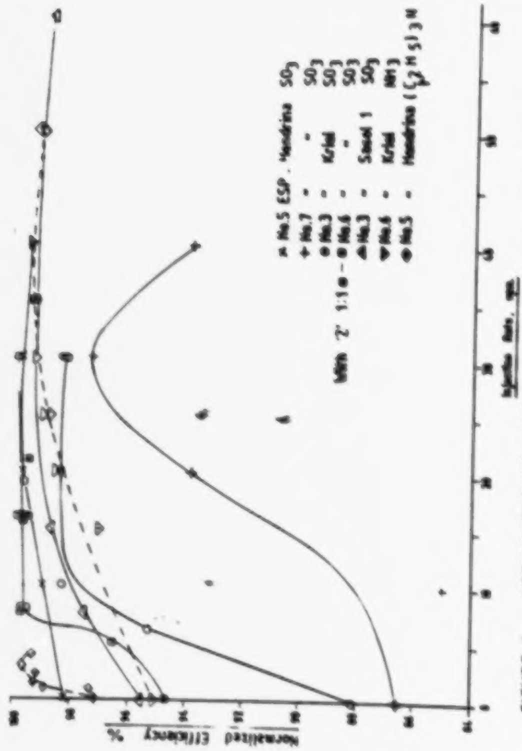

FIGURE 1 NORMALIZED COLLECTION EFFICIENCY V INJECTION RATES

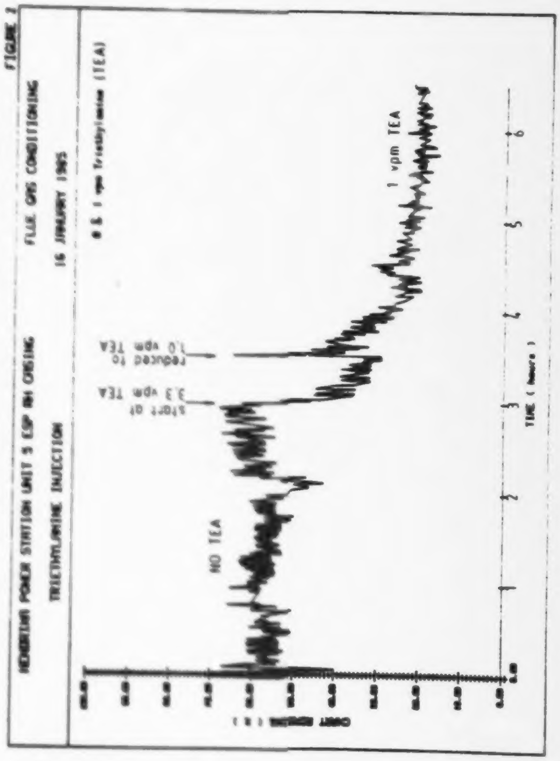

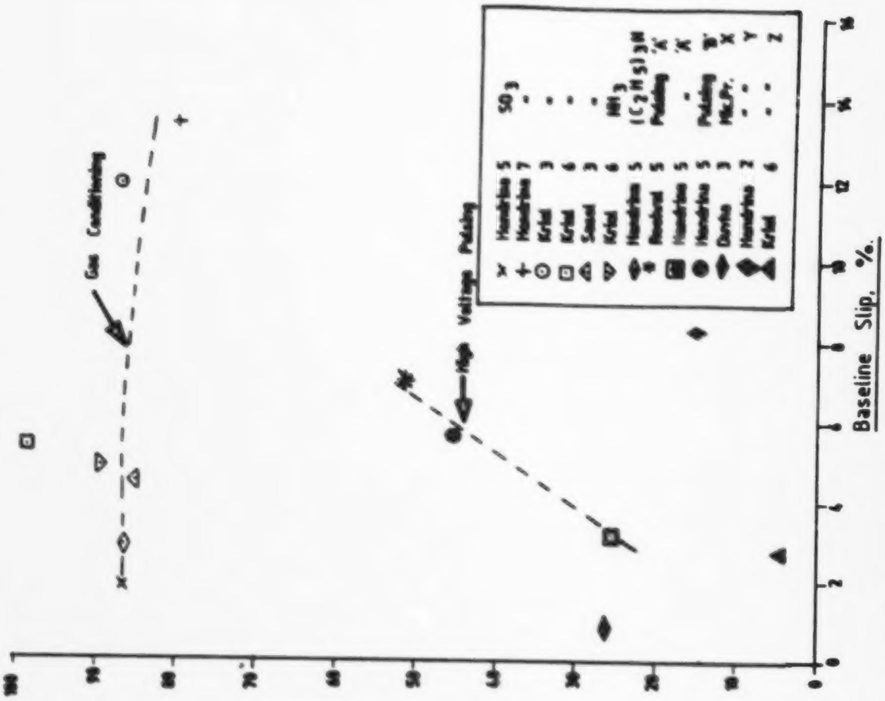

FIGURE 3 REDUCTION IN SLIP AS A FUNCTION OF BASELINE SLIP

FIGURE 4

EFFECT OF POWER-OFF RAPPING WITH AND WITHOUT TYPE 'A' PULSERS HENDRINA ESP 5

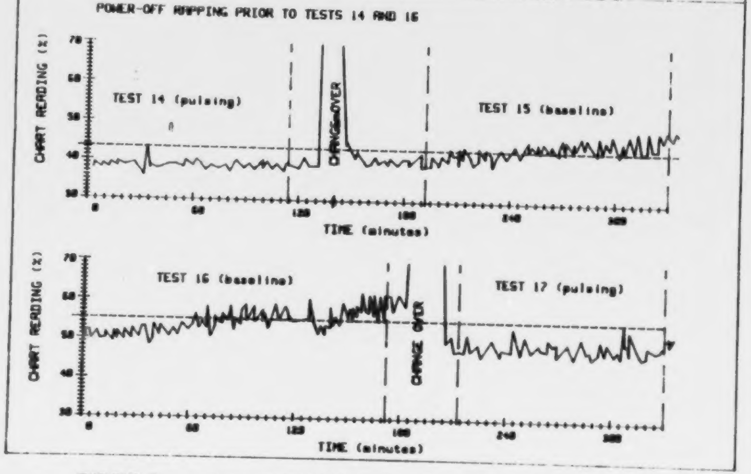

FIGURE 5. Emv ENHANCEMENT RELATED TO BASELINE SLIP

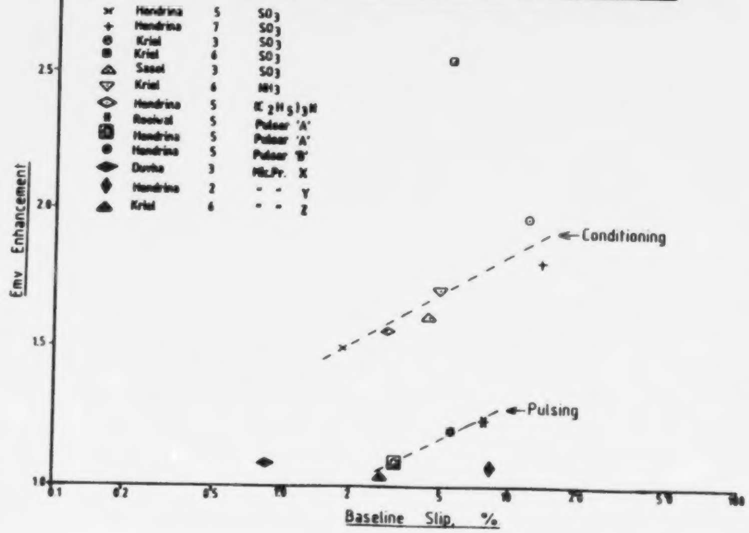

FIGURE 6. VOLTAGE-CURRENT CHARACTERISTICS

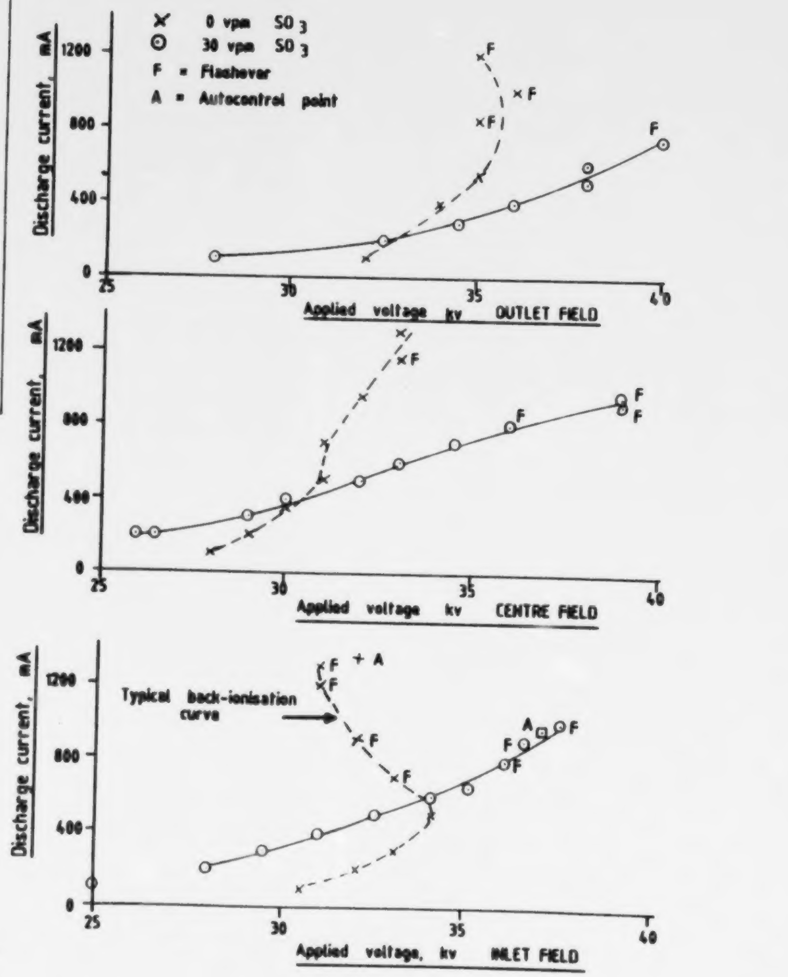

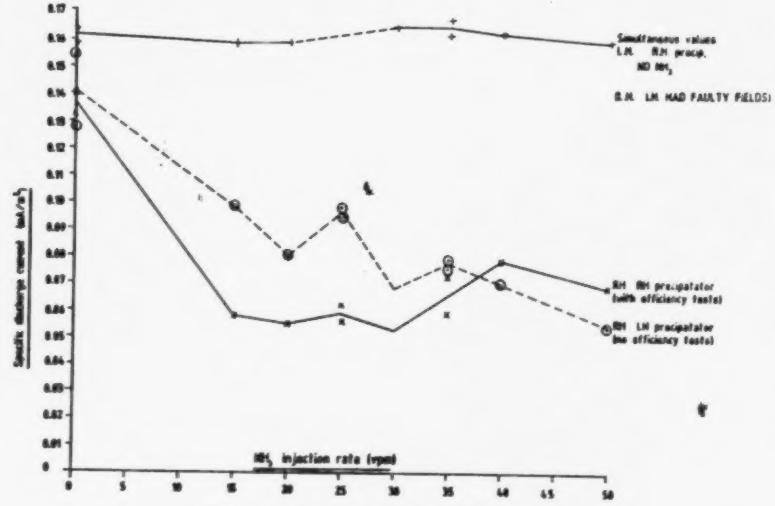

FIGURE 7 EFFECT OF INJECTION ON DISCHARGE CURRENT

FIGURE 8 EMV VERSUS SPECIFIC POWER

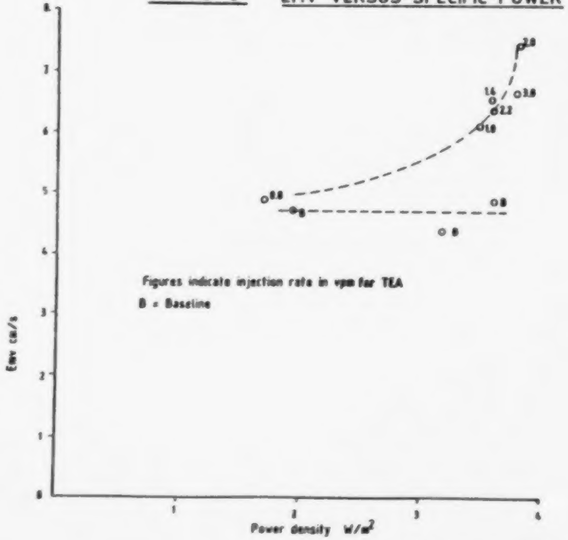

Figures indicate injection rate in vpm for TEA

B = Baseline

FIGURE 9 EFFICIENCY VERSUS SECONDARY VOLTAGE R.H. CASING ROOIWAL

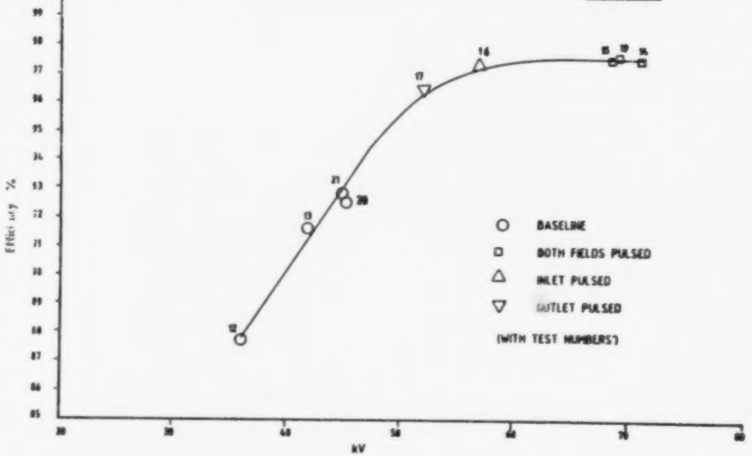

KRIEL 3

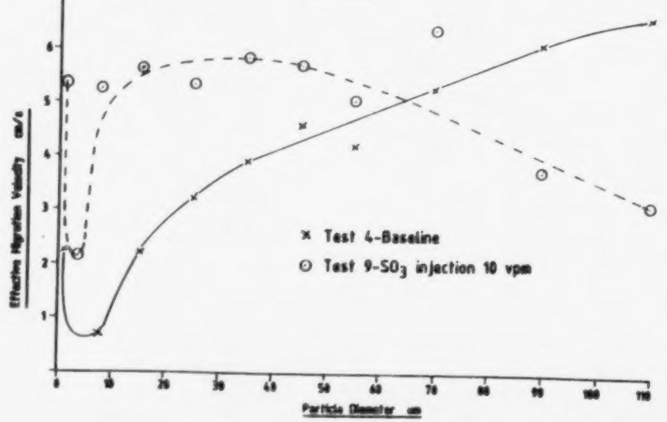

FIGURE 10 EFFECT OF INJECTION ON PARTICLE MIGRATION VEL.

Reproduced from best available copy.

BALTIMORE GAS & ELECTRIC EXPERIENCE WITH COMBINED SO_3/NH_3 INJECTION FOR PRECIPITATOR PERFORMANCE IMPROVEMENT

by: W. E. Cummings, Jr.
Wahlco, Inc.
Santa Ana, California 92704

W. H. Reamy
Baltimore Gas & Electric Company
Baltimore, Maryland 21203

ABSTRACT

Unit 3 of the H. A. Wagner Station built in 1966, is rated at 330 Mw gross, with a marginally sized electrostatic precipitator. When burning Eastern U.S. low sulfur coal, following a balanced draft conversion, a major load reduction was necessary to meet particulate emission limits. This paper describes the precipitator efficiency improvement obtained with sulfur trioxide alone, and with the subsequent highly effective addition of ammonia into the flue gas.

INTRODUCTION

This is a case history of the implementation of sulfur trioxide and ammonia-based gas conditioning systems installed at Baltimore Gas & Electric Company's H. A. Wagner Station, Unit 3. This unit consists of one supercritical, universal pressure, opposed fired steam generator manufactured by Babcock & Wilcox, Inc. The unit has a rated capacity of 330 Mw with a steam flow of 2,200,000 lbs/hr at 3605 psig. The boiler is equipped with one single chamber, four field, cold-side weighted-wire electrostatic precipitator (ESP), which was designed to maintain compliance with the State of Maryland emission requirements of 0.03 grains of particulate per dry standard cubic feet (gr/dscf) of flue gas when treating 900,000 cfm of flue gas with an inlet burden of 2.08 gr/cf and an average coal sulfur content of 3.0%. Following initial operation in 1966, compliance was demonstrated with the 188 specific collection area (SCA) precipitator achieving 99% collection efficiency.

In 1972, a change in the State of Maryland emission requirements necessitated a change in fuel chemistry from a sulfur content of 3.0% average to 1.0% maximum. A typical fuel analysis is detailed in Table 1. Emission compliance with this required fuel change coupled with the aging condition of the precipitator and the effects of balanced draft conversion required an operational boiler de-rating of 50 Mw, 15% of the units total capability.

To maintain emission compliance and recoup this lost generation, Baltimore Gas & Electric Company (BG&E) undertook exhaustive studies to determine feasible precipitator upgrade options. Table 2 details the upgrades and modifications implemented to enhance the mechanical/electrical condition of the unit. For all intents and purposes, BG&E has carefully and systematically insured that the precipitator was upgraded and maintained appropriately at its maximum physical capability. The balance of the text addresses the application and implementation of flue gas conditioning.

FLUE GAS CONDITIONING

Flue gas conditioning was first utilized in 1976 with the installation of a proprietary additive system. This system utilized an aqueous solution of ammonium sulfate as a means of controlling fly ash resistivity and particle cohesivity. This system enabled the boiler to demonstrate compliance at full load (330 Mw), however, continuous operation remained marginal, primarily due to the precipitators continuing low level of power input.

Following the balanced draft conversion, the performance of the precipitator diminished significantly. The change in draft conditions severely affected the ESP through an increase in the flue gas volume and a consequent increase of the precipitator gas velocity. Table 3 details the precipitator and process parameters before and after conversion. The proprietary additive system was modified to employ two dedicated additives. One injected upstream of the air pre-heater to control resistivity and one downstream of the air pre-heater to enhance particle agglomeration. Although generally recognized as being successful in controlling ash resistivity, emissions testing at full load did not indicate compliance operation (0.030 gr/dscf @ 50% excess air). In June of 1982, a reduction in net load to 270 Mw (283 gross) was necessary to continuously maintain emission compliance. At this operating level, particulate emission compliance was routinely achieved, however, the chemical feed rates necessary to do so were at the maximum levels allowed to avoid recombination and pluggage problems.

In 1983, the proprietary system was replaced with a Wahlco, Inc. SO_3 flue gas conditioning system. This decision was based on three factors:

1. Fly ash resistivity was viewed as the principle parameter affecting the precipitators inability to operate close to rated power.
2. Agglomerating agents, if required, could be added later.
3. The evaluated cost of the SO_3 conditioning system was equivalent to the cost of the proprietary systems (Table 4).

SULFUR BURNER OPERATION

The Wahlco system (Figure 1) utilizes a molten sulfur feed stock which is pumped via chemical proportioning pumps to a burner/converter chamber. Air as a carrier gas is passed through a series of duct heaters and elevated in temperature to 800°F. The heated air and sulfur are introduced into the burner/converter where combustion of the sulfur takes place and the molten sulfur is converted to SO_2. The SO_2 gas passes through a vanadium pentoxide catalyst bed where it is converted to SO_3. The 96% air/4% SO_3 mixture is transported to the point of injection through an insulated stainless steel manifold system. There SO_3 is introduced into the flue gas at approximately 700°F.

The injected SO_3 immediately combines with the available flue gas moisture and condenses on the surface of the ash particles as sulfuric acid (H_2SO_4). The sulfuric acid coating is highly effective in modifying the surface electrical conductivity of the ash to lower the apparent resistivity. Fly ash resistivities in the range of 10^9 - 10^{11} ohm/cm are generally recognized as optimum values for effective precipitation.

RESULTS

Following the initial operation of the sulfur burning system, the electrostatic precipitator power level improvement indicated that the resistivity of the H. A. Wagner Station, Unit 3 ash was indeed within the good operating range. The overall emissions, although in compliance at 283 Mw gross, were not significantly improved. Evaluation of the system operation at this point revealed that although the resistivity was effectively controlled, rapping losses were significantly contributing to the total emissions and that cohesive agents would be required.

AMMONIA CONDITIONING

In May of 1985, an anhydrous ammonia-based conditioning system was installed. This system was selected on the basis of ammonia's historical record as a cohesive agent and the ease of system installation and operation.

The ammonia conditioning system (Figure 2) utilizes agricultural grade anhydrous ammonia as a feed stock material. The ammonia (NH_3) is transported and stored under pressure in liquid form. The liquid NH_3 is pressure fed to a vaporizer vessel where it is maintained by immersion heaters at 40°F to produce 60 psig vapor. The 100% concentrated vapor is then pressure fed to a blower skid where it is intermixed with air as a carrier gas at a 96% air to 4% NH_3 concentration. The combined mixture is then transported (at approximately 2 psig) to the injection point downstream of the air preheater.

RESULTS

Prior to injection of NH_3, the station remained load limited due to emissions at 283 Mw gross with a 20% maximum opacity on a six minute average. Opacity spiking due to rapping losses constituted a large part of the total opacity (Figure 3).

Immediately preceding NH_3 injection, the SO_3 system feed rate was increased to pre-condition the precipitator. Additionally, a rapper sequence change was made extending the overall round trip time in an attempt to create a natural plate ash deposit to embed any sub-micron ammonia bisulfate, should it be created. Initial NH_3 injection commenced on May 14, 1985, with SO_3/NH_3 feed rates of 12 ppm and 7 ppm respectively. The initial response was a sharp increase in opacity followed by a slow, steady decline. This was interpreted as an increase in the quantity of sub-micron particles which affected the space charge characteristics of the first electrical field, causing an initial voltage increase and subsequent rise in field sparking. Seventy-two hours following the NH_3 addition, the opacity baseline had decreased to 7% and the rapping spikes were virtually eliminated (Figure 4).

On May 20, 1985, preliminary emission testing indicated that at 283 Mw gross the emissions were less than the requirement of 0.03 gr/dscf. Initial state compliance tests at this operating level indicated the emissions were on average 0.0217 gr/dscf.

On July 10 through July 12, 1985, a total of eleven emission tests were conducted at loads ranging from 312 to 320 Mw gross. The SO_3/NH_3 feed rates had been optimized to 12 ppm and 8-10 ppm respectively. The particulate emissions approached compliance levels, 0.0290 gr/dscf @ 50% excess air, at an increased gross generation level of 315 Mw. Compared to the previously experienced output of 283 Mw gross, an overall increase of the station output of 10% (32 Mw) was achieved.

The station is currently operating on a continuing basis (compliance tested) at 305 Mw gross and 12% opacity.

DISCUSSION

The significance of this program is not in the use of SO_3 and NH_3 as conditioning agents. These compounds have been utilized as conditioning agents since the inception of the conditioning industry. The significance here is that these compounds were delivered in such a fashion that independent control of the stoichiometry was achieved. Use of ammonium sulfate, ammonium bisulfate, or sulfamic acid for combined resistivity and cohesivity modification is subject to the natural disassociation of each chemical. Typically, the proportions of these chemicals through natural disassociation are incorrect for obtaining the best combination for precipitator performance enhancement. This program achieved direct control of the specific chemical compounds necessary for optimization of electrostatic precipitator performance.

ACKNOWLEDGMENTS

The authors wish to thank BG&E's excellent engineering and operating staff for their assistance and cooperation.

The work described in this paper was not funded by the U.S. Environmental Protection Agency and therefore the contents do not necessarily reflect the views of the Agency and no official endorsement should be inferred.

ENDNOTES

1. Baltimore Gas & Electric Company Particulate Emissions and Precipitator Diagnostic Test Program, H. A. Wagner Station, Unit 3, 1981. Unpublished report by KVB, Inc.

2. Baltimore Gas & Electric Company Particulate Emissions Test Program, H. A. Wagner, Unit 3, 1982. Unpublished report by KVB, Inc.

3. Baltimore Gas & Electric Company Particulate Emissions Test Report, H. A. Wagner, Unit 3, 1983. Unpublished report by KVB, Inc.

4. Baltimore Gas & Electric Company Particulate Emissions Tests - Additive Evaluation, H. A. Wagner, Unit 3, April 1983. Unpublished report by KVB, Inc.

5. Baltimore Gas & Electric Company Particulate Emissions Test Program, H. A. Wagner, Unit 3, 1983. Unpublished report by KVB, Inc.

6. Baltimore Gas & Electric Company, H. A. Wagner, Unit 3, Preliminary Particulate Testing, August, 1985. Unpublished report by ESS Environmental Source Samplers.

7. Baltimore Gas & Electric Company, H. A. Wagner, Unit 3, Electrostatic Precipitator Recommendations, August 1985. Internal communication by N. G. Lassahn, Jr.

8. Experience in Conditioning Electrostatic Precipitators in the United States, E. L. Coe, Jr., Wahlco, Inc., J. S. Lagarias, Lagarias Associates. Paper for IUPPA Conference, Sydney, Australia, August, 1986.

TABLE 1. TYPICAL CURRENT STATION FUEL AND ASH ANALYSIS

Coal Analysis	Percentage
Moisture	4.0%
Volatile	33.2%
Fixed Carbon	54.6%
Ash	8.2%
Sulfur	0.8%
Higher Heating Value (BTU/lb)	13,437

Ash Analysis	Percentage
SIO_2	57.00%
Al_2O_3	28.00%
Fe_2O_3	7.00%
TiO_2	1.3%
CaO	2.5%
M_gO	1.0%
Na_2O	0.5%
K_2O	1.7%
SO_3	0.5%

TYPICAL CURRENT STATION FUEL AND ASH ANALYSIS

TABLE 2. MAJOR PRECIPITATOR MODIFICATIONS 1974-1983

Year	Modifications
1974	Replacement of linear reactors, installation of an additional transformer recitifier to split the first field, substitution of high intensity impact rappers for the first field collection electrodes and installation of additional gas baffles.
1975	Substitution of high intensity impact rappers on the remaining collection electrode system.
1980	The unit was essentially rebuilt as part of a balanced draft conversion. The re-build included replacement of a substantial number of the collection electrode support rods, addition of internal support steel, re-alignment of the majority of the collection electrodes and an upgrade of the automatic voltage control hardware.
1981	75% replacement of the discharge electrode rapping system with impulse / impact rapping.
1983	Installation of thyristor-based control system coupled with a solid state sensor system and retrofit of rapper controls with solid state microprocessor control.

TABLE 3. PRECIPITATOR OPERATING DATA - TYPICAL

	Initial Design	Post Balanced Draft Conversion
Gas Volume acfm	900,000	990,000
Gas Temperature ^{0}F	274	315
Particulate Loading gr/acf	2.08	3.4
Gas Velocity FPS	7.64	8.4
Treatment Time (sec.)	4.71	4.3
SCA Ft^{2}/1000 acfm	188	171
Efficiency %	99.0	98
Power Levels KVA (primary)	-----	200

PRECIPITATOR OPERATING DATA - TYPICAL

TABLE 4. COMPARATIVE CONDITIONING COSTS

Supplier	**$/Ton of Coal Fired**
Proprietary No. 1	
Resistivity Modifier	$0.67
Cohesive Agent	0.66
Combination	$1.33
Proprietary No. 2	
Resistivity Modifier	$0.48
Cohesive Agent	0.53
Combination	$1.01
Proprietary No. 3	
Resistivity / Cohesive Agent	$0.50
Wahlco SO_3 System	
3 Year Lease	$0.61
7 Year Lease	$0.39
Wahlco NH_3 System	
2 Year Lease	$0.28
3 Year Lease	$0.21
Combination Worse Case	$0.89

Figures include capital costs, operating costs, and maintenanc

COMPARATIVE CONDITIONING COSTS

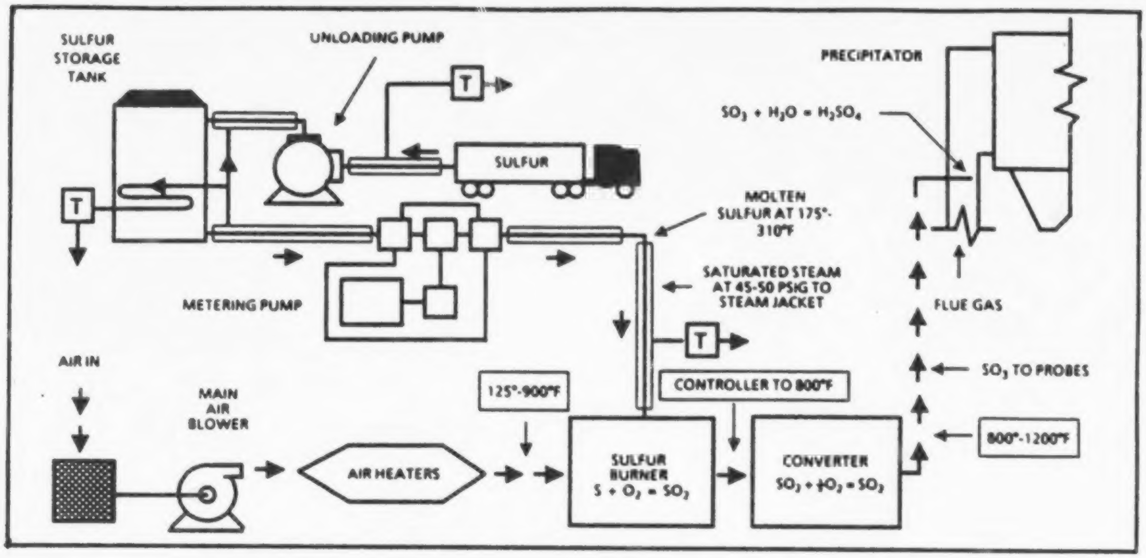

FIGURE 1: SCHEMATIC OF WAHLCO SO_3 CONDITIONING SYSTEM

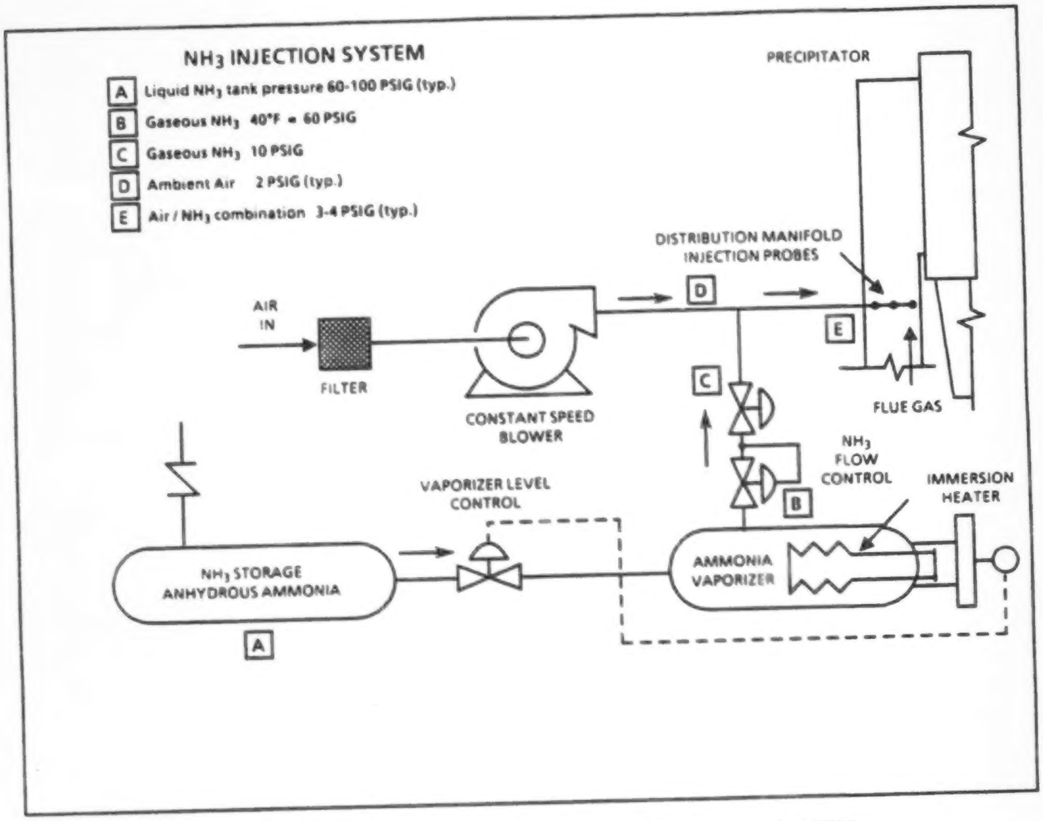
NH3 INJECTION SYSTEM
A Liquid NH3 tank pressure 60-100 PSIG (typ.)
B Gaseous NH3 40°F = 60 PSIG
C Gaseous NH3 10 PSIG
D Ambient Air 2 PSIG (typ.)
E Air / NH3 combination 3-4 PSIG (typ.)
PRECIPITATOR
DISTRIBUTION MANIFOLD INJECTION PROBES
D
E
AIR IN
FILTER
CONSTANT SPEED BLOWER
C
FLUE GAS
NH3 FLOW CONTROL
B
IMMERSION HEATER
VAPORIZER LEVEL CONTROL
NH3 STORAGE ANHYDROUS AMMONIA
A
AMMONIA VAPORIZER

FIGURE 2: SCHEMATIC OF WAHLCO NH3 CONDITIONING SYSTEM

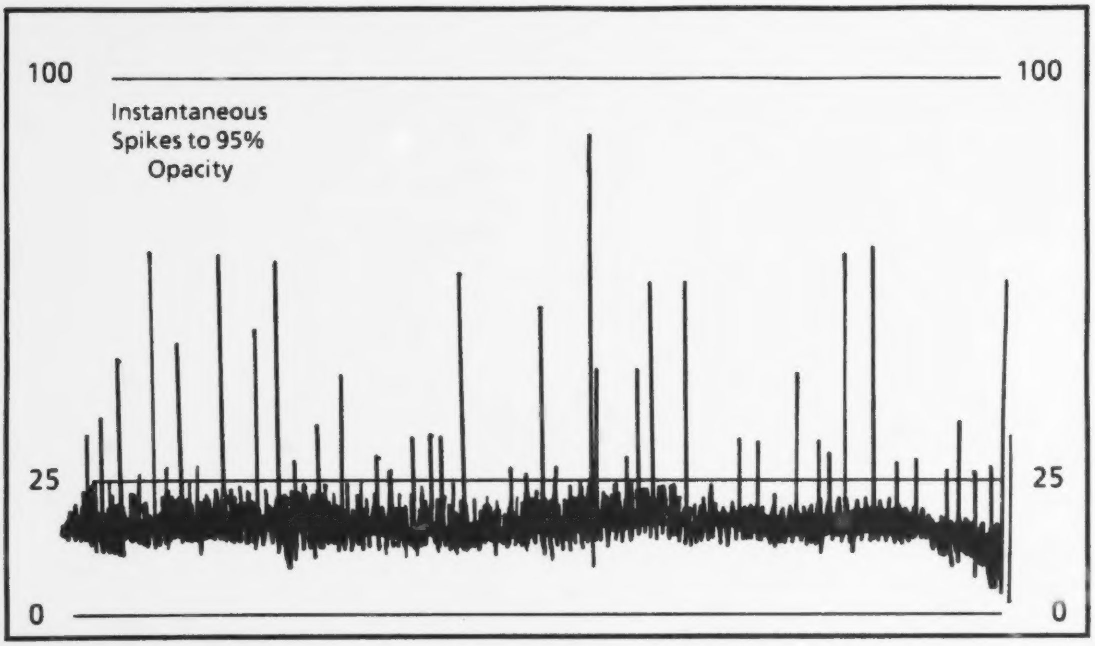

Date : 5/12/85

Load : 280 Mw. Gross

Opacity : 14% (6 min. average)

SO_3 : 5 ppmv

NH_3 : 0 ppmv

Figure 3. Pre-Ammonia Conditioning
Typical Opacity Trace H. A.. WAGNER NO. 3

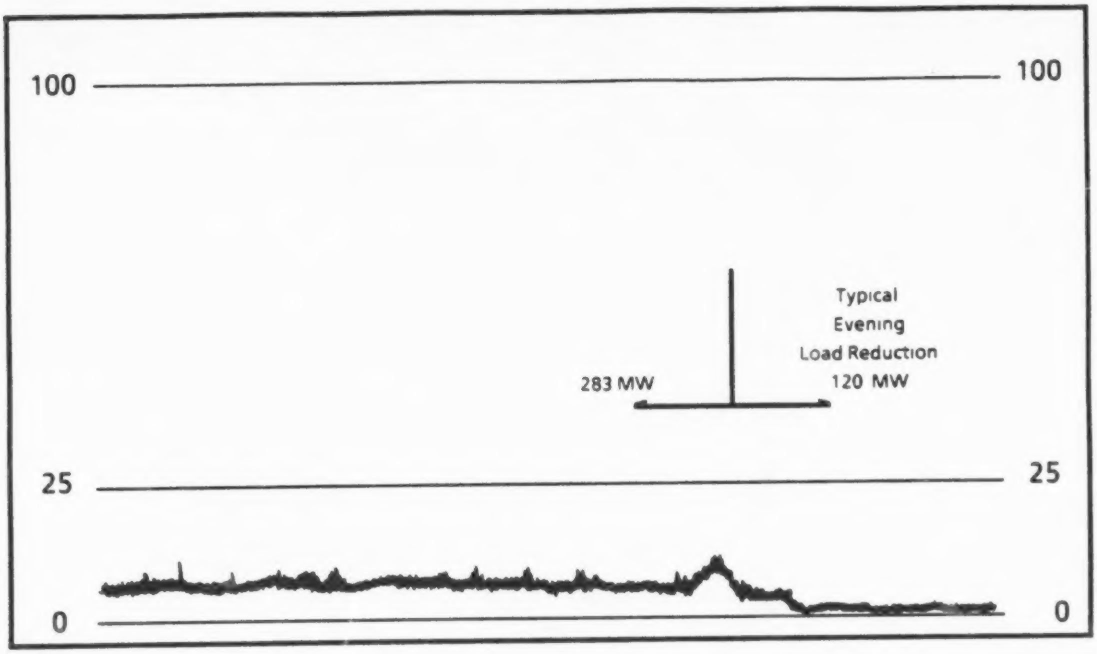

Date :	5/18/85	SO_3 :	12 ppm
Load :	283 Mw. Gross / 120 Gross	NH_3 :	7 ppm
Opacity :	7% (6 min. average) / 2% (6min. average)		

Figure 4. Post - Ammonia Conditioning
Typical Opacity Trace H. A.. WAGNER NO. 3

A DESIGN METHODOLOGY FOR OPTIMIZED WATER CONDITIONING OF HIGH RESISTIVITY FLY ASH

by: N.W. Frisch
N.W. Frisch Associates, Inc.
Kingston, NJ 08528

W.T. Hartshorn
Sonic Development Corporation
Parsippany, NJ 07054

ABSTRACT

A review of the literature on the effect of vapor phase moisture and temperature on the resistivity of particulate matter was made. Emphasis was directed to fly ash systems at temperature levels in the range of 125 to 200°C.

The sensitivity of ash resistivity to temperature and moisture was indicated for several sets of ashes and operating conditions. The general behavior of fly ashes was quantified in a design method which permits one to estimate the level of water injection required to achieve a desired reduction of resistivity. Performance benefits achievable by this technology may be directly estimated for an existing precipitator system.

Hardware considerations were discussed. The design method permits one to configure a nozzle system to attain complete, efficient and reliable humidification of gas streams in existing compact duct systems.

Examples are given of the level of benefits possible with this technology and also estimates of associated costs.

INTRODUCTION

Electrostatic precipitator performance is strongly influenced by the level of particulate resistivity. In fact ash resistivity is a prime variable which must be estimated in designing precipitators. Unfortunately a much too significant fraction of new ESPs fail to achieve their design performance and experience has shown that improper estimates of resistivity or optimistic sizings for a suitable resistivity level play an important role in these cases.

An owner faced with a malperforming precipitator needs to know the source(s) of performance losses before he moves to correct them. When ash resistivity is clearly higher that had been anticipated in the design of the unit, there are several possible upgrading approaches that may be investigated. These include ash conditioning, backfitting with an additional ESP or other emissions control device, modification of the electrical system including use of pulse energization as well as the exploration of alternate fuel sources including fuel blending. The costs associated with implementing these approaches and those related to plant downtime may vary considerably from plant to plant. Thus individual analysis of each situation is necessary.

Ash conditioning, by the use of SO_3, NH_3, water or other agents has been practiced mostly on an empirical basis in the past resulting in some failures. But as better knowledge of the chemistry of ash surfaces and also that of the interactions between these surfaces and the agents becomes available, it has become possible to apply more fundamental approaches to these situations.

This paper describes the development of a rational computer-based water conditioning methodology whose objectives include capability to assess the feasibility of reducing resistivity to an acceptable level consistent with operation within plant constraints. The latter, of course, may include the use of a specified fuel with an ESP of given SCA, configuration, rapping capability as well as an existing ductwork system which may restrict gas contact time upstream of the ESP.

LITERATURE REVIEW

The beneficial influence of gas phase moisture on ESP performance has been known for more than seventy years but quantification of some of these effects has occurred largely in the last forty. Sproull and Nakada (1) reported on the quantitative effects of moisture and temperature on the electrical resistivity of a number of dusts, including cement and various metal fumes. These effects were, in general, similar to those noted in Figure 1. Here it is observed that increasing levels of moisture, especially at cold-side conditions, resulted in a reduction in the resistivity level and also that resistivity can be lowered by raising or lowering temperature from that of a zone of maximum resistivity. Also evident is the fact that the temperature corresponding to the maximum resistivity value increases with increased moisture content of the gas.

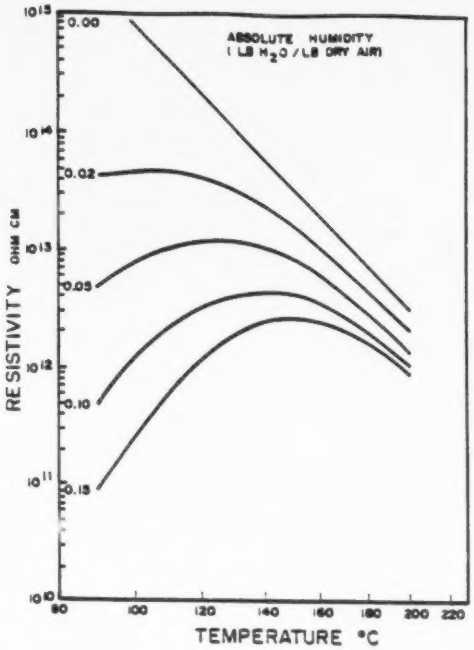

Figure 1 General Behavior of Fly Ash Resistivity with Respect to Temperature and Moisture Content of Gas.

Masuda (2,3,4) derived expressions for the influence of moisture and temperature on the conductivity of uniformly packed spherical particles. His analysis took into account the influence of both volume and surface conductivity; the effect of gas phase humidity was adequately represented by a multi-constant semitheoretical expression. Experimental measurements were conducted using glass, marble and cement particulate.

Busby and Darby (5) in a study of the role of coal properties in affecting ESP efficiency noted the benefits obtained with water conditioning using either water injection into the combustion chamber or atomization downstream of the air heater. Their results, using levels of 0.5-1.0 lb H_2O/1000 cu. ft. showed significant improvement in ESP performance; modified Deutsch migration velocity enhancements from 2.7 to 4.4 were achieved. Apparently, the field techniques available at that time were not sufficiently reliable to warrant permanent installation.

Maartmann (6) analyzed the effect of gas temperature and dew point on dust resistivity and thus on the performance of ESPs. His expression related the isothermal ratio of moist state- to dry state-resistivities to an exponential expression involving the dew point and gas temperatures. The data presented exhibited an excellent fit.

Sullivan (7) reported on techniques for characterizing fly ash based on the use of available fly ash samples, or in their absence, the use of a microfurnace facility to produce simulated ash samples from bore cores. The workers at ACIRL apparently were the first to standardize on a resistivity methodology which required the use of several (typically four) gas phase moisture levels.

Bickelhaupt (8) reported on the measurement of fly ash resistivity in the surface resistivity-controlling regime. This work indicated several species which influence fly ash surface conductivity.

McLean (9) produced an analysis of factors which affect the resistivity of a particulate layer in ESPs. His equation suggests that surface resistivity of a sample is proportional to exp(-Lp.exp(K/T)) where K and L are specific constants for the sample, T is absolute temperature and p is water vapor partial pressure.

In a later study, Bickelhaupt (10) reported on a procedure for predicting the resistivity of fly ash samples over wide temperature and gas phase moisture content ranges. Integrated within his procedure was the aforementioned McLean equation; Bickelhaupt's data did not exhibit a large range in the K and L parameters. Subsequently he (11) extended the method to accurately reflect the effect of sulfuric acid vapor on the surface resistivity of various classes of fly ash.

A joint USSR-US test program whose objective was to reduce fly ash resistivity by adding moisture to the gas and lowering temperature was reported (12). A centrifugal scrubber as well as a venturi scrubber was used to introduce the water. Resistivity reduction of one and two decades was accomplished by the use of the centrifugal scrubber or both scrubbers respectively. Back corona was completely eliminated with the use of two scrubbers but the extremely low resulting temperature (85°C) resulted in corrosion. (Initial gas temperature was 140°C).

ANALYSIS

Resistivity data of Sullivan (13) is shown on the preferred type of plot (Figure 2). Here log(resistivity) is plotted against reciprocal absolute temperature; the curve representing the bone-dry condition is a straight line. These results were produced at ACIRL in a study on the reproducibility of resistivity measurements conducted for EPRI. (The data shown represent the effect of moisture and temperature on resistivity in the absence of SO_3). In the U.S. it is customary to express the gas moisture content on a mol or volume basis but some prefer a mass ratio such as absolute humidity (lb H_2O/lb dry gas).

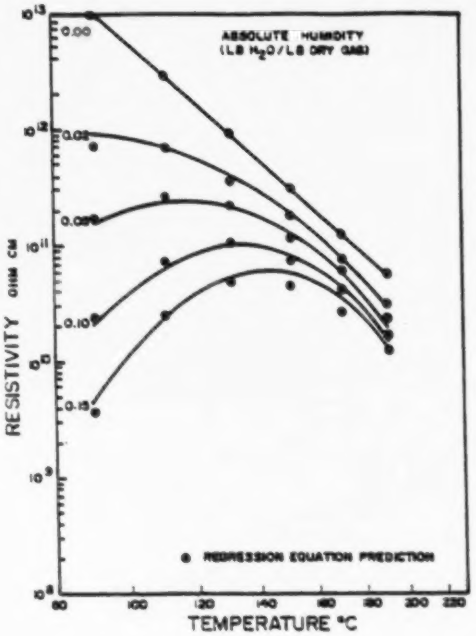

Figure 2 Resistivity Dependence on Gas Temperature and Moisture Content (13).

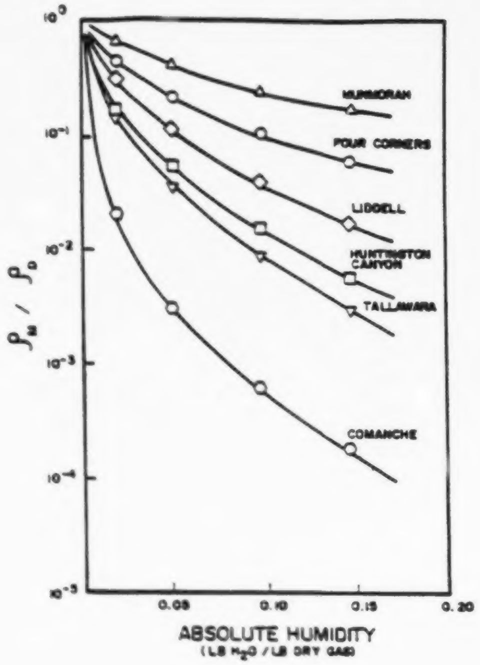

Figure 3 Range of Ash Resistivity Responses to Moisture at 130°C.

The response of resistivity to moisture is best quantified by reference to the bone-dry resistivity line. In this particular sample we note that the data are characteristic of an ash which exhibits a low resistivity response to added gas phase moisture. Figure 3 shows the range of responses exhibited at 130°C by the six samples of the Sullivan study. The depression of resistivity from the bone-dry level, with the molal humidity level m at least 0.032 moles H_2O/mole dry gas, can be represented by an equation of the form:

$$\rho_m/\rho_d = A \,.\, \exp\,(B.m) \qquad (1)$$

with

$$A = \delta + \varepsilon T + \zeta.B) \qquad (1a)$$

$$B = \alpha + \beta/T + \gamma/T^2 \qquad (1b)$$

Here ρ_m is the resistivity level at temperature T and molal humidity m, and ρ_d is the bone-dry resisitivity level at the same temperature. The constants α, β, γ, δ, ε and ζ are regression coefficients. The dependence of ρ_d upon temperature is simply expressed by the Rasch-Hinrichsen equation, namely:

$$\rho_d = A_o \exp\,(\Delta\, H/kT) \qquad (2)$$

where ΔH is the activation energy for conduction and k is the Boltzmann constant. On figure 2 we have reported (●) resistivity values calculated by the above relationships. It is clear that the fit is quite good.

Since we effect "moisture" conditioning by application of an adiabatic saturation process (see later) which results in a simultaneous change in gas moisture content and temperature, it is useful to examine resistivity changes on a t,m coordinate system. Figure 4 is a t,m plot which shows ρ_m contours. The high resistivity region coincides with the low temperature, low moisture content zone, namely B. For a system with an initial operating point O, adiabatic saturation will proceed along line OP. It is evident that major changes in resistivity are not to be expected with this ash unless very low temperatures or very high humidity levels are obtained.

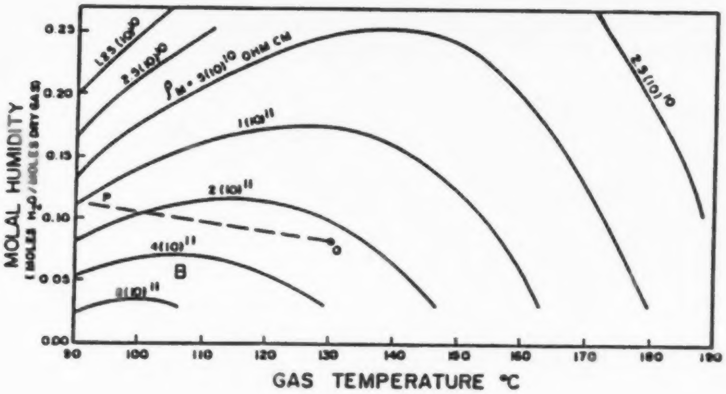

Figure 4 Contour Plot of Ash Resistivity Illustrating Adiabatic Saturation Process (unattractive situation).

It is of interest to quantify changes in resistivity resulting from conditioning. One sometimes refers, in a qualitative sense to the "moisture sensitivity" of ash resistivity but this appears to be a vague term. Actually we are interested in both the moisture and temperature sensitivity of ash resistivity; we present herewith our quantitative definitions and demonstrate their utility. Sensitivity of resistivity to moisture (or temperature or both) is related to the total derivatives of resistivity. Since resistivity of a specific ash is a function of both temperature and vapor phase moisture content we can write the total differential of resistivity as:

$$d\rho_m = \left[\frac{\partial \rho_m}{\partial m}\right] \cdot dm + \left[\frac{\partial \rho_m}{\partial T}\right] \cdot dT \qquad (3)$$

Thus the change in resistivity is related to the partial derivatives of resistivity with respect to temperature and moisture as well as the magnitude of the changes effected in the latter variables by the conditioning process. The relative resistivity sensitivity is conveniently referenced to the resistivity level. Thus we express the relative resistivity sensitivity level as:

$$\left[\frac{d\rho_m}{dT}\right] / \rho_m = 1/\rho_m \left[\left[\frac{\partial \rho_m}{\partial m}\right] \cdot \frac{dm}{dT} + \left[\frac{\partial \rho_m}{\partial T}\right]\right] \qquad (4)$$

Note that since we have referenced resistivity sensitivity to resistivity level, we can write for relatively constant resistivity sensitivity, the simple expression, in terms of temperature change:

$$\rho_f/\rho_i = \exp\ [\text{-Relative resistivity sensitivity} \times (T_i - T_f)] \qquad (5)$$

where f and i designate the final and initial states. Thus an average relative sensitivity of 0.046 $(\text{degree})^{-1}$ with respect to temperature is necessary to effect a two order of magnitude reduction of resistivity within a 100° range.

For isothermal and isohumidity conditions, the relative resistivity sensitivity based on equation (1) becomes respectively:

$$\left[\frac{\partial \rho_m}{dm}\right]_T / \rho_m = \alpha + \beta/T + \gamma/T^2 \qquad (6a)$$

$$\left[\frac{\partial \rho_m}{dT}\right]_m / \rho_m = \Big[- \Delta H/\ R.T^2 + (\varepsilon - \zeta.\beta/T^2 - 2.\zeta.\gamma/T^3)/ (\gamma + \varepsilon.T + \zeta\ (\alpha + \beta/T + \gamma/T^2)) - (\beta/T^2 + 2.\gamma/T^3)m\Big] \qquad (6b)$$

For adiabatic saturation conditions, the slope of the operating line is given by:

$$\frac{dm}{dT} = -c_p/\lambda \qquad (7)$$

where c_p is the molal heat capacity of the gas stream and is the heat of vaporization of water. The relative resistivity sensitivity of an ash exposed to an adiabatic saturation process is conveniently referenced to a unit temperature change. Hence

$$\left[\frac{\partial \rho_m}{dT}\right]_s / \rho_m = 1/\rho_m \cdot \left[-\left[\frac{\partial \rho_m}{\partial m}\right] . c_p/\lambda + \left[\frac{\partial \rho_m}{\partial T}\right]\right] \qquad (8)$$

Referring back to figure 4, at a local condition of 130°C and a molal humidity of 0.081, the relative resisitivity sensitivities are as follows:

$$\left[\frac{\partial \rho_m}{dm}\right]_T / \rho_m = 1/\rho_m = -9.39/\text{molal humidity}$$

$$\left[\frac{\partial \rho_m}{dT}\right]_m / \rho_m = -0.0247/K$$

$$\left[\frac{\partial \rho_m}{dT}\right]_s / \rho_m = -0.0179/K$$

Thus a 1° C decrease in temperature at fixed moisture content would, in this case, increase the resistivity level about 2.5%, while under adiabatic saturation conditions the increase is somewhat less, about 1.8%. The effect of increasing moisture content amounts to about a 9% reduction in ash resistivity for each 0.01 increase in molal humidity. As adiabatic saturation would proceed to lower temperatures, resistivity would begin to fall, but this situation would require very low temperatures. Clearly this is not a case for adiabatic cooling; even direct low pressure steam addition would be more effective.

A more attractive situation is evident here for a low sulfur coal which yields an ash with resistivity level of 1.9(10)^{12} ohm cm at 374°F (190°C). On figure 5, a contour plot of resistivity, with temperature-molal humidity coordinates, it is evident that water injection can reduce resistivity more than two orders of magnitude by dropping temperature to 260°F (127°C). This would require the injection of 0.14 gallons of water per 1000 cubic feet of gas.

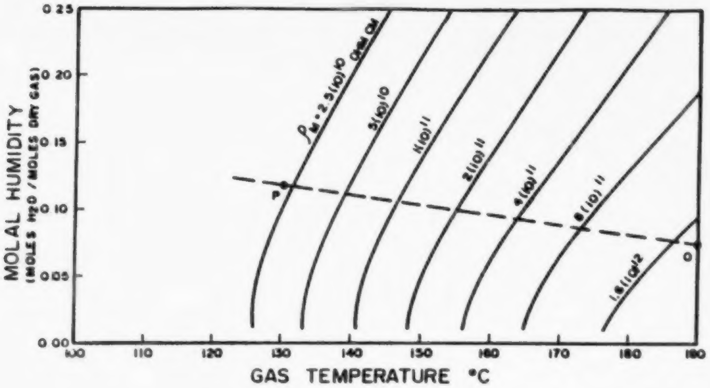

Figure 5 Contour Plot of Ash Resistivity Illustrating Adiabatic Saturation Process (attractive situation).

The relative resistivity sensitivity for the original condition, measured along the adiabatic saturation path is:

$$\left[\frac{d\rho_m}{dT}\right]_s / \rho_m = +0.035/K$$

Note here the sensitivity is positive, indicating that reducing temperature will result in lower resistivity levels. Also as temperature is reduced the sensitivity values increases rapidly; at 130° C the value has increased three fold to 0.10. In the previous situation the limited operating temperature range precluded taking advantage of the potential of water conditioning.

The effect of water conditioning on ESP performance for the figure 5 situation was estimated. The basis of these calculations was that the precipitator had been placed in satisfactory mechanical condition and was achieving 96.7% collection efficiency at the original design temperature. The results are shown in figure 6. By cooling to the 260° F level, resistivity will approach 1.4(10)^{10} ohm cm; emissions were estimated to be reduced to 14.8% of former levels. Similar estimates were made for the entire temperature range of 230 to 374° F. We have also shown the predicted acid dew point temperature for all operating temperature levels. The dew point approaches the operating temperature at about 235° F.

Two procedures were used to estimate the benefits which would be derived in the previous case had the precipitator not been upgraded mechanically. Both sets of results fell in a narrow band (figure 6); the performance benefits to be derived in such a situation are minimal in spite of the significant reduction in resistivity that can be achieved.

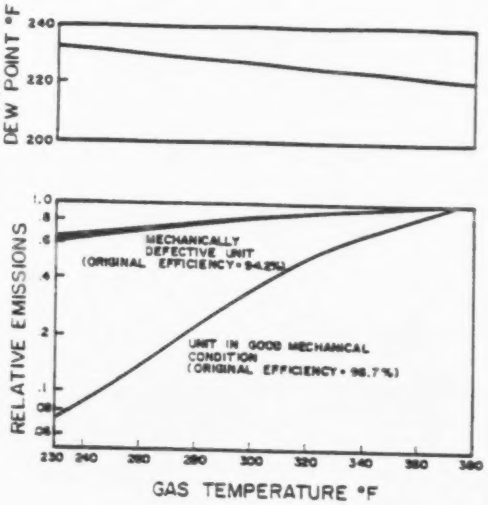

Figure 6 Predicted Dewpoint for Water Conditioning of Fly Ash (Figure 5 case) as a function of Outlet Gas Temperature.

MECHANISMS

The behavior of fly ash in an H_2O-containing environment may be best understood by reference to the appreciable glass literature on the subject. (As early as 1830 Faraday (14) recognized that the high adsorptive capacity of some glasses for water was related to the presence of alkali). We can summarize some important findings on the behavior of glasses in the following qualitative statements:

- The quantity of moisture adsorbed under a fixed set of conditions (humidity level, glass particle size, temperature etc.) is strongly related to the nature of the glass and the character of the surface. Silica-rich glasses, with low alkali content adsorb very small quantities compared to soda-flint glasses (with a 20% Na_2O content).
- Rates of adsorption roughly parallel the equilibrium extent of adsorption when glass particles of the same surface area are considered.
- Silica is largely insoluble in water below temperatures on the order of 250^oC (482^oF) but low temperature attack occurs in the presence of alkaline species such as Na_2O. The first step in the solubilization is the exehange of hydrogen ions from water for Na^+ at the glass surface, resulting in the formation of sodium hydroxide. The occurrence of lime and certain other oxides will reduce the ionic mobility of sodium ions as well as the overall solubility level.

- Razouk and Salem (15) found that the adsorption of water on a 12.5% Na_2O-70.9% SiO_2 glass followed a type II BET isotherm supporting the view of physical adsorption.

- In a study of the hydrophobicity of silica powder, Anderson and Kimpton (16) showed that adsorption did not occur below a certain critical partial pressure of water, which is greater the higher the temperature.

- Glasses rich in alumina can possess a glassy structure in which there is a deficiency of sodium-oxygen bonds, resulting in a serious reduction in the hydrogen-sodium exchange reaction, and subsequent hydroxide formation.

We have examined the water adsorption and also the electrical resistivity data of Pike and Hubbard (17) who exposed samples of powdered glasses to high humidity air. Our analysis led us to figure 7 which demonstrates a rather unique relationship between the conductivity of the exposed glass particulate and the specific adsorption of water. It is likely that an effective sodium level, largely determined by the actual sodium concentration and the presence of divalent species (calcium, barium, lead and zinc in the present instance) controls both the extent of water uptake and glass conductivity.

Awakuni and Calderwood (18) demonstrated that water is physically adsorbed on quartz at room temperature in accordance with a type II BET adsorption isotherm. Surface conductance is low, increasing significantly at relative humidities greater than about 55%. In terms of monolayer adsorption, the increased conductivity coincides with completion of the first monolayer (figure 8). These authors related the increased conductivity response to humidity to the existence of mobile water molecules on the surface after the completion of the first monolayer.

For cold-side temperature ESP situations, Bickelhaupt has reported (11) the quantitative effect of SO_3 adsorption on the resistivity of fly ash surfaces. The extent of adsorption increases with higher moisture level and especially with lower temperature at fixed SO_3 concentration. Figure 9, our calculated equilibrium data for the system H_2SO_4-H_2O-Air shows, via the dotted line AB, the adiabatic saturation process for a particular installation. (The specific path at the elevated temperature is not precisely known because of the lack of equilibrium data in that region). Nevertheless it is apparent that the lowering of the equilibrium partial pressure of the acid is nearly exclusively due to the reduction of temperature and not to the increase in gas phase moisture content. Here about four orders of magnitude reduction in acid equilibrium partial pressure are achieved due to reduction in temperature; the extent due to moisture increase appears to be only within a factor of 2 or 3.

Strongly reduced equilibrium H_2SO_4 partial pressure was shown by Frisch (19) to result in operation at an appreciably higher approach to saturation of acid in the gas phase (figure 10); this would enhance the extent of acid adsorption (and resistivity reduction).

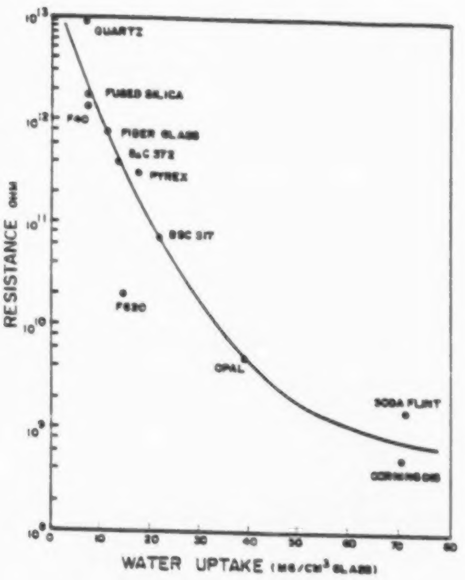

Figure 7 Relationship of Glass Resistivity and Extent of Water Adsorption.

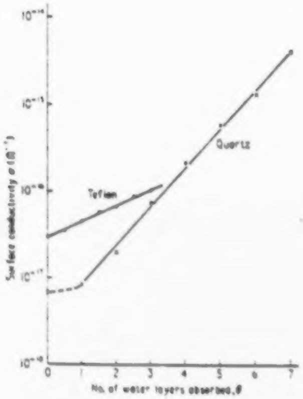

Figure 8 Surface Conductivity of Quartz and Teflon as a Function of Number of Adsorbed Water Layers (18)

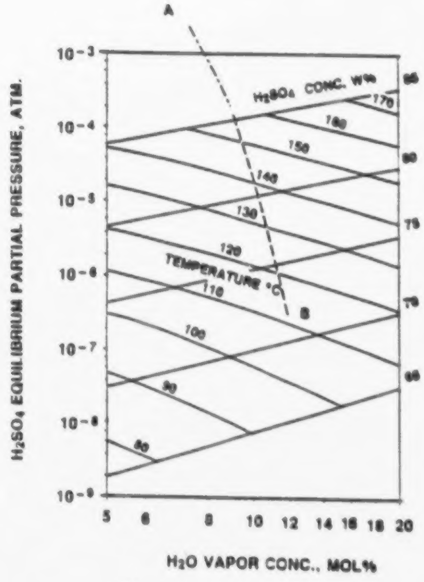

Figure 9 Adiabatic Saturation Path as Depicted on H_2SO_4-H_2O-Air Equilibrium Diagram (18).

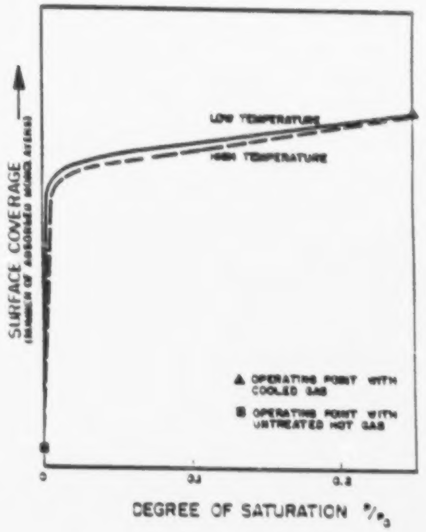

Figure 10 Comparison of H_2SO_4 Uptake by Ash Surface at Normal and at Water Conditioned State.

DESIGN METHODOLOGY

The basis for the programs was a modified Bickelhaupt approach coupled with appropriate use of mass and heat balances. Integrated into the programs were regression equations which relate to the performance of ESPs. The programs were written in a most convenient form for use by application engineers; input is generally from the keyboard but previously prepared data files may be recalled, updated and also may serve as a basis for current calculations. A series of up to 10 CRT screens are automatically presented by the program; the sequence of screens is determined by the user's various inputs which can be classified into fourteen possible cases. Figure 11 shows several of these screens. Many checks are built into the programs to reject inconsistent or conflicting data, or attempts at calculations in forbidden regions. Safeguards are incorporated to prevent the programs from "bombing out" when improper inputs are received. Similarly files can not be easily lost or unintentionally overwritten. A complete report summary is printed by the program.

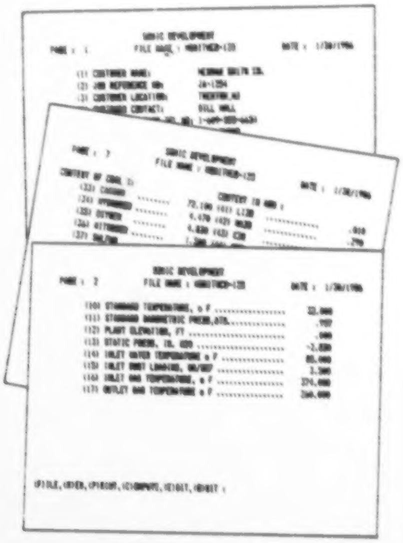

Figure 11   View of Several CRT Input Screens

While the basic program was designed to estimate resistivity reduction of fly ash occurring during an adiabatic cooling process, the program is also useful for simple cases of gas cooling. Data inputs are acceptable in a variety of forms; for example gas composition may be on a volume or weight basis, or may be based on the combustion of a fuel whose ultimate analysis is given; gas flow rates may be expressed on a mass, volumetric (actual or standard) or in the case of fuel firing, in terms of fuel rate. Regardless of the nature of the input data form, all pertinent input and output parameters are calculated and presented in a hard copy summary.

Heat balances use specific heat equations developed for gaseous species of interest. The enthalpy properties of water are well represented. The response of ash resistivity to adiabatic cooling is calculated for any desirable outlet temperature above the acid dew point. The acid dew point is an output of the program. In the absence of SO_3 in the gas, water dew points are presented.

When one desires to examine a complete database of coal and ash properties such as those for core boring in a new coal field, it is preferable to use the current version of our COALMASTER program which is capable of examining such data and to size ESPs for each sample for mass or opacity limitations for a variety of operating modes (water or SO_3 conditioning, pulse energization, etc.).

The program accepts various duct configurations (horizontal, vertical - up or downflow), descriptions of effective duct lengths, duct cross-sections, and gas velocities and for selected nozzle types, calculates feasible nozzle arrangements compatible with complete evaporation of the injected water. The basis for these calculations is knowledge of the size distribution of droplets produced by each nozzle under the required operating conditions. The output also lists the number of each type of nozzle needed, the required air flow and air pressure, the required system horsepower as well as the preferred nozzle spacing. Figure 12 shows an extract from the program print-out indicating some acceptable nozzle selections.

```
                                SYSTEM PARAMETERS

Gas  Flow  Gas Temp F   Water Flow  Duct Configuration   Gas Velocity   Emiss
Rate ACFM  Inlet Outlet    GPM      A  x B  x H ft- Dir      ft/s       Factor
---------  ----- ------    ---      ---- ---- ----- ----     ----       ------

  352,000   335   265      32.2     11.  12.  25.    D       44.4        0.30

                                NOZZLE SELECTIONS


Nozzle Type   No. of Nozzles   Spacing     Air Flow    Air Pressure     Power (Act)
-----------   --------------    inch         SCFM         PSIG             HP
                                ----         ----         ----             --

  SI - 47          190           8.3         1520          70.             300

  SI - 33          100          10.2         1500          70.             300
```

Figure 12 Example of Nozzles Selection Printout.

HARDWARE SYSTEM CONSIDERATIONS

Gas cooling by use of an evaporative technique offers several important potential benefits, including a) reduced gas flow rates and consequently the need for smaller, less costly downstream equipment, b) use of less costly materials of construction, c) reduced equipment maintenance and extended equipment life, d) possible higher production rates, e) higher collection efficiencies for existing downstream collector due to longer retention times, and f) significant advantages of severely reduced ash resistivity. However these benefits can be negated by inability to consistently and reliably achieve the desired temperature level without water carryover.

A study of water droplet evaporation was undertaken by SONIC in the past (20); the rate of evaporation over the inlet temperature range of 150 to 2500^{0}F was studied via a computer modeling approach. Figure 13, a print-out selected from an extensive set of data, shows the droplet distribution after a specific evaporation time. Such variables as inlet and outlet temperatures as well as the concentration of water vapor were explored; based on this output data it is possible to size cooling sections to provide sufficient residence time for complete evaporation. The importance of designing for complete evaporation of the largest water droplets became most evident from this study. Thus when one is constrained to conduct the evaporation in existing ductwork it becomes most critical to provide fine and uniform droplets.

```
                    SONICORE EVAPORATIVE COOLING PROGRAM

DROPLET          PERCENT          NUMBER OF          PERCENT
DIAMETER,        BY WEIGHT        DROPLETS           BY NUMBER
MICRONS

  3.83             0.69          0.52534E+09          85.32
  8.81             0.47          0.29493E+08           4.79
 13.54             0.54          0.93987E+07           1.53
 18.21             1.57          0.11130E+08           1.81
 22.85             2.33          0.83698E+07           1.36
 27.47             2.63          0.75025E+07           1.22
 32.09             2.55          0.33098E+07           0.54
 36.70             4.79          0.41564E+07           0.68
 41.31             5.47          0.33283E+07           0.54
 45.92             5.65          0.25020E+07           0.41
 50.53            11.12          0.36961E+07           0.60
 55.14            11.28          0.28856E+07           0.47
 63.14             7.33          0.12480E+07           0.20
 67.95             6.08          0.83104E+06           0.13
 76.95             8.96          0.84289E+06           0.14
 81.56            10.59          0.83743E+06           0.14
 90.96             7.31          0.41634E+06           0.07
 99.96             9.65          0.41428E+06           0.07

ORIGINAL GAS FLOW RATE                                120.0     CFM
GAS FLOW RATE AT THIS TIME                            119.7     CFM
GAS TEMPERATURE                                      1133.1   DEG F
GAS VELOCITY                                           19.9  FT/SEC
TOTAL DISTANCE TRAVELED                              0.0020      FT
TOTAL TIME FROM POINT OF INJECTION                    0.0001    SEC

WATER INJECTION RATE-60 F                              2.16     GPM
ORIGINAL WATER IN ELEMENT                          0.005000     LBS
AMOUNT OF WATER EVAPORATED                          0.000052     LBS
AMOUNT OF WATER REMAINING                           0.004948     LBS
PERCENT WATER VAPOR IN GAS                             0.01
THERMAL CONDUCTIVITY OF GAS                       0.0274  BTU/HR-FT-F
```

Reproduced from best available copy.

Figure 13 Sample Output of SONIC Droplet Evaporation Program

Effective gas cooling depends upon the use of atomizing nozzles which are capable of producing these fine liquid droplets (maximum droplet size in the range of 30-60 microns) over a wide flow rate range coupled with a control system capable of taking advantage of the modulating capability of the nozzles, injecting the correct rates of liquid to achieve the desired temperature. We achieve these fine droplets without any danger of nozzle clogging or wear by use of wide-bore units with convergent-divergent sections (figure 14) into which a compressible fluid (usually air) expands. The resulting shock wave serves to disintegrate the incoming water into fine droplets.

Our preferred control approach is based on a cascade feed-forward system (figure 15) which is capable of taking advantage of the modulating ability of our nozzles and provide rapid system response. This system is a two-loop system sensing temperatures at the inlet and outlet of the cooling system. The inlet temperature controllers dictate the required water flow to the nozzles. This loop anticipates changes in cooling system inlet temperature and corrects water flow at approximately the same time as the variation arrives at the nozzle location. The outlet loop (set point) resets the set point of the inlet loop if there is any deviation from the set point at the outlet which will result from unsensed volume changes at the inlet. This approach results in the control of temperature within 5° F.

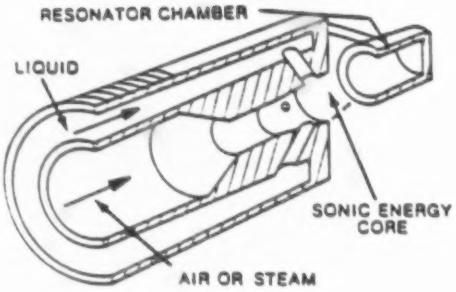

Figure 14 Cutaway view of SONIC atomizing nozzle.

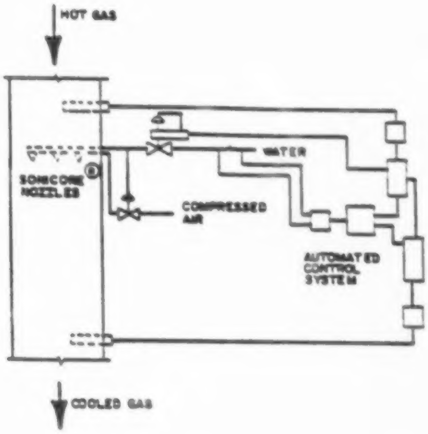

Figure 15 Cascade Feed Forward Control System.

Installed costs of systems for ESP performance enhancement by water conditioning downstream of air heaters typically run on the order of $ .5 to 1.5/cfm. This includes nozzles, lances, compressors, pumps, piping and control instrumentation.

CONCLUSIONS

- Fly ash resistivity exhibits variable sensitivity to both changes in moisture content and temperature of its environment.
- Water injection into a boiler system (combustion chamber, upstream or downstream of the air heater) can reduce ash resistivity from the unconditioned level. Adiabatic cooling conducted downstream of the air heater eliminates unattractive heat losses inherent in the other two injection processes.
- By far temperature, rather than moisture changes play the important role in producing resistivity improvement in the conditioning process.

- One and two decade reductions in ash resistivity are obtainable using a water conditioning approach.

- The feasibility of reducing ash resistivity to acceptable levels consistent with an installation's constraints is readily evaluated by use of SONIC's application engineering program. Precipitator performance improvement is an output of the program.

- Effecting desirable levels of ESP performance improvement in existing compact duct systems requires the use of nozzles which produce fine, uniform droplets, a careful design of the injection system and the use of two-loop control circuits.

- Nozzle selection and arrangement are outputs of SONIC's computer programs.

- Typical water injection levels may range from 0.06 to .14 gal/1000 ACF.

- Installed hardware systems costs range from about $.5 to 1.5/cfm.

The work described in this paper was not funded by the U.S. Environmental Protection Agency and therefore the contents do not necessarily reflect the views of the Agency and no official endorsement sould be inferred.

REFERENCES

1. Sproull, W.T. ad Y. Nakada. Operation of Cottrell Precipitators: Effect of Moisture and Temperature. Ind. Eng. Chem. 43: 1350-1358, 1951.

2. Masuda, S. Effects of Temperature and Humidity on the Apparent Conductivity of High Resistivity Dust. Electrotechnical J. Japan 7: No.3 108-113, 1962.

3. Masuda, S. The Influence of Temperature and Moisture on the Electrical Conductivity of High-Resistivity Dusts. Staub (English) 25: No.5 1-7, 1965.

4. Masuda, S., T. Onishi and H. Saito. Inlet-Gas Humidification System for Electrostatic Precipitator. Ind. Eng. Chem. Proc. Design. Devel. 5: 135-145, 1966.

5. Busby, H.G.T. and K. Darby. Efficiency of Electrostatic Precipitators as Affected by the Properties and Combustion of Coal. J. Inst. Fuel 36: 184-197, 1963.

6. Maartmann, S. The Effect of Gas Temperature and Dew Point on Dust Resistivity and Thus the Collecting Efficiency of Electrostatic Precipitators. Paper EN 34F presented at Second International Clean Air Congress of the International Union of Air Pollution Prevention Association, Washington, D.C. 1970.

7. Sullivan, K.M. The Laboratory Examination of Low Sulphur Coals in Relation to their Electrostatic Precipitability. ACIRL Report P.R. 73-5, 1973.

8. Bickelhaupt, R.E. Surface Resistivity and Chemical Composition of Fly Ash. J. Air Poll. Control Assoc. 25: 148-152, 1975.

9. McLean, K.J. Factors Affecting the Resistivity of a Particulate Layer in Electrostatic Precipitators. J. Air Poll. Control Assoc. 26: 866-870, 1976.

10. Bickelhaupt, R.E. A Technique for Predicting Fly Ash Resistivity. EPA-600/7-79-204, 1979.

11. Bickelhaupt, R.E. A Study to Improve a Technique for Predicting Fly Ash Resistivity with Emphasis on the Effect of Sulfur Trioxide. Paper to be presented at the Sixth Symposium on the Transfer and Utilization of Particulate Control Technology, Feb 26, 1986, New Orleans, LA.

12. Kropp, L.I et al. Joint US/USSR Test Program for Reducing Fly Ash Resistivity. J. Air Poll. Control Assoc. 29: 665-669, 1979.

13. Sullivan, K.M. and J.W. Baker. Reproducibility of Ash Resistivity Determinations. ACIRL Report 56 (draft copy, dtd Sept 30, 1975).

14. Faraday, M. Phil. Trans. Roy. Soc. (London) Part 1 49, 1830.

15. Razouk, R.I. and A.S. Salem. The Adsorption of Water Vapor on Glass Surfaces. J. Phys. & Colloid Chem. **52**: 1208-1226, 1948.

16. Anderson, S. and D.D. Kimpton. Some Phenomena Related to the Hydrophobicity of Silicate Glasses and Adsorbed Oxygen. J. Amer. Ceramic Soc. **43**: 484-488, 1960.

17. Pike, R.G. and D. Hubbard. Physicochemical Studies of the Destructive Alkali-Aggregate Reaction in Concrete. J. Nat. Bur. Stand. **59**: 127-132, 1957.

18. Awakuni, Y. and J. H. Calderwood. Water Vapour Adsorption and Surface Conductivity in Solids. J. Phys. D: Appl. Phys. **5** 1038-1045, 1972.

19. Frisch, N.W. Analysis of Air Heater-Fly Ash-Sulfuric Acid Vapor Interactions. Paper presented at the Fifth Symposium on the Transfer and Utilization of Particulate Control Technology, Kansas City, MO, Aug 27-30, 1984.

20. Korn, J., L. Kurylko and A. Muir. The Cooling of Gaseous Effluents Using Atomizing Nozzles. Paper A72-83 presented at AIME meeting, Feb 21-24, 1972.

A NEW CHEMICAL CONDITIONER TOGETHER WITH GOOD OPERATIONS AND MAINTENANCE PROGRAM MANAGEMENT HELPS MEET EMISSIONS OBJECTIVES

by: Rabi K. Sinha
Calgon Corporation
Pittsburgh, PA 15230

ABSTRACT

Chemical conditioning of fly ash remain a viable option to meet emissions objectives on coal fired boilers. However, chemical conditioners that are designed to lower the fly ash resistivity and make minor improvements in its cohesivity do not work well when the carbon content exceeds 12%. A new chemical conditioner that helps the fly ash retain the naturally present sulfur trioxide and moisture in the combustion gases has shown excellent results. Data will be presented that show how treatment with Calgon conditioner in conjunction with improved operation and maintenance helped further enhance the performance of recently rehabilitated electrostatic precipitators. Treatment with this chemical has shown that the mass emissions can be lowered from 0.4 lb/MM Btu to 0.07 lb/MM Btu and the opacity can be lowered from above 20% to less than 5%. The Calgon conditioner has been shown to work effectively on coals containing less than 1% sulfur in pulverized firing as well, but the discussions in this paper are restricted to a stoker operation in which the fly ash contained more than 30% unburned carbon and the coal contained about 2% sulfur.

INTRODUCTION

Electrical resistivity of dust particles is of prime consideration in the design of electrostatic precipitators. The parameters that affect the resistivity of dust are temperature, flue gas composition, and the chemistry of the dust itself (1-3).

In addition to the mechanical and electrical conditons under which a cold side electrostatic precipitator operates, the temperature of the flue gas, its moisture content and the level of sulfur trioxide play a major role in dictating its day to day performance. The impact of these parameters on an ash derived from a bituminous coal is shown in Figure 1 (4). It is generally considered essential that the dust resistivity must range between 1×10^7 to 2×10^{10} ohm-cm for acceptable performance (5). As seen in Figure 1, temperature, moisture and sulfur trioxide can be varied to keep the resistivity within the acceptable range.

Increasing the levels of flue gas moisture and sulfur trioxide, therefore, forms the basis of most chemical conditioning approach. Humidification or direct injection of sulfur trioxide or compounds that thermally decompose to produce sulfur trioxide are the most commonly exploited approaches of chemical conditioning. The exact mechanism by which the surface conduction in dust particles take place is not very well demonstrated but it is generally accepted that the conduction takes place by the migration of electrons (or ions) attached to the particle via an adsorbed layer of moisture on the surface. Many references strongly suggest that the adsorption of moisture on the dust surface is extremely important and that sulfur trioxide plays an important role in helping this process. The relationship between sulfur trioxide and moisture, also known as dew point, is well known (6) -- increasing moisture or sulfur trioxide in a given gas mixture increases the dew point. The role of moisture retention on the surface of photocopying paper for imparting conductivity is similarly well known (7).

In situations where re-entrainment of the collected ash during the rapping cycle becomes a problem, the ash cohesivity may have to be improved. The forces of cohesion increases with increasing geometric surface area of the particles which in turn increases with decreasing particle size. The cohesive force also depends upon the nature of the adsorbed layer on the surface. Adsorption of moisture, sulfuric acid, and compounds that can remain in the liquidus state on the surface of the dust particles such as organic fluids of high viscosity can also increase particle cohesion. Since the size of the dust particles generated in a process is fixed by the nature of the process itself, modification of the adsorbed layer or the extent by which the adsorption can be enchanced becomes a controllable factor in designing a chemical conditioner.

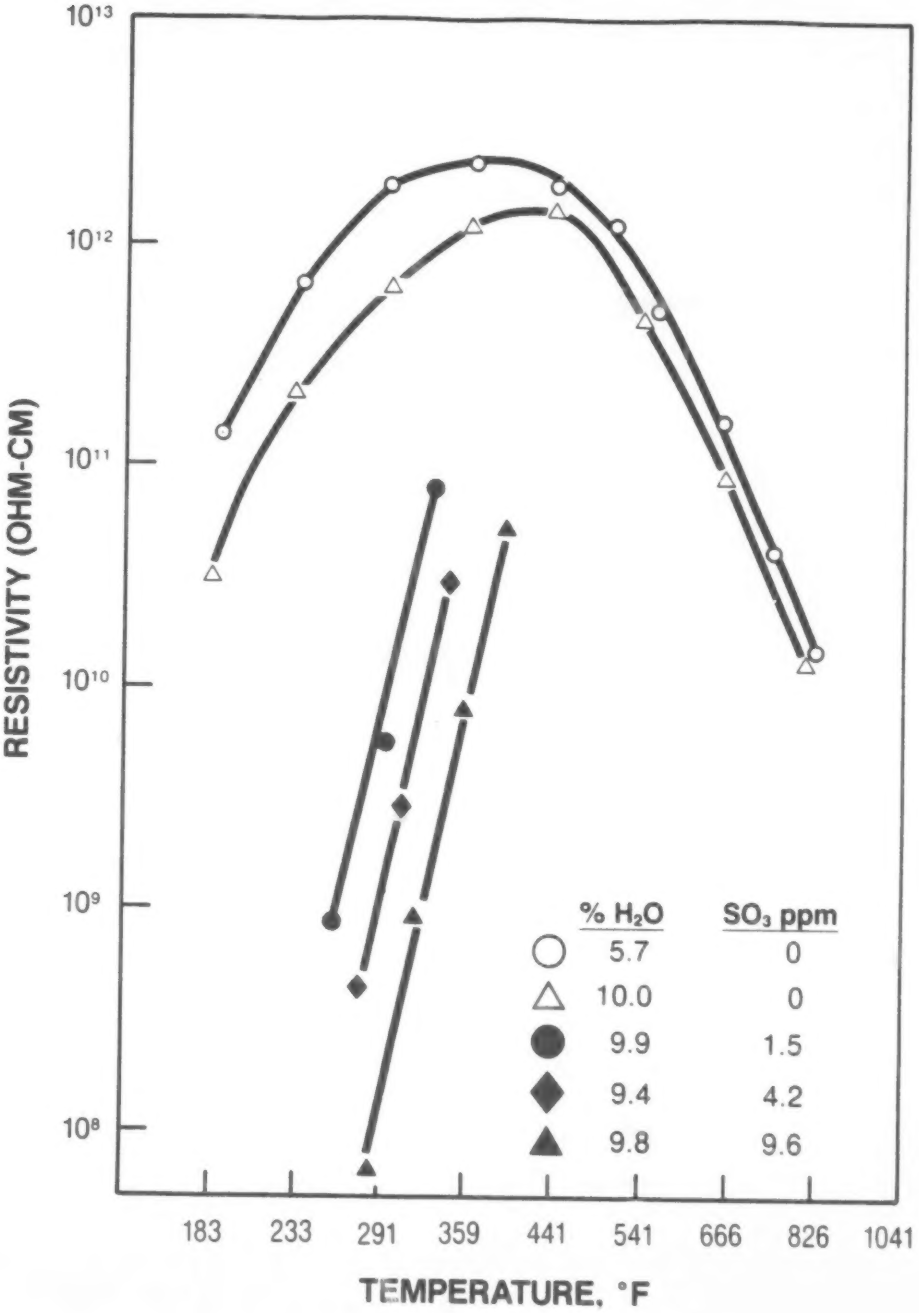

Figure 1—Effect of Water and Sulfur Trioxide Concentrations on Ash Resistivity.

In keeping with the perceived mechanisms of ash conditioning as discussed above, Calgon Corporation has developed a conditioner that is capable of increasing the surface conductivity and cohesivity of the dust particles. This product is a blend of a conductive organic co-polymer and ammonium nitrate in an aqueous base.

SYSTEM DESCRIPTION

Steam is raised in several boilers for meeting the demands of both the process and the turbine. These boilers are underfeed stoker design raising 140 to 180,000 lbs/hr of steam under steady load conditions.

In order to meet the emissions objectives on these stoker boilers the plant initiated a multiphase program:

Phase I

Initial problem identification and engineering investigations which led to the following control technologies:

A. ESP Rehabilitation
B. Overfire Air Turbulence System
C. Humidification

Phase II

Implementation/evaluation of initial control technologies.

Phase III

Identification/evaluation/implementation of additional technologies required to reach program goals. Some of these included:

A. Improved instrument/controls
B. Improved operation of boiler operating parameters
C. Fuel consistency and specifications
D. Improved maintenance of boilers and ESP
E. Operator training and supervision

Phase IV

Assessment of chemical conditioning option.

Phase V

Implementation of Calgon chemical conditioning program.

Electrostatic Precipitators

The ESP is a standard, American, weighted wire design. Flue gases from two boilers are led to one ESP box which then vents through a stack.

The original units were installed in 1967 with a quoted performance level of 95% efficiency.

The original design was for two field operations with a total plate area of 33,700 ft^2 to handle a gas volume of about 200,000 AcFM. There are 39 air gaps with an inlet loading of about 1.5 lb/MM Btu.

The retrofit was limited due to space and structure limitations. The ESPs are located on the roof of an old existing power plant in a congested plant area. Although no additional collecting area could be added, the rehabilitation program consisted of the following:

- Inspection and replacement of plates and wires
- Installation of microprocessor control
- Sectionalization from two to four electrical fields in series
- Installation of 500 and 600 MA TR sets from inlet to outlet fields with one TR set per field
- Gravity impact rappers on plates, wires and diffusion plates
- Based on air flow study, installation of turning vanes in the breeching, three diffusion plates in the inlet and one in the outlet

THE CHEMISTRY OF COAL AND FLY ASH

As described earlier in the paper, there are several boilers raising steam in underfeed stokers at the subject plant. The coal is a mixture of washed and run of mine, delivered in railroad cars as 2"x0" fraction. The specification and the typical analysis of the coal are presented in Table 1. The features to note here are that the coal is low in ash and contains a reasonably high level of sulfur. The constituent analysis of the ash (Table 2) further indicates that the sodium and the iron levels in the ash are sufficiently high to produce an ash of proper resistivity.

The screen analysis of the coal as it burns in the furnace, on the other hand, shows it to contain an excessive level of fines as seen from Table 3. For stoker boiler operation, it is generally recommended to keep the size fraction passing through 1/4" screen below 20% (6) otherwise excessive generation of fly ash and poor combustion may result.

TABLE 1. COAL PROPERTIES

Component	Specification	Current Range
Total Moisture	6% maximum	3-6%
Ash Content	8.5% maximum	6-8%
Volatile Matter(Dry)	45% maximum	35-40%
Fixed Carbon(Dry)	40% minimum	52-57%
Heat Content(Dry)	13,400 BTU/lb. min.	13,800-14,100
Sulfur(Dry)	1.9 lb/MM BTU max.	1.35-1.8(1.9-2.5% by wt.)
Fusibility(softening M=W)(Reducing Atmosphere)	2,200°F minimum	2,200-2,400
Free Swelling Index	6 min [illegible]	7-8
Size	2"x0" [illegible]	2"x0"

TABLE 2. CONSTITUENT ANALYSIS OF THE COAL ASH

Constituent	% (Wt)
SiO_2	46.3
Al_2O_3	25.91
TiO_2	1.02
Fe_2O_3	15.77
CaO	3.51
MgO	0.77
K_2O	1.15
Na_2O	1.26
SO_3	2.81
P_2O_5	0.32
S_2O	0.10
BaO	0.05
Mn_3O_4	0.03
Undetermined	1.00

TABLE 3. TYPICAL SCREEN ANALYSIS OF THE COAL(FEED TO FURNACE)

Screen Size	% Passing
2"	100
1-1/2"	100
1"	99
3/4"	95
1/2"	84
1/4"	53
#4	44
#8	28
#12	22
#16	18
#30	12
#50	8
#100	4
Pan	0

An investigation to first define the system was undertaken by Calgon. The chemistry of the fly ash and the composition of the flue gas together with the operating parameters of the ESP were analyzed. The chemical analysis of the fly ash collected from the various areas of the boiler system are given in Table 4. The following conclusions can be drawn from this investigation.

a. The level of unburned carbon, reported as loss on ignition ranges between 30-35%. This is about 10-15 percentage points higher than normally found in most stoker firing.

b. The LOI content in the ash does not drastically change from one point to another indicating no preferential re-entrainment of carbon from the ESP collector plates.

c. Particle size analysis on the ash indicated it to consist of a mixture of coarse and fine fractions. The carbon fraction of the ash had an average size in the 80-100 micron range whereas the inorganic ash had a mean size of about 15 microns. Microscopic examination of the ash did not reveal the presence of any lacey carbon characteristic of soot particles. This indicated that the carbon in the ash most likely comes from unburned coal or char.

d. The ash produced is highly acidic which is generally characteristic of stoker operation.

TABLE 4. FLY ASH ANALYSIS

Constituent	ESP Inlet	Hopper Ash Inlet	Hopper Ash Outlet	ESP Outlet
Al_2O_3	7	8	7	7
CaO	2	2	2	1
Fe_2O_3	10	11	8	10
P_2O_5	2	2	2	2
K_2O	1	1	2	2
SiO_2	30	32	30	29
Na_2O	4	5	4	5
SO_3	9	8	10	11
TiO_2	2	3	1	1
ZnO	<1	1	<1	<1
Unburned Carbon	33	32	35	35
pH @ 1% Slurry	2.55	2.50	2.40	2.35

THE CHEMISTRY OF THE FLUE GAS

The temperature of the flue gas entering the precipitator ranged between 380°-510°F and depended upon the boiler, steam rate and the extent to which the air preheaters were utilized. Operation at these temperatures suggest that the ash is expected to be highly resistive as neither the surface nor the volume conduction can play a significant role.

The sulfur trioxide level in the flue gas at various locations of the boiler was measured by utilizing an acid dew point meter. This is an indirect technique where the acid concentration is projected based on the relationship developed by Muller (8). As reported in Table 5, the dew point or the projected acid level remained about the same from the economizer outlet to the ESP outlet and corresponded to around 25 ppm of free sulfur trioxide in the gas. For a normal cold side precipitator operation, this acid level is considered sufficient to achieve proper conditioning of the ash. As a matter of fact, it is at a level high enough to produce a low resistive condition and impart a blue haze to the plume characteristic of acid emission.

TABLE 5. ACID DEW POINT AND PROJECTED SO_3 LEVEL

Boiler Location	ADP,°F	Projected SO_3 Level (ppm)
Economizer Outlet	275	20-25
ESP Inlet	274-275	20-25
ESP Outlet	280-295	20-50

Operation at high gas temperature, high levels of unburned carbon in the ash, high level of sulfur trioxide in the flue gas, and a bimodal particle size distribution together with the fact that the coal produced a highly resistive ash ($\sim 3x10^{11}$ ohm-cm) made interpretation of the data quite complicated. It was difficult to categorically recommend a specific conditioner without conducting trials with several.

As discussed earlier, this subject plant had evaluated the effect of humidification on the emissions. It was found that vaporization of water at a rate of 10-15 gallons per minute could bring the emissions within the objective. However, its role solely as a conditioning agent was not clear even though it increased the ESP power level by a factor of around two but it also lowered the flue gas temperature by 30-40°F. Therefore, the improvement could be interpreted as either due to a drop in temperature, or a result of conditioning by moisture or a combination of both.

EFFECT OF TREATMENT DESIGNED TO LOWER SO_3 IN THE FLUE GAS

Assuming that the poor performance is a result of overconditioning from an excessive level of naturally present sulfur trioxide in the flue gas, a patented stable suspension of $MG(OH)_2$ made by Calgon was fed into the boiler ahead of the superheaters. This product is known as Combustrol 500 and contains about 23% magnesium. The product was fed for 21 days at a rate of one gallon per hour per boiler. The effects of this treatment are shown in Table 6.

TABLE 6. EFFECT OF TREATMENT WITH COMBUSTROL 500

Treatment	ESP Outlet ADP, °F	Hopper Ash pH
None	280	2.55
Combustrol 500(4th Day)	265	6.0
Combustrol 500(11th Day)	260	8.0

As seen from this table, the product is effective in lowering the acid dew point and hence, the level of free sulfur trioxide in the flue gas. It is projected that the acid level in the gas was lowered from above 25 ppm to less than 5 ppm. The impact of this treatment is also noted from the ash pH; the acidic ash became basic in nature.

However, the mass emission test conducted on the 20th day of the treatment showed a disappointing result. Table 7 gives this result. Drop in power level together with increased emissions during this treatment clearly indicated that over-conditioning by the high level of sulfur trioxide present in the flue gas is not the reason for poor performance.

TABLE 7. MASS EMISSION TEST WITH COMBUSTROL 500 TREATMENT

Date	ESP Power Level, Watts	% Opacity	Mass Emission
11/12/84	10,000 to 12,000	8-12	0.228-0.313 lb/MM Btu

TREATMENT WITH FLUE GAS CONDITIONING AGENT

FACT-3000 which is Calgon's patented flue gas conditioning agent was next injected into the flue gas ahead of the ESP. The feed rate was initially varied between 0.5 to 2 lb/ton of coal fired into the boiler. Most investigations later were conducted at feed rates of 1.8 to 2 lb/ton as it was found to produce the desired results.

The beneficial effects of feeding FACT-3000 started to show after the second day of treatment. The level of opacity began to decline and the ESP power began to rise. By the fifth day, the opacity was down to less than 5% and the power level had increased to about 50,000 watts.

The acid dew point measured in the ESP outlet gas indicated that the treatment lowered the level of free sulfur trioxide in the gas but this time the lowering in the level was not due to some neutralization reaction as was the case when Combustrol 500 was the treatment chemical. The lowering in this case was due to a preferential adsorption of the sulfur trioxide by the conditioned ash. This is evident from the ash pH. The ash pH was depressed from 2.7 to 1.9.

The mass emission test conducted on two different occasions showed it to be well within the emissions objectives. The special feed system utilized for feeding this product is shown in Figure 2.

Results of the treatment on opacity is shown in Figure 3. As can be seen, the wide opacity range of 10-40% from no treatment condition has been made less variable and the range has been brought to less than 5%.

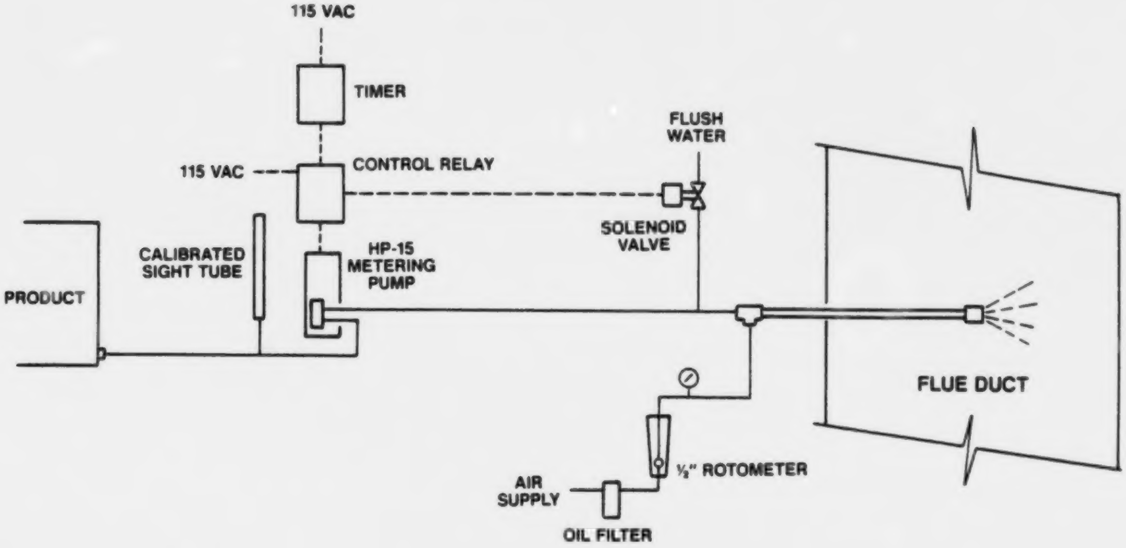

Figure 2—FACT 3000 Feed System.

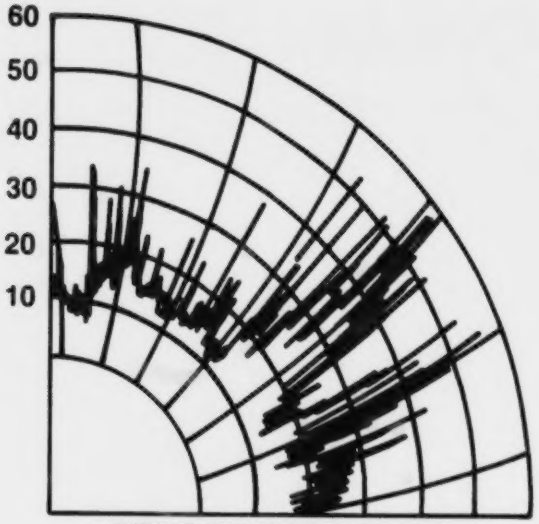

BEFORE TREATMENT

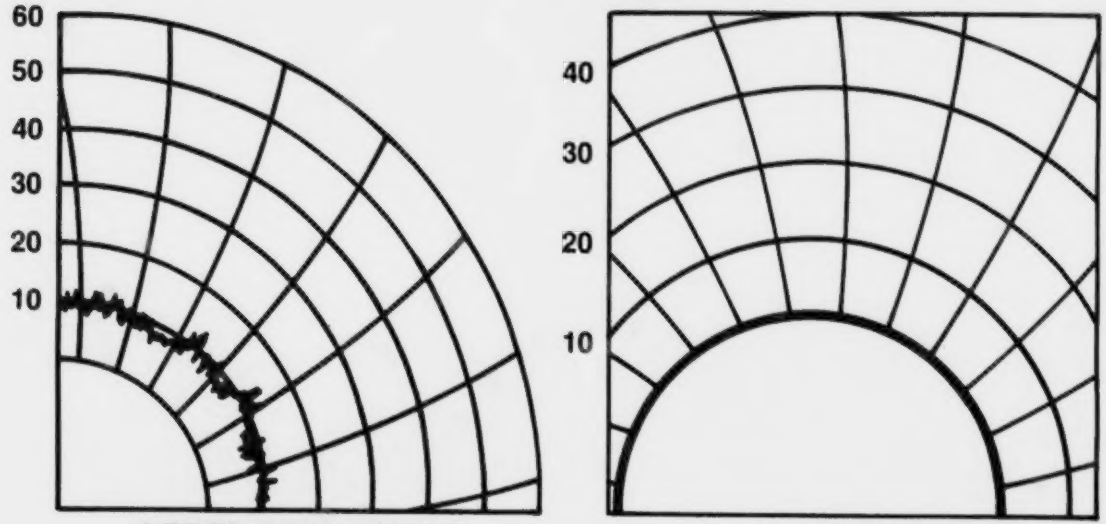

AFTER TREATMENT AFTER TREATMENT

Figure 3

The results of acid dew point depression and its attendant effect on fly ash pH are shown in Table 8. The results of the mass emission test are shown in Table 9, whereas the impact of various treatment on the ESP power level is shown in Figure 4.

TABLE 8. EFFECT OF TREATMENT WITH FACT-3000

Treatment	ESP Outlet, ADP,°F	Hopper Ash pH
FACT-3000(3rd Day)	278-280	2.4-2.6
FACT-3000(5th Day)	265	1.96
FACT-3000(20th Day)	262	1.98

TABLE 9. MASS EMISSION TEST RESULTS WITH FACT-3000 TREATMENT

Treatment	ESP Power Level, Watts	% Opacity	Mass Emission
None	10,000 to 20,000	8-20	0.3-0.5 lb/MM Btu
FACT-3000	19,000 to 60,000	1-5	0.08-0.18 lb/MM Btu

CONCLUSIONS

The following conclusions are drawn from this study:

a. The fly ash is high in unburned carbon and is highly acidic.

b. The flue gas contains a high level of sulfur trioxide, probably characteristic of most stoker operation.

c. The fly ash produced in the boiler consists of coarse and fine particles in which the inorganic components (ash derived from complete combustion of coal) are much finer than the unburned carbon.

d. Despite the presence of high levels of sodium and iron in the ash and sulfur trioxide in the flue gas, the ash must still be conditioned by a special chemical conditioner such as Calgon FACT-3000.

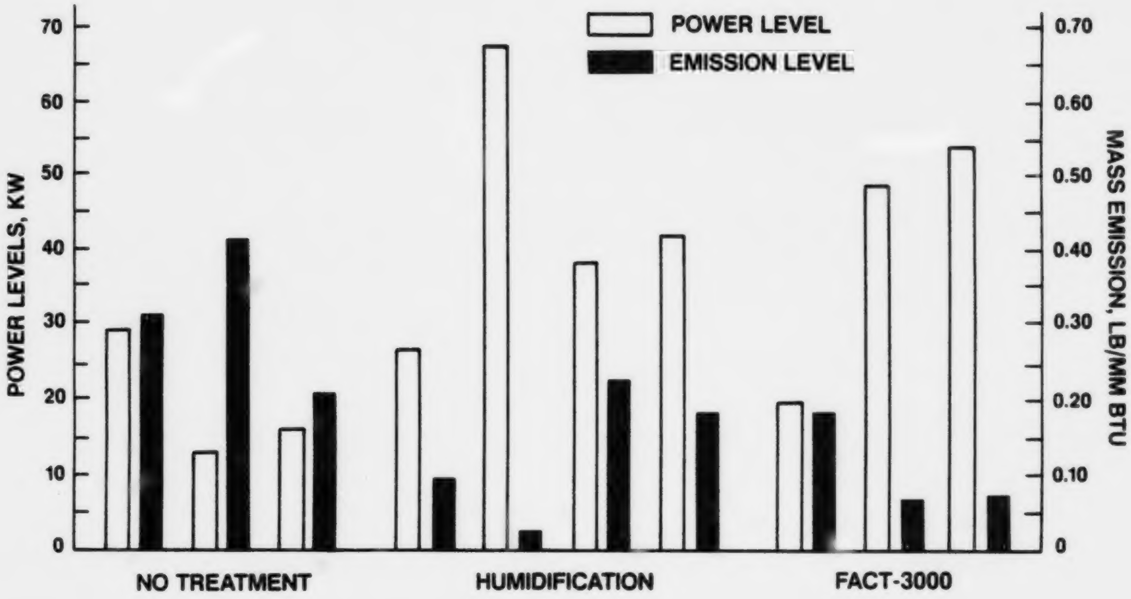

Figure 4—Power and Emission Levels with Treatments.

e. A good conditioning of fly ash containing high levels of unburned carbon and high acidity is brought when the treatment drives the naturally present sulfur trioxide in the flue gas to the fly ash. Such ashes, on account of high carbon,also need the presence of a cohesivity modifier which is brought about by the modification of the surface properties.

The work described in this paper was not funded by the U.S. Environmental Protection Agency and therefore the contents do not necessarily reflect the views of the Agency and no official endorsement should be inferred.

REFERENCES

1. Oglesby, S., Jr. and Nichols, G. Electrostatic Precipitation, Marcel Dekker, Inc., 1978. 123-131 pp.

2. Bickelhaupt, R.E. Symposium on Electrostatic Precipitators For The Control of Fine Particles, 1975. 237-255 pp.

3. White, H. J. Air Pollution Control Association, 1974. 313-338 pp.

4. Bickelhaupt, R. E. Bickelhaupt Associates, Inc. - Private communication, 1984.

5. A Study of Resistivity and Conditioning of Fly Ash - Prepared by Southern Research Institute for EPA, Contract CPA 70-149, February, 1972.

6. Additives for Boiler and Gas Turbine Fuels, Power Reprint, McGraw Hill, Inc., New York, 1980.

7. Hoover, M. F. and Carr, H. E. TAPPI, 1968. 379-396 pp.

8. Specifying Stoker Coal, Power, June, 1985. 62 pp. and MacDonald, J.R., Pulp and Paper, June, 1985. 111-113 pp.

9. Muller, P., Chem-Ing Tech, Vol. 31, No. 5, 1959. 345-351 pp.

Session A-3: PERFORMANCE ENHANCEMENT II

Ralph F. Altman, Chairman
Electric Power Research Institute
Chattanooga, TN

EVALUATION OF BROAD AND NARROW PULSE ENERGIZATION OF A COLD-SIDE ELECTROSTATIC PRECIPITATOR

by: Herman R. Osmers
Chemical Engineering & Policy Analyses
Rochester, NY 14609

Dennis J. Sugumele
Rochester Gas & Electric Corporation
Rochester, NY 14649

ABSTRACT

The effectiveness of broad (about one millisecond) and narrow (about one microsecond) pulse energization of a full-scale precipitator is presented based on two eight-week process test periods involving use of four coals with sulfur contents ranging from 1% to 3%, and fly ash resistivities in the range of 10^{10} to 10^{13} ohm-cm. The process tests were conducted on a coal-fired boiler with normal maximum operating load of 80 MW and a precipitator with a total of 32,000 ft^2 of plate area in three identical electric sections with a specific collection area of 128 ft^2/1,000 acfm. Different combinations of the inlet, center and discharge sections of the precipitator were pulsed. Data acquisition included intensive gas stream testing upstream and downstream of the precipitator, continuous opacity monitoring and analysis by computer, resistivity determination, coal and fly ash analyses, energy consumption, and particle size distribution determination. The latter include those particles smaller than one micron, the size range most important in human health effects. The effect of short-term, temporary cessation of conventional powering of the precipiator was also explored and found to be pronounced, with potentially large significance for precipitator operations under broad circumstances.

Presented to

EPA/EPRI Sixth Symposium
on the
Transfer and Utilization of
Particulate Control Technology

New Orleans, LA
February 25-28, 1986

INTRODUCTION

Pulse energization superimposes a relatively short duration high intensity pulse on top of the base voltage of an electrostatic precipitator (ESP). Normally, a base voltage with pulsing is set somewhat below the corona onset voltage maintained in the conventional operations. The pulse duration, the frequency, and its shape are significant parameters. The pulse voltage is nominally comparable to the DC voltage of the ESP, the frequency typically ranges between 50 and 200 Hz, and the pulse duration ranges from 1 to 1,000 microseconds. The expectation is that, with pulsing, the particulates will be more heavily charged, and thereby their migration velocity will be enhanced, with a concomitant improvement in the collection efficiency of the ESP. Pulsing is thought to be particularly affective with high resistivity fly ash, say on the order of 10^{11} ohm-cm or greater. It cannot, however, compensate for a poorly designed, a poorly maintained, or a poorly operated ESP.

Previous evaluations of pulse energization of a full-scale ESP have involved vendor demonstrations (1-13). The enhancement factor (the ratio of the migration velocity with pulsing to that without pulsing) has been shown to be as high as 2.1, but typically it ranged from 1.2 to 1.8. The corresponding fly ash resistivities ranged from 10^9 to 10^{13} ohm-cm with good results: the enhancement factor ranged from 1.3 to 1.6 with a fly ash resistivity as low as 6×10^{10} ohm-cm. A strong correlation between the resistivity and the resulting enhancement factors is not apparent in these data, although a careful examination does confirm that enhancement is significantly promoted at resistivities in excess of 10^{11} ohm-cm. Part of this absence of correlation undoubtedly can be associated with the difficulty of making resistivity measurements. Additionally, much of the data from these tests is not in the public domain, but rather is proprietary, and is therefore not subject to careful scrutiny. Pilot plant results of pulse energization have highlighted the great disparity between pilot-scale and full-scale results (14).

Consequently, this project was mounted to evaluate the effectiveness of broad (approximately 700 microseconds) and narrow (about 1 microsecond) pulse energization on a cold-side ESP. The field tests were conducted on Unit #12 of Rochester Gas & Electric Corporation. This unit has a tangentially fired, pulverized coal boiler with a gross nominal output of 80 MW. The effluent gas stream from the boiler is divided in two prior to entering the ESP where it goes through each half of the precipitator and combines downstream to feed a single stack. The ESP is a Research-Cottrell unit installed in 1959, and designed to accommodate 251,000 acfm of flue gas at 280F at a collection efficiency of 97.5%. The collecting plate area is 32,148 ft^2, with the collecting plates spaced 9 " apart and with a specific collection area of 128 ft^2/kacfm. The discharge electrodes are 0.109" in diameter and made of #430 stainless steel. Vertical impulse rappers are on the electrodes and magnetic impulse rappers are on the plates. There are three electric fields in series. The average gas velocity is 6.3 ft/sec at full load, which yields an average residence time of 2.9 seconds in the ESP.

Both narrow pulse powered (NPP) and broad pulse powered (BPP) energization were evaluated during two eight-week process test periods. Table 1 illustrates the conduct of a typical intensive test day at constant 100% load. Starting at midnight, the boiler was operated for one hour without soot blow to establish a reference state. At approximately 0100 hours, the power was turned off to the center and discharge sections of the precipitator to examine the effect of cessation of powering on the opacity's return to the reference state. The system was then operated for nearly four hours to enable it to get nearly to equilibrium again, and then the operating personnel were given the opportunity to blow soot in the boiler for one hour. At 0600 hours, the system was again operated at steady state to achieve a reference condition. At approximately 0800 hours, with conventional operation of the ESP, extensive gas stream testing was conducted as indicated by A2 in Table 1: these tests included temperature, pressure, velocity, particulate load, Orsat, sulfur oxides, and the fly ash resistivity. Simultaneously, the opacity was monitored by a transmissometer continuously and recorded on a strip chart recorder and 6-second values were accumulated in a computer data bank for subsequent analysis as well.

The testing begun at 0800 hours was conducted so that it would be completed as near as possible to 1100 hours, at which time the inlet, center, and discharge sections of the ESP were pulse energized. Intensive tests (A2) were again conducted in the intervening time between 1100 and 1700 hours, once at the beginning of the time period and a second time at the conclusion of the period. At 1700 hours the pulsers were disconnected and the precipitator returned to conventional operation, at which time another intensive test (A2) was conducted to be able to compare with the reference obtained about 0800 hours. The boiler was operated until 2200

TABLE 1. ORGANIZATION OF TESTS ON INTENSIVE TEST DAYS AT 100% BOILER LOAD

Nominal Start Time	ESP Sections Pulsed	Testing Phase	Blow Soot?	Remarks
0000	0		No	
0100	0		No	Power Off C,D
0105	0		No	Power On C,D
0500	0		OK	
0600	0		No	
0800	0	A2	No	
1100	I,C,D	A2	No	
1700	0	A2	No	
2200	0		OK	
2400	0		No	

hours without soot blow, at which time the operators were able to blow soot until midnight.

This project involved the following features and variations: (1) two types of pulsers (narrow and broad pulse); (2) three coals (average, lower and lowest sulfur content coal); (3) three load levels (100, 75 and 50%); (4) different sequencing of the pulsing of the electrical sections of the precipitator; (5) on-line continuous opacity measurement; (6) extensive flue gas, particulates, coal and fly ash measurements; and (7) power measurement of both the precipitator and the pulsers. The project is fully described elsewhere (15).

RESULTS AND ANALYSES

NARROW PULSE POWERING (NPP) EFFECTIVENESS

The effects of NPP on the stack emissions are shown in Table 2. For the sulfur content ranging from 1.0 to 2.5% and with the ash content ranging from 7.0 to 11.5%, the resistivities were found to range from 3.6×10^{11} to 1.35×10^{12} ohm-cm. For these conditions, the corresponding fractional reduction in the penetration of the fly ash discharging the ESP was 27, 6 and 48% for the average, lower and lowest sulfur content coals, respectively.

The discharge (penetration), D, may be expressed in terms of the efficiency, E, of the precipitator by the modified Deutsch equation:

$$D = 1 - E = e^{-(Aw/Q)^k} \qquad (1)$$

where A is the collecting plate area, w is the migration velocity, Q is the flue gas volumetric flow rate and k is an empirical factor that yields an improved fit of the data. The discharge with pulsing can also be described by the relation:

TABLE 2. EFFECT OF NARROW PULSE POWERING (NPP) ON STACK EMISSIONS

	Coal		
	Average	Lower	Lowest
Sulfur(%)	2.5	1.4	1.0
Ash (%)	7.4	7.0	11.5
Resistivity (10^{10} ohm-cm)	63	36	135
ESP Discharge (Penetration)(%):			
Conventional	8.6	5.5	14.0
Pulsing	6.3	5.2	7.3
Fractional Reduction (%)	-27	-6	-48

$$D_p = e^{-(Aw/Q)^k H^k} \qquad (2)$$

where the enhancement factor, H, is given by:

$$H = w_p/w \qquad (3)$$

namely the ratio of the migration velocity with pulsing to that without pulsing. It is seen that the enhancement factor maybe viewed as a parameter which effectively increases the collecting plate area with pulse energization. Substituting Equation 1 into Equation 3, there results:

$$D_p = D^{H^k} \qquad (4)$$

Equation 4 relates the discharge without pulsing, D, to the discharge with pulsing, D_p. Thus, the data that otherwise would be analyzed individually can be combined on a log-log plot, which should yield a straight line with a slope equal to H^k. This amounts to a single-parameter fit of all of the data available on pulsing with a given coal under similar conditions. The enhancement factor determined in this manor is independent of the other factors in the Deutsch equation, but does depend on the empirical factor k.

The effect of enhanced collection efficiency due to pulse energization as the ESP discharge decreases can be seen by rearrangement of Equation 4:

$$\frac{D_p}{D} = D^{H^k - 1} \qquad (5)$$

Here it is clearly desirable to have the ratio D_p/D as small as possible. Since the enhancement factor is, by definition, always greater than unity, one sees that as the discharge of the precipitator decreases the ratio D_p/D also decreases. In other words, for a given enhancement factor, this relationship indicates that the efficiency of a precipitator should improve more significantly with favorable pulse energization than without as the overall efficiency in conventional operation improves.

This is shown in Figure 1. Here, it is seen that for an enhancement factor of H = 1.8, the precipitator efficiency without pulsing improves from 90% to about 93.5%, but that at an efficiency of 99% without pulsing the efficiency would improve to approximately 99.8%.

The data points that were used to generate the overall results shown in Table 2 are shown in Figure 2 to determine the exponent in Equation 4. The point is that this method allows the use of all of the data simultaneously to arrive at an average enhancement factor for a given coal. It can be seen that the various symbols for a given coal concentrate rather well to yield the best-fit straight line through the data on a log-log plot. The

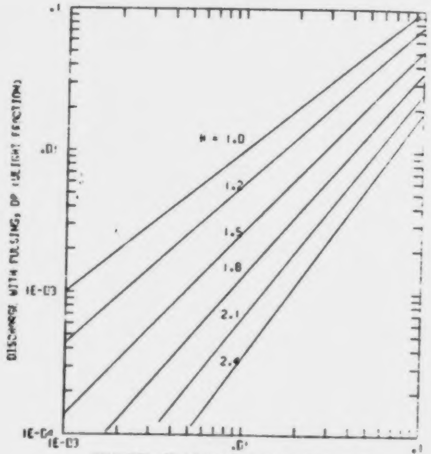

Figure 1. Correlation of the discharge (penetration) of an ESP with & without pulsing, for a given enhancement factor, H.

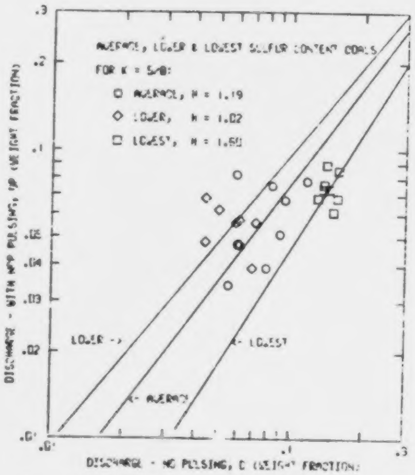

Figure 2. Correlation of discharge (penetration) results, NPP tests.

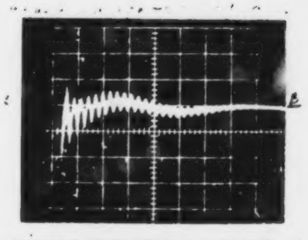

Figure 3. NPP pulser wave form, center section. The abscissa is 5 microsec cm and the ordinate is 10.5 kV cm. The base line is -44 kV and the first pulse peak is -31.5 kV. Initial pulse of approximately 0.8 microseconds.

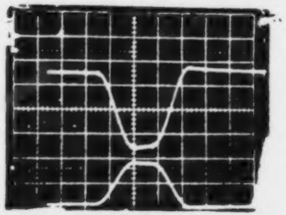

Figure 4. BPP pulser wave form. The upper curve is the pulse: ordinate at 10 kV cm, abscissa at 0.2 ms cm, and at a frequency of 30 Hz. The lower curve is a resonance capacitor voltage.

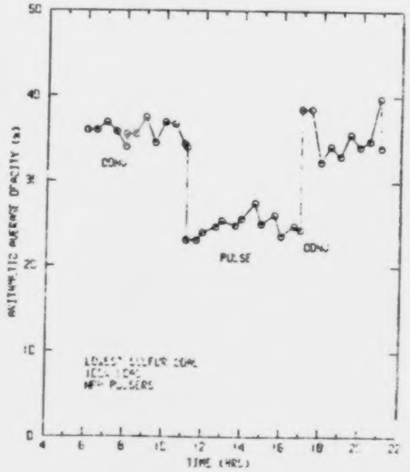

Figure 5. Opacity during NPP pulsing, full load, lowest sulfur content coal

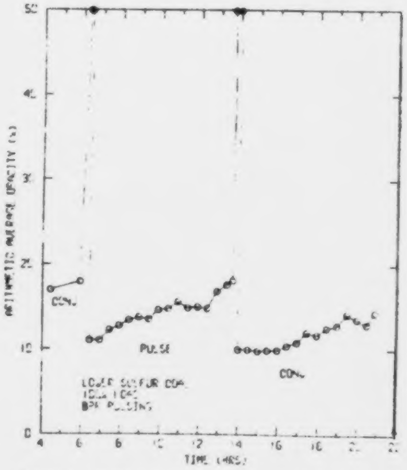

Figure 6. Opacity with BPP pulsing, full load, lower sulfur content coal.

Reproduced from
best available copy.

enhancement factor was found to be equal to 1.19, 1.02 and 1.60 for the average, lower and lowest sulfur content coals, respectively, using a k-factor = 5/8.

The base voltage on the ESP for both conventional and NPP powering of each section are shown in Table 3 for each of the three coals. These base voltages were established by using the highest base voltage that could be tolerated without an unacceptable degree of sparking. It can be seen that the voltages for the average and lowest sulfur content coals with NPP are comparable to or greater than the base voltage under conventional powering, and this undoubtedly aided the collection efficiency. However, the base voltage with NPP powering as compared to the conventional powering for the lower sulfur content coal is seen to be consistently lower, and this correlated to the decrease in the enhancement factor to 1.02. This can be explained in terms of erroneous setting of the base voltage on the ESP used when NPP pulsing to about 85% of that under conventional operation.

TABLE 3. ENHANCEMENT FACTOR AND THE ESP BASE VOLTAGE DURING NARROW PULSE POWERING (NPP)

	Coal		
	Average	Lower	Lowest
Resistivity (10^{10} ohm-cm)	63	36	135
Enhancement Factor: H (k = 5/8)	1.19	1.02	1.60
ESP Primary Volts:			
Inlet			
Conventional	276	315	200
NPP	346	293	215
Center			
Conventional	316	298	210
NPP	306	235	217
Discharge			
Conventional	298	307	180
NPP	303	243	187

The power consumption with conventional and NPP pulse energization of the ESP is shown in Table 4. The power consumption of the NPP unit is seen to be about constant, independent of the coal. On the other hand, the power consumption of the ESP itself increased with pulsing for both the average and the lowest sulfur content coals, and was approximately constant for the lower sulfur content coal when going from conventional to NPP pulsing. Also it can be seen that the power consumption generally decreased with the sulfur content of the coal.

A correlation of the ESP power requirements and the enhancement factor with NPP pulsing is shown in Table 5. The power ratio is the total power as compared to the ESP power only during the pulsing tests. This ratio is remarkably close to the enhancement factor for the average and lowest sulfur content coals, but is markedly different for the lowest sulfur content coal. If this apparent correlation is borne out by additional data, it suggests that the enhancement factor that would have been achieved with NPP pulsing of the lower sulfur content coal would be approximately 1.3 (equal to the power ratio), and this appears reasonable given the data on the coals and how one would expect the pulsers to perform with the respective coals.

A representative picture of a pulse from the NPP pulser is shown in Figure 3. The pulse appears to be a damped oscillation. The first peak of this pulse is essentially imperceptible because it was so faint as to be

TABLE 4. ESP POWER REQUIREMENTS DURING CONVENTIONAL AND NPP ENERGIZATION

	Power (kW)		
	ESP	NPP	Total
Average Sulfur Coal:			
Conventional	27	0	27
Pulsing NPP	35	6	41
Lower Sulfur Coal:			
Conventional	22	0	21
Pulsing NPP	21	7	28
Lowest Sulfur Coal:			
Conventional	7	0	7
Pulsing NPP	10	6	17

TABLE 5. CORRELATION OF THE ESP POWER REQUIREMENTS AND ENHANCEMENT FACTOR WITH NPP PULSING

	Coal		
	Average	Lower	Lowest
Power Ratio			
Total/ESP during Pulsing	1.18	1.32	1.62
Enhancement Factor	1.19	1.02?	1.60

almost unrecordable. The second peak is approximately half the magnitude of the first, and thereafter the damped oscillation is somewhat similar to the exponential decay of a damped system. It is difficult to characterize the wave form by a single parameter, but the time between the individual peaks may be approximated as 1.5 microseconds, and the exponential portion of the decay of the overall wave form has a time constant approximately equal to 10 - 15 microseconds.

I-V curves obtained throughout this project showed that the ESP did not exhibit back-corona.

ECONOMICS OF PULSE ENERGIZATION

There are two circumstances to consider when evaluating the economics of installing pulse energization on an ESP. The first of these is upgrading or retrofitting an existing ESP in order to improve its efficiency. The second circumstance is the decision as to whether to install pulse energization on a new precipitator that has yet to be constructed. For both situations, however, it is essential to note that in comparing the requirements for pulse energization versus conventional operation of a precipitator, one is constrained to comparing them at the same efficiency.

The collection plate area of a precipitator without pulsing, A, is related to the collection plate area of a precipitator with pulsing, A_p, by the expression

$$A = H A_p \qquad (6)$$

Let f_{PE} and f_{PL} represent the fixed capital costs per unit collecting plate area of installing pulse energization and the cost per unit plate area, respectively. The ratio of the total capital cost for the additional plate area to the total capital costs of including pulse energization for the retrofit of an existing ESP is then given by the expression

$$\frac{F_{PL}}{F_{PE}} = \frac{f_{PL}}{f_{PE}} (H - 1) \qquad (7)$$

For a new ESP, the comparable ratio is given by

$$\frac{F_{PL}}{F_{PE}} = \frac{(f_{PL}/f_{PE})\ H}{(1 + f_{PL}/f_{PE})} \qquad (8)$$

Clearly, it is desirable to have the ratio in each case greater than unity in order to favor pulse energization. It is worthwhile noting that both Equations 7 and 8 are independent of the size of the precipitator. Also, for a new ESP, the ratio in Equation 8 becomes equal to the enhancement factor in the limit where the ratio of the capital cost per square foot of adding plate area versus the addition of pulse energization becomes large with respect to unity. Therefore, for example, where the per unit area ratio is large (say on the order of 10) the total capital cost ratio is equal to the enhancement factor, which means that for the lowest sulfur coal used in this project and with the NPP units it would cost 60% more to construct the necessarily larger ESP without pulsing than a smaller ESP with pulsing.

By setting the total capital cost ratios in Equations 7 and 8 equal to unity, one obtains the break-even point in terms of the minimum enhancement factor that would be required in order for pulse energization and additional plate area to be equivalent:

$$H_{MIN} = 1 + (f_{PE}/f_{PL}) \qquad (9)$$

This equation shows that the minimum enhancement factor decreases as the ratio of pulse energization to plate area addition cost per unit area decreases.

Tables 6 and 7 show illustrations of the total capital costs of adding pulse energization versus adding plate area to an existing ESP and for a new ESP, respectively. In the case of the existing ESP the break-point is where

TABLE 6. COMPARATIVE INSTALLED CAPITAL COSTS OF USING PULSE ENERGIZATION OR INCREASING THE PLATE AREA TO RETROFIT AN ESP WITH A COLLECTING PLATE AREA OF 100,000 ft^2 TO ACHIEVE THE SAME PARTICULATE COLLECTION EFFICIENCY, ASSUMING A PULSE ENERGIZATION INSTALLED COST OF f_{PE} = \$5/ft^2 AND THAT THE ADDITION OF PLATE AREA COSTS f_{PL} = \$25 /ft^2.

Enhancement Factor, H	Pulse Energization	Addition of Plate Area
1.2	\$ 500,000	\$ 500,000
1.5	\$ 500,000	\$ 1,250,000
1.8	\$ 500,000	\$ 2,000,000

TABLE 7. COMPARATIVE INSTALLED CAPITAL COSTS USING PULSE ENERGIZATION TO ACHIEVE THE SAME ESP PARTICULATE COLLECTION EFFICIENCY FROM A NEW ESP FOR A 500 MW COAL-FIRED BOILER (APPROXIMATELY 440,000 ft^2 OF COLLECTION PLATE AREA) WITH A SPECIFIC COLLECTION AREA OF 300 ft^2/(1,000 ft^3/sec) ASSUMING A PULSE ENERGIZATION INSTALLED COST OF f_{PE} = \$5/ft^2 AND THAT THE ADDITION OF PLATE AREA COSTS f_{PL} = \$25/ft^2.

Enhancement Factor, H	ESP with Pulse Energization	ESP without Pulse Energization
1.2	\$ 11,000,000	\$ 11,000,000
1.5	\$ 8,800,000	\$ 11,000,000
1.8	\$ 7,330,000	\$ 11,000,000

the enhancement factor is equal to 1.2. The ratio of the capital costs increases dramatically as the enhancement factor goes up to realistic values. In Table 7 the break-point is the same as for additional plate area for an existing ESP. For a new ESP, the ratio of the cost is not as great as the enhancement factor increases, but the absolute difference in capital costs increases dramatically.

BROAD PULSE POWERING (BPP) EFFECTIVENESS

A summary of the results of the BPP powering of the ESP is shown in Table 8. The sulfur and ash parameters are nearly the same as those for the NPP tests shown in Table 2, with the exception of the ash content for the lowest sulfur coal which is slightly lower. These data do suggest that the coals were nearly the same and provided a reasonable basis for a comparison.

The ESP discharge percentage as shown in Table 8 is consistently higher for BPP pulsing than with conventional operation, and this is in contradiction to what one would expect given the resistivities of the fly ash. The collection efficiency of the precipitator with BPP gets closer to, but not better than, the efficiency with conventional operation as the coal resitivity increases. While the magnitude of the increase is not sufficent to provide an overall beneficial effect, it does infer that the broad pulse powering has greater effect on the higher resitivity coals, as has been suggested previously.

TABLE 8. BROAD PULSE POWERING (BPP) EFFECTS ON STACK EMISSIONS AND ESP POWERING

		Coal	
	Average	Lower	Lowest
Sulfur(%)	2.6	1.3	1.0
Ash (%)	7.6	7.2	9.2
Resistivity (10^{10} ohm-cm)	29	144	215
ESP Discharge (Penetration) (%):			
Conventional	9.0	6.0	15.5
Pulsing	25.8	11.0	16.3
ESP Primary Volts:			
Inlet			
Conventional	298	242	210
BPP	-	-	-
Center			
Conventional	289	191	206
BPP	149	119	119
Discharge			
Conventional	299	248	178
BPP	149	119	119

The reason for the lack of effectiveness of the BPP pulsers in improving the particulate emissions is evident on examination of the base voltage data for conventional and BPP operation of the ESP shown in Table 8. In these tests, there were two pulsers available to drive the three electrical sections of the ESP. Therefore, one of the pulsers was used to drive both the inlet and center sections of the ESP, and this is the reason for the absence of data at the inlet for BPP operation: namely it is the same as the center section. The basic reason that the pulser was not effective was that it required that the primary voltage to the precipitator be reduced by approximately 40% below the base voltage of conventional operation. This was simply too large a decrease for the pulsers to overcome, given the fact that the charge on the particle is proportional to the voltage squared.

A picture of the BPP pulse wave form is shown in Figure 4. The pulse in the upper portion of the figure is nearly the shape of a trapezoid with a ramp time of nearly 300 microseconds, and a total pulse duration of about 700 microseconds. The pulse magnitude is about 30 kV, and the frequency is approximately 30 Hz.

OPACITY AND CESSATION OF POWERING OF THE ESP

The opacity results are typified by those for the NPP pulser using lowest sulfur content coal shown in Figure 5. From approximately 0600 to 1100 hours, the ESP was operating in the conventional mode with an opacity of approximately 36%. At about 1100 hours, the pulsers were turned on for approximately six hours to yield an opacity of about 25%. Thereafter, conventional powering was resumed and the opacity returned to approximately the earlier reference level.

The opacity results obtained with the BPP pulser are typified by those in Figure 6, which represents the results obtained using the lower sulfur content coal. Here the reference opacity was approximately 18%, followed by a severe spike. The reason for this was that the BPP pulsers required the connection of wires which necessitated de-energizing one or more electrical sections of the precipitator. Upon resumption of powering - this time with pulsing - the opacity dropped immediately to approximately 11%, but then continuously increased until it achieved the reference opacity, even though the pulsers were still on. The pulsers were then disconnected (again requiring the cessation of powering of the electrical sections of the precipitator) and, upon resumption of conventional powering of the precipitator, the opacity dropped again below the reference opacity to at or below the initial opacity obtained when the pulsing began. Once again the opacity then continuously increased to approach the reference value.

Since the cessation of powering one or more sections of the precipitator was thought to have influenced these results very considerably, it was decided to make the cessation of powering the precipitator a programmed part of this project. Therefore, the center and discharge sections of the precipitator were de-energized for periods ranging from 30 down to one minute in duration. Typical results are shown in Figures 7 and

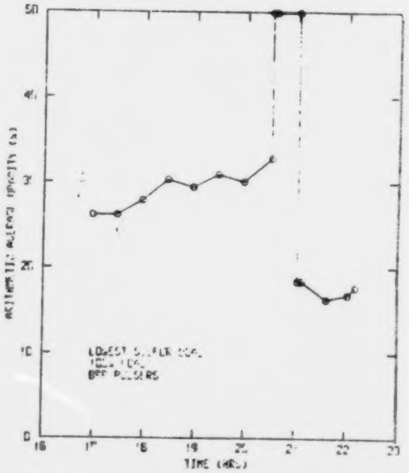

Figure 7. Cessation of conventional ESP powering for 30 minutes during BPP tests.

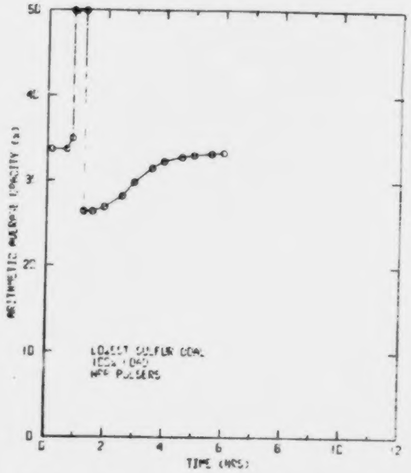

Figure 8. Cessation of conventional ESP powering for 15 minutes during NPP tests, with return to reference opacity during the recovery period.

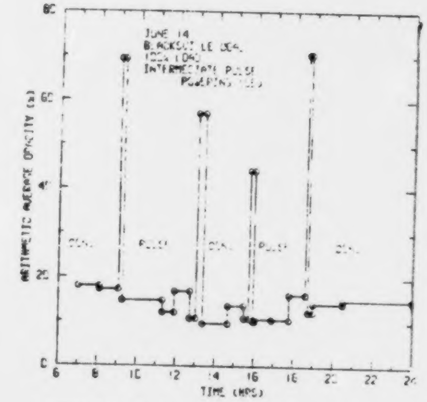

Figure 9. Opacity results with IPP powering using seven sets of parameter settings.

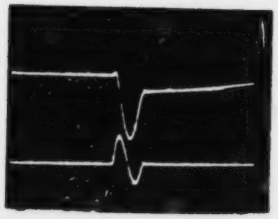

Figure 10. Intermediate pulse powered (IPP) pulser wave form; abscissa at 50 microseconds/cm, ordinate at 10kV/cm.

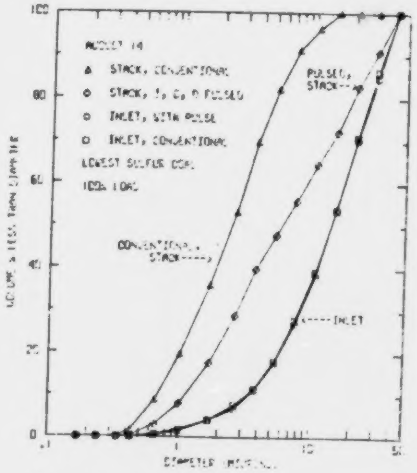

Figure 11. Effect of NPP pulsing on stack particle size distribution.

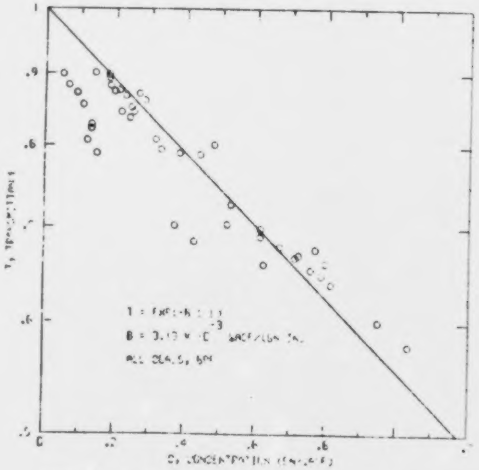

Figure 12. Beer's Law correlation of the measured transmittance and flue gas particulate concentration in the stack for the lower and lowest sulfur content coals used with the NPP pulse apparatus.

Reproduced from best available copy.

8. Each time the powering of the precipitator was discontinued, there would be a spike in the opacity, and then upon resumption of powering the opacity would decrease to a level considerably below the reference opacity achieved before cessation of powering. These results were reproducible and showed that the cessation of powering of the precipitator for times as short as one minute could reduce the opacity by 40%, and that it would then take a period of three to six hours for the opacity to return to the previous reference level prior to the cessation.

The rapping cycle on the precipitator took approximately 21.75 minutes. Since the rapping sequence was not coordinated with the cessation of powering of the precipitator, it could be expected that the sequence of rapping was intervened at different times by the cessation tests. This is one explanation for the erratic behavior of some of the data. It would also explain the different way in which the opacity returned to the reference level during the recovery period.

This behavior of the precipitator during the cessation periods suggests that a large portion of the buildup on the electrodes and plates within an ESP is held in place by electrostatic forces, rather than by physical/chemical means, and dislodging this material is not crucially dependent upon rapping the collection plates or electrodes.

INITIAL EVALUATION OF INTERMEDIATE PULSE POWERING

An intermediate pulse powered (IPP) prototype pulse energization unit was available for preliminary evaluation of its effectiveness in reducing the opacity. This IPP pulser used pulses with a duration of approximately 70 microseconds. It was installed on the center section of the ESP, and tested under full load boiler conditions with different settings of the IPP parameters. The tests were conducted with an average sulfur content coal (comparable to that of the average sulfur content coal used throughout the process tests) with a sulfur content of 2.3% and 10% ash.

The results of the tests conducted on a single day are shown in Figure 9. There is a general downward trend in the opacity, apparently due to pulsing during the first four adjustments of the pulser parameters up to 1302 hours. When the pulser was disconnected, an even lower opacity was observed during the conventional operation through to 1545 hours. The IPP pulser was reconnected at that time to yield a familiar spike in the opacity. In the subsequent period through to 1839 hours, three additional settings of the IPP pulsers were established. The latter parameter settings yielded opacity which ranged from 10.2% through 10.8%, which is to be compared to the reference opacities of 18.0% and 17.3% at 0700 and 0804 hours, respectively. However, the results up to this point are somewhat obscured because the connection and disconnection of the pulsers were comparable in duration to the cessation phenomenon discussed earlier. With cessation, one expects a decrease compared to an earlier reference level prior to the cessation, so that whether the decreases observed up to 1839 hours were due to IPP pulsing or to cessation is not clear.

Upon completion of the disconnect at 1847 hours, the opacity increased from 10.2%-10.6% achieved with the best parameter settings to 12.3% and 15.0% during conventional operations. These values of 12.3% and 15.0% are well below the reference opacity at 0700 and 0804 hours of 18.0% and 17.3%, respectively. This suggests that the IPP pulsing was beneficial in that it suppressed the emissions to even less than that expected on account of cessation of the conventional powering of the center section of the ESP. These results are encouraging, but they need to be replicated by additional, more comprehensive process tests prior to theer acceptance.

The wave form of the IPP unit is shown in Figure 10.

PULSING EFFECT ON PARTICLE SIZE DISTRIBUTION

High-volume samples of fly ash entering the precipitator and in the stack were collected for particle size analyses. A light scattering technique (16-18) was then used on these samples to determine the particle size distribution of the fly ash entering the ESP and in the stack. This was done for each of the coals during the NPP process tests. A representative result of the particle size distribution is shown in Figure 11 for the lowest sulfur coal at 100% load on the boiler.

The distribution is given in terms of the volume percent of particles at a given diameter or less. The density of the fly ash was nearly constant (approximately 2.4 g/cm^3) so that the volume percent is directly proportional to the mass percent. The inlet curves essentially superimposed, indicating that the particle size distribution was the same entering the percipitator both for the pulsing and conventional operation of the ESP. The particle size distributions in the stack, however, are markedly different. With NPP pulsing, a smaller fraction of the particles less than 10 microns is present than during the conventional operation.

The effect of the pulsing on the particle size distribution is compounded by the overall effect of the NPP pulsing on the total mass discharge from the ESP. For the lowest sulfur content coal, the NPP pulsing reduced the total emissions by nearly 50%. From Figure 11, it is seen that approximately 20% of the mass fraction of the particles are one micron or less in diameter with conventional operation of the ESP, whereas only about 8% of the particles are less than one micron in the case of NPP pulsing. Therefore, there is a five-fold decrease in the total mass emissions of particles of a size one micron or less when NPP pulsing was used. This general compounding effect is observed throughout the size range up to ten microns, and was generally apparent in all of the particle size distribution curves that were obtained.

It is fairly clear that the smaller fly ash particles, say less than ten microns, have potentially the largest deleterious effect on human health. This is currently being addressed by the promulgation of PM_{10} regulations now being developed by the EPA for ambient size distributions of particulates. From these results, it is clear that NPP pulsing can have a pronounced effect on the particle size distribution and thus provides another mechanism by which serious health effects can be addressed.

An additional observation based on all of the particle size distribution curves is that the 100% volume fraction is attained at a higher particle size with pulsing rather than with conventional operation. This apparent agglomoration of particles requires further examination.

PULSING EFFECTS AT REDUCED LOAD LEVELS

Process tests were conducted at reduced load levels, nominally at 50% and 75% boiler load to determine the effect of pulsing on the opacity. The penetration of fly ash with and without pulsing was not measured directly, but rather it was calculated using the measured opacity in the following manner. Figure 12 shows a Beer's law correlation of the measured transmittance versus the fly ash particulate concentration in the stack for all of the coals used with the NPP pulse apparatus. Thus, by measurement of the opacity (equal to 1-T), the concentration corresponding to any load condition in the stack was determined. The inlet particulate concentration was calculated assuming that at a given percentage load the flue gas loading would be equal to the percentage load multiplied by the average of the particulate concentrations measured during 100% load level. This enabled calculation of the enhancement factor by a plot according to Equation 4, as shown in Figure 13. The resulting enhancement factors were 1.17, 1.10, and 1.31 for the average, lower, and lowest sulfur content coals, respectively, using a k-factor of 5/8. These results demonstrate that pulsing can be effective at considerably reduced load levels, but they are not nearly as definitive as the earlier results because the inlet particulates and the discharges (penetrations) were calculated rather than measured directly.

ESP CLEANSING DUE TO PULSING

The data obtained during the intensive process testing suggested that there was a long-term beneficial effect due to pulsing because of cleaning the electrodes and the collecting plate. There appeared to be a slightly downward trend in the opacity values recorded as the tests progressed, in relation to earlier opacity values recorded under similar conditions.

The precipitator was inspected during shutdowns prior to the beginning of the BPP process tests, between the BPP and NPP process tests, and at the conclusion of the NPP process tests. A qualitative appraisal of the buildup on the electrodes and plates based on on-site visual inspection of the ESP during these shutdowns indicated that both BPP and NPP pulsing did have the effect of tending to clean the electrodes and collection plates of the precipitator. Prior to the pulsing tests the majority of the wires on the plates had a greater amount of buildup than the amount of buildup observed between and subsequent to the pulsing tests.

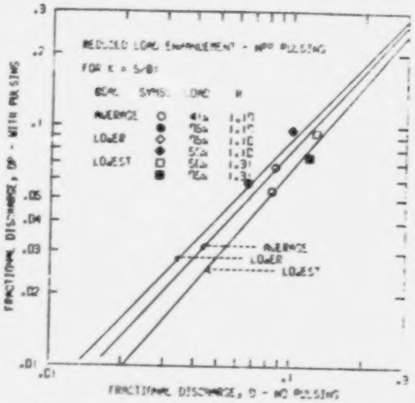

Figure 13. Correlation of discharges (penetrations) during NPF pulsing at reduced loads.

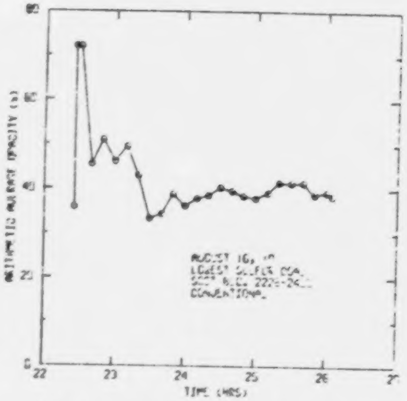

Figure 14 Return of opacity to steady state after a soot blow.

Reproduced from
best available copy.

The apparent cleansing effect of the pulsers took place despite the fact that the ESP was powered conventionally for the majority of the total process test time, with a variety of coals, and under different load and operating conditions. It would seem that cleansing would be even more pronounced with continuous pulsing, which would yield an even greater enhancement factor due to pulsing. Photographs bore out the claim that pulsing has a cleansing effect on the components of the precipitator, and lends support to the trend suggested by the earlier process data, notably that the opacity tends to decrease with time in the long-term, given pulse powering of an ESP.

EFFECT OF RAPPING AND NPP PULSING ON THE ESP

A way to get a measure of the effectiveness of an ESP due to rapping, without induced re-entrainment, is to turn off the rapping for periods of time and measure the particulate load or the opacity (19). The data in Table 9 were obtained during the NPP pulser process tests and demonstrate the effects of discontinuing the rapping of the electrodes and collection plates of the ESP at 100% load, without soot blow for the average sulfur content coal.

The opacity of 12.6% was obtained during conventional ESP operation with rapping on. The conventional powering was maintained and the rapping discontinued to yield an opacity of 5.3%. When all three sections of the ESP were NPP pulse energized, the opacity dropped to 4.2%. Upon returning to conventional operation with the rappers on, the opacity rose to 13.5%, which is quite close to the original reference opacity.

The opacity realized without rapping but with the pulsers on of 4.2% as compared to that of 5.3% with the pulsers off does not, at first glance, appear significant, but keeping in mind that the opacity is directly proportional to the discharge at low opacity levels, its reduction of approximately 20% is significant. It should also be noted that the opacity was decreased to less than one-half of its reference level by simply turning the rapping off.

TABLE 9. EFFECTS OF DISCONTINUING RAPPING OF ESP WITH AVERAGE SULFUR CONTENT COAL

ESP Powering	Rapping	Opacity(%)
Conventional	On	12.6
Conventional	Off	5.3
NPP	Off	4.2
Conventional	On	13.5

This reinforces the earlier statements that a large portion of the buildup on the electrodes and the collecting plates is held in place by electrostatic rather than physical/chemical forces. The reason for this is that, without rapping, the majority of the buildup is retained, rather than being intermittently emitted, and therefore the opacity decreases. Also, the large change in the opacity is indicative of the degree to which re-entrainment is promoted by a combination of rapping and the aerodynamics in an ESP.

These results obtained with the ESP rapping turned off suggests that it is worthwhile exploring a strategy in which alternating periods of, first, a minimum (or no) rapping is conducted, followed by cessation of the conventional powering of the ESP, during which intense rapping is conducted, perhaps augmented by pulsing during each period. It could be expected that the opacity would be lower during the conventional operation without rapping of the ESP as compared with rapping, and that the cessation period with heavy rapping to clean the electrodes and plates would not offset the expected emission improvement, the result being that there would be a net decrease of particulates discharged from the system over time.

DAMPING OUT OF THE EFFECTS OF SOOT BLOW

Figure 14 represents a typical operational soot blow followed by a return to normal operations. The data are for the period covering 2226 hours on one day until 0205 hours on the next, with the lowest sulfur content coal, at 100% load. Starting at a reference opacity with conventional powering of the ESP under normal conditions, the soot blow beginning at 2226 hours resulted in an expected spike in the opacity of 72.2% as an average over the ensuing 4-minute period. Thereafter, each datum represents the average over the previous 10-minute period. The opacity seems to drop rapidly after the first four minutes, and then decreases to steady oscillations around the opacity value of approximately 40%. The time it takes for the soot blow to damp out is seen to be somewhat less than one hour. The significance is that the process test schedules of this project allowed ample time for the effects of an operational or required soot blow to be damped out prior to commencing a subsequent process test.

NARROW PULSE POWERING DURING NORMAL OPERATIONS

On completion of the scheduled process tests with the NPP pulsers, it was decided to maintain the three NPP pulsers connected to the inlet, center and discharge electrical sections of the ESP so that the precipitator could alternately be conventionally powered and then powered by the pulsers for relatively protracted periods of time. During these times, the boiler was operated under normal conditions with two regularly scheduled trainloads of coal, and with soot blowing according to normal operational needs, but at constant load for given sets of process tests. Data were obtained for rather large blocks of time corresponding to either conventional operation or NPP powering. It was assumed that, by comparing opacity averages obtained for relatively large blocks of time, the comparison of the opacities would be valid. Table 10 shows representative results during which conditions were such that a period of time with pulsing could be compared with a period of time with conventional operations, with both periods of time under relatively comparable conditions. The coals consumed during these trials were comparable to the average sulfur content coal used during the scheduled process tests.

The data in Table 10 indicate that the pulse energization of the ESP with the NPP pulsers did indeed improve the opacity average when operated over relatively long periods under essentially normal operating conditions. The discharge of the precipitator is directly proportional to the opacity at these opacity levels. The fractional reduction in the opacity of 22% is especially significant in the context that average sulfur content coal was being consumed, and this would typicaly not have a high resistivity that would cause difficulties, and yet there was a measurable reduction in the opacity. Since these data were taken under normal operations with varying operating conditions and boiler load, they are felt to be reasonably representative and indicative of the type of performance to be expected from NPP pulers, and that much higher fractional reductions in emissions can be achieved with high resistivity fly ash.

CONCLUSIONS

Narrow pulse powering (about one microsecond) of an ESP was found to be effective in reducing particulate emissions. For a k-factor = 5/8, the enhancement factor was found to be equal to 1.6 with a coal that had 1% sulfur, 11.5% ash and a resistivity of about 1.4 X 10^{12} ohm-cm. Pulsing preferentially reduces the fraction of the smaller-sized particles emitted from a precipitator. When this is combined with the beneficial effect of NPP pulsing, the reduction in the particles smaller than one micron in size can be as much as five-fold.

Intermittent cessation of conventional powering of an ESP leads to a significant reduction in the opacity upon resumption of the powering of the ESP.

TABLE 10. NPP PULSERS IN NORMAL OPERATIONS FOR SIX DAYS

	Opacity(%)
Conventional ESP	12.0
NPP ESP	9.4
Fractional reduction	-22

This opacity reduction is maintained for approximately three to six hours before it returns to its prior reference level. Discontinuing rapping improves emissions, and the reduction in emissions is further promoted by NPP. The cessation and the discontinuance of rapping both suggest that the bulk of the buildup on the electrodes and collecting plates in an ESP are held in place by electrostatic forces rather than by chemical/physical forces.

The relation $D_p = D^{H^k}$ enables the correlation of all the discharge (penetration) data simultaneously to arrive at a fair average value for the enhancement factor. This same relation, based upon the Deutsh equation, indicates that the largest fractional improvement in discharge (penetration) is achieved as the efficiency of an ESP increases. An economic analysis shows that the minimum enhancement factor necessary for pulsing to be justified over the addition of plate area is equal to unity plus the ratio of the capital cost per square foot to add pulsing to the capital cost to add plate area, and that, for most cases, one can expect that this minimum enhancement factor would be 1.2 or less.

Opacity data accumulation by a computer on a continuous basis was shown to be invaluable in the analysis of the process tests. Broad pulse powering (about 700 micoseconds) is not effective in reducing stack emissions. However, preliminary results of the effectiveness of an intermediate duration pulse (about 70 microseconds) unit shows promise of reducing the stack emissions. The ESP power required for pulsing correlates with the enhancement factor. For this unit, without back-ionization, the power requirements of the ESP were not decreased with pulsing. It was also found that the power requirements to operate the ESP are rather inconsequencial.

Both BPP and NPP tend to maintain the electrodes and collection plates cleaner than does the conventional ESP operation. This would further promote the beneficial effects of pulsing. Given the choice, it is best to pulse all three sections of the ESP, but if only two sections are to be powered then it is best to power the center and discharge sections, or the center section if only one section is to be powered.

ACKNOWLEDGMENTS

This Project was supported by funding provided by the Empire State Electric Energy Research Corporation, the Rochester Gas & Electric Corporation, and the New York State Energy Research and Development Authority. The broad pulse powered (BPP) and the intermediate pulse powered (IPP) energization units were provided, operated and maintained by General Electric Environmental Services, Inc., and the narrow pulse powered (NPP) energization units were provided, operated and maintained by Ion Physics Company. These sources of support are gratefully acknowledged.

Entropy Environmentalists, Inc. conducted the flue gas, fly ash and coal analyses. Microtrac, a division of Leeds and Northrup, conducted the particle size distribution analyses. Their assistance was greatly appreciated.

The work described in this paper was not funded by the U.S. Environmental Protection Agency and therefore the contents do not necessarily reflect the views of the Agency and no official endorsement should be inferred.

REFERENCES

1. Feldman, P. L. and P. J. Aa, "Operating Results From The First Commercial Pulse Energization System To Enhance Electrostatic Precipitator Performance," American Power Conference, Chicago, April, 1981.

2. Feldman, P. L. and K. S. Kumar, "Enhanced Precipitation by Pulse Energization," Fine Particle Society 13th Annual Meeting, Chicago, April, 1982.

3. Kumar, K. S., P. L. Feldman, H. I. Milde and C. Schbert, "The Results of First Full-Scale Utility Demonstration of Pulse Precipitation," IEEE-IAS Annual Meeting Conference Record, 1333-1337 (1979).

4. Lausen, E., H. Henriksen and H. H. Petersen, "Energy Conserving Pulse Energization Of Precipitators," IEEE, 163-171 (1979).

5. Lausen, P., H. H. Petersen and H. J. Joergensen, "Theory In Application of Pulse Energization," International Conference On Electrostatic Precipitation, Monterey, California, October, 1981.

6. Lucidyne Data Sheet, Summary of Performance Unit 14 of Northern Indiana Public Service Company, Personal Correspondence, March 24, 1982.

7. Lugar, T. W, J. H. Brummer, T. W. Roesch, and J. Dalmon, "The Dynamic Response of Precipitator Performance to Pulse Powering," ASME/IEEE Power Generation Conference, Milwaukee, Wisconsin, October, 1985.

8. McGraw, M. G., "'Pulsed' Precip Could Lick Low-Sulfur Coal," 1979.

9. McIlvain Co., "Tests Of Pulse Energization Meet Expectations," Precip NewsLetter, No. 64, 1-2, May, 1981.

10. Milde, H. I. and P. L. Feldman, "Pulse Energization of Electrostatic Precipitators," IEEE-IAS 1978 Annual Meeting.

11. Niemeyer, J. W., R. A. Wright, and W. Love, "Pulsing On a Cold-Side Precipitator, Florida Power Corporation, Crystal River, Unit 1,"

EPA/EPRI Proceedings: 5th Symposium On the Transfer and Utilization Of Particulate Control Technology, Volume 2, Kansas City, August, 1984.

12. Petersen, H. H. and P. Lausen, "Application Of Energy Conserving Pulse Energization For Precipitators - Practical And Economic Aspects," EPA/EPRI Proceedings: 3rd Symposium on the Transfer and Utilization of Particulate Control Technology, Orlando, Florida, March, 1981.

13. Puille, W., L. E. Sparks, G. H. Marchant, Jr. and J. P. Gooch, "Evaluation of Performance Enhancement with Pulse Energization Systems on a Hot-Side Electrostatic Precipitator," EPA/EPRI Proceedings: 3rd Symposium on the Transfer and Utilization of Particulate Control Technology, Orlando, 1981.

14. Puille, W., D. C. Landham, J. L. DuBard and L. E. Sparks, "Estimate ESP Efficiency Gains From Pulse Energization," Power, 51(May, 1985).

15. Osmers, H. R. and Rochester Gas & Electric Corp., "Pulse Energization Electrostatic Precipitation," Research Report EP83-5, Empire State Electric Energy Research Corporation, New York, February, 1985.

16. Muly, E. C. and H. N. Frock, "Industrial Particle Size Measurement Using Light Scattering," Optical Engineering, 19, 861-869 (1980).

17. Plantz, P. E., "Particle Size Measurements From 0.1 to 1000 Micrometers, Based On Light Scattering And Diffraction," in Modern Methods of Particle Size Analysis, H. G. Barth, ed., Wiley, New York (1984).

18. Weiss, E. L. and H. N. Frock, "Rapid Analysis of Particle Size Distributions by Laser Light Scattering," Powder Technology, 14, 287-293 (1976).

19. Langan, W. T., J. H. Oscarson, and S. Hassett, "Electrostatic Precipitator Emission and Opacity Performance Control Thru Rapper Strategy," EPA/EPRI Proceedings: 2nd Symposium on the Transfer and Utilization of Particulate Control Technology, San Francisco, 1979.

D3.08

FULL SCALE DEMONSTRATION RESULTS OF ELECTROSTATIC PRECIPITATOR PULSE ENERGIZATION

by

Thomas W. Lugar
J. Mark Friday
General Electric Company
Environmental Services, Inc.
Lebanon, Pennsylvania 17042

ABSTRACT

General Electric has developed a commercially available electrostatic precipitator pulse energization system which can provide improved precipitator performance particularly on high resistivity flyash applications. Pulse energization is a modification to a conventional precipitator power supply output whereby short (microseconds) high voltage pulses are superimposed on the existing precipitator power supply DC output. Presented in this paper are results and characterization of pulse energization upon precipitator performance from full scale applications which utilized a mobile pulser demonstration system. Improved precipitator performance and simultaneous energy savings are described. This technology can be applied to electrostatic precipitators to enhance performance which may have degraded due to the burning of low sulfur coal or other factors. This technology will have major application to utility units affected by stack height or potential acid rain regulations who elect to comply through coal switching.

INTRODUCTION

Pulse energization is a modification of a conventional precipitator power supply output whereby short high voltage pulses are superimposed on the existing precipitator power supply DC output. Pulsing addresses the problem of reduced ESP collection efficiency when collecting high resistivity particulate. If the resistivity is too great, back corona and premature sparkover at low applied voltage will occur due to the large relaxation time constant of the dust particles. The key to overcoming this condition is to decrease the current density to lower the voltage drop through the ash layer on the collecting electrode. This can be done by applying short high voltage pulses with a relatively long duration between the pulses. Between the pulses the charge on the dust layer surface decays decreasing the average current density below a point where back corona would form. Thus the fundamental operating principle of pulse energization is an increased spark voltage level with back corona suppression by turning on and turning off the corona discharge at a predetermined rate (1,2).

Recent full scale tests on electric utility applications where the existing power supplies were retrofitted with pulse units have verified that improved precipitator performance can be obtained with pulse energization (3). Commercial high voltage pulse power supplies differ in the method of pulse generation, the philosophy of pulse output parameters and their optimum settings, i.e. pulse waveshape, pulse width, repetition rate and reference DC level. This has unfortunately resulted in a limited amount of consistent full scale performance related data with pulsing.

During the latter part of the 1970's GE Environmental Services (then Buell Envirotech) began investigating techniques to improve performance of precipitators operating with high resistivity particulate. This effort started with the Trielectrode Precipitator concept (4) and was followed by the Broad (1 ms width) Pulser system. Encouraging results were obtained with broad pulse energization at an EPRI funded test program at Gulf Power Lansing Smith Station on a hot side back corona application (5). In 1982 General Electric Company embarked on an extensive program to develop an optimized pulser system with more flexibility in pulse width to expand the system's applicability to a wider range of conditions, moderate to high resistivity with or without back corona. The need for pulse output adjustability was verified during a test program at Rochester Gas and Electric's Beebee Station in 1983. A broad pulse width output was found not to be optimum for this moderately high resistivity non-back corona application (6). A brief test with an early prototype of the new pulser utilizing a medium or microsecond pulse width resulted in a 40% reduction in opacity. This was a greater reduction than that provided with a narrow pulser (nanosecond width) system also tested during the program.

The result of these efforts is a commercially available, versatile pulser system that provides improved precipitator performance with enhancements in particle migration velocity greater than 2.0 possible. This paper describes recent full scale tests obtained with a mobile pulser demonstration system.

GE PULSER SYSTEM

Figure 1 is a basic schematic of the GE pulse power supply. A thyristor switch having a reversed conducting feedback diode supplies energy stored in C1 to the primary winding of a pulse transformer. The precipitator capacitance is reflected into the primary winding to act with inductor L1 as a series resonant, commutating circuit for the thyristor switch. The voltage is stepped up in the pulse transformer and is coupled to the precipitator through capacitor Cc. A DC reference voltage is supplied by the existing DC power supply and coupled to the precipitator through diode D1.

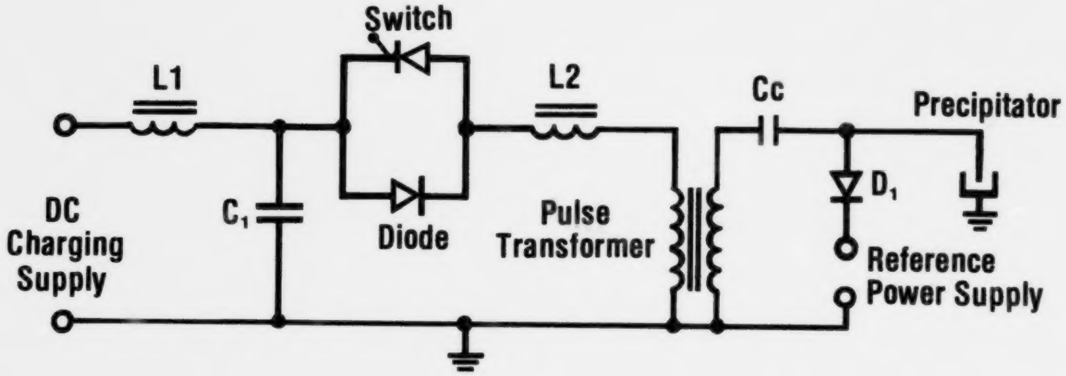

Figure 1. GE Pulse Power Supply Schematic Diagram

The pulse output consists of short high voltage pulses applied to a base DC voltage which is maintained at a level just below the sparking threshold or below the onset of back corona, depending on the condition, and provides a constant electric field to maintain ion and particle migration toward the collecting electrodes. The superimposed pulse width and frequency are adjusted to achieve the highest pulser amplitude at an increased spark threshold without the formation of back corona. The pulse voltage waveform is shown in Figure 2.

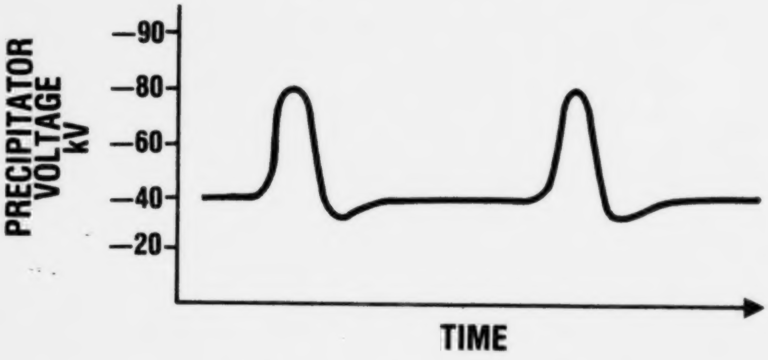

Figure 2. Pulse Voltage Waveform

The GE Pulse Energizer design parameters are as follows:

Powering Capability	to 55,000 ft^2 (5110 m^2) collecting plate area
Pulse Width	100 - 500 microsecond
Pulse Repetition Rate	1 - 300 Hz
Maximum Pulse Amplitude	50KV
DC Reference Voltage	to 40KV

The General Electric Pulse Energizer provides the following benefits to precipitator operation:

- Overcomes performance limitations due to high resistivity particulate
- Increases collection of fine particulate
- Reduced precipitator power consumption compared to conventional operation
- Reduces ash reentrainment after rapping
- Provides a more uniform distribution of current density
- Can be an alternative to increasing plate area or utilizing conditioning agents to upgrade performance of existing precipitators
- For new units, increased collection efficiency results in a reduction of collecting plate area required, i.e. for an enhancement in particle migration velocity of 1.5, collecting plate area can be reduced by 33%.

The pulser was designed to be as compact as possible and is housed in a standard precipitator transformer-rectifier tank that is placed alongside of and tied into the existing precipitator transformer with a short run of pipe and guard duct. The existing ESP transformers are thus retained to provide the DC base voltage. The GE pulse power supply and control cabinet are shown in Figure 3.

The pulser automatic controller provides spark response and maintains the optimum pulse output parameters. Pulse widths in the range of medium to broad allow greater flexibility in optimizing the pulse output to applications of moderate to high resistivity, with or without back corona.

Reproduced from
best available copy.

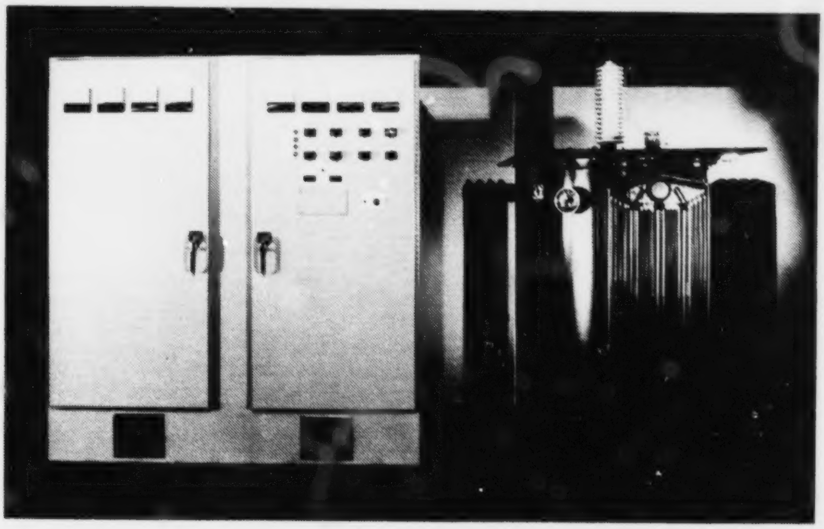

Figure 3. GE Pulse Energizer Power Supply and Control Cabinet

MOBILE PULSER DEMONSTRATION SYSTEM

Field testing of pulsing is accomplished using a specially designed mobile pulser demonstration system. Four pulse power supplies, mounted on a 48' (14.6m) long x 8-1/2' (2.6m) wide flat bed trailer, are capable of energizing a total of 220,000 ft^2 (20,438 m^2) of collecting plate area. Also included on the trailer is a control room housing control cabinets for the pulsers and four 90 KVA transformer-rectifiers with linear reactors. The pulser trailer is shown in Figures 4 and 5. The reference transformers provide the base full wave DC voltage output upon which high voltage pulses are applied. The mobile pulser system utilizes its own reference transformers instead of those on the precipitator due to the need for the pulser automatic controller to interface with the reference TR controller. In retrofit applications the existing precipitator transformers would be used.

Tie-in of the mobile pulser can be completed with the precipitator on line and has been designed to minimize alteration of existing precipitator equipment. After the trailer is positioned alongside the precipitator, a 2-3/8" (6 cm) O.D. dry high voltage insulated cable is run from the output of each pulser to the pipe and guard or transformer switch gear of each precipitator electrical field to be pulse energized. A three phase power connection and ground is supplied to the breaker panel in the pulser control room. This can be 380 to 600 VAC. Complete pulser tie-in generally requires one day.

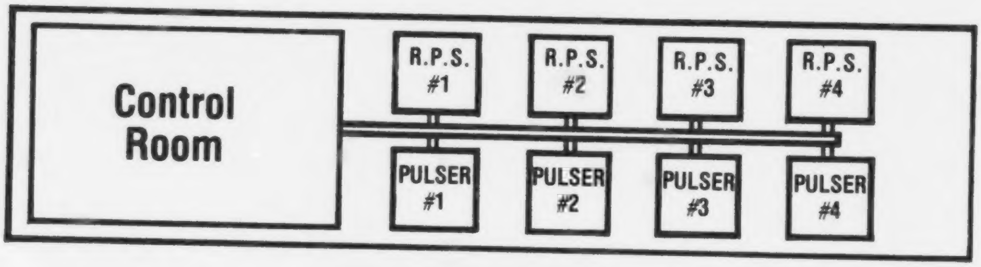

Figure 4. Plan View of Mobile Pulser System. R.P.S. refers to Reference Power Supply

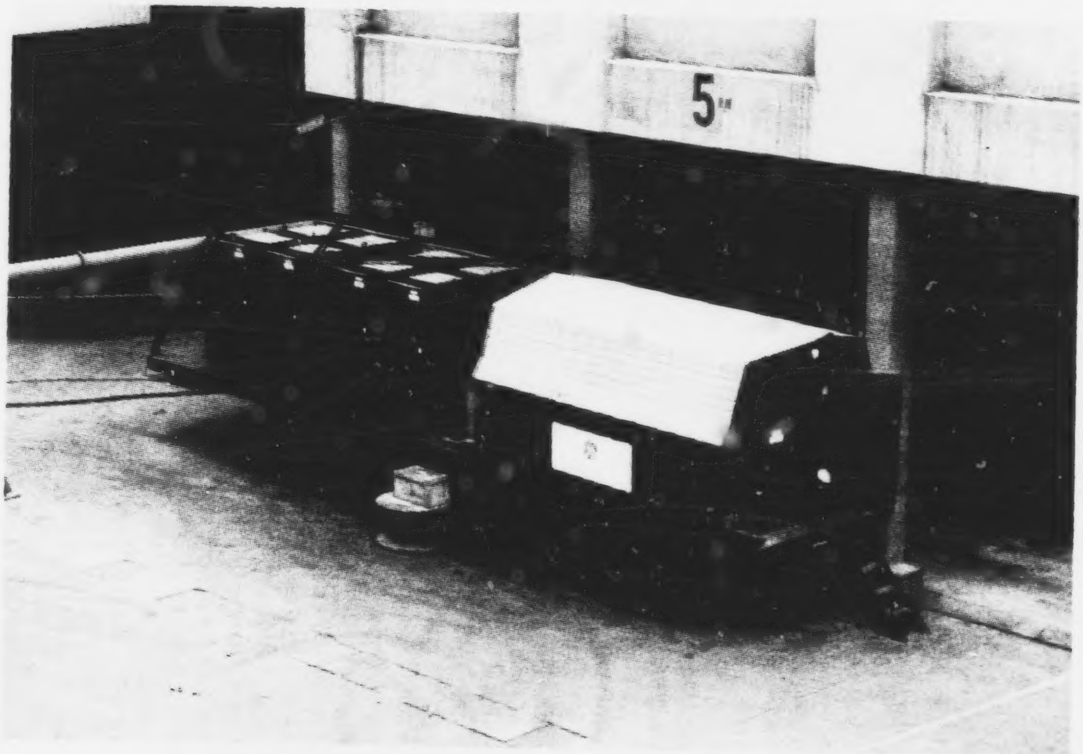

Figure 5. Typical Installation - Mobile Pulser Demonstration System

FULL SCALE TEST RESULTS

Pulse power demonstrations were conducted with the mobile pulser system in South Africa at Rooiwal Power Station - Pretoria Municipality and the Electricity Supply Commission (ESCOM) Hendrina Station and in the U.S. This paper describes test results from the Rooiwal and Hendrina Power Stations. Results from U.S. test sites will be presented in future publications.

ROOIWAL STATION UNIT #5

ESP Design Parameters

Unit #5 precipitator is a Lodge Cottrell two chamber rigid frame unit with two electrical fields per chamber. The unit is applied to a 60MW PC boiler and was installed in 1968.

Gas Volume - 238,930 ACFM (112 Am^3/s)
Gas Temperature - 291°F (144°C)
Inlet Dust Loading - 8.3 gr/ft^3 (19 gm/m^3)
Total Plate Area - 97,660 ft^2 (9072 m^2)
Plate Area Per Field - 24,415 ft^2 (2268 m^2)
SCA - 410
Efficiency - 96%
Coal Sulfur Content - 0.7-1.2%
Resistivity - 4×10^{12} - 1×10^{13} Ohm-CM
Transformers - 4 total, 25KVA

The unit is equipped with a mechanical drop hammer rapping system for both collecting and emitting electrodes and utilizes a basic variac and rotary rectifier powering system.

Precipitator Operation

Performance is in the range of 90-94% at a typical boiler load of 48MW. Mechanical and electrical integrity of the unit is very good. The rapping system however is not effective; excessive buildup occurs on both plate and rigid mast electrodes. The unit operates well within established back corona which is initiated shortly after corona onset potential is reached. Typical voltage-current curves are shown in Figure 6.

Pulser Installation and Powering Arrangement

The pulse powering arrangement for Rooiwal Unit #5 is shown in Figure 7. Pulsing was applied to both chambers of the precipitator, each pulser powering one electrical field for a total of four fields pulsed. The trailer mounted pulser system was located beneath the precipitator inlet ducts. A dry high voltage cable connected each pulser with the precipitator electrical field through a caged feed through insulator compartment in a control room located on the roof of each chamber.

The four existing variac operated 25KVA transformers with mechanical rectifiers were disconnected from the precipitator during the pulser test program. The four 90KVA transformers with Avcon control on the pulser trailer were used to energize the four electrical fields during periods of nonpulsing and the baseline tests.

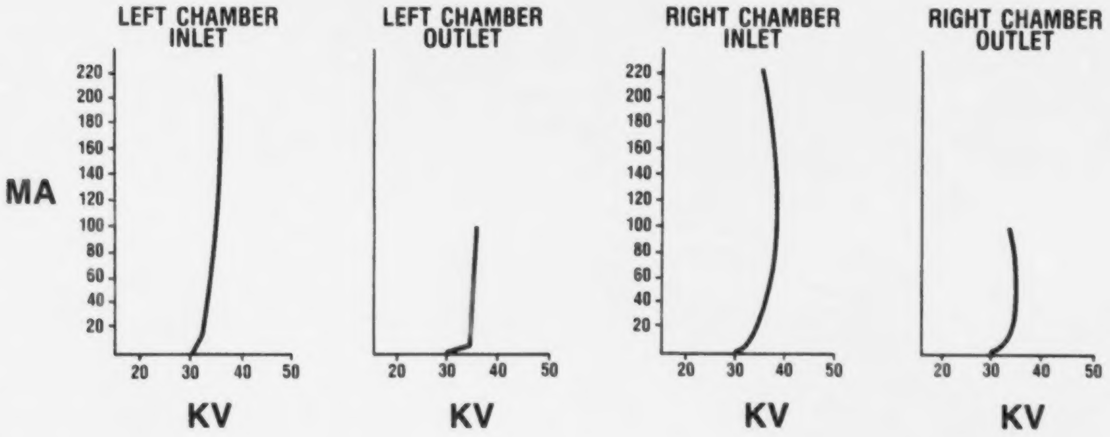

Figure 6. Voltage-Current Characteristics Rooiwal Unit #5

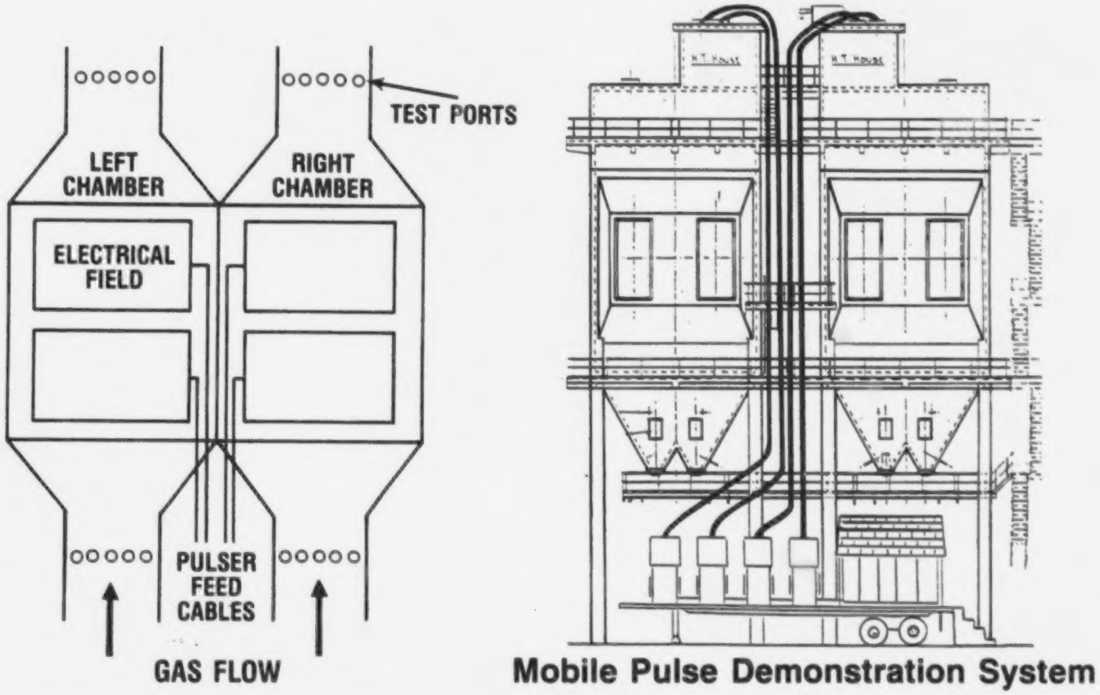

Figure 7. Pulser Tie-in and Powering Arrangement

Pre-Pulsing Tests

Prior to conducting the pulser test program, General Electric conducted a demonstration program on Unit #5 to assess other technologies - electromagnetic impact rapping and automatic voltage control of the conventional power supply. In order for an assessment to be made on the effect of plate ash buildup on pulsing enhancement the precipitator right chamber only was retrofitted with new rappers. The left chamber retained the existing rapping system and was used as the control. Automatic voltage control was evaluated by powering the four electrical fields with the pulser trailer's four standard precipitator power supplies that are used to provide a base DC level with pulsing applied. Mass efficiency testing was performed prior to the rapper retrofit to establish baseline performance with the existing rapper and variac control system. Tests were then performed with each of the new technologies so that their contribution to improved performance could be independently assessed and factored out of the pulsing results.

Baseline test results did not demonstrate a significant reduction in emissions due to new rappers but the effect of back ionization was moderated with precipitator voltages higher and current lower. The right chamber's voltage was 43kV versus the left's 39kV. This remained true during the pulsing tests with higher pulse voltages being obtained and thus greater enhancements on the right side versus the left.

A comparison of the mass collection efficiencies with automatic voltage control compared with the existing variac controls demonstrated that the mass collection efficiency with the new control system was greater, typically 89.9% vs. 88.6%. The reason for the approximately one percentage point increase in efficiency is that the automatic control prevented excessive sparking due to its spark response whereas the existing control had no response to sparking and is normally set at a high spark rate. A high spark rate is detrimental to the performance of a precipitator with only two electrical fields in depth.

Test Schedule - 1985

March 16-17	- Unit #5 Outage, washdown and inspection
March 22	- Baseline Tests - AVCON Control
March 25	- All Fields Pulsed
March 26	- Inlet Fields Pulsed, Outlets AVCON Control Outlet Fields Pulsed, Inlets AVCON Control
March 27	- All Fields Pulsed
March 28	- Baseline Tests - AVCON Control

Prior to pulse testing the precipitator was washed down and inspected. The mechanical integrity of the unit was very good. No close clearances existed and all gas passages, i.e. plates and wires, and inlet/outlet duct turning vanes, distribution baffles and duct floors were free of ash. The unit was brought back on line the evening of the 17th of March and within

48 hours was operating electrically as it had been before washdown. Therefore, the washdown did not affect the pulser baseline tests.

The dust sampled from the precipitator plates before washdown showed a sodium depleted layer next to the plate surface (7). This has been shown to be due to migration of sodium ions away from the plate electrode causing a highly resistive layer immediately at the plate surface (8).

Performance testing was performed by ESCOM (Electricity Supply Commission of South Africa) and CSIR (Council for Scientific and Industrial Research). The right-hand chamber was tested by ESCOM and the left by CSIR. The test methods are based on a British standard and are equivalent to the EPA Method 17 procedure.

Test Results

Performance tests results are shown in Table I for the right-hand chamber tested by ESCOM and Table II for the left chamber tested by CSIR. All tests were conducted at a constant boiler load of 48MW. Dust emissions were reduced by 73% for the right chamber and 51% for the left. For the case of all fields pulsed a results summary is as follows:

Right Chamber

Average Baseline Efficiency - 91.27%

Average Pulsed Efficiency - 97.60%

Migration Velocity Enhancement - 1.88 to 2.62

Left Chamber

Average Baseline Efficiency - 92.97%

Average Pulsed Efficiency - 96.55%

Migration Velocity Enhancement - 1.22 to 1.66

The difference in the pulsed performance between right and left chambers is due to the improved rapping on the right side with new impact rappers. The rapping was optimized prior to the tests using a portable opacity monitor installed in the right chamber outlet duct. In all cases with pulsing, the secondary voltages were higher on the right side than the left, resulting in a one percentage point increase in efficiency over the left side.

For both precipitator chambers the baseline efficiency without pulsing improved as pulse testing progressed. This phenomenon has been observed during other pulser test programs and is the residual effect of enhanced cleaning of the emitting electrodes due to the increased corona discharge points and their intensity during pulse energization.

Portable opacity meters were installed in both the right and left side outlet ducts. Reductions in opacity with pulsing averaged 50%. If only one field was pulsed, pulsing the inlet field was more effective in enhancing performance than the outlet field.

TABLE I. TEST RESULTS ROOIWAL UNIT #5 - RIGHT CHAMBER

Date	Condition	Inlet Loading gm/Am^3	Gas Volume Am^3/s	Percent Efficiency	ω_k[1] cm/sec	Enhancement*	Outlet Loading mg/Am^3 :	mg/Nm^3
3/22	Baseline	8.3	46.6	87.48	4.43		1037	1825
3/22	Baseline	9.7	46.0	91.53	6.18		824	1453
3/25	All Pulsed	11.1	45.4	97.60	13.92	2.62	265	460
3/25	All Pulsed	8.7	45.9	97.56	13.95	2.63	212	370
3/26	Inlet Pulsed	11.5	47.2	97.38	13.80	2.60	302	522
3/26	Outlet Pulsed	8.6	46.6	96.47	11.49	2.16	304	532
3/27	All Pulsed	9.5	50.1	*96.90	-			
3/27	All Pulsed	9.0	51.6	97.64	15.97	1.88	213	375
3/28	Baseline	10.1	58.9	92.47	8.68		763	1327
3/28	Baseline	11.9	54.2	92.79	8.26		855	1491

1. ω_k computed based on k = 0.5

* Test on 3/27 void due to 2 out of 6 traverses run with pulsers powered down due to communication problem with test crew; efficiency shown is estimate by ESCOM.

** Enhancement based on a baseline and pulsing test during the same time frame.

TABLE II. TEST RESULTS ROOIWAL UNIT #5 - LEFT CHAMBER

Date	Condition	Inlet Loading gm/Am^3	Gas Volume Am^3/s	Percent Efficiency	ω_k[1] cm/sec	Enhancement*	Outlet Loading mg/Am^3 :	mg/Nm^3
3/22	Baseline	10.7	55.2	91.51	7.4		879	1589
3/22	Baseline	11.1	55.1	92.06	7.8		849	1540
3/25	All Pulsed	13.4	49.1	96.54	12.25	1.61	497	892
3/25	All Pulsed	13.3	49.4	96.15	11.55	1.52	509	901
3/26	Inlet Pulsed	11.3	52.7	94.17	9.38	1.23	646	1154
3/26	Outlet Pulsed	11.6	52.8	93.73	8.93	1.17	707	1274
3/27	All Pulsed	11.0	51.4	95.92	11.60	1.22	436	781
3/27	All Pulsed	10.4	51.4	97.58	15.70	1.66	246	441
3/28	Baseline	12.3	53.2	94.23	9.54		706	1243
3/28	Baseline	12.4	53.3	94.08	9.40		727	1280

1. ω_k computed based on k = 0.5

* Enhancement based on a baseline and pulsing test during the same time frame.

Electrical Parameters

During pulser tests, the precipitator secondary voltage level was increased by over 80%, 39kV to 70 kV average.

Resistivity Measurement

$4.9\text{x}10^{12}$ Ohm-Cm (in-situ SRI Probe)
$1.0\text{x}10^{13}$ Ohm-Cm (in-situ Wahlco Probe)
$1.2\text{x}10^{12}$ Ohm-Cm (Laboratory)

Power Consumption

A wattmeter was installed by ESCOM in the pulser control room to determine power required for pulsing versus conventional operation. Power required for pulsing was the same as conventional powering, since, with the unit operating in established back corona, currents were very low, less than 100 MA for all power supplies. For a more moderate condition a power savings can be expected with pulsing as quantified during other tests.

Coal and Ash Analysis

Coal Analysis--

Ash	-	20.8%
Volatile Matter	-	25.2
Fixed Carbon	-	51.8
Water	-	2.2
Sulfur	-	1.09

Ash Analysis--

% Aluminum Oxide	Al_2O_3	-	30.65
% Calcium Oxide	CaO	-	5.15
% Iron Oxide	Fe_2O_3	-	4.52
% Magnesium Oxide	MgO	-	1.49
% Phosphorus Pentoxide	P_2O_5	-	0.85
% Potassium Oxide	K_2O	-	0.57
% Silica	SiO_2	-	50.00
% Sodium Oxide	Na_2O	-	0.15
% Sulfur Trioxide	SO_3	-	0.44
% Titanium Oxide	TiO_2	-	1.62
% Lithium Oxide	Li_2O	-	0.02
% Loss On Ignition	LOI	-	3.57

Mean inlet particle diameter - 10 to 13 microns

HENDRINA STATION UNIT #5

ESP Design Parameters

Unit #5 is a Lurgi two chamber rigid frame unit with three electrical fields per chamber and is applied to a 200 MW PC boiler.

Gas Volume	- 813,542 ACFM (384 Am^3/s)
Gas Temperature	- 280°F
Total Plate Area	- 319,808 ft^2 (29,722 m^2)
Plate Area Per Field	- 53,300 ft^2 (4953 m^2)
SCA	- 393
Efficiency	- 98%
Coal Sulfur Content	- 0.8%
Transformers	- 6 total, 66KVA

The unit is equipped with an electromechanical hammer rapping system for both collecting and emitting electrodes and utilizes Seimens automatic voltage controls.

Precipitator Operation

Performance is in the range of 92-96% at a boiler load of 200MW. The unit operates well within established back corona which is initiated shortly after corona onset potential is reached. Typical voltage-current curves are shown in Figure 8.

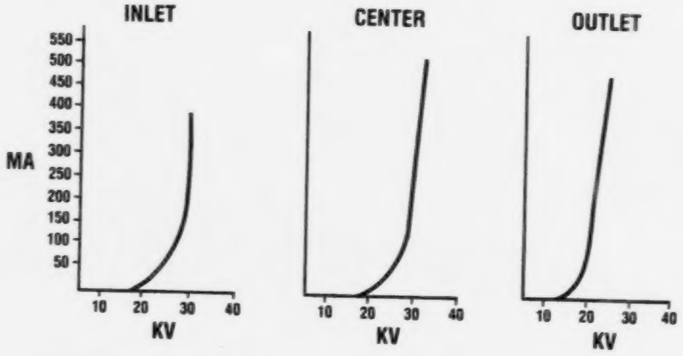

Figure 8. Voltage-Current Characteristics
Hendrina Unit #5

Pulser Installation and Powering Arrangement

The pulse powering arrangement for Hendrina Unit #5 is shown in Figure 9. Pulsing was applied to the right chamber only, with a total of three fields pulsed. Baseline tests were conducted utilizing the existing power supplies but thereafter the pulser trailer power supplies were used for periods of non-pulsing operation.

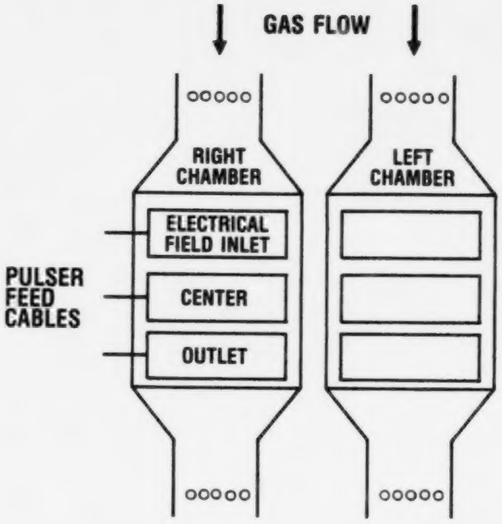

Figure 9. Pulse Powering Arrangement Hendrina #5

Test Schedule - 1985

April 18 - Baseline Tests (Seimens Power Supplies)

April 23 - Inlet Field Pulsed, Center and Outlet Conventional
Center Field Pulsed, Inlet and Outlet Conventional

April 24 - Outlet Pulsed, Inlet and Center Conventional

April 25 - All Fields Pulsed
Inlet and Center Field Pulsed, Outlet Conventional
Center and Outlet Field Pulsed, Inlet Conventional

April 26 - Baseline Tests (GE Power Supplies)
Inlet and Outlet Field Pulsed, Center Conventional

April 27-28 - Rappers Optimzed

April 30 - All Fields Pulsed
Center and Outlet Field Pulsed, Inlet Conventional

Test Results

Performance testing was conducted by ESCOM (Electricity Supply Commission of South Africa). Test Results are shown in Table III. All tests were conducted at a constant boiler load of 200MW. For the case of all fields pulsed and center and outlet field pulsed a results summary is as follows.

Average Baseline Efficiency	- 91.9%
Average Baseline Efficiency	- 97.5%
Migration Velocity Enhancement	- 1.95 to 2.20

TABLE III. TEST RESULTS HENDRINA UNIT #5

Date	Condition	Inlet Loading g/Am^3	Gas Volume Am^3/s	Percent Efficiency	ω_k[1] cm/sec	Enhancement	Outlet Loading mg/Am^3 :	mg/Nm^3
4/18	Baseline (Siemens)	11.0	207.8	92.62	9.50		869	1584
4/18	Baseline (Siemens)	11.7	198.6	91.26	7.94		969	1787
4/23	Inlet Pulsed	15.1	197.0	94.85	11.66	1.34	786	1435
4/23	Center Pulsed	16.3	197.6	96.03	13.84	1.59	660	1205
4/24	Outlet Pulsed	17.1	174.6	94.96	10.49	1.20	870	1598
4/25	All Pulsed	17.0	190.9	97.36	16.97	1.95	452	809
4/25	Inlet and Center Pulsed	15.3	197.1	96.51	14.93	1.71	538	974
4/25	Center and Outlet Pulsed	16.4	181.1	97.61	16.99	1.95	398	772
4/26	Baseline (AVCON)	14.4	197.3	95.73	13.20		625	1111
4/26	Inlet and Outlet Pulsed	14.8	195.0	96.49	14.72	1.69	524	946
4/30	All Pulsed	15.3	196.9	97.47	17.91	2.05	390	709
4/30	Center and Outlet	15.0	202.4	97.65	19.16	2.20	356	650

1. ω_k computed based on $k = 0.5$

Performance with all three fields pulsed was approximately the same as when only the center and outlet fields were pulsed. This is most likely related to the higher inlet dust loading suppressing the contribution to particle charging effect by pulsing. This is evident when comparing pulsing of the inlet only, with center only, Table III, 94.85% vs. 96.03%, respectively. Note that the increased baseline efficiency with GE power supplies versus that with the existing power supplies cannot be totally attributed to GE operation. As observed at Rooiwal and during other test programs, an enhanced cleaning of the emitting electrodes with pulsing occurs which can provide an improved precipitator performance for a baseline test conducted after pulse operation.

Electrical Parameters

During pulser tests the precipitator secondary voltage level was increased by 80% over conventional operation, 29kV to 52kV.

Resistivity Measurement

1.5×10^{12} Ohm-Cm (SRI Probe)
2.7×10^{12} Ohm-Cm (Wahlco Probe)

Power Consumption

A wattmeter installed by ESCOM in the pulser control room at Rooiwal was retained for use at Hendrina. Power consumed during pulsing was dramatically less than that used for conventional operation.

All Fields Pulsed - 8.5 KW
All Fields Conventional - 47.7 KW

Coal and Ash Analysis

Coal

Ash - 26.25%
Volatile Matter - 23.80
Fixed Carbon - 47.32
Water - 2.63
Sulfur - 0.94

Ash

% Aluminum Oxide Al_2O_3 - 27.86
% Calcium Oxide CaO - 3.24
% Iron Oxide Fe_2O_3 - 3.77
% Magnesium Oxide MgO - 1.11
% Phosphorus Pentoxide P_2O_5 - 0.68
% Potassium Oxide K_2O - 0.49
% Silica SiO_2 - 56.00
% Sodium Oxide Na_2O - 0.04
% Sulfur Trioxide SO_3 - 0.29
% Titanium Oxide TiO_2 - 1.40
% Manganese MnO - 0.02
% Loss On Ignition LOI - 3.79

COMPARISON TO OTHER PULSER TESTS

To compare General Electric's South African results with other pulser data, the results from Rooiwal and Hendrina Station are plotted on a published EPRI graph comparing penetration vs. pulsing enhancement factor for pilot and full scale utility ESP data (see Figure 10)(9). The GE Pulse Energizer results fall within the error bounds of pilot plant data from tests at EPRI's Arapahoe Facility. This is significant since pilot plant performance is usually better than full scale due to the former's more controlled conditions. The plotted left chamber Rooiwal results emphasize the importance of rapping on pulsing enhancement. Ineffective rapping will limit the maximum enhancement possible with pulsing due to the lower threshold of sparking.

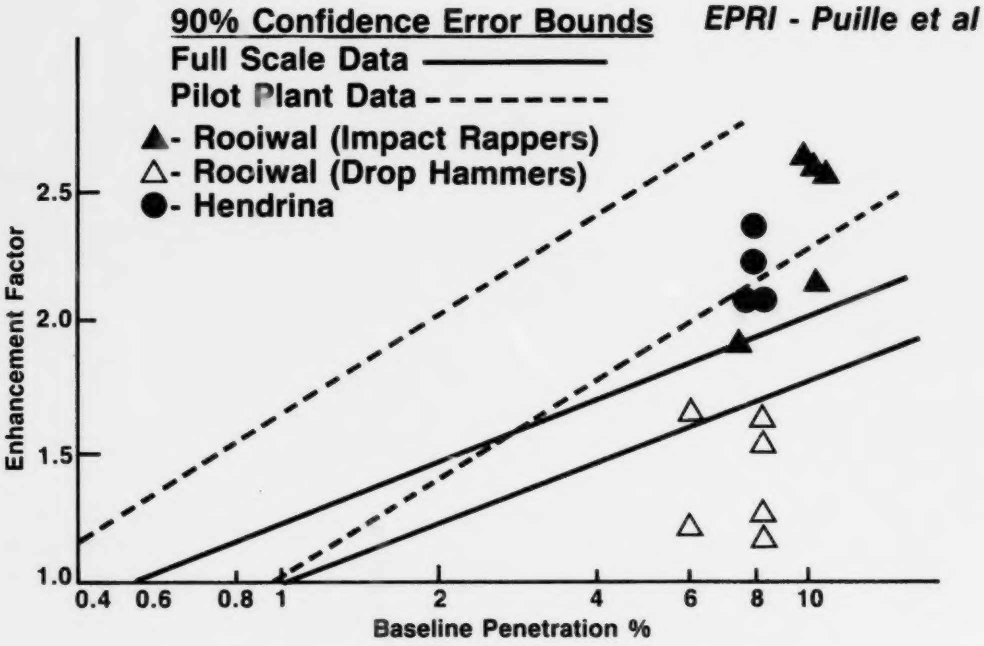

Figure 10. Penetration vs. Pulsing Enhancement Factor
South African Test Results Plotted on EPRI Graph

CONCLUSIONS

Full scale field tests with the GE Pulse Energizer have shown that the performance of precipitators collecting high resistivity ash can be greatly improved by pulse energization and at a significant reduction in power consumption. The degree of enhancement in performance obtained in South Africa with a difficult to collect ash is significant since these results were obtained with precipitator units of only two and three electrical fields in depth. Major test findings include:

- The large pulsing enhancements obtained were due to the high peak voltage achieved with pulsing, 80% increase over conventional operation.
- Consistent efficiency of approximately 97.5% was obtained with varying baseline performance.
- Effective rapping is required to obtain the maximum enhancement in performance with pulsing.
- Reduced power consumption with pulsing compared to conventional operation. Reduced power consumption may not be achieved with pulsing for applications with low power due to abnormally low secondary currents.

With reduced power consumption and low capital cost compared to gas conditioning and plate area addition, the GE Pulse Energizer provides a viable alternative to upgrade performance of existing precipitator units and allows a reduction in collecting plate area required for new unit applications. Pulse Energizer technology provides a cost effective electrical solution to the problem of meeting opacity and outlet emission requirements in applications where switching to lower sulfur coals is implemented.

The work described in this paper was not funded by the U.S. Environmental Protection Agency and therefore the contents do not necessarily reflect the views of the Agency and no official endorsement should be inferred.

ACKNOWLEDGEMENT

The authors wish to acknowledge Messrs. James Dalmon and Rod Hansen of the Electricity Supply Commission (ESCOM), Cris Albertyn of the Council for Scientific and Industrial Research (CSIR), and T. Rosch of Rooiwal Power Station, Pretoria Municipality, for their active participation, assistance and cooperation during the pulser demonstration programs. Their support was a major contribution to the successful completion of the test programs and is greatly appreciated.

REFERENCES

1. Chiang, T.K. and Lugar, T.W. Particle charging characteristics of a pulse corona discharge. IEEE-IAS Annual Meeting. October 1982.

2. Chiang, T.K. and Lugar, T.W., Leiby, R.H., Langan, W.T. Characterization of a pulse powered electrostatic precipitator. EPRI Conference. July 1982.

3. Yeager, K. R&D status report, Coal Combustion Systems Division. EPRI Journal, March 1985. pp. 42-45.

4. Penney, G.A. and Gelfand, P.C. The Trielectrode Electrostatic Precipitator for collecting high resistivity dust. J. APCA 28: 1, pp. 53-55, January 1978.

5. Piulle, W., Marchant, G.H. and Gooch, J.P. Evaluation of performance enhancement obtained with pulse energization systems on a hot-side electrostatic precipitator. EPA Symposium, March 1981.

6. Osmers, H.R. Pulse energization electrostatic precipitation. ESEERCO Research Report EP83-5. July 1985.

7. Dalmon, J., Bosch, F.J. and Hansen, R.S. Trial of a GE high voltage pulser on no. 5 electrostatic precipitator at Rooiwal Power Station. ESCOM Report M85/012. July 1985.

8. Bickelhaupt, R.E. and Altman, R.F. A method for predicting the effective volume resistivity of a sodium depleted flyash layer. J. APCA 34: 34, pp. 832-838.

9. Piulle, W., Landham, E.C., Dubard, J.L. and Sparks, L.E. Estimate ESP efficiency gains from pulse energization. Power. May 1984. pp. 51-53.

FIELD EVALUATION OF PULSE ENERGIZATION UNDER DIFFERENT OPERATING CONDITIONS

by: Senichi Masuda and Shunsuke Hosokawa
Department of Electrical Engineering,
University of Tokyo
7-3-1, Hongo, Bunkyo-ku, Tokyo 113, Japan

ABSTRACT

A series of field tests to evaluate pulse energization of electrostatic precipitators were made using "Direct-Coupled Submicrosecond Pulser" at three different plants: a pilot ESP combined with a coal-burning combustion rig, an ESP-type precharging section of an electrostatically augumented granular bed filter installed at a wooden-chip burning boiler, and an ESP installed at a glass melting furnace comprizing 3 series collection fields where the first and the second fields were pulse-energized. The pulse-energized collection area of these test ESP's was F = 5.57 m^2, 117 m^2, and 1522.4 m^2, respectively.

A great improvement was achieved in the first test for the coal flyash with the resistivity of 2 x 10^{13} ohm-cm, where its collection efficiency was raised from 84.2 % under dc energization causing severe back corona up to more than 99.0 % by pulse energization of this particular mode. Even in a lower resistivity level of 10^{10} - 10^{11} ohm-cm, pulse energization improved the collection efficiency.

In the second test, the wooden-chip burning boiler produced a large amount of unburnt carbon soot due to incomplete combustion. The dust resistivity was medium-high (10^{12} ohm-cm) to cause back corona with medium severity in dc energization. Pulse energization removed back corona, but no improvement was achieved in the collection performance. This was because of a very high space charge effect by unburnt carbon soot to produce corona quenching, which appeared as soon as back corona was removed and positive ion supply to reduce the space charge density was stopped.

In the third test, the dust resistivity was at an extremely high level close to 10^{14} ohm-cm, and even by pulse energization back corona could not be removed, with very little improvement in the collection performance. Moreover the exhaust gas contained the boron compounds fume condensed from the vapor

phase gradually during the passage of the ESP, and again the problem of high dust surface loading was recognized.

Using the same ESP, another test was made to examine the energy saving effect by pulse energization, where the gas from the furnace producing cathode-ray tube glass was used. The resistivity of dust in this test was at a moderate level where a high collection efficiency beyond 99 % was achieved in dc energization. By pulse energization, the performance remained unaltered, but the energy consumption became 1/16 of that in dc energization as a result of great reduction in current in pulse energization ($i = 0.078$ mA/m^2).

It was concluded that performance enhancement by pulse energization is possible only in the case where the cause of the trouble is restricted to a high dust resistivity but not exceeding say 10^{13} ohm-cm. In the case when the dust surface loading is large, the problem of corona quenching arises after back corona was removed. It was also confirmed that the energy saving effect is another big advantage of pulse energization.

INTRODUCTION

It is a matter of great concern whether pulse energization is really an effective means to enhance the collection performance of electrostatic precipitators suffering from the back corona troubles. In some cases pulse energization worked as expected, while in another case it failed. The cause of such uncertainty seems to be a hidden parameter which could never be identified in a laboratory precipitator.

Hence, the authors made a series of field evaluation tests of pulse energization at three different plant with different operating conditions. The tests were made with the direct-coupled mode of submicrosecond pulse energization using two proto-type pulser modules.[1,2,3] The test plants were a pilot ESP combined with a coal-burning combustion rig with the collection area of $F = 5.57\ m^2$,[4] an ESP-type precharging section of an electrostatically augumented granular bed filter installed at a wooden-chip burning boiler with $F = 117\ m^2$,[3] and an ESP installed at a glass melting furnace with three series fields where two fields with $F = 1522.4\ m^2$ were pulsed.[3]

In this paper are reported the results of these field tests and their assessments.

PRINCIPLES OF DIRECT-COUPLED PULSE ENERGIZATION

The principles of direct-coupled submicrosecond pulse energization used throughout the fields tests are briefly explained. Fig. 1 shows the basic pulse circuit where the pulse forming condenser and the rotating spark gap are used to generate pulse voltage. Fig. 2 shows the pulse voltage wave form in three different time scales. It is in a shape of a saw-tooth with a transient LC oscillation in its leading edge. The first peak of the LC oscillation acts for submicrosecond pulse energization and the dc average voltage in the saw-tooth produces a collecting field. The voltage is divided into two decay phases (decay phases I and II). The sharp decay (decay phase I) is produced by the migration of negative ions across the field, followed by the decay phase II where small leakage current or dc corona current exists provided back corona does not occur. However, when back corona occurs, it produces a constant and sharp decay even in decay phase II because positive ionic current flows during the entire period. Pulse voltage parameters are shown in the figure in which V_M (maximum voltage), V_R (final voltage in a pulse period), T_r (pulse rise time) and decay phases I and II are often referred in this paper.

TEST RESULTS AT PILOT ESP EQUIPPED WITH COAL-BURNING COMBUSTION RIG

TEST FACILITY

Fig. 3 shows the block diagram of the pilot ESP equipped with a coal-burning combustion rig. It consists of a coal pulverizer, a boiler, and a gas cooling system so as to make the precise simulation of a practical utility boiler. The specifications of the ESP is indicated in the figure. The gas temperature is set at Tg = 110 °C and 150 °C in order to test at two different dust resistivities, r_d. The measurement using a parallel-plate resistivity cell made in room air with 7 vol% water content shows $r_d = 2 \times 10^{13}$ ohm-cm at both Tg = 110 °C and 150 °C. But the performance of the conventional dc-energized collection field as well as its V - I characteristics are different between these two cases as shown later. The operating resistivity is greatly affected by SO_3 in the exhaust gas at a lower gas temperature (Tg < 120 °C in this case) so that its value at Tg = 110 °C is probably much lower, less than 10^{11} ohm-cm. The dust mass loading is measured by a constant dust monitor based on light scattering, calibrated by dust sampling made occasionally.

PRIMARY TEST

Fig. 4 shows the V-I characteristics in the conventional dc-energized collection field. Here V denotes the average voltage applied to the ESP and I the average current of the high voltage rectifier outlet. In Fig. 4(a) with Tg = 110 °C, the V-I curve represents ordinary corona characteristics indicating no back corona is occurring. On the other hand in Fig. 4(b) with Tg = 150 °C, a large hysteresis typical to severe back corona is recognized.

Fig. 5 shows the light activity at both the corona electrode and the collection electrode photographed at Tg = 150 °C. This is observed from the downstream side of the EP where the outlet duct is removed just after the gas flow is stopped. In the case when dc-energized field (Fig. 5(a)), the light of negative dc coronas appears only at local regions on the corona electrode opposite to the dust layer domains where back corona induced light is observed. Fig. 5(b) shows the light activity when pulse-energized. Luminous regions of back corona still remain on the collection electrode, yet their extent and luminosity are remarkably reduced. The most significant feature is the uniformity in corona activity on the corona electrode. Moreover, corona appears not only at the spikes of barbed wires, but also their between. Consequently, the ionic current distribution becomes very uniform on the entire collection electrode.

Fig. 6 shows the saw-tooth voltage wave form of pulse energization measured at the inlet terminal of the corona electrode. Fig. 6(a) is for Tg = 150 °C with T_r = 2 µs and V_M = -63 kV, and Fig. 6(b) for Tg = 110 °C with T_r = 2 µs and V_M = -68 kV. A difference exists between Figs. 6(a) and (b) in the magnitude of final voltage, V_R. In Fig. 6(a) (Tg = 110 °C) without back corona, V_R = -25 kV is obtained, whereas in Fig. 6(b) (Tg = 150 °C), a continuous decay produces V_R = -10 kV. The decay continues even below the dc corona threshold, V_c = -18 kV in this case. Back corona is not removed even by pulse energization, yet the collection performance is greatly improved as described in the next paragraph.

COLLECTION PERFORMANCE ENHANCEMENT BY PULSE ENERGIZATION

In Table 1 is summarized the performance enhancing effect by pulse energization compared with dc energization measured at I = 0.3 mA/m^2 and V_p = -65 kV where I is the average current density in the dc-energized field, V_p the maximum voltage in the pulse-energized field, η the collection efficiency, w the Deutsch migration velocity, and H the enhancement factor by pulse energization based on w. When no back corona takes place (Tg = 110 °C), the dc-energized collection field shows a high collection performance (η = 99.48 %, w = 15.1 cm/s). But the collection performance drops to η = 84.2 % and w = 5.3 cm/s when severe back corona takes place. Pulse energization produces a high collection efficiency in both cases of Tg = 110 °C and 150 °C (η = 99.83 % and 99.02 %, respectively). Even at Tg = 110 °C where no back corona occurs, pulse energization enhances distinctly the performance (H = 1.21). A very large enhancement is obtained at Tg = 150 °C when severe back corona takes place (H = 2.50).

Fig. 7 shows the effects of I and V_p on the collection efficiency of the dc-energized and pulse-energized fields, respectively, at Tg = 110 °C. Fig. 8 indicates the same results measured at Tg = 150 °C. The collection efficiency with dc energization increases with increasing current density, I, in both Figs. 7(a) and 8(a), but the value of w increases only by 2 cm/s in both cases by increasing current density from I = 0.1 mA/m^2 to 0.5 mA/m^2. This suggests that the high current operation of dc-energized field is not reasonable solution, especially considering energy consumption. The collection efficiency by pulse energization rises with increasing V_p in both cases of Figs. 7(b) and 8(b). This is because the uniformity and the intensity of the pulse-induced coronas are raised with increasing V_p. In Fig. 8(b), the flash over voltage is -70 kV. V_p with 80 % of the flash over voltage measured at this small plant (V_p = -56 kV), which is considered to be the no sparking operation voltage in practical plants shows a very high collection efficiency η > 98 % (Fig. 8(b)).

TEST RESULTS BY PRECHARGING ESP SECTION OF ELECTROSTATICALLY AUGUMENTED GRANULAR BED FILTER

TEST FACILITY

The small-sized ESP is used as a precharging section of a practical electrostatically augmented granular bed filter, being used for cleaning of an exhaust gas from a wooden-chip burning boiler. Fig. 9 shows the schematic of the plant. The exhaust gas from the wooden-chip burning boiler is introduced through two screen grid for gas distribution into the precharging section where dust particles are precharged, and then to the filter section where charged particles are collected on the surface of pebbles. Pulse energization is made at this precharger. The gas load is changed according to the fuel feed rate regulated by the screw revolutions, R_s, of a belt conveyor. The full gas load is produced at R_s = 1000 rpm.

The resistivity of the flyash sampled from the hopper of the precharging section is measured in a laboratory with the absolute humidity at 15 vol%. This resistivity is around 10^{13} ohm-cm at the operating temperature, 220 °C. However, it is anticipated that the working resistivity in the precharger is about one order of magnitude lower because very higher water content in the combustion gas. The flyash contained a substantial amount of carbon soot. However the dust resistivity is not affected much by carbon in this particular case. Silica with a very small particle size represents a major chemical component.

BEHAVIORS UNDER DC-ENERGIZATION

Fig. 10 shows V-I characteristics of this ESP-type precharger measured with the gas flow stopped. A smooth curve without back corona and corona quenching is observed. Fig. 11 indicates V-I curves measured under operating conditions. The solid curves show the characteristics with the full gas load (R_s = 1000 rpm) and a half gas load (R_s = 500 rpm) measured on the same day and the dotted curves with the full gas load (R_s = 1000 rpm) and 1/3 gas load, (R_s = 330 rpm) measured on the other day. Although the exhaust gas conditions fluctuate and the data scatter, it is clearly recognized that back corona is taking place with gas load under dc energization.

Visual observation is made with both naked eyes and an image intensifier from a man-hole installed at the ceiling of the precharger. Back corona in a form of many tiny breakdown points is recognized on the entire surface of grounded mesh electrodes. Its light is very luminous and active, while negative coronas on the wires are so feeble that they can not be observed by naked eyes. The round corona wires with 4 mm in diameter are covered with dust deposit of 1 - 2 mm thickness. The state of back corona changes in time, affected by the furnace conditions, and concurrent changes occur in operating voltage and current in the precharger. When streamer mode back corona is taking place, the voltage lies at a higher level of V_{dc} = -30 kV and the current fluctuates because of sparking. When glow mode back corona occurs, the voltage drops to the level of V_{dc} = -20 - -24 kV, with the current becoming stable at I = 50 mA (0.42 mA/m^2).

BEHAVIORS UNDER PULSE ENERGIZATION

At first pulse energization is tested at T_g = 205 °C with the gas flow stopped. Both the grounded electrodes the and corona electrodes are covered with high resistivity dust deposit. Fig. 12 shows the saw-tooth voltage on the precharger measured at its inlet terminal at $V_M = -45$ kV and $T_r = 400$ ns. It is a typical CR-decay in phase I, followed by a flat phase II. All the corona wires produce very strong light activity of pulsed coronas, while back corona on the grounded electrode disappears completely.

Then, the load test is carried out by allowing the exhaust gas to pass through the precharger. Fig. 13 shows the change in the voltage wave form in accordance with the increase in the load expressed by R_s, where the peak voltage is kept in the range of $V_M = -45 - -48$ kV. In Fig. 14 the mean current density in the precharger calculated from the saw-tooth voltage wave forms and the inter-electrode capacity is plotted against the screw revolutions, R_s. It can be seen from these two figures, that with increasing R_s the decay speed of the voltage is lowered, resulting a reduction of corona current. The excessive sparking takes place at a higher load, $R_s > 800$ rpm, when the smoke from the stack becomes noticeably black.

The visual observation of the inside of the precharger reveals that back corona is not occurring in any case of the load test when pulse-energized. However, there is a drastic change in the negative corona activity or the wires. The first wire in each duct indicates an active pulsed corona, but the coronas become feeble on the second and third wires and much less or completely disappears on the succeeding wires. Fig. 14 indicates that the mean current density at $R_s = 1000$ rpm becomes about one half of that at no load test ($R_s = 0$ rpm), which corresponds to the reduction in number of active corona wires confirmed by the visual observation.

These clearly indicate the corona quenching effect taking place in the precharger. Its severity increases with the increase in the fuel feed rate, R_s. Carbon soot produced in the furnace owing to incomplete combustion will be charged in the region of the first corona wire and form a large space charge density in the succeeding region. The field intensity around these wires should be reduced to stop corona production (corona quenching effect). Moreover, the field near the grounded electrodes will be enhanced to cause excessive sparking.

Table 2 shows the test results with both pulse energization and dc energization. The emission concentration of dust is measured at the outlet of the granular bed filter, and the precharging performance is estimated from these data, assuming the total collection performance being determined by the charging performance of the precharger. The peak voltage, V_M, in pulse energization is kept as high as possible ($V_M = -45$ to -48 kV in the test number 1,2,and 5-9, and $V_M = -52$ kV in the test number 10-12). No difference is likely to be existing in the emission concentration between pulse and dc energizations when a large fluctuation of the combustion conditions is taken into account. The peak voltage is limited by sparking, and the operation at a higher voltage to increase corona current is not possible.

CORONA QUENCHING EFFECT

The level of the corona current density when pulse-energized is very small compared with its ordinary level ($i = 0.43$ mA/m^2 in this case; see Fig. 14), but its charging time constant is calculated to be $t_{ch} = 0.15$ s by Pauthenier's equation. It is still much shorter than the residence time of dust in corona field ($t = 1.2$ s). Even when the active corona field be limited to the region of the first corona wire and the effective residence time be 1/6 (6 wires in one duct), the saturation charge should be given to the dust particles because the charging time constant becomes also 1/6.

A picture of what is going on in this particular case of severe space charge effect might be drawn as described in following:

(1) The gas containing a large quantity of carbon soot with a high magnitude of S (dust surface loading) is introduced to the first corona wire region of the precharging field where active pulsed corona is taking place. Although the current density in this region is high enough to satisfy the saturation charging condition for a single particle model of Pauthenier's equation, the amount of negative ions is not sufficient to provide enough charge to all of the particles as a result of too large magnitude of S.
(2) Indivisual particles poorly charged in the first wire region are brought to the succeeding corona wire region, with a very high overall space charge density. They reduce the field intensity around the wire below the corona onset. Especially in this particular case when round and smooth wires are used, this quenching effect may be pronounced. Moreover, the field near the ground electrode is greatly enhanced to produce the break down of dust layer, which will trigger a sparking.
(3) The poorly charged particles can not acquire additional charge in the succeeding regions, and be collected effectively.
(4) Hence, the collection performance would not be enhanced by pulse energization even though it can remove back corona effectively.

When operated in dc energization mode and the back corona trouble is occurring, the space charge effect does not appear at all. Back corona supplies copious positive ions to the space filled with negatively charged particles to compensate its high negative space charge density. As a result, the high dust surface loading effect is masked, and the level of overall current density consisting of both negative and positive ions remains high.

However, once back corona is completely removed by pulse energization and the space charge effect, hidden behind back corona, appears to play another role of trouble-maker. In order to solve both troubles of back corona and space charge effect electrostatically, the use of the preagglomerater in front of the pulsed collection field is likely to be effective.[5] The preagglomerater should consist of a back corona free precharger and a parallel plane collection field. Then, the pulsed collection field would perform most effectively.

TEST RESULTS BY ESP FOR GLASS MELTING FURNACE

TEST FACILITY

Fig. 15 shows the gas cleaning system for the glass melting furnace. It consists of a lime reaction chamber aimed to remove HF in the exhaust gas (lime conditioning) and an electrostatic precipitator out of 3 series fields. Water spray is being made before the reaction chamber. At both of the inlet and outlet ducts of the precipitator are measured the dust mass loading and the boron content in the vapor phase. Two series of tests are made by using the exhaust gas either from the furnace producing fiber glass or from the one producing cathode-ray tube glass. The gas conditions of these two cases are shown also in the figure.

Fig. 16 shows the schematic top view of the precipitator tested. Fields 1 and 2 are pulse-energized in parallel by inserting the "cassette type pulser module" between the existing dc power supply and their H.V. inlet. These fields have a standard duct spacing of 2D = 300 mm and the collection area F = 1523.2 m^2 in total. Not only direct-coupled pulse energization but also dc-biased pulse energization is tested by connecting an additional dc power supply in series. DC-biased pulse energization in this case is used to raise the average voltage (namely increase V_R as described later) where the oscillatory pulse shape is the same as those by direct-coupled pulse energization. Field 3 has a wide duct spacing with 2D = 500 mm, and is operated in dc energization during the entire experiments.

In dc energization mode, the dc power supply is automatic-controlled to maintain the corona current at:

Fields 1 and 2 : I = 400 mA (i = 0.53 mA/m^2)
Field 3 : I = 400 mA (i = 0.81 mA/m^2).

However, sparking in Fields 1 and 2 prevents a stable operation, and both the current and the voltage fluctuate greatly.

BACK CORONA CORRECTION TEST

This series of tests are made using the gas from the furnace producing fiber glass. The dust mass loading at the inlet of the ESP is in the range of 200 - 300 mg/Nm^3 without lime conditioning, and 1000 - 2500 mg/Nm^3 with lime conditioning. The dust contained boron compounds with very high resistivity in about 40 - 50 weight% in the case no lime conditioning is made. The dust resistivity measured at a laboratory is about 10^{13} ohm-cm at 250 °C. The working resistivity, however, seems to be a higher, close to 10^{14} ohm-cm. Lime conditioning does not change the resistivity. It is assumed that the $Ca(OH)_2$ particles are covered with boron compounds producing high resistivity.

V-I Curves under DC Energization

Fig. 17 shows the V-I characteristics of Field 3 with lime conditioning stopped. Two examples measured on the same day are shown. The curve shows a very steep rise and a tendency of hysteresis even in this case of a wide duct spacing of 2D = 500 mm. The visual observation reveals that a very severe back corona is occurring on the entire collection plates, and that the dust layer opposite to the corona wires emitts very bright lights of back coronas.

With lime conditioning off, the excessive sparking occurs in Fields 1 and 2 preventing the measurement of V-I characteristics. With increasing the voltage, the current suddenly jumps to a high level of about 140 mA, and sparking takes place concurrently. As a result, the stable operation becomes impossible, and the voltage and the current make a cyclic change with current jump from 0 mA to 140 mA at V = -30 to -32 kV, followed by V = 0 kV and I = 0 mA with sparking. This extremely unstable V - I characteristics with excessive sparking is usually observed in the case of back corona at a lower dust resistivity, $r_d = 10^{10} - 10^{11}$ ohm-cm. However, the dust resistivity in this case is around $r_d = 10^{14}$ ohm-cm, so that another mechanism must be sought to explain this strange characteristics of excessive sparking. This mechanism is not clear yet, however, the following hypothesis may be built. As described later, a large quantity of extremely fine fumes of boron compounds are introduced and also condensed from the vapor phase continuously. They suppress the corona current by forming a dense space charge to enhance considerably the electric field near the dust layer on the collection electrode. The effects of the space charge is magnified by an increased duct spacing. In this stage, however, enough ionic current does not reach the dust layer. By raising the voltage the corona current reaching to the layer exceeds a threshold, and back corona suddenly takes place. Back corona is enhanced by the enhanced field near the layer easily to turn into sparking. This hypothesis should be supported by more precise experiments.

Pulse Voltage Wave Form

Fig. 18 shows the pulse voltage wave form of direct-coupled pulse energization operated under the condition : $V_M = -50$ kV, $T_r = 900$ ns and $F_p = 50$ Hz with lime conditioning off and water spray on. The saw-tooth voltage shows a continuous decay in the entire decay phase resulting a very low level of the final voltage of $V_R = -10$ kV. This indicates that severe back corona takes place in Fields 1 and 2 even when pulse-energized.

The pulse voltage with both lime conditioning and water spray on is observed at the same magnitudes of V_M, T_r and F_p, and the effect of lime conditioning on the voltage wave form is tested. No distinct difference is observed in the voltage wave forms between lime conditioning on and off. It is anticipated that lime conditining alters neither corona production in the corona wires nor back corona severity. The high dust surface loading will also remain unaffected by lime conditioning.

Fig. 19 indicates the effect of the pulse repetition frequency, F_p, on the voltage wave form measured at $V_M = -50$ kV. It is astonishing to see that the decay speed in the decay phase increases with increasing F_p and, concurrently, the magnitude of the final voltage remains unchanged at about $V_R = -10$ kV, although V_R shows a slight increase with F_p. It is anticipated that with increasing F_p the average number of negative ions arriving at the surface of the dust layer in a unit time increases proportionally, tending to raise its surface potential. However, with the increase in the surface potential beyond the breakdown threshold, which is originally a statistical value scattering around its average, the number of the breakdown points would increase to produce an increased emission of positive ions, and thereby keeping the magnitude of the surface potential almost unaltered. As a result, the supply of the positive ions by back corona per each pulse should be increased in proportion with F_p, and the decay time will be decreased. with F_p, concurrently.

Effect of DC Bias Voltage

By connecting a dc power supply in series to the outlet terminal of the direct-coupled pulse power supply (see Fig. 16) without using any coupling means, the effect of the dc bias voltage is tested. Fig. 20 shows the voltage wave form of this dc-biased pulse energization at $V_M = -55$ kV. Its bottom is increased with the aid of the dc bias voltage. The bottom is not flat, but fluctuating in accordance with the frequency of the dc power supply (full-wave rectification : 120 Hz). It should be noted that the dc corona onset voltage in this particular case is $V_c = -24$ kV, and the dc voltage with pulse off remains flat up to this level. The negative ionic current induced by the pulse voltage should disappear in the first 2 - 4 ms, and the later voltage fluctuation in the dc bias voltage is caused by the positive current produced by back corona. This is another evidence of back corona occurring in the pulse energized fields. The back corona extinguishing voltage in this case may be as low as blow -10 kV, resulting in the continuous voltage decay when the dc bias voltage is removed.

Visual Observation of Pulse Energized Field

Although the voltage wave form indicates a distinct sign of severe back corona taking place, no light activity is observed by the visual observation both by naked eyes and by a potable image intensifier on the collection electrode of the pulse energized fields (Fields 1 and 2) with lime conditioning on and off. The observation is made from the man-holes on the roof of both Fields 1 and 2. According to the author's experience, such mode of back corona with a very feeble light activity is caused by an extremely high resistivity dust with say $r_d > 10^{14}$ ohm-cm.

Measurements of Collection Performance

The collection performance by pulse energization is tested using a dust sampler with lime conditioning on and off. Comparison tests for dc energization are also made. These results are shown in Tables 3 and 4. The inlet conditions fluctuate greatly, so that the effect of pulse is difficult to estimate. However, it can be concluded that the collection performance indicates no distinct improvement by pulse energization. The change of the operation mode in pulse energization does not indicate any significant difference in collection performance either. It should be noted that the boron compounds (shown by B_2O_3 in the table) in vapor phase decreases in the precipitator due to condensation. The quantity of the condensation is estimated to be about 220 mg/Nm^3, which is as large as the total of the inlet dust mass loading. The collection efficiency indicated does not take this factor into account.

According to the other tests, the boron compounds continue to condense from the vapor phase with the decreasing gas temperature down to about 70 °C. This continuous condensation produce a large quantity of very fine fumes with less than 1 μm diameter responsible to a large dust surface loading in the precipitator.

Discussions

This is another example of the co-existence of extremely high dust resistivity and a large quantity of very fine particles. The space charge effect produced by such fine particles is masked by extremely severe back corona under dc energization, and completely hidden behind. However, a very unstable operation in dc energization in the Fields 1 and 2 with a standard duct spacing is likely to be related to a very high dust surface loading.

This series of tests indicate that back corona can not be removed even by pulse energization when the dust resistivity approaches the level of 10^{14} ohm-cm. In such case, parallel plane collection fields [6] or pulse-energized collection fields with a very low current operation, both combined with a back corona free precharger, may be one of the solutions. A suitable chemical agent to lower the dust resistivity below $r_d = 10^{13}$ ohm-cm may be another solution.

ENERGY SAVING EFFECT

The second series of tests using the same electrostatic precipitator is made by introducing the exhaust gas from the furnace producing cathode-ray tube glass. Lime conditioning is also being made in order to remove HF components in the gas. The dust contained in the exhaust gas has a much lower resistivity, and there is no fume condensation in the temperature range of the ESP. The collection performance even by dc energization is very high beyond 99 %. The target of this series of tests is to examine the energy saving effect by pulse energization.

Pulse Voltage Wave Forms

Figs. 21 shows the pulse voltage wave forms in two different time scales. The saw-tooth voltage wave form with clearly defined decay phases I and II represents a typical example when back corona does not exist. The decay phase I lasts 3 - 4 ms, and in the decay phase II the voltage wave form is almost flat with $V_R = -20$ kV in a wide range of the pulse repetition frequency of $F_p = 25 - 100$ Hz. This also indicates a quantity of the negative current produced by one pulse to be almost same, and the ionic current increases in proportional to the pulse repetition frequency in this range of F_p (see Table 5).

Reduction in Energy Consumption

The tests are made with three different pulse repetition frequencies, and compared with dc energization. The maximum voltage in pulse energization is kept as high as possible within sparking limit ($V_M = -50$ kV). Table 5 shows the test results. The outlet mass loading is below 10 mg/Nm^3 in all cases tested and the collection efficiency is higher than 99 %.

The total power consumption in Fields 1 and 2 for energization is also shown. In dc energization with automatic control, 22.2 kWh is consumed. A great reduction occurs in direct-coupled pulse energization. The reduction rate increases with the decrease in the pulse repetition frequency. The power consumption at F_p = 25 Hz is as low as only about 1/16 of the one under dc energization, with the collection performance remaining unaltered.[7] Energy saving effect is also expected even with intermittent energization, which, however, does not produce such a great reduction.

CONCLUSION

In the series of the field tests made to evaluate the effectiveness of pulse energization, the following conclusions are obtained:

(1) When the cause of performance degradation is restricted only to the back corona trouble, pulse energization is likely to enhance the performance.
(2) In the moderate level of dust resistivity where dc energization performs very well, pulse energization still enhances or at least does not lower the collection performance.
(3) These is an upper limit of dust resistivity beyond which pulse energization can not correct back corona trouble. This is likely to be around 2×10^{13} ohm-cm. Beyond 10^{14} ohm-cm back corona can never be abated by pulse energization, with the collection performance not improved.
(4) In the case high dust resistivity and high dust surface loading co-exist, the space charge trouble like corona quenching appears as soon as back corona is eliminated by pulse energization. Collection performance can not be raised due to the shortage in the charge of indivisual dust particles.
(5) The energy saving effect of pulse energization is very substantial even in the case of moderate dust resistivity at which no back corona takes place in dc energization. This effect becomes more pronounced at a higher resistivity level to produce back corona.

It is concluded that pulse energization is a good solution for a high resistivity problem, but that a careful attention must be paied on the so-called hidden variables like an excessively high dust surface loading.

The work described in this paper was not funded by the U.S. Environmental Protection Agency and therefore the contents do not necessarily reflect the views of the Agency and no official endorsement should be inferred.

REFERENCES

[1] S.Masuda and S.Hosokawa; Pulse Energization System of Electrostatic Precipitator for Retrofitting Application, Proc. of the 5th EPA-EPRI Symp. on Transfer and Utilization of Particulate Control Technology, (Aug. 1984 in Kansas City)

[2] S.Masuda and S.Hosokawa; Submicrosecond Pulse Energization for Retrofitting Application, Proc. of 2nd International Conference on Electrostatic Precipitation, pp613-622 (Nov. 1984 in Kyoto)

[3] S.Hosokawa; Pulse Energization in Electrostatic Precipitator, Doctoral Dissertation, Univ. of Tokyo, (1986)

[4] S.Masuda, S.Hosokawa, N.Tachibana, T.Ando, and Y.Matsumoto; Fundamental Behaviors of Direct-Coupled Submicrosecond Pulse Energization in Electrostatic Precipitators, Record of IEEE IAS 1985 Conference, pp1288-1294, (Oct. 1985 in Tronto)

[5] S.Masuda and J.Moon; Electrostatic Precipitation of Carbon Soot from Diesel Engine Exhaust, Record of IEEE IAS 1982 Annual Conference, pp1086-1094, (Oct. 1982 in San Fransisco)

[6] S.Masuda and S.Hosokawa; Performance of Two-Stage Type Electrostatic Precipitators, Trans. of IEEE/IAS, vol IA-21 No. 4 May/June, pp724-732, (1984)

[7] T.Ando, Y.Nakayama and Y.Matsumoto; Reduction of Power Consumption in Precipitators, Proc. of 2nd Int. Conf. on Electrostatic Precipitation, pp219-227 (Nov. 1984 in Kyoto)

Table 1 Collection Performance of DC-Energized and Pulse-Energizated Collection Fields in Typical Cases

Gas Temperature T_g (°C)	DC-Energization ($I = 0.3$ mA/m^2)		Pulse-Energization ($V_M = -65$ kV)		Enhancement Factor H
	η(%)	w(cm/s)	η(%)	w(cm/s)	
110	99.48	15.1	99.83	18.2	1.21
150	84.19	5.3	99.02	13.2	2.50

key

I : ionic current density in dc-energized collection field
V_M : maximum voltage applied in pulse-energized collection field (peak voltage in the first cycle of LC oscillation)
η : collection efficiency
w : Deutsch migration velocity
H = w (pulse-energization) / w (dc-energization) : enhancement factor
r_d = 2×10^{13} ohm-cm at T_g = 150 °C
$10^{10} - 10^{11}$ ohm-cm at T_g = 110 °C

Table 2 Results of Comparative Tests of Dust Emission Measured at the Outlet of Granular Bed Filter (ESP-Type Precharger : either dc-energization or pulse-energization)

Test NO.	Mode of Energiza-tion	Speed of Fuel Feeding Screw R_s (rpm)	Gas Volume Q_g (Nm^3/h)	Gas Temparature T_g (°C)	Outlet Dust Mass Loading W_o (g/Nm^3)	Average Current Density i (mA/m^2)	Remarks
1	pulse	800	21,100	190	0.107		
2	pulse	800	20,500	195	0.088		
3	dc	800	21,600	190	0.083		
4	dc	800	22,900	200	0.060		
5	pulse	1000	21,600	180	0.101	0.052	
6	pulse	900	23,100	220	0.092	0.054	
7	pulse	850	23,600	215	0.117	0.058	
8	pulse	800	23,800	220	0.156	0.037 - 0.060	Excesive Sparking
9	pulse	800	24,000	230	0.094		
10	pulse	850	23,400	200	0.159	0.043	Excesive Sparking
11	pulse	850	23,600	205	0.115	0.041	
12	pulse	850	23,000	210	0.219	- 0.052	Excesive Sparking
13	dc	850	20,600	200	0.083		
14	dc	850	23,200	205	0.196		
15	dc	850	22,400	215	0.110		

Note: Soot appears from the stack in Test NO. 8, 10, 12, and 14.

Table 3 Results of Comparative Tests of Collection Performance Between DC-Energization and Pulse-Energization Under No Lime Conditioning

Test Conditions		Dust Mass Loading (mg/Nm^3)	Dust Components		B_2O_3 in Vapor Phase (mg/Nm^3)
			$Ca(OH)_2$ (mg/Nm^3)	B_2O_3 (mg/Nm^3)	
Direct-Coupled Pulse Energization V_M=-50kV, F_p=50Hz, i=0.056mA/m^2	Inlet	214	10.1	78.9	----
	Outlet	85.1	3.0	36.5	----
Direct-Coupled Pulse Energization V_M=-55kV, F_p=10Hz, i=0.005mA/m^2	Inlet	200	5.6	87.9	1140
	Outlet	75	1.7	31.9	781
DC Biased Pulse Energization V_M=-55kV, V_{bias}=-20kV, F_p=50Hz	Inlet	220	7.2	82.1	1240
	Outlet	100	3.2	42.9	871
DC Energization	Inlet	250	---	---	---
	Outlet	63	---	---	---

Note: Water Spray = 6 ℓ/min
Lime Conditioning : Off

Table 4 Results of Comparative Tests of Collection Performance Between DC-Energization and Pulse-Energization With Lime Condioning On

Test Conditions		Dust Mass Loading (mg/Nm^3)	Dust Components	
			$Ca(OH)_2$ (mg/Nm^3)	B_2O_3 (mg/Nm^3)
Direct-Coupled Pulse Energization V_M=-50kV, F_p=50Hz, i=0.056mA/m^2	Inlet	2315	1285	180.2
	Outlet	601	416	69.5
DC Energization	Inlet	1067	682	165.7
	Outlet	327	207	52.7

Note: Water Spray = 6 ℓ/min
Lime Conditioning : On

Table 5 Energy Saving Effect of Pulse Energization
(Furnace: Cathode-Ray Tube Glass)

	Energy Consumption (kWh)	Dust Mass Loading		Collection Efficiency (%)
		Inlet (mg/Nm^3)	Outlet (mg/Nm^3)	
Direct Coupled Pulse Energization V_M=-50kV, F_p=25Hz, i=0.023mA/m^2	1.4	916	10.6	98.84
		869	5.4	99.38
Direct Coupled Pulse Energization V_M=-50kV, F_p=50Hz, i=0.044mA/m^2	2.3	896	----	-----
		974	9.1	99.07
Direct Coupled Pulse Energization V_M=-50kV, F_p=100Hz, i=0.078mA/m^2	4.8	959	4.9	99.49
		1010	9.8	99.03
DC Energization	22.2	926	2.2	99.76
		1080	3.8	99.65

Note: Water Spary = 6 ℓ/min, Lime Consumption = 25 kg/h.

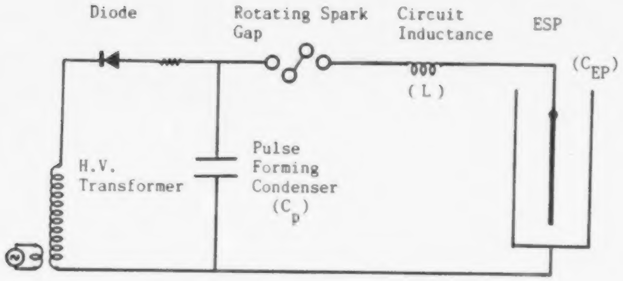

Fig. 1 Circuit Diagram of Direct-Coupled Submicrosecond Pulse Energization

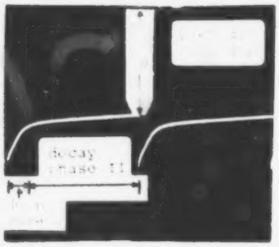

(a) [illegible]

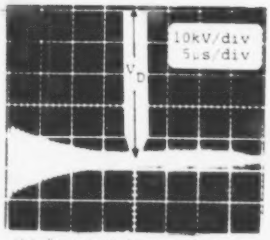

(b) Transient LC oscillation

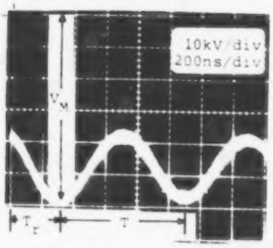

(c) [illegible]

[illegible]

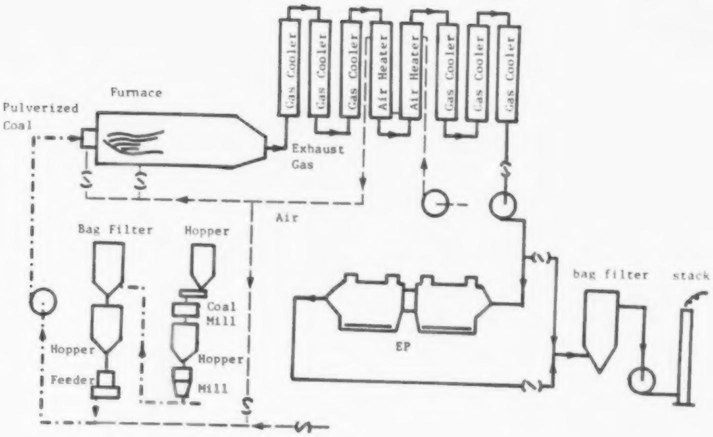

EP: 2D = 300 mm (duct spacing)
Corona Electrode: Berved Wires
$F = 5.57\, m^2$ (collection area)
$f = 35\, s/m$ (specific collection area)
$V_g = 0.9\, m/s$ (gas speed)

Fly Ash: $S_i = 4.5 - 5.5\, g/Nm^3$ (inlet dust mass loading)
$d_m = 6.5\, \mu m$ (mass median diameter)
$r_d = 2 \times 10^{13}$ ohm-cm at $T_g = 150\,°C$
$10^{10} - 10^{11}$ ohm-cm at $T_g = 110\,°C$
(dust resistivity)

Fig. 3 Test Facility of Pilot EP Combined with Coal-Burning Combustion Rig

Reproduced from best available copy.

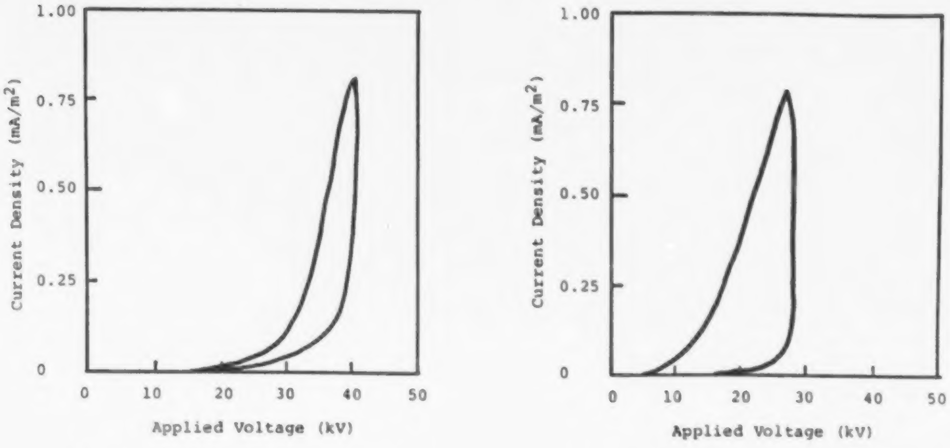

(a) normar curve without back corona (T_g = 110 °C : $r_d = 10^{10} - 10^{11}$ ohm-cm)

(b) hysteresis curve with severe back corona (T_g = 150 °C : $r_d = 2 \times 10^{13}$ ohm-cm)

Fig. 4 V - I Characteristics in DC-Energized Field

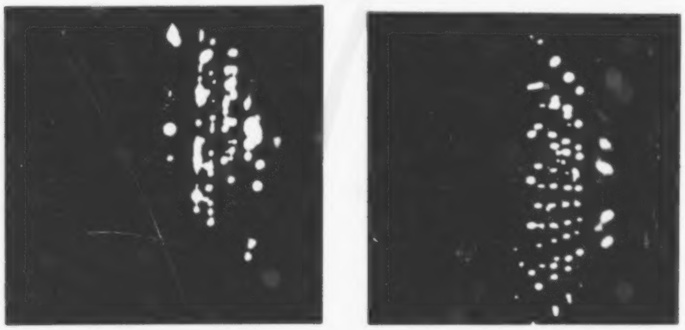

(a) dc-energized field (b) pulse-energized field

Fig. 5 Correction of Back Corona and Enhancement of Uniformity in Light Activity of Corona Wires by Pulse-Energization (T_g = 150 °C)

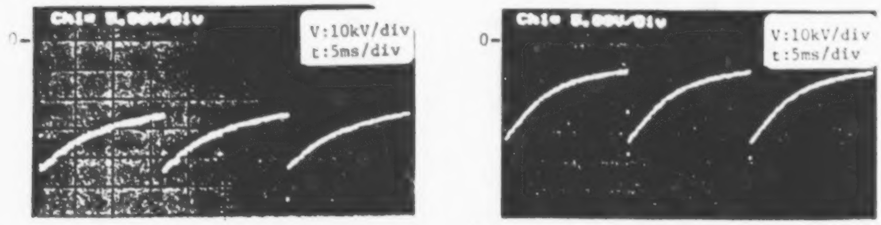

(a) No Back Corona (T_g = 110 °C; $r_d = 10^{10} - 10^{11}$ ohm-cm)

(b) Slight Back Corona (T_g = 150 °C; r_d = 2×10^{13} ohm-cm)

Fig. 6 Saw-Tooth Voltage Wave Forms Under Two Different Dust Resistivities

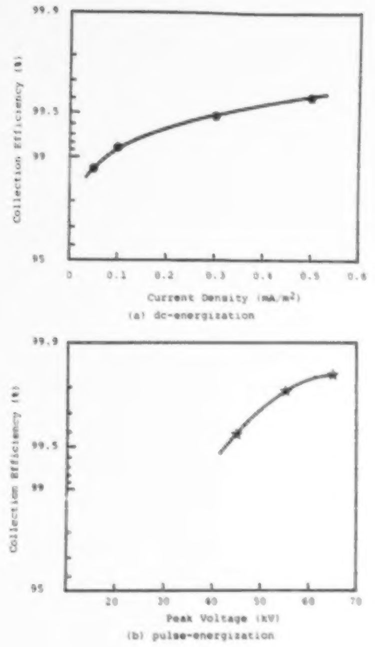

Fig. 7 Enhancement of Collection Performance by Pulse Energization (T_g = 110 °C ; r_d = 10^{10} - 10^{11} ohm-cm, no back corona in both dc-energized and pulse-energized fields)

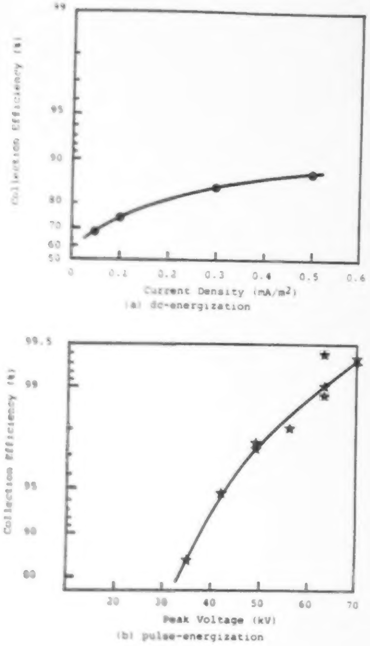

Fig. 8 Enhancement of Collection Performance by Pulse Energization (T_g = 150 °C ; r_d = 2 x 10^{13} ohm-cm, severe back corona in dc-energized field and slight back corona in pulse-energized field)

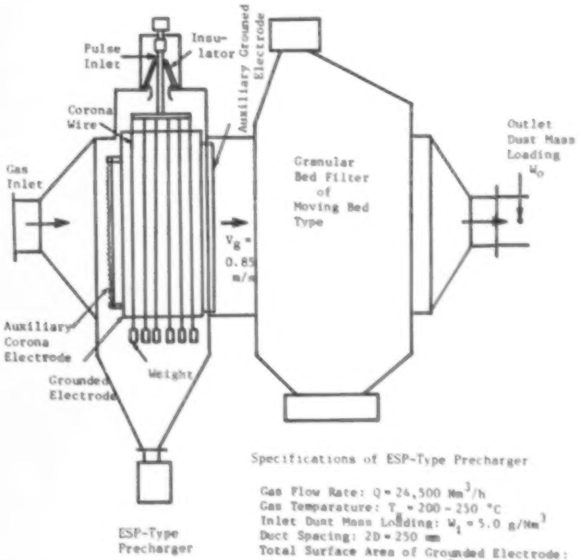
Pulse Inlet
Insu-lator
Auxiliary Grounded Electrode
Corona Wire
Gas Inlet
Granular Bed Filter of Moving Bed Type
V_g = 0.85 m/s
Outlet Dust Mass Loading W_o
Auxiliary Corona Electrode
Weight
Grounded Electrode
ESP-Type Precharger

Specifications of ESP-Type Precharger

Gas Flow Rate: Q = 24,500 Nm^3/h
Gas Temparature: T_g = 200 - 250 °C
Inlet Dust Mass Loading: W_i = 5.0 g/Nm^3
Duct Spacing: 2D = 250 mm
Total Surface Area of Grounded Electrode:
F = 117 m^2
Corona Wire: Smooth Round Wire with 4 mmϕ
6 wires spaced at 140 mm
Gas Residence Time in Precharger: t = 1.2 s

Fig. 9 Electrostatically Augumented Granular Bed Filter Installed at a Wooden-Chip Burning Boiler

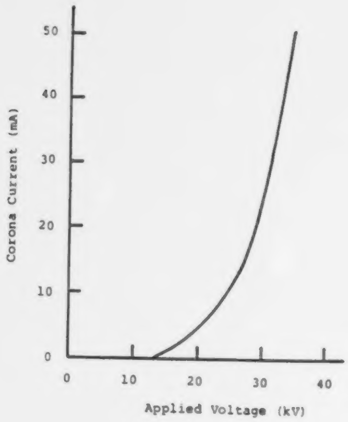

Fig. 10 V - I Characteristics of DC-Energized Field of ESP-Type Precharger under No Gas Load (Tg = 250 °C)

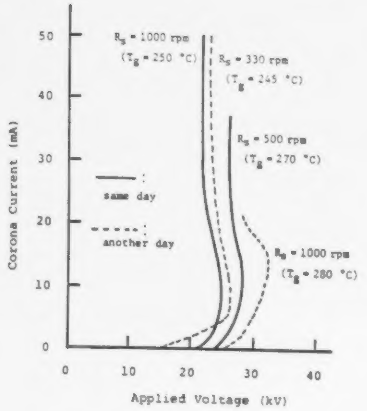

Fig. 11 V - I Characteristics of DC-Energized Field of ESP-Type Precharger under Gas Load (full gas load : R_s = 1000 rpm)

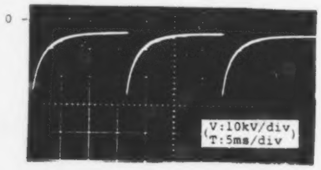

Fig. 12 Pulse Voltage Wave Form Under No Gas Load (T_g = 205 °C)

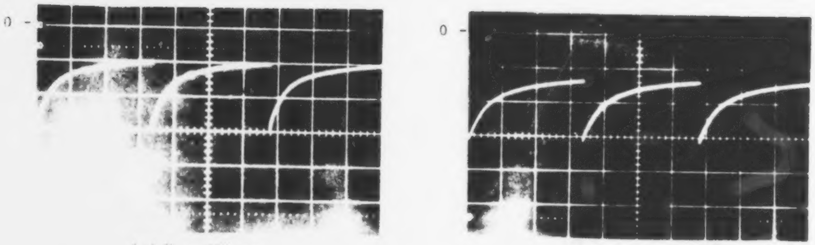

(a) R_s = 100 rpm

(b) R_s = 400 rpm

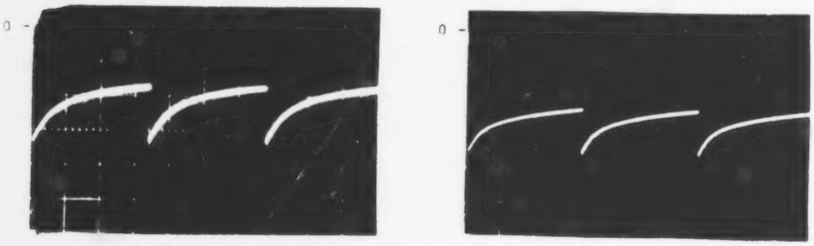

(c) R_s = 800 rpm

(d) R_s = 1000 rpm

Fig. 13 Change of Pulse Voltage Wave Form with Increase in Gas Load (maximum gas load : R_s = 1000 rpm)

Reproduced from best available copy.

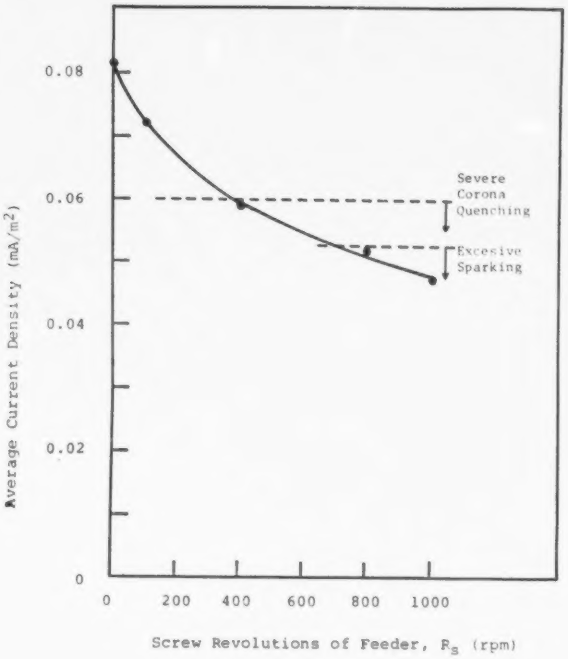

Fig. 14 Change in Current Density Due To Space Charge Effest
(Severity of space charge effect increases with increase in gas load changed by screw revolutions of fuel feeder, R_s.)

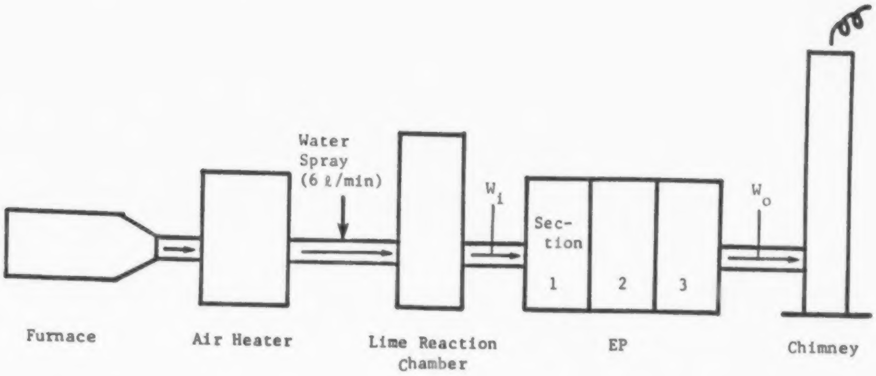

Furnace	Lime Consumption	Gas Temperature (EP Inlet)	Gas Volume (EP Inlet)
Glass Fibler	50 kg/h	T_g = 250 °C	Q = 17,000 - 20,000 Nm^3/h
Cathode-Ray Tube	25 kg/h	T_g = 340 °C	Q = 17,00 - 19,000 Nm^3/h

Fig. 15 Schematic Diagram of Gas Cleaning System of Glass Furnace

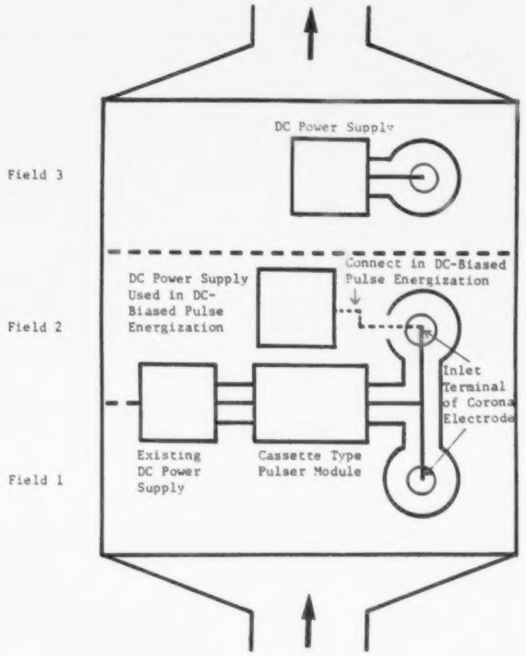
Field 3
DC Power Supply
Field 2
DC Power Supply Used in DC-Biased Pulse Energization
Connect in DC-Biased Pulse Energization
Inlet Terminal of Corona Electrode
Field 1
Existing DC Power Supply
Cassette Type Pulser Module

Field 1 : collection area, $F_1 = 761.2\ m^2$; duct spacing, $2D = 300$ mm
Field 2 : collection area, $F_2 = 761.2\ m^2$; duct spacing, $2D = 300$ mm
Field 3 : collection area, $F_3 = 492.8\ m^2$; duct spacing, $2D = 500$ mm

Fig. 16 Schematic Top Vie of EP in Pulse Operation
Fields 1 and 2 : Direct-Coupled Pulse Energization or
DC-Biased Pulse Energization
Field 3 : DC Energization

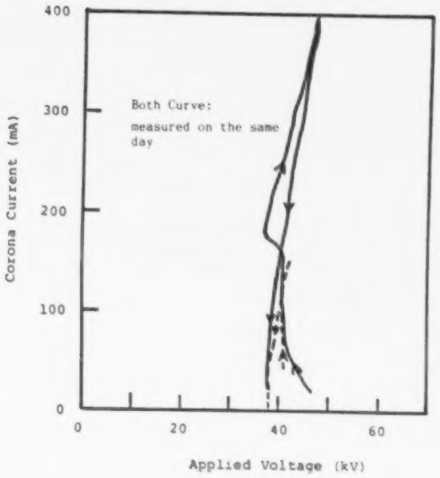

Fig. 17 V-I Characteristics of Field 3 under DC Energization (Furnace: Glass Fiber, Lime Conditioning: Off, Water-Spray: Off, Gas Temperature: $T_g = 210$ °C)

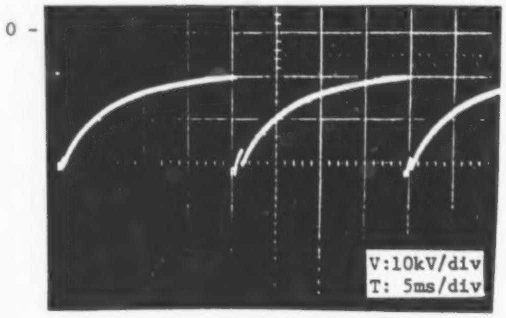

Fig.18 Pulse Voltage Wave Form Measured By Using Furnace Producing Fiber Glass With Lime Conditioning Off
($V_M = -50$ kV; $T_r = 900$ ns; $F_p = 50$ Hz)

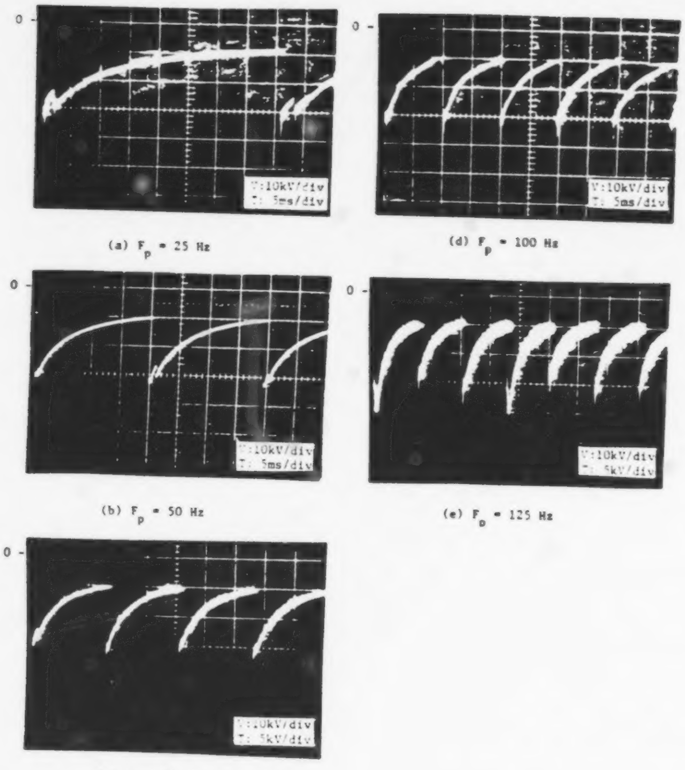

(a) F_p = 25 Hz

(b) F_p = 50 Hz

(c) F_p = 75 Hz

(d) F_p = 100 Hz

(e) F_p = 125 Hz

Fig. 19 Effect of Pulse Repetition Requency, F_p, on Pulse Voltage Wave Form (Furnace: Fiber Glass, Lime Conditioning: Off, Water Spray: On, Gas Temperature: T_g=210°C, Pulse Parameters: V_M=-50kV and T_r=900ns)

Reproduced from
best available copy.

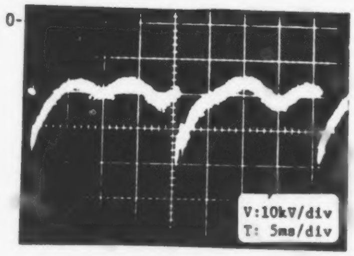

Fig. 20 Effect of DC Bias Voltage on Pulse Voltage Wave Form (Furnace: Fiber Glass, Lime Conditining: Off, V_M = -55 kV, T_r = 900 ns, F_p = 50 Hz)

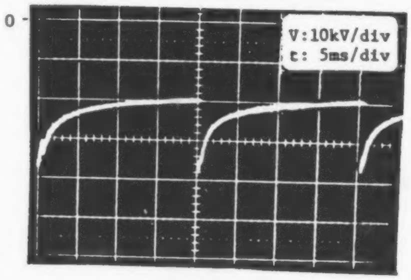

Fig. 21 Pulse Voltage Wave Form Measured By Using Furnace Producing Cathode-Ray Tube Glass With Lime Conditioning On (V_M = -50 kV, T_r = 900 ns, F_p = 50 Hz)

LONG-TERM EXPERIENCE WITH PULSED ENERGIZATION OF ESP's AT A DANISH POWER STATION

By: Kjell Porle and Reine Karlsson
Fläkt Industri AB, Växjö, Sweden
and
Bent Kirkegaard
Ensted Power Station, Åbenrå, Denmark.

ABSTRACT

Ensted Power Station fires various types of imported coal. Experience gained since 1983 from pulsed energization of the plant's electrostatic precipitators has confirmed the previously documented advantages offered by pulsing.

Ensted's 75 MW boilers have ESP's equipped with microsecond pulsed T/R sets. These units, which operate on the basis of the Multipulse Concept (MPC), decrease outlet emissions by two thirds for high resistivity fly ash. The MPC units have operated trouble-free since their installation.

The ESP's for the plant's 630-MW boiler are sized with an SCA of 82 $m^2/m^3/s$, or 420 $ft^2/1,000$ acfm, and was equipped with Fläkt Electrostatic Precipitator Management Systems (EPMS) in 1983. The EPMS incorporates Fläkt's Semipulse Concept (SPC), generating millisecond pulses. In addition to 80-percent power savings, the EPMS reduces emissions to less than 50 mg/m^3 NTP for low sulphur (0.5 %), low sodium (0.1 %) and low iron (1.5 %) coals.

A data acquisition system was installed to monitor ESP performance. The system supervises 300 variables and continuously calculates and stores 400 values 15 times per hour. It facilitates real time access to data and is used for statistical evaluations of ESP performance.

This paper describes the equipment, the two pulsing concepts and the results obtained when firing various imported coals. Results are also reported on the influence of gas temperature and ammonia conditioning in combination with pulsing.

INTRODUCTION

Ensted Power Station, Abenrå, in Denmark, has used pulsed energization of its electrostatic precipitators (ESP's) since mid-1983. Two different systems provide substantial power savings and reduced emissions in high resistivity fly ash applications. The performance of the ESP's and the high voltage transformer-rectifiers (T/R) supplying the pulses has been excellent.

This paper presents the two systems, in addition to experience and results gained under different conditions. The powerful system for automatic retrieval of performance data is also described.

The power plant consists of three sections, all of them currently firing coal. Section one -- commissioned in 1958 -- comprises two 30-MW boilers, equipped with a Fläkt high-ratio fabric filter installed in 1976.

Section 2 -- commissioned in 1965 -- comprises two 75-MW cyclone-fired, wet-bottom boilers manufactured by KSG-Sulzer. Fly ash is collected by two ESP's converted to Fläkt design in 1983. Two mills, with a capacity of 7 kg/s, supply coal to 12 burners/boiler arranged on two levels. Two Ljungström air preheaters are used. Coals with ash fusion temperatures below 1,400°C must be used to avoid the build-up of slag in the boiler.

The Section 3 boiler -- commissioned in 1979 -- has a continuous capacity of 630 MW and a maximum capacity of 685 MW with disconnected high-pressure preheater. This overload capacity is limited to 500 hrs/year. The boiler is a Benson type supplied by Völund Babcok & Wilcox, with critical circulation and balanced draft, designed for 100 % coal or, alternatively, 100 % oil firing. The combustion air system and flue gas plant comprises six radial fans for primary air, two axial flow FD fans and two ID fans. The unit is equipped with auxiliary steam preheaters, two air preheaters -- based on the Ljungström principle -- and six coal mills, each feeding 6 burners. Unit 3 has two Fläkt ESP's, each comprising two cells and five fields.

Table 1 presents technical data for the boilers and ESP's.

Coal from major exporters like the U.S., South Africa, Australia, Columbia, and Poland have been fired. Annual average consumption is 1.7 million tons, or 5,000 tons per day.

PULSED ENERGIZATION OF ESP's

The old type of power supplies energize the ESP with current of essentially DC character. High resistivity fly ash requires that the DC current is reduced substantially to avoid back-corona. This low DC current cannot be effectively distributed in the ESP; parts of the ESP will be devoid of current resulting in great loss of collection efficiency. By supplying the current in short pulses, the average current still being low, the current distribution is improved.

TABLE 1

	Unit 2	Unit 3
Max. output from generator, MW:		
continuous	2 x 75	630
short-term	2 x 78	685
Fuel consumption, kg/s		
coal	19.6	72
oil	7.6	40
ESP collecting area, m^2	9,156	65,800
Specific collecting area, $m^2/m^3/s$	39.1	82.5
Number of fields	2	5
Total number of bus sections	4	20
Guaranteed emission, mg/m^3 NTP	400	150
T/R sets, rated kV/mA	70/1000	70/1000
Discharge electrodes	spirals	spirals

The ability of pulsed energization to provide proper precipitator collection efficiency for high resistivity ash from low-sulphur coals offers an alternative to the large ESP's which would otherwise be required. Pulsed energization is also an attractive option when upgrading existing ESP's to comply with new emission regulations, or to accommodate more difficult ashes. The alternative of adding fields to a precipitator requires space which may not be available. Flue gas conditioning with NH_3 or SO_3 is also an option, but adds capital and operating costs throughout the unit's lifetime. Pulsed energization offers a reduction in the precipitator's power consumption, resulting in significant savings.

Pulsed energization can be connected to a bus section without switching off the rest of the precipitator. No changes in the internal components are required and no extra maintenance or supervision is needed.

Years of research and development, combined with test programs on numerous ESP installations, have culminated in Fläkt's development of two distinct pulsing systems:

o The Multipulse Concept (MPC). Bursts of 50 to 100 microsecond pulses at 7 to 100 millisecond intervals.

o The Semipulse Concept (SPC). Millisecond pulses formed by blocking the powerline halfwaves for 30 to 150 millisecond intervals.

Both concepts are presented in Appendix 1.

The MPC requires a specially designed T/R unit, while the SPC is a software feature incorporated into the Fläkt microprocessor T/R controller (EPIC). The EPIC controller with SPC forms a more compact unit than most controllers available today. The unit can be added easily to existing control panels, with minimum expense.

ENSTED UNIT 2

BACKGROUND

The boilers currently operate as a peak load station on a daily basis, with frequent stops and starts. Before conversion to Fläkt design the emission level had increased from 600 mg/m^3 NTP at the time of commissioning in 1965, to 1,000 - 1,200 mg/m^3 NTP by the early 1980s. The primary underlying factors were the nonavailability of suitable coals that generate easily collected fly ash, and worn-out internal components. The revised emission target was set at 400/mg/m^3 NTP -- an acceptable level given the intermittent operation.

Difficult coals, from precipitation point of view, were expected to dominate in the future. Because of space limitations the precipitator casing could be extended only slightly. Therefore high performance electrodes were needed to reach the goal. Spiralized wires were judged to be the best choice for the discharge electrodes.

In evaluating the most cost-effective solution it was decided to use standard T/R sets comprising EPIC controllers with SPC and one MPC unit per casing. Tests were performed to evaluate maximum improvement by the MPC units -- in the front fields or in the rear fields.

The MPC units have controls designed to vary burst frequency, pulses/burst and pulse amplitude. Automatic control of spark rate, current and voltage is included. Each MPC unit is installed in parallel with a conventional T/R set. The reason for installing both an MPC unit and a conventional T/R set to one bus section at this installation was to compare performance of conventional, SPC and MPC energization.

Double gas distribution screens at the inlet and one at the outlet were inserted to ensure excellent gas distribution in the ESP. Manual gas flow adjustment took place prior to start-up. The rebuilt ESP's were taken into service in 1983.

OPERATING EXPERIENCE OF UNIT 2

Initial testing confirmed that optimal performance was achieved with the MPC units energizing the rear fields. The plant has been operated permanently in this mode since 1983. Complete reliability over more than 12,000 operating hours has now been achieved.

SPC is used continuously in the front fields, with a charging ratio (CR) of 1:3 in order to save energy without reducing the ESP efficiency.

Table 2 shows data at full boiler load. Modified migration velocity, w_k (k = 0.5) is used for comparative purposes. CC represents conventional energization. The w_k enhancements are typical for the whole operating period.

TABLE 2

Resistivity	Emission, mg/m^3 NTP			Migration velocity w_k			w_k enhancement	
Ohm cm	CC	SPC	MPC	CC	SPC	MPC	SPC	MPC
10^{12}	290	200	145	25	30	37	1.2	1.6
10^{13}	800	560	275	12.5	16	26	1.3	2.1

Note the following observations:

1. Optimum results with MPC are obtained with 7 pulses/burst at a burst frequency of 20 Hz. The corresponding average corona current density is 0.023 mA/m^2.

2. Energy savings in the first field ranges from 60 to 70 percent and in the rear field from 80 to 90 percent. Power consumption for the MPC unit is around 3 kW.

3. No performance improvement was noted with the conventional T/R set operating in parallel with the MPC unit. Optimum performance is obtained when the voltage between the bursts is kept at corona onset voltage.

The results with MPC energization at Ensted correspond with data from other coal-fired power stations (India, Australia, South Africa). However, the positive effect by applying MPC on the first field at Ensted is less than in other power stations (dry bottom boilers). This is attributed to a higher than normal space charge in the front field thus leading to current supression. The high space charge is mainly due to recycling of precipitated fly ash and high temperature in the wet bottom boilers.

During the start-up phase, the MPC unit created some disturbances on the mains supply. Consequently, the automatic control of the power station's 24 V DC power supply was affected. The problem was immediately solved by installing an RC link across the inlet terminals to the MPC unit. This problem has not arisen in any other installation.

The MPC units have occasionally tripped during boiler start-up procedure. The reason being that the low voltage alarm was set rather high. Prior to normal boiler conditions the ESP voltage is sometimes rather low.

At an early stage, oil leaks occurred in the T/R sets but this was easily corrected. The units have frequently operated at an ambient temperature above 50°C without any damage.

ENSTED UNIT 3

BACKGROUND

The daily load profile at unit 3 is full load at 600 MW between 06:00 and 23:00; part load from 23:00 to 06:00, at 250 to 300 MW from November to April, and 150 to 200 MW during the remainder of the year. Support oil firing, approximately 0.7 kg/s, is used at the 150 - 200 MW load level.

The ESP's were designed for West Canadian coal, with a sulphur content of 0.17 to 0.29 percent, and a sodium content of 0.36 percent. Design flue gas temperature was 130°C. Table 1 presents data for unit 3.

Some of the commercially attractive coals formed very high resistivity conditions in the ESP's, which led to higher emissions than permitted. A modification of the existing ESP's was thus required to comply with the demands. In 1980, equipment for NH_3-conditioning between air preheaters and ESP's was installed with a maximum injection rate of 25 ppm. At the same time an outlet screen was installed for improved gas distribution in the rear field. By decreasing the temperature to 110°C it was demonstrated that the outlet emission could be kept below 150 mg/m^3 NTP for all available coals.

The T/R control system was upgraded in 1983 to save energy. The controllers for all 20 T/R's were replaced with EPIC microprocessors -- one for each T/R. EPCC microprocessors, each one controlling the ten EPIC's for one ESP chamber, form the basis of the Flakt Electrostatic Precipitator Management System (EPMS). The system is described in ref.(2). Each EPCC monitors the outlet dust concentration by means of an opacity meter.

The EPIC unit comprises the Semipulse Concept. The charging ratio can be changed from 1:1 to 1:15 , either from a switch on the microprocessor, from the EPCC unit or from a central host computer.

A dense-phase conveying system transports collected fly ash to silos. This continuous dust discharge system keeps the hoppers empty at all times, thereby minimizing the risk of dust build ups.

DATA ACQUISITION

A computerized data acquisition system has been installed at unit 3 -- the Test Data Management System (TDMS). Fläkt EPMS is a vital part of the system which is designed for continuous collection of data and instantaneous evaluation of ESP performance under varying conditions. A major subject of study is the long-term effect of pulsed energization. A simplified TDMS flow sheet is presented in Figure 1.

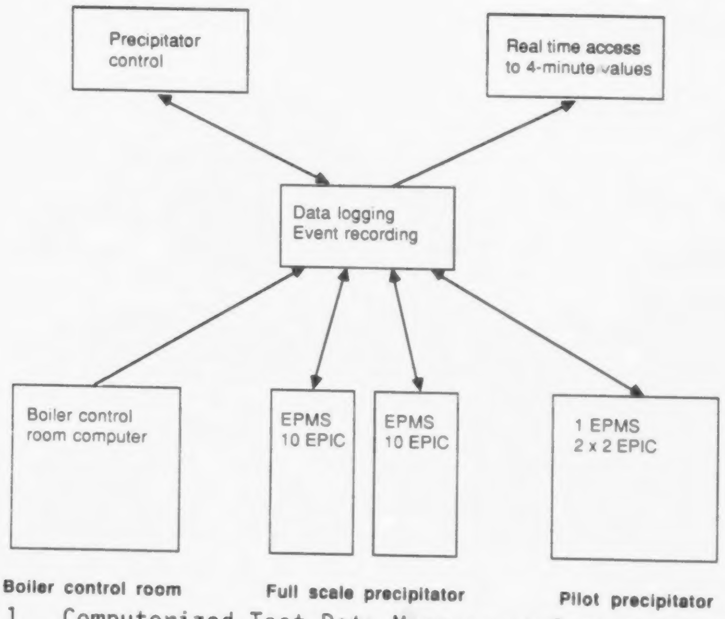

FIGURE 1. Computerized Test Data Management System for unit 3.

TDMS controls the ESP's and continuously and automatically samples about 300 parameters, including all relevant data on ESP operation and process data. The actual values for important parameters are established by repeated calibration measurements with traditional techniques. The TDMS calculates time averages every four minutes and stores the results in a data base. All values are available in real time, thus permitting data to be accessed from the moment of storage.

The TDMS is also connected to a pilot ESP unit operating on a slip-stream from the main flue gas. The pilot unit consists of two parallel identical ESP's, used for development of ESP concepts.

If required, the computer can be set up to run predefined test programs and store data for evaluation over a period of months. The test facility is powerful since the parallel full-scale ESP's and pilot ESP's can be controlled independently. The four sets of simultaneous data are used for evaluation.

The TDMS continuously stores about 400 collected and calculated values. The most important values are:

- Outlet dust concentration -- from opacity meters.
- Inlet dust concentration -- calculated from the flow of precipitated fly ash through the dense phase conveying system. Records of dust drop-out lengthwise in the ESP's become available.
- Gas flow, temperature and boiler data.
- Electrical data.
- Migration velocity.

For maximum use of the data acquired by the TDMS, complete knowledge about the plant and plant operation is required. Consequently, all tests at Ensted are conducted in cooperation between plant technicians and ESP specialists. This procedure provides insight into factors influencing ESP performance.

OPERATING EXPERIENCE OF UNIT 3

The SPC operating mode was introduced in July 1983 and has run continuously since then. The full-scale ESP's including the T/R sets have operated without problems and providing virtually 100-percent availability. With the low flue gas temperature, SPC and NH_3-injection, a redundancy has been built in and all collecting area is not required to comply with emission limits. No extra maintenance, supervision or tunings have been required for operational purposes. The low flue gas temperature, often 105 to 110°C, have not resulted in any significant corrosion in air preheaters, gas ducts, ESP's, induced draught fans or stack.

The long-term average power consumption for ESP energization is as low as 170 kW, with an outlet emission of about 20 to 60 mg/m^3 NTP. This corresponds to a power saving of about 80 percent compared with conventional charging. Full utilization of EPMS, to take advantage of low load conditions, permits power consumption to be further reduced.

The reduced emissions resulting from SPC minimize the need for NH_3-injection. The cost for NH_3 for 1985 was less than USD 15,000 corresponding to an average of 2,5 kg/h or 2 ppm. NH_3 is injected when opacity increases. Emission is then reduced within 30 minutes. NH_3 supply is switched off and the positive effect continues for a few hours.

ESP PERFORMANCE WITH HIGH RESISTIVITY FLY ASH

One of the most interesting tests was performed in November 1984. During the test period, Ulan coal, from Australia, yielding a low precipitability fly ash was fired. Table 3 shows coal and coal ash characteristics for this coal.

The main parameters studied were semipulse charging ratio, temperature and ammonia conditioning. The study was based mainly on data sampled and averaged continuously by TDMS.

Pulsed energization provided low emissions and a significant power saving compared with conventional charging. Figure 2 illustrates the typical performance improvement when switching to SPC.

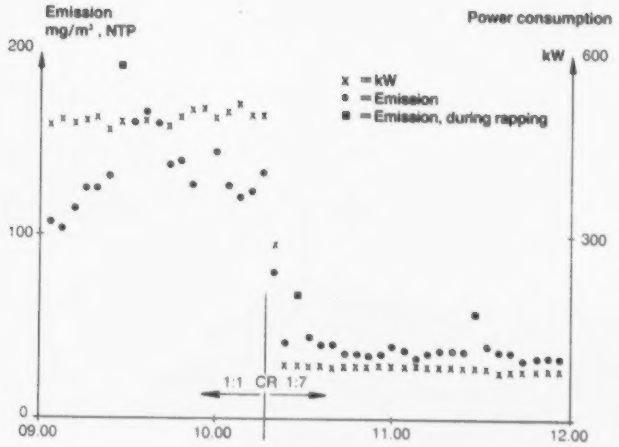

FIGURE 2 Emission and power consumption versus time, when CR was changed from 1:1 to 1:7

Each symbol represents a 4-minute average. The power saving and reduced emission are obvious.

The temperature influence on emission firing Ulan coal is shown in Figure 3. The ESP flue gas temperature was increased from 106°C to 130°C by preheating the combustion air before the Ljungström type A/H. The cycle time of the temperature loop was 3 hours.

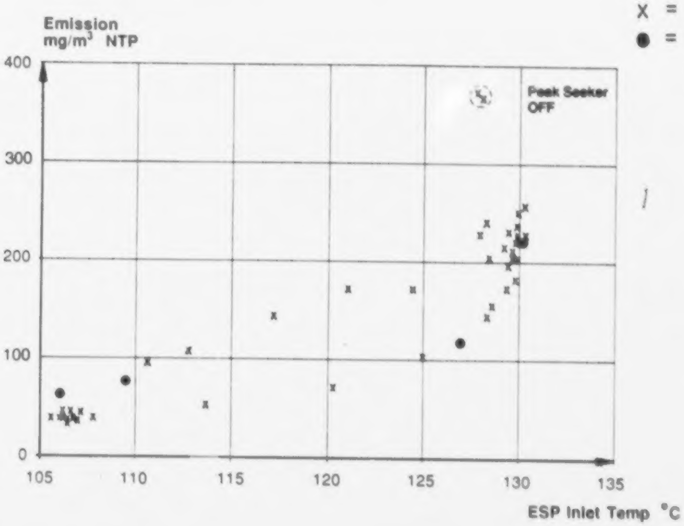

x = Emission
● = Emission, during rapping

FIGURE 3. Effect of temperature on emission

TABLE 3

Coal		Ulan Sample 1	Ulan Sample 2	U.S.-Au.mix
Moisture	% a.r.	10.6	10.5	5.7
Ash	% a.r.	13.7	13.8	12.2
Volatile	% d.a.f.	36.5	36.1	35.2
Sulphur	% a.r.	0.46	0.50	1.68
Heating value	MJ/kg a.r.	25.0	25.0	28.0
Coal ash analysis				
P_2O_5		0.04	0.20	
SiO_2		80.3	73.7	
Fe_2O_3		1.27	2.53	
Al_2O_3		16.1	18.5	
TiO_2		0.71	0.86	
CaO		0.25	1.09	
MgO		0.10	0.26	
SO_3		0.05	0.75	
K_2O		0.41	0.49	
Na_2O		0.07	0.06	
Li_2O		0.03	0.04	

Coal and ash data of Ulan coal and a mixture of Mid Appalachian high sulphur US coal and Australian Illawara coal.

The increase in emission from 40 to 240 mg/m^3 NTP corresponds to a 50 percent reduction in migration velocity, w_k. This pronounced temperature dependence tallies with repeated observations in Ensted and also with previously reported temperature trends, see ref.(3) and (4). The hysteresis shown in Figure 3, is due to the time delay between the temperature of the dust layer on the collecting plates and the ESP inlet flue gas temperature.

Table 4 gives typical data over a 10-day-period with proper boiler conditions when firing homogeneous Ulan coal. Coal was sampled automatically on a daily base and coal as well as coal ash was analysed by the plant laboratory.

TABLE 4

Mode of operation	Temperature °C	Emission range mg/m³ NTP	
		West EP	East EP
CC	105	70 - 100	60 - 90
SPC	105	40 - 50	30 - 40
SPC	130	300 - 350	230 - 300
SPC + NH_3	105	15 - 20	15 - 20
SPC + NH_3	130	75 - 95	70 - 85

The table shows the positive influence on emission by low temperature, ammonia and SPC. In general these parameters give positive combined effects on emission.

LONG TERM SPC EFFECTS

When widening the scope to general long-term effects of SPC, different coals and operating conditions have to be considered. Figure 4 illustrates relations between emission and power consumption at unit 3 for various SPC charging ratios (CR). Ulan coal -- the upper curve -- is a high resistivity case while the lower curve represents an easy case with U.S.-Au. mix coal -- see Table 3.

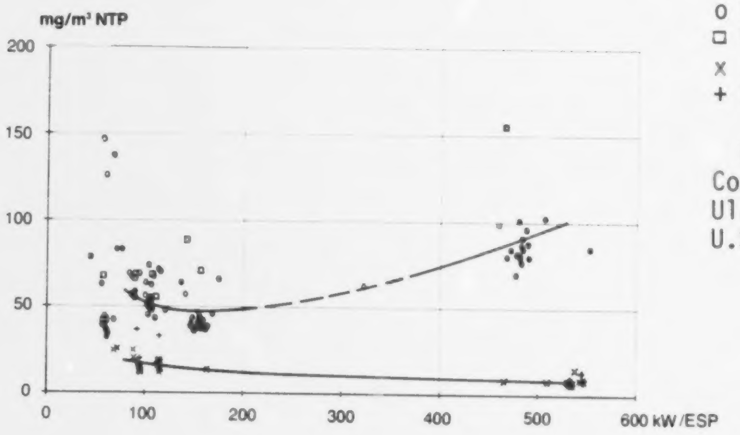

o Ulan coal
□ Ulan, during rapp.
x U.S.-Au. mix
+ U.S.-Au.,during rapp.

Extraction keys:

Coal	MW	Temp.
Ulan	620-630	105-110
U.S.-Au	590-610	115-125

FIGURE 4. Emission versus power consumption for two coals. The variations in power consumption results from changes in the charging ratio. 4 minutes average values.

A moderate increase in emission is seen for the U.S.-Au. mix when switching from conventional energization (500 kW) to SPC (100 kW). However, the emission is still well below the emission for Ulan coal and SPC for easy-to-collect fly ash is justified in regards of the considerable power savings. A total power saving for the two ESP's of 800 kW is gained.

Curves such as those in the Figure 4 can be used to calculate the change in emission for semipulse compared with conventional charging for different resistivities. As the ESP's meet various conditions the effect of semipulse on average emission can be described on a diagram like Figure 5. The X-axis in Figure 5a. represents the emission with conventional charging of the ESP. It can also be said to represent the dust resistivity as increased resistivity gives increased emission. The Y-axis indicates the change in emission with semipluse. Each curve in Figure 4 gives one point for construction of each curve in 5a. The upper curve describes the effect of operation at a fixed charging ratio and the EPMS curve describes the effect when using optimum charging ratio for every condition.

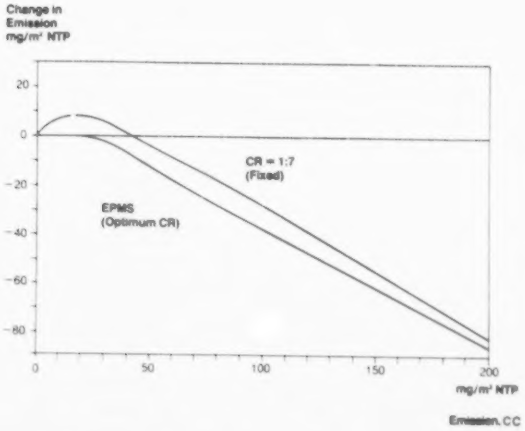

FIGURE 5a.
Semipulse effect on emission.

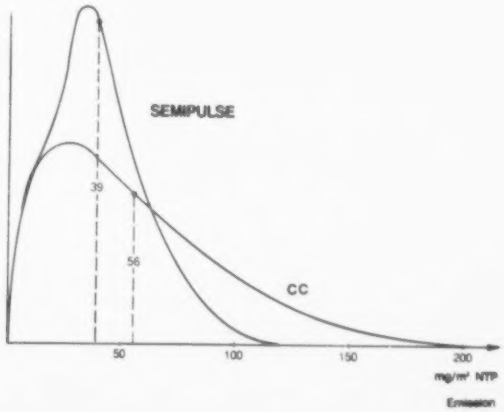

FIGURE 5b.
Yearly emission distribution for Ensted unit 3.

A yearly emission distribution for Ensted unit 3 can look like the curves in Figure 5b. The CC-curve illustrates the situation if neither SPC nor NH_3 is used for the presently fired coals. By applying SPC with optimum CR a considerable shift of the curve is obtained. The emission is drastically reduced for high resistivity cases. The average emission is lower for the SPC- than for the CC-curve. An important gain is that a more narrow distribution curve is obtained for SPC in addition to substantial power saving. This is also illustrated by the decreased spread in emission in Figure 2 when switching to SPC.

CONCLUSION

For high resistivity fly ash the use of MPC results in a significantly higher collection efficiency per ESP unit volume compared with conventional energization. MPC is highly suitable for retrofits. For Ensted unit 2 it would have been necessary to double the collecting area in order to obtain the same emission without pulsing.

The experience with Ensted unit 3 proves that an ESP with an SCA of 82 $m^2/m^3/s$ (420 $ft^2/1,000$ acfm) can provide sufficient collection performance for all coals available. The methods to obtain this are pulsed energization, NH_3-injection, back-end temperature control, reliable continuous dense phase dust handling and the ESP Management System.

The Ensted long-term experience confirms the advantages of pulsed energization in terms of collection efficiency and power savings. The enhanced performance levels have been maintained over a 3-year period on a power station in normal commercial operation. The energization equipment has been totally reliable throughout these years. There is now sufficient knowledge to apply these pulse technologies on new or retrofit applications.

The work described in this paper was not funded by the U.S. Environmental Protection Agency and therefore the contents do not necessarily reflect the views of the Agency and no official endorsement should be inferred.

REFERENCES

1. Porle K., Bradburn K. Full scale experience with pulsed energization of electrostatic precipitators. The 5th Symposium on the Transfer and Utilization of Particulate Control Technology. Kansas City, Miss., U.S., August 27-30, 1984.

2. Matts S. The Fläkt EP Management System. CSIRO Conference. August 1983.

3. Maartmann S. Experience with cold-side precipitators on low-sulfur coals. Symposium on the Transfer and Utilization of Particulate Control Technology. Denver, Colorado. July 24-28, 1978.

4. Matts S. Cold-side electrostatic precipitators for high resistivity fly ash require different design philosophy. Journal of APCA No. 2. February 1975.

THE MULTIPULSE CONCEPT

Figure A1 shows the circuit diagram of the Fläkt pulse power supply. A storage capacitor placed after the high-voltage rectifier is charged. The energy is transferred via an inductance to the ESP by thyristors. The energy oscillates between the ESP and the storage capacitor until an essential portion has been used by the ESP.

Figure A2 shows the high-voltage waveform for the MPC system. When the energy generated in the storage capacitor is released, the pulse burst is generated. The pulse amplitude declines in line with the progressive use of the energy to form corona in the ESP. By means of short pulses, peak voltages higher than used for conventional energization are used in the ESP without leading to sparking. Better corona current distribution results and back-corona formation is suppressed.

A separate conventional base rectifier is not required for the DC since the Multipulse unit is designed to supply an inherent base voltage equal to corona onset voltage. Any change in the corona onset voltage is automatically tracked. Table A1 shows technical data for the MPC units at Ensted unit 2.

TABLE A1

Pulse amplitude	40 kV	Pulses/burst	up to 8
Pulse width	90 uS	DC voltage	65 kV
Pulse frequency	up to 300 Hz	Size	1.2 x 1.2 x 1 m
Corona current	200 mA	Weight	1,470 kg

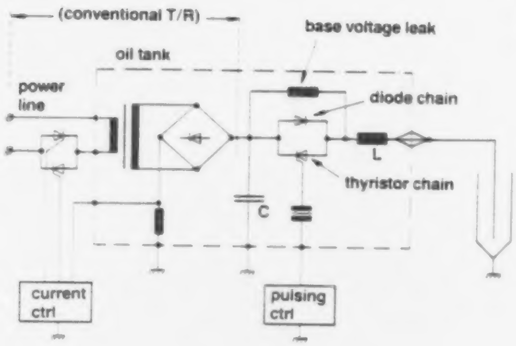

FIGURE A1 MPC unit

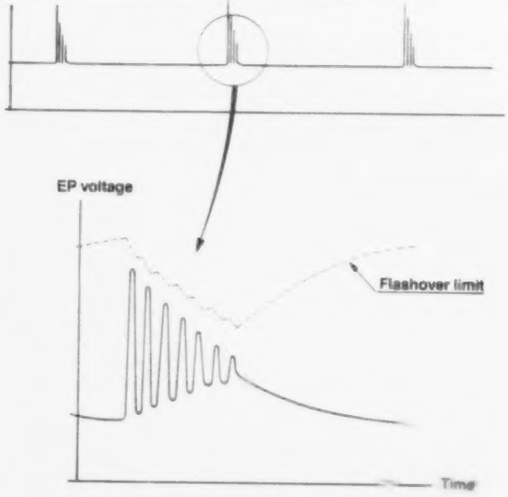

FIGURE A2 MPC voltage

THE SEMIPULSE CONCEPT (SPC)

Figure A3 shows current and voltage from a conventional T/R set. Here, the controlling thyristors are fired for each half cycle of the line power. It is now possible to control the firing of the thyristors by still using the same standard T/R set. This is done in a manner which permits only each third half-wave to pass, resulting in the waveforms shown in Figure A4.

By maintaining the same amplitude on each half wave in Figure A4, the average current decreases to one-third of the original. The voltage waveform in Figure A4 has a more pronounced ripple than in Figure A3. By increasing the number of blocked pulses, the ripple is incrased. The voltage curve form now becomes a DC base level with "pulses" superimposed on it. These pulses are of a much longer duration -- 3 to 5 milliseconds -- than those of the MPC -- Figure A2.

The total number of unblocked pulses in relation to the total number of half cycles is referred to as the charging ratio (CR). Semipulsing can be realized by replacing the T/R controller with a Fläkt EPIC microprocessor and the benefits can be attained without any modification to the standard T/R set, apart from the change in the control.

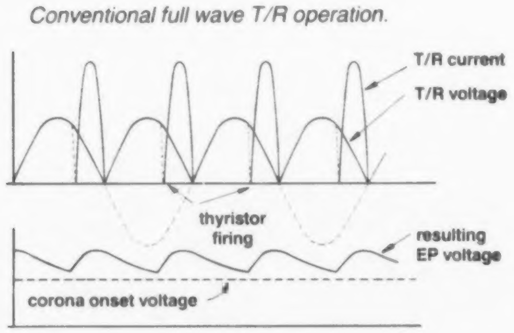
Conventional full wave T/R operation.

FIGURE A3 Wave forms for conventional energization

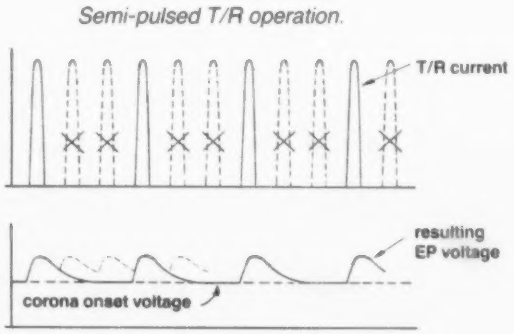
Semi-pulsed T/R operation.

FIGURE A4 SPC Wave forms

Session A-4: PERFORMANCE ESTIMATING (MODELING)

Ronald B. Mosley, Chairman
U. S. EPA/AEERL
Research Triangle Park, NC

AN IMPROVED MODEL FOR PREDICTING FLY ASH RESISTIVITY

by: Roy E. Bickelhaupt
Bickelhaupt Associates, Inc.
Carbondale, Illinois 62901

Leslie E. Sparks
Air and Energy Engineering Research Laboratory
U.S. Environmental Protection Agency
Research Triangle Park, North Carolina 27711

ABSTRACT

Research has been conducted to improve and extend the capabilities of a technique for predicting fly ash resistivity from the ultimate coal analysis and the coal ash composition. Emphasis was placed on determining the quantitative effect of adsorbed sulfuric acid vapor on resistivity. Ten fly ash samples were used to have available a reasonable spectrum of ash composition. Resistivity was determined as a function of temperature in air environments containing 5% and 10% water. Isothermal resistivity measurements were made for each ash at three temperature levels using three concentrations of sulfur trioxide. With respect to resistivity predictions for conditions not including sulfur trioxide, the present data did not suggest any modification of the original resistivity predictive model. However, the much larger and improved data base recently acquired with respect to environments containing sulfur trioxide has required a new approach for predicting this effect. This paper presents these data and illustrates an improved model for the resistivity prediction.

This paper has been reviewed in accordance with the U.S. Environmental Protection Agency's peer and administrative review policies and approved for presentation and publication.

INTRODUCTION

A model (1) with which the electrical resistivity of fly ash can be predicted as a function of temperature and important flue gas constituents was developed several years ago. Input data for the model are the as-received ultimate coal analysis and the coal ash composition. Instead of these data, one can use known values for flue gas sulfur dioxide and water concentrations and the fly ash composition.

Fly ash resistivity can be extremely sensitive to the concentration of sulfur trioxide (sulfuric acid vapor) in the flue gas. There are two points to be made regarding this with respect to predicting resistivity. One must be able to accurately estimate the sulfuric acid vapor concentration of the flue gas present in the precipitator. One must also have confidence in the predicted quantitative effect of the acid vapor on resistivity. Regarding the development of an improved resistivity model, the first point was treated by a more conservative approach based on the review of an old compilation of field test data. The second point was addressed by greatly increasing the laboratory test data base. This paper describes the results and an improved model for predicting resistivity.

The research scope centered on the evaluation of the quantitative effect of air/water/sulfuric-acid environments on fly ash resistivity as a function of: fly ash composition, sulfuric acid vapor concentration, water vapor concentration, temperature, and electric field intensity. Ten fly ashes exhibiting wide variations in important chemical constituents were characterized for the experimentation. The physical and chemical data regarding these ashes are shown in Table 1. The principal experiment was to determine resistivity at three temperatures using three concentrations of sulfuric acid vapor. Over 100 data points were generated using the 10 ash samples.

EXPERIMENTAL PROCEDURE

Resistivity as a function of temperature in an air environment containing nominally 5% and 10% water using an electric field intensity of 4 kV/cm was determined prior to the experiments with sulfuric acid vapor. These tests were done in accordance with IEEE Standard 548-1981, descending temperature technique (2).

The equipment used for the isothermal resistivity tests in environments containing acid vapor has been described in detail (3). An ash layer positioned between two concentric electrodes is equilibrated with the test environment in an environmentally controlled chamber within a thermally controlled oven. A schematic diagram of the test cell is shown in Figure 1.

The ash sample was thermally equilibrated in dry air overnight at the highest temperature of interest for the experiment being conducted. The environment was converted from dry air to moist air, and when the monitored

TABLE 1. PHYSICAL AND CHEMICAL CHARACTERIZATION OF FLY ASHES

	Chemical Composition*														Bahco Data		
No.	Li_2O	Na_2O	K_2O	MgO	CaO	Fe_2O_3	Al_2O_3	SiO_2	TiO_2	P_2O_5	SO_3	Sum	SO_3†	LOI	mmd µm	GSD	Density g/cc
301	0.03	0.51	1.7	1.3	4.4	5.0	25.8	59.0	1.7	0.31	0.35	100.1	0.34	5.4	12.2	3.3	2.36
302	0.01	0.29	0.71	1.8	12.6	4.1	24.6	52.9	1.0	0.13	0.24	99.4	0.26	0.9	21.2	4.0	2.30
303	0.05	0.34	0.42	6.3	19.5	4.3	24.1	41.2	1.5	0.31	0.94	99.0	0.68	1.4	11.5	3.9	2.44
304	0.04	0.19	2.7	0.85	0.56	4.1	32.2	56.4	2.3	0.15	0.18	99.7	0.18	3.2	12.4	3.1	2.26
305	0.05	0.34	3.1	1.1	2.2	12.5	27.1	50.5	1.8	0.33	0.57	99.6	0.43	1.1	22.0	4.5	2.44
306	0.03	0.46	2.4	0.91	3.8	21.4	20.7	46.9	1.5	0.29	1.2	99.6	0.92	3.9	19.8	4.1	2.49
307	0.01	2.8	0.62	1.1	12.8	4.1	25.6	50.4	0.84	0.19	0.41	98.9	0.43	0.4	11.7	4.8	2.04
308	0.02	1.8	0.32	6.2	30.9	5.5	19.8	30.8	1.7	1.1	4.1	102.2	2.5	0.5	6.1	3.3	2.86
311	0.10	0.54	2.4	1.2	2.1	8.1	30.8	51.6	2.1	0.51	0.33	99.8	0.20	5.2	16.5	3.8	2.19
312	0.07	0.20	0.76	1.7	7.9	3.9	32.8	48.7	2.3	0.98	0.53	99.8	0.33	4.1	15.0	3.8	2.40

* Elemental analysis performed on ignited samples and reported in weight percent as oxides.

† Water soluble sulfur reported as SO_3 in weight percent.

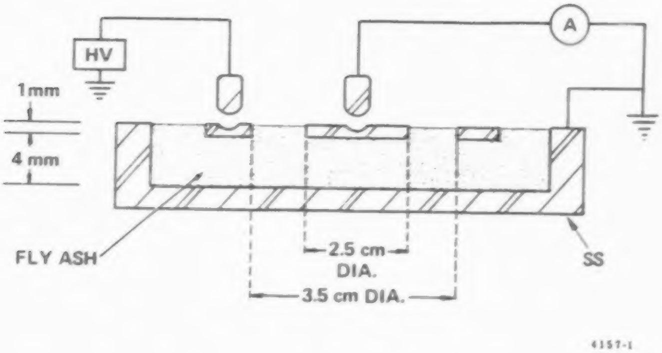

Figure 1. Schematic drawing of radial test cell for measuring fly ash resistivity in an environment containing sulfuric acid vapor.

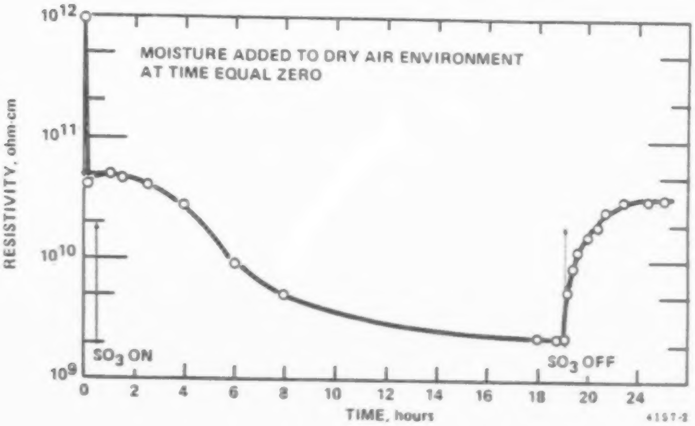

Figure 2. Resistivity/time relationship after injection of sulfur trioxide in an environment of air containing water.

current resulting from a periodically applied 2 kV voltage no longer increased, the injection of sulfur trioxide into the system was started. Resistivity was periodically determined until the 1 mm thick ash layer under test had equilibrated with the environment. This equilibration was arbitrarily defined as a resistivity decrease of <30% in a 24-hour period. After the resistivity data for the highest temperature had been recorded and without breaking the continuity of the test, the equilibration was repeated for successively lower temperatures. At the lowest temperature in the series and after equilibration had been achieved, resistivity was determined as a function of field strength intensity. The concentration of water and sulfuric acid vapor in the environmental exhaust was evaluated at least daily, and average values were reported.

Figure 2 illustrates the resistivity data obtained from one isothermal test for a specific set of environmental conditions. Each data point indicates a 1-minute application of voltage. The data point on the vertical axis represents the resistivity in an environment of dry air. At time equals zero the environment was converted from dry to moist air. Resistivity reached a minimum as a function of water vapor after about 15 minutes. The desired concentration of sulfur trioxide was introduced at time equals 30 minutes. After about 19 hours in this illustration, the environment containing sulfuric acid vapor had equilibrated with the ash volume under test. It is believed that the resistivity/time relationship shown in Figure 2 is analogous to the response of the electrical characteristics of a precipitator with ash-laden plates when a flue gas containing sulfuric acid vapor enters.

RESULTS

RESISTIVITY DETERMINATIONS

Resistivity as a function of temperature was determined in an air environment containing nominally 5% and 10% water using an average electric field intensity of 4 kV/cm. These data represent the baseline for the experiments involving sulfur trioxide. Ten fly ash specimens were used to determine the effect of ash composition on the sensitivity of resistivity to the environmental sulfur trioxide concentration. At least nine data points illustrating the effect of temperature and sulfur trioxide concentration were obtained for each ash. Typical resistivity data for air environments containing either 5% or 10% water and no sulfur trioxide, as well as the data for air environments containing about 10% water and sulfur trioxide concentrations of about 1.5, 4, and 10 ppm are shown in Figures 3 and 4. Although the principal data acquired relate to environments containing sulfur trioxide, the acquisition of baseline data using environments free of sulfur trioxide allows one to compare these recent measurements with values predicted from the model established several years ago.

The laboratory-measured resistivity data are presented on semi-logarithmic graphs with resistivity plotted on the logarithmic ordinate versus the reciprocal of the absolute temperature in degrees Kelvin. The curves have an inverted vee-shape. Because the high-temperature portic

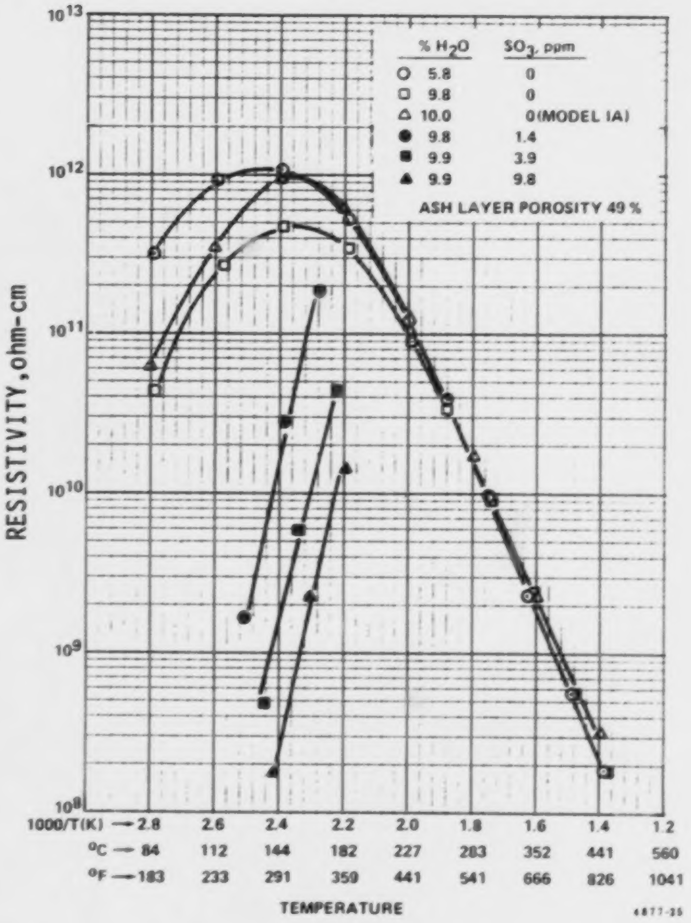

Figure 3. Effect of water and sulfur trioxide concentrations on ash 305 resistivity.

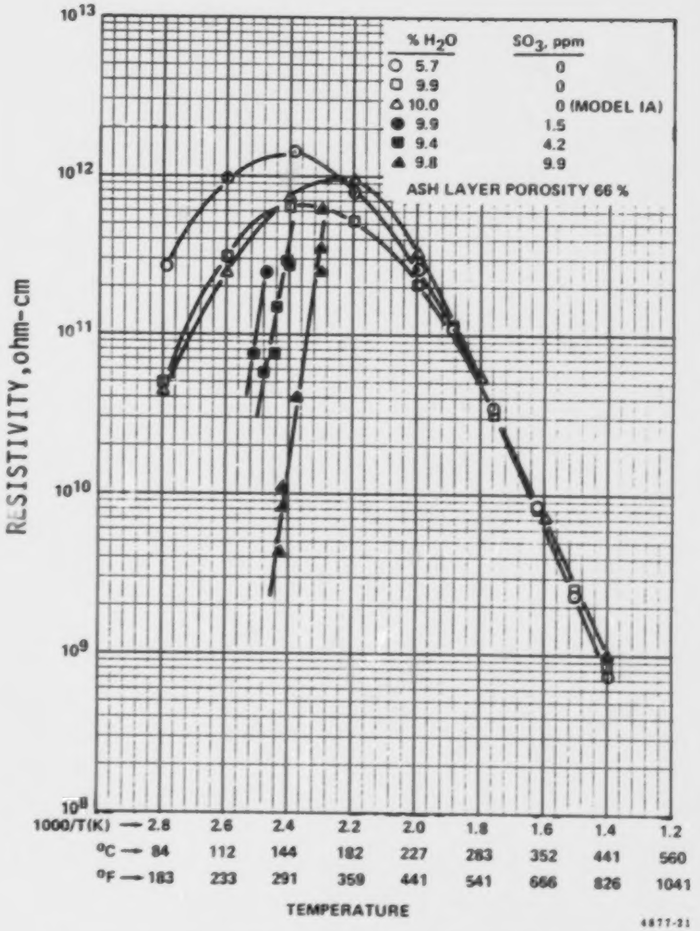

Figure 4. Effect of water and sulfur trioxide concentrations on ash 301 resistivity.

of the curve obeys an Arrhenius-type of equation, a straight line results when resistivity is plotted in this manner. The various elements of the resistivity curve will be defined and discussed below as: volume resistivity, ρ_v; surface resistivity, ρ_s; and acid resistivity, ρ_a.

In the discussion that follows, Model I refers to the technique for predicting resistivity as presented in reference 1. Model IA represents an interim modification of Model I to account for the extra sensitivity of ashes high in calcium and magnesium to the effect of water concentration on resistivity. Model II is the end result of the new data described elsewhere in detail (4).

Volume And Surface Resistivity

The predicted volume and surface resistivity values using Models I/IA were compared with the laboratory-measured values for the 10 fly ashes used in this study. Also, the information generated for Models I/IA and that obtained in the present study were compared with respect to the slope of the high-temperature leg of the resistivity/temperature curves and the effect of temperature on the sensitivity of resistivity to environmental water concentrations. These observations are discussed in reference 4. In summary, the resistivity data for the [illegible] fly ashes used in this study do not indicate a need for modification of th[illegible] I/IA resistivity predictor with respect to environments containing no [illegible] acid vapor.

Acid Resistivity, ρ_a

The effect of environmental sulfuric acid vapor on resistivity was determined for nine or more combinations of concentration and temperature for each of the 10 fly ashes. Typical measured data are shown by solid symbols in Figures 3 and 4. For each acid concentration, a line of linear regression was determined for resistivity as a function of reciprocal absolute temperature. The slopes of these lines and the resistivity values at the reciprocal absolute temperature of 1000/T(K) = 2.4 were recorded. These data were used to correlate the effect of environmental sulfuric acid vapor on resistivity with fly ash composition.

In Figure 5, the resistivity values at 1000/T(K) = 2.4 for the three levels of acid concentration have been plotted as a function of measured acid concentration. The resistivity value measured when no sulfur trioxide was injected has been plotted on the ordinate where the acid concentration is 0.1 ppm. From these curves, one observes a linear relationship between the resistivity and equilibrium acid concentration when plotted on logarithmic coordinates. For the applicable cases, linear regression analyses were used to determine the slope of the lines and the resistivity values for the 4 ppm ordinate.

Two average slopes are shown: -5.0000 for two ashes that do not respond to small acid concentrations under the subject conditions, and -2.0502 for eight ashes that are sensitive to small acid concentrations. Comparison of these results with the ash chemical compositions suggests that the ashes that contain either moderate to high concentrations of alkaline earth elements

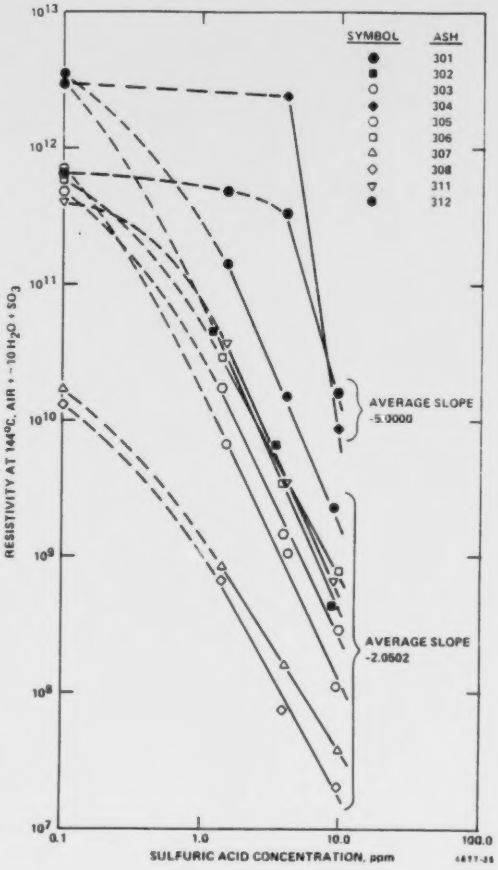

Figure 5. The effect of acid concentration on resistivity at 1000/T(K) = 2.4 for all ashes.

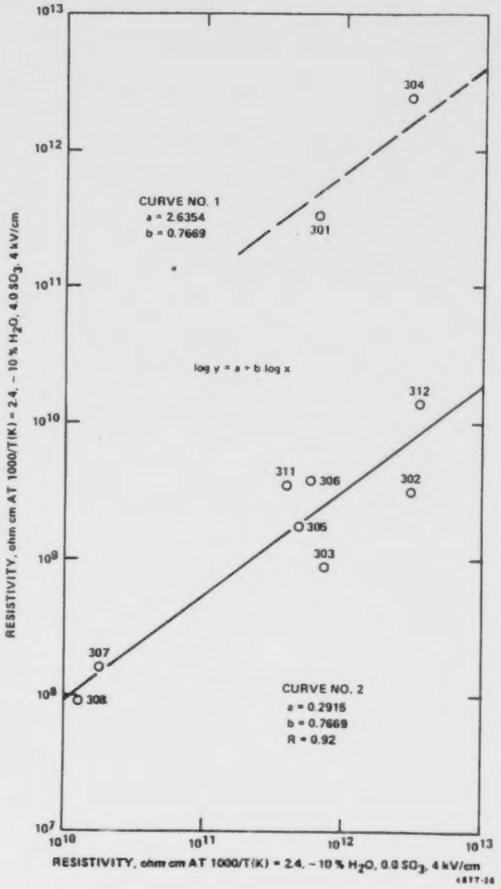

Figure 6. The effect of 4.0 ppm SO_3 on resistivity at 1000/T(K) = 2.4 in an air/water environment.

(MgO + CaO) or moderate to high amounts of iron (Fe_2O_3) respond more readily to small concentrations of acid and produce the lower slope in Figure 5. The two ashes that contain low concentrations of both alkaline earth elements and iron do not respond well to low acid values and produce the greater slope. It is conceivable that with a very large amount of data one could develop a smooth transition of slope as a function of one or more compositional features.

The resistivity values for a 4.0 ppm sulfuric acid concentration that were computed from the linear regression lines for each ash in Figure 5 were plotted versus the resistivity values that were measured under similar conditions with 0.0 ppm acid concentration. This relationship is shown in Figure 6. Again the data fall into two groups: the group of eight ashes that are chemically characterized by moderate to high concentrations of either alkaline earth elements or iron, and the other two ashes that contain small amounts of these elements. A least-squares linear regression was performed for the group of eight ashes. The coefficient of correlation for the calculated line and measured data was 0.92. The slope and intercept for this line are given in Figure 6, curve 2. Curve 1 was given the same slope as curve 2 and was arbitrarily placed at the mid-point between the two available data points.

In the next section it will be seen that the prediction of resistivity related to adsorbed acid begins with Figure 6. The amount of resistivity attenuation predicted for a given set of conditions will depend on ash composition (selection of curve 1 or 2) and the resistivity value without acid. For this reason, the amount of water in the environment is ignored with respect to the effect of adsorbed acid on resistivity. The amount of water in the environment will have been previously taken into account in the prediction of ρ_{vs}.

For those ashes that readily respond to environmental sulfuric acid vapor, the resistivity is attenuated more than two orders of magnitude by the presence of 4 ppm in an air/water environment at 144°C (291°F). The resistivity level produced under these conditions by the adsorbed acid is in the range of 1×10^9 ohm-cm to 1×10^{10} ohm-cm. The ashes containing moderate amounts of sodium, 307 and 308, perhaps have a lower resistivity because of the significant conduction related to this element. The lack of response to adsorbed acid by ashes 301 and 304, which have low iron and alkaline earth concentrations, is not understood. The obvious intuitive explanation would be to suggest that these ashes fail to adsorb the available acid vapor. Water soluble sulfate values were used to monitor the adsorption of acid vapor. From the limited amount of data available using this monitor, one concludes that the ashes that do not readily respond to the effect of adsorbed acid on resistivity nevertheless have adsorbed as much as those ashes that do respond.

The second consideration to be given to the experimental data such as shown in Figures 3 and 4 involves the slope of the lines of linear regression for resistivity versus reciprocal absolute temperature at the three levels of acid concentration.

The very significant decrease in resistivity with decreasing temperature is a result of an alternate conduction mechanism related to the adsorption of acid vapor. At constant temperature and equilibrium, the amount of adsorbed acid per unit mass of fly ash should be proportional to the acid vapor concentration. For a series of temperatures at equilibrium and a constant absolute acid concentration, the amount of adsorbed acid per unit mass of fly ash should be proportional to the acid relative humidity or the partial acid vapor pressure divided by the saturated pressure.

When this vapor pressure ratio is plotted as a function of temperature using the same coordinates as Figure 3, the resultant straight line has a slope of about +9.0. The positive sign indicates that the acid relative humidity is increasing as the temperature is decreasing. The magnitude of this slope is similar to the average slope of the resistivity versus reciprocal temperature curves for various concentrations of acid for many of the ashes. For example, the three lines shown in Figure 3 for ash 305 have a slope of approximately -9.0. If this were observed for all ashes, one could attempt to relate resistivity to acid relative humidity on a first principle basis. However, as in the case of the magnitude of resistivity attenuation due to acid concentration, other factors influence the relationship. As a consequence, a matrix of slopes is used in the prediction of resistivity. This matrix is based on ash composition and acid concentration. Far too little data are available to precisely define this parameter. As a result of the required averaging, the fit between experimental data and the computed curves varies from ash to ash.

After the equilibrium resistivity value was determined for an average electric field intensity of 4 kV/cm at the lowest test temperature to be used, resistivity as a function of electric field intensity was determined for the range 2 kV/cm to 12 kV/cm. The relationship between resistivity measured at 12 kV/cm and the values obtained at the conventional electric field intensity used in the laboratory measurement is shown in Figure 7.

Two major points are observed. First, the effect of field strength on resistivity that is influenced by adsorbed acid can be greater than the effect observed when the acid vapor is not present in the test environment. That a difference exists is not unexpected since the conduction mechanisms with and without acid present are different. Second, Figure 7 shows that an increase in average field intensity from 4 kV/cm to 12 kV/cm can reduce the resistivity an order of magnitude at high levels of resistivity and has little effect if the resistivity is low, $<1 \times 10^9$ ohm-cm. Apparently the effect of field intensity is greatest when the effect of adsorbed acid on resistivity is lowest.

The equation shown in Figure 7 describes the least-squares linear regression analysis for the data shown. This expression is used to attenuate resistivity values, predicted on the basis of 4 kV/cm, to the levels expected for higher field intensities experienced in commercial practice.

OUTLINE OF RESISTIVITY PREDICTION METHOD

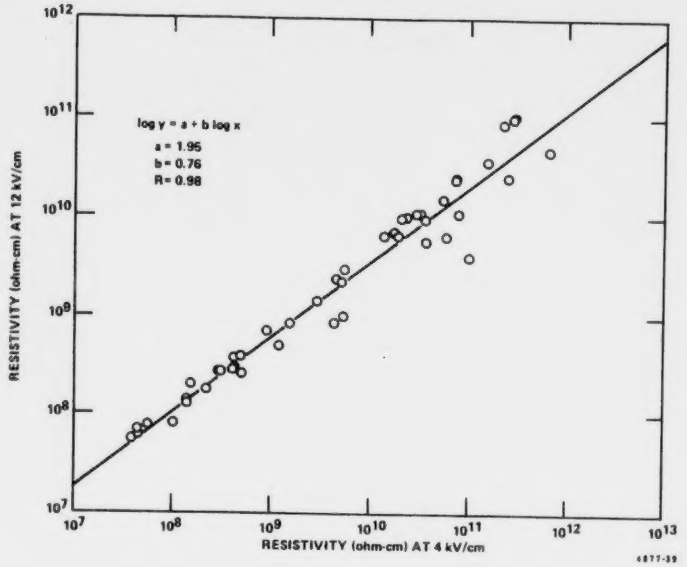

Figure 7. The effect of electric field intensity on resistivity in environments containing sulfur trioxide.

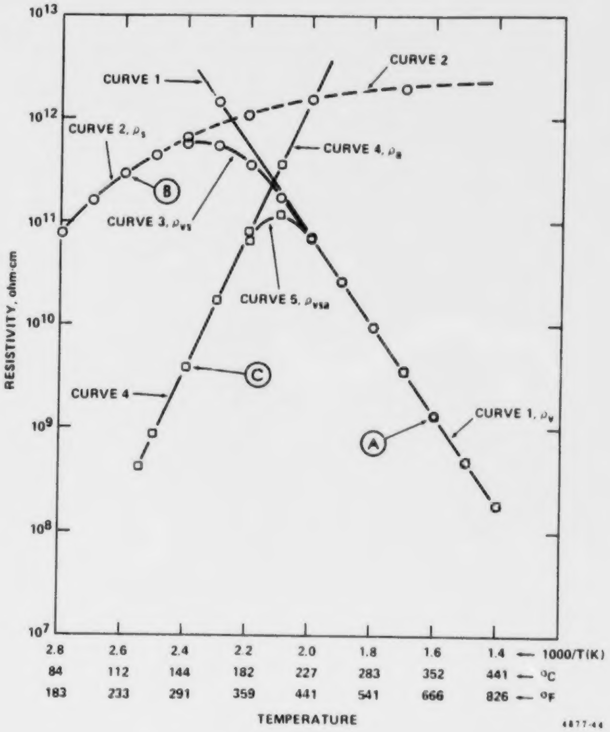

Figure 8. Resistivity/temperature relationships demonstrating the calculation of ρ_v, ρ_s, ρ_a, ρ_{vs}, and ρ_{vsa}.

The predictive method accommodates the most general case; that is, the prediction of fly ash resistivity from a core bore sample of coal that has not been commercially fired. The technique can also be used for situations involving known flue gas analyses and commercially produced fly ash compositions. The steps used in the prediction are outlined below. The details of the various calculations and a computer program to execute the model are given in reference 4.

INPUT DATA

The input data are obtained from the as-received, ultimate coal analysis and the chemical analysis of the coal ash. Using the ultimate coal analysis, a stoichiometric combustion calculation based on 30% excess air is made to determine the expected flue gas composition. Two factors from the computed flue gas analysis are used in the resistivity prediction: the water concentration in volume percent and the sulfur dioxide concentration expressed as the wet volume fraction in parts per million.

For the computation of fly ash resistivity due to adsorbed sulfuric acid vapor, an estimate of the sulfur trioxide concentration in the flue gas must be made. In Models I/IA of the resistivity predictor, the sulfur dioxide value was multiplied by 0.004 to obtain an estimate of the sulfur trioxide concentration. No improvement has been made in the ability to estimate sulfur trioxide concentration; however, in Model II, two multipliers are used to better reflect in situ measurements of sulfur trioxide/sulfur dioxide ratios. A review of the flue gas data acquired for 16 field tests has led to the following change. In predictive Model II, the calculated sulfur dioxide value is multiplied by 0.001 to determine the sulfur trioxide value if the combined atomic concentration of magnesium and calcium in the ash is greater than 5.0%. The 0.004 multiplier is used when the value is 5.0% or less.

For a constant sulfur concentration in the as-received ultimate coal analysis, the calculated percentage of sulfur dioxide in the flue gas increases with increasing ash content. Reasoning that the additional particulate surface resulting from higher ash content will compensate for the disproportionately high sulfur trioxide concentration resulting from the higher sulfur dioxide percentage, a factor has been included in Model II to minimize this effect.

The coal ash data are reported as oxides in weight percent. After normalizing the weight percentages to sum 100%, each oxide percentage is divided by the respective oxide molecular weight to obtain the mole fraction. Each mole fraction is divided by the sum of the mole fractions and multiplied by 100 to get the molecular percentage as oxides. Each molecular percentage is multiplied by the fraction of cations in the given oxide to obtain the atomic concentration. The following atomic concentrations are utilized in the resistivity prediction: (a) the sum of lithium and sodium, (b) the sum of magnesium and calcium, and (c) iron.

CALCULATION OF RESISTIVITY

Using the aforementioned flue gas and ash compositional data, resistivity can be calculated as a function of the temperature for the temperature range experienced by both cold-side and hot-side precipitators. The resistivity-reciprocal absolute temperature curve is produced from the combination of three separately calculated curves. These three resistivity-temperature relationships are commonly referred to as: (a) volume resistivity, ρ_v; (b) surface resistivity influenced by adsorbed water, ρ_s; and (c) surface resistivity influenced by adsorbed acid, ρ_a. Figure 8 serves to demonstrate the various resistivity relationships.

Calculation of Volume Resistivity, ρ_v

Volume resistivity, ρ_v, can be described as the resistivity of a fly ash layer excluding the influence of the flue gas composition. It is principally affected by ash composition, temperature, and the physical characteristics of the particulate layer. Conduction is dependent upon the migration of thermally activated charge carrying ions such as sodium through and over the surface of the particles with movement from one particle to another at the contacts. Volume resistivity as a function of reciprocal absolute temperature is shown as curve 1 in Figure 8.

The Model II expressions used to produce curve 1 are identical to those previously described in reference 1 for Models I/IA. Point A on curve 1 is established using an expression relating resistivity to the atomic concentrations of lithium plus sodium, iron, and magnesium plus calcium for a laboratory-test level of electric field intensity. This resistivity value is then extrapolated to a lower value commensurate with field intensities near electrical breakdown. Finally, curve 1 is obtained from the value of point A using an Arrhenius-type equation for which an average experimental activation energy has been determined.

Calculation of Surface Resistivity, ρ_s

Surface resistivity, ρ_s, is herein defined as the resistivity of a fly ash layer resulting from the interaction of the ash surface with adsorbed water vapor. The effect of adsorbed acid vapor is excluded. Surface resistivity is affected by ash composition, temperature, water concentration, and the physical characteristics of the layer. Conduction is dependent upon the migration of charge carrying ions such as sodium over the surface of the ash particles with movement from one particle to another at the contacts. Adsorbed water has the role of increasing the number of mobile charge carriers and increasing the mobility of these ions. Surface resistivity as a function of reciprocal absolute temperature is shown as curve 2 in Figure 8.

The Model II computation of the surface resistivity is also no different from the procedure used in Models I/IA. The calculation of point B of curve 2 begins using an expression utilizing the atomic concentration of lithium plus sodium for a flue gas water concentration of 9% and a low level of field strength. The value is then adjusted for a field strength near breakdown, for the water concentration determined from the combustion calculation, and for extra sensitivity of resistivity to water as affected by the calcium concentration. Having established point B, the other data points making up curve 2 are computed from eq. 8, ref. 1, relating the effect of temperature on the sensitivity of resistivity to water conditioning.

Calculation of Combined Volume and Surface Resistivities, ρ_{vs}

Although in the absence of sulfuric acid vapor the surface and volume conduction mechanisms are both dependent on alkali metal ions for charge carriers, the two processes can be treated as separate conduction paths through the ash layer. Resistivity as a function of temperature for the combined effect of surface (ρ_s) and volume (ρ_v) resistivities can be calculated using the expression for the sum of parallel resistances expressed in terms of resistivity. It is apparent that, when $\rho_v \gg \rho_s$ at low temperatures, then $\rho_{vs} = \rho_s$ and, when $\rho_s \gg \rho_v$ at high temperatures, then $\rho_{vs} = \rho_v$. Curve 3 in Figure 8 shows the resultant ρ_{vs}.

Calculation of Acid Resistivity, ρ_a

Fly ash resistivity responds to the presence of environmental sulfuric acid vapor, reaches an equilibrium minimum value for a given concentration and temperature, and then loses the effect of the acid vapor when the environment is purged of acid. It has been concluded that surface conduction resulting from the interaction of water vapor with the ash surface and surface conduction resulting from adsorbed acid are separate phenomena.

Although a separate mechanism, conduction due to adsorbed acid is linked to the ash chemistry. In the Results section above, it was apparent that the sensitivity of resistivity to acid concentration varied from ash to ash. It was also shown that the effect of temperature on resistivity for a given acid concentration varies with ash type. Consequently the prediction of acid resistivity is closely tied to ash composition. The effect of adsorbed acid on the complete resistivity/temperature relationship is incorporated by combining ρ_a with ρ_{vs} using the expression for parallel resistances.

The first step in the calculation of resistivity due to adsorbed acid is to determine the effect for a fixed set of conditions; e.g., 4 ppm SO_3, 144°C, 10% H_2O, and 4 kV/cm using the information shown in Figure 6. Note that in all calculations of ρ_a the water concentration is 10%. The effect of the design water concentration is accounted for in the calculation of ρ_s. The values of resistivity on the abscissa of Figure 6 were determined when curve 3 of Figure 8 was established. If the calcium plus magnesium concentration is <5.0 atomic percent and the iron concentration is <1.0 atomic percent, curve 1 of Figure 6 is used. Curve 2 is used if the atomic percent calcium plus magnesium is 5.0 or more or the iron concentration is 1.0 or more atomic percent.

Having found the resistivity level for a fixed set of conditions and a specific type of ash composition, the resistivity value for the acid concentration of interest can be computed. The sulfuric acid concentration of interest is the value computed from the coal analysis or a value arbitrarily selected. The value of ρ_a calculated from the equations of

Figure 6 is used with the appropriate slope in Figure 5 to calculate the line intercept. Knowing this value, resistivity for any acid concentration can be calculated for the conditions 144°C, 4 kV/cm, and 10% water. The slope of -5.000 is used for ashes containing <5.0 atomic percent calcium plus magnesium and <1.0 atomic percent iron, and -2.0502 is used for ashes containing 5.0 or more atomic percent calcium plus magnesium or 1.0 or more atomic percent iron. In the computer program detailed in reference 4, all acid resistivity calculations are made for acid concentrations of 1, 4, and 10 ppmv as well as the value resulting from the coal analysis, C_a.

The value of ρ_a calculated from the equations in Figure 5 for the sulfur trioxide concentration obtained from the coal analysis is used to calculate acid resistivity as a function of temperature from an Arrhenius-type of equation. The slope to be used in the calculation of ρ_a as a function of reciprocal absolute temperature varies with ash compositional characteristics and the acid concentration as shown below. The slopes shown are averages of slopes determined from figures such as 3 and 4 for the 10 ashes used in the study.

Ash Compositional Characteristics	Acid Concentration in ppmv		
Atomic % of Elements	<2.75	2.75 to 6.50	>6.50
Li + Na >1.0 and Mg + Ca >5.0	-4.74	-4.85	-4.85
Fe <1.0 and Mg + Ca <3.0	-28.39	-28.39	-28.39
Fe = 1.0 or greater or Mg + Ca = 3.0 or greater	-8.67	-9.71	-10.59

Using the appropriate slope, the value of ρ_a calculated from Figure 5 for the sulfur trioxide value C_a, and $1000/T(K) = 2.4$, the intercept for an Arrhenius-type equation can be calculated. Knowing the intercept, ρ_a values for all applicable temperatures can be determined.

The calculation of ρ_a must be done at a sufficient number of temperatures so that curve 4 of Figure 8 is adequately defined and the calculation of ρ_{vsa} can be made.

Each of the resistivity values determined as a function of reciprocal absolute temperature is based on an electric field intensity of 4 kV/cm. These data can be used for comparison with other laboratory determinations. However, for design or comparison with in situ spark data, the results must be corrected to an electric field intensity of 12 kV/cm. This can be done using the equation shown in Figure 7. The data adjusted to an electric field intensity of 12 kV/cm are shown as curve 4 in Figure 8.

Calculation of Combined Volume, Surface, and Acid Resistivities, ρ_{vsa}

The curve for resistivity as a function of temperature is completed to include the effect of adsorbed sulfuric acid vapor by combining the values for ρ_a, ρ_s, and ρ_v using the equation for parallel resistances expressed in terms of resistivity. Depending on the temperature and flue gas composition, any one of the three conduction modes can dominate. Curve 5 in Figure 8 illustrates the combined effect of ρ_a, ρ_v, and ρ_s.

REFERENCES

1. Bickelhaupt, R.E. A technique for predicting fly ash resistivity. EPA-600/7-79-204 (NTIS PB80-102379), U.S. Environmental Protection Agency, Research Triangle Park, North Carolina, 1979. 114 pp.

2. IEEE Standard 548-1981. Criteria and guidelines for the laboratory measurement and reporting of fly ash resistivity. The Institute of Electrical and Electronics Engineers, Inc., 345 East 47th Street, New York, New York 10017, April 24, 1981.

3. Bickelhaupt, R.E. Measurement of fly ash resistivity using simulated flue gas environments. EPA-600/7-78-035 (NTIS PB278758), U.S. Environmental Protection Agency, Research Triangle Park, North Carolina, 1978. 29 pp.

4. Bickelhaupt, R.E. Fly ash resistivity prediction improvement with emphasis on sulfur trioxide. EPA-600/7-86-010 (NTIS PB 86-178126), U.S. Environmental Protection Agency, Research Triangle Park, North Carolina, 1986.

A SELECTED REVIEW OF CRITICAL PARAMETERS AND FORMULAE FOR DESIGN AND PERFORMANCE EVALUATION OF ELECTROSTATIC PRECIPITATORS

by: Herbert J. Hall
President
H. J. Hall Associates, Inc.
Princeton, New Jersey 08540

ABSTRACT

It is necessary to apply effective and practical parameters, formulae and techniques in the design and performance evaluation of electrostatic precipitators. This is especially critical in today's climate requiring very high efficiencies and reliability at optimum size and cost with emphases on fine particle collection and low stack opacities. The coordinated assembly of some of the more important relationships, esoteric factors, techniques and their application is the purpose of this paper. The contents should be of special use to those engaged in research, design, application, operation and upgrading, as well as to those interested in the quantitative proposal evaluation and in the use of advanced technologies in the precipitation process. It is often said that ESP design is a judicious blend of science and art; or perhaps better, mainly sound science tempered by wide and esoteric experience among the many and varied application and process conditions extant in the field. There are areas of knowledge yet unrevealed and unexplored, but we are still learning new scientific things about this old and venerable art.

INTRODUCTION

Electrostatic precipitation emerged from a laboratory curiosity about 75 years ago when F. G. Cottrell and his associates laid the early foundations for the practical application of the process whose basic physical viability rested on the work of Coulomb two centuries ago. The beginnings of a systematic science and technology recall such names as Anderson, Deutsch, Pauthenier, Penney, Mierdel, Loeb, and others. Until about 1950, the process was empirical and batch at 90-97% efficiency; design was largely by analogy, experience and extrapolation of available operating data to select suitable effective migration velocities, each peculiar to its own application. The importance of process variables, e.g. gas properties and some particle sizing, chemical and electrical properties of aerosols, were recognized early, as was the effect of conditioning agents such as moisture and trace amounts of SO_3. Our work at the Research Laboratory of the Research Corporation (later Research-Cottrell, Inc.), starting about 1946 under the direction of H. J. White, had by late 1950's explored many fundamental aspects of precipitation and added solid structure and new developments to good foundations for a more scientific approach to the design, analyses and evaluation of electrostatic precipitators. The precipitation edifice has added many new stories in the last 15-20 years with the advent of strict pollution laws and expanded research and development efforts worldwide. Above the massive SCA and the quietly humming computer rooms, the view from the top can look down upon many modern ESPs operating at very high performance (99-99.9%) under difficult conditions, as well as upon not a few ESPs still not meeting acceptable long-term standards. Occasional trips to the lower floors containing the fundamentals and some of the esoteric arts can be worthwhile.

The necessity for applying effective and practical parameters, formulae, and techniques in the design and performance evaluation of electrostatic precipitators is especially critical in today's climate requiring very high efficiencies and reliability at minimum size and cost with emphases on fine particle collection and low stack opacities. The coordinated assembly of some of the more important relationships, factors, techniques and their application is the purpose of this paper. It is hoped that the contents will be useful to those engaged in research, development, design, application, operation and upgrading, as well as to those interested in the quantitative proposal evaluation and in the use of advanced technologies in the precipitation process.

Valuable comprehensive reviews and treatises on the theory and practice of electrostatic precipitation are available - e.g. White (1, 2), Rose and Wood (3), Robinson (4), Oglesby (5), Böhm (6), Proceedings of the First and Second International Conferences (7, 8). Practical aspects of operation and maintenance are reviewed in references (9, 10); EPRI (11) has issued a manual on fly ash ESPs specifically for utility engineers. Useful background information, various precipitator application and operating data, plus notes on new developments drawn from the current technical literature are contained in the McIlvaine publications (12).

SOME PRECIPITATOR FUNDAMENTALS

An electrostatic precipitator, being fundamentally an electric field device, requires a collecting area of adequate size, structured so that said electric fields can be suitably established, and otherwise only sufficient to store collected particles in a controlled fashion while they are being removed to hoppers with least loss. The overall system arrangement must provide for the following basic things:

1. Effective electrical energization.
2. Optimum electrode geometry in which maximum electric field strengths can be established and maintained, and so that all particles can be properly exposed thereto and collected therein. This typically takes the form of parallel plate ducts or gas passages with coplanar corona discharge electrode (DE) elements centered therein - a single stage, horizontal flow ESP universally used in most dry particle industrial applications extant. Wet ESPs generally use single or two stage pipe types, vertical flow.
3. An optimum treatment gas velocity and distribution within particle erosion limits.
4. Sufficient time and number of series fields, etc., for collecting the finer particles.
5. Rapping devices for removing the collected material in a controlled manner consistent with minimum reentrainment.
6. Minimum uncontrolled dust losses.

These basic functions and processes are strongly and synergistically interrelated. The net particle migration velocity and required SCA are thus mainly functions of required performance efficiency; particle size distribution; electrode geometry; gas flow rate and velocity level with its vectors, distribution and aerodynamic qualities; and the electric field strengths. Other important factors include particle dielectricum, drag forces resisting particle collection, and net dust loss factors. Migration velocity increases with larger particles (>1 μm), higher field strengths, wider ducts with optimum geometry, reduced drag forces (very fine particles), lower gas viscosities, and highly conducting particles. Minimum migration velocities typically occur in the range 0.2-1 μm diameter particles in the transition region between diffusion and electric field particle charging. The optimum gas treatment velocity typically increases with electric field strengths available. However, very low resistivity dry material may exhibit excessive losses requiring restricted velocities, even at relatively high corona power densities near electric field removal levels of collected material. Electric field strengths are associated with electrode geometry and useful electric energy density - a function of gas flow rate, operating voltage and current, as well as stability and uniformity of current density distribution throughout the ESP. These latter electrical factors are in turn controlled principally by collected dust resistivity, gas density, space charge phenomena, efficacy of rapping, electrode alignment, and power supply design.

With reduced gas velocities below optima, the observed reduction in active migration velocities may well be associated with decreased turbulent mixing to move, statistically, finer particles close to collecting surfaces where fast capture by electric field forces is possible. At very low gas treatment velocities, electric wind effects may have a significant influence not only in aiding fine particle motion to plates, but also away from plates, and in pushing some gas flow above and below collecting zones to aggravate sneakage difficulties. With a fixed ESP size, reducing gas velocity increases SCA, thus introducing a variation in overall migration velocity according to changes in particle size distribution with ESP length. At low gas velocities, some net loss factors can also reduce. Note, however, that at low velocities, dust dropout in flues and transitions can materially change gas flow conditions and alter chemistry properties, resistivity, and particle size distributions of the material entering the ESP to reduce performance. The overall net effects of gas velocity vs the effective Deutsch or Matts migration velocities achievable are thus the net result of several factors involved. If all particles could be properly exposed to electric fields and, once collected, could all be transferred to hoppers without loss, the size of conventional ESPs could indeed be much smaller than those now in service under variable conditions of optimization. Net loss factors are considered to comprise gas sneakage, hopper sweepage, gas velocity erosion, rap-reentrainment, saltation and excessive ESP sparking - factors neither included in basic theory nor easily provided for in modern computer modeling techniques. These too are interdependent becoming generally more serious with high gas velocity, low aspect ratios, reduced field strength and poor ion current, poor gas flow distribution and variable temperature-process conditions. While dust losses from near outlet fields may often be critical, it is clear that failure to provide adequate high performance in inlet fields merely pushes larger dust quantities into subsequent fields to exacerbate exposure to increased dust losses. So-called rap-reentrainment losses are often not so much due to improper rapping, per se, as due to subnormal performance of inlet fields where 65-80% by weight of material should be collected, for example, in typical fly ash ESPs. Massive SCA and many series fields may well compensate for other design deficiencies, but at high cost.

It is evident that precipitation is a fairly complex process, per se, and it is always associated with an equally complex industrial process. Nothing less than a total overall system approach with expert attention to critical details is satisfactory in ESP design, operation, trouble-shooting, and upgrading performance.

SUMMARY BASIC CONCEPTS AND FACTORS

To fix our ideas and to emphasize the strong, synergistic relationships among the various aspects of the process, we conveniently summarize the basic concepts and factors of importance in electrostatic precipitation.

ESP FUNDAMENTAL FACTORS

1. Electric fields - particle charging and collecting - negative polarity corona discharge generally; small radii discharge electrode (DE) elements. Positive corona used in two-stage air cleaning ESPs to limit O_3 production; very limited industrial application, but can be used successfully on high resistivity ash with needle point DE, as long as points remain dust free due to electric wind.
2. Collecting area - large surface; parallel plate gas passages divided into a number of chambers and/or cells transverse to gas flow and a number of series sections or fields in series with gas flow.
3. Effective electrical energization - maximum electric field strengths continuously maintained; Power Supply design.
4. Optimum electrode geometry, arrangement.
5. Optimum gas treatment velocity-vectors, distribution, and aerodynamics.
6. Adequate time and series fields to collect finest particles.
7. Industrial process factors and effects.
8. Effective rapping and dust removal.
9. Minimum uncontrolled dust losses.

NET MIGRATION VELOCITY AND SCA (Specific Collecting Area)

1. Required performance - regulations and process factors influence.
2. Particle size distribution, dielectricum.
3. Drag forces.
4. Electrode geometry.
5. Gas flow rate.
6. Gas velocity factors.
7. Electric field strengths.
8. Net dust losses.
9. Formulae and methods used in performance calculations.

MIGRATION VELOCITY

1. Increase - for larger particles $>\approx 1$ µm diameter; higher field strengths; wider ducts and optimum geometry; reduced drag forces (very fine particles); lower gas viscosity (lower gas temperatures); electrically conducting particles.

2. Minimum - typically in range ≈ 0.2-1.0 µm diameter particles in transition region between diffusion and field charging of particles. Note that maximum light scattering and maximum stack opacity also

occur in the same above particle size range. Visible light wave lengths are in the range 0.55 μm ± 0.2 μm. We emphasize the importance of assessing ESP design performance capability in this critical particle size range. Minimum performance requirements are often controlled by opacity regulations rather than by mass emissions regulations.

3. Decrease - very low gas velocities; excessive net loss factors; high resistivity ash; non-uniform current density distribution; poor gas distribution.

OPTIMUM GAS TREATMENT VELOCITY

1. Electric field strengths.
2. Gas flow erosion limits and dust reentrainment.
3. Low resistivity materials.
4. Optimum bulk dust resistivity.
5. Gas velocity to aspect ratio - v/AR.
6. Gas distribution quality.

ELECTRIC FIELD STRENGTHS

1. Electrode geometry and alignment; thermal stresses; mechanical and structural design.
2. Useful electric energy density.
3. Power supply design - TR matching to load, optimum waveforms, ESP sectionalization, reliability, automatic control system and quality.
4. Dust resistivity; anode asperities.
5. Operating voltages and currents - corona starting voltage; gas density.
6. Current density at anode - distribution and stability.
7. Particulate space charge effects.
8. Process factors and ion mobilities.
9. Electrode dust buildups, efficacy of rapping.
10. Electrostatic field strength.

NET DUST LOSSES

1. Gas sneakage) 2. Hopper sweepage)	Gas vectors; vertical gas and dust distribution; air inleakage.
3. Gas velocity erosion) 4. Rap-reentrainment)	Turbulence; electric wind; resistivity; particle adhesion, agglomeration, shear forces.

5. Excessive sparking.
6. Saltation.
7. General aggravation synergism.
    a. Low power density.
    b. High v/AR.
    c. Gas distribution quality - jets.
    d. Conditioning system effects.
    e. Poor ion current distribution.
    f. Poor power supply and automatic control design.
    g. Shorted ESP sections.
    h. Improper rapping system.
    i. Poor performance inlet fields.
    j. Non-optimum process conditions.

PROCESS FACTORS AND ESP DESIGN, OPERATIONS

These are some important factors for consideration typically illustrated for coal-fired, utility boilers and fly ash collection - the largest single ESP application.

1. Load - steady, cyclic, variable - fuel/air ratios; boiler type.
2. Gas temperature control for resistivity adjustment.
3. Coal sources - range of fuel properties to be dealt with. Uniformity best, coal-ash indices, washed coal.
4. Coal grind, carbon generation, good combustion, particle sizing.
5. Excess air combustion, air inleakage (local).
6. Coal types - eastern, western, imports - mixtures - ash properties, chemistry, critical elements.
7. Gas flow rates, composition, H_2O, SO_3 availability, stratification, O_2/CO_2 traverse.
8. ΔT across face due to air preheater (AH) rotation - (AH speed), gas mixing.
9. Temperature balance - multiple AH, ID fans.
10. Pyrite rejection in mills - critical loss of S and SO_3/H_2SO_4.
11. Coal feeder hang up, wet coal, puffing.
12. Boiler size, heat release, slagging, fouling (loss Na_2O).
13. High excess air to control slagging.
14. Cenosphere production - vapor SiO condense → SiO_2; submicron fume.

15. Ash carryover.

16. Reduced loads/long flues - ash dropout, changes in particle sizing and ash chemistry; gas temperature variation.

17. Start up and shut down procedures.

18. Rate of load changes.

19. Concise, valid measurements and records.

20. Serious tube leaks - sticky ash, condensation, electrode fouling.

21. High carbon in hoppers.

22. Unburned hydrocarbons deposition on ESP electrodes - polymerization at high temperature and formation of high resistivity, tenacious layers.

USEFUL, PRACTICAL FACTORS AND FORMULAE

PARTICLE SIZE PROPERTIES

Various techniques are available for industrial dust particle size distribution measurement and data usage (13-17), e.g. sieving, elutriation, sedimentation, centrifugal classifiers, cascade impactors, electrical aerosol analyzers, optical and electric instruments, electron microscopes, etc. In situ cascade impactors for sizing 0.3-10 μm diameter particles and electrical aerosol analyzers in range below 0.5 μm are commonly used today. The well-known Bahco classifiers have been applied in range ≈1 μm-44 μm. Agglomerative fines have been examined usefully by electron microscope techniques; liquid dispersion methods also break up larger agglomerates; the EL-ZONE electric method (17) gives good results, especially for small amounts of material in ESP outlet flues or stacks for correlation with optical opacity meter data. The need for representative dust sampling, preferably isokinetic traverse data, and very careful, valid techniques with methods specified are paramount.

Some typical parameters and formulae of interest are shown in Table 1.

TABLE 1. SUMMARY USEFUL PARTICLE SIZE PROPERTIES AND FORMULAE*

Parameter	Symbol	Formula
Geometric median diam, μm	$\bar{X}_g$	50% weight above and below $\bar{X}_g$ from cumulative size distribution plotted on log-probability paper
Standard deviation	σ_g	$\frac{\bar{X}_g}{\approx 16\%\ \text{diam}^{\dagger}}$ or $\frac{84\%\ \text{diam}^{+}}{\bar{X}_g}$
Modal diameter, μm	$\bar{X}_p$	$\bar{X}_g e^{-\ell n^2 \sigma g}$
Mean diameter Weight to surface, μm	X	$\bar{X}_g e^{-0.5\ \ell n^2 \sigma g}$
Specific surface, cm^2/g	S_o	$\ell n S_o = \ell n \frac{6}{\rho_p} - \ell n \bar{X}_g + 0.5\ \ell n^2 \sigma_g$
Average particle density, g/cm^3	ρ_p	Measured or calculated
Average particle radius, μm Weight to surface	a	$\frac{3}{\rho_p S_o}$
Particulate surface density $\frac{cm^2}{cm^3}$ gas	S	$S = c_i S_o$ (c_i = inlet conc. g/cm^3)
Average particle number density, no./cm^3gas at average particle radius weight to surface	N_p	$N_p = \frac{3c_i}{4\pi a^3 \rho_p} = \frac{S}{4\pi a^2}$

---

*Basis equivalent spherical particles.

†Per cent by weight less than size indicated on plotted graph.

Example: A fly ash ESP might have the following inlet aerosol properties: $\bar{X}_g$ = 12 μm, σ_g = 3.3, $\bar{X}_p$ = 2.88 μm, X = 5.88 μm, S_o = 4433 cm^2/g (0.44 m^2/g), a = 2.94 μm, ρ_p = 2.3 g/cm^3, and S = 0.0252 cm^2/cm^3 (2.52 m^2/m^3).

One of the most useful procedures is a plot of particle diameter on a logarithmic scale ordinate vs per cent by weight less than indicated size on a probability scale. Most industrial dusts of interest in precipitation can be represented quite well by the log-normal distribution giving straight lines on such a plot, or possibly by two or three segments of straight lines of different slopes where analyses can be easily handled. Distributions can also be represented on a volume, number or surface basis in various ways to suit specific purposes. In the literature one often sees differential plots of $\frac{dM}{d(\log D)}$ vs particle diameter, for example, where M is the mass of material in suitable units in a small range of particle diameters D and D + ΔD - the area under such a curve in said range. The area under the total curve represents the total inlet mass concentration typically. Some fly ash inlet concentrations show mass concentration peaks in the neighborhood of ≈10 μm diameter; others are often at smaller diameters - including bimodal effects. Tests on several coal-fired boilers (18) have also shown a small peak in the region of 0.1 μm diameter ascribed to volatile species condensation fume. Such material can adhere to larger fly ash particles acting as nucleii. In smaller (0-10 μm) sizes, measurements can exhibit considerable variation spreads among different methods and investigators. In a large ESP, it is not uncommon to find significant differences in particle size distributions, mass inlet concentrations, gas temperatures, particle chemistry and bulk resistivity, gas velocity distributions, electrical operating conditions, and net loss factors within and among say eight different chambers. Good data acquisition is difficult, time consuming and costly. Precipitator design, analyses and performance evaluation, trouble shooting, upgrading, etc., of necessity must resort to judicious practical compromises to focus upon fundamental issues. Effective methods and techniques are available, albeit perhaps not so widely disseminated as we might wish.

Note that for high performance most of material <1 μm diameter must be collected. A useful check on ESP design quality lies in examining performance capability in this fine particle range. The actual performance ultimately may come down to how well net losses can be controlled. Overall this means high quality equipment and design by experienced people.

ELECTRICAL ENERGIZATION

Previous publications (19-22) on high voltage power supplies and automatic controls have discussed historical developments, technological trends, fundamental design and application factors, as well as electrical operations, maintenance, and trouble-shooting aspects of securing maximum electric field strengths and high, reliable performance in modern precipitators. In a later paper (23) emphasis is on a number of recent and current technical developments and trends such as microprocessor computer controls, wide duct technology, pulse energization and energy management systems related to effective power supply design and application.

Table 2 summarizes some important parameters, factors and formulae related to the optimum design and application of standard high voltage power supplies for industrial electrostatic precipitation. Systems typically use a transformer-rectifier (TR) set at 460 ±5% line input voltage, 60 HZ, 1 Ph, with SCRs and linear reactor in series with the primary winding, and modern microprocessor, computer type automatic controls. Table 3 summarizes some electrical factors in ESP operations, analyses and evaluation.

TABLE 2. SUMMARY FACTORS AND FORMULAE - HIGH VOLTAGE POWER SUPPLY DESIGN AND APPLICATION[*]

Parameter	Symbol/ Factor	Formula	
1. ESP duct width	2b	Typical 228-305 mm	Wide Duct 400-600 mm
2. Nominal TR rated output voltage[o]	KV DC	45-55	80-120
3. TR rated peak voltage at load	KV_p = 1.57 KVDC	70-86	125-190
4. Rated ESP DC current/TR, MA	I_{av}	Nominal 250-1500 (max)[+]	
5. TR secondary voltage, RMS	KV	1.19 KV DC	
6. TR secondary winding form factor	I_{rms}/I_{av}	$\simeq \frac{1.11}{\sqrt{t/T}} = 1.2$ design	
7. Transformer capacity	KVA	1.43 KV DC x I_{av} (Amp)	
8. Max DC current fractional conduction (full wave)	t/T	0.86 design	
9. Transformer turns ratio (o.c.)	n	$\frac{\text{Rated sec volts}}{\text{Rated pri volts}}$	
10. Rated primary current, amp	I_{pri}	$n(I_{rms})$	
11. Rated TR primary impedance, ohms	Z_p	$\frac{\text{Rated pri volts}}{\text{Rated pri current}}$	
12. Minimum linear reactor impedance, ohms	Z_L	0.5 Z_p at full load	
13. Minimum linear reactor inductance[†], Henry	L	$Z_L/377$	

---

[*] Special conditions may require variations in some parameters for optimum results, rel. gas densities $<<\simeq 0.65$; possibly heavy space charge in inlets - not recommended with wider ducts.

[o] By convention TR design ratings are based upon a resistance load.

[+] Some at 2000-3000 MA - generally not recommended with 1 Ph circuit.

[†] Large size TR sets operating at $\lesssim$50% rated load current require load matching with appropriately larger size L for best stability, maximum ESP Iav, and maximum performance capability.

TABLE 3. SUMMARY ESP ELECTRICAL OPERATING FACTORS AND FORMULAE FOR PERFORMANCE ANALYSES AND EVALUATION

Parameter	Symbol/ Factor	Formula
1. Typical operating voltage ratio	KV_{av}/KV_p	0.65-0.75+
2. Optimum fractional DC current conduction	t/T	0.65-0.86
3. Optimum TR set operation	% rated load	≈70-100
4. Average current density (max controlled by resistivity)	J, $\mu a/ft^2$ na/cm^2	$\frac{I_{av}}{A} = \frac{\text{ESP current}}{\text{Coll. area served}}$
5. Average corona power*, watts	P_c	$\sum (KV_{av} \times I_{av}(MA)$ /TR
6. Average specific power density	P_c/Q	watts/1000 ACFM
7. Average power density	P_c/A	$watts/ft^2$ area
8. Avg. energy density, $Joules/m^3$	G	P_c/m^3/sec gas flow
9. Average specific current density	I_{av}/Q	MA/1000 ACFM related to (SCA)(J)
10. Specific collecting area	SCA	ft^2/1000 ACFM
11. Sectionalization	A/TR	Coll. area per TR set
12. Rel. gas density (=1 @ 70F, 1 atm)	δ	Standard function of gas temperature, pressure, elevation of site
13. ESP sparking voltage	V_{sp}	Function of δ, geometry, alignment, dust resistivity, A/TR, dust build, air inleakage, space charge, etc.
14. Nominal corona starting voltage[†] in pipes or ducts	KV_o	$f_r(30\ r\ \delta + 9 \sqrt{r\delta}) \ell n\ b/r$
a. DE roughness factor	f_r	Varies ≈0.7-1.0
b. DE corona radius	r	Typically ≈0.10-0.14 cm clean wires or points, clean gas
c. Distance corona to collection surface	b	Typically ≈11.4-20 cm

---

*Not including excess sparking effects.

[†] Peek formula for pipes but reasonably good for typical ducts with f_r closer to ≈1.0; δ strictly referred to ≈ air on mol. wgt. of gases; see also ref. (4).

ASH RESISTIVITY

In many applications such as fly ash, the electrical resistivity of collected dust is a very important factor in determining the allowable voltages, current densities and their distribution that can exist. In the ESP, this impact upon maximum operating electric field strengths thus largely determines the required size and cost of the equipment. Resistivity is defined as the electrical resistance of one cubic centimeter of material and is expressed in units of ohm-cm. Operatively speaking, it is Ohm's law in action. The passage of corona current through dust layers results in a voltage drop which, if large enough, causes internal breakdown or ionization of the gas in particle interstices. Critical values of bulk ash resistivity are reported typically $\approx 10^{10}$ ohm-cm in low temperature $\lesssim$400F gases and order one magnitude lower in high temperature or low density gases (21). Note that limited current density operation with conventional power supplies requires that the operating voltage must be reduced accordingly in order to maintain acceptable ESP sparking rates in the incipient back-corona stage ($\approx 10^{10}$-10^{11}+ ohm-cm), and to eliminate the seriously deleterious effects of well developed or stable back corona ($\approx 10^{12}$+ ohm-cm) - arising from large amounts of positive ions in the interelectrode gas space. Net effects are drastic reductions in normal negative ion particle charging, increasing amounts of positively charged particles which deposit on DE, high negative ion and electron currents at very low voltages, and highly localized corona distribution - hence very poor performance. With high resistivity dusts, the presence of asperities, projections, sharp edges, etc., on the anode or collecting plate surfaces causes high local electric field concentrations and premature initiation of sparking. As with lightning discharges, the initiation of an ESP spark or arc starts at the anode with a positive ion leader.

Resistivity of fly ash, for example, and other cases too, depends mainly on ash chemical properties, gas temperature and the presence of other conditioning agents - chiefly moisture and SO_3/H_2SO_4. In the normal temperature range for fly ash 230-350F+, adsorption processes improve rapidly with gas temperature below ≈290F, where particle surface conduction can be very efficient and effective. Above ≈350F, the effects of SO_3 in controlling resistivity diminish and disappear in the neighborhood of 400-450F, where typically volume conduction through the material takes over.

Methods of coping with high ash resistivity problems in ESPs include the following:

1. Gas temperature control (15-20 degrees F can be critical).
2. Gas/dust conditioning - e.g., Na_2O, SO_3, H_2O, NH_3, $(NH_4)_2SO_4$, etc.
3. Pulse energization.
4. Coal blending or process change.
5. Large ESP size - low J operation.
6. Electrical optimization.
7. Wet ESP (limited application, but effective).

The first six methods are effective and are being used in large industrial scale ESPs. We have applied all of these successfully, including NH_3 in both cold and hot ESPs - a favorable case with high silica-alumina type ashes. First use of NH_3 on a low temperature industrial case was by White (25) on cat-cracker dust. Amines have been used commercially in Australia. Cooled anodes, two-stage ESP, studied by White and Hall 30 years ago, have recently been revived by Denver Research Institute - although basically effective, can have difficult problems in large systems at low surface temperatures required. High quality precipitator designs with careful attention to critical details can handle ash resistivities on the order of one magnitude higher than that possible in poorer designs.

Theory, techniques and practical factors re resistivity are contained in the works of Bickelhaupt (24), White (25), Masuda (7, 8), Hall (26), and others. Bickelhaupt's prediction methods for fly ash resistivity as functions of chemistry, temperature, H_2O and SO_3 gas contents, and sodium depletion are available on computer programs. Hall summarizes several useful, practical coal-ash indices and equations for estimating typical fly ash resistivities from low S ($\leq$1%) coals at typical operating conditions circa 300F.

PRECIPITATOR PERFORMANCE

Precipitator performance comprises a normal capability level plus a long-term realistically, achievable level. How close these cases approach each other thus depends first upon having optimized all critical interrelated factors in a practical way in the design which has also taken into account the reasonably expected variations in important process factors to be dealt with. Secondly, it depends upon said design having been transformed into a high quality, functional equipment in which maximum electric field strengths can indeed be maintained without costly ongoing maintenance and shutdowns. Thirdly, it depends upon the existence of an effective routine plant monitoring and maintenance program, so that potential troubles can be detected early and promptly corrected. In principle, a good ESP design is one that has acceptable short-term reliability - i.e., no forced process shutdown over at least one year between planned outages; good long-term reliability - continuously maintains design performance guarantees over many years of service; achieves all this in minimum practical size and cost.

Methods used over the years for designing ESPs include: trial and error, analogy, theory, proper field test data analyses and evaluation, experience, on-site pilot ESP studies, and computer modeling. The last five methods comprise current usage. The familiar Deutsch equation provides a theoretical physical basis and has been derived by White (1) on statistical probability grounds with certain assumptions which, on a micro-scale, have proved acceptable and very useful. White describes methods for incorporating particle size distribution data, as well as variable gas distribution quality effects. The Deutsch equation forms the basis for the SoRI/EPA (27) mathematical computer modeling technique in which integration for particle sizing, gas flow distribution, particle space charge, and electric field strengths as functions of ESP length and series fields, etc., are carried out for specified physical design parameters. Empirical correction factors - so far based upon seventeen fly ash field performance evaluations and tests - are applied to account for discrepancies between calculated and measured performance.

Matts-Ohnfeldt (28) suggested an empirical approximation in the form, dust loss $P = \exp\left[- \frac{A}{Q} \omega_K\right]^K$, where ω_K is a precipitation parameter, like an effective migration velocity; though not so dependent upon SCA, it is still a function of electric field strengths. K is a number <1 representing the statistical spread of variable factors. For typical fly ash, cement dust, etc., $K = 0.5$; K increases for finer dust size distributions, and $K = 1$, the equation reverts to Deutsch. The Matts form is now widely used in the industry for design with ω_K values based upon field tests, and for extrapolating performance expectations as a function of SCA. Feldman (29) has presented another semi-empirical performance equation having some interesting features; its use has also been incorporated into computer modeling estimates for ESP performance.

Electric field strengths in practical precipitators are very difficult or impossible to calculate accurately - particularly in duct geometries with the wide range of configurations used. The critical factors vary significantly both in time and space throughout the ESP. Individual cases can be treated with as much rigor as is possible or may be justified; useful formulae involving suitable approximations, together with esoteric experience and judgment, are commonly employed for practical application. Of the various approximations for electric field strength at the collecting surfaces, we have found that of DuPuy (30) to be especially useful for the ion current component. Satisfactory comparisons on relative performance capabilities of different full-scale and laboratory ESPs regarding electrode geometry effects have been noted over many years (31).

Items 6, 8, 9 of Table 3 are useful indices for assessing ESP performance as functions of specific corona power/energy density, current density, and SCA effects. In any given case, collection efficiency (log scale ordinate) normally increases with increasing values of said indices (linear scale abscisca). The shape of curves and levels involved give information on the presence and extent of excessive dust losses, relative particle size effects, and relative dynamic resistivity of material being collected under conditions extant. Corona power density, within limits, can be traded for ESP size. A balance for minimum cost exists between a larger number of smaller size TR sets at reduced SCA vs a smaller number of large capacity TR sets with increased SCA. If collecting area installed costs ≈\$20/ft^2, and a TR set installed runs ≈\$25,000+, I would much prefer to have the TR set than a few thousand square feet of extra collecting area - factors especially critical with the narrower duct widths. Optimum electrode geometry and alignment, and uniformity of current density distribution yield performance premiums and minimum size-cost ESPs. Table 4 summarizes some useful factors in ESP performance evaluation.

TABLE 4. SUMMARY USEFUL FACTORS IN ESP PERFORMANCE EVALUATION

Parameter	Symbol	Formula
1. Deutsch equation (1922) (Anderson, 1919)	$(1-\eta)=P$	$\mathrm{Exp}\left[-\frac{A}{Q}\omega\right]$; eff. % = (1-P)100
2. Force on particle	F	qEp ; q = particle charge
3. Drag force	F	$6\pi a\mu\omega/C$; μ = gas viscosity; a = particle radius
4. Migration velocity, m/sec for given size particle	ω	$\frac{4\varepsilon_o k a E_o E_p C}{6\mu}$ (MKS units)
5. Dielectricum factor	k	$3\varepsilon/\varepsilon+2$ (ε = particle dielectric const.)
6. Cunningham slip correction	C	$\approx\left(1+1.26\frac{\lambda}{a}\right)$; λ = mean free path gas mol. at conditions
7. "Effective" migration velocity	ω_e	$(1-\alpha)\omega$
8. Loss factor	α	Typically varies $\approx v^{1.75}$; ≈ 0.03-0.1 typ.
9. Matts-Ohnfeldt	P	$\mathrm{Exp}\left[-\frac{A}{Q}\omega_K\right]^K$; $K \simeq 0.4$-0.9
10. Cochet factor°	C'	$\left[\left(1+\frac{\lambda}{a}\right)^2+\frac{2}{(1+\lambda/a)}\right]$ for fine particles. At a >>λ reverts to 3 = max value of k.
11. DuPuy equation, V/m (ion current component)*	E_p'	$\left[\frac{i}{\pi\varepsilon_o K}\left(\frac{\pi b}{2c}-\ell n2\right)\right]^{\frac{1}{2}}$; i = amp/m of DE length; K = ion mobility m^2/V-sec; ε_o = permittivity free space
12. Average charging field, V/m	E_o	V/b ; b = dist. corona-plate, m; V = volts
13. Average "effective" part. radius, meters or cm	a_e	aCDf; D = relative increase due to diffusion charging for fines; f = turbulence and electron charging factor; a = physical radius equivalent sphere
14. Geometry factor†	g	$\left(\frac{\pi b}{2c}-\ell n2\right)$; 2c = wire-wire spacing
15. Nom. gas flow shear stress, dynes/cm^2 (Blasius law)	T_o	$0.04\ \rho_g v^2/R_e^{\frac{1}{4}}$; ρ_g = gas density, g/cm^3 v = gas vel. cm/s; R_e = Reynolds number

---

°Our experience - underpredicts particle charge including diffusion effects. Cochet factor is used in typical computer modeling programs.

*Total electric field E_p must include dust space charge and electrostatic field effects where applicable.

†Electrode geometry factor = $\frac{2c}{b}$ important in increasing E_p' at constant J or i.

CONCLUSIONS

1. An electrostatic precipitator is a many splendored thing.
2. The many functions, processes and parameters affecting its design, operation, evaluation, upgrading, and performance are strongly and synergistically interrelated. Nothing less than a total overall systems approach with expert attention to the critical details, including knowledge of some esoteric arts, is satisfactory in dealing with precipitation.
3. Reliable designs for very high performance under difficult conditions can indeed be produced and have been produced to meet modern requirements. Application of sound science and advanced technologies, e.g., power supply and automatic control design, wide duct technology, pulse energization, and others to control resistivity and to control excess dust losses offers great promise for optimization toward minimum practical ESP size and cost.

REFERENCES

1. White, H. J. Industrial Electrostatic Precipitation, Addison-Wesley, Reading, Massachusetts, 1963.
2. White, H. J. Electrostatic Precipitation of Fly Ash. APCA Reprint Series, Air Pollution Control Association, Pittsburgh, PA, 1977.
3. Rose, H. E. and Wood, A. J. An Introduction to Electrostatic Precipitation in Theory and Practice, 2nd Ed. Constable, London, 1966.
4. Robinson, M. Electrostatic Precipitation. In: W. Strauss (ed.), Air Pollution Control, PT 1, Wiley-Interscience, New York, 1971, p. 227.
5. Oglesby, Jr., S. and Nichols, G. B. A Manual of Electrostatic Precipitation Technology, Parts I, II. Southern Research Institute, Birmingham, Alabama, 1970.
6. Böhm, J. Electrostatic Precipitators. Elsevier, New York, 1982.
7. White, H. J. (ed.). Proceedings of the First International Conference on Electrostatic Precipitation, Monterey, Calif. Air Pollution Control Association, Pittsburgh, PA, 1981.
8. Masuda, S. (ed.) Proceedings of the Second International Conference on Electrostatic Precipitation, Kyoto, Japan. Air Pollution Control Association, Pittsburgh, PA, 1984.
9. APCA (ed.). A Specialty Conference on: Operation and Maintenance of Electrostatic Precipitators. APCA, Pittsburgh, PA, 1978.

10. Katz, J. The Art of Electrostatic Precipitation. Published by Precipitator Technology, Inc., Munhall, PA, 1979.

11. Gallaer, C. (ed.). Electrostatic Precipitator Reference Manual, CS-2809, Research Project 1402-4. Electric Power Research Institute, Palo Alto, Calif., 1983.

12. McIlvaine Co. (ed.) The Electrostatic Precipitator Manual and Precip Newsletter. McIlvaine Co., Northbrook, Illinois, ≈1976-present.

13. Galeski, J. B. Particle Size Definitions for Particulate Analysis. EPA-600/7-77-129. Environmental Protection Agency, Office R & D, Washington, D. C., Nov., 1977.

14. Friedlander, S. K. Smoke, Dust and Haze: Fundamentals of Aerosol Behavior. John Wiley and Sons, Inc., New York, 1977.

15. Herndan, G. Small Particle Statistics, 2nd Ed. Elsevier, New York 1960.

16. Lapple, C. E. Particle Size Analysis and Analyzers. Chemical Engineering, May 20, 1968.

17. Particle Characterization and Technology, Vol. 1. CRC Press, Boca Raton, Fla., 1984.

18. McElroy, M. W., Carr, R. C., Ensor, D. S., Markowski, G. R. Size Distribution of Fine Particles from Coal Combustion. Science 215:4528, 1 Jan. 1982.

19. Hall, H. J. Trends in Electrical Energization of Electrostatic Precipitators. In: Proceedings of the Electrostatic Precipitation Symposium, Birmingham, Alabama, Feb. 1971, pp. 77-116. EPA, Durham, N. C.

20. Hall, H. J. Design and Application of High Voltage Power Supplies in Electrostatic Precipitation. J. Air Pollution Control Association, 25:132, Feb., 1975.

21. Hall, H. J. Solving Problems in the Electrical Energization of Electrostatic Precipitators. J. Air Pol. Control Assoc., 28:870, Sept., 1978.

22. Hall, H. J. Summary Overall Concepts for Design, Energization and Control of Electrostatic Precipitators. Paper 83-57.6 presented at 76th Annual Meeting APCA, Atlanta, GA, 20-24 June 1983. Published by APCA.

23. Hall, H. J. High Voltage Power Supplies and Microprocessor Controls for Electrostatic Precipitators. Proceedings for First International Conference on Electrostatic Precipitation, Monterey, Calif., October, 1981, pp. 668-699. Published by APCA, 1982.

24. Bickelhaupt, R. E. A Technique for Predicting Fly Ash Resistivity. EPA-600/7-79-204, Symposium on the Transfer and Utilization of Particulate Control Technology, U. S. EPA, Research Triangle Park, N. C., Aug. 1979. (Also later reports, e.g., EPRI CS-4404, Vol. 2, Project 1835-6, Feb. 1986.

25. White, H. J. Resistivity Problems in Electrostatic Precipitation. J. Air Pollution Control Assoc. 24: April 1974, pp. 313-338.

26. Hall, H. J. Fly Ash Chemistry Indices for Resistivity and Effects on Electrostatic Precipitator Design and Performance. Presented at 4th Symposium on Transfer and Utilization of Particulate Control Technology, Houston, Texas, 11-14 Oct. 1982. EPA-600/9-84-025b, Nov. 1984.

27. McDonald, J. R. A Mathematical Model of Electrostatic Precipitation (Rev. 1): Vols. 1, 2. EPA-600/7-78-111a, b. U.S. EPA, IERL, Research Triangle Park, N. C., 1978. Also Revision 2 - EPA-600/7-80-034, 1980.

28. Matts, S. and Ohnfeldt, P. Efficient Gas Cleaning with SF Electrostatic Precipitators. A. B. Svenska Flaktfabriken, Stockholm, Sweden.

29. Feldman, P. Effects of Particle Size Distribution on the Performance of Electrostatic Precipitators. Paper 75.02-3 Presented APCA Annual Meeting, Boston, Mass., Feb. 1975.

30. DuPuy, J. Comptes Rendus 242, 1140-43, 1956.

31. Hall, H. J. Some Electrode Geometry, Electric Field and Performance Effects in Electrostatic Precipitation. In: Proceedings 2nd International Conference, Kyoto, Japan, Nov. 1984, publ. APCA, pp. 354-361.

The work described in this paper was not funded by the U. S. Environmental Protection Agency and therefore the contents do not necessarily reflect the views of the Agency and no official endorsement should be inferred.

PREDICTING COLD-SIDE PRECIPITATOR PERFORMANCE BASED UPON COAL AND ASH CHEMISTRY

By: Fay A. Horney and Victor H. Belba
Stearns Catalytic Corp.
4500 Cherry Creek Drive
Denver, Colorado 80222

ABSTRACT

Electrostatic precipitator performance with respect to the collection of fly ash from pulverized coal-fired combustion is dependent upon flue gas and ash properties. An empirical model has been developed by the correlation of a large data base of precipitator efficiency tests with coal and ash chemical analyses of coal samples taken concurrently with the tests. This model is described in this paper. The model relates cold-side precipitator performance to one performance parameter, rather than the two variables (ω_k and k) required for the solution of the currently popular Modified Deutsch-Anderson equation. The precipitator performance parameter is determined from coal and ash analyses without direct consideration of ash resistivity or particle size distribution. The only constituents which determine the performance parameter are the amount of moisture, hydrogen, ash and sulfur in the coal and the amount of sodium, iron, potassium, calcium and magnesium in the ash. Flue gas temperature is not directly considered in this model and has been found to have little significance in sizing precipitators for normal cold-side precipitator temperature ranges.

INTRODUCTION

Traditionally, precipitator SCA's (i.e., size in terms of square feet of collection surface per 1000 actual cubic feet per minute of flue gas flow) have been determined by using the Deutsch-Anderson equations. Stearns Catalytic determines SCA's for cold-side precipitators, i.e., precipitators placed after the air-heaters of a coal-fired boiler for the collection of fly-ash, by using an empirical model. This model was developed through the correlation of actual stack test data, coal and ash analyses, and precipitator SCA. The model considers the coal's heating value, percents moisture, ash, sulfur, and hydrogen, as well as the chemical analysis for five of the ash constituents. In so doing, the model accounts for such phenomena as resistivity and particle size effects without directly solving for these values. Also, the model uses empirical results to predict, more reliably than the traditional Deutsch-Anderson equation, the minimum SCA required for a given fly ash.

PRECIPITATOR SIZING EQUATIONS

The first equation developed that reasonably described precipitator performance was the familiar Deutsch-Anderson equation (circa 1922) which takes the form of Equation (1):

$$E = 1 - \exp\left[-(\omega A/Q)\right] \qquad (1)$$

where,

E = collection efficiency
ω = migration velocity (precipitation rate parameter)
A = total collection area
Q = volumetric flow rate

The quantity "A/Q" is essentially the SCA. Knowing either the SCA or the required efficiency, the other value can be determined if the migration velocity is known. One difficulty in using the traditional Deutsch-Anderson equation lies in the choice of a migration velocity (or precipitation rate parameter) that is representative of the actual particulate matter to be collected. Also, as more stringent emission standards have required larger and more efficient precipitators and more experience has been gained in sizing precipitators, it has been realized that the traditional Deutsch-Anderson equation does not adequately describe precipitator performance for high efficiencies greater than 96% and SCA's greater than 250.

Various modified Deutsch-Anderson equations were published in the 1960's and early 1970's and were developed to more closely describe actual precipitator performance. The Matts-Ohnfeld form of the Modified Deutsch-Anderson equation is the most widely used version and is presented as Equation (2):

$$E = 1 - \exp\left[-(\omega_k A/Q)^k\right] \qquad (2)$$

where "k" usually equals 0.5 and typically varies from 0.4 to 0.8(1). The value of "k" in the modified Deutsch-Anderson equation accounts for the fact that the migration velocity is not constant but decreases over the length of the precipitator. This is because each successive field handles ash which is more difficult to collect than the previous field. Note that with "k" equal to one, the modified equation becomes the traditional Deutsch-Anderson equation. The problem of choosing a meaningful migration velocity (ω_k) still remains for the person not privy to large amounts of empirical data. Also, a suitable value of "k" must be selected.

Stearns Catalytic started development of its precipitator performance model in the early 1970's. The Stearns Catalytic model is in the form of Equation (3):

$$E = 1 - [A + (C)(SCA)]^{-P} \qquad (3)$$

where "C" is a constant for all fly ash from coal and equals 0.01; and "A" is a function of the amount of ash measured in terms of pounds per million Btu which enters the precipitator. "A" varies from 1.0 to 1.3 for inlet loadings of 0 to 50 lb/mm Btu and greater, respectively, and accounts for the effects of inlet grain loading on precipitator efficiency. "SCA" (specific collecting area) is the collecting plate area in square feet divided by the flue gas volume calculated stoichiometrically and expressed in thousands of acfm. The single unknown "P," called the Precipitator Performance Parameter, ties in the ash (particulate) characteristics to the performance of the precipitator for the Stearns Catalytic model. In other words, "P" represents the precipitability of the fly-ash.

A previous form of this model set "A" equal to one and adjusted for the effects of ash loading in the equations for "P" (2). However, a slightly better correlation has been obtained by accounting for the effects of the inlet grain loading on collection efficiency in the efficiency equation itself.

"P" varies from 2.0 to 5.0 and is determined empirically just as the migration velocity must be empirically determined to solve the Deutsch-Anderson equations. However, a relationship has been determined which relates "P" to the amount of moisture, ash, and sulfur in the coal and the amount of sodium and other ash chemical constituents such as iron, potassium, calcium, and magnesium.

The relationship for "P" was empirically determined based on a correlation of a large data base of precipitator performance tests and concurrent coal and ash analyses. Thus, knowing the coal and ash analyses for a particular coal, the efficiency of a given precipitator or the required SCA to achieve a particular collection efficiency can be reliably determined by using the above model.

Figure 1 is a plot of collection efficiency versus SCA. The straight line represents a plot of the Deutsch-Anderson equation for a migration velocity (ω) of 6.31 cm/sec. The curved lines represent a plot of the Stearns Catalytic model for a value of precipitator performance parameter (P) of 3.04 and a plot of the Modified Deutsch-Anderson equation for a migration velocity (ω_k) of 35.23 cm/sec and with "k" equal to 0.5. Note that a line for either the Deutsch-Anderson Equations or the Stearns Catalytic model represents the performance of a precipitator on a given ash. Actually, a family of curves representing different migration velocities and precipitator performance parameters can be generated for the Deutsch-Anderson equations and the Stearns Catalytic model, respectively.

Inspection of the curves indicates that the Stearns Catalytic model predicts better performance than the Deutsch-Anderson equation for very small SCA's. On the other hand, the Stearns Catalytic model indicates a drop-off in performance relative to the Deutsch-Anderson equation for larger SCA's. The Modified Deutsch-Anderson equation shows close correlation to the Stearns Catalytic model for the moderately precipitable ash plotted with "k" set equal to 0.5. For more easily precipitated ash (i.e., higher values of "P" and "ω_k"), the modified Deutsch-Anderson equation shows better correlation to the Stearns Catalytic model if "k" is increased to 0.6 or higher.

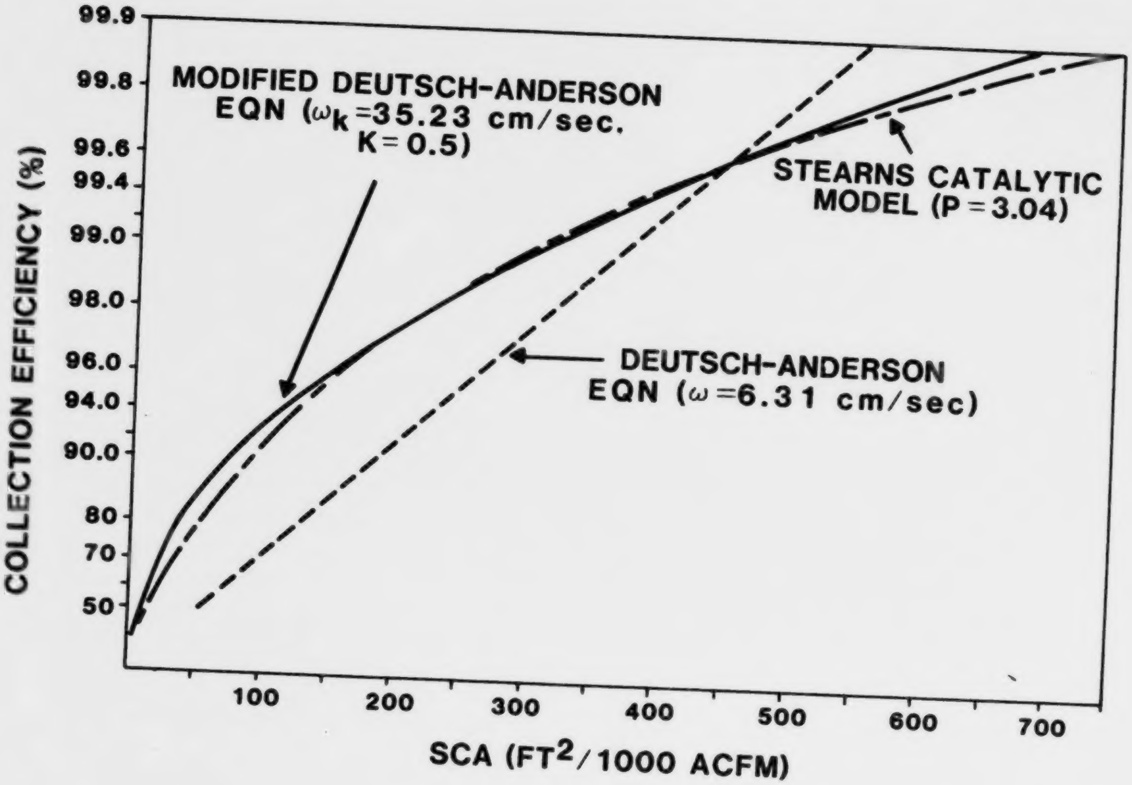

Figure 1. Precipitator Collection Efficiency vs SCA

DETERMINING ASH PRECIPITABILITY

The Precipitator Performance Parameter, "P", expresses how easily a particular fly-ash is collected in a given precipitator for the Stearns Catalytic model. In other words, "P" expresses the precipitability of the ash. The migration velocities (ω and ω_k) express the precipitability of the ash for the Deutsch-Anderson equations.

The relationships for "P" were empirically determined by correlating a large number of precipitator efficiency tests with the chemical analyses of coal and ash samples which were taken concurrently with each of the tests. The relationships for "P" follow in functional form:

$$P = f(P_T) \quad (4)$$

$$P_T = f(P_S + P_N + P_H) \quad (5)$$

$$P_S = f(\text{Sulfur}, Fe_2O_3, \text{Ash}, CaO, MgO, K_2O) \quad (6)$$

$$P_N = f(Na_2O, MgO, K_2O, CaO, H_2O, H_2) \quad (7)$$

$$P_H = f(H_2O, H_2, \text{Ash}) \quad (8)$$

Equation (4) is the primary equation of the model in that it relates the coal and ash chemistry, "P_T", to the ash precipitability, "P". "P_T" is in turn a function of three other relationships as shown in equation (5). Each of these three other relationships express the impacts of sulfur in the coal, the sodium in the ash and the total moisture in the coal on ash precipitability. In solving the equations to obtain "P" for a specific ash, the coal's sulfur, moisture and hydrogen contents are used in terms of pounds per million Btu; whereas, the ash mineral constituents are used in terms of percent by weight of ash.

Currently, the best curve fit for this data base of concurrent performance tests and coal and ash analyses is a third order polynomial equation in the form of Equation (9):

$$P = a - (b)(P_T) + (c)(P_T)^2 - (d)(P_T)^3 \quad (9)$$

where, "a", "b", "c" and "d" are constants. The relationship for "P" versus "P_T" (equation 4) is plotted in Figure 2.

This curve fit has a correlation coefficient (R) of 0.98 ($R^2 = 0.95$). Initially a straight line correlation was used (16). Intuitively, we prefer the current, S-shaped third order polynomial since we feel that a straight line fit should taper off towards its end points. At the lower limits of precipitability, we feel that there is an intrinsic precipitability despite the lack of the chemical compounds which are advantageous to precipitability. At the upper end of precipitability, the advantages of large amounts of chemicals such as sulfur and sodium taper off. In fact, there can be too much of a good thing with respect to precipitability. There have been cases of very high sulfur coals requiring ammonia flue gas conditioning to improve precipitator performance - presumably by increasing ash resistivity. We feel that the shape of the curve depicted in Figure 2 is overly optimistic for lower precipitabilities. Therefore, for "P_T" values of less than 0.2 we force the curve into a straight line fit.

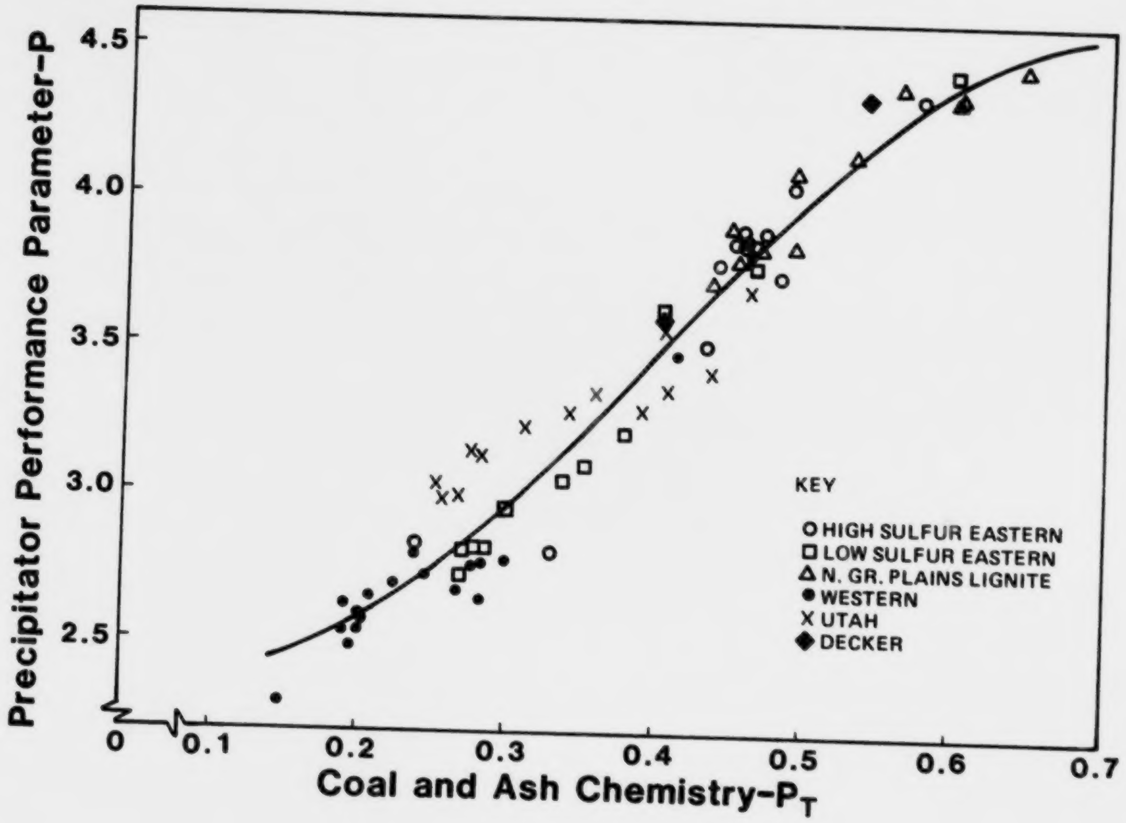

Figure 2. Precipitator Performance Parameter (P) vs Coal and Ash Chemistry (P_T)

Equation (6) expresses the impact of sulfur in the coal on ash precipitability. The amount of iron in the ash (reported as FE_2O_3) has an impact on the influence of the sulfur. It is thought that the iron acts as a catalyst in the conversion of sulfur dioxide to sulfur trioxide. Traditionally, a sulfur trioxide coating on the ash particles has been considered to be the primary mechanism which promotes ideal surface resistivity of the ash. Generally, as the amount of sulfur and/or iron increases, the ash precipitability increases due to the beneficial resistivity effects of increased sulfur trioxide. The amount of ash relative to the sulfur in the coal determines how widely the sulfur trioxide must be distributed. The less ash relative to the amount of sulfur trioxide, the greater the impact of the sulfur trioxide.

Calcium, magnesium, and potassium (reported as CaO, MgO, and K_2O) have an adverse impact on the beneficial effects of sulfur. Presumably, these constituents combine with the sulfur dioxide and thus reduce the amount of sulfur trioxide to improve the surface resistivity of the ash. In addition, compounds formed such as gypsum ($CaSO_4$) have a high intrinsic (bulk) resistivity and thus detract from the overall ash precipitability.

Equation (7) expresses the impact of sodium in the ash (reported as Na_2O) on the ash precipitability. Traditionally, sodium has been considered as having the major beneficial impact on the intrinsic resistivity of the ash. Sodium ions are very mobile charge carriers. As the amount of sodium increases, the resistivity decreases, and hence the precipitability of the ash improves.

However, it is thought that sodium is beneficial to the precipitability in ways other than by improving resistivity. Apparently, relatively large amounts of sodium affect particle size - mostly through agglomeration. Agglomerated masses of particles improve precipitability by reducing rapping re-entrainment losses and due to the well-known phenomenon that larger particles are easier to collect than fine ones.

The magnesium, potassium and calcium oxides shown up in the relationship for P_N due to their mitigating impacts on the beneficial effects of sodium on precipitability. Like sodium, the potassium ion is rather mobile and thus an effective charge carrier. It is expected that the potassium would then have a beneficial impact on the intrinsic resistivity of the ash, and thus a beneficial effect on the precipitability. Traditionally, and in early investigations into this model, potassium has been looked at as a beneficial ash constituent. However, it was not until potassium was considered as having a negative impact on the beneficial effect of sodium in Equation (7) that any relationship connecting the Eastern and Western coals could be demonstrated with a reasonable correlation.

The H_2O and H_2 in Equation (7) represent the total moisture in the flue gas and impact the beneficial effects of the sodium. As the total moisture increases, the beneficial aspects of the sodium increase - presumably through increased particle agglomeration.

Equation (8) relates the impact of total moisture to ash precipitability. It is thought that the moisture affects the particle size. Many Western coals with high moisture content exhibit very fine fly-ash particle sizes when compared to the national average fly ash particle size of approximately 13 microns (3). It is thought that a high intrinsic coal moisture creates fine particles by a "popcorn" effect in which the high furnace temperatures cause the moisture to expand rapidly and burst the ash particles (3). The amount of ash in the coal determines how effective the moisture is at reducing particle size. As the amount of ash increases, a given amount of moisture will be less effective at reducing particle size and thus have less of a mitigating influence on precipitability.

Figure 3 is a plot of ash precipitability (P) as determined by Stearns Catalytic's model for each of 33 Eastern bituminous coals versus the percent sulfur in the corresponding coal (2). The "shotgun" scatter of the data values indicates that factors other than the percent sulfur determine how precipitable the ash from a particular coal is. Note that for a given precipitator, performance increases as "P" increases. It is apparent that consideration of percent sulfur alone for the prediction of precipitator performance becomes less and lesss reliable as the percent sulfur in the coal decreases. The convergence of the data values at higher sulfur contents reflects general knowledge that the beneficial effects of coal sulfur on precipitator performance eclipse the effects of other chemical constituents and peak in the 3.5 to 4.0 percent sulfur range. Plots of Deutsch-Anderson migration velocities versus percent sulfur for the same coals would exhibit a similar scatter.

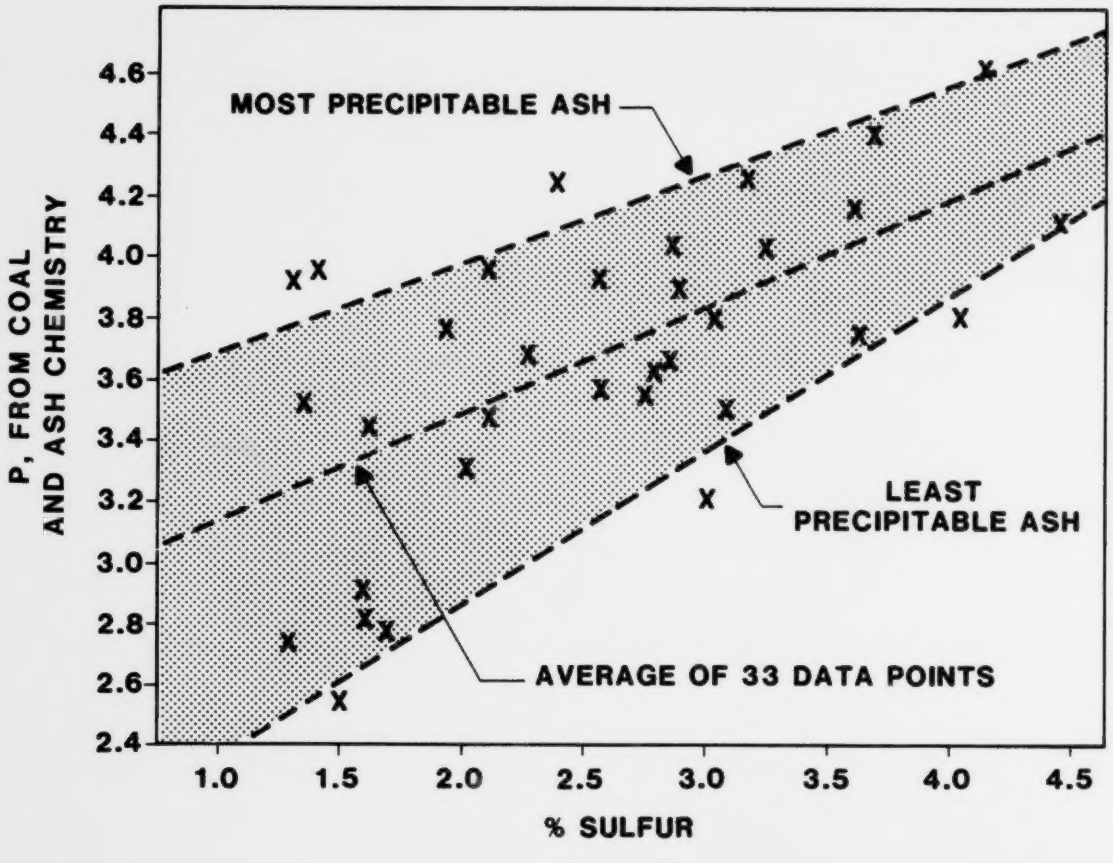

Figure 3. Stearns Catalytic Model - Precipitator Performance Parameter (P) vs Percent Sulfur

FACTORS NOT DIRECTLY CONSIDERED

Several factors such as particle size distribution, resistivity, flue gas temperature, and other ash chemical constituents are known or thought to be important with respect to ash precipitability. However, the Stearns Catalytic model exhibits a good correlation of precipitability to coal and ash chemistry without directly considering or solving for such values.

Although resistivity and particle size distribution have been used as rationalizations to consider the impacts of several chemical constituents on precipitability, resistivity and particle size are never directly considered or determined in this model. Ideally, it would be beneficial to have a measurable quantity such as resistivity upon which one could base ash precipitability. However, it is clear that resistivity is not the only mechanism at work which determines ash precipitability. Also, methods have yet to be developed which can reproducibly measure or predict the ash resistivity as it exists at all points on the collecting plates throughout the precipitator.

Although ash resistivity can give us an idea of how easily a particle can take on and give up charge, the dielectric strength of the collected ash layer is the electrical property that becomes important for high resistivity ash (4). This property tells us about the onset of back corona, which is the true limiter of precipitability. Also, it is now known that for many ashes the resistivity of the collected ash layer apparently degrades (increases) over time, in the case of hot-side precipitators. This deteriorative effect on cold-side precipitator performance has just recently been documented (15).

Figure 4 is a version of a classic curve relating ash resistivity to Deutsch-Anderson migration velocity, and was taken from Reference 6. This curve suggests rather good, and much better correlation of resistivity and migration velocity for high resistivity ash than indicated by such curves reported earlier (7, 8). This good correlation suggests that resistivity may actually be a good indicator of precipitability for high resistivity ash. However, the scatter of the data points for lower resistivity suggests that mechanisms other than resistivity are at work in determining precipitability. Such factors could likely be particle size and/or agglomeration.

Figure 5 is another example of the difficulty in using resistivity to predict precipitability. Figure 5 is a plot of fly-ash resistivity versus flue gas temperature for many coals, and was adapted from reference 4. This Figure is a compilation of such curves from many other sources (9, 10, 11, 12). The large shaded areas for Wyoming Subbituminous, North Dakota Lignite, and Arizona and Wyoming Subbituminous coals suggest the data scatter observed by Stearns Catalytic in its attempts to relate ash resistivity to precipitability. Such efforts were finally abandoned in favor of the precipitability approach.

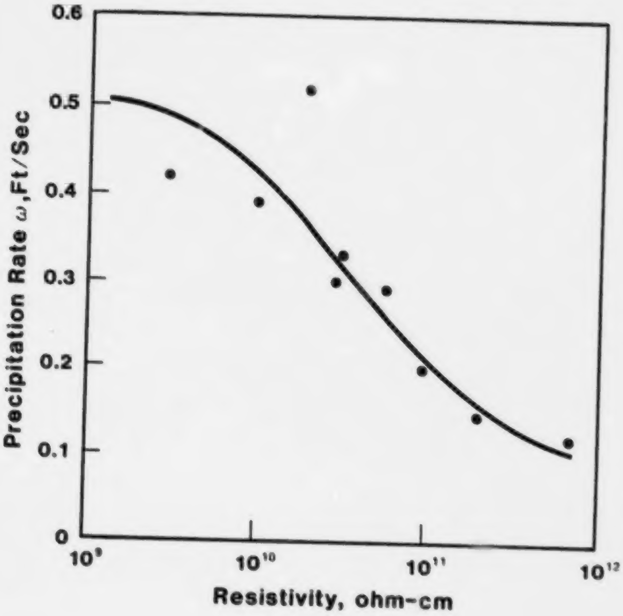

Figure 4. Precipitation Rate vs Fly Ash Resistivity

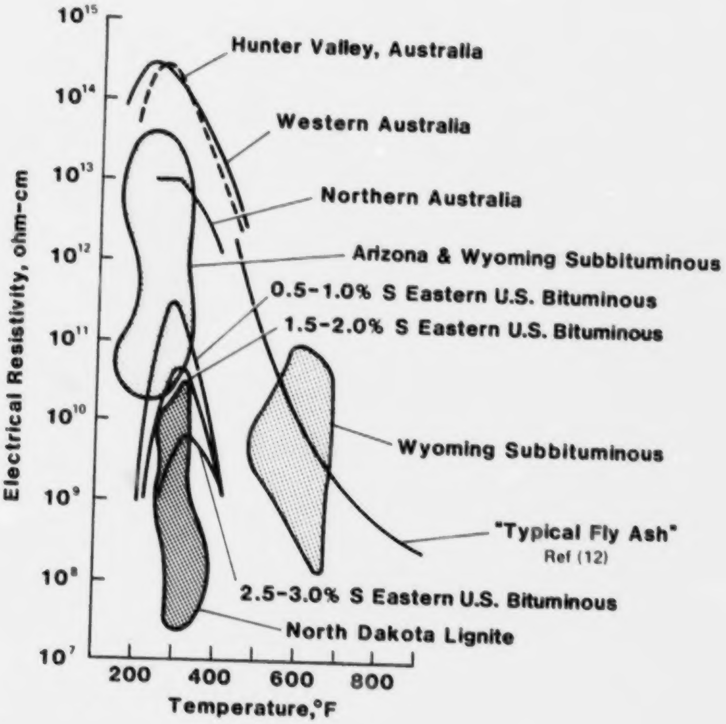

Figure 5. In-Situ Fly Ash Resistivity vs Temperature

Note that the correlation of coal and ash chemistry to precipitability (P) for cold-side precipitators of Figure 2 was obtained without consideration of flue gas temperature. Figure 5 demonstrates the difficulty of relating flue gas temperature to resistivity and then to precipitability.

Inspecting the resistivity curves in Figure 5, it becomes apparent that the resistivity does not change appreciably over the range of typical cold-side gas temperatures (250°-350°F) since the curves have peaked out and are at their points of inflection. These resistivity changes typically are approximately one-half an order of magnitude or less. In that the gas temperature out of the air heaters can vary by as much as 100°F, it appears that attempting to pin down an ash resistivity can be a futile effort. The average flue gas temperature at the precipitator is a function of the coal being fired and the boiler design and operation and therefore, can vary from the design temperature by as much as plus or minus 25°F. Following a regenerative air-heater the flue gas temperature at any point across the face of the precipitator can vary from the average temperature by a minimum of plus or minus 30°F. Therefore, the precipitator designer does not have the luxury of a design flue gas temperature upon which to base an ash resistivity across the face and throughout the precipitator.

At the hot-side of the air heater, the resistivity differences of a given ash are in terms of orders of magnitude and are thus important to consider. However, the industry's commitment to hot-side precipitators during the early- to mid-1970's led to many unpleasant surprises. The degradation in performance of many hot-side precipitator installations demonstrated even further that in-situ resistivity is not an adequate design tool in itself.

Ash constituents other than those considered by Stearns Catalytic's model are reported in the literature as having significant impact on ash resistivity. One of these constituents is lithium (reported as LiO_2) which is considered to be as effective as sodium at improving intrinsic resistivity due to an exceptional ion mobility (13,14).

Lithium typically shows up in ash as trace amounts and traditionally has seldom been reported with ash mineral analyses. Similarly, the test data and coal and ash analyses available to Stearns Catalytic for development of its model have not included lithium. It is primarily for this reason that lithium is not considered in Stearns Catalytic's model. Nevertheless, good correlation exists for the Precipitator Performance Parameter versus the coal and ash parameters considered for the Stearns Catalytic Model without considering lithium.

Since lithium is typically available only in trace amounts in fly-ash, it seems possible that its effect is eclipsed by the other more plentiful ash constituents - despite lithium's exceptional mobility. In that lithium is even more mobile than sodium, it also seems possible that the lithium ion, in its trace amounts, succumbs even more rapidly to the sodium ion depletion phenomenon hypothesized by Bickelhaupt (5).

Other ash constituents, such as alumina (Al_2O_3) and silica (SiO_2) are reported in the literature as having an impact on ash resistivity (4). However, alumina or silica are not considered in determining the ash precipitability for the Stearns Catalytic model. It is thought that the other coal and ash constituents considered by the model effectively account for the effects of alumina or silica and/or have a greater impact than the alumina and silica.

CONCLUSIONS

An empirical model has been developed which directly relates cold-side electrostatic precipitator performance to coal and ash chemistry. The model was developed by correlating precipitator performance tests and precipitator size with coal and ash analyses.

The model relates cold-side precipitator performance to one performance parameter rather than the two variables which are required to solve the modified Deutsch-Anderson equation. The Precipitator Performance Parameter, "P", represents the ash precipitability and is easily determined from coal and ash analyses without direct consideration of ash resistivity. Flue gas temperature is not directly considered in this model and has been found to have little impact on the ash precipitability for normal cold-side precipitator temperature ranges.

The coal and ash chemical constituents which are considered by the Stearns Catalytic model and have been found to have the major impacts on ash precipitability are: sulfur, moisture, hydrogen, sodium, magnesium, potassium, calcium and iron. As shown by Figure 2, this model exhibits a good correlation of ash precipitability to coal ash chemistry without the consideration of lithium, alumina, and silica.

NOTICE

The work described in this paper was not funded by the U.S. Environmental Protection Agency and therefore the contents do not necessarily reflect the views of the Agency and no official endorsement should be inferred.

REFERENCES

1. R.W. Scheck, S.D. Severson, et al, Economics of Fabric Filters versus Precipitators, EPRI FP-775, June 1978.

2. V.H. Belba, F.A. Horney, "The Future of Electrostatic Precipitation for the Collection of Fly-Ash from Pulverized Coal-fired Steam Generators," Coal Technology 1981, Volume 3, (Proceedings of the Fourth International Coal Utilization Exhibition and Conference, Houston, Texas; November, 1981).

3. F.A. Horney, "Coal Ash Characteristics: Do They Allow Predictability of Fabric Filter Performance?" Proceedings of the 4th International Fabric Alternatives Forum, Arizona State University and American Air Filter Company, Inc. December 5-6, 1979.

4. J.G. Singer, Combustion-Fossil Power Systems. Combustion Engineering, Inc. Windsor, CT, 1981.

5. R.E. Bickelhaupt, "An Interpretation of the Deteriorative Performance of Hot-Side Precipitators," Journal of the Air Pollution Control Association 30:882 (1980).

6. H.J. White, "Resistivity Problems in Electrostatic Precipitation" Journal of the Air Pollution Control Association 24:315 (1974)

7. H.J. White, Industrial Electrostatic Precipitation, Addison-Wesley Publishing Co., Inc.; Reading, Mass. 1963.

8. S. Oglesby, Jr. and H.J. White, "Practical Design and Operating Considerations for Industrial Electrostatic Precipitators" Proceedings of the Electrostatic Precipitator Symposium, February 23-25, 1971 Birmingham, Alabama, U.S. Env. Prot. Agency.

9. Kenneth J. McLean, Survey of Australian Experience in Collecting High Resistivity Fly Ash with Electrostatic Prescipitators. Final Report. Report no. PB-221 139 (EPA-R2-73-258). Springfield, VA: National Technical Information Service, 1972.

10. Alan B. Walker, "Operating Experience With Hot Precipitators on Western Low-Sulfur Coals." Proceedings of the American Power Conference, 39: 582-594, 1977. Chicago: Illinois Institute of Technology, 1977.

11. Harry J. White, "Electrostatic Precipitation of Fly Ash; Part II, Section 3: Fly Ash and Furnace Gas Characteristics," Air Pollution Control Association Journal, 27(2): 114-120, Pittsburgh 1977.

12. C.C. Shale, J.H. Holden, and G.E. Fasching, "Electrical Resistivity of Fly Ash at Temperatures to 1500°F.," U.S. Bureau of Mines Report of Investigations 7041. Washington: U.S. Government Printing Office, 1968.

13. G.B. Nichols and R.E. Bickelhaupt, "Electostatic Collection of Fly-Ash from Western Coals: Some Special Problems and the Approach to their Solution," 1975 Lignite Symposium, Grand Forks, N.D., May 14-15, 1975.

14. R.E. Bickelhaupt, A Technique for Predicting Fly Ash Resistivity, EPA-600/7-79-204, Prepared for Industrial Environmental Research Laboratory, U.S. EPA, August 1979.

15. H.R. Fletcher, Operating Experiences at Detroit Edison with Various Flue Gas Conditioning Systems, Paper No. 82-49.1, 75th Annual Meeting of the Air Pollution Control Association, New Orleans, Louisiana, June, 1982.

16. Fay A. Horney and Victor H. Belba, *An Empirical Model of Cold-Side Precipitator Performance Based upon Coal and Ash Chemistry, Presented to the 1982 IEEE/IAS, Annual Conference on Electrostatics*; San Francisco, California; October 1982.

APPROXIMATE METHOD TO CALCULATE CHARACTERISTICS OF CONTAMINATED-WIRE AND STRIP-DISCHARGE ELECTRODES

Kenneth J. McLean
University of Wollongong
Wollongong, NSW, 2500, Australia

Leslie E. Sparks
Geddes H. Ramsey
Air and Energy Engineering Research Laboratory
U.S. Environmental Protection Agency
Research Triangle Park, N.C., 27711

ABSTRACT

A new method has been developed to calculate the voltage-current characteristics and current density distribution for contaminated-wire and strip-discharge electrodes. The method is based on the characteristics of the individual tuft discharges which have the same Warburg law and current density distribution as the needle-plane geometry except that part of the pattern is truncated by the discharge electrode shape and the proximity of other discharges. These effects are examined experimentally and expressions found for the truncation loci. The technique is then applied to a contaminated-wire electrode and to a scallop-strip rigid-discharge electrode and the calculated and experimental results compared.

This paper has been reviewed in accordance with U.S. Environmental Protection Agency's peer and administrative review policies and approved for presentation and publication.

INTRODUCTION

To effectively model an electrostatic precipitator, it is necessary to calculate the electric and current density fields in the gas space and on the collecting plate. Because of the space charge and the need to satisfy the current continuity equation, the following equations must be solved:

$$\nabla^2 V = -\rho/\epsilon o \quad , \quad E = \nabla V$$
$$j = \rho\mu E \quad , \quad \nabla x j = 0 \tag{1}$$

By eliminating j and E, these equations become:

$$(\nabla V)^2 + (\nabla V)\cdot(\nabla\nabla^2 V) = 0 \tag{2}$$

Since this equation is non-linear, exact analytical solutions can only be obtained for parallel planes, coaxial cylinders, and concentric spheres (1).

In order to solve these equations for the electrode geometry used in commercial electrostatic precipitators, it is usual to make several simplifying assumptions, the most important being that the discharge electrodes are wires and that the corona discharge is uniformly distributed along the length of the wire as with positive corona. With these assumptions, it is possible to obtain approximate analytical or numerical solutions (2)(3)(4)(5)(6).

In practice the discharge is not uniform. If the discharge electrode is a contaminated wire, negative corona forms a series of discrete tuft discharges along its length. Alternatively, if preformed electrodes are used, the corona discharge is forced to form at predetermined locations, and this results in a non-uniform discharge.

An alternative approach is to model the corona in terms of the characteristics of the individual tuft discharges, their interaction with one another, and with the shape of the discharge electrode on which they form (7)(8). This method can be easily applied to different shaped, strip or barbed, as well as to contaminated wire, electrodes.

This paper will first discuss the characteristics of the individual discharges formed on different shaped electrodes and calculate the extent of their interaction with one another and with adjacent electrodes. The results will be applied to a wire electrode and to a typical scallop-strip electrode.

TUFT CORONA CHARACTERISTICS

One of the important features of the individual corona discharge points is that their characteristics can be derived from those of the needle-plane geometry.

The current density distribution pattern is an important feature of this geometry, and it has been found experimentally to follow the Warburg law very closely (1):

$$J(\theta) = J(0)\cos^n\theta \tag{3}$$

where n is approximately in the range 4.6 - 5.5, and θ is the angle with respect to the perpendicular from the needle to a point on the plate.

The magnitude of the current density at any point on the surface is given with good approximation by the saturated current density [Equation (1)] but has been modified to take into account the voltage drop across the discharge region (9):

$$J = \epsilon_o\mu(V - Vd)^2/L^3 \tag{4}$$

Where ϵ_o is the permittivity, μ the negative ion mobility, V the applied voltage, Vd the voltage drop across the discharge , and L the length of the flux path. This equation is used to calculate the value of J(0) in Equation (3). In this case L = S, where S is the gap between the needle point and the plate.

The total current can be found by using Equation (4) to find J(0), substituting in Equation (3), and then integrating over the whole area to give:

$$I = 2\pi S^2 J(0) \int_o^{\theta_c} \cos^{n-3} d(\mathrm{Cos}\,\theta) \tag{5}$$

$$= 2\pi B\, \epsilon_o\mu(V - Vd)^2/S^{(n-2)} \tag{6}$$

where θ_c is the cutoff angle; and B is a correction factor that allows for changes of n with applied voltage, especially at low voltages, and takes into account the variation in the gap spacing as the voltage increases due to the increase in the discharge size and the streamer penetration into the gas space. It varies from 1.0 to 1.4.

Alternatively, the following empirical expression may be used:

$$I = Kg\, \mu\, V(V - Vt)/(S)^{1.5} \tag{7}$$

where Kg = 0.85, and Vt is the corona onset voltage.

The current field pattern can be truncated by any one, or a combination, of the following:

(a) The diameter of the rod on which the corona forms.

(b) The shape of the discharge electrode on which the discharge is formed or to which the rod is attached.

(c) The proximity of adjacent discharges.

(d) The proximity of adjacent discharge electrodes.

The effect of the electrode geometry on the current density footprint is shown in Figure 1. For the rod-plane geometry, there is a cutoff of the outer current depending on the diameter of the rod and the average electric field, E_{av}. For a 2.5 mm diameter rod, the cutoff angle θ_c is approximately 55^o for E_{av} = 1.5 kV/cm.

The strip-plane geometry has a truncation loci that is approximately an ellipse, $(x/a)^2 + (y/d)^2 = 1.0$. The ratio of d/a = 2 and a has values depending on W/P. For W/P = 2, a = 60 mm, and for W/P = 8, a = 33 mm.

The wire-plane geometry truncation locus follows the equation, $x^2 = 0.01y + T$, where T varies with the applied voltage and has values of 3.0 and 6.8 mm for voltages of 25 and 50 kV, respectively.

The scallop-strip rigid-discharge electrode truncation locus follows the equation, $y = 0.02x^2 + Eo$, where Eo is 10 and 70 mm at 40 and 20 kV, respectively. Equal amounts of current flow to both plates.

For each shape, part of the needle-plane current density pattern is truncated and reduced to zero: but, in the unaffected region, it continues to follow the Warburg law. The effect of the electrode geometry truncation is to reduce the total current from the discharge and this current, expressed as a per unit value of the unmodified needle-plane current, is called the electrode modification factor, Ke.

The truncation of the current due to adjacent discharges or electrodes is taken into account by the truncation modification factor, Kt. Its value depends on the shape of the current density distribution and needs to be evaluated for each geometry. One example is given later for the scallop-strip discharge electrode.

STRIP DISCHARGE ELECTRODES

In practice there are a wide range of discharge electrodes that are not wires (10). These are constructed in such a way that they have clearly defined regions where corona forms and include the scallop, barbed stud, and pointed strip. The important characteristic of these electrodes is that the corona forms at fixed locations along the electrode and their number per unit length does not change with voltage.

In order to illustrate this new technique, a scallop-strip discharge electrode will be considered. The discharge forms at the edge of each scallop, and the footprint of the current on the plate is shown in Figure 2. For this electrode, the effect of truncation due to adjacent discharges on the same electrode and of the parallel electrodes is given by Kt, and typical values are shown in Figure 3.

If H is the total length of the discharge electrode, and N is the total number of discharge points per unit length, the total current becomes:

$$I = (1 + F)\ Kg\ Kt\ \mu\epsilon\ HNV(V - Vt)/(S)^{1.4} \qquad (8)$$

where Equation (7) gives the current from a needle-plane geometry. An

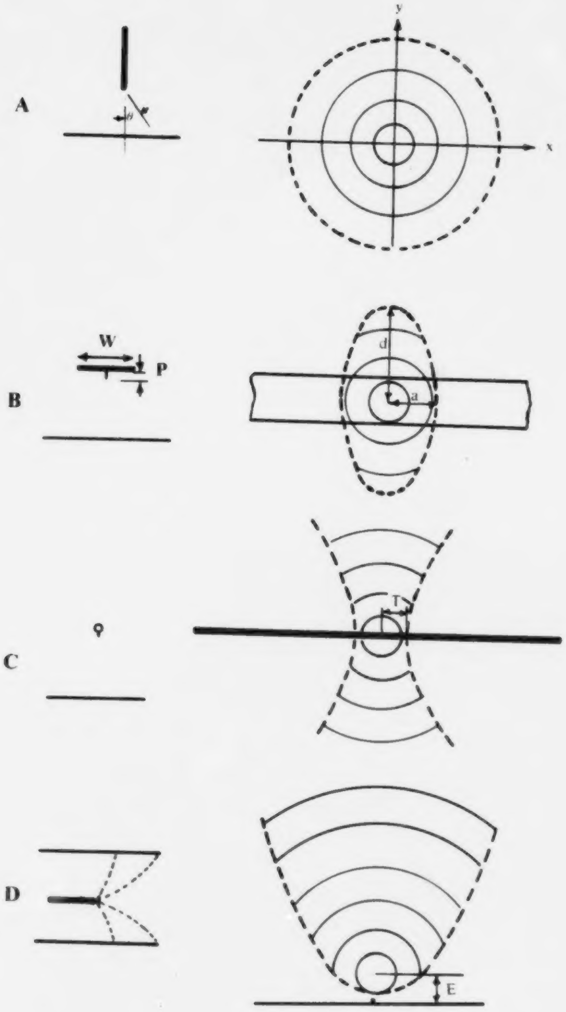

Figure 1. Current density footprints for different discharge electrodes. Electrode-plate spacing is 115 mm

A Rod-plane B Strip-plane
C Wire-plane D Scallop strip-plane
---- Truncation loci

alternative expression could be obtained, using Equation (6). F is the measure of the fraction current going to the opposite plate to which the discharge is pointing. For the scallop-strip electrode, F = 1.0, since equal amounts of current flow to both plates. A set of measured and calculated voltage-current characteristics are shown in Figure 4.

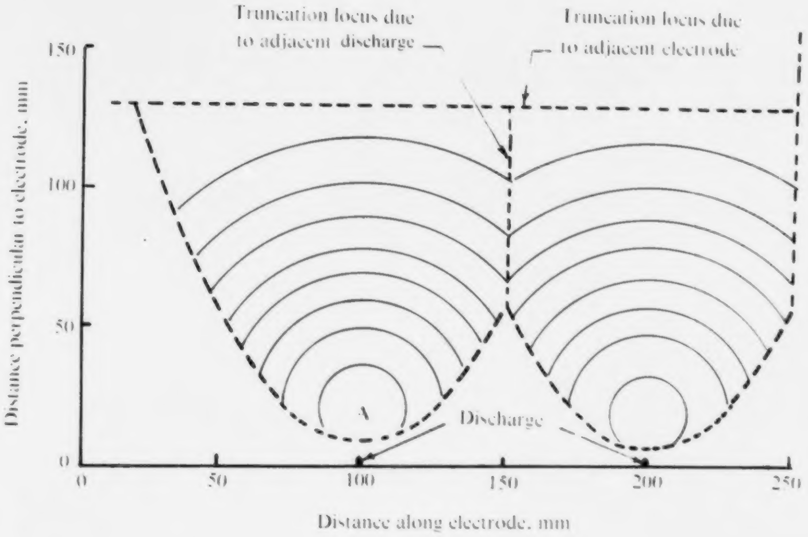
Truncation locus due to adjacent discharge
Truncation locus due to adjacent electrode
150
100
50
0
Distance perpendicular to electrode, mm
A
Discharge
0
50
100
150
200
250
Distance along electrode, mm

Figure 2. Current density footprint of scallop strip electrodes showing truncation effects of adjacent discharges and electrodes

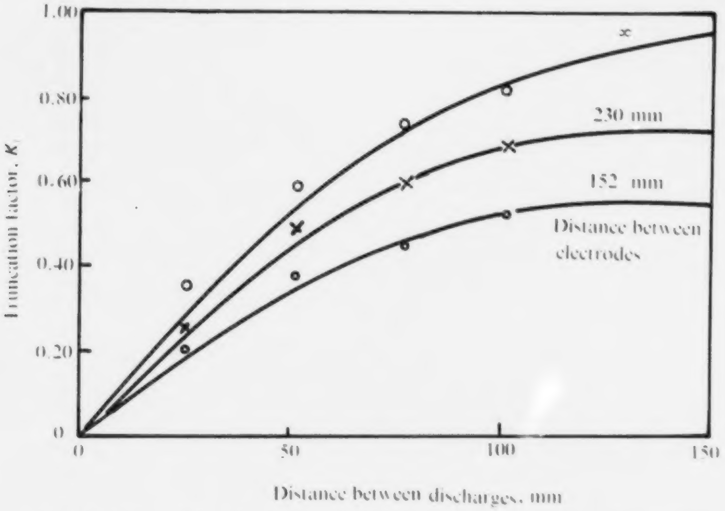

Figure 3. Variation of the truncation factor, Kt, for the scallop-strip rigid-discharge electrode

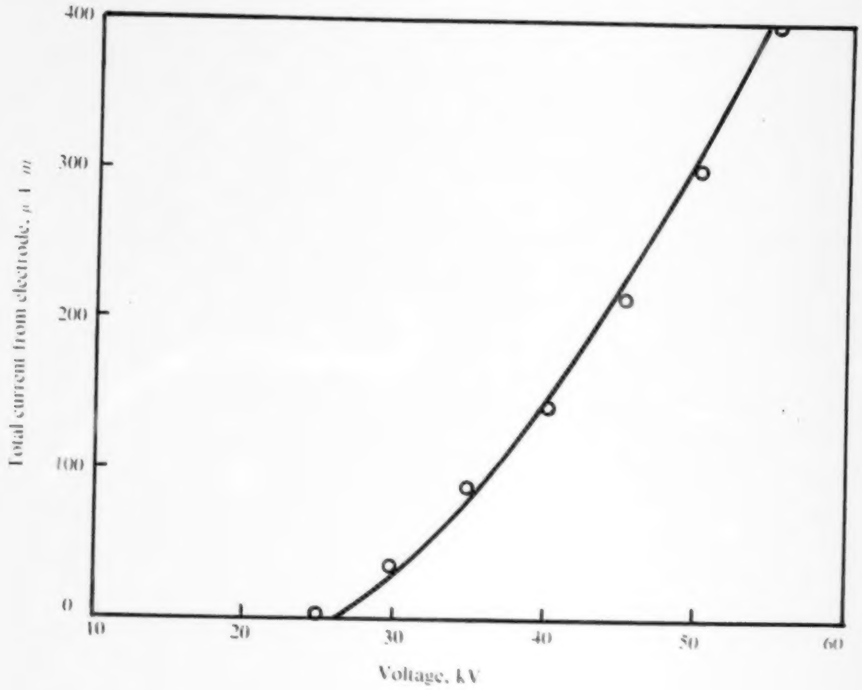

Figure 4. Voltage-current characteristic of scallop-strip rigid-discharge electrode

WIRE DISCHARGE ELECTRODES

For a clean and polished discharge wire, negative corona will start at Peeks onset voltage, Vc, and the voltage-current characteristic is given by the solid curve in Figure 5 and may be calculated by classical methods. For these conditions, the corona discharge appears as a uniform glow similar to positive corona, but is more turbulent and unstable. As the wire becomes contaminated, the glow discharge becomes unstable and degenerates to a series of unstable tuft discharges. When the wire is completely contaminated, the discharges become reasonably stable tufts which form uniformly along the wire length but pointing in all directions around the surface (7).

The contamination of the wire has several important effects on the voltage-current characteristics (8). For a given voltage, the current increases, which has the effect of shifting the curve to the left as shown in Figure 5. Considering the slope of this new curve, the corona onset appears to be reduced to Vo, which is traditionally taken to be Vc multiplied by the roughness factor of about 0.9. In practice, the corona onset is substantially lower at approximately 0.5 Vc, and there is a new region of corona discharge between Vt and Vo. In this partial corona region, the individual tuft discharges form arbitrarily along the wire in such a manner that their current fields do not overlap. Their number increases with voltage until at Vc, no more can be added without their current fields overlapping. The current per meter is given by:

$$I = \frac{0.392\ \epsilon o \mu Vc^2}{S^2} \left[\frac{V-Vt}{Vc-Vt}\right]^2 \tag{9}$$

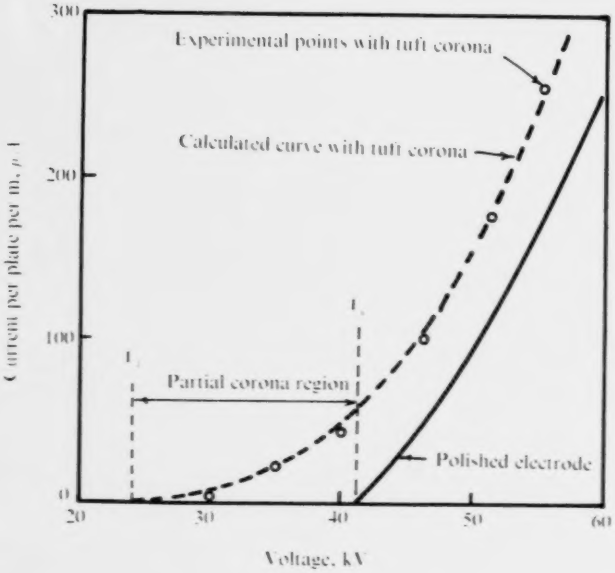

Figure 5. Voltage-current characteristic of negative corona with wire discharge electrode

For voltages above Vc, the current fields overlap and truncate one another, and the total number of discharges increase with voltages. The net result is that the current increases more rapidly than for the partial corona region, and has the same slope as the glow corona curve. This is called the full corona region, and the current is given by:

$$I = \frac{4\ \epsilon o \mu V^2}{3\ Df\ S^2} \tag{10}$$

where Df is the field modification factor (it starts at 3.4 for voltages below Vc, and decreases to about 1.6 for voltages of 1.5 Vc). S is the discharge electrode-plate spacing.

DISCUSSION

A new method to calculate some of the important electrical characteristics of duct electrostatic precipitators has been developed and is applicable to a wide range of discharge electrode shapes. The method requires a knowledge of the electrical characteristics of the individual discharges and their interaction. These can be related to those of the needle-plane geometry where the current density distribution obeys the Warburg law, and the current densities can be calculated from the modified saturated current density equation (9).

The new method has a number of important advantages over the classical approach, of which the following are particularly important:

(a) The method is applicable to all shapes of discharge electrodes.

(b) The method models the contaminated wire electrodes and explains the shift in the corona characteristic.

(c) It identifies the existence of a new corona region for wire electrodes well below the Peek onset voltage. This is of importance for large diameter discharge electrodes.

(d) The maximum current density can be calculated, and a good estimation made of the current density distribution on the plate.

The accuracy of the method is approximately 10 percent, but this can be improved with a better understanding of all the mechanisms involved. Additional work needs to be done to fully investigate the characteristics of the individual discharge.

ACKNOWLEDGEMENTS

This work was supported under U.S. Environmental Protection Agency Contract 68-02-3907 with the University of Wollongong.

The authors are grateful to D.A. Cunningham, S. Zedi, and B.S. Judibrata of the University of Wollongong for their assistance in measuring the characteristics of the discharges from different shaped electrodes, and to T.S. Ng and A.I. Ansari for their helpful comments and suggestions.

REFERENCES

1. Sigmond, R.S. Simple approximate treatment of unipolar space-charge-dominated coronas: The Warburg law and the saturated current. J. Appl. Phys. 53, 1982, 891 pp.

2. Cooperman, P. A theory for space-charge limited currents with application to electrostatic precipitation. AIEE Tran. Pt.1, 79, 1960, 47 pp.

3. Cooperman, G. A new current-voltage relation for duct precipitators valid for low and high current densities. IEEE Trans., Ind. Appl. IA-17, 1981, 236 pp.

4. Sekar, S. and Stomberg, H. On the prediction of current-voltage characteristics for wireplate precipitators. J. of Electrostatics, 10, 1981, 35 pp.

5. McDonald, J.R., Smith, W.B., Spencer, H.W., and Sparks, L.E. A mathematical model for calculating electrical conditions in wire-duct electrostatic precipitation devices. J. Appl. Phys. 48, 1977, p. 2231.

6. Lawless, P.A. and Sparks, L.E. Prediction of voltage-current curves for novel electrodes--arbitrary wire electrodes on axis. In: Proceedings: Fifth Symposium on the Transfer and Utilization of Particulate Control Technology, Volume 2, EPA-600/9-86-008b (NTIS PB86-167160), February 1986.

7. Lawless, P.A., McLean, K.J., Sparks, L.E., and Ramsey, G.H. Negative corona in wire-plate electrostatic precipitators. Part I : Characteristics of individual tuft-corona discharges. Accepted for publication in J. of Electrostatics, 1986.

8. McLean, K.J., Lawless, P.A., Sparks, L.E., and Ramsey, G.H. Negative corona in wire-plate electrostatic precipitators. Part II : Calculation of electrical characteristics of contaminated discharge electrodes. Accepted for publication in J. of Electrostatics, 1986.

9. McLean, K.J. and Sparks, L.E., Electrical characteristics of large-diameter discharge electrodes in electrostatic precipitators. In: Proceedings: Fifth Symposium on the Transfer and Utilization of Particulate Control Technology, Volume 2, EPA-600/9-86-008b (NTIS PB86-167160), February 1986.

10. Hall, H.J. Some electrode geometry, electric field and performance effects in electrostatic precipitation. Presented to the Second International Conference on Electrostatic Precipitation, Kyoto, November 12-15, 1984.

Session A-5: ADVANCED TECHNOLOGY

Leslie E. Sparks, Chairman
U. S. EPA/AEERL
Research Triangle Park, NC

PILOT-SCALE EVALUATION OF ESP WIDE PLATE SPACING

by: R. F. Altman
Electric Power Research Institute
Chattanooga, TN 37411

E. C. Landham, Jr.
J. L. DuBard
Southern Research Institute
Birmingham, AL 35255

Harry L. Wheeler
Combustion Engineering, Inc.
Birmingham, AL 35243

ABSTRACT

A 1 MW pilot-scale ESP at the EPRI Arapahoe Test Facility was operated with four different plate spacings in the range of 230 mm (9 inches) to 560 mm (22 inches). The tests were conducted with nominal gas flows of 1.65 m^3/s (3500 acfm) and 2.25 m^3/s (4800 acfm) and fly ash resistivities in the range of 10^{10} to 10^{12} ohm-cm. Total mass concentration and particle size distribution measurements indicated that the ESP collection efficiency was relatively insensitive to increases in plate spacing up to 460 mm (18 inches) as the spark-limited operating voltages increased roughly in proportion to the plate spacing. At the widest plate spacing, the ESP performance deteriorated. Final results of the project are summarized in this paper.

INTRODUCTION

In recent years, there has been a significant revival of interest in improving the design and operation of electrostatic precipitators, the principal means of controlling fly ash emissions at power plants. This interest, which to some degree is prompted by increasingly stringent particulate emission standards for utility boilers, has resulted in laboratory, pilot- and full-scale studies of flue gas conditioning, pulsed power supplies, intermittent energization, two-stage precipitation, and wide plate spacing.

The interest in the last topic, wide plate spacing, results primarily from experience overseas. There are over 200 precipitators in operation (mostly in industrial as opposed to utility applications) with collection plate spacings greater than 305 mm (12 inches). The principal advantage of precipitators with increased plate spacings is a reduced capital cost. Figure 1 contains a graph of some of the results from an economic study sponsored by the Electric Power Research Institute which indicates that the capital cost of a precipitator can be reduced by 12 to 16% by increasing the plate spacing. The 16% reduction results if it is assumed that the precipitator will maintain a constant collection efficiency as the plate spacing is increased. The 12% figure results if it is assumed that the precipitator length must be increased by 10% to achieve a constant collection efficiency. In addition to a reduction in the capital cost, precipitators with increased plate spacings will have fewer discharge electrodes, fewer collection plates, and, for some designs, fewer components in the rapping system. This reduction in the number of components should also reduce the maintenance costs for the precipitator.

Because an increased collection plate spacing can lower precipitator capital costs and produce a precipitator that is easier and less costly to maintain, the Electric Power Research Institute has sponsored a pilot-scale study to determine the effect of plate spacing on collection efficiency and to estimate the effect on capital and operating costs. The Environmental Systems Division of Combustion Engineering, Inc. was the prime contractor and co-sponsor of the work. Sumitomo Heavy Industries of Japan and Walther & Cie of Germany were also co-sponsors and served as consultants during certain phases of the study. Southern Research Institute was responsible for the operation of the pilot precipitator used in the study and for gathering and analyzing data from the pilot tests. A preliminary report on this study was made at a previous symposium (1). The study has now been completed, and this paper contains a more complete summary of the results.

EXPERIMENTAL APPROACH

The tests were conducted at the Public Service Company of Colorado's Arapahoe Power Plant in Denver, Colorado. The Environmental Control Systems Department of EPRI operates a number of pilot plants at Arapahoe (2). The pilot ESP used in this study was designed to treat a flue gas flow rate of 3500 to 4800 acfm (1.65 to 2.25 m^3/s) and has three electrical fields in the direction of gas flow. When the plates are spaced at 9 inches (230 mm), the ESP has four gas passages and total plate area of approximately 1,400 ft^2 (130 m^2) giving it an SCA in the range of 280 to 400 $ft^2/1000$ acfm (55 to 78 $m^2/m^3/s$). When collection plates are removed to increase the spacing between the plates, the SCA is reduced.

The values of the principal parameters during wide plate spacing tests are listed in Table 1. As indicated by the table, data were taken with the plates spaced at 9, 12, 18, and 22 inches (230, 305, 460, and 560 mm). For each of those plate spacings, tests were conducted with a high flue gas flow rate of approximately 4800 acfm (2.25 m^3/s) and at a low flue gas flow rate of approximately 3500 acfm (1.65 m^3/s). For each flow rate, the precipitator was operated both with and without SO_3 conditioning. Without SO_3 conditioning, the fly ash electrical resistivity was high, since a low-sulfur Colorado coal is burned at the plant. With SO_3 conditioning, the fly ash resistivity was 2 to 5 x 10^{10} ohm-cm, a resistivity that is in the optimum range for electrostatic precipitation.

For each test condition, comprehensive measurements were made. Inlet and outlet mass concentrations were measured using EPA Method 17 so that overall mass collection efficiency could be determined. Particle size distributions at

TABLE 1. TEST PARAMETERS FOR PILOT-SCALE PROJECT AT ARAPAHOE

Test Condition	Plate Spacing Inches	SCA (Nominal) ft^2/1000 ACFM	Flue Gas Flow Rate ACFM	SO_3 Conditioning
9-1	9	370	3,630	not used
12-1	12	275	3,690	not used
18-1	18	185	3,600	not used
22-1	22	185	3,600	not used
9-2	9	260	4,900	not used
12-2	12	195	5,220	not used
18-2	18	130	4,670	not used
22-2	22	130	4,900	not used
9-3	9	370	3,520	used
12-3	12	275	3,630	used
18-3	18	185	3,600	used
22-3	22	185	3,600	used
9-4	9	260	5,000	used
12-4	12	195	4,720	used
18-4	18	130	4,900	used
22-4	22	130	4,900	used

the inlet and the outlet of the precipitator were measured so that the particle size dependent collection efficiency could be determined. Outlet opacity was monitored continuously to alert the operators to any changes in ESP operation. Fly ash resistivity was measured regularly in situ so that the effect of this important parameter on the results could be determined. Coal and ash samples were gathered for chemical analysis.

At the beginning of the tests for each plate spacing, voltage-current data were taken at ambient conditions to verify that no electrical clearance problems existed which would limit the discharge electrode voltage. During all of the tests, a conventional spark rate controller was used to energize the transformer-rectifier sets. There was no attempt made to force the voltage to be proportional to plate spacing or to maintain a constant current density at all plate spacings. This approach was adopted because spark-rate controllers are used almost universally for precipitator controls in utility applications. This approach also eliminated the need to select a base voltage or current density, a task that would have been difficult in view of the wide range of test conditions.

The discharge electrodes used during all of the tests were round wires with a diameter of approximately 0.1" (2.5 mm) spaced 6 inches (150 mm) apart.

Laboratory measurements made early in the project indicated that this diameter and spacing would produce reasonable voltage-current curves and reasonably uniform current distributions at the plate for all the plate spacings under consideration. Time and budget constraints did not allow the optimization of the discharge electrode design at the wider plate spacings.

EXPERIMENTAL RESULTS

The resistivity measurements made during all of the tests are plotted in Figure 2. The numbers beside the resistivity ranges in this figure correspond to the test conditions identified in Table 1. When SO_3 conditioning was not being used, there were some substantial shifts in fly ash resistivity. During the 9 inch tests without SO_3 conditioning, fly ash resistivity was unusually low. The resistivity during the 12 inch tests without fly ash conditioning was high, usually greater than 2×10^{12} ohm-cm. During the 18 inch tests, the resistivity was lower than it was during the 12 inch tests but not as low as it was during the 9 inch tests. These changes in fly ash resistivity are reflected in the collection efficiency data presented later. During the tests that were conducted with SO_3 conditioning, the resistivity was consistently below 10^{11} ohm-cm, but there was still scatter in the resistivity data. The test period stretched over many months, and there were unavoidable changes in the coal supply at Arapahoe that were responsible for these rather significant changes in fly ash resistivity.

Figure 3 contains a plot of the average collection efficiency data taken during the high flow rate tests for all plate spacings. The solid line on the graph is a projection of precipitator performance versus fly ash resistivity for a precipitator with a 12 inch plate spacing. This curve was generated using the Southern Research Institute computer model of electrostatic precipitation, in order to indicate the expected trend in the data. The data gathered with no SO_3 conditioning are grouped in the upper right hand corner of the figure. The average efficiency data in this group for 9, 12, and 18 inch plate spacings roughly parallel the computer projection of performance. The interpretation of this result is that there was very little, if any, loss in collection efficiency, even though there were fewer plates in the precipitator (smaller SCA) as the plate spacing was increased. There was, however, a significant loss in performance when the plate spacing was further increased to 22 inches.

The efficiency data gathered with SO_3 have a similar appearance in the lower left hand corner of the figure. The average data for 9, 12, and 18 inches roughly parallel the computer projection of performance, indicating that there was little loss in collection efficiency as the plate spacing was increased to 18 inches. There was a loss in performance when the spacing was increased to 22 inches. During the tests conducted with the plates spaced at 9 inches, the operation of the precipitator shifted in a noticeable fashion. The data taken before and after that shift in operation are distinguished by the opened and closed circles. Apparently, a significant change in the coal burned during the 9 inch tests produced a measurable change in the operation of the pilot precipitator.

The data gathered when the precipitator was operating at a low flue gas flow rate are plotted in Figure 4 and show the same trends. When SO_3 conditioning was not being used, the collection efficiencies measured with the plates spaced at 9, 12, and 18 inches roughly parallel the computer projection of the performance. The performance deteriorated when the plate spacing was increased to 22 inches. When SO_3 conditioning was being used, the collection efficiencies fell in a cluster around an average value of 99.9%. Again, the collection efficiency was lower when the plates were spaced at 22 inches. Two shifts in precipitator performance are indicated by these data. One took place when the plates were spaced at 22 inches and SO_3 conditioning was not being used (indicated in Figure 4 by the opened and closed diamond symbols). The second shift in operation occurred when the plates were spaced at 18 inches and SO_3 conditioning was being used (indicated by the opened and closed triangles). These shifts were similar to the one that took place when the plates were spaced at 9 inches. Although there is scatter in the data, these results indicate that the spacing between plates can be increased up to 18 inches with no significant loss in performance. As stated earlier, this result was achieved using a conventional discharge electrode design and a conventional spark rate controller.

The fractional efficiency or particle size dependent collection efficiency data taken during the high resistivity, low flue gas flow rate tests are plotted in Figure 5. These results indicate that the collection efficiency for the 9 inch plate spacing tests was slightly better than the efficiencies measured when the plates were spaced at 12, 18, and 22 inches. However, the fly ash resistivity during the 9-1 tests (see Table 1 and Figure 1) was lower than the resistivity during the other tests. That difference in resistivity probably accounts for the difference in these fractional efficiency curves. The results also indicate that performance of the ESP with the plates spaced at 22 inches was as good as it was with 12 and 18 inch plate spacings. But the resistivity during some of the 22-1 tests was unusually low.

The fractional efficiency curves for all of the plate spacings in Figure 5 are similar. The minimum in every case occurs for particles with diameters in the one micron range. The minimum is around 85% for 9 inch plate spacing and around 70% for the other plate spacings. The fractional efficiency data taken at the other test conditions were very similar. The most significant result of the particle size dependent collection efficiency study is that the dependence did not change with plate spacing. There was no systematic shift in the way the precipitator collected fly ash as a function of particle size as the plate spacing was increased.

In addition to the collection efficiency data, the electrical operating points of the transformer-rectifier sets were recorded during all of the tests, and voltage-current curves were measured. Figure 6 contains a plot of the average voltages and current densities for the tests conducted with no SO_3 conditioning, with the flue gas flow rate set at the lower level. There is a clear trend in the voltage data for all three fields. The voltage increased at a rate that was roughly proportional to the plate spacing when the spacing was increased to 12 and 18 inches. When the plate spacing was further increased to 22 inches, the operating voltage did not increase as sharply. A conventional spark rate controller was used during all of the tests. The trends in current density are not as simple or consistent. The average current density increased slightly when the plate spacing increased from 9 to 12 inches but then decreased when the plate spacing was increased to 18 and 22 inches. An attempt was made to correlate collection efficiency with energy consumption and plate spacing for these data and for the data taken at the other test conditions, but there was too much scatter in the data to allow a useful correlation to be developed.

Two facts should be considered in any attempt to analyze the electrical data plotted in Figure 6. First, current density, not total current to the precipitator, is plotted in the figure. The current density must be multiplied by the plate area to obtain the total current. If the current density had remained constant for all plate spacings, then the total current would have been inversely proportional to the plate spacing since the plate area was inversely proportional to the spacing. The second fact concerns the usefulness of the current plotted in Figure 6. These data were taken when the precipitator was collecting fly ash with a high resistivity, and there was some degree of back corona present during all of the high resistivity tests. Therefore, not all of the current sensed by the current meters and recorded in Figure 6 was useful current for charging and collecting particles.

One way to judge the degree of back corona is to examine the voltage-current curves recorded during the tests. Figure 7 contains a plot of the V-I data for the outlet field, for the tests with low gas flow rate and high resistivity. The curves for the tests conducted with plates spaced at 9 and 12 inches show clear indications of back corona or back ionization. Both of these curves have very steep vertical portions and actually bend back toward the vertical axis. In contrast, the curves obtained with the plates spaced at 18 and 22 inches have a different appearance. The indications of back corona are much less apparent. This effect could result from the design of the discharge electrodes or it could be an indication that back corona has a less pronounced effect on precipitator operation at the wider plate spacings. It was impossible to make a definitive determination of the cause for the difference in appearance from the limited tests conducted during this pilot study.

CONCLUSIONS AND OBSERVATIONS

The conclusions that can be drawn from this preliminary study can be summarized as follows. The spark rate controller increased the voltage applied to the discharge electrodes at a rate that was roughly proportional to the plate spacing, for spacing up to 18 inches. The overall collection efficiency of the precipitator changed very little when the precipitator was operated with 9, 12, and 18 inch plate spacings. The collection efficiency decreased slightly when the plate spacing was increased to 22 inches. The appearance of the voltage-current curves for the high resistivity test conditions changed when the plate spacing was increased to 18 and 22 inches. An attempt to correlate the electrical operating points with plate spacing and efficiency did not produce useful results.

The implications of these findings are significant. First, the results indicate that an existing precipitator with a 9 inch plate spacing can be rebuilt with a larger plate spacing to take advantage of new discharge electrode designs, with no loss in performance even though the rebuilt precipitator will have fewer plates than the original precipitator. The results also imply that a new precipitator can be built with a wide plate spacing with a potential capital cost savings of 10% or more. (Plate spacing of 400 mm (16 inches) is becoming the standard in Europe.) Finally, the results justify further work on wide plate spacing at a larger scale. In future tests, more emphasis should be placed on discharge electrode design.

REFERENCES

1. Altman, R., et al. Technical Evaluation of Plate Spacing Effects on Fly Ash Collection in Precipitators. EPA/EPRI Fifth Symposium on the Transfer and Utilization of Particulate Control Technology, Kansas City, MO, August 1984. EPRI CS-4404, Volume 2, February 1986.

2. Altman, R. and Carr, R. EPRI Sponsored Research at the Arapahoe Test Facility. DOE/METC/84-13 Volume 2. US Department of Energy, Grand Forks, ND, February 1984. p. 783.

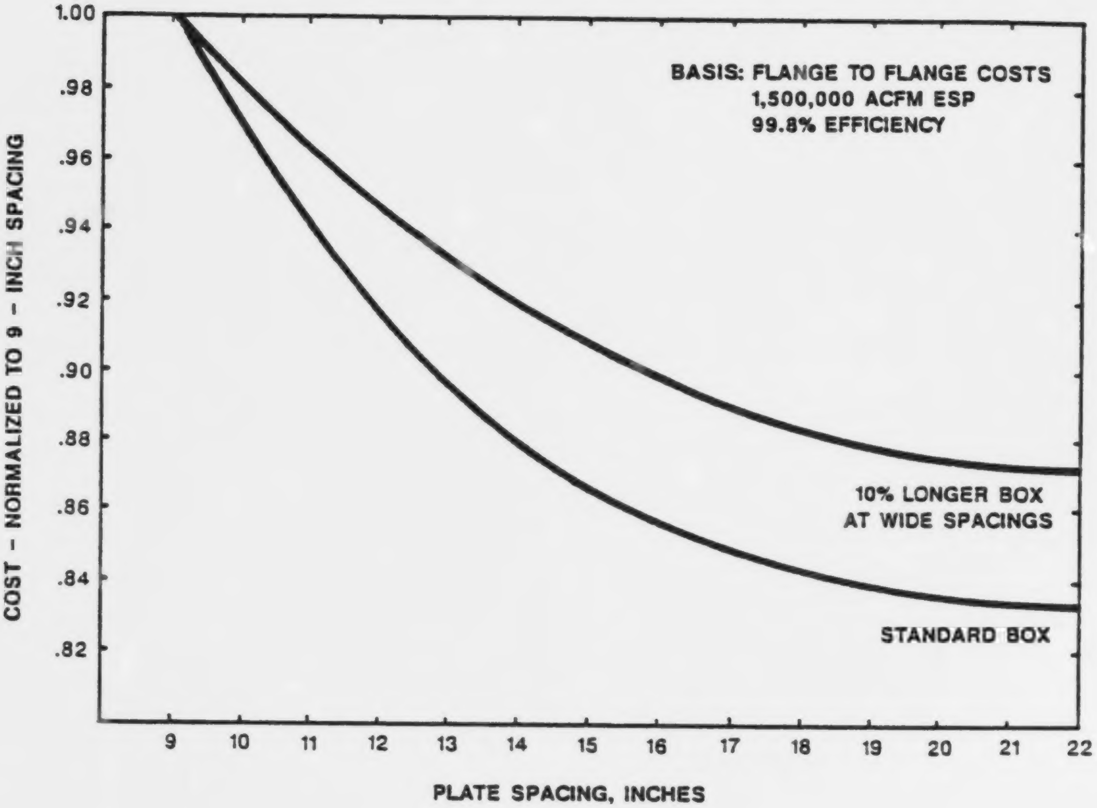

Figure 1. Normalized cost - vs - plate spacing for a large precipitator.

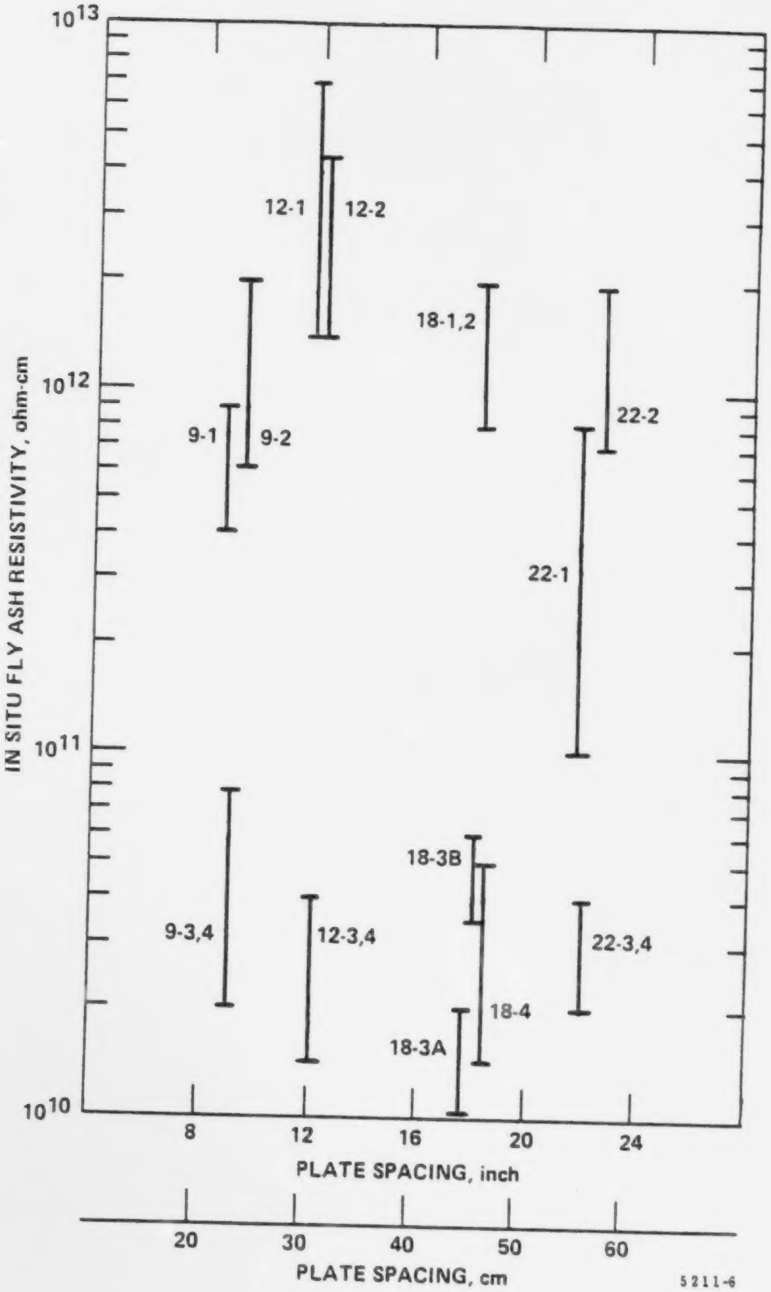

Figure 2. Resistivity ranges for all plate spacings and test conditions.

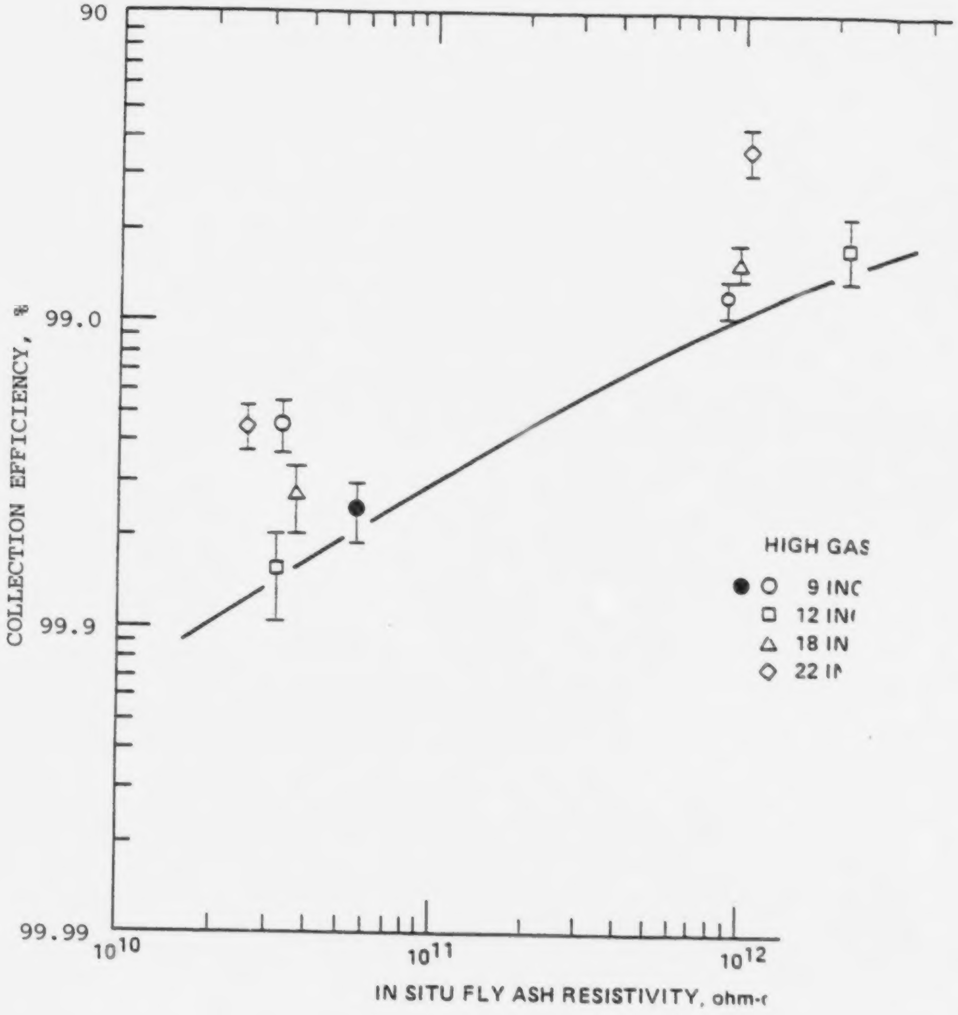

Figure 3. Collection efficiency versus resistivity compared with a computed trend for 12-inch plate spacing - high gas flow.

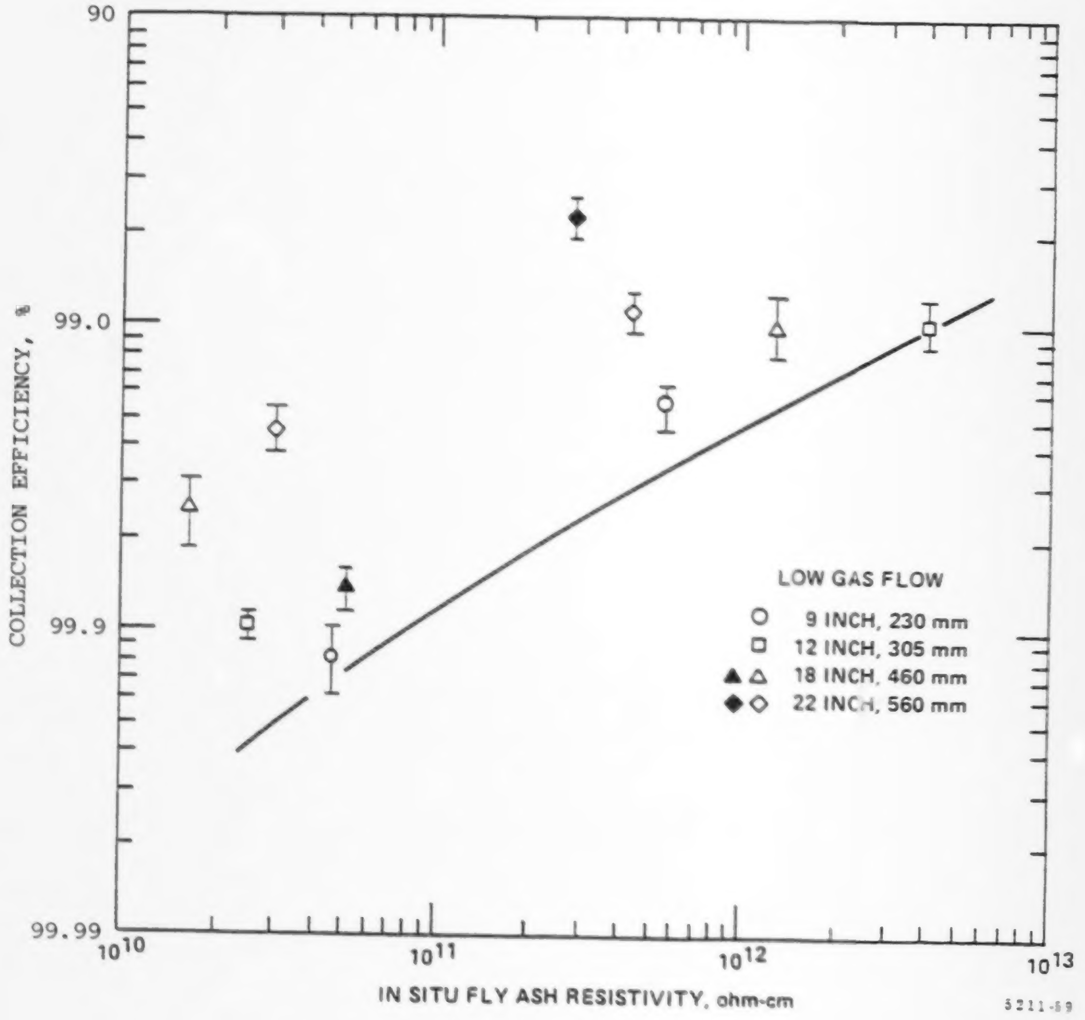

Figure 4. Collection efficiency versus resistivity compared with a computed trend for 12-inch plate spacing - low gas flow.

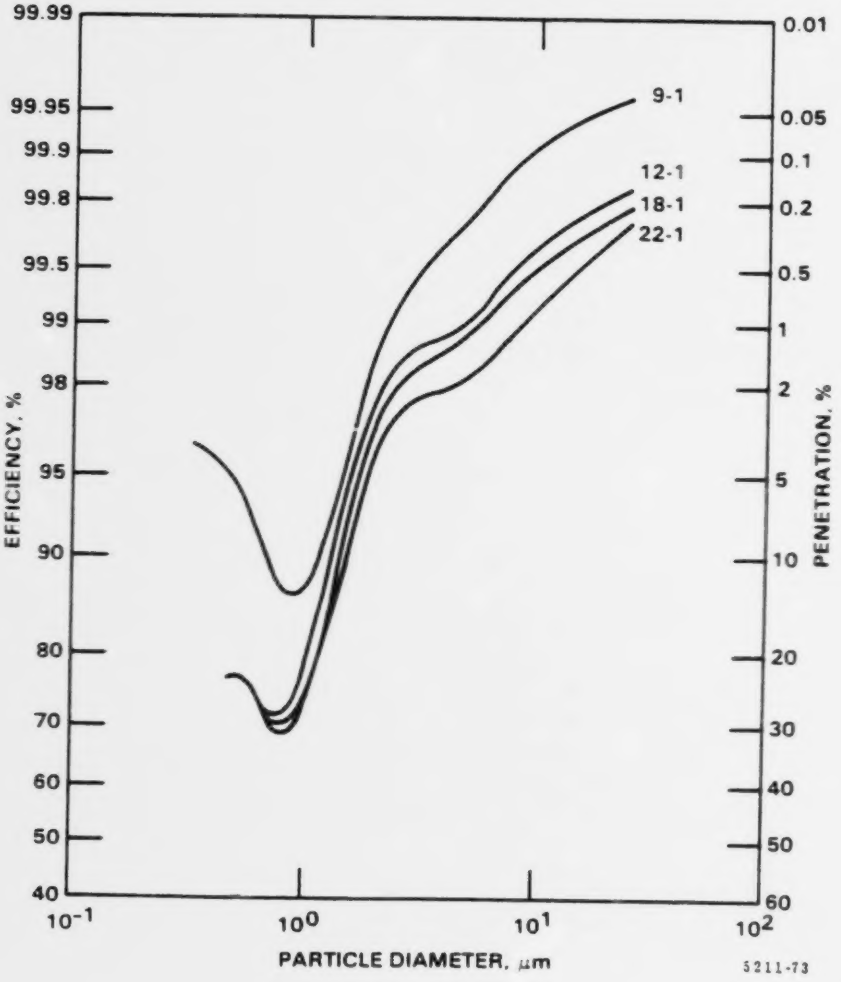

Figure 5. Fractional efficiency curves - high resistivity, low gas flow.

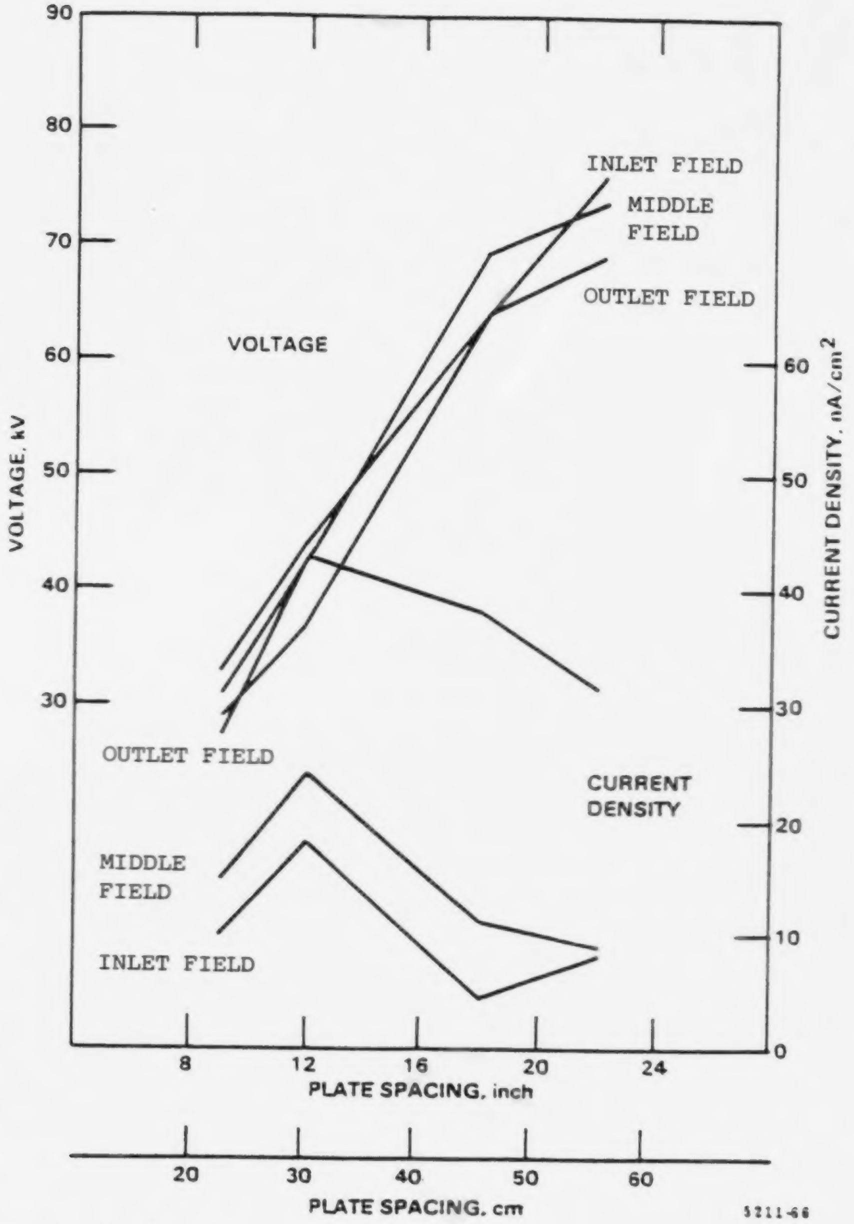

Figure 6. Measured electrical operating points - high resistivity, low gas flow.

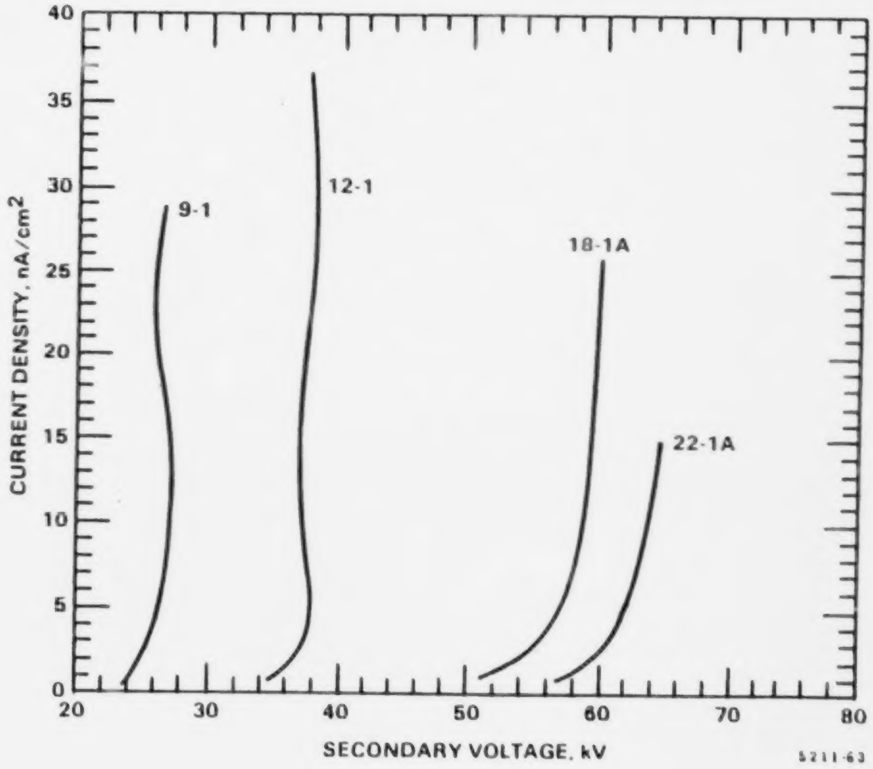

Figure 7. Voltage-current curves for the outlet field - high resistivity, low gas flow.

PILOT-SCALE EVALUATION OF ESP INTERMITTENT ENERGIZATION

E. C. Landham, Jr.
J. L. DuBard
Southern Research Institute
Birmingham, Alabama

Walter Piulle
Louis F. Rettenmaier
Electric Power Research Institute
Palo Alto, California

ABSTRACT

ESP transformer-rectifier controls which have the capability of intermittent energization were evaluated on the EPRI one-megawatt pilot-scale precipitator at the Arapahoe Test Facility. The commercially available system evaluated for this project can produce either normal energization (full-wave rectified DC) or can block and pass any combination of half-cycles. Results presented in this paper indicate that intermittent energization can maintain, or under certain conditions improve, ESP collection performance while significantly reducing transformer-rectifier power consumption. Direct comparison was made between the performance of a true pulser system and the intermittent energization system.

INTRODUCTION

Intermittent energization (IE) is a method of modifying the voltage and current waveforms used to energize electrostatic precipitators (ESPs). The benefits of IE operation include reduction in transformer-rectifier (T-R) power consumption and, under certain conditions, improvement of ESP collection efficiency. The Electric Power Research Institute (EPRI) has funded a research project to evaluate the usefulness of the IE technology to the American utility industry. This paper reports on a study of IE conducted on a pilot-scale ESP.

The purpose of the pilot-scale study was to develop techniques for predicting the effect of IE on full-scale ESPs. Major emphasis was placed upon determining the reduction in T-R power consumption which could be obtained without degrading ESP performance. Several different types of ESP electrical operating conditions, which appear to strongly affect IE performance, were evaluated. To determine if the process is sensitive to discharge electrode type, both round wire and barbed electrodes were tested. The performance of IE was directly compared to that of a true pulser system.

DESCRIPTION OF THE IE PROCESS

SYSTEM HARDWARE

As opposed to other electrical ESP enhancement technologies, such as pulsing, an IE system requires minimal hardware changes. The commercially available systems on the market today incorporate the IE system into a state-of-the-art T-R controller. The silicon-controlled rectifiers (SCRs), T-R sets, and other existing hardware need not be modified. A block diagram of an IE system is shown in Figure 1. Since modifications are made only to the low voltage side of the T-R set, one controller can be replaced at a time eliminating plant down-time for installation.

Companies known to have IE capable T-R controls on the market include Belco Pollution Control, Environmental Elements, NWL, Sumitoma Heavy Industries (Combustion Engineering), and Mitsubishi. The IE units utilized for this project were Merlin@ Microprocessor Controls manufactured by Belco Pollution Control.

THEORY OF OPERATION

During normal operation, the high-voltage waveform used to power the ESP fields is generally full-wave rectified DC. Examples of the voltage and current waveforms which appear in various parts of the system with normal operation are shown in Figure 2a. Conventional controllers maintain maximum T-R output current by continually seeking the point where sparking occurs in the field. The output of each T-R set is adjusted by using the SCRs on the T-R primary to block a portion of each AC half-cycle. The percentage of each half-cycle allowed to pass the SCRs determines the power to the ESP field. This method of adjusting AC power output is termed phase control.

To produce intermittent energization the IE control utilizes the same SCRs to alternately block and pass integral numbers of half-cycles. During the time when the IE control allows half-cycles to pass, normal phase control maintains the peak currents at spark-limit. Examples of two different IE waveforms are displayed in Figures 2b and 2c. Figure 2b shows the waveforms produced by turning the SCRs on for one half-cycle and then off for two half-cycles. Figure 2c indicates the waveforms due to energizing the SCRs for two half-cycles and de-energizing them for four half-cycles. The waveforms in Figure 2 do not show the result of phase control on wave shape, but represent 100% full output of the SCRs.

The advantages claimed for IE include reduction in power consumption and also an improvement in ESP performance for high resistivity ash. The improvement in performance has been attributed to elimination of back corona. IE may achieve this by reducing the ESP current to less than the amount necessary to produce the voltage drop across the dust layer at which back corona occurs (1, 2). To reduce the current to these values the number of energized half-cycles is set at two for some commercial systems. Other systems, such as the Belco studied at Arapahoe, are infinitely variable.

Regardless of the number of energized half-cycles utilized, the number of de-energized half-cycles should always be an even number. This will prevent polarization and potential damage to the T-R set. As seen in Figures 2b and 2c, correct operation always produces subsequent AC half-cycles of opposite polarity on the T-R primary.

Notation

The notation for describing the ratio of the off to on half-cycles in the IE waveforms is termed here IE ratio and is defined as:

$$\text{IE Ratio} = \frac{\text{Number of Half-Cycles Energized}}{\text{Number of Half-Cycles Energized + Half-Cycles De-energized}}$$

The IE ratios evaluated in this test program were varied in seven to nine increments from 1/1, 2/2, and 4/4 (which are normal operation) to 1/21, 2/40, and 4/80. An example of the general notation used to describe a series of tests with two half-cycles energized followed by a variable number de-energized is 2/x.

Power Consumption vs IE Ratio

The IE ratio could also be described as the duty cycle of the waveform. In theory, the power consumed by the T-R set would be decreased by this ratio. In fact, the true power savings is less than would be expected, as shown in Figure 3. The deviation of actual data from the theoretical line, down to an IE ratio of about 0.2, is caused by increasing T-R output peak current values with decreasing IE ratio. The actual data begins to converge with the theoretical line below 0.2 because the T-R set was not able to produce enough current to reach spark-limit of the ESP field.

ESP Voltage and Current

As the IE ratio decreases the peak and average values of ESP current and voltage change. Both peak and average T-R output current are plotted as a function of IE ratio in Figure 4. The relationship for peak and average ESP voltage is shown in Figure 5. The peak T-R output current should not be confused with the peak current available for charging and collecting particles in the ESP field. The peak current in the ESP field will be proportional to the peak ESP voltage. Therefore, the peak values of both ESP voltage and current increase with decreasing IE ratio until the peak output of the T-R set is reached. The maximum output limit of the T-R set can be seen in both the peak voltage and current values as a rolling off or flattening of the rate of increase. The roll-off is most serious for 1/x, less serious for 2/x, and does not occur for 4/x at the lowest ratio tested. The charge which flows between the ESP electrodes will be proportional to the average current.

EPRI PULSER SYSTEM

The IE process is often erroneously compared with the pulser systems currently on the market. Several of the terms used to describe IE (semi-pulsing, pulse-blocking, poor-man's pulser) seem to justify that comparison. The IE and true pulsing techniques are actually quite different. A major practical difference is hardware cost, which may be 10 to 20 times higher for a pulser system. To determine the differences in ESP performance, the IE process was directly compared with a true pulser system. The hardware and performance of the pulser system utilized for these tests have been described elsewhere (3).

The pulser superimposes a fast (125 microsecond) pulse on top of a DC bias voltage. Typical voltages for the Arapahoe unit are a 25 kV pulse height on top of a DC bias of 25 kV producing peak voltages of 50 kV. During operation the pulse height is held constant while the DC bias voltage is adjusted to operate at spark-limit. The pulse repetition rate which produces the best effect at Arapahoe is 50 pulses/sec. All of the ESP fields are operated at the same pulse rate. An example of the ESP voltage waveform produced by the pulser system is shown in Figure 6.

PILOT-SCALE RESEARCH PROGRAM

ARAPAHOE TEST FACILITY

The pilot-scale ESP utilized for this test program is located at EPRI's Arapahoe Test Facility in Denver, Colorado. The ESP is nominally rated at one-megawatt equivalent although the gas flow was varied for the tests to produce specific collection areas from 250-400 ft^2/1000 acfm (49-79 $m^2/m^3/s$). The unit has three separate electrical fields in the direction of gas flow, each of which is capable of IE. Flat collection plates without baffles were used with a nominal plate-to-plate spacing of nine inches. Two different styles of discharge electrodes, supported by harp frames, were used for the tests. Round wire electrodes with a diameter of 0.115 in. (2.92 mm) were utilized for most of the test program, but limited tests were conducted with a barbed type discharge electrode similar to Figure 7.

The flue gas to operate the ESP is obtained from Colorado Public Service Company's Arapahoe Unit 4. Unit 4 is a Babcock & Wilcox down-fired, pulverized coal boiler rated at one million pounds of steam per hour. The fuel consists of a variety of western subbituminous coals from the Rocky Mountain region.

TEST PROGRAM

The test program was designed to provide information on the operation of IE for a variety of ESP operating conditions. The electrical characteristics of the ESP appear to be the dominant force in determining the effect of IE. A number of different electrical conditions were experienced over the life of the project due to changes in the coal supply. A summary of the conditions tested are as follows:

Electrode Type	Electrical Conditions
Round Wire	Good Electrical Conditions
	Slightly degraded but without severe back corona
	Degraded with Severe Back Corona
Barbed	Good Electrical Conditions
	Low Current Density, Spark-Limited Operation

Because of the unpredictability of the coal supply, identical conditions were not obtained for both of the two electrode types. Enough overlap did occur that comparisons can be developed.

The test program was designed to approach the evaluation of IE in two steps. First, parametric tests were performed to determine the operating characteristics of IE for many operating conditions. Secondly, comprehensive tests were conducted to quantify the ESP performance and power consumption for optimized operation. These two test series will be discussed separately in the results section.

POWER CONSUMPTION MEASUREMENTS

The measurement of T-R primary power consumption was of principal interest in this study. Although the techniques for accurately determining the particle collection performance of an ESP have been thoroughly documented, insuring the accurate measurement of T-R primary power during IE required a significant effort. The use of phase control during normal operation can produce AC waveforms which are difficult to measure due to their non-sinusoidal nature and added harmonics. Addition of high waveform crest factors, associated with the discontinuous IE waveform, to the phase control distortions already present compounds the difficulty of the measurement. A separate paper discussing the steps taken to insure accurate measurement of the T-R primary power consumption is presented at this symposium (4). For the purposes of this discussion, it is sufficient to state that electronic, integrating watt-hour meters were used for the measurement of IE power savings.

RESULTS

OPACITY VS POWER CONSUMPTION

The principal data collected during the parametric tests consisted of the measurement of T-R power consumption and outlet opacity at various IE ratios. Opacity at the outlet of the Arapahoe pilot ESP has consistently proven to be proportional to particulate emissions. Opacity measurements give a real-time output of changes in ESP performance allowing much faster optimization of operation.

Optimum IE Ratio for Different ESP Fields

The data discussed in the following sections were taken with all three ESP fields operating at the same IE ratio. On this ESP, no apparent advantage was achieved by using different IE ratios in the various fields. However, on ESPs with high SCA and a large number of electrical fields in the direction of gas flow, it may be useful to vary the IE ratio to optimize performance. It would seem that the best results might be obtained with the most current input (highest IE ratio) in the inlet fields followed by smaller IE ratios toward the outlet fields. A somewhat higher IE ratio might be useful in the outlet field to reduce particle loss due to rapping reintrainment.

Number of Energized Half-Cycles

The performance of the pilot unit was evaluated for IE ratios utilizing one, two, and four energized half-cycles. Figure 8 shows the effect of the various IE combinations on power consumption and opacity with round wires installed in the ESP. Operation with 1/x and 2/x produced approximately the same effect while the 4/x ratios consistently resulted in poorer performance. The same type of data taken with barbed electrodes is displayed in Figure 9. With these electrodes the 1/x ratios produced the best ESP performance, 2/x was second, and 4/x caused opacity increases in all tests. In spite of the slight apparent advantage to using 1/x operation, 2/x was given preferential consideration during testing because of the availability of commercial systems. The 4/x mode of operation will not be discussed further since it produced significantly poorer performance in all tests.

Elevated Background Output

Some vendors have advocated the use of elevated background levels during IE operation. That is, rather than turning the SCRs completely off during the de-energized periods, the output level is simply reduced to a low value. There would be some output from the T-R set during all half-cycles with output periodically increased to the spark point. When tests were conducted in this manner on the pilot unit, the performance of the ESP was no better than when the SCRs were completely turned off. However, T-R power consumption was higher for the elevated background tests. All test data discussed subsequently were taken with the SCRs turned completely off during the de-energized periods.

Good and Slightly Degraded Electrical Conditions with Round Wires

During a large part of the project, the electrical resistivity of the fly ash was in the range of 2-6E11 ohm-cm. The ESP electrical conditions varied from good to what could be considered slightly degraded. Although little difference in the performance of IE could be consistently measured between the good and slightly degraded conditions, general trends were observed. Therefore, even though the distinctions are not clear enough to justify separate groups of data, they will be discussed separately for better illustration. Figure 10 contains the data measured during this period using the round discharge electrodes.

Figure 11 shows ESP voltage-current (V-I) curves which indicate good electrical operation of the ESP. The spark-limit operating points for both normal and 2/10 IE operation are also indicated on the figure. There is no evidence of back corona and the maximum current density is very high. This indicates that the performance of the ESP should not be limited by its electrical operating conditions. During this period, the performance of the ESP either was unchanged or tended to degrade slightly as power consumption was reduced with IE. These data tended to populate the top half of the data band in Figure 10. In the worst case, the opacity was increased by a factor of 1.10 at a power saving of 50%. In an ESP installation which is not bordering on compliance violations, such a slight increase in opacity is not likely to be noticed.

Figures 12 and 13 indicate V-I curves which could be considered slightly degraded. Figure 12 is very difficult to distinguish from the good electrical conditions discussed previously (Figure 11). However, when carefully compared, the slope of both the middle and outlet field V-I curves of Figure 12 is much steeper at high current density. This may indicate that some back corona is starting to develop in these fields, thus degrading the performance of the ESP slightly and wasting some power. The V-I curves in Figure 13 are considerably reduced in maximum current density and show slight evidence of back corona, mainly evident in the middle field. During the periods when these slightly degraded electrical conditions were observed, IE tended to either produce no change in ESP performance or to improve it slightly with a 50% reduction in power consumption. The best results for this condition indicated that IE reduced opacity by a factor of 0.96 at a power reduction of 50%.

Good Electrical Conditions with Barbed Electrodes

With the barbed discharge electrodes installed in the ESP only one set of electrical conditions corresponded to the round wire data. Figure 14 indicates the V-I curves which indicated good electrical conditions in the ESP. As would be expected of this type electrode, the operating voltages are from 4 to 8 kV lower than that measured at the same current density with the round wires.

The effect of IE under these conditions is demonstrated by Figure 15. The data seem to indicate that the barbed electrodes respond more favorably to IE than do the round wires with good electrical conditions in the ESP. For a 50% power savings, the opacity values ranged from 0.83 to 1.03 times the normal opacity. The barbed discharge electrode data were taken over a very short period of time at the end of the project; our confidence is not as high as for the round wire data. Whether barbed electrodes would show a long term advantage is uncertain.

Degraded Conditions with Severe Back Corona - Round Wires

For a short period of time during the project a change in the ash characteristics produced ESP electrical operating conditions indicative of severe back corona. The measured values of ash resistivity increased for several days into the 1-3E12 ohm-cm range before dropping back into the 2-6E11 ohm-cm region. During the time that most of the tests were conducted, the resistivity was the same as for the slightly degraded test condition. However, the high resistivity ash collected in the ESP continued to affect performance for several weeks. This is an example of ESP performance being dominated by the history of the ash layer rather than by the coal burned at that time. This type of operational effect has been observed during other projects at Arapahoe.

The V-I curves which are indicative of severe back corona are displayed in Figure 16. Back corona is obvious in the middle and outlet fields from the negative slope of the upper portion of the curves. The "useful" current density of the fields is less than 10 nA/cm . Most of the current above that point is wasted in generating back corona. With this type of operating condition present in the ESP, the effect of IE was as indicated by the lower set of data on Figure 17. The opacity was reduced to 0.40 - 0.60 times the original value with a reduction in power consumption of 60% - 80%.

The extent of the back corona which exists in the ESP appears to produce a dramatic change in the performance of IE. ESPs which regularly operate with indications of severe back corona would appear to enjoy significant improvements in performance and larger power savings than ESPs which do not show those characteristics. However, while some ESPs may continually operate in one or the other of these modes, the changes in the Arapahoe unit from one to the other indicate that caution should be used in estimating performance improvements based on currently existing electrical conditions.

Low Current Operation With Barbed Electrodes

Another increase in the ash resistivity into the range of 1-3E12 ohm-cm caused the ESP to operate spark-limited with very low current density in all fields. Barbed electrodes were in use at that time. Figure 18 shows the V-I curves measured during that period. No evidence for severe, power consuming back corona is obvious in the shape of the curves. The performance of IE is indicated in Figure 19. With this type of operation, all of the tests indicated some degradation in opacity at a 50% power reduction with the worst run increasing opacity by a factor of 1.25.

Even though the target of 50% power savings was not possible with no degradation in ESP performance, un-degraded operation is still possible in this case with a smaller power savings. An insignificant degradation in performance was observed for a power savings of 30%.

Reducing Power Consumption by Other Means

Energy management systems attempt to save T-R power consumption by means other than IE. Typically the power input to the ESP T-R sets is reduced until a preset maximum opacity is reached. The power input is reduced by the normal SCR phase control. In order to compare the two systems on the same basis, the manual T-R set controls were used to adjust the power consumption during normal operation to the same values obtained at the various IE ratios. An example of the result is shown in Figure 20. In all cases IE produced better ESP performance than phase control for a given power savings. The data from 7/18/85 are with round wire electrodes while the 12/4/85 results were measured with barbed electrodes.

ESP PERFORMANCE AND POWER CONSUMPTION

The performance of the ESP was more thoroughly quantified for three major conditions. The conditions tested were as follows:

1. Round Discharge Electrodes without Severe Back Corona
2. Barbed Discharge Electrodes without Severe Back Corona
3. Round Discharge Electrodes with Severe Back Corona

The operation of the IE system was adjusted using the data from the parametric tests. The goal in choosing IE ratios was to operate with a power savings of 50% without any degradation in ESP performance. Although a larger power savings might be possible without degradation, 50% was felt to be conservative. IE ratios of 1/9 and 2/10 appeared to satisfy this general requirement for the conditions tested.

The mass collection efficiency and power consumption data are shown in Table 1. Table 2 indicates the change in ESP penetration and power consumption and the omega-k enhancement calculated from the data of Table 1. Omega-k is the effective migration velocity as defined by the Matts-Ohnfeldt equation with $k = 0.5$. This performance indicator is a more effective means of comparing ESP performance because it is relatively insensitive to changes in SCA. The omega-k enhancement is the ratio of the omega-k with IE or pulsing to the omega-k for normal operation. An omega-k enhancement of 1.0 indicates no change in ESP performance while a number greater than 1.0 means performance has improved. The data are discussed in the following two sections.

Without Severe Back Corona

The data indicate that without severe back corona present in the ESP, IE maintained constant ESP performance and reduced T-R power consumption by approximately 50%. The response of the round and barbed electrodes to 2/10 IE was not significantly different. The slightly larger reduction in power consumption measured with 1/9 is not considered significant. Operation with 2/14 would have saved more power and probably not changed performance.

The pulser system did produce an enhancement in performance under these operating conditions. With the round electrodes, the pulser produced an omega-k enhancement of 1.75 which is consistent with previous performance of the system (3). The pulser also improved the performance with the barbed electrodes although the omega-k enhancement was only 1.21. The reason for the poorer performance is undetermined. The power consumption of the pulser system was not measured during these tests. The research pulser was not designed to be conservative of power but to generate several different types of pulses. A power comparison between this type of uncommercial pulser system and IE is therefore not meaningful. We would expect that a pulser system would consume more power than IE to produce the measured improvements in performance.

With Severe Back Corona

The IE system reduced particle penetration of the ESP by almost half when operating with severe back corona. Omega-k was enhanced by a ratio of 1.25 while the power savings exceeded 60%. Again there was no significant difference between the round and barbed electrodes.

The pulser system reduced ESP particle penetration more than 70% with severe back corona. This corresponds to an omega-k enhancement of 1.42 which is almost twice as high as the improvement due to IE. As stated above, it is likely that this improvement in performance would require an increase in power consumption.

SUMMARY OF PILOT-SCALE STUDY

- Intermittent energization was consistently capable of reducing T-R power consumption by 50% or more.
- The effect of intermittent energization on ESP collection performance was dependent on the electrical operating conditions measured in the ESP. The relationship was as follows:
    1. When severe back corona was obvious in the V-I curves, particle penetration of the ESP was reduced more than 40% and T-R power consumption was reduced by more than 60%.
    2. With good electrical operating conditions in the ESP, the particle penetration was largely unaffected while a power savings of approximately 50% was achieved.
    3. With very low current density operation, opacity was increased by from 1.10 to 1.25 times the normal opacity at a power reduction of 50%. A 30% power savings could be achieved with no loss of ESP performance.
- Intermittent energization produced better ESP performance than manually reducing T-R set power input to obtain a comparable power savings.
- The performance of intermittent energization was not significantly affected by the two styles of discharge electrodes studied.
- Power meters are desirable for accurate measurement of the power savings effected by intermittent energization.
- The EPRI/SoRI pulser system improved the collection efficiency of the ESP more than intermittent energization in all comparative tests. The pulser would likely increase power consumption at the level of performance tested.

REFERENCES

1. Masuda, S. Mitsubishi Intermittent Energization System for Electrostatic Precipitator. EPA Contract 68-02-3686. Report 82.01. January 8, 1983
2. Ando, T., N. Tachibana, and Y. Matsumoto. A New Energization Method for Electrostatic Precipitators - Mitsubishi Intermittent Energization System. EPA Fourth Symposium on the Transfer and Utilization of Particulate Control Technology. Houston, TX. October, 1982.
3. Landham, E. C., J. L. DuBard, W. Piulle, and L. E. Sparks. Precipitator Performance Enhancement with Pulsed Energization. EPA/EPRI Fifth Symposium on the Transfer and Utilization of Particulate Control Technology. Kansas City, MO. August, 1984.
4. Gelfand, P., E. C. Landham, and L. Rettenmaier. Electrostatic Precipitator Power Measurements. EPA/EPRI Sixth Symposium on the Transfer and Utilization of Particulate Control Technology. New Orleans, LA. February, 1986.

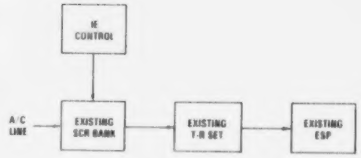

Figure 1. Block diagram of IE System.

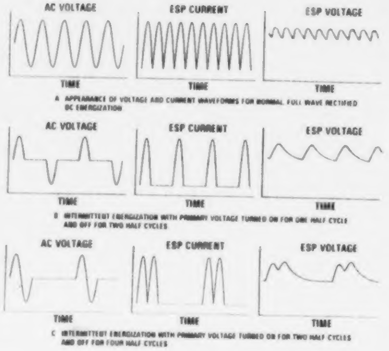
AC VOLTAGE
ESP CURRENT
ESP VOLTAGE
TIME
TIME
TIME
A APPEARANCE OF VOLTAGE AND CURRENT WAVEFORMS FOR NORMAL, FULL WAVE RECTIFIED DC ENERGIZATION
AC VOLTAGE
ESP CURRENT
ESP VOLTAGE
TIME
TIME
TIME
B INTERMITTENT ENERGIZATION WITH PRIMARY VOLTAGE TURNED ON FOR ONE HALF CYCLE AND OFF FOR TWO HALF CYCLES
AC VOLTAGE
ESP CURRENT
ESP VOLTAGE
TIME
TIME
TIME
C INTERMITTENT ENERGIZATION WITH PRIMARY VOLTAGE TURNED ON FOR TWO HALF CYCLES AND OFF FOR FOUR HALF CYCLES

Figure 2. Examples of IE waveforms.

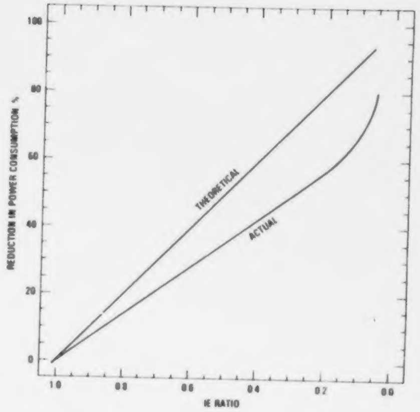

Figure 3. T-R power consumption as a function of IE cycle ratio.

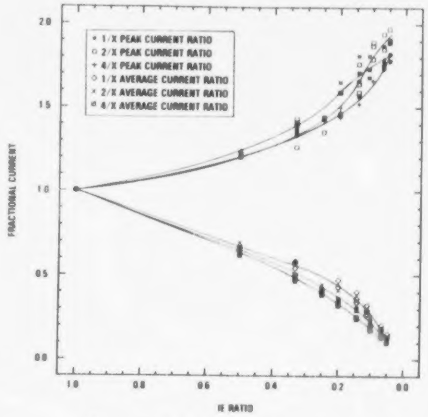

Figure 4. Peak and average current as a function of IE ratio.

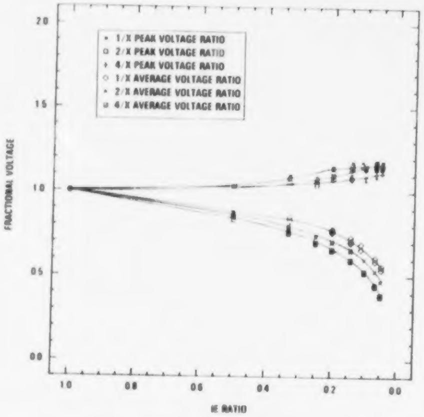

Figure 5. Peak and average voltage as a function of IE ratio.

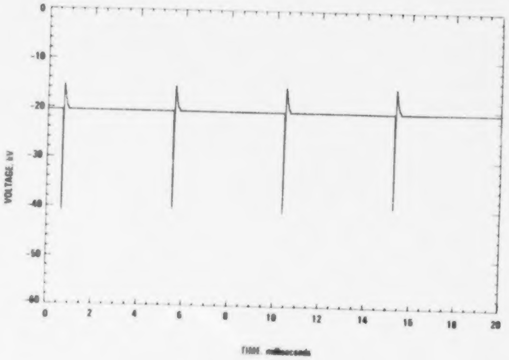

Figure 6. Fast pulse from EPRI/SoRI pulser system.

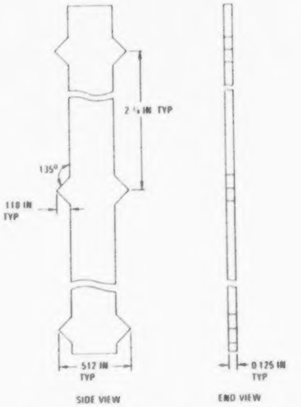

Figure 7. Barbed discharge electrode style tested.

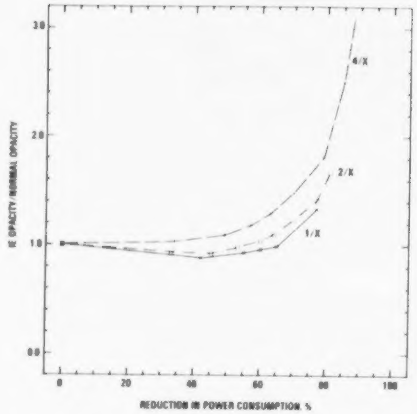

Figure 8. Effect of number of half-cycles energized on IE performance with round electrodes.

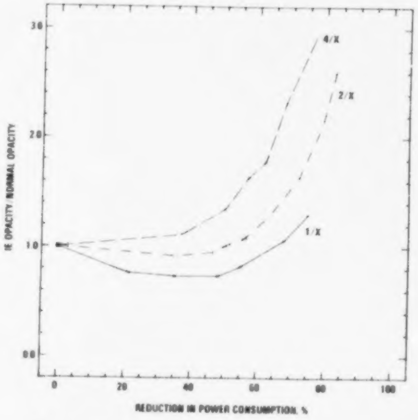

Figure 9. Effect of number of half-cycles energized on IE performance with barbed electrodes.

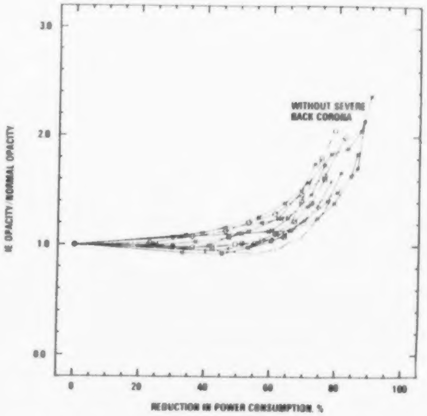

Figure 10. Effect of IE on T-R power consumption and ESP outlet opacity.

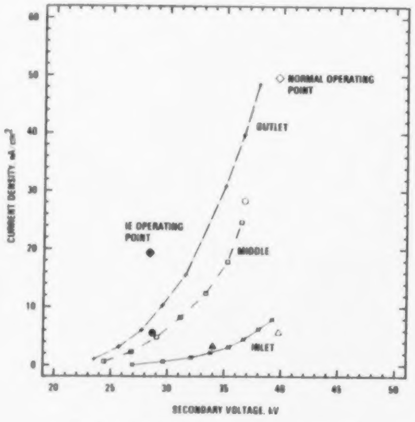

Figure 11. ESP voltage-current curves indicating good electrical conditions.

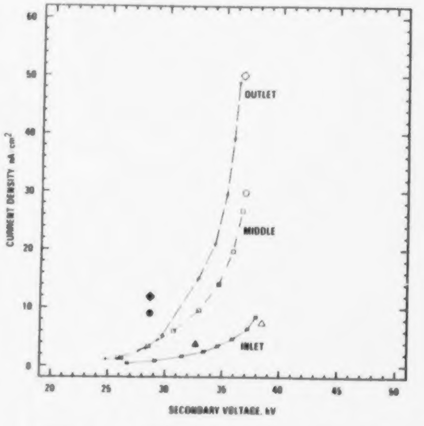

Figure 12. ESP voltage-current curves indicating slight degradation of electrical conditions.

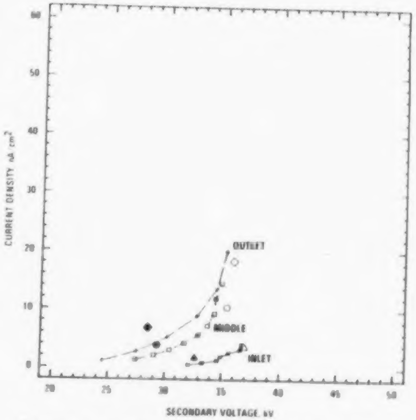

Figure 13. ESP voltage-current curves indicating slight degradation of electrical conditions.

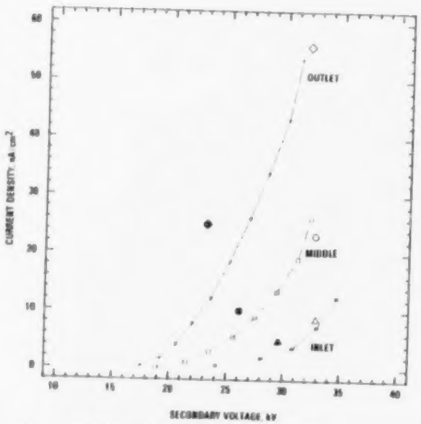

Figure 14. ESP voltage-current curves indicating good electrical conditions with barbed electrodes.

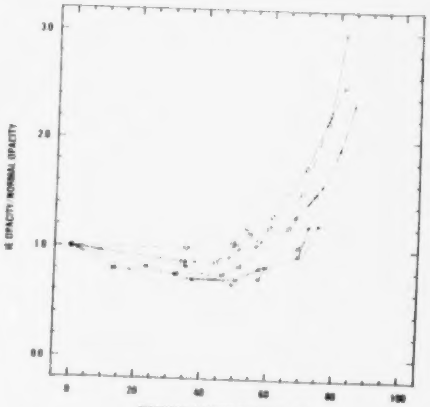

Figure 15. Effect of IE on T-R power consumption and outlet opacity with good electrical conditions and barbed electrodes.

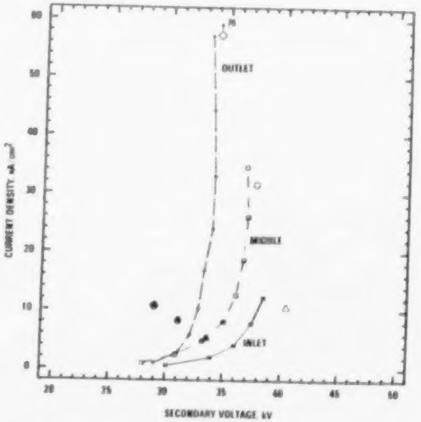

Figure 16. ESP voltage-current curves indicating severe back corona.

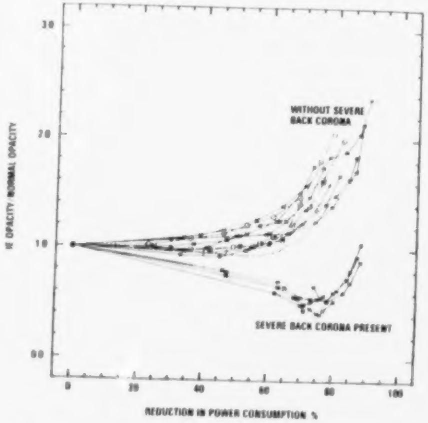

Figure 17. Effect of IE on T-R power consumption and ESP outlet opacity - round electrodes.

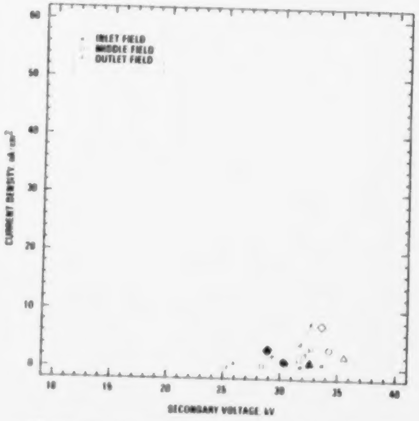

Figure 18. ESP voltage-current curves during very low current-density operation.

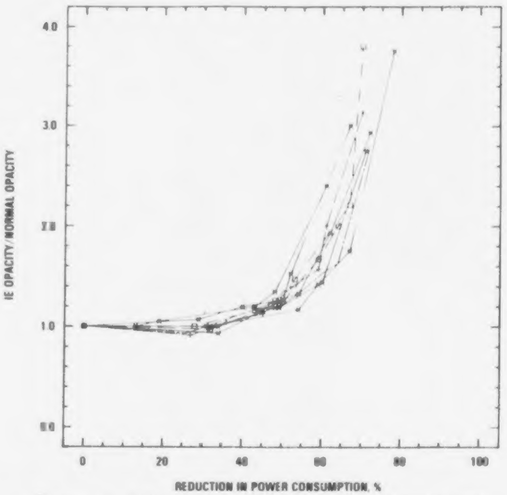

Figure 19. Effect of IE with low current density and barbed electrodes.

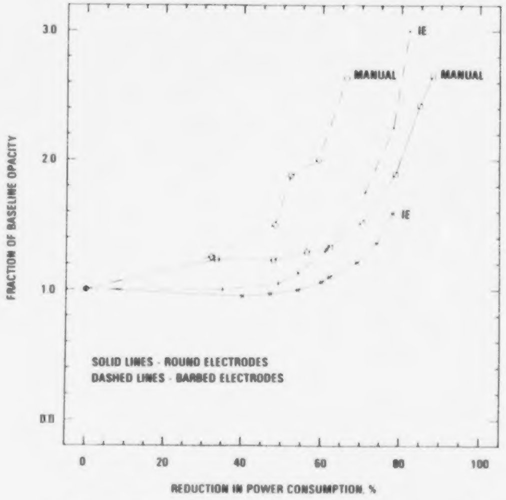

Figure 20. Comparison between IE and manual reduction of T-R power consumption.

Table 1.

ESP MASS PERFORMANCE AND POWER CONSUMPTION

TEST CONDITION	DISCHARGE ELECTRODE STYLE	ESP EFFICIENCY, %	EMISSION RATE, lb/10^6 Btu	SCA, ft^2/kacfm	PRIMARY POWER, Watts
		WITHOUT SEVERE BACK CORONA			
Normal	Round	98.90	0.055	255	710
1/9 IE	"	98.91	0.050	250	338
Normal	"	99.66	0.020	361	822
2/10 IE	"	99.64	0.021	360	449
Normal	"	99.68	0.021	408	695
Pulsed	"	99.95	0.005	402	—
Normal	Barbed	99.53	0.031	341	1370
2/10 IE	"	99.59	0.029	342	723
Normal	"	99.59	0.026	331	1350
Pulsed	"	99.77	0.013	332	—
		WITH SEVERE BACK CORONA			
Normal	Round	99.37	0.034	348	1510
1/9 IE	"	99.65	0.019	348	543
Normal	"	99.39	0.039	350	1570
2/10 IE	"	99.65	0.022	347	533
Normal	"	99.42	0.035	352	1190
Pulsed	"	99.83	0.010	353	—

Table 2.

EFFECT OF IE AND PULSED OPERATION ON ESP PERFORMANCE AND PRIMARY POWER CONSUMPTION

DISCHARGE ELECTRODE STYLE	TEST CONDITION	PENETRATION REDUCTION, %	OMEGA-K ENHANCEMENT	POWER REDUCTION, %
		WITHOUT SEVERE BACK CORONA		
Round	1/9 IE	1.0	1.02	52
"	2/10 IE	–6.9	1.01	45
"	Pulsed	98.4	1.75	—
Barbed	2/10 IE	12.8	1.04	47
"	Pulsed	43.9	1.21	—
		WITH SEVERE BACK CORONA		
Round	1/9 IE	44.0	1.26	64
"	2/10 IE	42.6	1.24	66
"	Pulsed	70.7	1.42	—

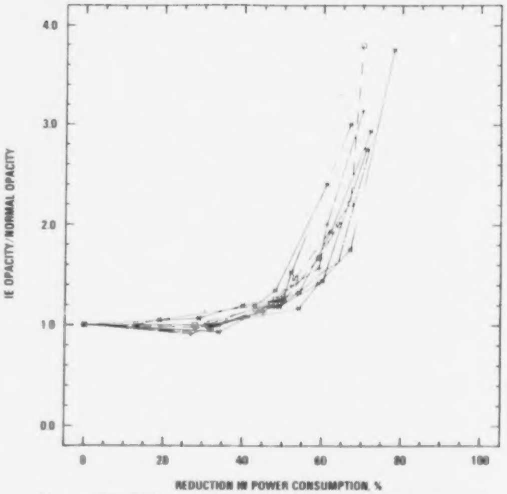

Figure 19. Effect of IE with low current density and barbed electrodes.

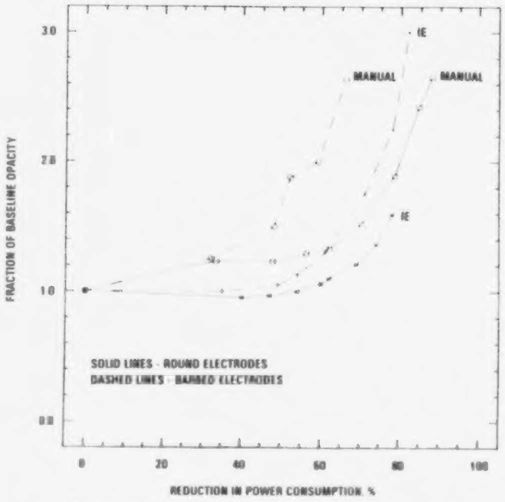

Figure 20. Comparison between IE and manual reduction of T-R power consumption.

Table 1.

ESP MASS PERFORMANCE AND POWER CONSUMPTION

TEST CONDITION	DISCHARGE ELECTRODE STYLE	ESP EFFICIENCY %	EMISSION RATE $lb/10^6$ Btu	SCA ft^2/kacfm	PRIMARY POWER Watts
		WITHOUT SEVERE BACK CORONA			
Normal	Round	98.90	0.056	255	710
1/9 IE	"	98.91	0.050	250	338
Normal	"	99.66	0.020	361	822
2/10 IE	"	99.64	0.021	360	449
Normal	"	99.68	0.021	408	695
Pulsed	"	99.96	0.005	402	—
Normal	Barbed	99.53	0.031	341	1370
2/10 IE	"	99.59	0.029	342	723
Normal	"	99.59	0.026	331	1350
Pulsed	"	99.77	0.013	332	—
		WITH SEVERE BACK CORONA			
Normal	Round	99.37	0.034	348	1510
1/9 IE	"	99.65	0.019	348	543
Normal	"	99.39	0.039	350	1570
2/10 IE	"	99.65	0.022	347	533
Normal	"	99.42	0.036	352	1190
Pulsed	"	99.83	0.010	353	—

Table 2.

EFFECT OF IE AND PULSED OPERATION ON ESP PERFORMANCE AND PRIMARY POWER CONSUMPTION

DISCHARGE ELECTRODE STYLE	TEST CONDITION	PENETRATION REDUCTION, %	OMEGA-K ENHANCEMENT	POWER REDUCTION, %
		WITHOUT SEVERE BACK CORONA		
Round	1/9 IE	1.0	1.02	52
"	2/10 IE	-5.9	1.01	45
"	Pulsed	88.4	1.75	—
Barbed	2/10 IE	12.8	1.04	47
"	Pulsed	43.9	1.21	—
		WITH SEVERE BACK CORONA		
Round	1/9 IE	44.0	1.26	64
"	2/10 IE	42.6	1.24	66
"	Pulsed	70.7	1.42	—

OPERATING RESULTS OF MOVING ELECTRODE TYPE ELECTROSTATIC PRECIPITATORS FOR COAL-FIRED BOILERS

by : H. Asano, H. Yabuta, M. Ohtsuka
Hitachi Plant Engineering & Construction Co., Ltd.
Tokyo, Japan 170

ABSTRACT

The moving electrode type electrostatic precipitators (ESPs) which show the great effect in precipitation of high electrical resistivity dust or fine dust, have been applied for ten coal-fired boilers. To comply with the specific requirements of the customers, that is, an optimum ESP effective for flyash having high electrical resistivity in a range of 10^{10} to 10^{14} ohm-cm produced by burning overseas coal, the moving electrode type ESP has a chance for showing its superior properties. The first moving electrode type ESP for coal-fired boiler was installed at Tokuyama Soda Industry Co., Ltd. in 1981, and has been operating for four and a half years. Thereafter, the moving electrode type ESP was applied to Mizushima Power Station of Chugoku Electric Power Co., Inc. as a first ESP for the utility boiler in 1984, and proves its reliability and high performance.

1. INTRODUCTION

It is well known that the electrical resistivity of the flyash produced by burning the low sulfur coal is high and makes the collecting performance decrease by the back ionization phenomena due to the dust accumulated on the collecting electrode. The hammering device used in the conventional fixed electrdode type ESP cannot adequately dislodge the dust from the collecting electrodes. Therefore, it is very difficult to prevent the back ionization phenomena.

The problem caused by the back ionization was solved by means of the moving electrode type ESP. The point of the solution is to adopt brushing as a method of dislodging dust substantially on the collecting electrode. As the results , the moving electrode type ESP continuously keeps high collecting performance for the high electrical resistivity dust. Because, as shown in Figure 1, the migration velocity of dust in the moving electrode type ESP is higher than in case of the fixed electrode type ESP so that it is possible to design the moving electrode type ESP's collecting area smaller than the fixed electrode type ESP's. This tendency is remarkable as the higher electrical resistivity dust.

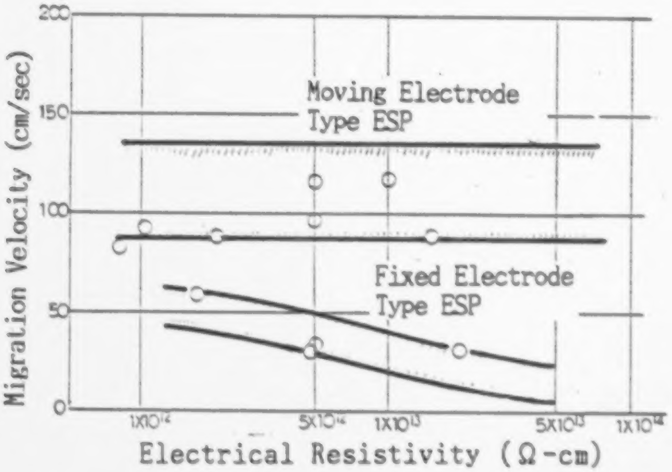

Figure 1. Relation between Electrical Resistivity and Migration Velocity of Dust

2.STRUCTURE OF THE MOVING ELECTRODE TYPE ESP

The moving electrode type ESP has two features as shown in Figure 2. One is that the collecting electrode plates are continuously moving and another is that the dust on the collecting electrodes is dislodged completely by the rotating brush instead of hammer. The collecting electrode is divided into dozens of plates and each plate is connected with the endless link-chains. The link-chains are driven slowly at adequate speed by means of the driving wheel.

The dust adhered to collecting electrodes are dislodged into the hopper by means of the rotating brush which is located at the noncollection zone in hopper without reentrainment. As the result of application of brushing, the moving electrode type ESP keeps the surface of collecting electrode so clean that the back ionization phenomena is completely suppressed, therfore, the collection efficiency is kept high.

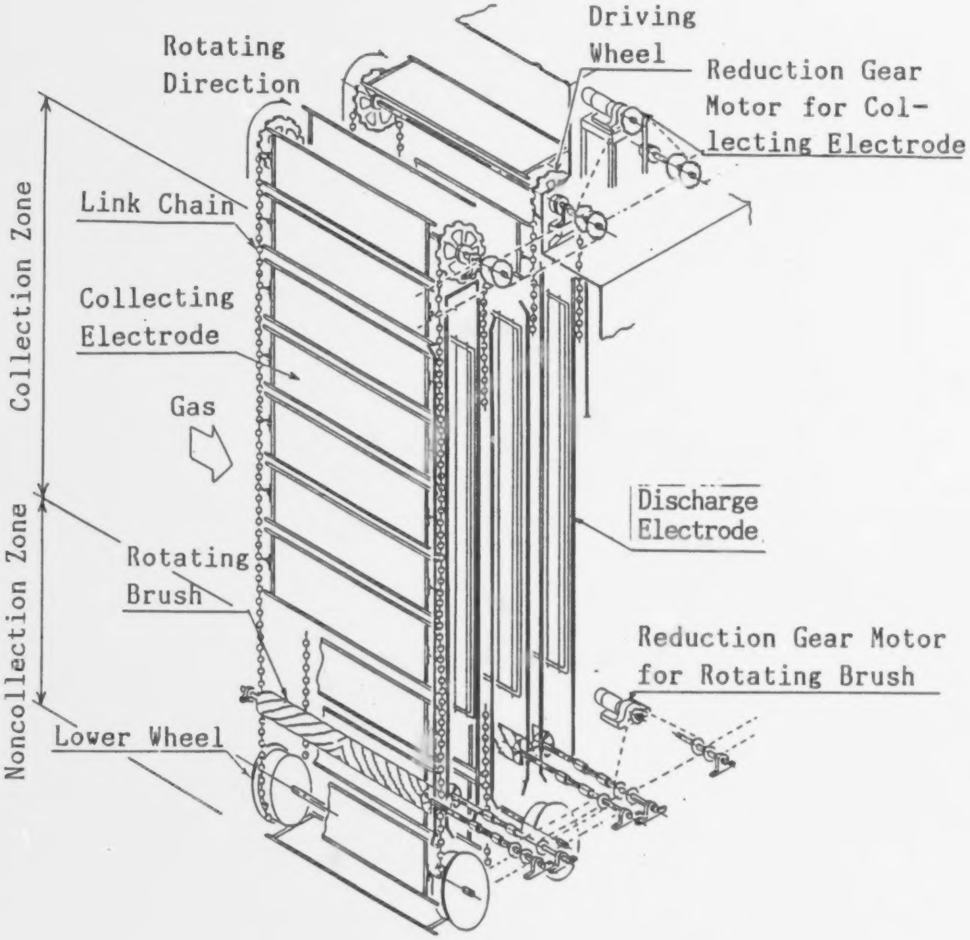

Figure 2. Structure of the Moving Electrode Type ESP

In case that the ESP's inlet dust concentration is high and the particle size is comparatively coarse like the flyash produced from the coal-fired boilers, the most suitable method is to adopt the combined ESP of the fixed electrode type ESP in the inlet zone and the moving electrode type ESP in the outlet zone as shown in Figure 3. Because the dust particle size at inlet zone is enough coarse to be easily dislodged by the hammering device ,but the dust particle size at outlet zone is so fine that it is difficult to dislodge sufficiently by means of the hammering device.

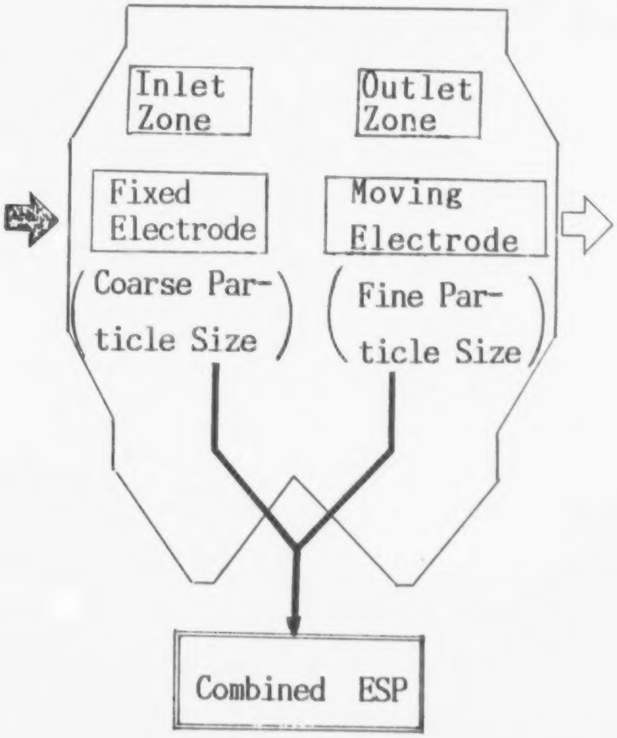

Figure 3. Combined ESP for Coal-Fired Boiler

3.ESTABLISHMENT OF RELIABILITY OF THE MOVING COMPONENT PARTS

Establishment of reliability of the moving component parts is the most important factor to evaluate general reliability including stable operation and prevention of wear. The considerations on designing to keep the reliability of the moving electrode type ESP are shown in Table 1.

TABLE 1. CONSIDERATION ON DESIGNING FOR CONFIRMATION OF RELIABILITY

Condition	Component Part	Item
Stable Movement	Collecting Electrode	Speed Limitation (1m/min. or less)
		Prevention of Swing (Attachment of Guide)
		Smooth Insertion to Brushes (Attachment of Guide)
	Link-Chain	Strength
		Matching with Driving Wheel(Test in Factory)
	Brush	Lower Speed
		Elasticity
		Unification of Torque(Spiral set Brush Wire)
		Smooth Reception of Collecting Electrode (Spiral Set Brush Wire)
Prevention of Wear	Driving Wheel	Lower Speed
		Hardness (Quenching)
	Link-Chain	Hardness (Quenching)
	Bearing for Driving Device of Collecting Electrode	Prevention of Wear by Dust (Positioned at outside of ESP's Casing)
	Bearing for Driving Device of Brush	Prevention of Wear by Dust (Coverd by Box)
	Brush	Lower Speed
		Ajustment of Distance between each Brush (Once Time for 2 years)

4.OPERATING RESULTS OF THE MOVING ELECTRODE TYPE ESPS FOR COAL-FIRED BOILERS

We have applied ten moving electrode type ESPs for coal-fired boilers. Among of them, we herein describe the operating results of the moving electrode type ESPs for coal-fired boilers of Chugoku Electric Power Co., Inc., Tokuyama Soda Industry Co., Ltd. and Teijin Ltd.. As an example of process flow diagram of boiler plant, we show the process flow diagram of Chugoku Elecric Power Co., Inc. in Figure 4. Although various kinds of coals such as American, Australian and South African coals were burned by these boilers, the collection efficiency of any case is higher than the design value as shown in Table 2. Especially, Tokuyama Soda Industry Co., Ltd. has been operated satisfactory with good use of the features of moving electrode type ESPs such as to be able to collect the high electrical resistivity dust even though its boiler is burning many kinds of coals practically.

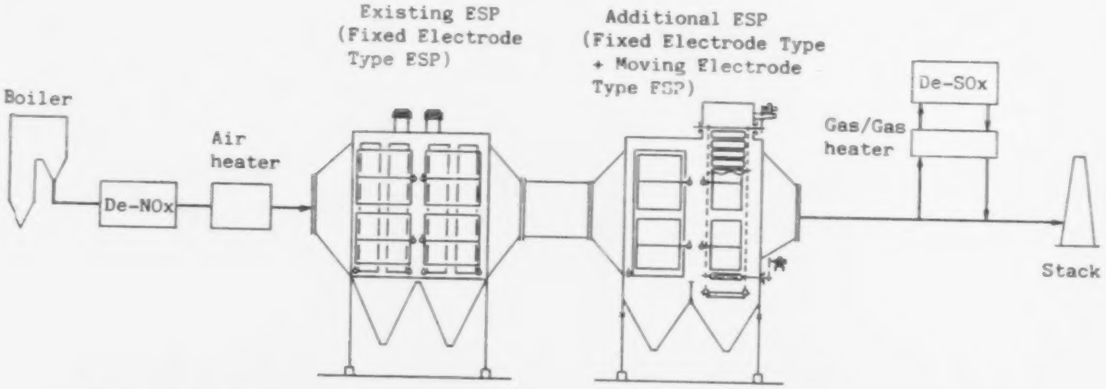
Boiler
De-NOx
Air heater
Existing ESP (Fixed Electrode Type ESP)
Additional ESP (Fixed Electrode Type + Moving Electrode Type ESP)
Gas/Gas heater
De-SOx
Stack

Figure 4. Process Flow Diagram of Chugoku Electric Power Co.,Inc.

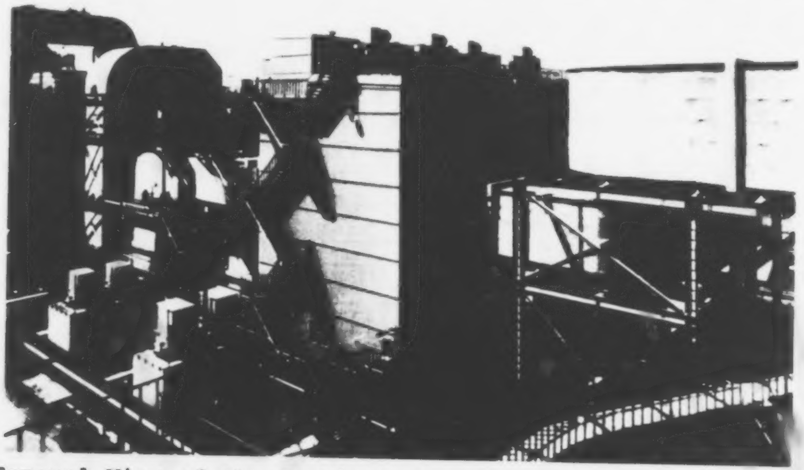

Figure 5. General View of the Combined ESP for Chugoku Electric Power Co.,Inc.

TABLE 2. PERFORMANCE TEST RESULTS

1	Client	Chugoku Electric Power Co.,Inc. Mizushima Power Station (№2 Unit)		Tokuyama Soda Industry Co., Ltd. (№5 Unit)		Teijin Ltd. Matsuyama Works (№1 Unit)	
2		Design	Actual	Design	Actual	Design	Actual
	Gas Flow (m^3N/H)	600,000	529,000	209,000	193,000	101,500	101,100
	Gas Temperature (℃)	136	132	150	150	180	191
	Collection Efficiency (%)	98.73	99.46	99.75	99.93	99.33	99.8
3	Coal	Ulan(Australia) Wambo(Australia) Coalex(Australia)		Soldier Canyon(U.S.A.) Orchard Valley(U.S.A.) King Coal(U.S.A.) Red Fox(U.S.A.) Plateau(U.S.A.) Siera(U.S.A.) Drumont(U.S.A.) Abadare(Australia) Bayswater(Australia) Ulan(Australia) Goedenhoop(South Africa) Ombilin(Indonesia)		Hunter valley(Australia) Wallarah(Australia)	

These coals were actually burned in each boilers.

Further, as for the change of collection efficiency with the lapse of time as shown in Figure 6, all ESPs maintain stable performance for a long time.

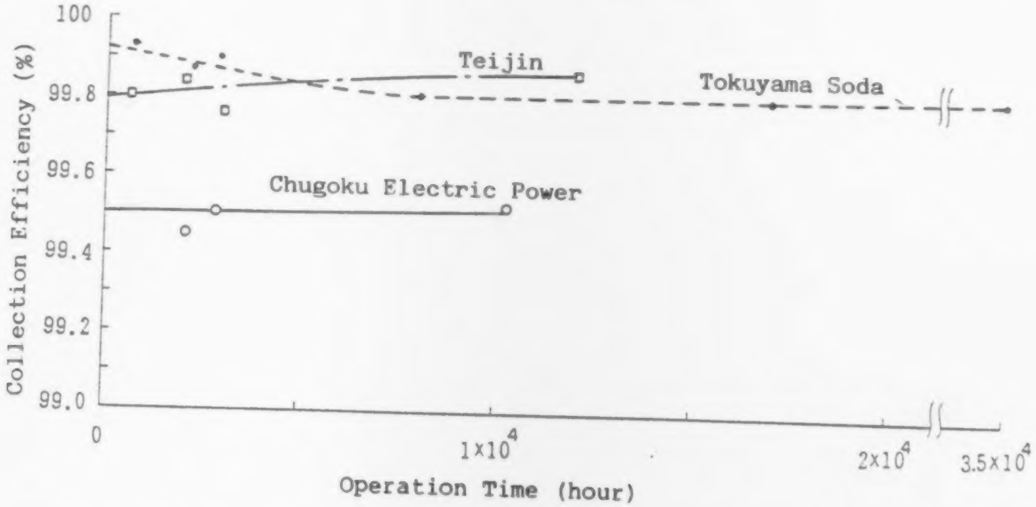

Figure 6. The Change with the Lapse of Time of Collection Efficiency

The wear states of each parts after the operation of the ESPs are as follows;

(1) Driving wheel and collecting electrode plate

As the results of application of low speed driving and suitable selection of materials, the wear of driving wheel and collecting electrode plate was so minor as not to be able to measure.

TABLE 3. WEAR OF DRIVING WHEEL AND COLLECTING ELECTRODE PLATE

(mm)

Item	Chugoku Electric Power Co.,Inc. (after 9.2×10^3 hours operation)	Tokuyama Soda Industry Co., Ltd. (after 3.5×10^4 hours operation)	Teijin Ltd. (after 1.9×10^4 hours operation)
Driving wheel	0.3>	0.3>	0.3>
Collecting Elec--trode Plate	0.3>	0.3>	0.3>

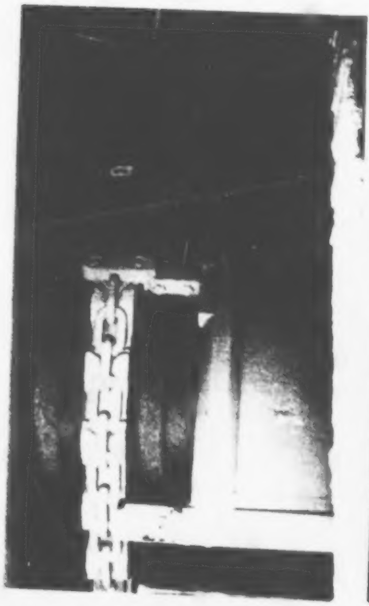
Figure 7. Chugoku Electric Power's Driving Wheel

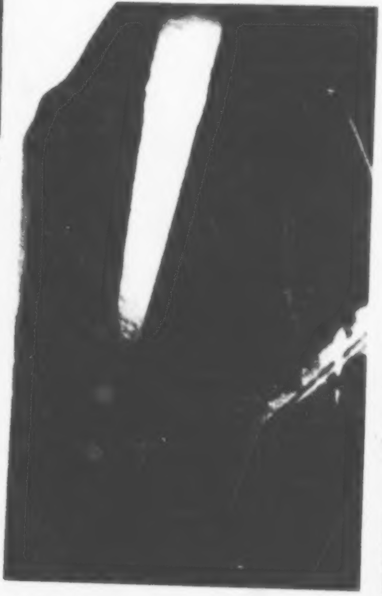
Figure 8. Tokuyama Soda's Driving Wheel

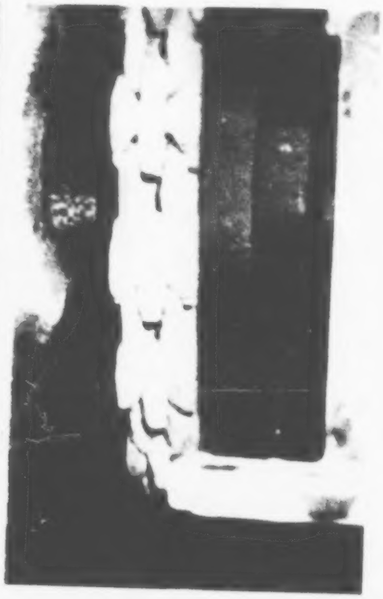
Figure 9. Teijin's Driving Wheel

Reproduced from best available copy.

(2) Link-chain

The wear of link-chain increased little by little after occurrence of initial wear.

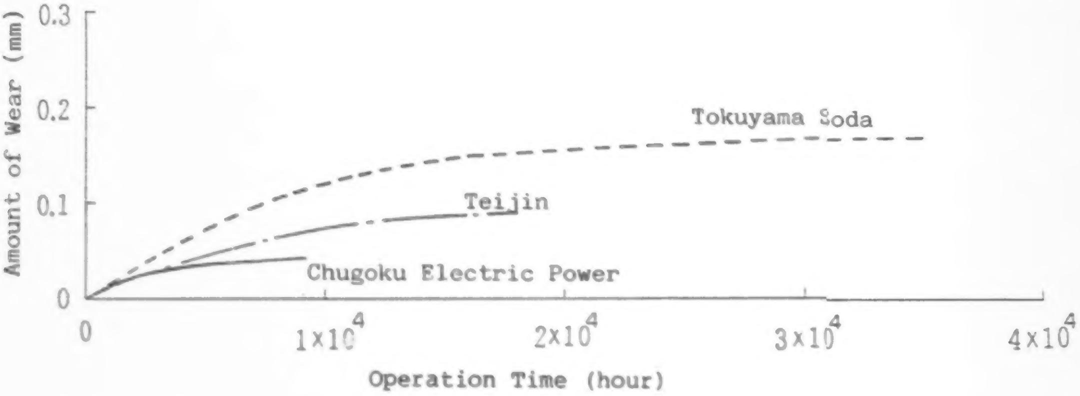

Figure 10. The Change with the Lapse of Time of Link-Chain's Wear

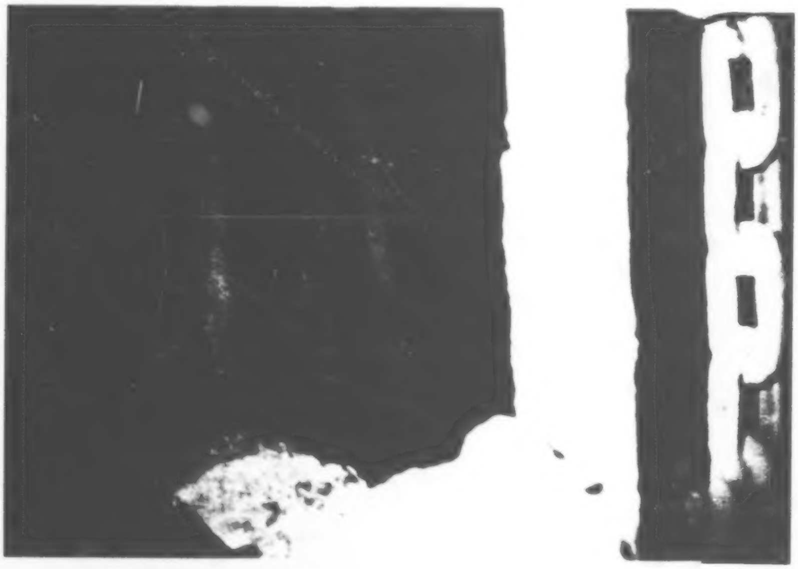

Figure 11. Chugoku Electric Power's Link-Chain after $9.2x10^3$ hours Operation

(3) Bearings

Ball bearings, which are positioned at outside of ESP's steel casing, are used for supporting the driving devices of collecting electorode. Then the wear by dust was not able to find out on any ball bearings.

But, in case of the combined ESP, oilless bearings for driving devices of brush are settled in inside of ESP.
Chugoku Electric Power's oilless bearings, as shown in Figure 13, were covered to prevent the wear by dust.

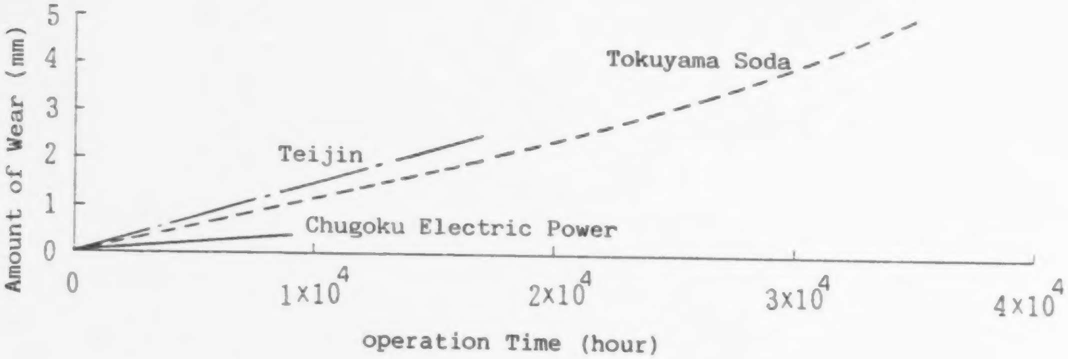

Figure 12. The Change with the Lapse of Time of Oilless Bearing's Wear

Figure 13. Chugoku Electric Power's Oilless Bearing

(4) Brush

The wear of brushes increased little by little after occurrence of initial wear as well as link-chain.

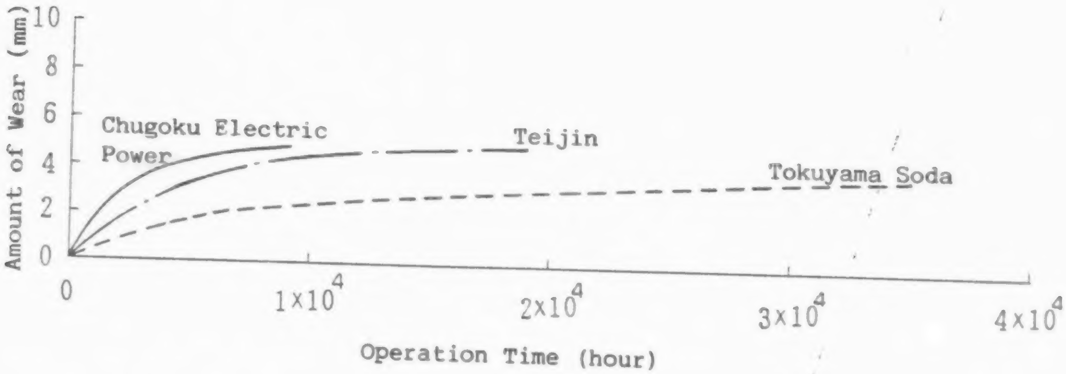

Figure 14. The Change with the Lapse of Time of Brush's Wear

Figure 15. Chugoku Electric-Power's Brush after 9.2×10^3 hours Operation

Allowable value, actual results and possible operating life concerning wear of each part are shown in Table 4. These parts have good results which are lower than expected value.

TABLE 4. INSPECTION RESULTS OF WEAR OF THE MOVING ELECTRODE TYPE ESPS

(mm)

Item	Allowable Value	Inspection Result			Possible Operating Life (years)
		Chugoku Electric Power Co.,Inc. (after 9.2×10^4 hours operation)	Tokuyama Soda Industry Co.,Ltd. (after 3.5×10^4 hours operation)	Teijin Ltd. (after 1.9×10^4 hours operation)	
Driving Wheel	3	0.3>	0.3>	0.3>	7
Collecting Electrode Plate	1	0.3>	0.3>	0.3>	7
Link-Chain	0.5	0.045	0.17	0.09	7
Oilless Bearing	5	0.5	5	2.5	2
Rotating Brush	10	5	4	5	4

5.COMPARISON OF SPECIFICATION AND ECONOMICS BETWEEN THE CONVENTIONAL FIXED ELECTRODE TYPE ESP AND THE COMBINED ESP FOR COAL-FIRED BOILER

Comparison of specification and economics between the conventional fixed electrode type ESP and the combind ESP for coal-fired boiler is shown in Table 5. As shown in Table 5, the moving electrode type ESP has the following three merits over the fixed electrode type ESP.

(1) Floor space is smaller.
(2) Power consumption is smaller.
(3) Price is lower.

Therefor, in case of improving collecting performance of existing ESP by retrofiting or adding ESP, the moving electrode type ESP is very effective at the view point of saving floor space and Price.

TABLE 5. COMPARISON OF SPECIFICATION AND ECONOMICS BETWEEN THE FIXED ELECTRODE TYPE ESP AND THE COMBINED ESP FOR COAL-FIRED BOILER

Item	Fixed Electrode Type ESP	Combined ESP
Collecting System	gas → Fixed Electrode Type ESP Fixed Electrode Type ESP Fixed Electrode Type ESP	gas → Fixed Electrode Type ESP Moving Electrode Type ESP
Ratio of SCA (%)	100	50
Ratio of Floor Space (%)	100	49
Ratio of Power Consumption (%)	100	65
Price (%)	100	75

Estimating Condition;

① Inlet Dust Concentration	15g/m^3N
② Outlet Dust Concentration	0.05g/m^3N
③ Collection Efficiency	99.67%
④ Electrical Resistivity of Dust	1×10^{13} ohm-cm

6. SUPPLY LIST OF THE MOVING ELECTRODE TYPE ESP FOR THE HIGH ELECTRICAL RESISTIVITY DUST

Table 6 and 7 show supply lists of the moving electrode type ESPs which maintain high collecting performance against the high electrical resistivity dust. Thus the sufficient reliability on operating has been proved. And now the moving electrode type ESPs show the great effect in regard to high electrical resistivity dust for not only coal-fired boiler plants but also another use without for coal-fired boilers.

TABLE 6. SUPPLY LIST OF THE MOVING ELECTRODE TYPE ESPS FOR COAL-FIRED BOILERS

Client	Application		Gas Flow (m^3N/H)	Gas Temperature (℃)	Collection Efficiency	Completion Year
Tokuyama Soda Industry Co.,Ltd.	220T/H Boiler (NO.5 unit)	Design	209,000	150	99.75	1981
Coal Mining Reserch Center	20T/H Fludized Bed Boiler	Design	24,000	150	80.0	1983
Teijin Ltd.	80T/H Boiler (Matsuyama NO.1unit)	Design	101,500	180	99.33	1983
Chugoku Electric Power Co.,Inc.	125MW Boiler (Mizushima P/S NO.1unit)	Design	500,000	153	98.73	1984
Chugoku Electric Power Co.,Inc.	156MW Boiler (Mizushima P/S NO.2unit)	Design	600,000	136	98.73	1984
Sanuki Engyo Co.,Ltd.	80T/H Boiler	Design	85,000	130	99.75	1984
Teijin Ltd.	80T/H Boiler (Matsuyama NO.2unit)	Design	101,000	180	99.33	1985
Joban Joint Power Co.,Ltd.	75MW Boiler (Nakoso P/S NO.4unit)	Design	342,000	[illegible]	99.11	1985
Nitto Boseki Co.,Ltd.	55T/H Boiler (Fukuyama NO.7unit)	Design	72,000	[illegible]	99.22	1985
Tokuyama Soda Industry Co.,Ltd.	530T/H Boiler (NO.10 unit)	Design	567,000	127	99.03	1987

TABLE 7. SUPPLY LIST OF THE MOVING ELECTRODE TYPE ESPS FOR ANOTHER USE WITHOUT FOR COAL-FIRED BOILER

Client	Application		Gas Flow (m^3N/H)	Gas Temperature (℃)	Collection Efficiency	Completion Year
Nippon Petroleum Refining Co.,Ltd.	Fludized Catalytic Cracker	Design	74,900	180	90.0	1979
Iwaki Glass Co., Ltd.	Glass Melting Furnace	Design	23,000	250	90.0	1982
Yokohama City	Sewage Sludge Incinerator (NO.1)	Design	19,000	330	99.85	1982
Toa Nenryo Kogyo Co.,Ltd.	Fludized Catalytic Cracker	Design	292,000	240	85.0	1984
Yokohama City	Sewage Sludge Incinerator (NO.2)	Design	20,000	320	99.85	1985
Yokohama City	Sewage Sludge Incinerator (NO.3)	Design	18,500	220	99.98	1987

7.CONCLUSION

Six years have passed since application of the first moving electrode type ESP in 1979.

This paper has described the application of the moving electrode type ESPs for coal-fired boilers.

Through the investigation up to the present, the following results have been obtained.

(1) The collection efficiency exceeded higher than expected value was obtained and superiority of the moving electrode type ESP was proved. Moreover, it was confirmed that the moving electrode type ESP could maintain its stable performance against the change with lapse of time and change of kinds of coals as well.

(2) Reliability was confirmed through the commercial operation .

(3) Successful results of the moving electrode type ESP have convinced us the possibility of applying to the larger ESP and for inexperienced fields.

8.REFERENCES

1. Hiroshi Asano, et al., "Recent Results of Application of the Moving Electrode Electrostatic Precipitator for Coal-Fired Utility Boilers, "Second International Conference on Electrostatic Precipitation, November 12th-15th, 1984, Kyoto JAPAN.

2. Hiroaki Yabuta, "Moving Electrode Type Electrostatic Precipitators" ,Hitachi Hyoron 64,105-110(1982).

3. Hiroshi Asano, et al., "Development and Application of the Moving Electrode Electrostatic Precipitator for High Resistivity Dust Collection", The second CSIRO Conference and Course on Electrostatic Precipitation, August 15th-19th,1983,Bowral AUSTRALIA.

4. Takeshi Nakayama, Makoto Ohtsuka,"Application of Moving-Electrode Type Electrostatic Precipitators to Coal-Fired Utility-Use Boilers",Hitachi Review 34,225-228(1985).

The work described in this paper was not funnded by the U.S. Environmental Protection Agency and therefore the contents do not necessarily reflect the views of the Agency and no official endorsment should be inferred.

Session A-6: FUNDAMENTALS I

Sidney A. Self, Chairman
Stanford University
Stanford, CA

MEDIUM-SULFUR COAL AND FLY ASH RESISTIVITY

by: W. A. Harrison, J. K. Nicholson
Southern Company Services, Inc.
Birmingham, AL 35202

J. L. DuBard, J. D. Carlton
Southern Research Institute
Birmingham, AL 35255

L. E. Sparks
Air and Energy Engineering Research Laboratory
U.S. Environmental Protection Agency
Research Triangle Park, NC 27711

ABSTRACT

Electric generating plants burning medium-sulfur coal need a way to predict when ESP performance will be limited by high resistivity of the collected fly ash. The main uncertainty in mathematical predictions of fly ash resistivity lies in the marginal effect of SO_3 vapor naturally occurring in the flue gas. This paper describes a project to expand the data base of SO_3/SO_2 concentrations, in situ fly ash resistivities, and electrical operating points measured in operating utility fly ash precipitators. Recent data are presented. In situ resistivity data are compared with laboratory measurements and mathematical predictions.

This paper has been reviewed in accordance with the U.S. Environmental Protection Agency's peer and administrative review policies and approved for presentation and publication.

INTRODUCTION

This paper describes a joint endeavor between the U.S. Environmental Protection Agency (EPA), Southern Research Institute (SRI), and Southern Company Services (SCS) to enlarge the existing data base on the relationship between fuel sulfur and the production of sulfur trioxide (SO_3) available for fly ash resistivity modification in the flue gas. This work was performed in support of the EPA research program in the fundamental science of electrostatic precipitation.

The reasons for selecting medium-sulfur coal for this program are related to the impact of fly ash characteristics on the electrical operating condition of the electrostatic precipitator (ESP). Medium-sulfur coal is defined as coal having between 1 and 2 percent sulfur. It is known that the combustion of low-sulfur coals (<1 percent sulfur) with highly alkaline ash will produce a very small amount of SO_3. The low-sulfur coal fly ash will have high electrical resistivity, severely limiting the electrical power input to a cold-side ESP. It is also known that the combustion of a high-sulfur (>2 percent sulfur) coal will produce sufficient SO_3 to condition the ash, resulting in low-resistivity fly ash and presenting few operating problems to a cold-side ESP. However, the existing data exhibit a large degree of scatter in the relationship between the SO_2 and SO_3 produced when burning medium-sulfur coal in a utility boiler. This large scatter in the data makes the prediction of SO_3 values extremely difficult. It is advantageous to be able to predict what levels of SO_3 will be available from a particular fuel; as one can then predict the impact that the fuel will have on an operating ESP.

The data collected in this program consisted of in situ resistivity measured with two probes, in situ SO_2 and SO_3, ash samples, fuel samples, boiler operating data, and ESP electrical conditions. As many data as possible were collected over a 3-day period at each of three plants.

SRI has been involved in particulate sampling and control technology development for a number of years. SRI has developed many of the methods and techniques used in ESP performance evaluation. The point-plane probe and the Bickelhaupt computer model are two techniques developed at SRI and used for collecting and analyzing the data presented in this paper.

SCS is the engineering and design company for The Southern Company, one of the nation's largest public utility holding companies, with some 232 generating units providing over 24,000 MW of electrical power. Some 80 percent of these units are coal-fired and use precipitators for particulate control. SCS has been involved in numerous research programs concerning ESP control technology, with support from EPA and EPRI, and in many internal research and development programs. SCS has a responsibility to its operating companies, Alabama Power, Georgia Power, Gulf Power, and Mississippi Power, to remain abreast of current particulate control technology and the fundamental processes that affect electrostatic precipitation.

PROGRAM PLAN

Representative data sets from three plants in the Southern electric system are presented here. They include in situ resistivity, flue gas composition including SO_2 and SO_3, fuel sample analyses, and fly ash analyses. The data are correlated with computer generated resistivity values from Versions I and II of the Bickelhaupt computer model and with laboratory resistivity measurements (IEEE Standard 548-1984). In situ data, flue gas data, ash samples, and fuel samples were collected simultaneously. It should be noted that variations in fuel and boiler firing conditions make it essential that all data for this type of comparison be collected simultaneously.

There are three methods used by SRI and SCS to obtain fly ash resistivity values:

1. Bickelhaupt computer program, Model I.
2. Laboratory measurement, IEEE Standard 548-1984, descending temperature.
3. In situ measurement, point-plane probe, spark method.

For this particular program, the point-plane resistivity probe provides the reference resistivity measurement. Therefore, the following program objectives were established:

1. to compare the three methods when given the same data and fuel,
2. to compare the computer models (Models I and II) with in situ and laboratory data, and
3. to compare the computed SO_3 concentrations with the measured concentrations.

RESISTIVITY MODELS

There are presently two versions of the Bickelhaupt resistivity prediction program. Model I is available from the National Technical Information Service (1). Model II is in the final review phase by EPA. There are two significant differences in the two models. First, Model I gives a tabulated data format of resistivity versus temperature, with two columns of data representing the resistivity with no SO_3 present and the resistivity when the ash has been conditioned by the amount of SO_3 calculated from the fuel and ash analyses. Model II gives a computer generated plot of resistivity versus temperature, including curves for the effect of 0, 1, 4, and 10 ppm SO_3 in the ash. The curve for the SO_3 concentration predicted by the model (from the fuel and ash analyses) is also plotted. Second, the models each use an empirical SO_3/SO_2 ratio to predict the SO_3 concentration in the flue gas at the ESP inlet. However, Model II uses a different mathematical approach for determining the effect of the SO_3 on the fly ash resistivity. This algorithm tends to shift the maximum peak of the curves to a higher temperature. Model II also takes into account the percentage of ash and the mineral analysis of the ash in predicting the SO_3 concentration. Therefore, there will often be small differences in the predicted SO_3 concentration between Models I and II. In the absence of SO_3, there is no difference in the resistivity predictions of Models I and II.

The model predictions of the effect of SO_3 concentration on fly ash resistivity are based on laboratory resistivity measurements on a large number of fly ashes having large variations in their ash mineral analyses. This field test program is the first systematic comparison of the laboratory resistivity measurements with resistivity values measured in situ.

RESULTS

Complete data sets from the coal, ash, and gas analyses are presented in Tables 1, 2, and 3. Water vapor in the flue gas is given in volume percent, and SO_2 and SO_3 are given in volume ppm. The ultimate coal analyses (in weight percent) and the ash mineral analyses (in weight percent as the oxide) constitute complete input data for the resistivity models. Representative comparisons of measured and computed resistivities are shown in the figures following the tables.

Data collected at Plant 3 are shown in Figures 1 and 2. Figure 1 shows that Model I predicts an SO_3 concentration of 2.4 ppm when 1.6 ppm was actually measured. The two rectangular data points represent the in situ resistivity measurements, one obtained by SCS and the other by SRI. In this case, Model I overpredicts the measured resistivity by almost an order of magnitude. Figure 2 is a plot of Model II predictions using the same data as Figure 1, with additional data points from laboratory measurements of resistivity with 0.0 and 3.8 ppm SO_3 in the laboratory chamber. The in situ measured resistivity is shown by the same two rectangular data points. It can be seen that the predicted value is now lower than the measured value, primarily due to the model prediction of slightly more SO_3 than was actually present. The laboratory measured values agree well with the predicted curves for 0.0 and 4.0 ppm SO_3. The laboratory measurements were performed on samples collected in the SRI point-plane probe during in situ measurements.

Data collected at Plant 1 are shown in Figures 3 and 4. This plant had the highest fuel sulfur of the three. This fact is reflected in the higher SO_3 concentrations measured and predicted. The SO_3 concentrations of 6.6 ppm and 5.9 ppm predicted by Models I and II, respectively, are compared with the measured value of 7.6 ppm. Since the measured SO_3/SO_2 ratio can vary widely about the average value that is used in the resistivity models (even at the same sampling point, as a result of variations in boiler operation) this level of agreement between measurement and prediction is considered to be good. Figure 3 shows the predicted resistivity values from Model I compared with the in situ data. Figure 4 shows the same comparison using Model II. The resistivity values predicted by Model II are much closer to the in situ data points. The comparisons of the predicted values and the laboratory measured values are reasonably good.

The differences between Model I and II are compared again in the data presented in Figures 5 and 6. These data taken at Plant 3 show good agreement between the predicted SO_3 values and the measured SO_3 values: 2.3 versus 2.0, respectively, for Model I, and 2.1 versus 2.0, respectively, for Model II. However, Model I overpredicts the in situ resistivity values by an order of magnitude. Model II gives a predicted value much closer to the in situ measured values, due to the way it computes the effect of SO_3 on the fly ash resistivity. Ash samples for laboratory measurements were not obtained at the same time as the in situ measurements.

Data collected at Plant 2 are shown in Figures 7 and 8. These data illustrate the comparisons of predicted values and measured values when the computer models predict much more SO_3 than was actually present. Figure 7 shows the Model I resistivity prediction. It appears to correspond closely to the in situ resistivity until one realizes that it predicts 5.2 ppm SO_3 when only 0.5 ppm was actually measured. In Figure 8, the Model II prediction is almost two orders of magnitude lower than the in situ resistivity because it predicts 4.6 ppm SO_3 when only 0.5 ppm was actually measured. The reason for the unusually low SO_3 concentration in the flue gas at Plant 2 was not determined. However, these data from Plant 2 illustrate the possible pitfalls in relying solely on a computer model prediction of resistivity. The laboratory measured data points shown in Figure 8 are from two different ash samples collected simultaneously. The hopper sample data compare well with the model prediction. The other sample was taken from one of the in situ resistivity probes. Its measured resistivity compares closely with the in situ resistivity measurements at 0.5 ppm SO_3.

It is not surprising to see a difference in fly ash resistivity measurements made on in situ samples and hopper samples, because it is known that an ESP selectively collects certain ash particle size fractions in certain areas. Typically, the larger particles are collected in the inlet fields, with the smaller particles penetrating to the middle and outlet fields. This is not a uniform fractionation, however, as rapping reentrainment tends to redistribute the particles among the middle and outlet fields.

CONCLUSIONS

In conclusion, the following major points are evident:

1. Good agreement between the three methods of determining fly ash resistivity was usually obtained when using simultaneously collected data.
2. Model II of the Bickelhaupt computer program gave consistently better agreement with in situ measured resistivity than Model I.
3. The SO_3 concentrations predicted by the models are usually close to the measured values. However, there can be large differences.

The in situ data were obtained with two different point-plane probes manufactured by two different shops and used by four different operators. Very consistent data were obtained. At this stage in the knowledge of the relationships between fuel chemistry and fly ash resistivity it is advisable to measure the resistivity with a point-plane probe whenever possible (2). If the resistivity is to be predicted from fuel and ash analyses, Model II of the Bickelhaupt computer program should be used. If possible, the SO_3 concentration in the flue gas should be measured by the Cheney-Homolya method (2) and used as input data for the computer model instead of depending on the model to predict a value of SO_3. A combination of all three methods of determining fly ash resistivity is strongly recommended in order to discern any unexpected anomalies in the fly ash properties.

REFERENCES

1. R. E. Bickelhaupt. A Technique for Predicting Fly Ash Resistivity. EPA-600/7-79-204, August 1979. U.S. EPA, Research Triangle Park, NC. NTIS PB80-102379.

2. W. B. Smith, K. M. Cushing, J. D. McCain, and D. B. Harris. Procedures Manual for Electrostatic Precipitator Evaluation. EPA-600/7-77-059, June 1977. U.S. EPA, Research Triangle Park, NC. NTIS PB269698.

TABLE 1. PLANT 1
COAL, ASH, AND GAS ANALYSES

	8/28/85 am		8/28/85 pm	8/29/85 am		8/29/85 pm
Coal Analysis						
C	69.50		71.44	68.41		68.80
H_2	4.26		4.44	4.05		4.16
O_2	5.41		5.31	4.65		4.60
N_2	1.52		1.58	1.44		1.47
S	2.15		2.18	1.65		1.73
H_2O	4.99		2.72	5.90		5.72
Ash	12.07		12.22	13.83		13.44
Computed Gas Composition						
H_2O	7.4		7.2	7.4		7.4
SO_2	1520.0		1500.0	1200.0		1240.0
SO_3 (Model I)	6.6		6.4	5.2		5.3
SO_3 (Model II)	5.9		5.9	4.6		4.8
Measured Gas Composition						
H_2O	8.5		8.5	8.6		8.6
SO_2	1580.0		1386.7	1178.8		1190.0
SO_3	7.6		7.1	7.7		7.9
	SRI in situ	SCS in situ	SRI in situ	SRI in situ	SCS in situ	SRI in situ
Ash Analysis						
Na_2O	0.25	0.26	0.26	0.23	0.24	0.22
K_2O	2.91	2.87	2.94	2.85	2.94	3.09
MgO	1.02	1.01	1.04	1.04	1.08	1.09
CaO	0.76	0.86	0.80	0.60	0.67	0.66
Fe_2O_3	17.04	15.64	11.43	11.58	11.69	9.80
Al_2O_3	23.10	23.10	24.60	24.60	25.10	24.80
SiO_2	45.30	47.10	48.30	48.50	49.80	51.00
TiO_2	0.93	0.96	1.06	1.00	1.01	0.98
P_2O_5	0.28	0.33	0.32	0.32	0.31	0.49
SO_3	0.45	0.40	0.38	0.38	0.30	0.35
LOI	7.65	7.04	8.48	8.56	6.44	7.31

TABLE 2. PLANT 2
COAL, ASH, AND GAS ANALYSES

	8/20/85 pm		8/21/85 pm		8/22/85 am		8/22/85 pm	
Coal Analysis								
C	69.28		71.24		68.99		69.58	
H_2	4.55		4.77		4.55		4.66	
O_2	5.73		6.44		5.35		6.03	
N_2	1.66		1.70		1.66		1.69	
S	1.69		1.38		1.36		1.29	
H_2O	3.58		4.08		5.41		5.24	
Ash	13.49		10.32		12.66		11.49	
Computed Gas Composition								
H_2O	7.5		7.7		7.7		7.8	
SO_2	1200.0		939.0		950.0		900.0	
SO_3 (Model I)	5.2		4.1		4.1		3.9	
SO_3 (Model II)	4.6		3.7		3.7		3.5	
Measured Gas Composition								
H_2O	9.8		9.2		8.9		8.9	
SO_2	1051.0		995.0		965.0		924.0	
SO_3	0.50		0.82		0.42		0.37	
	in situ	hopper	in situ	hopper	in situ	hopper	in situ	hopper
Ash Analysis								
Na_2O	0.43	0.43	0.39	0.41	0.43	0.41	0.45	0.41
K_2O	3.66	3.38	3.30	3.30	3.60	3.24	3.65	3.31
MgO	1.27	1.21	1.14	1.16	1.29	1.14	1.31	1.17
CaO	1.02	0.98	1.18	1.10	1.02	1.12	1.07	1.02
Fe_2O_3	8.45	8.43	10.13	8.66	9.05	8.44	8.42	8.27
Al_2O_3	26.30	24.00	26.00	24.30	26.40	23.80	26.90	24.60
SiO_2	52.90	45.40	51.70	45.40	52.60	43.40	52.50	45.70
TiO_2	1.17	1.06	1.25	1.12	1.12	1.03	1.18	1.07
P_2O_5	0.38	0.44	0.48	0.42	0.43	0.44	0.37	0.39
SO_3	0.30	0.95	0.27	1.05	0.20	1.00	0.53	0.70
LOI	3.87	13.49	3.97	12.84	3.70	15.75	3.43	13.12

TABLE 3. PLANT 3
COAL, ASH, AND GAS ANALYSES

	7/30/85 pm		7/31/85 pm	8/1/85 am	
Coal Analysis					
C	73.29		74.16	72.72	
H_2	4.36		4.34	4.39	
O_2	5.55		4.55	5.11	
N_2	1.54		1.58	1.53	
S	0.84		0.78	0.81	
H_2O	1.69		1.71	1.96	
Ash	12.60		12.00	12.50	
Computed Gas Composition					
H_2O	6.9		6.8	7.0	
SO_2	570.0		530.0	560.0	
SO_3 (Model I)	2.4		2.3	2.4	
SO_3 (Model II)	2.2		2.1	2.2	
Measured Gas Composition					
H_2O	9.3		9.3	9.4	
SO_2	626.0		543.0	594.0	
SO_3	3.6		2.0	1.6	
	SCS in situ	SRI in situ	SCS in situ	SCS in situ	SRI in situ
Ash Analysis					
Na_2O	0.41	0.49	0.44	0.11	0.43
K_2O	2.58	2.84	2.63	2.55	2.84
MgO	0.00	1.19	1.17	1.25	1.23
CaO	1.39	1.42	2.23	2.18	1.85
Fe_2O_3	8.62	6.15	7.43	8.88	6.35
Al_2O_3	28.00	27.60	28.20	27.15	26.40
SiO_2	53.79	54.70	55.23	53.40	53.70
TiO_2	1.33	1.36	1.36	1.31	1.27
P_2O_5	0.47	0.29	0.57	0.47	0.27
SO_3	0.43	0.13	0.22	0.47	0.15
LOI	--	3.34	--	--	5.11

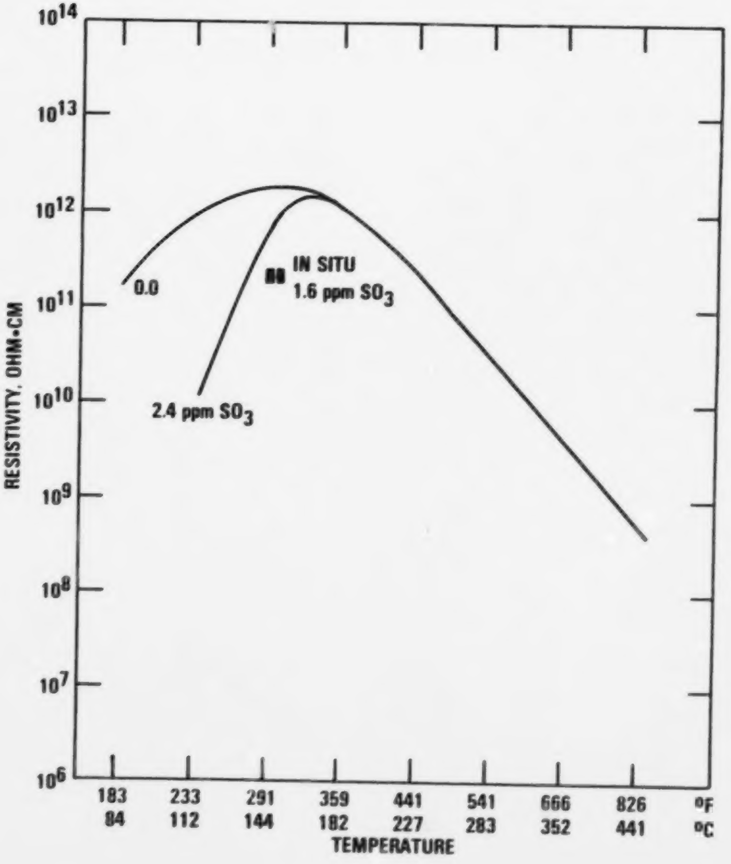

Figure 1. Plant 3, 8/1/85 am,
Model I resistivity curves.

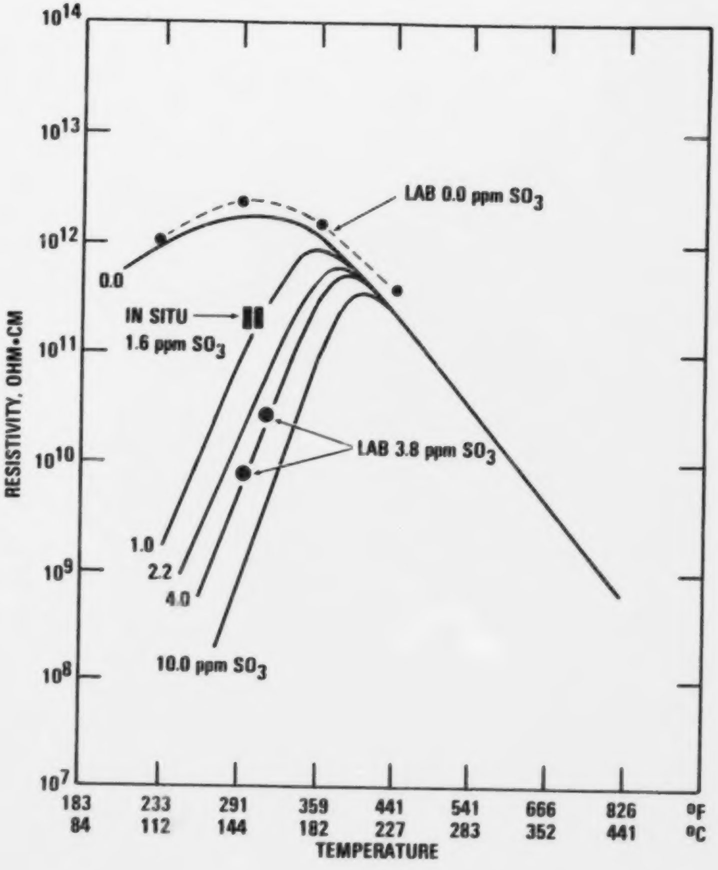

Figure 2. Plant 3, 8/1/85 am,
Model II resistivity curves.

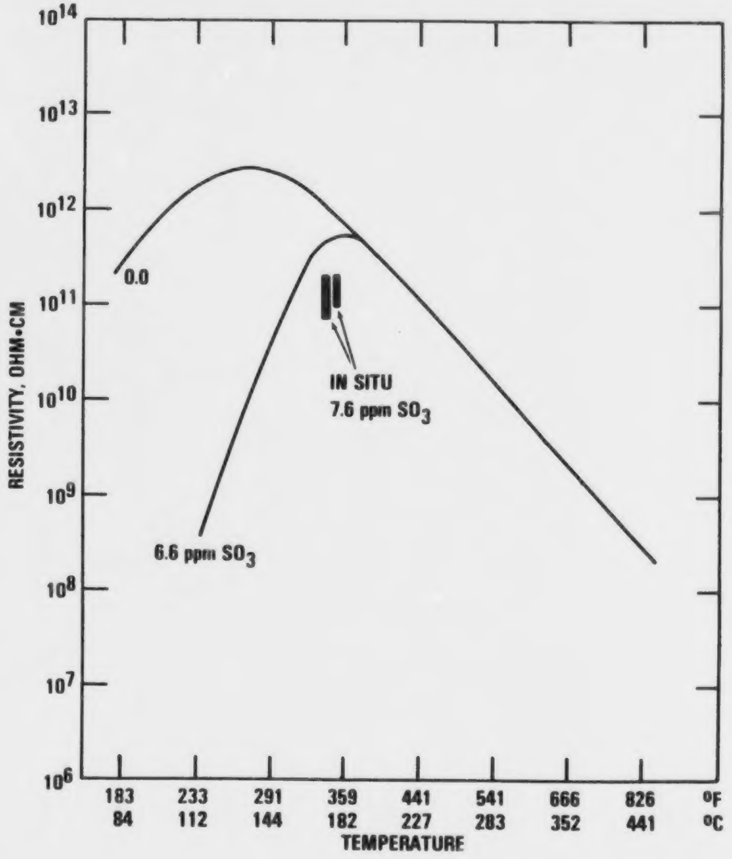

Figure 3. Plant 1, 8/28/85 am, Model I resistivity curves.

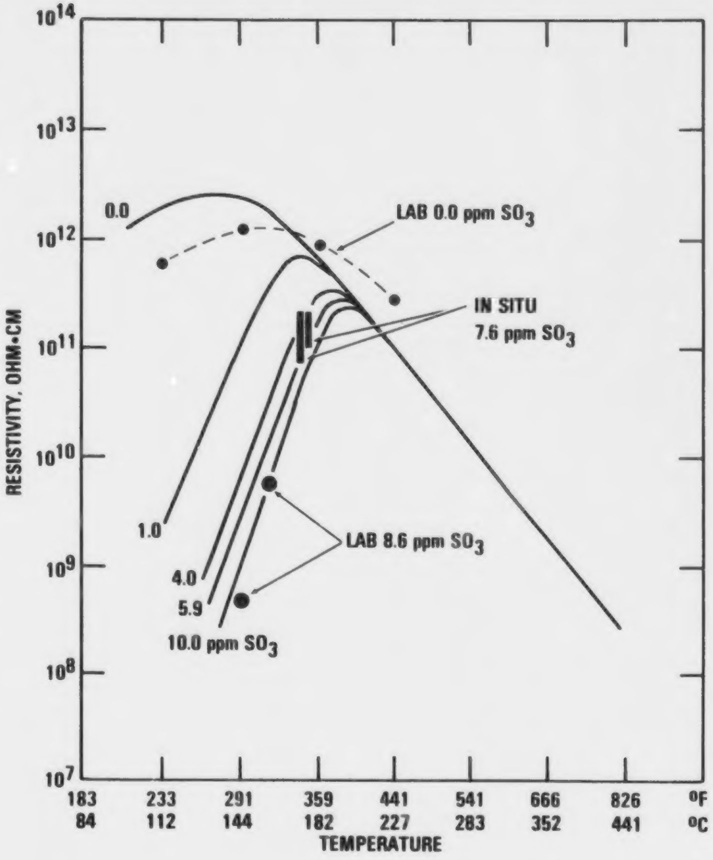

Figure 4. Plant 1, 8/28/85 am, Model II resistivity curves.

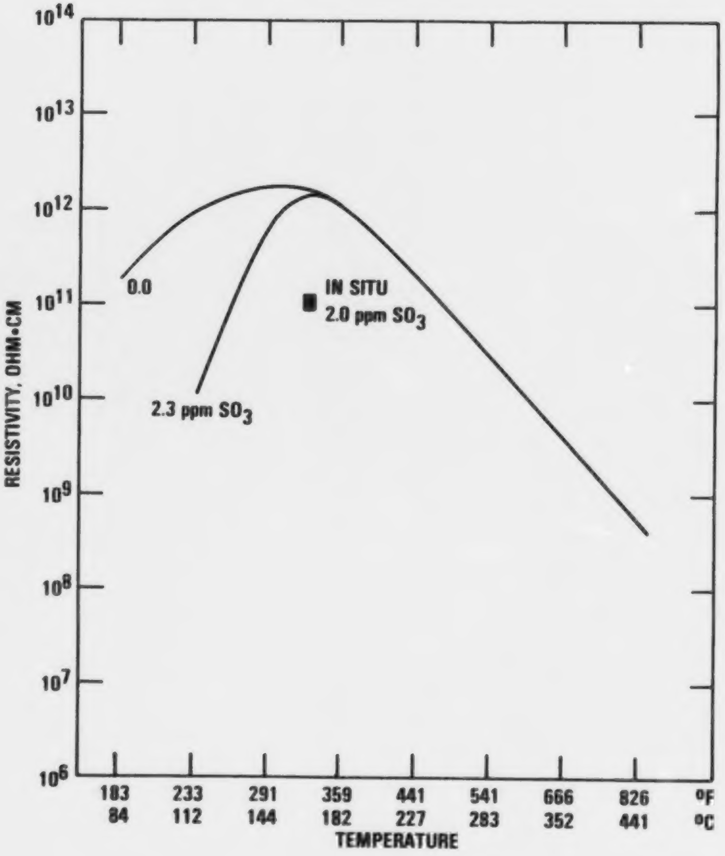

Figure 5. Plant 3, 7/31/85 pm, Model I resistivity curves.

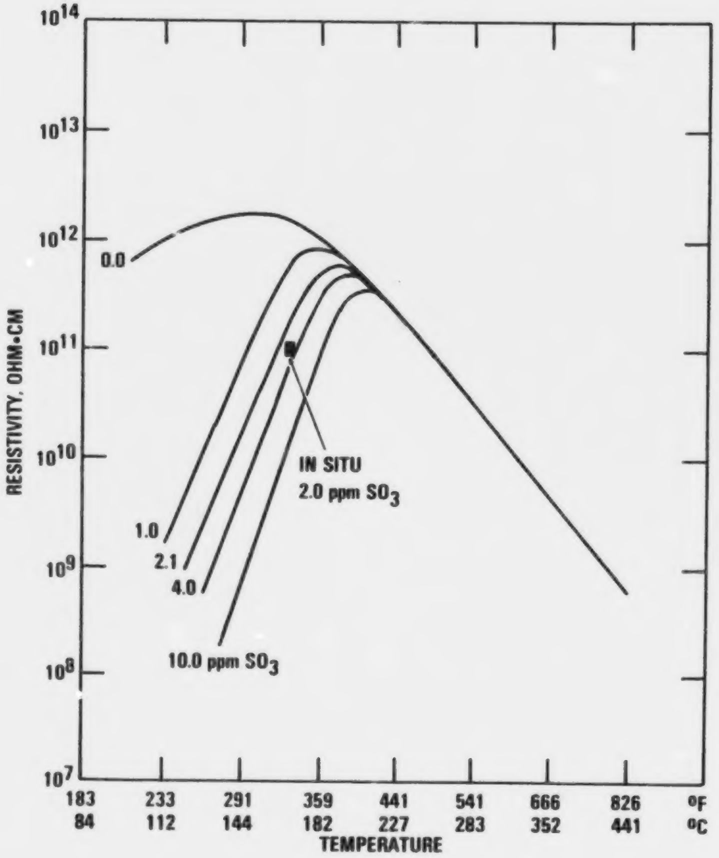

Figure 6. Plant 3, 7/31/85 pm, Model II resistivity curves.

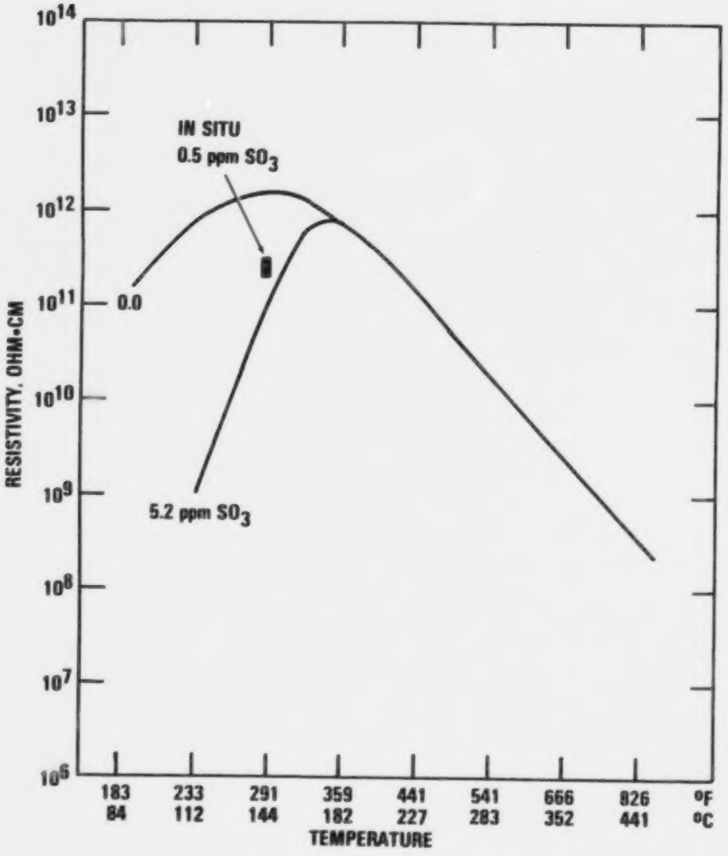

Figure 7. Plant 2, 8/20/85 pm, Model I resistivity curves.

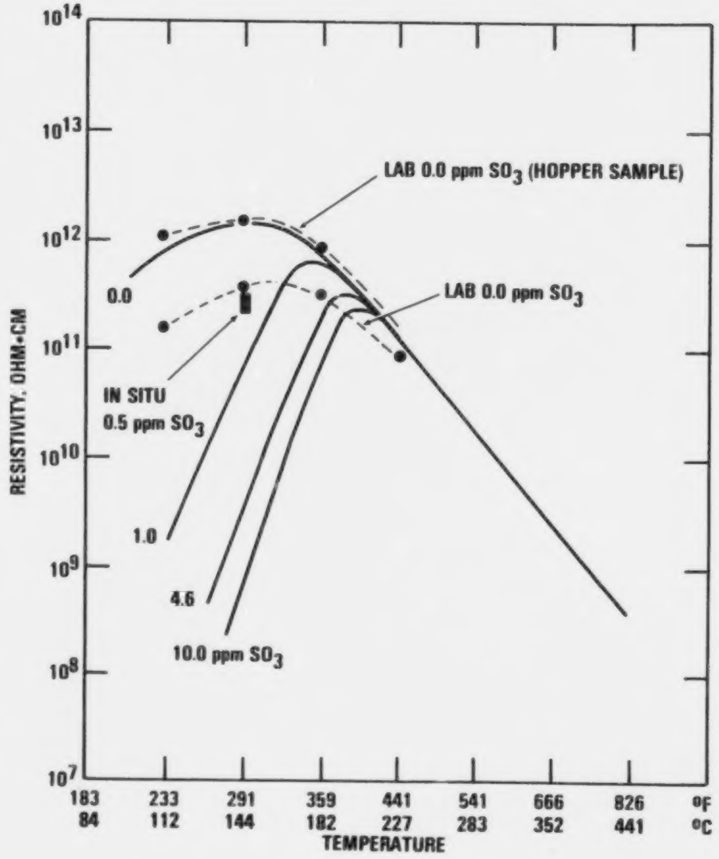

Figure 8. Plant 2, 8/20/85 pm, Model II resistivity curves.

THE EFFECT OF HIGH MASS LOADING ON FLY ASH PRECIPITATORS

by: M. G. Faulkner
J. L. DuBard
Southern Research Institute
Birmingham, AL 35255-5305

L. E. Sparks
Air & Energy Engineering Research Laboratory
US Environmental Protection Agency
Research Triangle Park, NC 27711

ABSTRACT

Dry sorbent injection techniques for SO_2 control are expected to increase the fine particle concentration in the flue gas. In order to study the effects of increased space charge, a laboratory ESP has been modified so that the plate current may be measured in small increments along its length and recorded by a computer data acquisition system. This ESP was used with flue gas generated by the SRI 300 kW (10^6 Btu/h) coal combustion facility. Current distribution data were taken with flue gas containing fly ash, fly ash and hydrated lime, and an ammonium sulfate fume. These data show the development of corona suppression and back corona. The data are being used to improve the particle charging and collecting calculations in the EPA/SRI ESP Model.

This paper has been reviewed in accordance with the U.S. Environmental Protection Agency's peer and administrative review policies and approved for presentation and publication.

INTRODUCTION

One of the techniques being investigated for the control of SO_2 in flue gas is the furnace injection of a dry sorbent material such as hydrated lime (LIMB). One of the results of sorbent injection is the addition of a large quantity of small particles to the flue gas. These additional particles affect the operation of the ESP being used to clean the gas in the following ways: 1) they increase the total dust load on the ESP, 2) the added particles fall in the size band where ESPs are least effective, 3) as the particles are charged, they form a space charge cloud which may suppress the corona in the ESP, and 4) the sorbent material may change the net resistivity of the collected particulate layer.

In order to study the effects of increased space charge with sorbent injection, a laboratory ESP has been modified so that the plate current may be measured in small increments along its length. A schematic of the segmented plate ESP is shown in Figure 1. The ESP has six wires on 15 cm (6 in.) centers. The wires may be powered by a single supply or by multiple supplies. One of the collection plates is a 66 x 122 cm (26 x 48 in.) circuit board which has been machined into conductive strips as shown in Figure 1. There are 43 conductive strips measuring 2.2 x 51 cm (7/8 x 20-1/4 in.) and 2 end strips measuring 6 x 51 cm (2-3/8 x 20-1/4 in.). The length of the conductive strips corresponds to the length of the corona wires. Each of the narrow strips has an area of 114 cm^2 (1/8 ft^2). The area of all 45 strips is 5,560 cm^2 (6 ft^2). The other collection plate is a grounded stainless steel sheet. The duct width is 23 cm (9 in.).

The segmented plate ESP is located in the SRI Coal Combustion Facility. The combustor is a 300 kW (10^6 Btu/h) down-fired furnace which burns pulverized coal to produce fly ash which is very similar to the ash produced by a full-scale utility boiler. The furnace has provisions for the injection of hydrated lime to test the LIMB process. The ESP processes the entire gas stream, with a typical SCA of 5.3 $m^2/m^3/s$ (27 ft^2/1000 acfm) at 150°C (300°F).

Each of the 45 plate segments in the ESP is monitored by an electrometer circuit which produces a voltage proportional to the current on the plate strip. The 45 voltages are then scanned by a Cyborg/Isaac relay multiplexer, converted to a digital signal, and processed and stored by an Apple IIe computer.

PRELIMINARY TESTING

Results of preliminary testing with the segmented plate ESP are shown in Figure 2, in which the current is plotted for each plate strip. The strips are numbered 0 through 44 from the ESP inlet to the outlet. The location of the corona wires is indicated by the squares on the x-axis of these graphs. The ambient air curve (Figure 2a) shows significant corona occurring only on the first and last wires. Dominance by the first and/or last wires is typical of all of the data taken by this device. Figure 2b shows the increase in current using flue gas provided by the combustor operating on natural gas. A shift to fly ash laden gas reduced the current. The total current densities for these curves were 2.4 nA/cm^2 for ambient air, 30 nA/cm^2 for flue gas, and 5.6 nA/cm^2 with fly ash. It is interesting to note that the current peaks are not located over the wires. In the flue gas curve (Figure 2b), the peaks for the end wires are shifted outward and the peaks for the inner wires lie equally spaced between the outer peaks. With fly ash (Figure 2c) the peaks for wires 2-6 are shifted downstream of the wires.

FLY ASH AND LIME

In an effort to achieve a higher concentration of fine particles, a test was run with hydrated lime $[Ca(OH)_2]$ injected into the furnace at $Ca/S \cong 2$. Figure 3 shows the total plate current as a function of time for this test. The current shown for time t less than 0 was for fly ash only. At $t = 0$, when lime injection began, the current density dropped by about 50%. The times during which the two 45 channel current measurements were made are shown by the horizontal lines in the figure. The duration of the first measurement was 6 minutes, during which the 45 channels were read 10 times and averaged. During this period, the current rose from 0.075 to 0.57 mA, which corresponds to a rise in the current density of 5 to 37 nA/cm^2. The second test was shortened to 2 minutes by reducing the number of times the data were averaged. During this test, the current rose from 2.0 to 2.7 mA, which corresponds to an increase in current density of 130 to 170 nA/cm^2. Previous in situ resistivity data taken in the Coal Combustion Facility have shown that the addition of hydrated lime at the furnace raises the resistivity of the ash from 2×10^{10} to 2×10^{12} ohm-cm. The high resistivity and the uncontrolled rise in current indicate that the system went into severe back corona during this test.

Figure 4 shows the 45 channel current measurements for this test. Figure 4a shows the data for fly ash only ($t < 0$). The peaks are similar to the fly ash peaks in Figure 2c, but are more pronounced due to the higher voltage (45 kV instead of 40 kV). Figure 4b shows the first multi-channel data taken with lime injection (Figure 3). Although the area around wires 2 and 3 may indicate corona suppression, wire 6 is showing the beginnings of back corona. By the second test (Figure 4c), the system is well into back corona. In an attempt to return to normal operation, the voltage was reduced and the plates were vibrated. A large drop in current occurred, after which the current rose again. Figure 4d shows data taken during this period. The voltage had been reduced from 45 to 37 kV. Wires 1 and 6 are still in back corona. There is no apparent emission from the inner wires. The current density rose from 13 to 22 nA/cm^2 during the test. The back corona problem was remedied only by opening up the ESP and cleaning it.

FLY ASH + LIME + SO_3

To counter the problems caused by high resistivity, the previous test was repeated with the addition of SO_3. The hydrated lime was again furnace injected at $Ca/S \cong 2$. The estimated dust loadings for coal only and coal + lime were 2.3 and 6.9 g/m^3 (1 and 3 gr/acf), respectively. The in situ resistivity of the ash + lime + SO_3 mixture was 2 x 10^{10} ohm-cm, which was very close to that of the fly ash alone. The V-I curves for this test are shown in Figure 5. The upper V-I curve is for fly ash. The irregularity in the curve is due to shutting the power off and checking the wires in the middle of taking V-I data. The lower curve is for ash + lime + SO_3. Figure 6 shows the current on the ESP during the lime + SO_3 injection test. The SO_3 conditioned sorbent injection reduced the current by about a factor of 3. The current was stable at the lower level for the 3 hours of the injection test. When the injection was stopped, the current returned to the higher level. Figure 7 shows the 45 channel current measurements for the test, in which the current suppression during the lime + SO_3 injection and the recovery afterward are clearly illustrated. The current in Figure 7d may have been affected somewhat by an effort to clear the wires of deposits before the data were taken.

AMMONIUM SULFATE FUME

In an attempt to observe the effects of fine particles without the presence of fly ash, a test was made using an ammonium sulfate fume in flue gas. To perform this test, the combustor was run on natural gas. An excess of ammonia was introduced into the gas flow upstream of the ESP. SO_3 was then added between the ammonia source and the ESP so that the two chemicals could react to form an ammonium sulfate fume before entry into the ESP. Figure 8 shows the results of this test. The upper curve shows the current for flue gas only. Then, as ammonia was added, the current unexpectedly dropped to about 25% of what it had been, implying there was SO_3 present in the system. As the combustion system had not been cleaned prior to this test, this was possible. (Subsequent tests showed 0.8 ppm SO_3 present when no SO_3 was injected.) The quenching effect of this fume is shown in Figure 9. In order to make additional quenching effects visible, the voltage was raised to 44 kV at this point. The depressed V-I curves in Figure 8 show the results of the addition of SO_3. Figure 10 shows the multi-channel data for the SO_3 addition. Again, the quenching effects are clearly visible. The current density using an estimated 12 ppm SO_3 (Figure 10c) was 1.5 nA/cm^2. This is a factor of 6 less than the 44 kV value for ammonia (Figures 8 and 10a).

APPLICATION OF RESULTS

The EPA-SRI ESP Model has been used to estimate collection efficiency and outlet particulate emissions for a full-scale ESP based on the results of the tests with coal + hydrated lime + SO_3. The ESP was chosen to represent an older unit of the type that would be retrofitted for sorbent injection. The ESP has 23 cm (9 in.) plate spacing, weighted wires, and an SCA in the 30 to 60 m^2/m^3/sec (150 to 300 ft^2/1000 acfm) range. The simulations were run for the four conditions listed below:

1. High-sulfur coal only. For this case the mass loading was assumed to be 5.3 g/m^3 (2.3 gr/acf).

2. Coal + hydrated lime (Ca/S = 2) + ~100 ppm SO_3. For this case, the mass loading was increased by about a factor of 3 and the mmd of the particle size distribution was reduced from 30 to 15 µm to match data taken at the SRI Coal Combustion Facility. The electrical operating conditions were the same as for case 1.

3. Coal + hydrated lime + SO_3. This case is the same as case 2 except that the current in the first half of the first electrical section has been reduced in proportion to the V-I curves in Figure 5.

4. Coal + hydrated lime + SO_3. This case is the same as case 2 except that the current in the first half of the ESP has been reduced in proportion to the V-I curves in Figure 5.

The results of the simulations are shown in Figure 11. The largest change in emissions was caused by the increase in the dust loading and the shift in the particle size distribution to account for the large increase in the number of fine particles due to the hydrated lime. By comparison, the additional increase in emissions due to current suppression is small.

CONCLUSION

The segmented plate ESP described here promises to be a useful tool in the exploration of corona quenching effects. Preliminary results have been used to model corona quenching effects in an ESP collecting ash from coal + hydrated lime + SO_3. The modeling showed that the effects of corona suppression are overshadowed by the effects of the higher inlet mass and finer particle size distribution.

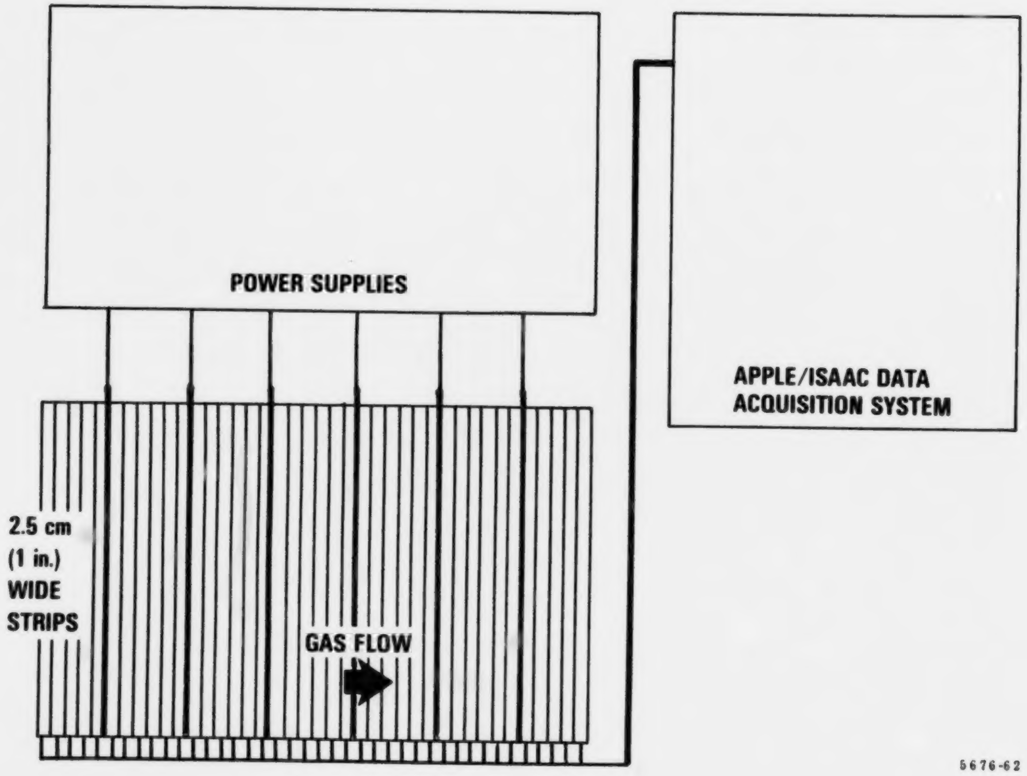
POWER SUPPLIES
APPLE/ISAAC DATA ACQUISITION SYSTEM
2.5 cm (1 in.) WIDE STRIPS
GAS FLOW
5676-62

Figure 1. SRI segmented plate electrostatic precipitator.

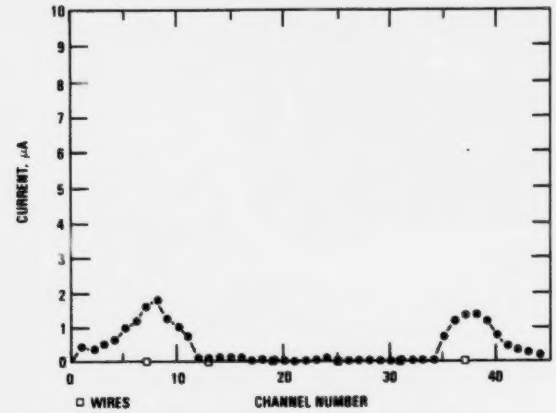

a. AMBIENT AIR

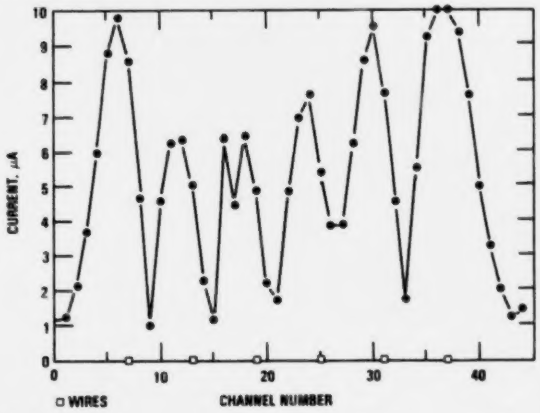

b. FLUE GAS

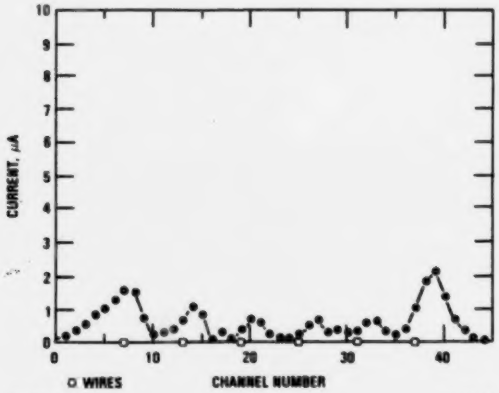

c. FLY ASH

5676-43

Figure 2. Current on each plate strip for three gas conditions at 40 kV.

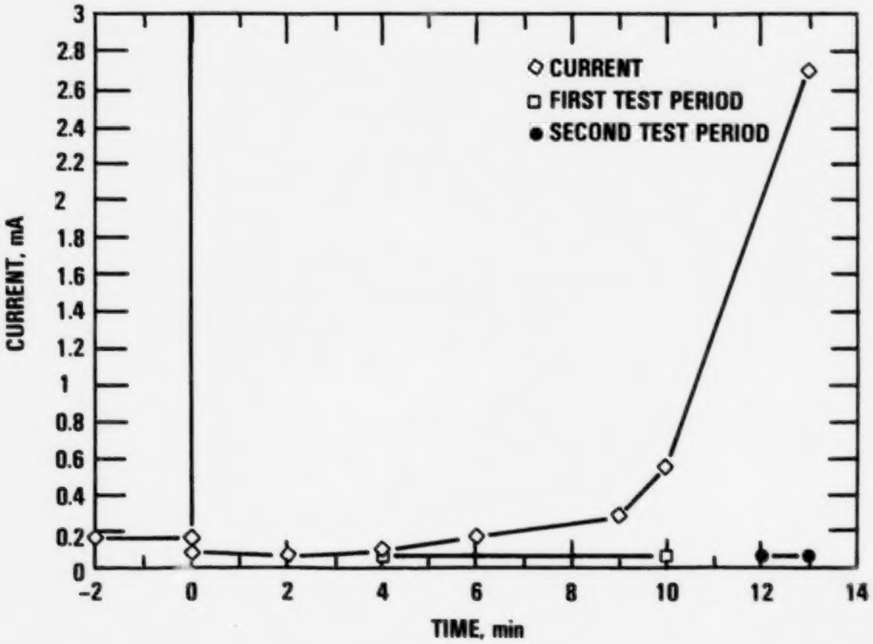

Figure 3. Variation in current with time for fly ash and hydrated lime at 45 kV. Lime injection began at time = 0 min.

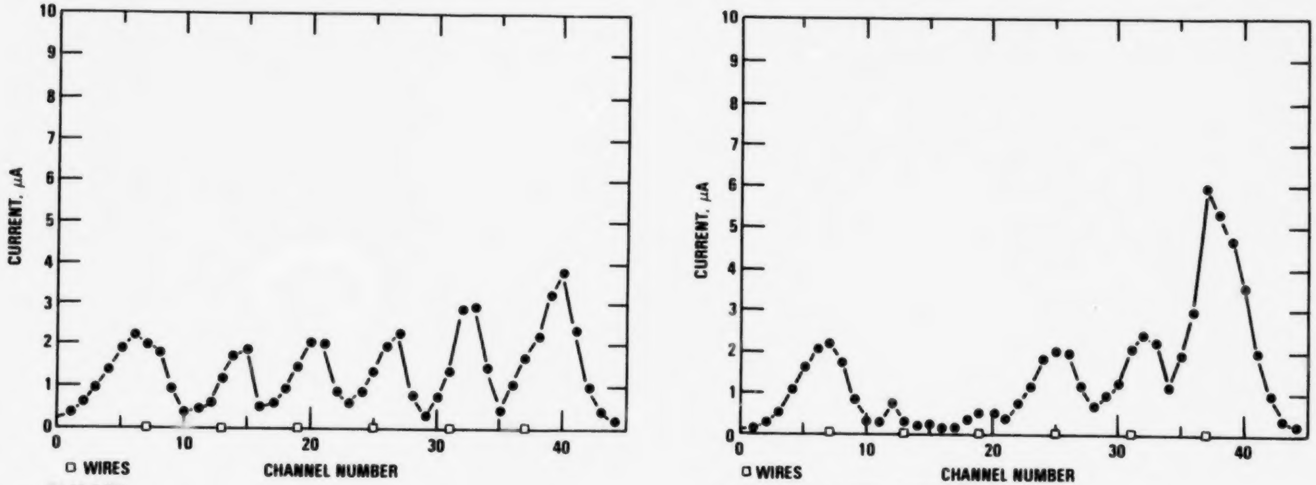

a. FLY ASH

b. FLY ASH + LIME, FIRST TEST

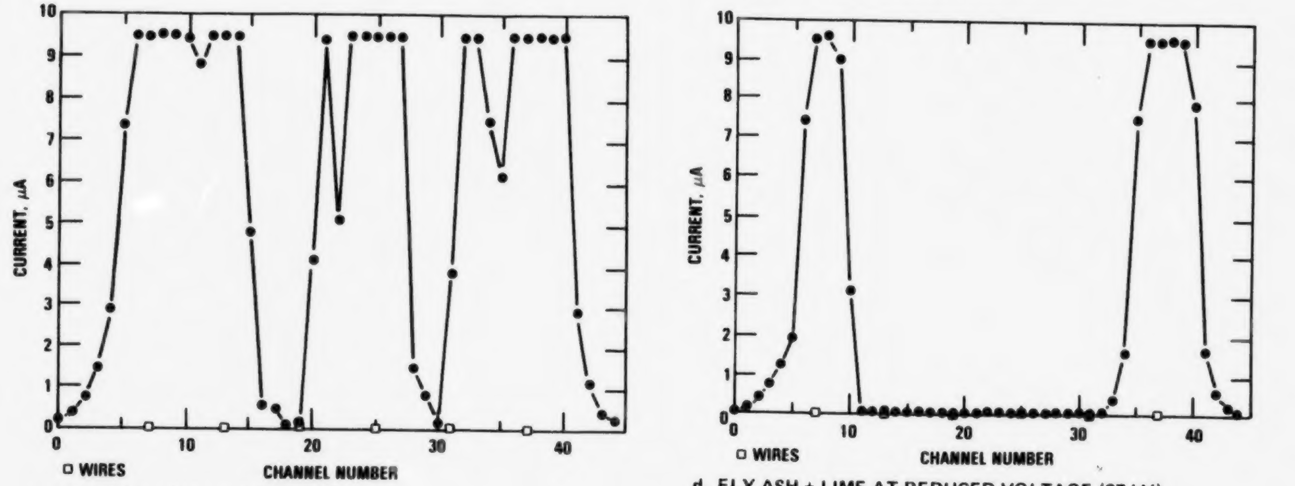

c. FLY ASH + LIME, SECOND TEST

d. FLY ASH + LIME AT REDUCED VOLTAGE (37 kV)

5676-64

Figure 4. Current on each plate strip for fly ash and lime at 45 kV.

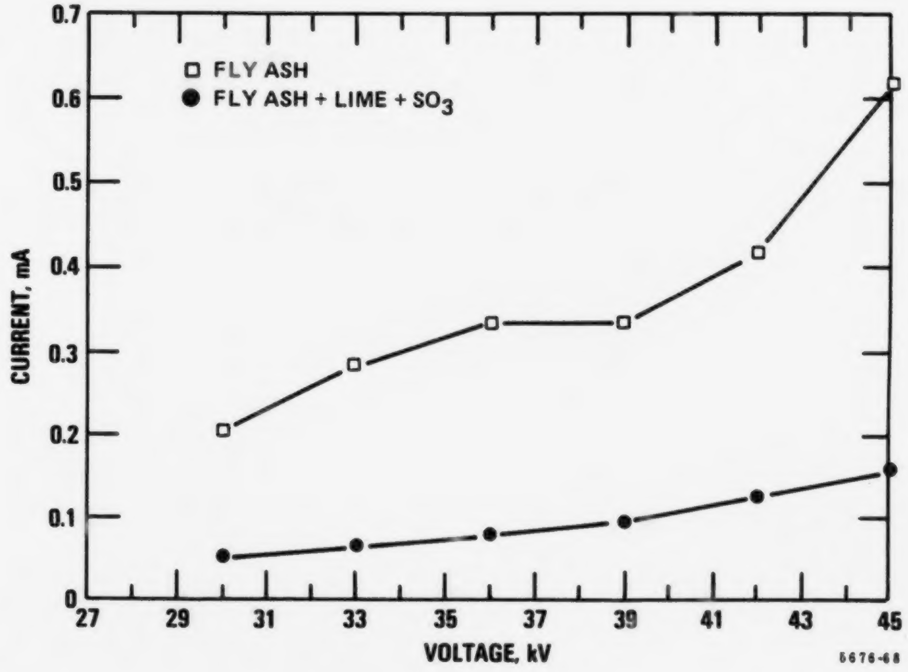

Figure 5. V-I curves for fly ash and fly ash + hydrated lime + SO_3.

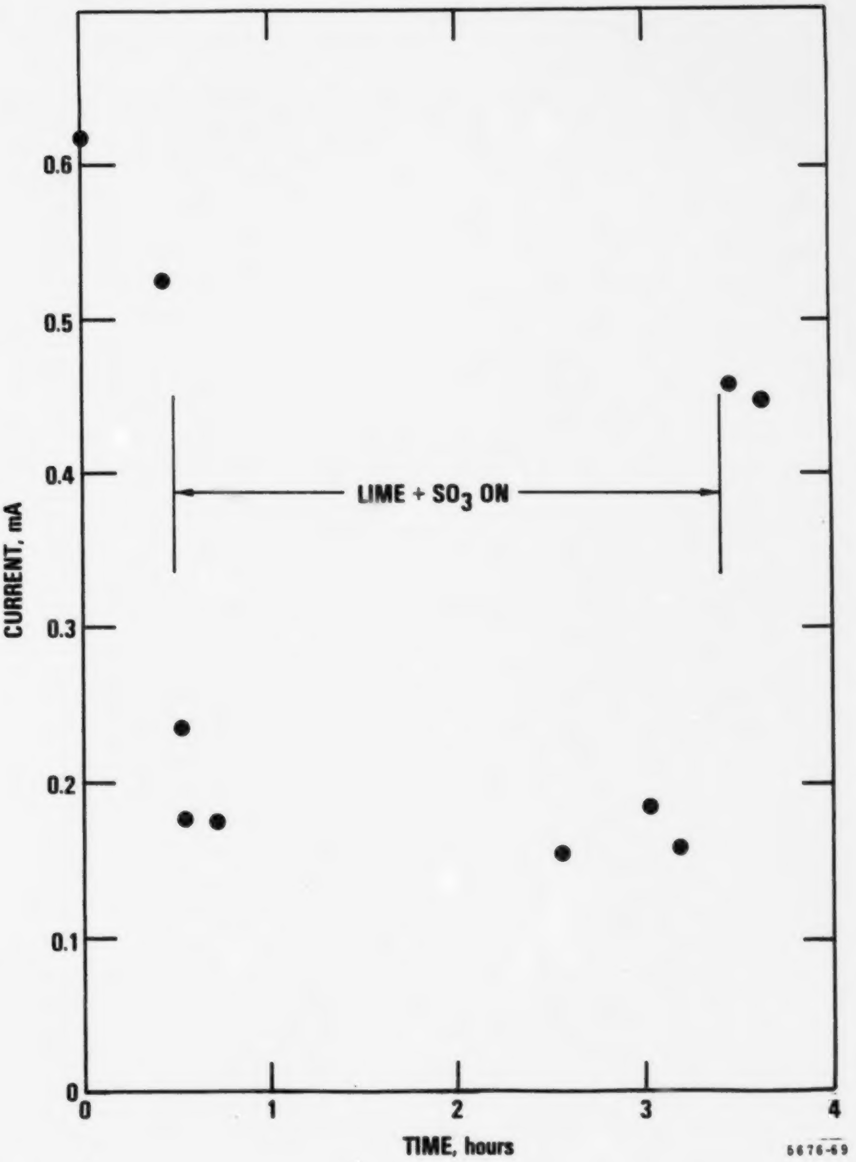

Figure 6. Variation in current with time for fly ash with hydrated lime and SO_3 conditioning at 45 kV.

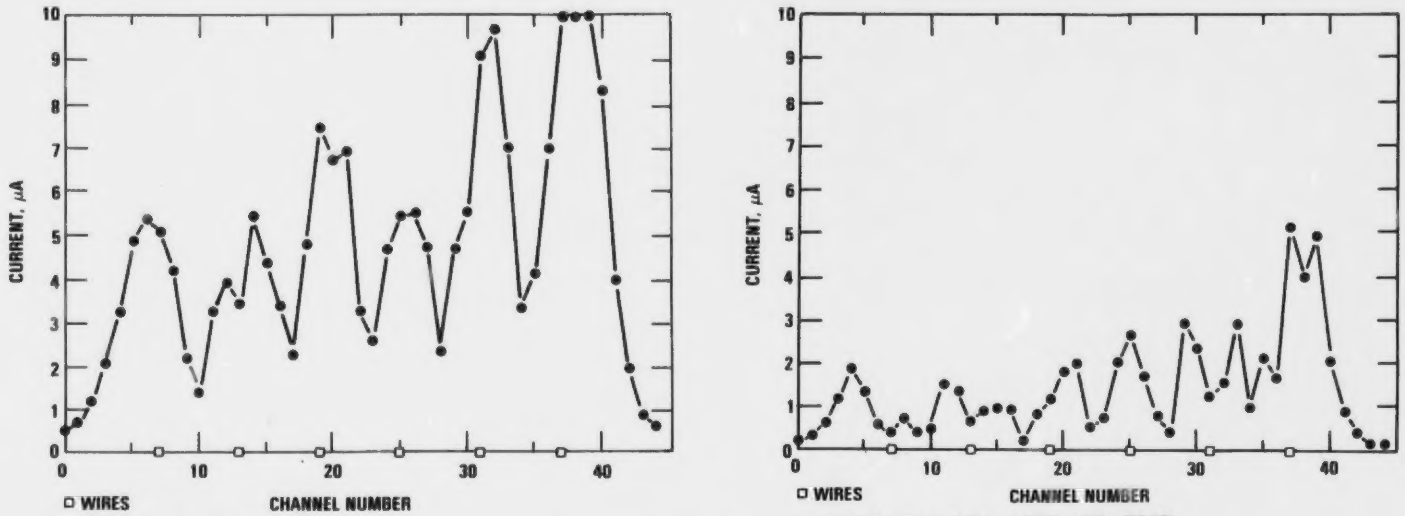

a. FLY ASH BEFORE CONDITIONING

b. INITIAL FLY ASH + LIME + SO_3 TEST

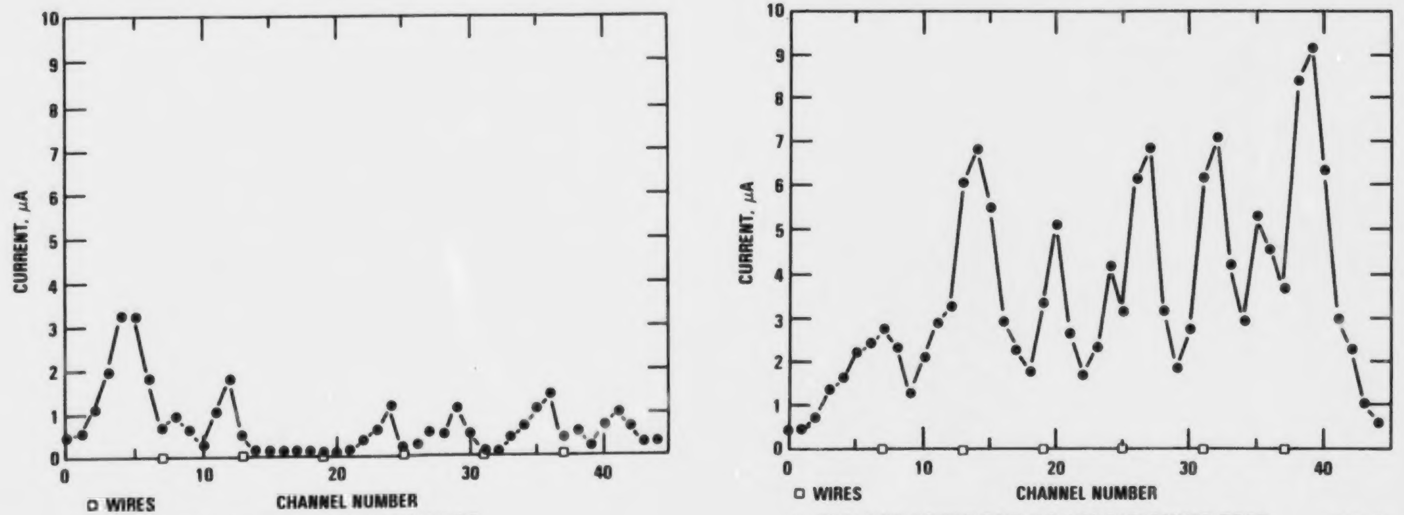

c. FLY ASH + LIME + SO_3 AFTER 3 HOURS

d. FLY ASH AFTER END OF CONDITIONING TEST

5676-70

Figure 7. Current on each plate strip for fly ash with hydrated lime and SO_3 conditioning at 45 kV.

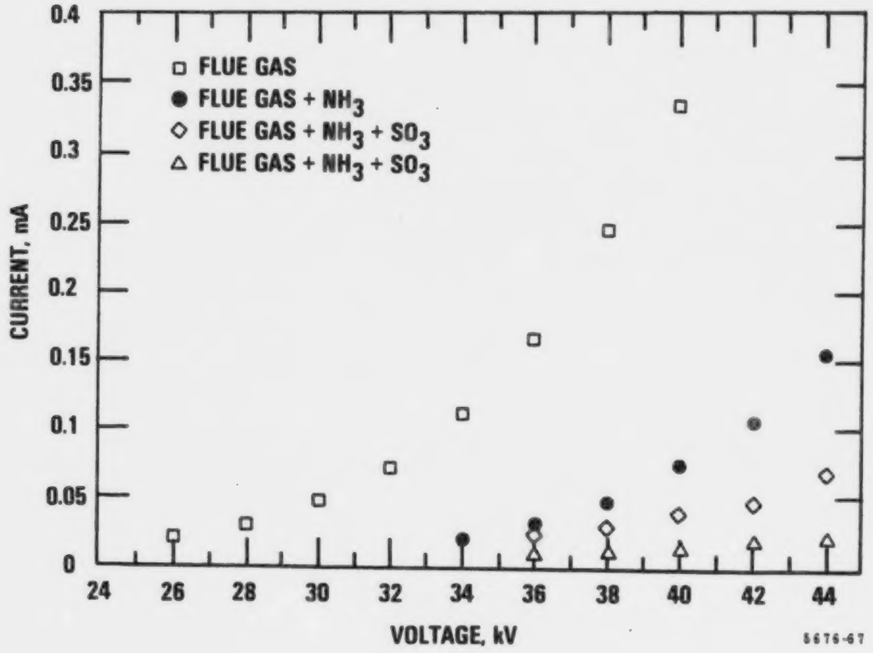

Figure 8. V-I curves for flue gas with ammonia and SO_3 addition.

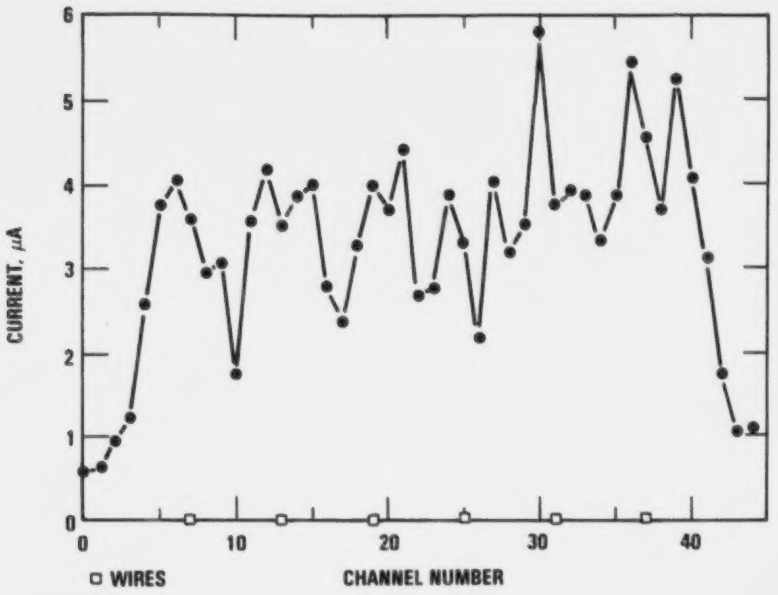

a. FLUE GAS

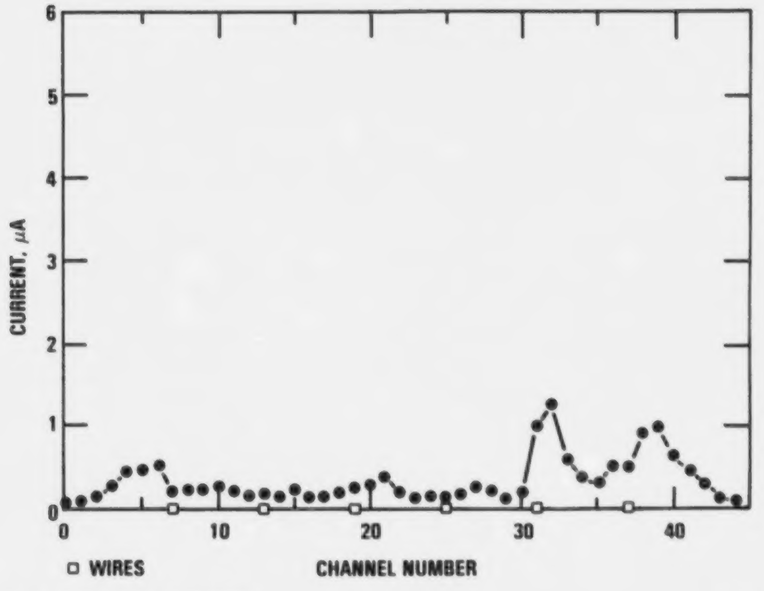

b. FLUE GAS + AMMONIA

5676-66

Figure 9. Current on each plate strip for flue gas with ammonia at 40 kV.

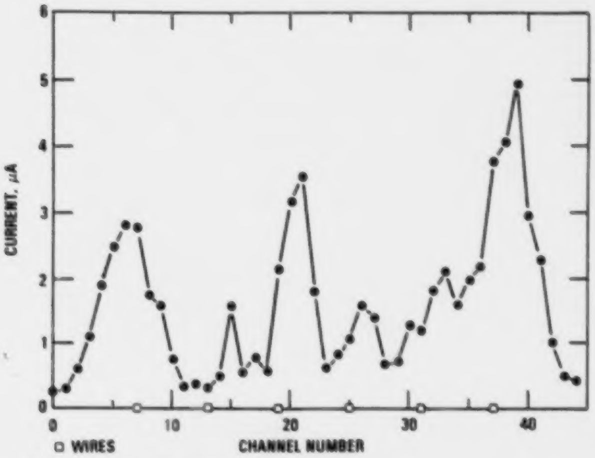

a. FLUE GAS + AMMONIA

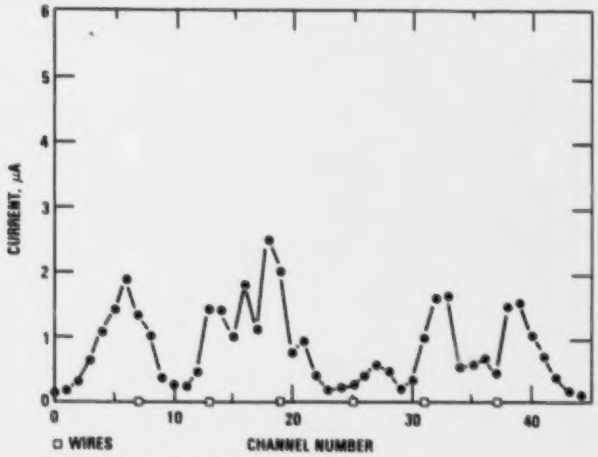

b. FLUE GAS + AMMONIA + 6 ppm SO_3

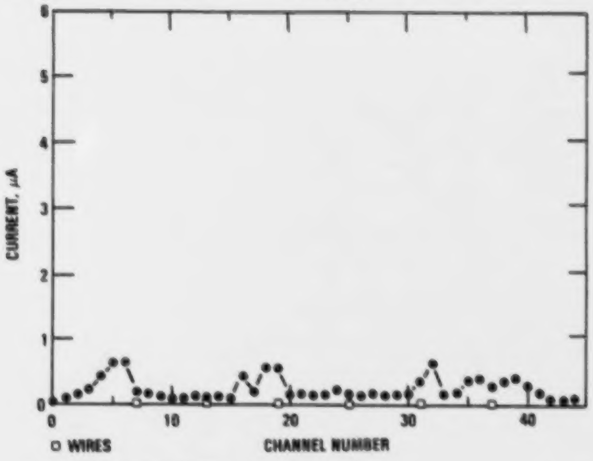

c. FLUE GAS + AMMONIA + 12 ppm SO_3

5676-66

Figure 10. Current on each plate strip for flue gas and ammonia and for flue gas, ammonia, and SO_3 at 45 kV.

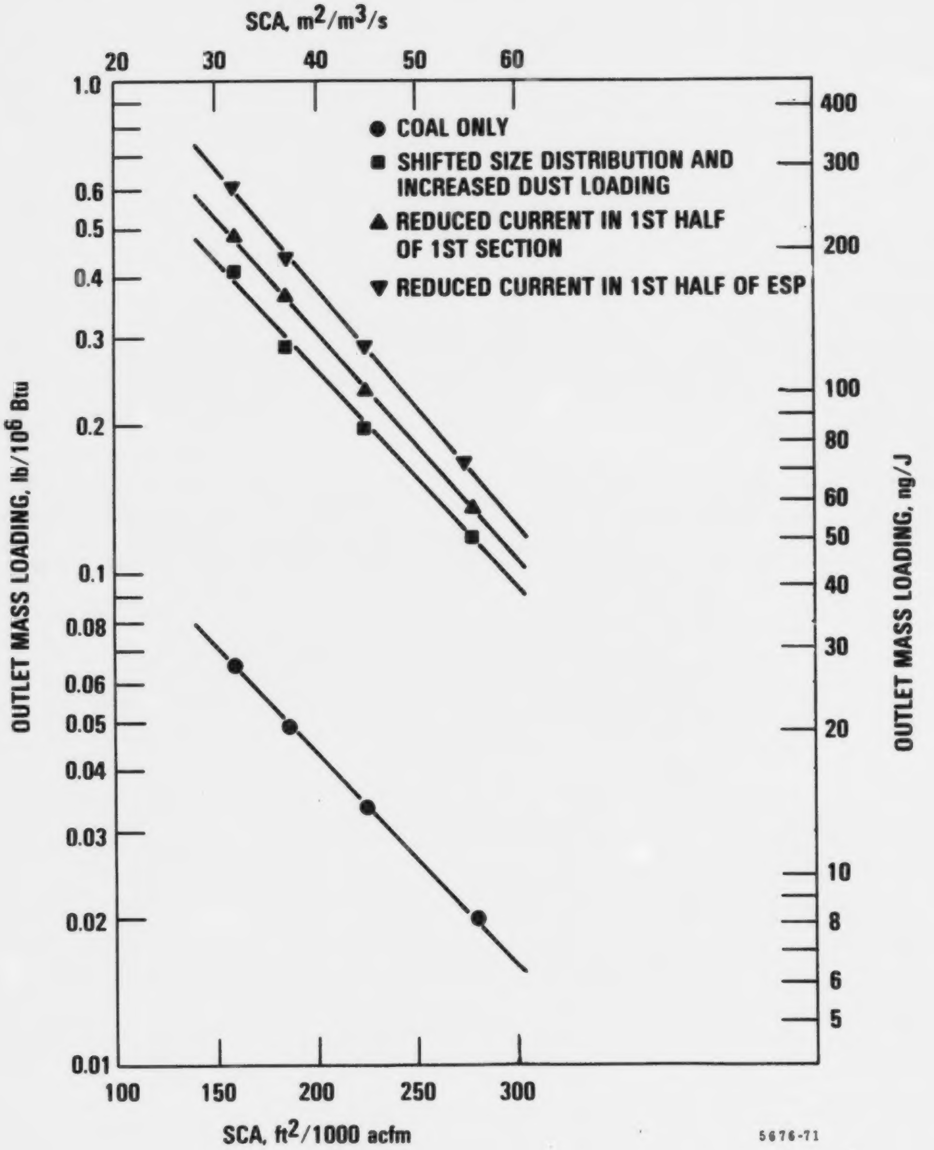

Figure 11. Outlet mass loading as a function of SCA for an ESP collecting coal with hydrated lime and SO_3.

THE EFFECTIVE DIELECTRIC CONSTANT OF FLY ASH

by: R. P. Young
J. L. DuBard
Southern Research Institute
Birmingham, Alabama 35255-5305

L. E. Sparks
Air and Energy Engineering Research Laboratory
U.S. Environmental Protection Agency
Research Triangle Park, North Carolina 27711

ABSTRACT

The electrical breakdown of a fly ash layer usually occurs at average electric fields which appear to be too small to produce the breakdown. AC dielectric measurements performed on a fly ash layer, in conjunction with the theory of Debye, can be used to determine an effective static dielectric constant at a given temperature. Using this dielectric constant in an expression for the local electric field which combines the effects of dielectric polarization and space charge in the layer, enhanced values of the local electric field are obtained which are sufficiently large to produce breakdown in the relatively large, gas-filled voids between particles. The effect of temperature and layer thickness on the onset of electrical breakdown within the fly ash can also be explained by the dependence of the effective dielectric constant on these parameters.

This paper has been reviewed in accordance with the U.S. Environmental Protection Agency's peer and administrative review policies and approved for presentation and publication.

INTRODUCTION

It has been established (1) that electrical breakdown within a dust layer is an ordinary electron avalanche process originating in voids within the dust layer and obeying Paschen's Law. This law states that the breakdown potential applied across a gas-filled gap is a function of the product of pressure (or gas density) and gap height. The dependence of breakdown field on the average particle size distribution of the fly ash can then be explained in terms of the average void dimension (gap height) associated with the distribution. However, Paschen's Law is of no help in explaining the influence of ash layer thickness on the onset of breakdown and of only limited use in explaining the role of temperature. By employing dielectric measurements, the complex dielectric constant of the fly ash can be obtained. An effective dielectric constant is then assigned to the ash which can be used to explain how temperature and layer thickness affect the electric field at breakdown. The technique of using dielectric measurements to obtain the complex dielectric constant of a coal fly ash has been previously demonstrated by Tassicker (2) and by Evans (3).

COMPLEX DIELECTRIC CONSTANT

When a sinusoidal voltage is applied to a dielectric material, a leakage current will be induced within the dielectric in addition to the resulting charging current. The existence of both the leakage and charging currents is conventionally represented by the use of a complex dielectric constant

$$\varepsilon^* = \varepsilon' - i\varepsilon'' \qquad (1)$$

to describe the dielectric. Here, both ε' and ε'' are functions of frequency. The real part of the dielectric constant, ε', is related to the equivalent parallel capacitance, C_p, of the material by

$$C_p = \varepsilon' C_0 \qquad (2)$$

where C_0 is the geometrical (air) capacitance of the measuring electrodes separated by a distance equivalent to the thickness of the dielectric. The imaginary part of the dielectric constant, ε'', is related to C_0 and the conductance, G, of the material according to

$$\varepsilon'' = \frac{G(\omega)}{\omega C_0} \qquad (3)$$

where ω is the angular frequency. By measuring C_p and G, ε' and ε'' can be determined from equations (2) and (3), respectively.

If the dielectric material is sufficiently dipolar in nature, the theory of Debye (4) can be applied to ε^*:

$$\varepsilon^* = \varepsilon_\infty + \frac{\varepsilon_{dc} - \varepsilon_\infty}{1 + i\omega t_0} \qquad (4)$$

where ε_∞ and ε_{dc} are the dielectric constants in the high and low frequency limits, respectively; and t_0 the characteristic relaxation time. Equation (4) can be separated into its real and imaginary parts:

$$\varepsilon'(\omega) = \varepsilon_\infty + \frac{\varepsilon_{dc} - \varepsilon_\infty}{1 + (\omega t_0)^2} \qquad (5)$$

$$\varepsilon''(\omega) = \frac{\omega t_0(\varepsilon_{dc} - \varepsilon_\infty)}{1 + (\omega t_0)^2} \qquad (6)$$

Cole and Cole (5) have shown that the Argand diagram of equation (4) is a circular arc from which ε_{dc} can be extrapolated.

When the data for ε' and ε" are somewhat scattered, Cole (6) has shown that more useful forms of equations (5) and (6) are obtained by multiplying both sides of each equation by $(1+i\omega t_0)$ and solving for ε' in terms of ε" and ε_{dc}:

$$\varepsilon'(\omega) = \varepsilon_{dc} - t_0(\omega\varepsilon'') \qquad (7)$$

For the purpose of extrapolating to ε_{dc}, equation (7) has the advantage of being a linear equation with intercept ε_{dc} and slope $-t_0$.

Auty and Cole (7) have shown that the contribution to ε" from the dc conductance of the layer must be corrected for in equation (3) before using equation (7). This can be done by subtracting the dc conductance, G_{dc}, from the conductance at higher frequencies:

$$\varepsilon''(\omega) = \frac{G(\omega) - G_{dc}}{\omega C_0} \qquad (8)$$

where $G(\omega)$ is the conductance obtained from the measured parallel resistance of the sample.

Because of the particulate nature of a fly ash, its dielectric constant will vary with position in the material. However, when Debye's theory can be applied to the layer, an average, "effective" dielectric constant (ε_{dc}) can be ascribed to the fly ash.

MATERIALS AND METHODS

The components of the apparatus used in these experiments are shown schematically in Figure 1. The fly ash was hand-deposited between the parallel plates of the test cell to a uniform depth of 0.5 cm, using a constant surface areal loading of 10 g/cm^2. A digital RLC bridge (GenRad model 1689) was connected to the cell electrodes as shown. The loaded test cell was then placed into an environmental chamber where the temperature and water vapor in the atmosphere could be controlled.

For each temperature and test frequency, the measuring circuit was zeroed for its open- and short-circuit impedance to obtain accurate values for the ash layer impedance. Then the equivalent parallel capacitance and resistance were measured for several different frequencies between 12 Hz and 100 kHz. For measurement temperatures above 250°C, a standard resistivity cell (IEEE Standard 548-1984) was used in place of the cell shown in Figure 1. The transition from measurements made with one cell to those of the other cell was smooth. Thus, it was concluded that no offset or error was introduced into the measurements by changing test cells.

Eleven different fly ash species were examined here. Since generally similar qualitative features were observed for these samples, the discussion will focus on the coal fly ash from the Wabamun Power Plant in Canada. The fly ash particles were predominantly spherical in shape and amorphous, with a mass median diameter of 33.5 μm.

RESULTS

The variation of ε' with frequency for the fly ash at 266°C and 9% water vapor (by volume) in the test environment is shown in Figure 2. The corresponding data for ε'' are shown in Figure 3. Here the value of G_{dc} in equation (8) has been approximated by the conductance at 12 Hz (the lower limit of the RLC bridge). As a result, the data of Figure 3 begin at 20 Hz rather than 12 Hz. Notice that the sudden decline in ε' for frequencies greater than 10 kHz is accompanied by a sudden increase in ε'' in these regions. This resonance behavior was predicted by Debye (4) and lends support to the validity of using Debye's analysis on fly ash. Figure 3 suggests that another resonance occurs in the low frequency limit which is not clearly resolved in Figure 2.

A plot of equation (7) for the data of Figures 2 and 3 is shown in Figure 4. Due to the broadness of the resonance in Figure 2 in the low-frequency region (indicating a distribution of relaxation times rather than a single t_0), better correlation of the data results if the use of equation (7) is restricted to measured (solid circles) and interpolated (open circles) values of ε' and ε'' in Figures 2 and 3 obtained at frequencies of 100 Hz or less. The interpolated values picked from the curves of Figures 2 and 3 are necessary because of the scarcity of data in this frequency range. Application of linear regression to the data in Figure 4 yielded a value of 16.4 for ε_{dc} with a correlation coefficient (r^2) of 0.99.

Applying the foregoing extrapolation procedure to data obtained at many different temperatures results in Figure 5. Generally, ε_{dc} is quite sensitive to temperature changes in the high temperature limit but becomes progressively less sensitive as the temperature decreases, approaching an asymptotic behavior in the low temperature limit. Also, the presence of moisture in the test atmosphere had little or no effect on the value of ε_{dc} obtained at a given temperature. Figure 6 shows the variation of ε_{dc} with dust layer thickness at three different temperatures. The relationship is essentially linear for the range of thicknesses used.

DISCUSSION

Previous work (1) has shown that the electrical breakdown originates in relatively large voids (on the order of tens of micrometers) and obeys Paschen's Law. For the ash layers used in this study, Paschen's Law predicts electric field strengths at breakdown in the range of 235 to 365 kV/cm, depending on the temperature of the layer (7). Figure 7 shows the dependence of the average electric field across the dust layer at breakdown, E_{BD}, on temperature for Wabamun fly ash in the presence of the indicated amounts of atmospheric moisture (volume percent). Since the average fields in this figure are in the range of 4 to 10 kV/cm, it is clear that an enhanced local electric field in a void space between particles, E_{loc}, corresponds to the breakdown field of Paschen's Law. McDonald, et al. (8), by treating the dust layer as a collection of spherical particles all of the same size and arranged in a cubic array, have shown that the combined effects of polarization and space charge due to a potential applied across the layer result in a maximum local electric field strength given by

$$E_{loc} = 1.5 \, [1 + 1.25 \, (\varepsilon_{dc} - 1)] E_0 \qquad (9)$$

where E_0 is the applied electric field. Using values of ε_{dc} of 12 and 31 at the temperature extremes of Figure 5, equation (9) predicts local electric fields which are 22 to 58 times that of the applied field, in rough agreement with the predictions of Paschen's Law. Table 1 compares the values of E_{loc} obtained from Paschen's Law from the data of Earhart (9), E(P), and those obtained using Figure 7 (9% H_2O) and equation (9), E(9). The two values agree within a factor of about two, which is remarkable considering the uncertainties and approximations involved in this comparison.

The dependence of ε_{dc} on temperature has been shown by many investigators, including Debye (4). A rather complete review of the important early work in this area was given by Frohlich (10). For temperatures above about 200°C, ε_{dc} increases rapidly with increasing temperature (Figure 5). Then equation (9) predicts that progressively lower values of E_0 (E_{BD}) will be required to produce an E_{loc} of sufficient magnitude to initiate breakdown as the temperature increases. This agrees with the data of Figure 7. For lower temperatures, ε_{dc} becomes nearly independent of temperature and E_{BD} remains relatively constant as temperature decreases. It has been previously shown (7) that the presence of moisture affects the conduction mechanism, thereby reducing the magnitude of E_{BD} necessary to initiate breakdown. The fact that ε_{dc} is not sensitive to the presence of moisture (Figure 5) for temperatures below about 150°C, where surface conduction is dominant over volume conduction (11), indicates that this constant is not affected by the condition of the surface of the particles.

Since the charge carriers within the dust layer are ionic (11,12), the metal electrode in the test cell is incapable of exchanging charge carriers with the layer surface. When an electric field is applied, this "blocking electrode" causes charge to build up just inside the dust layer at the electrode-layer interface. This layer of charges and the corresponding charges on the metal electrode constitute a "double layer" of charge at the interface. A detailed analysis concerning the nature of this double layer is contained in the work of Conway (13). For our purpose, it is sufficient to note that the existence of the double layer at each electrode makes the test cell arrangement functionally equivalent to three capacitors in series. Then assigning an effective dielectric constant to the entire dust layer is tantamount to replacing the three capacitors by a single equivalent capacitor, using the usual reciprocal relationship for combining capacitors in series. The dependence of ε_{dc} on layer thickness then arises quite naturally from this replacement process and the dependence of each capacitance term on the thickness of the dielectric.

Figure 8 shows the dependence of E_{BD} on dust layer thickness for the fly ash. In general, E_{BD} decreases as the thickness increases for a given temperature. This behavior is readily explained by equation (9) and the data of Figure 6: thicker dust layers have larger effective dielectric constants so they require smaller values of E_{BD} to produce a given E_{loc}.

The data of Figures 6 and 8 can also be used to check the validity of the predictions of equation (9). Table 2 shows the correlation between the ratios of ϵ_{dc} for 250°C to the ratios of E_{loc} from equation (9), E(9), normalized to the data for a 0.1 cm thickness (el and El). The agreement is quite good considering the roughness of the comparison. Thus, the technique used by McDonald et al. of combining the contributions of polarization and space charge within the layer appears to be justified.

CONCLUSIONS

Using ac dielectric measurements of dust layers and applying the theory of Debye allows the determination of an effective dielectric constant to characterize the layer. Combining this constant with an expression for the enhanced local electric fields across the voids between particles in the bulk where electrical breakdown occurs produces agreement with values of electrical field at breakdown predicted by Paschen's Law. The effective dielectric constant increases with increasing temperature and explains the corresponding decrease in applied electric field necessary to produce breakdown. For increasing dust layer thickness, the effective dielectric constant also increases, accompanied by a decrease in the applied field which will initiate breakdown.

REFERENCES

1. Young, R., DuBard, J., and Sparks, L. The onset of electrical breakdown in dust layers. In: Proceedings: Fifth Symposium on the Transfer and Utilization of Particulate Control Technology: Volume 2, EPA-600/9-86-008b (NTIS PB86-167160), February 1986.

2. Tassicker, O., The temperature and frequency dependence of the dielectric constant of power-station fly ash. Staub-Reinhalt. Luft, 31(1971)23-8.

3. Evans, R., The Dielectric Properties of Fly Ash from Western Coals. Thesis, U. of North Dakota, 1978.

4. Debye, P., Polar Molecules. Chemical Catalog Co., New York, (1929).

5. Cole, K. and Cole, R., Dispersion and adsorption in dielectrics. I. Alternating current characteristics. J. Chem. Phys., 9(1941)341-51.

6. Cole, R., On the analysis of dielectric relaxation measurements. J. Chem. Phys., 23(1955)493-9.

7. Auty, R. and Cole, R., Dielectric properties of ice and solid D_2O. J. Chem. Phys., 20(1952)1309-14.

8. McDonald, J., Mosley, R., and Sparks. L., An approach for describing electrical characteristics of precipitated dust layers. APCA J., 30(1980) 372-6.

9. Earhart, R., The discharge of electricity through gases at various temperatures. Phys. Rev., 31(1910)652-61.

10. Frohlich, H., Theory of Dielectrics. Oxford University Press, London (1949).

11. Bickelhaupt, R., Surface resistivity and the chemical composition of fly ash. APCA J., 25(1975)148-52.

12. Bickelhaupt, R., Electrical volume conduction in fly ash. APCA J., 24(1974) 251-5.

13. Conway, B., Theory and Principles of Electrode Processes. The Ronald Press Company, New York (1965).

Table 1. COMPARISON OF E_{loc} FROM PASCHEN'S LAW AND FROM EQUATION (9).

Temp. (°C)	Fig. 7 E_{BD} (kV/cm)	Fig. 5 ε_{dc}	E(9)* (kV/cm)	E(P)† (kV/cm)	$\frac{E(P)}{E(9)}$
155	8	12.5	185	286	1.6
260	4	15.2	113	235	2.1

*Calculated from equation (9)
†Obtained from Paschen's Law, Reference 9

Table 2. CORRELATION OF ε_{dc} WITH E_{loc} FROM EQUATION (9) AT 250°C.

Layer Thickness (cm)	ε_{dc}	E(9) (kV/cm)	$\frac{\varepsilon_{dc}}{\varepsilon 1^*}$	$\frac{E1^*}{E(9)}$	% Difference of Ratios
0.1	7.8	249	--	--	--
0.2	10.1	223	1.29	1.12	13
0.4	13.3	160	1.71	1.56	9
0.5	14.8	137	1.90	1.82	4
0.95	21.9	108	2.81	2.31	18

*Value for 0.1 cm thick layer.

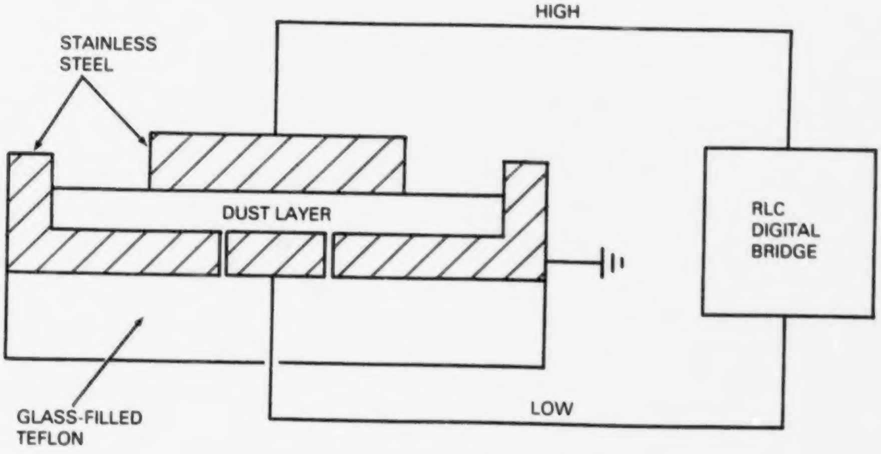

Figure 1. Schematic diagram for ac dielectric measurements.

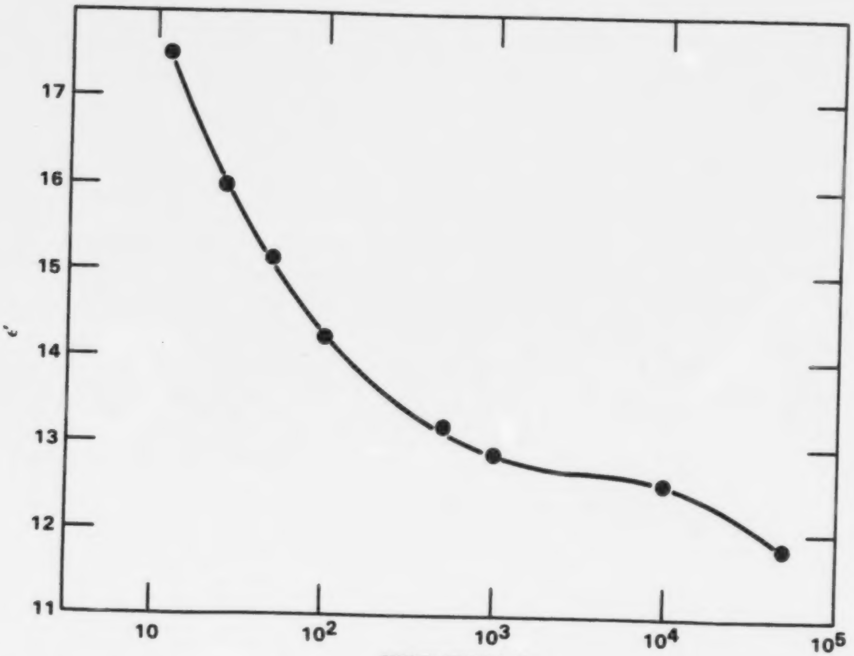

Figure 2. Real part of the dielectric constant of Wabamun fly ash at 266 °C and 9% water vapor.

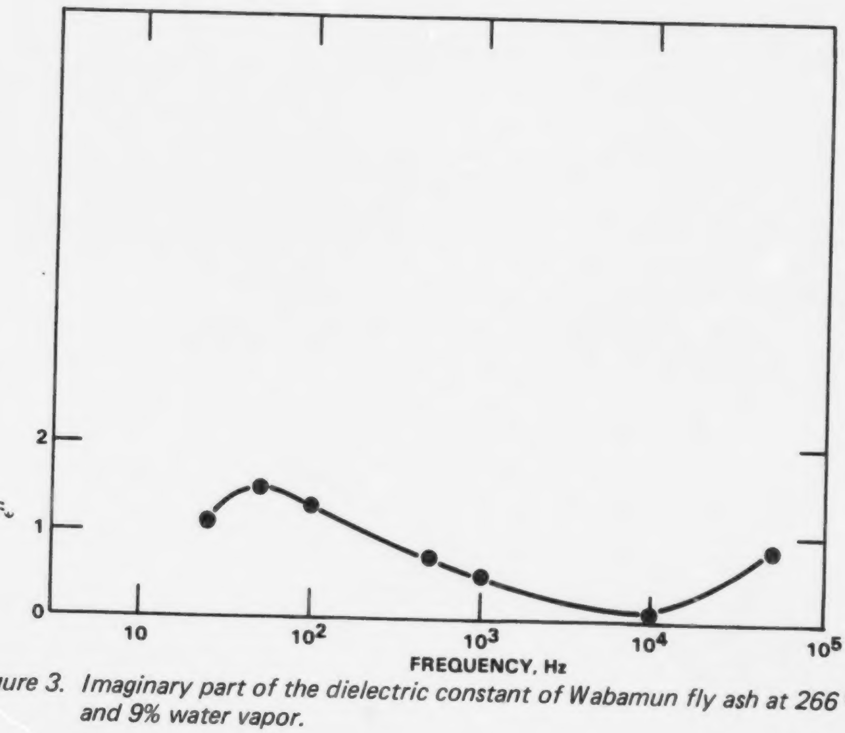

Figure 3. Imaginary part of the dielectric constant of Wabamun fly ash at 266 °C and 9% water vapor.

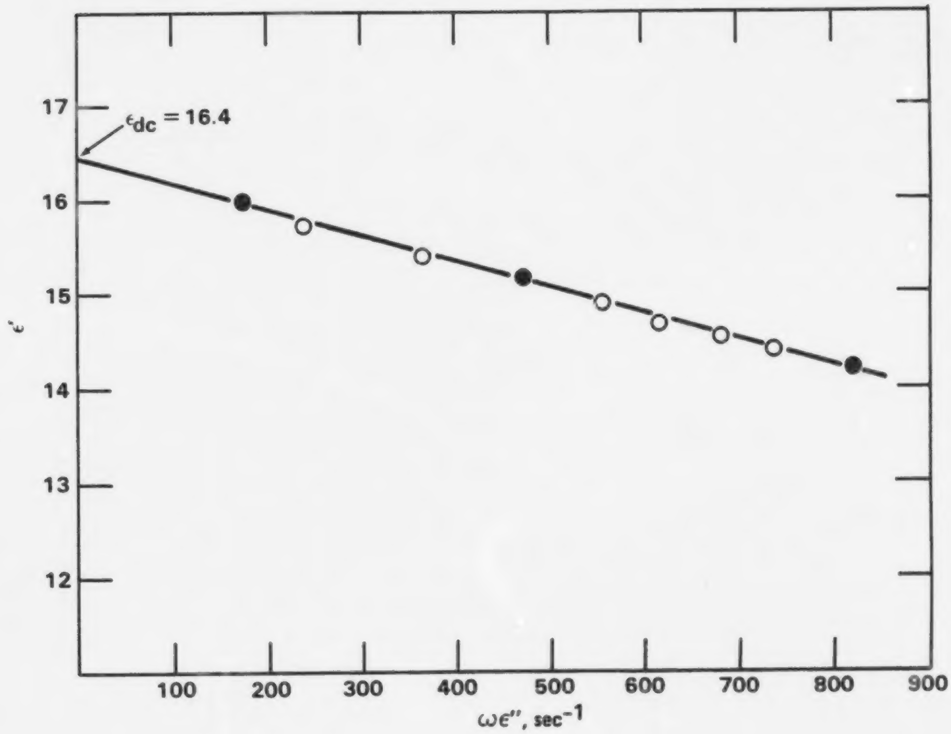

Figure 4. Plot of equation (7) for Wabamun fly ash at 266 °C and 9% water vapor.

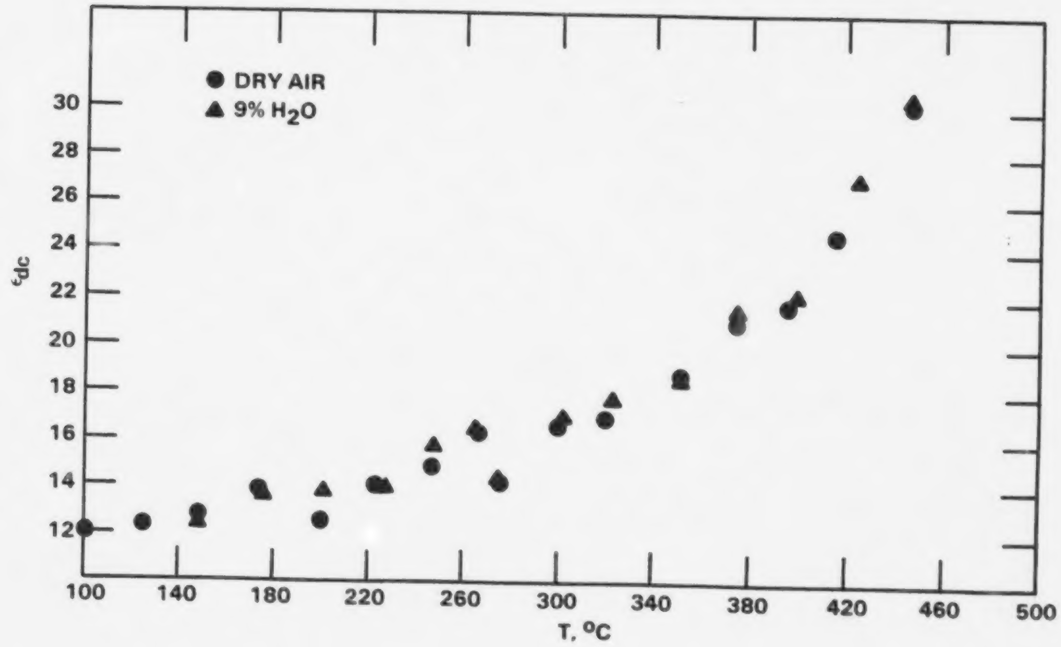

Figure 5. Variation of ϵ_{dc} with temperature of Wabamun fly ash.

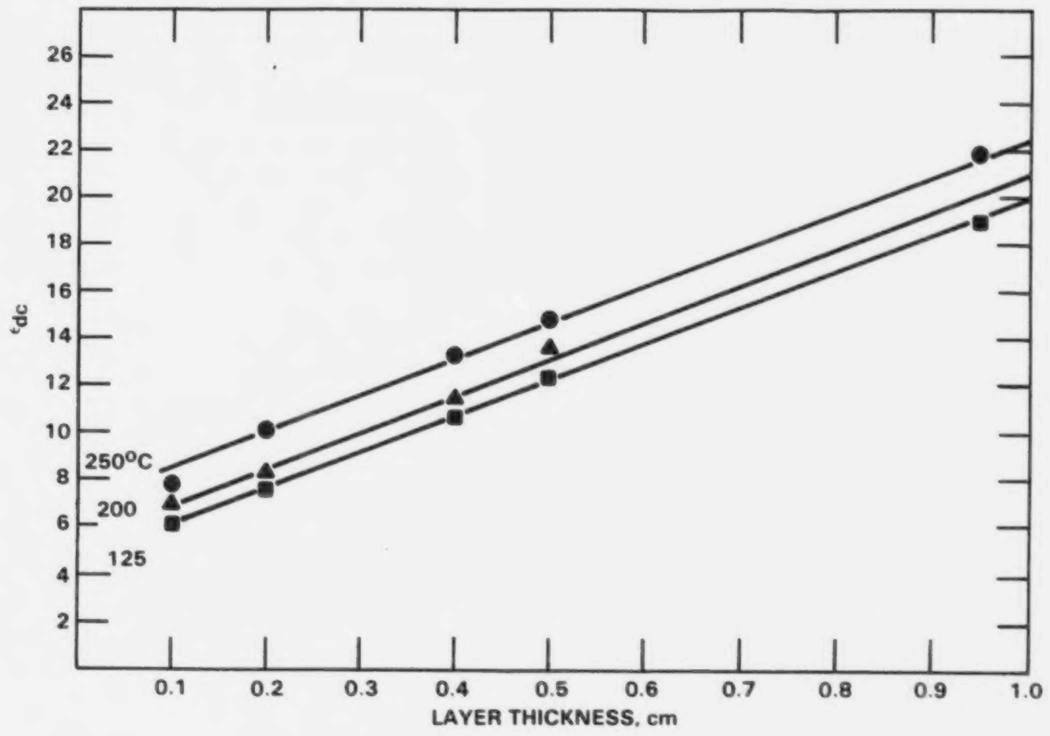

Figure 6. Variation of ϵ_{dc} with layer thickness of Wabamun fly ash.

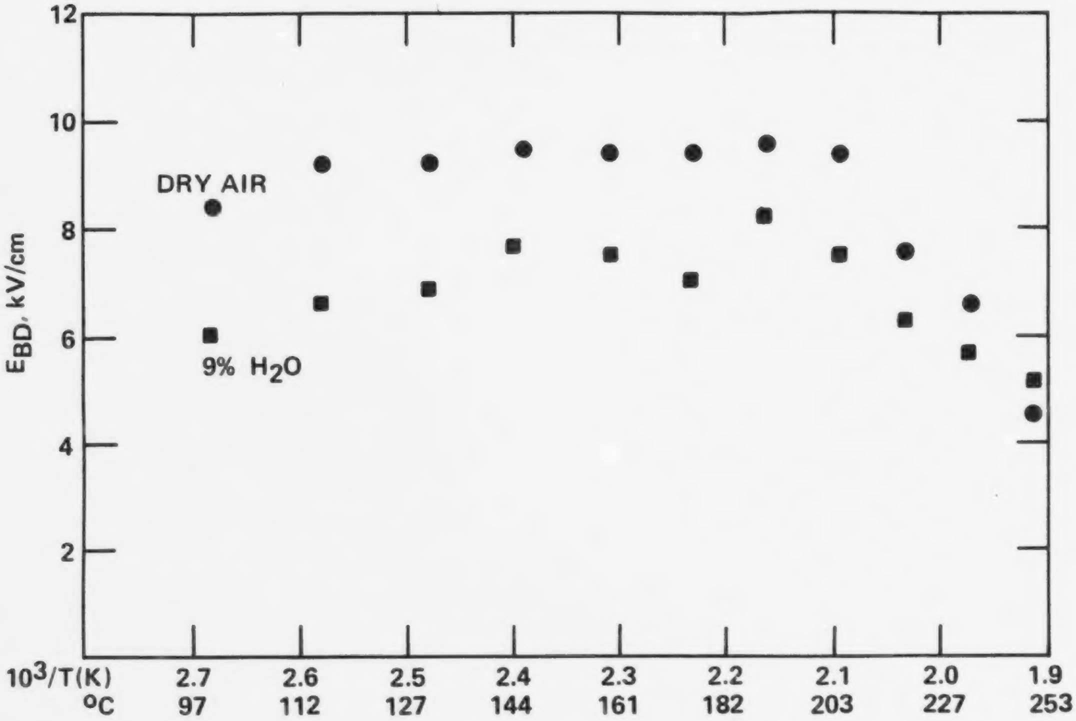

Figure 7. Variation of E_{BD} with temperature and moisture of Wabamun fly ash.

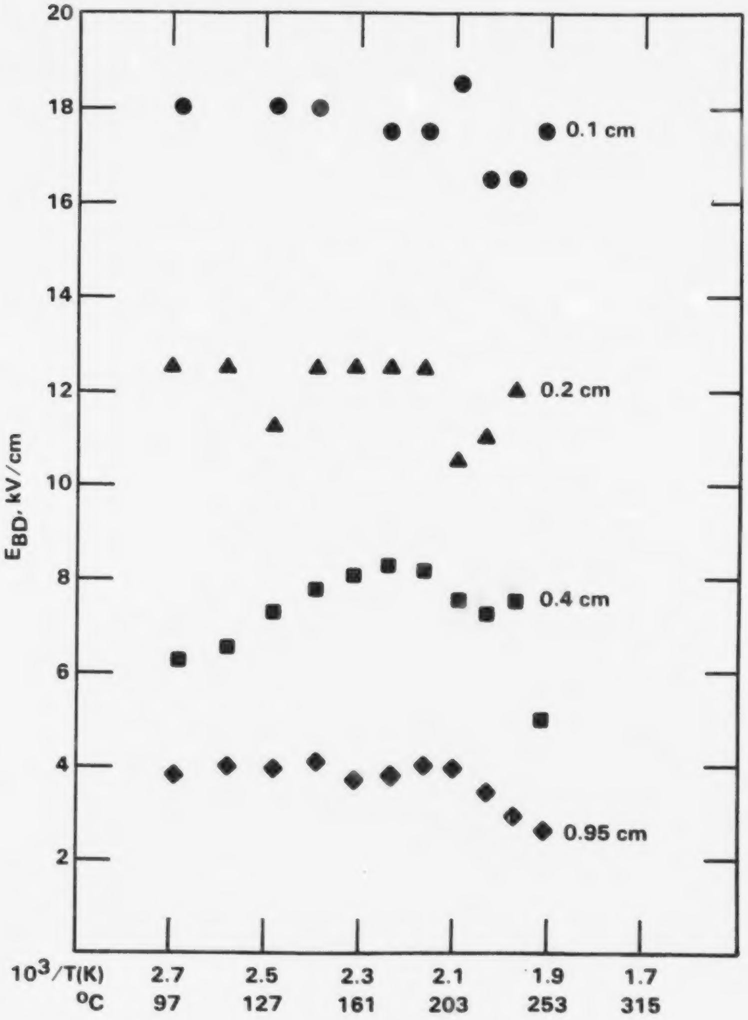

Figure 8. Variation of E_{BD} with layer thickness of Wabamun fly ash at 9% water vapor.

DIAGNOSTIC TECHNOLOGY OF PRECIPITATOR OPERATION

By: Senichi Masuda, Toshifumi Itagaki, and Shunsuke Hosokawa
Department of Electrical Engineering,
University of Tokyo
7-3-1, Hongo, Bunkyo-ku, Tokyo 113, Japan

ABSTRACT

The importance of in-situ diagnosis of operating variables determining performance of electrostatic precipitators has been recognized. An on-line bipolar current probe and an on-line dust surface loading meter have been developed and modified to be suited for the fields tests. The former is used to measure the back corona severity and the latter provides an information on the space charge effect. When they are used together with the conventional instruments such as a dust resistivity meter, a continuous dust monitor, an image intensifier, and so on, better understanding of precipitation variables known and unknown, is expected to be in our hand.

INTRODUCTION

The diagnosis of an electrostatic precipitator under operation becomes important to clear the causes of performance degradation. There are many unfavorable conditions for an ESP such as back corona, reentrainment, corona quenching, difficult particle size (submicrometer in diameter) and so on. In a practical plant, however, the observable parameters are restricted to the mean voltage and current of the high voltage power supply indicated in a front panel of a controller, and in some cases to the opacity of the exit gas. Occasional dust sampling provides the overall collection performance. They gives very little information on the causes of performance degradation and there are many misunderstanding in practical fields.

Moreover, as reported in another paper,[1] a hidden parameter behind back corona such as corona quenching under dc energization comes out as soon as back corona is corrected by pulse energization. The dust with extremely high resistivity produces back corona even under pulse energization. In such cases, the necessity of the diagnosis under operation is pronounced.

The authors has been using the conventional instruments as a voltage divider, an image intensifier, and a constant dust monitor in the field tests. The pulse voltage wave form indicates both back corona and corona quenching effect. The light activity on a collection electrode observed by an image intensifier indicates the occurrence of back corona. The dust space charge induced trouble like corona quenching can be detected by observing corona electrodes, active in corona only on the wires on the upstream side, but drastically diminished or completely quenched on the downstream side. However, the more precise measurements of the back corona severity and corona quenching effect on a quantitative basis are needed for diagnosis and trouble-shooting of a substandard ESP.

The authors has developed a bipolar ionic current prove [2-4] to measure the severity of back corona, and an instrument for measuring "dust surface loading" (total surface of dust particles contained in a unit volume of gas) which is a parameter determining the dust space charge effect. This paper reports on these two instruments developed for the field use.

BIPOLAR IONIC CURRENT PROVE

The bipolar ionic current probe has been developed to measure the back corona severity and field distribution in an ESP, and it is now usable in a field test.[4] Fig. 1 shows the probe with three electrodes (electrodes 1, 2 and 3). When it is inserted in an ESP and its potential is set equal to the local undisturbed potential (balanced condition), the electric line of force becomes symmetric as shown in Fig. 2 and the positive ions flow into the electrode 3 and the negative ions into the electrode 1. As the result, both negative and positive ionic currents can be measured separately.

In order to attain the balanced condition one, a variable dc bias voltage has been applied to the probe. However, this method fails in the cases when the voltage fluctuates owing to severe back corona, and when pulse energization is applied. However, when the bias voltage is produced by a voltage divider connected between the corona and collection electrodes, the balanced condition is kept unaltered at any instant of voltage. But the ratio of a divider is not easy to change. As a result, the modification is made in such a way that its ratio set at a fixed value, and the probe position is changed so as to attain the balanced condition. A motor traverses the prove in the direction of electric field.

THEORETICAL BACK GROUND

Let us consider the case of the asymmetric probe (see Fig. 2). The electrodes 2 and 3 are divided by the center plane. When the prove with its potential V is inserted in an ESP with the electrode 1 facing to the corona wire, the ionic currents measured by the electrodes 1, 2, and 3 are:

$$I_1 = i_+\ell\{-4a\cos\delta' - \frac{(\pi/2 - \delta')Q}{\pi\varepsilon_0 E_0}\} \qquad (Q < -4\pi\varepsilon_0 aE_0) \qquad (1)$$

$$= i_+\ell\{4a(\cos\theta_0 - \cos\delta') - \frac{(\theta_0 - \delta')Q}{\pi\varepsilon_0 E_0}\}$$

$$+ i_-\ell\{-4a\cos\theta_0 - \frac{(\pi/2 - \theta_0)Q}{\pi\varepsilon_0 E_0}\} \qquad (-4\pi\varepsilon_0 aE_0 \leqq Q < -4\pi\varepsilon_0 aE_0 \sin\delta') \quad (2)$$

$$= i_-\ell\{-4a\cos\delta' - \frac{(\pi/2 - \delta')Q}{\pi\varepsilon_0 E_0}\} \qquad (-4\pi\varepsilon_0 aE_0 \sin\delta' \leqq Q) \qquad (3)$$

$$I_2 = i_+\ell\{4a(\cos\delta' - 1) - \frac{\delta' Q}{\pi\varepsilon_0 E_0}\} \qquad (Q < -4\pi\varepsilon_0 aE_0 \sin\delta') \qquad (4)$$

$$= i_+\ell\{-4a(1 - \cos\theta_0) - \frac{\theta_0 Q}{\pi\varepsilon_0 E_0}\}$$

$$+ i_-\ell\{-4a(\cos\theta_0 - \cos\delta') - \frac{(\delta' - \theta_0)Q}{\pi\varepsilon_0 E_0}\} \qquad (-4\pi\varepsilon_0 aE_0 \sin\delta' \leqq Q < 0) \qquad (5)$$

$$= i_-\ell\{-4a(1 - \cos\delta') - \frac{\delta' Q}{\pi\varepsilon_0 E_0}\} \qquad (0 \leqq Q) \qquad (6)$$

$$I_3 = i_+\ell(4a - \frac{Q}{2\varepsilon_0 E_0}) \qquad (Q < 0) \qquad (7)$$

$$= i_+\ell\{4a\cos\theta_0 - \frac{(\pi/2 + \theta_0)Q}{\pi\varepsilon_0 E_0}\}$$

$$+ i_-\ell\{4a(1 - \cos\theta_0) + \frac{\theta_0 Q}{\pi\varepsilon_0 E_0}\} \qquad (0 \leqq Q < 4\pi\varepsilon_0 aE_0) \qquad (8)$$

$$= i_-\ell(4a - \frac{Q}{2\varepsilon_0 E_0}) \qquad (4\pi\varepsilon_0 aE_0 \leqq Q) \qquad (9)$$

where $\theta_0 = \sin^{-1}(-\frac{Q}{4\pi\varepsilon_0 aE_0})$,

$$\delta' = \frac{d}{a} \qquad (10)$$

where the undistorted local field around the probe is assumed to be uniform with its intensity E_0, Q represents the total change induced on a unit length of the probe, i_+ and i_- the positive and the negative ionic current densities in the local field, and a, d, and l the dimensions of the probe (see Fig. 1; d is the length along the circle).

When the probe is traversed in the direction of electric field, the magnitude of Q change as:

$$Q = \frac{2\pi\varepsilon_0 E_0}{\ln\frac{h}{a}}(h - h_0)(1 + \frac{a^2}{hh_0}) \qquad (11)$$

where h is the position of the probe measured from the collection electrode and h_0 position of the balanced point for the probe potential, V. As a result, I_1, I_2, and I_3 become functions of h. At the balanced position the ratio I_2/I_1 gives a fixed value (balanced ratio) determined by the ratio $\delta' = d/a$.

TEST OF THEORY

A needle to plane electrodes system without back corona is used in combination with an asymmetric probe having the balanced ratio $I_2/I_1 = 0.166$ to check the probe theory described above. Fig. 3 shows both the test plots and the theoretical line. The value of h_0 is determined by the detection of the balanced ratio, and this is used as a reference point to draw the theoretical line. It can be seen from this figure that the correlation between the plots and the theory is very satisfactory, and that this probe traverse method is applicable.

PRACTICAL PROBE SET-UP

Fig. 4 shows the new probe set-up based on the probe traverse method. The box unit, where a probe holder, a current meter, and a power supply are installed, is moved with the probe by a stepping motor so that the probe position from the collection electrode, h, is changed.

DUST SURFACE LOADING METER

It has been discovered recently in Japan, concerning the carbon soot induced space charge effect, that:

(1) The corona current drops by 10 - 20 % at 1 % excess air in a boiler from its value at 2 % excess air.

(2) The corona current becomes one order of magnitude smaller at 10 - 20 % carbon content in flyash than that without carbon soot.

(3) The space charge induced performance drop becomes distinct at the dust surface loading $S = 10\ m^2/m^3$, and very detrimental at $S = 50\ m^2/m^3$.

These are the informations obtained from the boiler plants subjecting to the carbon soot induced space charge troubles, now very often occurring by the use of "Low NOx Burners" and "Low NOx combustion" being operated at a reduced excess air ratio. Moreover, the authors discovered in field tests that the space charge effect is masked when back corona occurs providing the positive ions to reduce space charge level, but as soon as back corona is removed by pulse energization, corona quenching immediately begins to appear. This may provide one of the possible explanations on the current confusing results of pulse energization.

In consideration of the utmost importance to investigate the space charge effect, as the hidden variable behind back corona, the authors developed an instrument for measuring the dust surface loading, S. It consists of a precharger possible to impart Pauthenier's theoretical charge to suspended particles and a suction-type Faraday cage combined with an electrometer. A ceramic-made cylindrical "Boxer-Charger" is used as the precharger. Fig. 5 shows the schematic diagram of this dust surface loading meter and Fig. 6 the photographs of its main components: "Boxer-Charger" and Faraday case.

BOXER-CHARGER

The detailed descriptions on the design and charging performance of "Boxer-Charger" are omitted, because they have been reported separately.[4-7]

A cylindrical tube with 40 mm in the inner diameter, made of 92 % alumina and attached with a pair of ionizer electrodes is used for the "Boxer-Charger" to be operated at an elevated temperature up to 300 °C. Even at such a high temperature alumina ceramic is a stable and reliable insulator. Although the electric field of the charging zone in the cylinder is distorted because of its electrode configuration, it can provide uniform and stable charging. It is confirmed by the dynamic probe test that both position-dependent and time-dependent changes in the charge is small.

Under the standard operating condition of "Boxer-Charger" (main ac voltage: square wave, frequency = 200 Hz, Peak-to-peak voltage = 8 kV; excitation voltage: frequency = 10 kHz, peak-to-peak voltage = 6 kV), the average charging field is E = 2 kV/cm and the mean current density I = 0.34 mA/m^2. The charging time constant becomes T = 21 ms.

SUCTION-TYPE FARADAY CAGE

The suction-type Faraday cage consists of an inner screen electrode holding a filter inside and an outer cylinder electrode serving as a gas dust. The gas passes through the filter and inner-electrode, whereas the charged particles are captured by the filter to provide an electrometer with a current equal to the convection current carried by the charged particle stream.

PRINCIPLE

The current supplied from the Faraday cage is given by:

$$I = G \sum_i N_i \, q_i \quad (A) \qquad (12)$$

where

$q_i = q_{\infty i} \, f(t)$ = charge of i-th particle by Boxer-Charger

$q_{\infty i} = 4 \pi \varepsilon_o P a_i^2 E$ = saturation charge of i-th particle

$P = 3 \varepsilon_s / (\varepsilon_s + 2)$ = permitivity parameter

$f(t) = t / (t + T)$ = charging time constant

$T = 4 \pi \varepsilon_o / J$ = charging time constant

G = gas flow rate (m^3/s)

a_i = radius of i-th particle (m)

N_i = number of i-th particle in a unit volume of gas (m^{-3})

The dust surface loading is given by:

$$S = \sum_i 4 \pi a_i^2 N_i \tag{13}$$

and I can be expressed by S as:

$$\begin{aligned} I &= G\, f(t)\, E\, \varepsilon_o\, P\, S \\ &= C\, \varepsilon_o\, P\, S \end{aligned} \tag{14}$$

where

$C = G\, f(t)\, E$ = operation parameter

P = permitivity parameter

As a result, the current, I, provides a measure directly proportional to the dust surface loading, S. In this case, the constant, C, is determined by the charging efficiency of "Boxer-Charger" and the gas suction rate, G. The permitivity parameter, P, depends on the dust material, and the measurement of the dielectric constant of a dust is needed. However, assuming P = 2, the error will be within 25 % within the range of the specific dielectric constant between 2 and 10. In the case when the measurement of the dielectric constant is difficult, the above assumption gives a rough estimation.

When "Boxer-Charger" is not energized, this instrument becomes an ordinally suction-type Faraday cage. The current in this case, I', provides a charge-to-mass ratio, and the ratio, I'/I, with "Boxer-Charger" on and off, provides an information on the charging performance of the collection fields of an electrostatic precipitator.

PRIMARY TEST

By supplying lycopodium powder from the constant dust feeder, the dust surface loading meter is tested. Lycopodium powder is monodisperse in particle size distribution and suited for this test. Fig. 7 shows the test result where Q is the charge in a unit gas volume passed through the Faraday cage and given by Q = I / G. The solid line in the figure is the theoretical curve estimated from the theoretical relation between I and S, using the values of $f(t{=}79\text{ms}) = 0.79$, $G = 4\ \text{m}^3/\text{h}$ and $a = 15\ \mu\text{m}$.

It is recognized that the test results and the theoretical curve show a good agreement. This type of dust loading meter works as expected.

CONCLUSIONS

The bipolar ionic current probe and the dust surface loading meter have been developed as the in-site diagnostic means for precipitators. It is confirmed by laboratory tests that they work as expected. The diagnosis of a practical ESP using these instruments will be reported separately.

REFERENCES

[1] S.Masuda and S.Hosokawa; Field Evaluation of Pulse Energization Under Different Operating Conditions, to be presented at EPA-EPRI 6th Symp. on Transfer and Utilization of Particulate Control Technology, (1986).

[2] S.Masuda and Y.Nonogaki; Sensing of Back Discharge and Bipolar Ionic Current, Journal of Electrostatics, vol. 10, Elsevier, Amsterdam, Netherlands, p73, (1981).

[3] S.Masuda and Y.Nonogaki; Bi-Ionized Structure of Back Discharge Field in an Electrostatic Precipitator, Record of IEEE/IAS 1981 Annual Conf. (1981).

[4] S.Masuda, T.Itagaki, S.Nohso, S.Tanaka, K.Hironaga, and N.Fukushima; Bipolar Current Probe for Diagnosing Full-Scale Precipitators, presented at EPA-EPRI 5th Symp. on Transfer and Utilization of Particulate Control Technology, (1984).

[5] S.Masuda, K.Akutsu and T.Saito; Electrostatic Continuous Dust Monitor Using Boxer-Charger, Record of IEEE/IAS 1980 Annual Conf. p918, (1980).

[6] S.Masuda M.Washizu, A.Mizuno, and K.Akutsu; Boxer Charger - A Novel Charging Device for High Resistivity Powder, Record of IEEE/IAS 1978 Annual Conf. p16, (1978).

[7] S.Masuda, S.Hosokawa, and S.Kaneko; Ceramic-Made Boxer-Charger For Precharging Applications, reported at EPA-EPRI 5th Symp. on Transfer and Utilization of Particulate Control Technology, (1984).

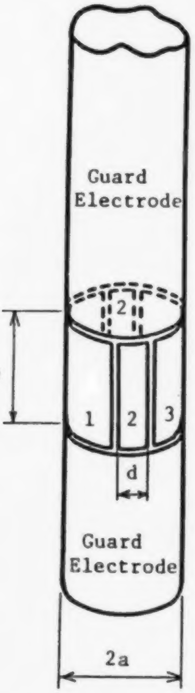

Fig. 1 Electrode Configuration of Bipolar Ionic Current Probe (Cylindrical Probe)

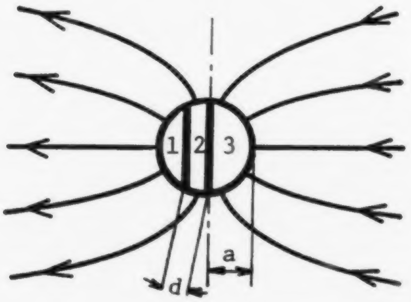

$$I_2/I_1 = 1/\cos(d/a) - 1$$

$$I_1 + I_2 = -4a\ell\, i_-$$

$$I_3 = 4a\ell\, i_+$$

d: distance along circle

Fig. 2 Electric Field Around Asymmetric Probe Placed at Balanced Potential

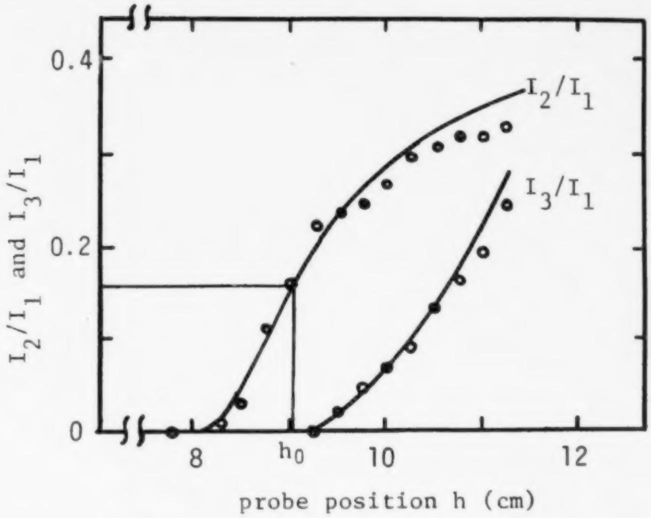

Fig. 3 Comparison Between Theory and Test Results of Bipolar Ionic Current Probe Under Clean Electrode Condition (needle-to-plane, gap = 18 cm, Probe Traverse Method)

Reproduced from best available copy.

Fig. 4 Photograph of Bipolar Current Probe System

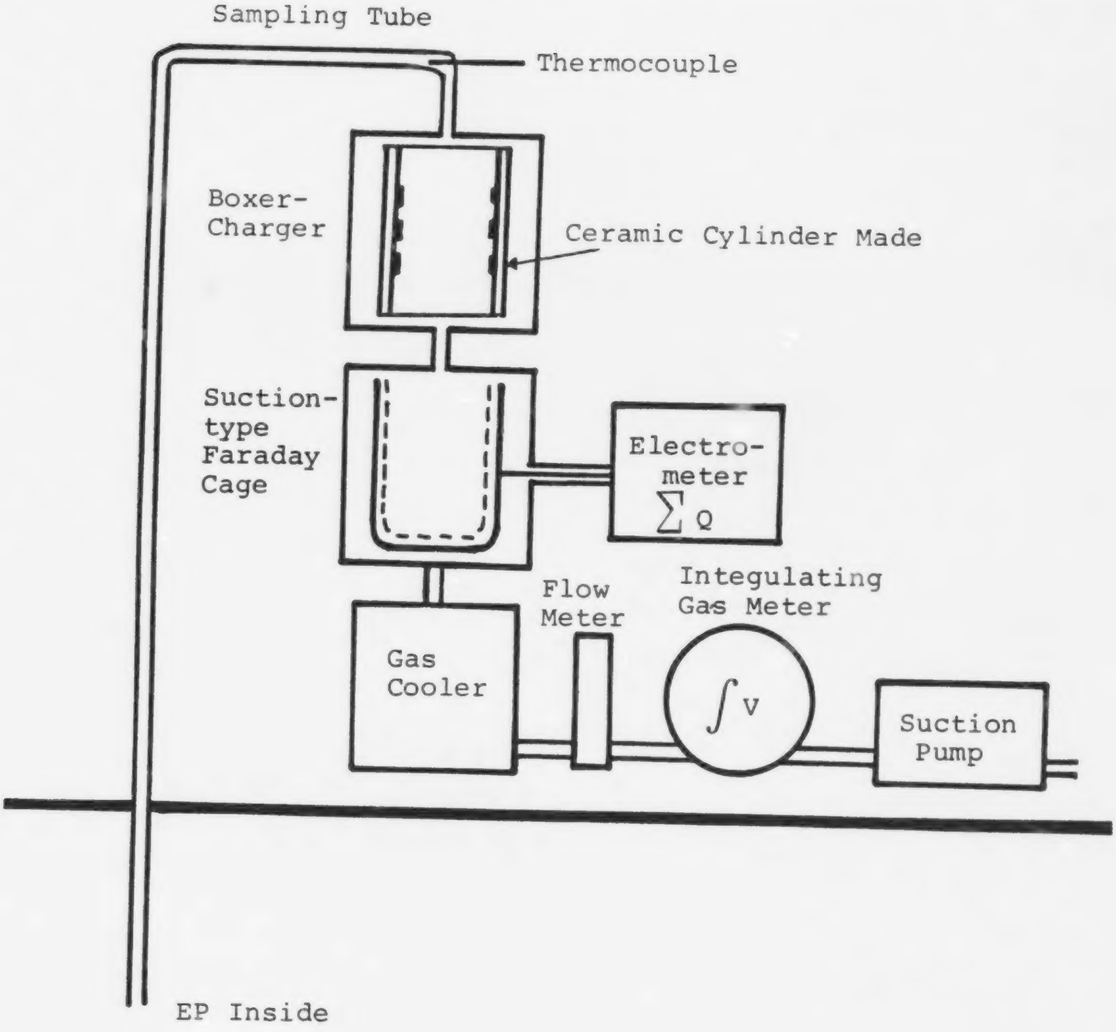

Fig. 5 Schematic Diagram of Dust Surface Loading Meter

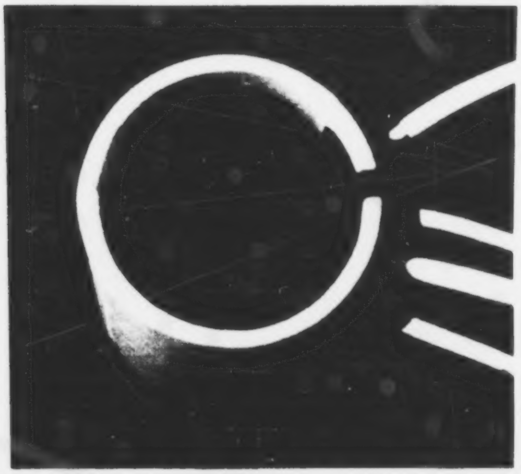

(a) Ceramic-Made Cylindrical Boxer-Charger

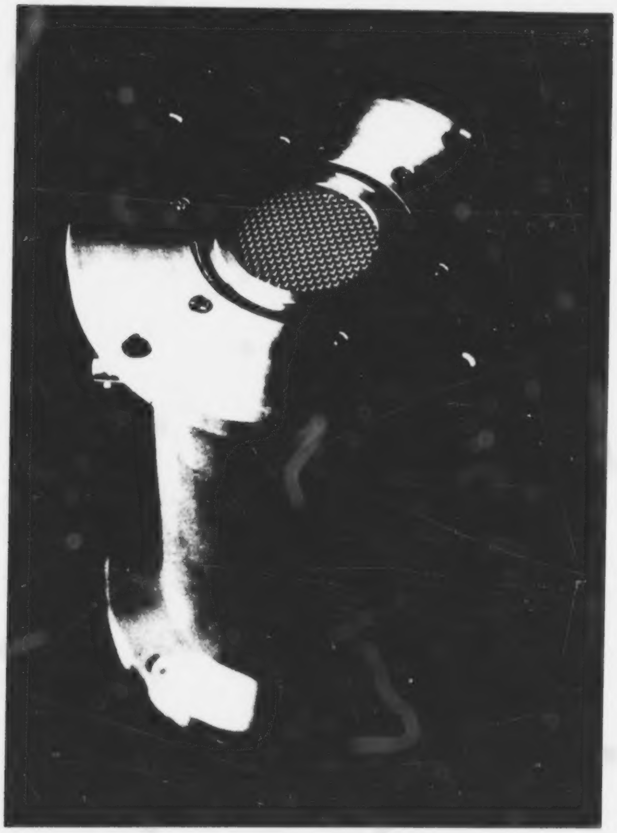

(b) Suction-Type Faraday Cage

Fig. 6 Photographs of Main Components of Dust Surface Loading Meter

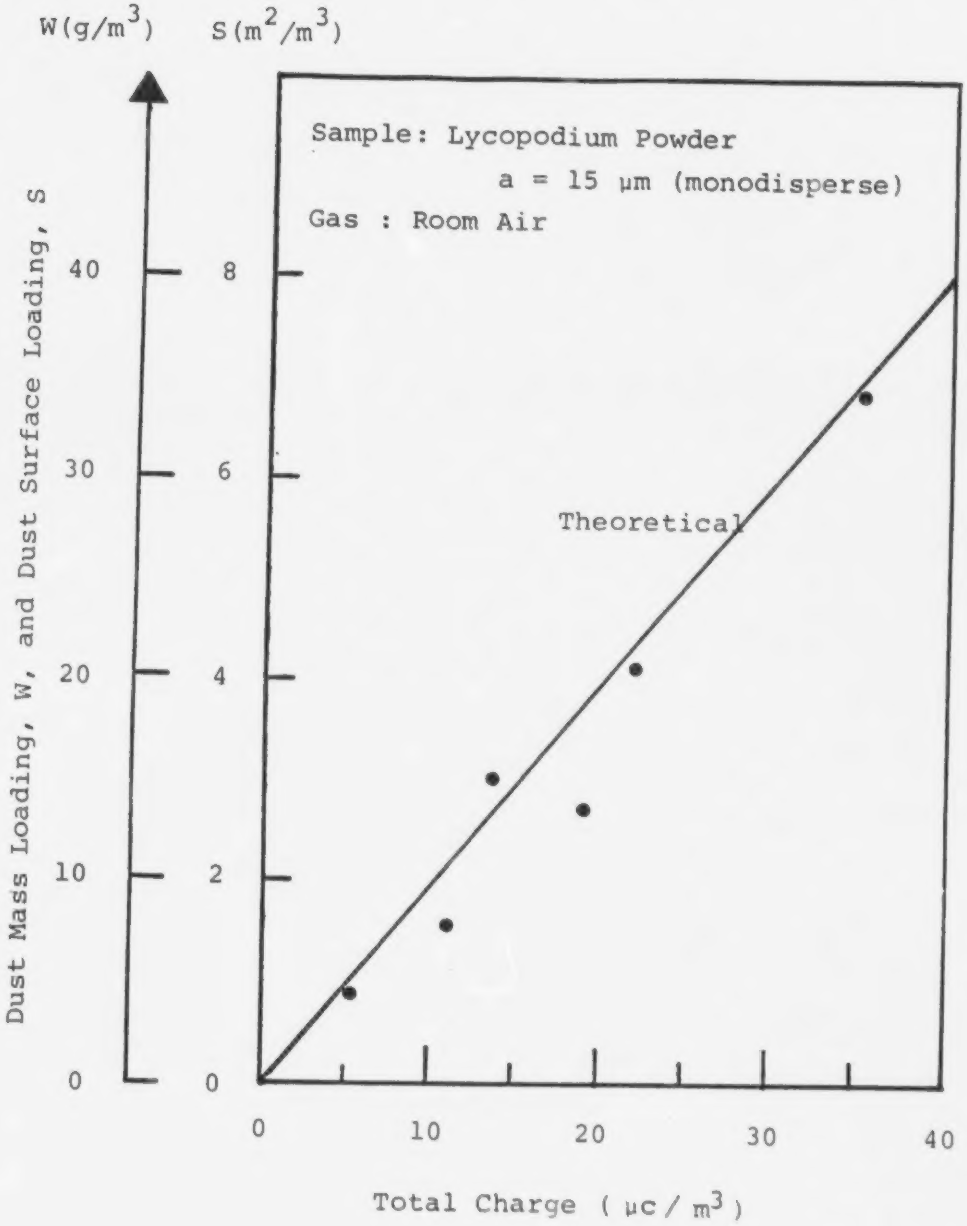

Fig. 7 Comparison Between Theory and Test Results of Dust Surface Loading Meter

The work discribed in this paper was not funded by the U.S. Environmental Protection Agency and therefore the contents do not necessarily reflect the views of the Agency and no official endorsement should be inferred.

Session B-6: CONTROLS AND ENERGY CONSUMPTION

James L. DuBard, Chairman
Southern Research Institute
Birmingham, AL

ELECTROSTATIC PRECIPITATOR POWER MEASUREMENTS

Peter Gelfand, P.E.
P. Gelfand Associates
Trumbull, Conn.

E. C. Landham, Jr.
Southern Research Institute
Birmingham, Alabama

Louis F. Rettenmaier
Electric Power Research Institute
Palo Alto, California

ABSTRACT

Modern electrostatic precipitators consume large ammounts of power to achieve the collection efficiency needed to meet today's stringent environmental regulations. An Electric Power Research Institute project is aimed at making significant reductions in precipitator energy use through a process referred to as intermittent energization. Evaluation of the process requires precise measurement of the power consumed by the precipitator's transformer-rectifiers. The application of silicon-controlled rectifiers as high speed, low voltage regulating circuits provide a unique set of AC and DC waveforms making accurate measurement of energy and power difficult. The intermittent energization process further compounds this problem. This paper discusses the measurement of AC and DC waveforms, energy, and power in a pilot-scale ESP.

INTRODUCTION

The Electric Power Research Institute (EPRI) is conducting an investigation of the benefits of intermittent energization (IE) of electrostatic precipitators (ESP). The potential effects of IE can be to both reduce transformer-rectifier (T-R) power consumption and to modify ESP performance. The initial phase of this work is a pilot-scale study which has been conducted at EPRI's Arapahoe test facility. A companion paper is presented at this symposium describing the effects of IE on the performance and power consumption of the ESP (1).

Since reduction in power consumption is perhaps the major benefit of the IE process, the accurate measurement of T-R primary power consumption is crucial. However, the AC waveforms produced by IE are affected by several types of distortion, requiring sophisticated instrumentation for accurate measurement. This paper will describe the techniques used to measure the power consumption of the pilot-scale ESP and will compare these with some more conventional techniques. A power audit was also performed to quantify the losses in various parts of the ESP power delivery system.

BACKGROUND

NORMAL ESP OPERATION

A schematic diagram of the ESP power supply is shown in Figure 1. During normal operation of the ESP, the silicon-controlled rectifiers (SCR) adjust the T-R set input power, and therefore the ESP voltage and current, by proportioning the percent of "on" time during each half-cycle on the AC line. This process of adjusting the percent of output during each half-cycle is termed phase control. Figure 2 indicates the AC voltage and current waveforms which typically are seen at the T-R set primary during normal operation. The voltage and current waveforms measured at the AC line connection are shown in Figure 3. The waveforms produced at the T-R output are similar to those shown in Figures 4 and 5. Although the current waveform (Figure 4) is not continuous, the amount of off time between each energized period is relatively short. The capacitance of the ESP prevents the voltage (Figure 5) from dropping to zero between the energized periods. The only time that a continuous current waveform is delivered is when the T-R set is operating at current limit with the SCRs full on.

The non-sinusoidal waveforms produced by phase control are rich in harmonic distortions. These distortions increase the difficulty of measuring the RMS and power values of the waveforms accurately. Many of the instruments currently in use by the utility industry for killowatt-hour calculation were not designed for measuring such waveforms.

DESCRIPTION OF INTERMITTENT ENERGIZATION

IE modifies the normal ESP voltage and current waveforms by periodically blocking and passing integral numbers of AC half-cycles. It is technically fairly simple to modify the SCR phase control to turn off the power entirely for a preset number of half-cycles. During the time when the IE control allows power to flow, phase control is used to adjust output to spark-limit. The process of power control by passing and blocking whole half-cycles can be termed integral half-cycle control. In such a system the duty cycle established by the integral half-cycle control is used to adjust the ESP power input. The notation used in this paper to describe this duty cycle is:

$$\text{IE ratio} = \frac{\text{Number of half-cycles energized}}{\text{Number of half-cycles energized} + \text{half-cycles de-energized}}$$

The IE ratio which generally provided the best performance in the pilot-scale tests was two half-cycles energized followed by eight half-cycles de-energized. This is notated "2/10" and was the mode of operation for which the power measurements discussed in this paper were made.

Figures 6 and 7 show the ESP voltage and current waveforms which result from the 2/10 IE method of energization. The ESP voltage (Figure 6) still does not drop to zero during the "off" periods but is maintained near the corona quench voltage by the ESP capacitance. However, the off time observed in the current waveform (Figure 7) is approaching 67 milliseconds. This off time is approximately 20 times longer than seen in Figure 2 for normal operation. The AC waveforms on the T-R set primary with this mode of operation are displayed in Figure 8. Figure 9 shows the waveforms at the AC line connection.

In addition to the harmonic distortions produced by phase control, which are still present with IE, the long off times common to the IE process produce crest factors beyond the rated capability of conventional metering systems. Crest factor is defined as the ratio of the maximum or crest of a wave to its RMS value. A pure sinewave has a crest factor of 1.414. Most hand-held multimeters can accurately measure waveforms with crest factors of 3 at full range, which is sufficient for most measurements. With IE the crest factor would theoretically increase as a function of the number of off cycles between on cycles of applied power. For example, an IE ratio of 2/10 would have a crest factor of 4.47. If the crest factor rating of the meter is exceeded the meter continues to record but accuracy falls off.

DEFINITION OF AC POWER AND ENERGY

Electrical energy is measured in units of joules or watt-seconds. Power is the time rate of energy conversion or transport. The units are joules/second or watts. In power systems we use the unit of watt-hour to calculate the energy consumed where one watt-hour equals 3.6E6 joules.

In electric circuits the instantaneous power is the product of the instantaneous voltage and current present. For direct current, where voltage and current do not vary in time, the instantaneous power and the average power are equal. However, in alternating current circuits the instantaneous and average power are very different, requiring more difficult measurement techniques. For AC systems, power means the average power taken over a full cycle, while energy is the integration of average power over time. The definition of power for any shape AC waveform is:

$$P = 1/T \int_{0}^{T} \text{Voltage}(t) * \text{Current}(t)\,dt$$

where voltage(t) and current(t) are instantaneous values at time = t and T is the time required for one complete cycle.

CONVENTIONAL POWER INSTRUMENTS

The traditional instruments used to measure power and energy in AC systems are quite different in design. The electrodynamic wattmeter utilizes a moving coil to measure voltage and a fixed coil for current detection. The electrodynamic wattmeter is very accurate if the voltage and current waveforms are sinusoidal, continuous, and slowly varying. The induction watt-hour meter (IWM) is the most widely used energy measuring device and has been the standard of the electric industry for years. IWM design also assumes the presence of sinusoidal voltages and currents at the frequency of the supply. Physically the IWM employs a moving disk and registers. Both the Wattmeter and the IWM are affected by distorted waveforms, transients, and discontinuous energy flow. (2),(3),(4)

The IWM must meet ANSI standard C12-1975 which requires calibration to +/- 0.5% at unity power factor. The IWM has been shown to maintain its accuracy to within a few percent when measuring distorted power waveforms (4). However, the addition of discontinuous energy flow, produced with IE, to the distorted waveforms from phase control has the potential to compound the error.

ELECTRONIC POWER METERS

An instrument which can be used to accurately evaluate the effect of IE on power consumption must meet strict requirements. The instrument must be able to maintain accuracy when measuring waveforms with the following characteristics:

- Distorted sinewaves which are rich in harmonics.
- Rapidly varying amplitude (as sparking is controlled in the ESP).
- High crest factors.
- High speed transients caused by ESP sparking and arcing.

The Joule Electronic Meter@ (JEM) from Scientific Columbus was found to meet these requirememts. This instrument divides the voltage and current waveforms into about 11.3 segments/cycle. Each segment is then evaluated by analog circuits. The specific instrument selected was model 402-E-06. The meter provides simultaneous output of watt-hours and watts. The specifications are as follows:

Range: 1-4800 watt-hours/watts as single element (2x as double).
Accuracy: Watt-hour = +/-0.1% of reading plus 0.01% of class.
Speed of Response: 0-99% reading in 400 millisec. (processing delay).
Detection speed: 680 Hz. or detection rate of 1.5 milliseconds.
Watt Output: Continuous analog signal.
Watt-hour Output: Electronic register with 1 watt-hour resolution.

COMPUTER CALCULATED POWER

Although the specifications of the JEM instruments indicated that they were capable of measuring the power of an IE waveform, an independent determination of the JEMs accuracy was desired. The method of determining the voltage, current and power which we felt was most accurate involved calculation from fundamental equations using the actual waveforms. This was done by recording the voltage and current waveforms simultaneously in a digital oscilloscope and then reading the values into a computer where the calculations were performed. The waveforms stored in this fashion typically had a resolution of approximately 1000 data points/cycle. Average power was determined by summing the product of simultaneous points from the voltage and current waveforms then dividing by the number of data points. The RMS and average values of the voltage and current waveforms were also calculated. The oscilloscope used for these measurements was a Nicolet 2090-III with a Nicolet 204A input module. The Nicolet was interfaced to a Hewlett-Packard 9825A desktop computer.

RESULTS

PRIMARY AC INSTRUMENT ACCURACY

The primary of the T-R set is driven by 480 volt, single-phase AC power. The original AC meters installed on the T-R controls were not sufficiently accurate to consider for comparison. The AC voltage was measured directly with a Fluke 8040A RMS Voltmeter. The AC current was determined by an AEMC 2011 multimeter installed directly in the 480 volt line. The Oscilloscope was connected to the AC voltage with a Tectronics A6902A Isolator and the current signal provided by a Fluke Y8100 amp probe. Neither of these devices exhibited measurable phase shift.

The measured RMS primary voltage and current are compared to the oscilloscope/computer calculated RMS values in Figures 10 and 11. The instruments accurately measured these distorted waveforms, even though the crest factor was 3.7 - 4.8 for an IE ratio of 2/10. The RMS values of AC voltage and current cannot be used to determine the T-R power consumption by a simple product. This is discussed in a later section on power factor.

Although the RMS value of AC current may be reduced with IE, the peak values may be increased. This can be seen by comparison between Figures 2 and 7. During normal operation, the current waveform (Figure 2) had a peak value of 3.4 amps with a measured RMS value of 1.7 amps. The IE waveform (Figure 7) indicates that the peak value was increased to 4.1 amps while the RMS value dropped to 0.96 amps. Although this increase is only 20%, which would not cause a problem in most situations, this is a point to consider during the selection of equipment. Some IE control systems may be capable of limiting peak current, to avoid damage to the T-R, while others may act on RMS values.

POWER METER ACCURACY

The JEM meters, which were used to collect the data for the performance tests, were compared to the oscilloscope/computer calculation method. In addition, the JEM instruments were compared with IWM devices under both normal and IE operation.

Joule Electronic Meters

Figures 12 and 13 compare the power measured by the JEM meters with that calculated from the oscilloscope/computer technique. Both IE and normal operation values are displayed in these graphs. Figure 12 is the power at the line connection (before the SCRs) while Figure 13 is the power at the input to the T-R primary. The results indicate that the values measured with the two techniques are in agreement within experimental uncertainty. Perfect agreement is shown by the solid line. The JEM instruments are accurately measuring power and energy.

Induction Watt-Hour Meter

The IWM standards call for an accuracy of +/-2.0% over the full range of test conditions, including low power factor. The accuracy of the JEM instruments is not sensitive to power factor. For the energy comparison tests, the JEM and the a conventional IWM were connected in series so as to monitor the energy consumed by all Three T-R sets of the ESP. Separate readings were taken during normal operation and when operating with an IE ratio of 2/10. The results indicate that the IWM was indicating about 1.6% higher than the JEM in normal operation and approximately 3.0% higher in IE mode. This level of agreement is considered within experimental error for this particular test.

POWER FACTOR

We have calculated the power factor according to the formula,

$$\text{Power Factor} = \frac{\text{Real Power}}{(\text{RMS Voltage} * \text{RMS Current})} ,$$

at the T-R and at the input line. The results for continuous powering and IE are plotted separately in Figures 14 and 15. Both sets of power factors are varying normally. The low power factors obtained at the line are due to the low operating power levels.

It is obvious from the power factor data that the product of the AC voltage and current is not an accurate means of exactly determining the T-R power consumption. Comparison of the data from the two figures indicates that the power factors with normal and IE operation may not be equivalent, depending on the line current. Therefore, the most accurate method for measuring power savings due to IE remains the power meters.

ESP HIGH-VOLTAGE POWER

The oscilloscope/computer method was also used to investigate the DC power applied to the high-voltage ESP load. In this case the power was calculated using the simultaneous waveforms of ESP high-voltage and T-R output current. The connection of the oscilloscope to the ESP high voltage was accomplished with a calibrated voltage-divider of SoRI construction. The divider has an input impedance of 120E6 ohms and provides signal attenuation of 10,000x. Even with such a high impedance, the voltage divider draws a significant amount of current compared to the small pilot ESP field. This leakage current has been subtracted from the data where appropriate. The current was input to the oscilloscope as the voltage drop across the ground return resistor of the rectifier bridge. The same signals were utilized for the meter measurements of ESP voltage and current. A Keithly 616 digital electrometer operating in voltage mode was used to measure the voltage-divider output while the current was determined with a Hewlett-Packard 3403C voltmeter. A comparison was also performed with the conventional analog meters installed on the T-R controls.

Figures 16 and 17 compare the values of the voltage and current measured with the H-P and Keithly meters to the calculated values. Agreement is very good, indicating that the meters are accurate even though the flow of power from the supply is discontinuous.

Figures 18 and 19 compare the ESP high-voltage power calculated by the oscilloscope/computer method and the product of the average values of the secondary voltage and current. The good agreement on Figure 18 confirms that power flowing to the ESP load under normal operation is equal to the product of the T-R secondary voltage and current. However, Figure 19 indicates that with IE in use the power flowing to the ESP may exceed the simple product of the average values. This disagreement occurs because the average ESP voltage during the time that current flows to the ESP greatly exceeds the average voltage over an entire cycle.

On most ESPs the secondary voltage and current is measured by analog meters with D'Arsonval movements. Although such meters were not provided with the IE controls, typical meters were installed for this test. Results from a typical comparison between the analog meters and the oscilloscope/computer calculated average values are shown below:

Mode of Operation	Secondary Voltage			Secondary Current		
	Analog KV	Scope KV	% Error	Analog MA	Scope MA	% Error
Normal	34.2	34.4	0.6	10.0	8.9	-12.4
2/10 IE	25.5	25.2	1.2	2.3	1.9	-21.1
2/20 IE	22.0	22.4	1.8	1.2	1.3	7.7

The data indicate that the analog KV meters were reasonably accurate for both normal and IE operation even out to 2/20. The analog current meters were not as accurate as the voltage meters although they were close to the manufacturer's specifications of 2% of full range. For normal and 2/10 the ballistics of the meter movements seem to be over-responding to the peak currents to give numbers which are higher than the true average value. At 2/20 the high crest factor appears to dominate the operation of the meters producing low indications.

POWER AUDIT

To identify the power losses within the components of this ESP system, a power audit was performed. This series of tests consisted of power measurements at various points in the power delivery system. The measurements were conducted both with and without IE and with the ESP load connected and disconnected.

High Voltage Transmission Losses

With the ESP field disconnected from the T-R set, the power dissipated due to high voltage transmission losses was measured. The total power loss (square symbols) is plotted vs the T-R secondary voltage in Figure 20. To help account for the losses the theoretical power consumption of the voltage divider high-voltage measuring circuits has been plotted on Figure 20 as the solid line. Clearly, the no-load losses are almost entirely due to these metering resistors. The triangular symbols show the adjusted power loss after subtraction of the voltage divider leakage. Since the ESP was never operated above 45 KV, except for the no-load test, the high voltage transmission losses were insignificant for both normal and IE operation.

The power consumed by the high-voltage metering resistors are losses which are not significant on a full-scale ESP. However, because of the small plate area of the pilot-scale ESP these losses are proportionally as much as 50 times higher than those expected at full-scale. Any calculations of economic benefit from IE, which are based on the pilot-scale data, will subtract out the effect of the metering resistors to determine as closely as possible the amount of power consumed by the ESP itself.

T-R Set Magnetization Losses

The normal operation power losses attributable to magnetizing the T-R set and other low current effects are plotted as a function of primary voltage on Figure 21. These losses are obtained by subtracting the high voltage transmission losses from the power measured at the T-R primary during the no-load tests. The least square fit to these data has an r coefficient of 0.908 indicating acceptable agreement. Operation with an IE ratio of 2/10 produced T-R losses which were effectively zero. This is most likely due to the lower effective primary voltage and the long de-energized period of each cycle of IE.

SCR, Reactor, and T-R Load Losses

A short circuit test of the T-R set is the desired means of determining the losses in the primary control circuit. Unfortunately, when this test was attempted, the amount of current that could be applied was limited to such small values by the reaction of the AVC control, that meaningful results could not be obtained.

The no-load tests were used to develop an estimate of these losses. The primary circuit power consumption was determined by taking the difference between the power measured at the line and at the T-R primary. Figure 22 graphs the power loss as a function of the square of primary current along with a least square fit to the data.

Calculation of Total Power

In a circuit such as formed by an ESP's HV supply, the principle of power conversion applies. Regardless of waveform, frequency, continuity or discontinuity of current flow, at any instant the sum of the power consumed by the load (the ESP field) plus the HV transmission and the internal losses within the components of the supply must equal the power drawn from the lines. That is, the line power is equal to the sum of the following:

1. High-voltage transmission losses

2. T-R magnetization, coil, and rectifier losses

3. Losses in the SCRs and the linear reactor

4. Power dissipated in the ESP

The previously measured values of these four power consumption components has been summed for a number of test conditions to produce an independent estimate of the line power. This calculated power is compared to measurements made with a JEM at the line connection in Figure 23. The readings plotted and compared are those of both normal and IE operation. Agreement is generally good, providing additional support for the accuracy of the JEM instruments.

Power Transfer Ratio

The amount of power measured at the T-R primary divided by the amount of power measured at the AC input line is defined as a power transfer ratio. For example, 100 watts of power measured at the lines and a transfer ratio of .95 would say that 95 watts is applied to the T-R. In other words, 5 watts is lost in the transfer process. In the same way we can define an overall transfer ratio, comparing the input line power to the power delivered to the high voltage load by the T-R . The T-R output for this comparison is determined by subtracting the T-R losses from the JEM reading obtained at the T-R primary. This T-R output is divided by the JEM power measured at the AC line connection to determine the transfer ratio.

In general the transfer ratio between input watts and high voltage watts increases as line current increases, since operating losses are a smaller fraction of the watts used by the load. In most cases the transfer ratio is greater than 0.85, increasing to nearly 0.90 at higher loads. Since the power supply has a rated line current of 6196 mA and we operate in the range of 10-30 % of rating, our transfer ratio is likely on the low side.

SUMMARY

- These measurements demonstrate that the JEM electronic power meters are able to accurately measure the power consumption of the ESP during both normal operation and intermittent energization.
- Comparison of the solid state energy meter to the IWM meter indicates that the difference between the two instruments was within 3.0% experimental error for both normal and 2/10 IE operation. However, the scope of these tests was limited. Proper operation of this type of instrument should be verified for a particular application if high accuracy is required.
- The product of ESP voltage and current (either primary or secondary) may not be a reliable measure of power saving when IE is used. Power meters are advisable for high accuracy evaluation of IE power reductions.
- High waveform crest factors in excess of 3.7 were obtained during IE at 2/10. Careful attention should be paid to peak current values with IE, which may be significantly higher than for normal operation, to avoid inadvertent overload of the power supply.
- About 85-90 watts out of every 100 measured at the line was delivered to the high voltage load.

REFERENCES

1. Evaluation of Pilot-Scale ESP Intermittent Energization, E.C. Landham, Jr., J. L. DuBard, W. Piulle, and L. F. Rettenmaier, Sixth EPA/EPRI Symposium on the Transfer and Utilization of Particulate Control Technology, New Orleans, LA, February 1986.

2. The Effect of Waveshape Distortions on the Measurement of Energy Tariff Meters, A. J. Baggott, Nov 15-17, 1977 IEE Conference Publication #156, Third International Conference on Metering Apparatus and Tariffs.

3. Errors in Measurements of Thyristor-Controlled AC Loads, M.M. Kalifa, et al, Nov 15-17, 1977 IEE Conference Publication #156, Third International Conference on Metering Apparatus and Tariffs.

4. Evaluation of Electrical Interference to the Induction Watt-Hour Meter, EPRI EL-2315, Project 1738, April 1982.

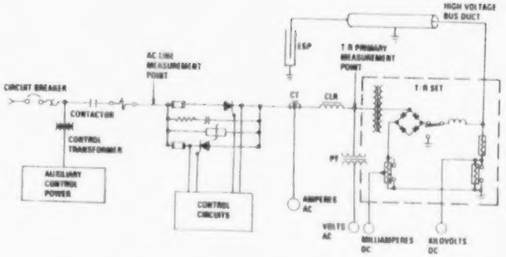

Figure 1. Schematic diagram of ESP power supply.

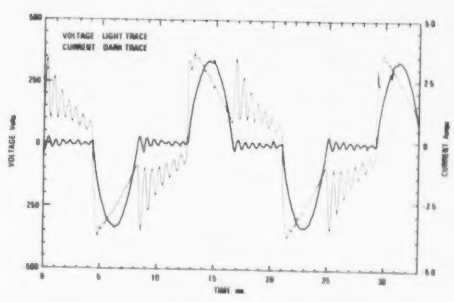

Figure 2. T-R set primary voltage and current waveforms during normal operation.

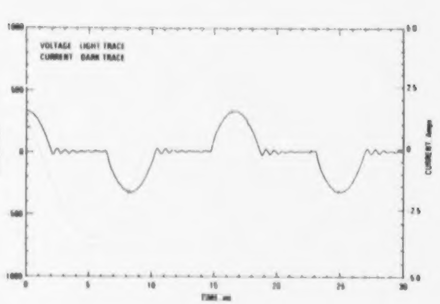

Figure 3. AC line voltage and current waveforms during normal operation.

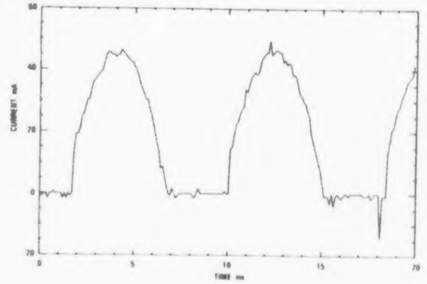

Figure 4. T-R set secondary current waveforms during normal operation.

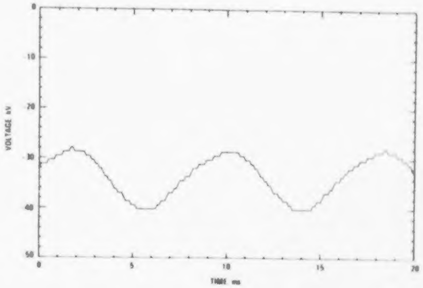

Figure 5. ESP high-voltage waveform during normal operation.

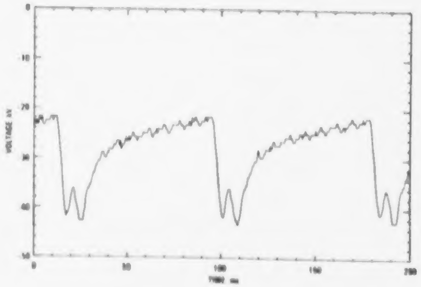

Figure 6. ESP high-voltage waveform during 2/10 IE operation.

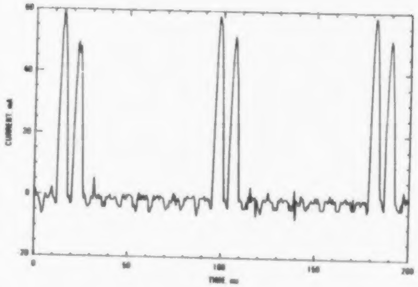

Figure 7. *T-R secondary current waveform during 2/10 IE operation.*

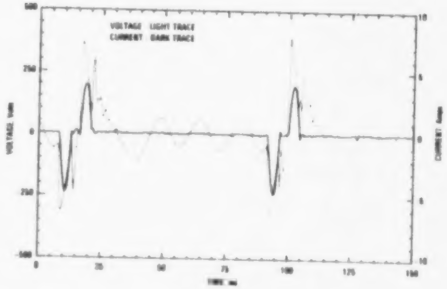

Figure 8. *T-R set primary voltage and current waveforms during 2/10 IE operation.*

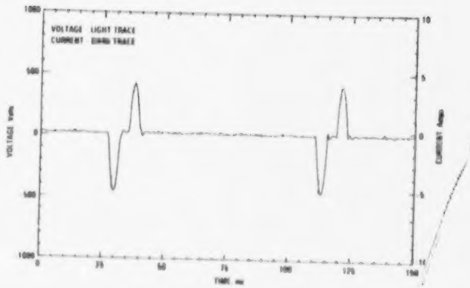

Figure 9. *AC line voltage and current waveforms during 2/10 IE operation.*

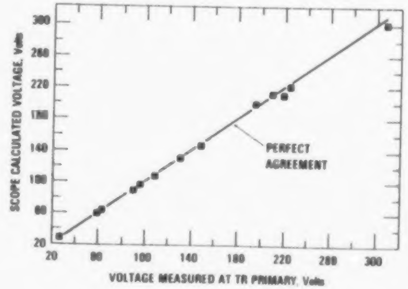

Figure 10. *Comparison of measured and calculated AC voltage at the T-R primary.*

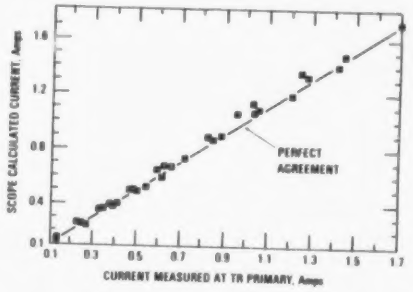

Figure 11. *Comparison of measured and calculated AC current at the T-R primary.*

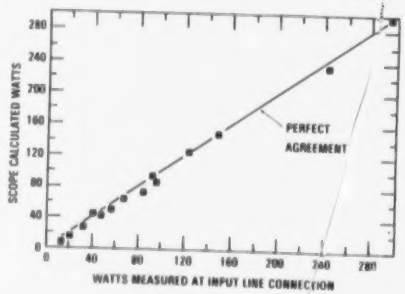

Figure 12. *Comparison of JEM measured and calculated AC power at the line connection.*

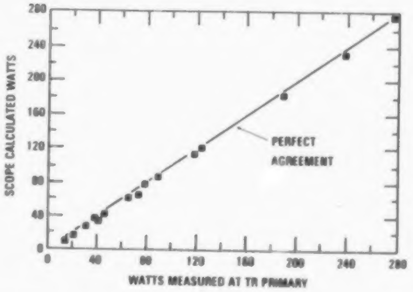

Figure 13. Comparison of JEM measured and calculated AC power at the T-R primary.

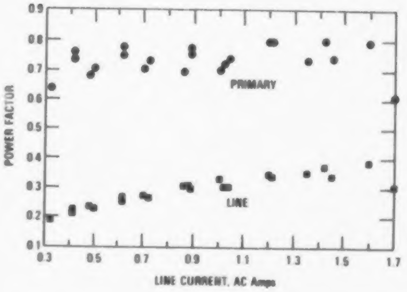

Figure 14. AC power factor for normal operation.

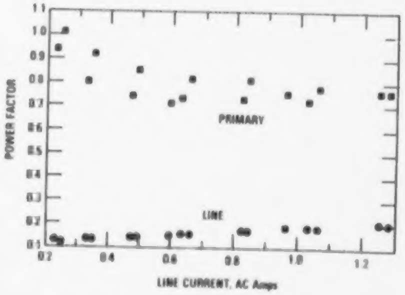

Figure 15. AC power factor for IE operation.

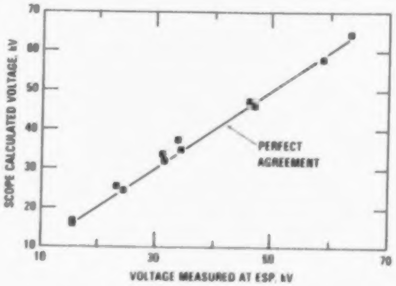

Figure 16. Comparison of measured and calculated precipitator high voltage.

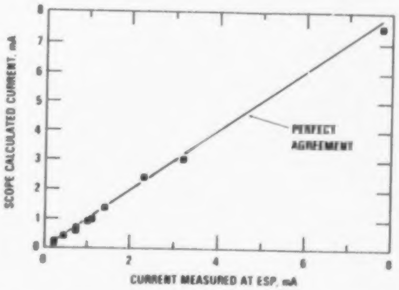

Figure 17. Comparison of measured and calculated T-R secondary current.

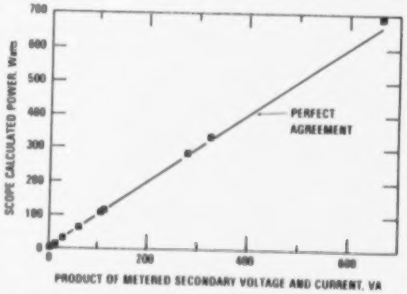

Figure 18. Comparison of scope calculated ESP power and the product of T-R secondary voltage and current for normal operation.

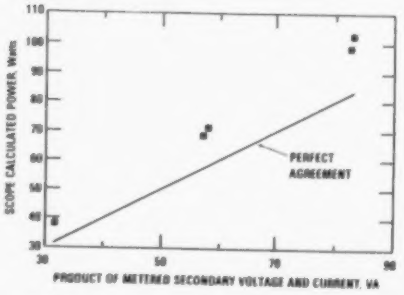

Figure 19. Comparison of scope calculated ESP power with the product of T-R secondary voltage and current for 2/10 IE operation.

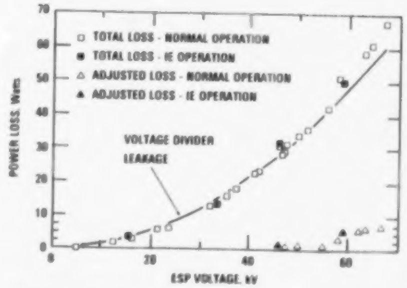

Figure 20. High-voltage transmission losses.

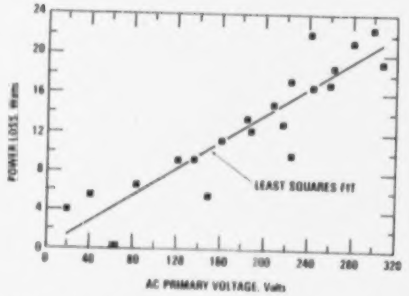

Figure 21. Transformer-rectifier power losses.

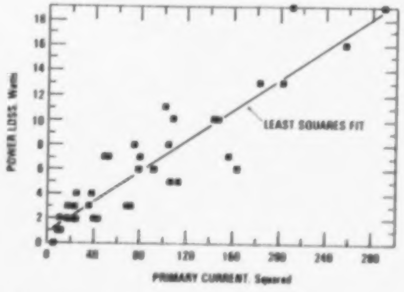

Figure 22. Estimated power loss in SCR and linear reactor.

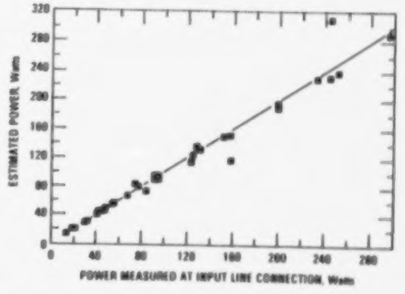

Figure 23. Comparison of measured input power with power estimated from loads and losses.

ESP ENERGY MANAGEMENT AND OPTIMIZATION OF COLLECTION EFFICIENCY

by: Bill Borowy, Mac McLauchlin,
William F. Frazier
Virginia Power
Richmond, Virginia 23261

ABSTRACT

This paper relates the authors' experience in energy management and efficiency improvement through reduced voltage (KV) operation of ESPs with design specific collection areas (SCA's) of 280 to 660 ft^2/1000 ACFM. Up to 90% energy savings and increased collection efficiency were achieved without a central energy management system.

Opacity was used as a guide to adjust power supplies at lower levels. EPA Method 5 or 17 was used to determine the mass emission rate at each level. Several units in the system were adjusted with varying degrees of success. A curve was plotted to show power input versus mass emission rate and based on the curve the operating parameters were set for each ESP tested.

INTRODUCTION

To date, Virginia Power has converted 2270 MW of coal-capable capacity from oil to coal, making this conversion program the largest in the country. Future plans for this decade include conversion of an additional 200 MW of capacity from oil to coal. As part of this conversion, nine new electrostatic precipitators (ESPs) have been installed and two ESPs upgraded as of February, 1986. Two additional ESPs are planned to be installed by the end of 1987.

All of the new ESPs were conservatively sized to ensure compliance when burning a wide variety of coal. Consideration of numerous possible future coal sources was the primary reason for the conservative desfgns.

The available coal supplies produce fly ash with a resistivity range of approximately 5 x 10^{10} to 5 x 10^{11} ohm-cm. The current ash is considerably easier to collect than that which would be produced by some of the worst case scenarios considered during initial design. It was therefore recognized that considerable power savings could be achieved by re-tuning the new ESP's while using present coal supplies. The re-tuning was also used on two small existing precipitators of an older vintage. Company concerns about energy savings at the cost of increased emissions prompted a commitment to save power without substantially increasing emissions. A comprehensive program of testing and tuning was developed which maintained or reduced existing emissions when limiting power input to the ESP's. Most of the new units tested were designed at 540 to 660 SCA. Actual SCA's encountered during tests were higher. The older units tested had a design SCA of 280 ft^2/1000 ACFM. The older units showed improvements, but could not attain the percentages of power reduction possible with the larger units.

SELECTION OF CANDIDATE UNITS

A brief survey was made of all the ESPs in the system. Three ESPs in the range of 200 to 240 SCA were not used because of a lack of reserve collecting area. Four of the nine new ESPs were also initially rejected as candidates. The rejections were due to 1) high exit temperatures (≅350°F) on two units, and 2) malfunctioning high voltage controllers on the other two units. Programs are now under way to improve the thermal efficiency of the two units with high gas temperatures and replacement controllers have been selected for the other two ESPs. Tuning and testing of the new units that were rejected will proceed after improvements are completed. A summary of the design information for each of the tested precipitators is provided in Table I.

ESP TUNING

After a new precipitator is brought into service at Virginia Power, two acceptance tests are generally performed to determine if the ESP meets the guaranteed emissions performance. The first test is scheduled 30 days after start-up and the second test is scheduled one year later. In addition to the ESP acceptance tests, a State compliance test is generally performed to verify that the particulate emissions do not exceed the allowable emission rate established by the Virginia State Air Pollution Control Board. If the ESP manufacturer meets or exceeds guaranteed efficiencies, they usually have no economic incentive to further tune the ESP. In-house procedures were, therefore, developed to tune Virginia Power's ESPs to save power while maintaining or improving existing low emission levels.

The tuning procedures involved 1) lowering secondary voltage levels (KV) or current settings on the ESP automatic high voltage controllers, 2) cutting back on rapping frequency, 3) energizing only the first 3 or 4 fields of collecting plate rappers, and in some cases, 4) shutting off transformer rectifier (TR) sets for the back fields of the ESP. All of the tuning was performed while observing visual and metered opacity.

TEST PROGRAM

Testing took two forms, electrical tests and mass emission tests. The electrical tests were performed to determine the amount of power savings possible between tuned and untuned states. The mass emission rate tests were performed on all the new units to develop mass emissions versus opacity data. The data was for possible future use as guidelines during equipment malfunctions or other abnormal situations and not for opacity feedback management. As discussed earlier, all of the power savings were achieved without any substantial increase in opacity. In the case of the two 280 SCA units opacity actually dropped.

ELECTRICAL TESTS

Total input power to the ESP was monitored either by measuring the volts, amps and power factor at the main supply transformer for the ESP tested or by measuring secondary amps and kilovolts at each TR controller. TR controllers were then backed down by either placing them in manual and reducing the power or by reducing the secondary voltage limits on controls so equipped. The controls with the secondary voltage limits were allowed to remain in full automatic. All front field controls were left in full automatic without any reductions. Typically, the front fields consume very little power because of control reaction to sparking conditions. In most cases the electrical power was reduced in steps to a level where metered opacity increased to about 20%. Power levels for opacities between 0% and 20% were recorded. Reduced power levels which maintained opacities at 0% or below 5% were selected for follow-up mass emission tests.

MASS EMISSION TESTS

Mass emission test formats varied from ESP to ESP. Station needs at the time of the tests, requests from individual state inspectors, and equipment availability all caused variations in the test procedures and the amount of data taken.

The mass emissions were determined using either E.P.A. method 5 or EPA method 17. The principal difference between the two methods is the location of the particulate collected during the test. In method 5 the particulate must be pulled through a heated probe and collected on a filter contained in an external chamber that is kept at an elevated temperature. The method 17 uses a flat pack filter holder that is heated in the stack by stack gases.

The greatest amount of data was taken on Possum Point Unit 4 and Chesterfield Unit 5. These units were the first ones tested. Figure 1 shows the power reduction test results for these units. Mass emissions (lbs/MBtu) were determined as a function of the secondary power levels of the transformer rectifier sets. These results indicated that there were minimal increases in mass emissions when power levels were adjusted to approximately 10% of the full power levels. Later test programs were abbreviated when run on similar units burning similar types of coal. The results of these tests are summarized in Table II. Tuning of the two 280 SCA units resulted in a reduction of opacity from the 12% range to the 8% range. Mass emission tests for these smaller units are scheduled for summer of 1986. Power savings for the two units was estimated at .75 MW. The lack of secondary voltage metering circuits and numerous auxiliary circuits on the ESP main supply transformers made the determination of an exact percentage of power savings difficult. More power consumption data will be generated on these units when mass emission tests are performed.

HARDWARE CONSIDERATIONS

AUTOMATIC VOLTAGE CONTROLS (AVCs)

AVCs with secondary voltage limits which can run in full automatic under a set secondary voltage were found to be best for our energy management applications. It was felt that possible emission problems could result if current limits were used to reduce power to more than 70% of full rated values. The basic reasoning was that 1) if resistivities of the ash dropped, a secondary voltage limit would let the current rise to provide the extra clamping forces needed to hold ash to the collector plates, 2) if resistivities increased, the secondary voltage limits would keep the fields below the threshold of back corona while an ash related (but not always desirable) form of energy management would take place. Lower resistivities were encountered during start-ups when temperatures are lower and moisture content of the flue gases are higher. Current-voltage relationships were developed for the units tested and high resistivity problems such as back corona were not detected.

Another consideration in selecting secondary voltage over secondary current was the full scale accuracy of the metering circuits involved. A power reduction of 90% will result in secondary currents in the range of 10% of full rated values. Since several components in the metering circuits for most AVCs are specified to tolerances of ±10%, minor problems can result. Secondary voltage levels for the same power reductions, however, will be in the range of 50 to 70% of full rated values due to exponential current-voltage relationships.

RAPPERS

Rapper adjustments are an important part of tuning for energy saving while minimizing emissions. If rapper intensities and frequencies are not lowered when power is lowered, increased emissions may result. This is mostly due to decreased clamping forces holding the ash to the collector plates. The end result is that rapper intensities which were previously needed to dislodge ash held at full power may cause rapping reentrainment at reduced power levels.

Internal inspections on two of the new ESPs revealed fly ash deposits less than 1/16" thick in areas where rappers had not been working on outlet fields. In light of the relatively clean condition of the rear collector plates, it was decided that rapping was unnecessary on these fields. Before turning off the rear field rappers, rapping cycles were checked. Rapping frequencies as often as once every seven minutes were found on some outlet fields. As part of the program, the rappers on the last two fields were turned off and round trip times for the front fields were adjusted to cut rapping frequency. The rapper tuning in conjunction with reduced power settings resulted in lowered emissions as well as an approximate 91% power reduction on Chesterfield Unit 5. The emission rate dropped about .002 lbs/10^6 Btu while metered and visual opacity stayed near zero. The total power savings was approximately 1.27 MW on this unit over full power settings. It should be noted that all emitter rappers should remain in service and that all fields should be rapped down as part of shutdown procedures.

CONCLUSIONS

ESPs which run well and can easily meet guaranteed emissions can often be tuned further for energy savings. For selected Virginia Power precipitators savings of up to 90% were achieved without substantial increases in emissions, and in some cases, with a decrease in emissions over full power settings. The precipitators achieved the above without the added cost of a central energy management system. Rapper tuning and AVCs with secondary voltage limits can play an important role when running ESPs at reduced power.

TABLE I. SUMMARY OF ESP DESIGN INFORMATION

Station	Unit	Design Efficiency	Specific Collection Area (ft^2/1000 ACFM) With Redundancy	Specific Collection Area (ft^2/1000 ACFM) Without Redundancy	Gas Flow Rate (ACFM)
Chesterfield	5	99.7%	750	660	1,300,000
Mt. Storm	1	99.7%	280	220	2,300,000
Mt. Storm	2	99.7%	280	220	2,300,000
Portsmouth	4	99.7%	650	540	951,000
Possum Point	4	99.7%	650	540	951,000
Yorktown	2	99.7%	720	600	652,000

TABLE II. SUMMARY OF ESP TUNING/TESTING RESULTS

Station	Unit	Power Reduction	Opacity (%) Full Power	Opacity (%) Reduced Power	Emissions (lb/MBtu) Full Power	Emissions (lb/MBtu) Reduced Power
Chesterfield	5	91%	2	2	0.007	0.005
Portsmouth**	4	90%	0	5	0.010	0.018
Possum Point	4	94%	0	2	0.005	0.017
Yorktown	2	87%	6	7	0.009	0.011

**Reduced power tests had 4½ fields in service, full power tests had 6 fields in service.

FIGURE 1

REDUCED POWER TEST RESULTS

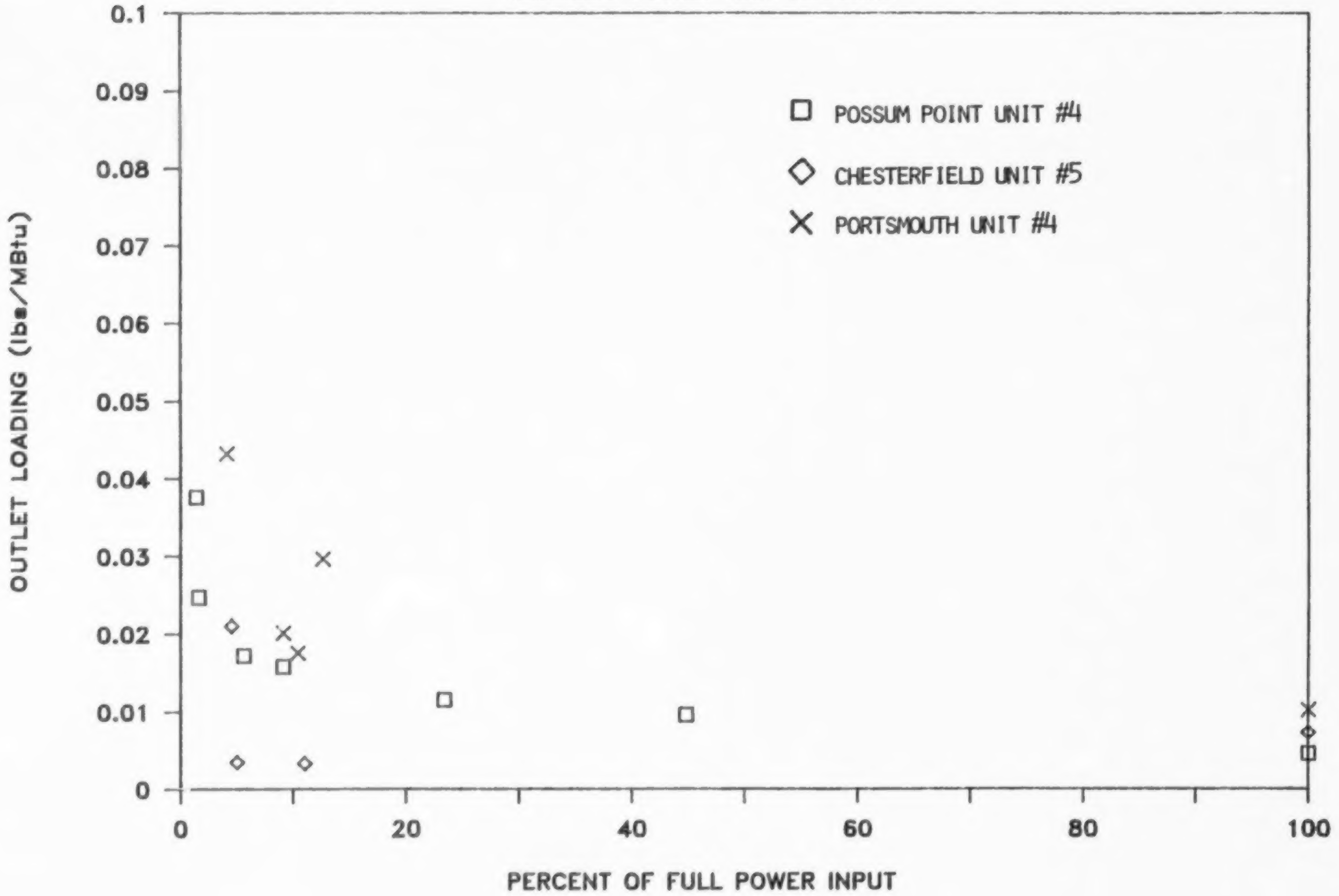

The work described in this paper was not funded by the U.S. Environmental Protection Agency and therefore the contents do not necessarily reflect the views of the Agency and no official endorsement should be inferred.

REFERENCES

1) White, H. J., Industrial Electrostatic Precipitation. Addison-Wesley, Reading, Massacausetts, 1983.

2) Lynch, J. G., and Kelly D.S., A Review of Rapper System Problems Associated with Industrial Electrostatic Precipitators. Proceedings: Operation and Maintenance of Electrostatic Precipitators. APCA, Pittsburgh, PA, April, 1987.

3) Frazier, W. F., and Borowy, W. J., Evaluation of Utility Cold-Side Electrostatic Precipitators. Paper Presented at the Joint ASME/IEEE Power Generation Conference, Milwaukee, Wisconsin, October 20-24, 1985.

THE EVALUATION OF TESTS AND THE ECONOMIC IMPLICATIONS OF POWER REDUCTION OF ELECTROSTATIC PRECIPITATORS

by: D. L. Lueckenotte, P.E.
V. L. Kunzweiler, P.E.
Burns & McDonnell Engineering Company
P.O. Box 173
Kansas City, Missouri 64141

ABSTRACT

This paper will discuss the test results and economics leading to the consideration of a system for the automatic reduction of power consumption on a high-efficiency electrostatic precipitator.

We will examine the results of a series of load tests that were run. We will discuss the test results and their implications, and the use of the Southern Research Institute's precipitator program in this evaluation.

The economic evaluation of the power saving device will be covered through the analysis of tests results.

INTRODUCTION

The high-efficiency, cold-side, electrostatic on a minimal 700-MW coal-fired plant was tested to evaluate both the technical and economic feasibility for consideration of a system for the automatic reduction of power consumption.

It was our intention to determine if it was economically feasible to install a precipitator power reduction system which did not degrade unit opacity more than 2 percent. That is, assuming that the unit is of recent design and normally running at 0 to 3 percent opacity. The system we were proposing is unique in that it does not control precipitator power off of opacity, but only uses opacity as a fine turning or trim device.

The unit was tested at two load levels; full load and 65 percent load. Three test runs were made on the full load test and four test runs were made on the lower load test. Each test run consisted of uniformly distributed manual power reduction in precipitator power.

The specific tests that were performed during each test run in accordance with predefined procedures were:

- Precipitator power consumption.
- Stack particulate emissions.
- Precipitator inlet particulate loading.
- Ash particulate sizing.

- Ash resistivity-in-situ.
- Precipitator inlet and stack gas flow.
- Coal and ash analysis.

The method or procedure for each test will be described under the Test Procedure section. It should be pointed out that all particulate testing was done in accordance with EPA Methods 1, 2, 3, 4, and 5, as published in the Federal Register's, "Standards of Performance for New Stationary Sources, Protection of the Environment" Parts 53 to 80.

EPA formulas were used in the calculation of the results from the data obtained during the tests.

Another useful tool in the data analysis was the Southern Research Institute Precipitator Model program. This program provides a detailed mathematical model of the precipitator from the test results. The model can be used to predict results at different unit load and performance conditions as well as different precipitator power levels.

Selected field power measurements, supply bus measurements, and transformer-rectifier (T-R) readings were taken to determine both useful power and actual input power.

In order to determine the economic feasibility of a power reduction system, data from the tests and the Southern Research Model were used in conjunction with predicted load conditions and fuel costs. Of course, the assessed value of the system took into account payback or return on investment (ROI).

TEST PROCEDURE

DESCRIPTION OF TESTED FACILITIES

The air pollution control system tested was on a 700 MW coal fired steam generator plant equipped with an electrostatic precipitator using two casings, each handling one-half of the rated 2,643,000 acfm at 302 degrees F. The precipitator is designed for a removal efficiency of 99.4 percent.

The precipitator arrangement is as indicated in Figure 1. Each casing is five fields deep by six paths wide. Fields and paths are identified in the figure for clarification.

The source of the particulate is the steam generator rated at 4,500,000 pounds of steam per hour at 2400 psi. The unit is fired with pulverized western subbituminous coal fed from seven coal bunkers.

Precipitator Power Tests

Precipitator power tests were conducted to:

1. Correlate actual field input power to the primary ac and secondary dc readings.
2. Correlate field readings to precipitator supply bus readings.
3. Determine power reduction capability of the precipitator.

Precipitator power reduction tests were run with each TR primary ac and secondary dc current and voltage logged during each test run along with precipitator supply bus ac data. In addition, the power was monitored on a continuous strip chart on the primary side of each TR in a path of fields (one field wide) in the direction of flow through Casing A. The first field in the series was monitored using a power recorder with primary voltage inputs and clamp-on current transformer inputs. This provided a continuous record trend for actual field power supplied corrected for power factor. The remaining four fields in the series were similarly monitored with power transducers temporarily installed in each TR control cabinet utilizing the primary voltage input with the existing current transformers. Monitoring the power in this flow path series established power correlation factors for other fields and for the Southern Research modeling program.

Particulate Sampling

A high-volume EPA Method 5 stack sampler was used at one precipitator inlet and in the stack. The south precipitator inlet was tested for temperature, and gas velocity.

Gas analyses was with an orsat analyzer for concentrations of CO_2, O_2, and CO.

All sampling procedures were by standard EPA methods. The number of sampling points and positions of the points in the flue at the sampling locations, and the sampling time at each point were determined by standard EPA methods.

Particle sizing was with an Anderson head cascade sampler. The precipitator inlet was sampled isokinetically in accordance with the procedures for particle sizing sampling.

The fly ash resistivity measurement procedures were done according to the recommended procedures using a Wahlco, Inc., resistivity probe. The probe is an in-situ field device for use in testing fly ash resistivity. This means of collection is mechanical, so no dust characteristics are destroyed during the sampling process.

Coal samples were taken during each test and composites were sent to a laboratory for analysis.

TEST DATA

Plant Computer Data

The following data was printed every 5 minutes by the plant computer:

- Barometric pressure
- Unit steam flow
- Generator gross MW
- Generator net MW
- Stack opacity
- Flue gas oxygen A
- Flue gas oxygen B
- ID fan inlet pressure

- Precipitator gas inlet temperatures
- Coal feeder coal flows

PLANT DATA READINGS

Manually taken plant data readings consisted of the following:

- ID fan amps
- Unit MVAR
- Buss Voltage and Amperage
- Barometric pressure

PRECIPITATOR CONTROL PANEL READINGS

Precipitator control panel readings taken from the automatic voltage control cabinet:

Secondary volts (kV dc)
Average secondary current (mA dc)
Primary volts (V ac)
Primary current (A ac)

These readings were taken initially and after each power reduction step.

PRECIPITATOR AND STACK FIELD DATA

The data gathered in the field at the precipitator inlet and at the stack is as follows:

- Pitot differential pressure
- Gas temperature
- Normal EPA Method 5 data
- Percent CO_2
- Percent O_2
- Ash resistivity (precipitator inlet only)
- Ash particle sizing (precipitator inlet only)

LABORATORY DATA

Samples were analyzed after the test in the laboratory for the following:

- Particulate sizing
- Particulate loading
- Coal and ash analysis

TEST RESULTS

GENERAL

The data gathered during testing was analyzed to determine specific power consumption and actual particulate removal efficiency.

First, power readings were utilized to correlate actual TR secondary data to actual power consumption. Next, TR secondary readings were corrected to show actual power consumed for each test run accounting for all precipitator inefficiency. Third, specific power consumption curves were developed from the data and the correlation. To support and analyze the actual opacity readings, particulate sizing and loading data was also analyzed. And finally, the Southern Research Institute Modeling Program was used to verify and predict precipitator performance.

Stack Particulate Emissions

Run	Date	Unit Load	Emission Rate
1	5-22-85	691 MW	0.018 lb/MMBtu
2	5-23-85	691 MW	0.014 lb/MMBtu
3	5-23-85	691 MW	0.026 lb/MMBtu
4	6-7-85	450 MW	0.009 lb/MMBtu
5	6-7-85	450 MW	0.009 lb/MMBtu
6	6-8-85	450 MW	0.011 lb/MMBtu
7	6-8-85	450 MW	0.015 lb/MMBtu

The highest emission rate occurred on Run 3 at 691 MW and at a reduced precipitator power input of 493 watts per 1000 acfm, which was 0.026 lb/MMBtu. This is well below the 0.1 lb/MMBtu allowable.

The precipitator efficiency and inlet loading tests were run on only one inlet, the north duct. Temperature and velocity were run only on the south inlet duct. From the data obtained on the south duct, a flue gas volume in acfm was calculated. With this information and the test information on the north duct, the duct loadings for the south duct were calculated. Then a precipitator removal efficiency was generated. The calculated precipitator removal efficiencies are as follows:

Precipitator Efficiency

Run No.	Date	Removal Efficiency
1	5-22-85	99.59%
2	5-23-85	99.65%
3	5-23-85	99.44%
4	6-7-85	99.82%
5	6-7-85	99.77%
6	6-7-85	99.77%

At no time did the precipitator collection efficiency drop below that shown for run number 3.

PRECIPITATOR PROGRAM

The Southern Research Institute Precipitator Model program was used in the analysis of the test data. This computer program was developed by the Southern Research Institute under contract to the Environmental Protection Agency. This model is the most widely used model for electrostatic precipitation, according to the Electric Power Research Institute's Precipitator Reference Manual.

The model predicted precipitator operation, removal, and opacity at various conditions based upon actual test data. Test data input to the program was the actual operating levels of voltage and current, inlet dust loading, inlet dust particle size, ash resistivity, gas composition, gas volume flow rate, and physical precipitator data. With this data base, the program could be manipulated to produce outlet conditions at any desired load and/or voltage and current levels.

Predicted curves from the program are shown in Figure 3. It should be pointed out that the program accounts for all reduced efficiencies by averaging them over the whole precipitator. The effects of this will be outlined under the heading "DISCUSSIONS."

ASH RESISTIVITY

Ash resistivity was run using the in-situ resistivity probe. A description of the sampler and its operation is provided in Test Procedure.

A total of test runs were made. All test runs were on the north precipitator inlet duct. The results of the ash resistivity tests are presented below:

Run		Date	Ash Resistivity
High Ld.	1	5-23-85	4.0×10^{13}
	2	5-23-85	4.0×10^{13}
	3	5-23-85	4.0×10^{13}
Low Ld.	4	6-6-85	1.2×10^{12}
	5	6-6-85	1.2×10^{12}
	6	6-6-85	1.2×10^{12}

COAL AND ASH ANALYSIS

Coal and ash data reports indicate some minor variations from the high load to the low load. This might account for some variation in precipitator performance, however, variances were minimal.

ECONOMIC EVALUATION

The purpose of this series of tests was to gather actual data by which to evaluate the feasibility, economics, and payback or cost benefit ratio of a power reduction system. The actual test data has been applied to the Southern Research Institutes modeling program to generate a series of situations each with its own set of economics.

Power consumption and power savings is reported in ac power units. The precipitator power readings were taken in dc power units and the Southern Research Program's inputs and outputs were also in dc units.

In the evaluations, a 2 percent opacity level has been used in the economics. After analyzing the data, it was felt that this should have actually been a 0 percent or near 0 change in opacity. (See DISCUSSION).

The unit heat rate fuel costs, unit availability, and hours of operation were supplied by the utility. All other values were taken from actual test data. A sample calculation is summarized as follows:

$$\text{Coal Flow} = \frac{(\text{MW})(1000\ \text{kW/MW})(\text{Btu/kWh})}{(\text{Btu/lb})}$$

$$\text{Air Flow} = \left[1 + \frac{\%\ \text{Leakage}}{100}\right]\left[\text{lb coal/hr}\right]\left[\text{\#Air/\#Coal}\right]\left[1 + \frac{\%O^{2}}{20.9\%\ O^{2}}\right]$$

$$\text{Gas Flow} = \frac{[(\text{lb air/hr}) + (\text{lb coal/hr} - \text{ash})]\ [\text{cu ft/lb}]}{(60\ \text{min/hr})(1000)}$$

$$\text{Power Required} = (\text{Gas Flow})\ \frac{\text{Watt Required}}{1000\ \text{kacfm}}$$

$$\text{Fuel Saved} = (\text{kW actual-kW req'd})(\%\ \text{avail}/100)(\text{hrs/day})(365\ \text{days})(\text{Cost/kW})$$

$$\text{C/B Ratio} = \frac{\text{Annual Savings}}{(\text{Installed Cost})(\text{Worth Money}) + \text{Annual O\&M}}$$

DISCUSSION

Power monitoring on this precipitator, as well as many other precipitators and other 480-volt users in power plants normally do not have indication or record of power consumption. A technique was developed in this test program to use existing precipitator monitors to determine actual input power. The power correlation factor that was arrived at, shows that approximately 33 percent more power is required than is actually used in the fields. It should be noted that in Figure 2 this relationship holds fairly closely past the 50 percent power reduction.

The power data and specific power consumption curves demonstrate that significant power can be removed from the precipitator before significant increases occur in opacity. Previous tests on a different precipitator demonstrated that the specific power consumption curves were close to ideal as depicted in Figure 3. The actual specific curves from the test indicate that power was pulled from fields where it should not have been removed.

Close examination of the power data on Table 1 through Table 7 show that the technique of uniform power reduction, as agreed upon prior to the test program, was probably the primary reason for the increase in opacity at each reduction. Flow Path B in Casing A was only contributing 9 percent of the total casing power initially. Subsequent reductions from the test program's uniform reduction approach maintained that ratio at approximately the same percentage. The 9 percent power level was marginal in terms of specific power consumption.

The reasons for the reduced power levels in the B flow path is not clearly known. It is suspected that a gas flow distribution problem caused the problem since the first three fields in the path have low power levels along with the first two fields in the adjacent paths. Review of the layout of the inlet breeching as schematically shown in Figure 1 could have easily allowed for a flow maldistribution of this nature. Other contributing factors such as stratification have not been ruled out.

An important observation to be made is to note the shift in the opacity level of the high-load tests vs. the low-load tests in the specific power curves in Figures 2 and 3. This is primarily the result of the differences in volumetric flow which causes higher sneakage and reentrainment at the higher load.

The Southern Research Institute Modeling Program is an excellent tool to predict data as was utilized in this test program. However, there is one major fallacy, that is--exterior simplifying assumptions must be made particularly in the area of flow distribution and uniformity of particulate loading and averaging of power across a given field. In this test, the low power level in the B path of Casing A was averaged over the whole casing. The model should not average the power in all paths in a casing. As a result of this program, additional modeling is being done to rectify this situation and additional testing with fine power profiling is intended.

The slight variations in coal, composition, size and resistivity could have had a slight contribution to the offset in opacity since the low-load test was run 2 weeks later than the high-load test.

Economically, an automatic power reduction control system could be justified when specific power consumption curves can be demonstrated similar to the ideal curves in Figure 3. Cycling units such as the one tested or ones which operate at reduced loads are good candidates for automatic power reduction. Because this test program had such a broad spectrum of objectives and because of the prior agreement to uniformity reduced power levels, proper profiled power reduction was not achieved. It is anticipated that additional testing will demonstrate the required power reduction for economic justification without increases in opacity.

The work described in this paper was not funded by the U.S. Environmental Protection Agency and therefore the contents do not necessarily reflect the views of the Agency and no official endorsement should be inferred.

* * * * *

Figure 1. Precipitator arrangement

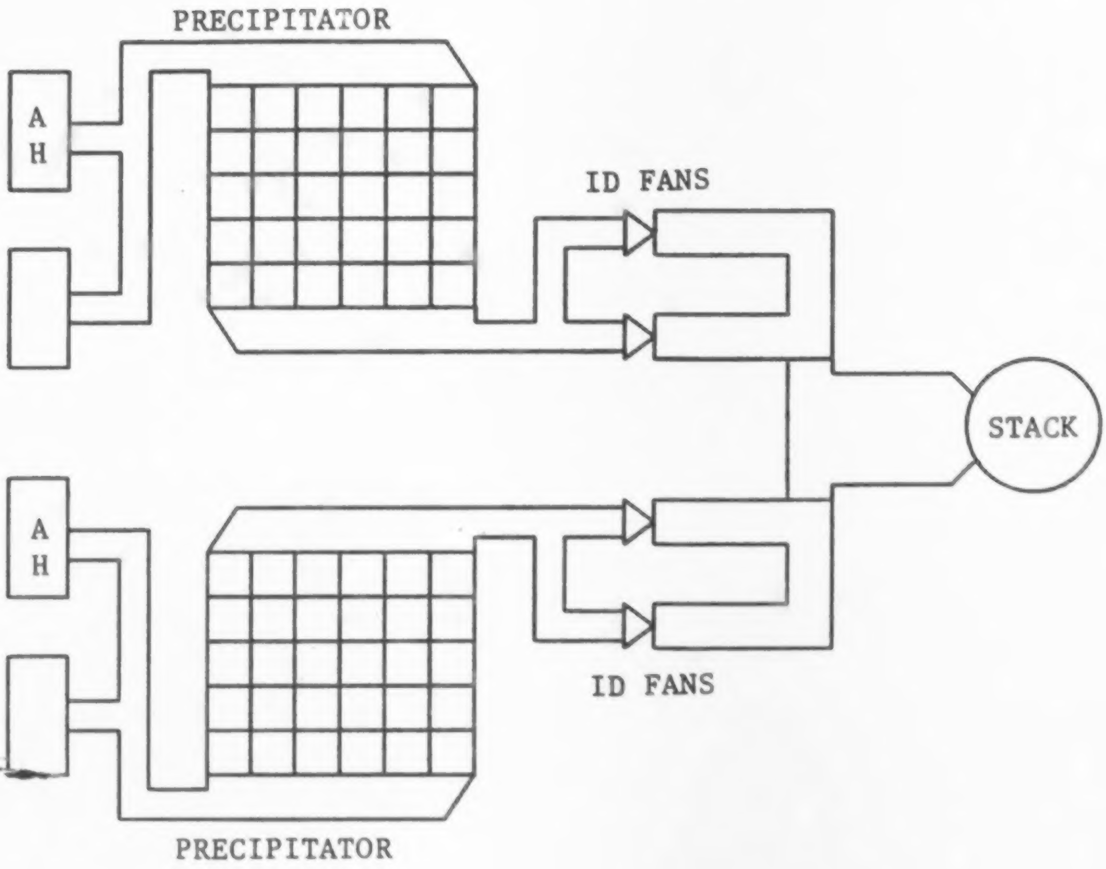

Figure 2. Predicted ideal curves

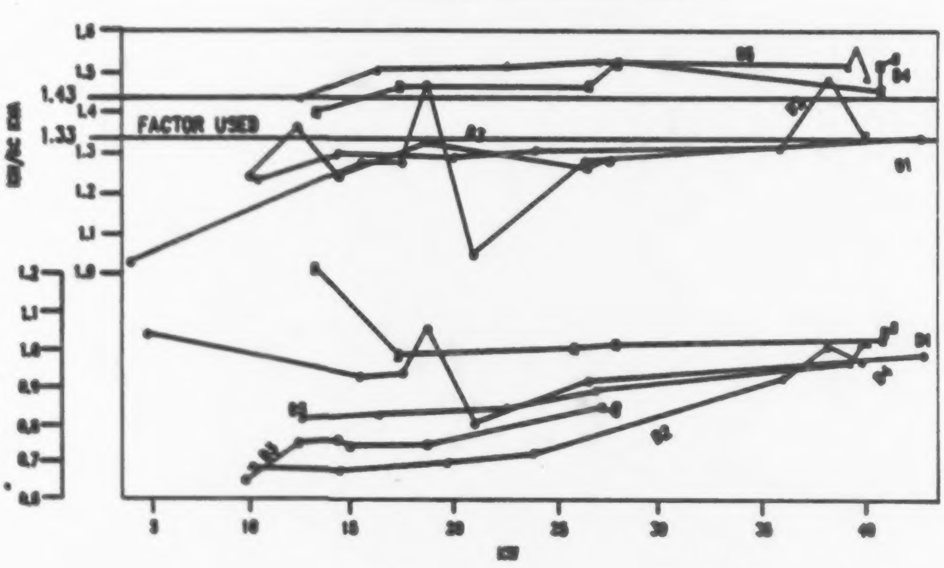

Figure 3. Opacity vs. power consumption
Low load

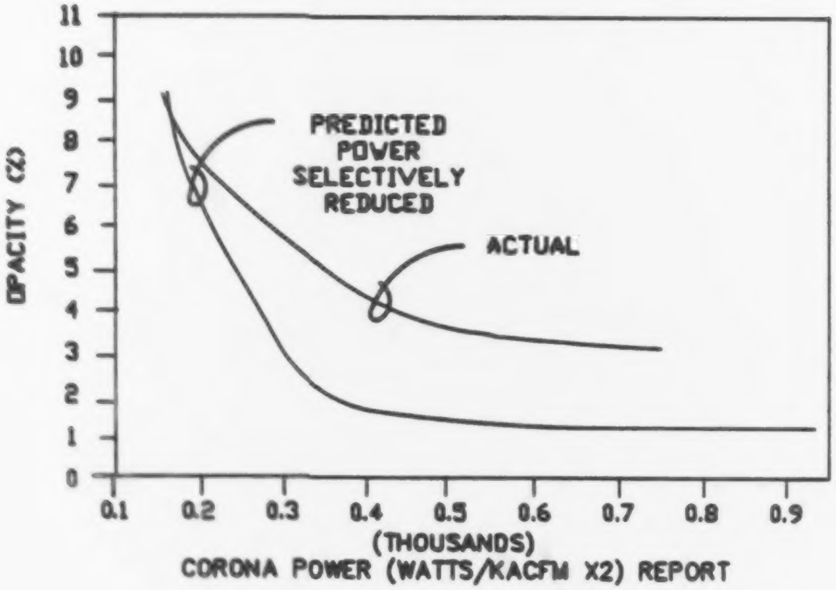

Figure 4. Opacity vs. power consumption
High load

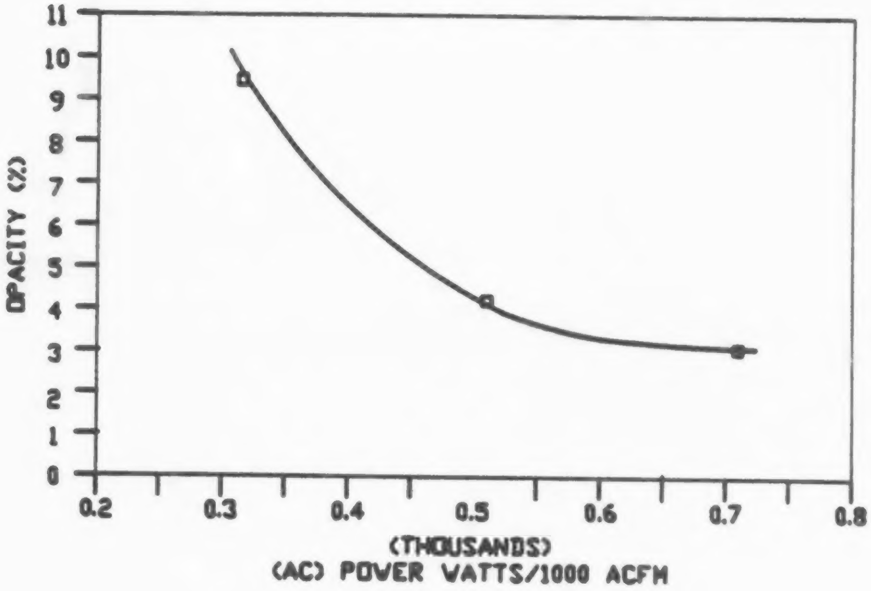

Figure 5. Opacity vs. power consumption
reduced load

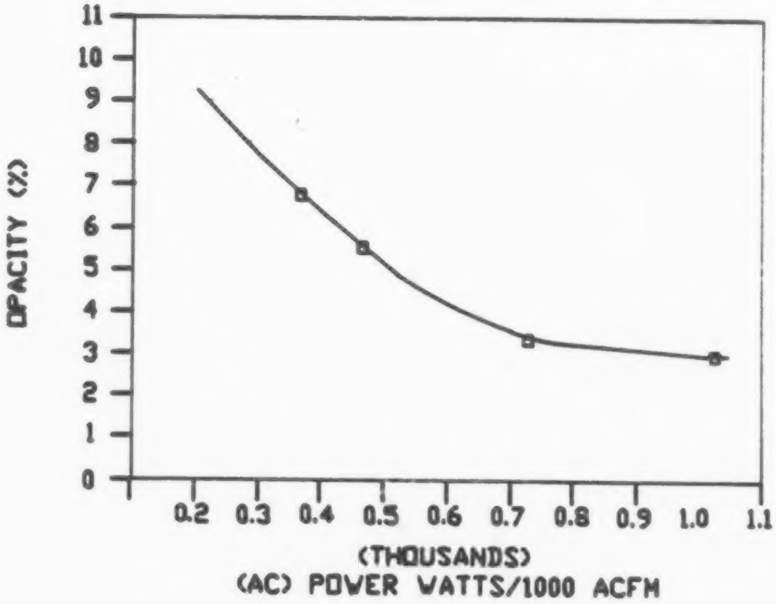

Table 1. Test run No. 1

FIELD	A	B	C	F	E	D	TOTAL W	AVG W	%TOTAL W
1	8645	8938	6145	35272	17130	26367	102496	17083	13
2	5187	1303	559	31920	37506	33350	109825	18304	14
3	21107	1962	25696	38663	43198	33350	163976	27329	20
4	38570	21280	42055	30324	34188	34580	200996	33499	25
5	28249	39348	38891	51604	33888	33197	225177	37529	28
TOTAL W	101758	72831	113344	187783	165911	160844	802470	133745	20

CASING A WATTS 802470
CASING B WATTS 880646
TOTAL WATTS 1683116

FIELD	A	B	C	F	E	D	TOTAL W	AVG W	%TOTAL W
1	17556	3724	4323	1410	30750	31654	89416	14903	10
2	30856	51950	42879	33011	10374	31840	200910	33485	23
3	37346	37905	37027	40804	36256	34381	223719	37287	25
4	35950	13393	35963	39341	31721	34381	190749	31791	22
5	31202	28130	21440	30590	31933	32558	175853	29309	20
TOTAL W	152910	135101	141632	145156	141033	164814	880646	146774	20

CASING A WATTS 802470
CASING B WATTS 880646
TOTAL WATTS 1683116

Table 2. Test run No. 2

FIELD	A	B	C	F	E	D	TOTAL W	AVG W	%TOTAL W
1	3511	9576	10214	27624	14151	16226	81303	13550	11
2	3458	1192	0	32718	36509	35312	109188	18198	15
3	16758	1962	25696	38284	41656	27930	152285	25381	21
4	34713	16492	40565	29566	35910	35910	193156	32193	26
5	28249	39102	38663	32558	33250	34580	206403	34400	28
TOTAL W	86689	68323	115138	160750	161475	149958	742334	123722	20

CASING A WATTS 742334
CASING B WATTS 707686
TOTAL WATTS 1450021

FIELD	A	B	C	F	E	D	TOTAL W	AVG W	%TOTAL W
1	16040	2873	6145	2128	3511	14470	45167	7528	6
2	0	0	0	30949	9576	22264	62789	10465	9
3	36575	40113	35312	37413	34873	35478	219763	36627	31
4	35950	14450	35963	39042	32319	32585	190310	31718	27
5	36628	35112	22823	30590	33250	31255	189658	31610	27
TOTAL W	125193	92548	100242	140122	113529	136052	707686	117948	20

CASING A WATTS 742334
CASING B WATTS 707686
TOTAL WATTS 1450021

Table 3. Test run No. 3

FIELD	A	B	C	F	E	D	TOTAL W	AVG W	%TOTAL W
1	359	0	0	7302	5426	4628	17716	2953	5
2	1596	0	0	11850	12801	20090	46337	7723	14
3	5772	665	10374	19019	22131	15441	73403	12234	22
4	12449	4096	14364	17290	20854	22484	91537	15256	27
5	15082	17130	17636	18554	21566	18554	108521	18087	32
TOTAL W	35258	21892	42374	74015	82779	81197	337514	56252	20

CASING A WATTS 337514
CASING B WATTS 427469
TOTAL WATTS 764983

FIELD	A	B	C	F	E	D	TOTAL W	AVG W	%TOTAL W
1	2660	0	2886	0	3192	3618	12356	2059	3
2	13500	23913	19471	9736	1197	8472	76289	12715	18
3	19711	19737	17636	19711	19751	21027	117572	19595	28
4	19884	5938	20628	17742	16958	21546	102696	17116	24
5	20801	17157	12236	17742	20948	29672	118556	19759	28
TOTAL W	76555	66746	72857	64931	62045	84335	427469	71245	20

CASING A WATTS 337514
CASING B WATTS 427469
TOTAL WATTS 764983

Table 4. Test run No. 4

FIELD	A	B	C	F	E	D	TOTAL W	AVG W	%TOTAL W
1	1463	0	3298	45619	34134	41297	125811	20969	15
2	7342	0	3298	37932	35870	38450	122892	20482	15
3	26440	0	33051	37985	43970	24605	166051	27675	20
4	42879	23169	44409	33516	33888	34580	212441	35407	25
5	30829	44409	42999	33237	33915	32585	217974	36329	26
TOTAL W	108954	67577	127055	188288	181778	171517	845168	140861	20

CASING TOTAL W 845168
CASING B TOTAL 943861
4 1789030

FIELD	A	B	C	F	E	D	TOTAL W	AVG W	%TOTAL W
1	1330	3538	7129	5187	41602	35378	94164	15694	10
2	25536	51006	49742	40991	10374	28302	205951	34325	22
3	39341	41656	49077	44528	61074	34527	270203	45034	29
4	40233	12209	37346	29925	33516	33915	187144	31191	20
5	37307	30630	20828	31202	33237	33197	186400	31067	20
TOTAL W	143746	139038	164122	151833	179803	165319	943861	157310	20

CASING A TOTAL 845168
CASING B TOTAL 943861
TOTAL WATTS 1789030

Table 5. Test run No. 5

FIELD	A	B	C	F	E	D	TOTAL W	AVG W	%TOTAL W
1	0	0	1410	24299	19391	27651	72751	12125	13
2	5027	0	2274	25935	31202	17955	82394	13732	14
3	17556	0	20748	25935	31202	17955	113396	18899	20
4	31282	15415	30324	25376	24379	23754	150529	25088	26
5	20828	33942	33649	23248	23248	22743	157658	26276	27
TOTAL W	74693	49356	88405	124794	129422	110058	576728	96121	20

CASING A TOTAL 576728
CASING B TOTAL 598181
TOTAL WATTS 1174909

FIELD	A	B	C	F	E	D	TOTAL W	AVG W	%TOTAL W
1	1277	1809	4190	3086	23528	21785	55674	9279	9
2	18514	33942	30829	26334	8459	19285	137362	22894	23
3	26281	27132	25589	29260	24419	26281	158962	26494	27
4	29327	8751	25536	18434	21067	22743	125858	20976	21
5	20948	19445	16253	20948	22145	20588	120325	20054	20
TOTAL W	96345	91078	102397	98061	99617	110683	598181	99697	20

CASING A TOTAL 576728
CASING B TOTAL 598181
TOTAL WATTS 1174909

Table 6. Test run No. 6

FIELD	A	B	C	F	E	D	TOTAL KW	AVG KW	%TOTAL KW
1	0	0	0	15428	10853	17742	44023	7337	12
2	1463	0	0	16958	16279	14364	49064	8177	13
3	9576	0	12768	15561	20189	12010	70104	11684	19
4	18620	9510	19365	19790	15082	15082	97449	16242	27
5	14989	23514	24758	15268	14723	13832	107085	17847	29
TOTAL KW	44648	33024	56891	83005	77127	73030	367725	61288	20

CASING A TOTAL 367725
CASING B TOTAL 385580
TOTAL WATTS 753305

FIELD	A	B	C	F	E	D	TOTAL W	AVG W	%TOTAL W
1	0	0	1516	1303	15162	13646	31627	5271	8
2	11278	24419	19365	17875	6384	12848	92169	15362	24
3	17503	17955	16878	18248	16944	18753	106280	17713	28
4	17729	5453	18301	11411	13726	14896	81516	13586	21
5	12768	12130	10055	12768	13300	12968	73988	12331	19
TOTAL W	59278	59956	66114	61606	65516	73110	385580	64263	20

CASING A TOTAL 367725
CASING B TOTAL 385580
TOTAL WATTS 753305

Table 7. Test run No. 7

FIELD	A	B	C	F	E	D	TOTAL W	AVG W	%TOTAL W		
1	0	0	0	11172	7953	13899	33024	5504	12	CASING A TOTAL	285870
2	1357	0	0	12130	13034	10866	37386	6231	13	CASING B TOTAL	297747
3	7581	0	10986	15215	13034	10361	57177	9529	20	TOTAL WATTS	583617
4	15322	7754	14337	15295	11930	12236	76874	12812	27		
5	11372	16944	19152	11411	11411	11119	81409	13568	28		
TOTAL W	35631	24698	44475	65223	57363	58480	285870	47645	20		

FIELD	A	B	C	F	E	D	TOTAL W	AVG W	%TOTAL W		
1	0	0	1436	572	11704	8618	22331	3722	7	CASING A TOTAL	285870
2	6916	19737	16386	13899	3112	9722	69772	11629	23	CASING B TOTAL	297747
3	13167	14869	14071	12236	12236	16519	83098	13850	28	TOTAL WATTS	583617
4	14178	4150	12768	8858	10906	11119	61978	10330	21		
5	10334	11930	10108	8512	9576	10108	60568	10095	20		
TOTAL W	44595	50686	54769	44076	47534	56086	297747	49625	20		

FIRST UTILITY APPLICATION OF A NEW MICR PROCESSOR-BASED DISTRIBUTED CONTROL SYSTEM FOR ELECTROSTATIC PRECIPITATORS

By: Gary R. Gawreluk, Maoz Barav
Research-Cottrell, Inc.
Air Pollution Control Division
Somerville, NJ 08876

Salvatore R. Coco
Lutz, Daily & Brain
Consulting Engineers
Shawnee Mission, KS 66202

ABSTRACT

This paper describes a state-of-the-art system for controlling energization equipment, rappers, and auxiliary equipment for electrostatic precipitators. The various elements of the distributed control system are discussed with emphasis being placed on hardware configuration, operator interface and control strategies.

Specific attention is paid to the role of a central control and the attendant benefits of the graphic displays and the reports.

Finally, the actual application of this control approach to a precipitator installation at Associated Electric's Thomas Hill plant is discussed. The discussion centers around actual operating experience to date and specific benefits derived including lower power consumption and improved control capability.

INTRODUCTION

Microprocessor-based control systems are becoming quite commonplace in the power plant environment. Applications range from critical boiler, turbine, and generator control schemes down to the more mundane tasks assigned to the stations' paper copying machines. One set of criteria for examining the utility of these microprocessor controls may broadly be considered in terms of the number of tasks that must be performed, the complexity of the tasks, and the speed at which they must be completed.

It is not surprising then that control of electrostatic precipitators has been long viewed as an ideal application for microprocessors. These devices have permitted extensive refinement to spark sensing circuits where damaging arcs must be detected and quenched in milliseconds. They have permitted development of control strategies which link subsystems together to improve performance, reduce power consumption, and extend component life; and the real time information transfer, data acquisition capability, and self-diagnostic systems permit the operators and plant maintenance personnel to better understand the precipitator operation and troubleshoot when necessary.

This paper describes the first application of a newly developed microprocessor-based distributed control system for electrostatic precipitators at Associated Electric Cooperative's Thomas Hill Power Plant. The key elements in the system are the transformer-rectifier control, rapper control, ash handling control, and central control station.

PROJECT BACKGROUND

The Thomas Hill Power Plant is located roughly midway between Kansas City and Hannibal, Missouri. The station consists of three (3) coal-fired generating units which burn locally mined coal. The microprocessor control system was part of a new Research-Cottrell rigid electrode precipitator package which was retrofitted to Unit #1, a 180 megawatt cyclone fired boiler.

The precipitator is a four-field machine with 40 foot high collecting plates and nearly 50 feet of treatment length. It was designed with a low treatment velocity and variable intensity rappers in order to keep rapping reentrainment losses to an absolute minimum. This design consideration was extremely important given the low emission limit of 0.005 grains per actual cubic foot and opacity guarantee of less than 10%.

CONTROL SPECIFICATION

The project specification was prepared by the consulting engineering firm of Lutz, Daily and Brain in conjunction with Associated Electric Cooperative. It detailed the requirements for supply and installation of a full scope precipitator backfit.

Considerable emphasis was placed on the design of the precipitator control system, with more than a dozen pages devoted to this alone. The control specification outlined a system that was configured around a distributed control philosophy permitting lower level, dedicated microprocessors to perform specific tasks while a central controller would provide overall command control, system monitoring, and data acquisition. Each of the controllers in the system were rigorously specified with regard to functionality, features, and operational modes. A key system requirement was the implementation of an energy management control scheme which utilized the stack opacity monitor for optimizing transformer-rectifier power levels.

The overall objective was to furnish Associated Electric with a reliable, flexible, easily operated control system that would consistently maintain high performance levels with minimal power consumption.

SYSTEM DESCRIPTION

OVERVIEW

The microprocessor-based precipitator control system installed at Thomas Hill represents the culmination of three years of developmental effort. The development program was geared towards establishing a truly integrated system of precipitator control components while refining the control strategies and improving the reliability of currently available lower level controls.

System configuration relegates the fundamental tasks of controlling transformer-rectifier output and rapper intensity, for example, to lower level microprocessors. These controls may operate independently or in concert when tied to a high speed data link. With the data link connected to a central computer, the operator has the tools to monitor, diagnose, and optimize the performance of his precipitator in response to changing fuels and boiler operation (Figure 1).

TRANSFORMER-RECTIFIER CONTROL

Design Philosophy

The basic operating philosophy of most transformer-rectifier (T-R) controls is to maximize the amount of power input into the precipitator for any given operating condition. In many instances, however, maximizing power input does not necessarily mean maximizing precipitator efficiency. This control, therefore, has been designed to optimize power input with computerized control strategies that follow actual precipitator operation.

Hardware

The T-R control hardware may be classified into two categories; the power level components and the system logic components. The power level components include devices like the primary SCR's, linear reactor, current transformer, circuit breaker, and contactor. The logic components include the microterminal, which serves as the operator interface; the control processor, which executes the control algorithms and handles communication with two independent CPU's; and the phase controller, which controls the gating of the power SCR's.

Each transformer-rectifier control includes three independent microprocessors; one for operator interface, one for power control, and one for communications. This redundancy affords fast spark/arc response and considerable flexibility in control options, resulting in an extremely powerful and reliable system. And even if any one or all of the microprocessors for a given T-R fail, the T-R will still continue to operate. A manual back-up system will automatically take over. This manual backup still has the ability to sense sparks and arcs, extinguish them, and then ramp up to an operator-selectable maximum power level. Features like this, incorporated with unbreakable electrode designs and conservatively rated transformers, can provide strong rationale for questioning the traditional levels of conservatism typically applied to precipitator design in the form of spare fields or bus sections.

The microterminal, which serves as operator interface, is an extremely powerful tool designed to provide nearly limitless flexibility in control adjustment (Figure 2). The high-impact, Lexan^R encased unit contains a keyboard with 24 keys and a 16 character, alphanumeric LED display for clear, understandable readout of data and messages. The microterminal itself is panel mounted next to an array of 10 discrete status LED's for viewing control mode and status at a glance. This panel also contains a manual/automatic selector switch and a full range potentiometer for manual fall-back control.

The microterminal, with its message writing ability, adds a new dimension to the ease of control and degree of information transfer. The software has been written to make it self-prompting, virtually taking the operator by the hand and walking him through initial set-up and subsequent optimizing adjustments. This minimizes the amount of formal training required, reduces the potential for incorrect inputs, and eliminates the need for printed tables or programming instructions. Further, two level password access has been incorporated in order to limit control adjustment to the responsible operating personnel.

Operation

The T/R control is designed to differentiate between sparks and arcs and react differently to each of the occurrences. For the purposes of simple definition, sparks may be considered as low current discharges of short duration and self-extinguishing in nature. Arcs, on the other hand, are more damaging, high current discharges which are relatively self-sustaining.

Spark and arc detection is accomplished by a newly developed proprietary sensing circuit which takes full advantage of the microprocessor's capability. Detection and discrimination is based on a combination of both amplitude and energy level, permitting identification at any point on the wave form. This holds true even at locations close to the zero crossing point where many controls lose sensitivity.

When a spark is detected the control automatically phases back the firing angle of the SCR's and then begins to ramp voltage back up. When an arc is detected, the control phases back to 0% firing angle and remains there for a minimum of one full cycle to quench the arc. The control then initiates voltage recovery on a steep ramp, which is termed a pedestal. Degree of phase back, ramp rate, pedestal rate, and quench time are fully adjustable by simple keypad input (Figure 3).

Aside from the basic control function of spark/arc detection and power-up, there are a few other operator-selectable control modes that deserve mention:

1. Automatic Process Follower™ - reacts to short term upsets, such as soot blowing, and hastens power recovery;

2. Back Corona Control - operates at a level below the onset of back corona (when it exists) for improved collection and reduced power; and

3. Power Down Rapping - reduces T-R voltage to an operator selected level upon receipt of a signal from the rapper control for improved performance on select applications.

Features

The amount of information available at the local controller in the form of data, set-points, status, and alarms also represents a significant advancement in control design. The alphanumeric display provides information, either on demand or in a continuous scrolling readout that, in many cases, has been only available on back-lit alarm panels or CRT terminals in a central control room. Some examples of the types of readouts available at the local level include:

1. primary and secondary voltage and current readings (in pairs);
2. spark and arc rates (separately);
3. undervoltage and overcurrent trips;
4. processor failure;
5. T-R low oil level and high temperature;
6. T-R cabinet high temperature;
7. hopper high level;
8. T-R in remote; and
9. all set-points and limits.

RAPPER CONTROL

Design Philosophy

The rapper control is designed to control magnetic impulse, gravity impact (MIGI) type rappers. Basic control philosophy is geared towards addressing the three primary control variables: rapping intensity, cycle time, and rapping sequence.

Proper adjustment of rapping intensity is required to maintain relatively clean collecting surfaces and minimize rapping reentrainment losses as a function of ash characteristics. The improvements in performance due to the ability of matching rapping forces to changing fuel scenarios is well-supported in industry literature (1,2,3,4) as well as by Research-Cottrell's own experience.

Optimizing the rapping cycle is generally a function of the particulate loading that a given field in the precipitator is treating and is also aimed at reducing rapping reentrainment losses.

Rapping sequence, or the order in which individual rappers are fired, is the least critical of the three variables. Sequence is usually established during initial commissioning of the equipment and may never require modification again.

Hardware

The rapper control hardware utilizes logic components nearly identical in design to those previously described for the T-R control. The three main components, again, are the microterminal, the control processor and the phase controller. Three dedicated microprocessors are also used in the rapper control for operator interface, system control, and communications.

The microterminal used for operator interface incorporates the basic design and operating features that were described for the T-R control. It is of the same durable construction with alphanumeric display and status LED's for quick and clear information transfer (Figure 4). The rapper control software has also been developed to be self-prompting for ease of operation.

Operation

The control is designed for three operational modes; timed, power down rap, and rap all. Additionally, a test mode has been included which can be utilized while any of the other operational modes are functioning normally.

The "timed" mode may be considered normal operation. In this mode, rappers are assigned to timer groups, normally on a per T-R section basis, and identified as either collecting plate, discharge electrode, or perforated plate rappers. Each rapper group may be programmed to fire on different time cycles based upon its location in the precipitator. Rapping cycles are generally progressively longer from inlet to outlet as ash concentration decreases. The rapping intensity in the "timed" mode may be established for individual rappers, groups of rappers, or for the entire precipitator. Further, a few simple key strokes accesses the master intensity adjustment which can change the rapping intensity for the whole precipitator by the same percentage. This feature would be particularly useful in installations where changing fuels yield ashes of widely varying resistivities.

The "power down rap" mode is initiated by the rapper control on a separate time basis. After sending a power down signal to its respective T-R, a given group of rappers will fast rap through the group and then tell the T-R to power-up again. Performance enhancements with this mode of operation are generally limited to large, multi-field precipitators on high resistivity ashes.

The "rap all" and "test" modes are situational in nature. "Rap all" permits all the rappers on the precipitator to be fired sequentially on two second intervals for a given number of cycles programmed by the operator. A typical use of this mode would be for quick clean-up of the electrodes prior to an internal inspection. The "test" mode permits the operator to single out individual rappers and to test fire them at will to verify operation.

Features

One important feature that has been incorporated in this new rapper control design addresses a common problem observed on some of the larger precipitator installations, that being the effect of rapper wire resistance on rapping intensity. This control incorporates a special compensation algorithm to solve the problem. Simply described, the firing of any individual rapper involves a train of pulses which are controlled by the gating of an SCR (Figure 5). The first, low energy pulse is a test pulse which checks to see if the rapper is open or shorted. If a fault is detected, the rapper will not be fired and an alarm will be recorded. If there is no fault, a full-on wake-up pulse then follows. During this period, the total resistance of the circuit is calculated. By comparing this value to the lift (or intensity) programmed for that rapper and entering the value into look-up tables in the microprocessor program, the appropriate firing angle to achieve the desired intensity is calculated and the control pulse is then initiated. All this activity takes place in a fraction of a second.

CENTRAL CONTROL

Design Philosophy

The central control serves as the primary operator interface point as well as the system supervisor. It has been designed to provide the operator with all of the information and control adjustments that are available at the local control level. It also serves to implement integrated control strategies, such as energy management, which require system coordination.

Hardware

Physically, the central control consists of a color CRT, keyboard, central computer, and printer (Figure 6). The high resolution, color graphics monitor utilizes a menu-driven, self-prompting format for ease of operation. The use of graphic displays and dynamic color changes for status indication further simplify operator interface. The keyboard is detachable and contains a full ASCII character set along with 16 function keys.

The central computer is actually a powerful software development station which has been configured and programmed to serve as a front-end central station. It contains 896K bytes of dynamic RAM for the dual purpose of general software storage and graphics data storage. Additionally, a mass data storage system is provided which consists of 1 Mbyte of floppy disk and 5 Mbytes of Winchester disk. Lastly, an expansion card cage is provided with card plug-in access from the rear panel of the control unit chassis. This allows for convenient future system expansion and customization through addition of I/O channel and bus compatible cards.

System communications are handled by a dual redundant Ethernet local area network (LAN). This is a highly reliable, extremely fast communications system with a baud rate orders of magnitude faster than systems which use RS422 loops. Local level controllers are arranged in a multi-drop configuration along standard coaxial cable. Non-intrusive connectors are used for tie-in, eliminating the need for breaking the cable at connection points. Maximum transmission distance is in excess of 1-1/2 miles.

Operation

The central control performs the following major tasks:

1. system monitoring of status and alarms;
2. on/off and parameter adjustment of local controllers;
3. monitoring and start/stop control of ash handling system;
4. implementation of automated, integrated control strategies such as energy management; and
5. data acquisition, storage, trending, and report generation.

Graphic displays assist the operator in equipment identification and simplify the task of system monitoring. For example, if the operator wishes to observe the general trend in power levels through the precipitator, he may call up the "T-R readings" screen (Figures 7 & 8). By pressing one key, a screen is generated which shows a plan view of the precipitator with all of the real-time T-R input and output power levels displayed, updated every few seconds. A single T-R may be more closely scrutinized by pressing another key and entering the T-R's identification number. This is the "T-R control" screen and it gives the operator in-depth knowledge of the T-R as well as full capability to make setpoint adjustments (Figure 9). This screen gives the T-R rating, lists all limit settings and operating setpoints, provides dynamic readout of voltage and current levels and spark/arc rate, and furnishes an alarm listing. Control capability duplicates what is available at the local controller including fine tuning ramp rates and quench times, for example.

The "rapper control" screen is a particularly useful tool for visualizing and setting up rapper sequence, cycle, and intensity (Figure 10). As with the T-R's, a plan view of the precipitator is displayed which presents an I.D. for each individual rapper along with its operating status. Rapper status includes enable/disable, open or shorted rapper, and intensity of each rapper. Dynamic color change with alarm message permits quick location of a faulted device, if one should occur, so that maintenance may be promptly performed. Since the rappers are roof-mounted, inspection and maintenance of the device may be performed while the precipitator remains on-line.

The "energy management" screen utilizes a control strategy integrated with a stack opacity monitor to optimize performance while minimizing power consumption (Figure 11). Operator programmable selection include auto or manual control, opacity limits, voltage limits, lag time, steps of change, alarm setpoints, and series or parallel field sequencing. A companion screen, the "energy management plot," makes use of the computer mass data storage capability and shows the effectiveness of the chosen energy management control strategy over time. Separate graphs of both total power consumption and opacity are displayed against a time frame of either 1 to 48 hours or 1 to 32 days.

The central computer also interfaces with a programmable controller which controls the ash handling system. A graphic depiction of the hopper area clearly indicates status of the ash handling system, such as valve position and vacuum level, as well as status of the hopper heaters and vibrators. Start/stop control of system sequencing is also provided from the central control.

The central control can also play a key role in diagnosing precipitator performance problems. Hard copy power levels, setpoint changes, and alarms can be generated as required and analyzed against opacity printouts. Voltage-current curves can be screen-generated and printed out to further evaluate the cause of a performance shortfall. Additionally, communication ports are provided to enable information access by the plant's host computer.

OPERATING EXPERIENCE

The microprocessor control system was commissioned in August, 1985. System start-up was relatively troublefree with more concern being centered around some marginally sized motor control center contactors and breakers than on the microprocessor control elements. No discernable problems were detected in the operation of the local controllers and only minor software flaws were detected in the central control programming. The smooth start-up and subsequent operation was due in large part to the system testing performed at two different field sites as well as the full system staging and checkout done in the shop prior to shipment.

Microprocessor component reliability has been very good. There have been no card failures to date, nor has the central computer gone down. The Ethernet communications network has functioned as designed with no indication of noise on the lines, even though the local controllers are located at the precipitator roof level and the central computer is in the boiler control room. There was, however, some noise interference on the RS-232 link which ties into the ash handling programmable control, but this has since been resolved.

The client has expressed satisfaction with the operation of the controllers and in particular the energy management system. With one transformer-recitifer de-energized and the opacity limit set at 10%, the system has demonstrated the ability to operate with power consumption less than 20% of installed values.

The ash handling control has also been identified as one of the bright spots in the system. The graphics provide an excellent depiction of system operation and there have been no incidences of full or plugged hoppers since start-up.

Plant operating personnel have indicated that the considerable amount of information available to them in the boiler control room permits them to gain a better understanding of the precipitator operation. Over time, as more experience is acquired, this should translate into improved performance, refined maintenance procedures, and reduced energy consumption.

SUMMARY AND CONCLUSIONS

A fully integrated, microprocessor-based distributed control system for electrostatic precipitators has been installed and commissioned at Associated Electric's Thomas Hill Power Plant. The system utilizes a multi-drop configuration with all local level controllers tied by a high speed data link to a central control complete with menu-driven CRT and keyboard. The central control gives the operator all of the control and monitoring functions of the local controllers in addition to mass data storage and energy management capability.

The system satisfies not only the project specifications, but a desire to address emerging control strategies and design enhancements under consideration, for this, or any future projects. The ultimate utility of this new control system is bounded only by the researcher's and applications engineer's ability to develop improved performance relationships in the precipitation process and design algorithms to describe them.

ACKNOWLEDGMENTS

The authors gratefully acknowledge the cooperation of the following personnel from Associated Electric Cooperative in the preparation of this paper: Carl R. Jansen, Jr., Supervisor, Instruments & Controls (Headquarters); Terry Ross, Electrical Maintenance Superintendent (Power Station); and Dick Stearns, Assistant Operations Superintendent (Power Station).

The work described in this paper was not funded by the U.S. Environmental Protection Agency and, therefore, the contents do not necessarily reflect the views of the Agency and no official endorsement should be inferred.

REFERENCES

1. White, H.J., Industrial Electrostatic Precipitation , Addison-Wesley, Reading, MA, 1963, p. 365.

2. Oglesby, S. Jr. and Nichols, G.B., "Electrostatic Precipitation Technology for Source Emission Control," Recent Advances in Air Pollution Control , American Institute of Chemical Engineers Symposium Series 137, Vol. 70, 1974, pp. 354-5.

3. Katz, J., The Art of Electrostatic Precipitation (Supplement to the 2nd printing), Precipitator Technology Inc., Munhall, PA, 1/81, pp. 379-80.

4. Gooch, J.P. and Piulle, W., "Studies of Particle Reentrainment Resulting from Electrode Rapping," Conference Proceedings on Particulate Collection Problems Using Electrostatic Precipitators in the Metallurgical Industry, 1977, pp. 107-8.

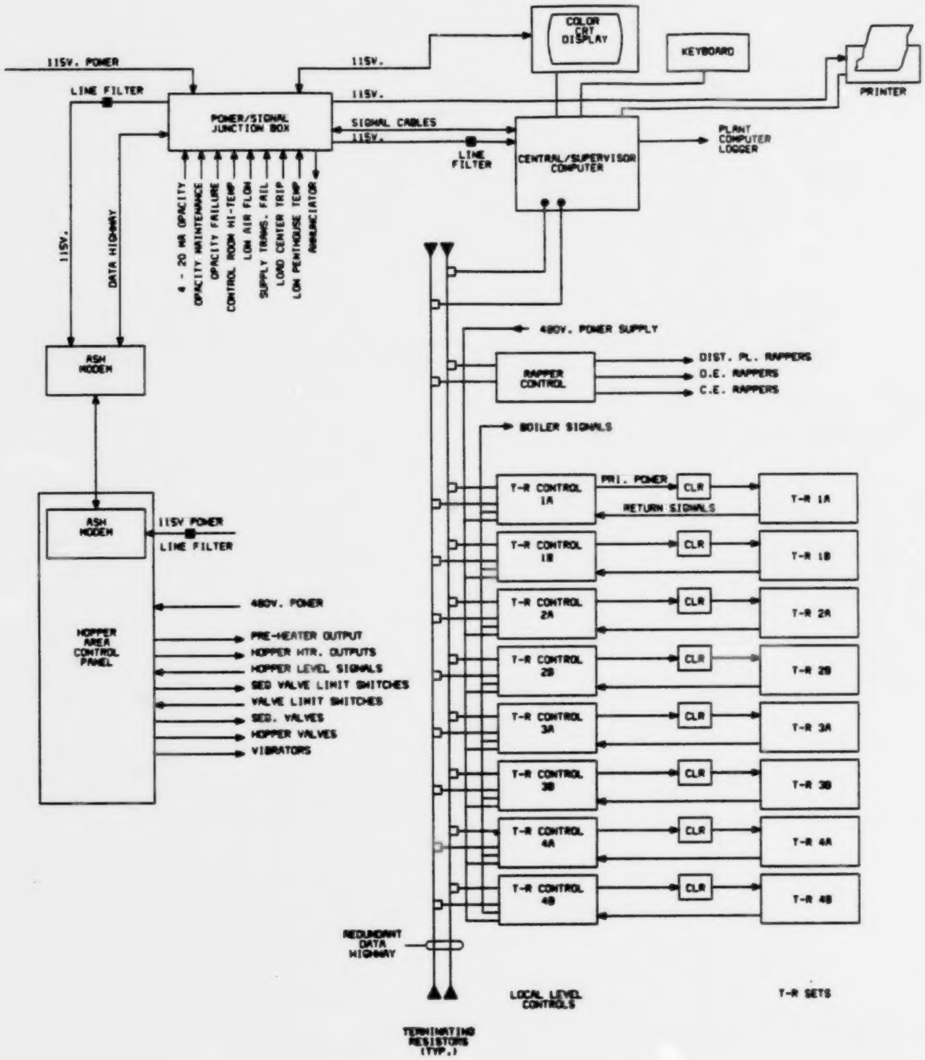

Figure 1. Microprocessor-Based Distributed Control System For An Electrostatic Precipitator

Reproduced from
best available copy.

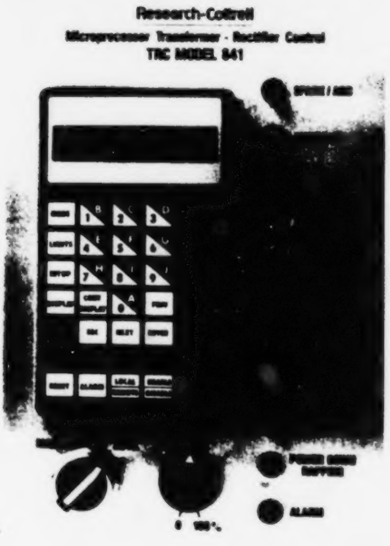

Figure 2. Microterminal For Transformer-Rectifier Control

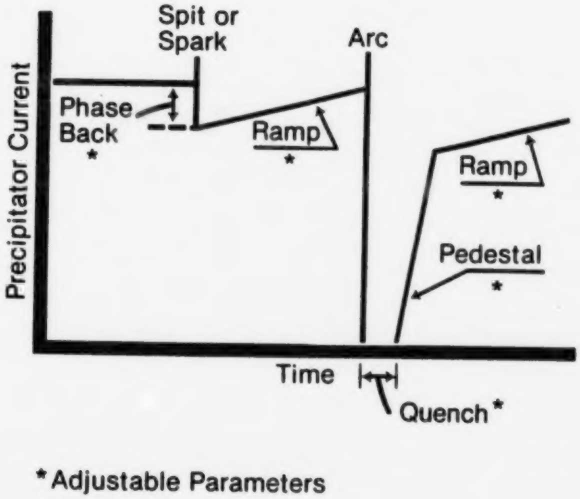

Figure 3. Transformer-Rectifier Control Operation

Figure 4. Microterminal For Rapper Control

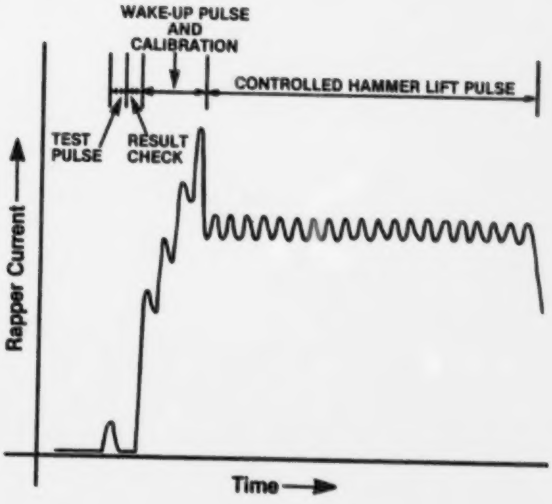

Figure 5. Rapper Control Pulse Train

Reproduced from
best available copy.

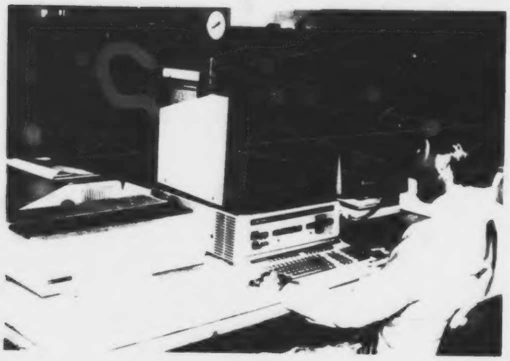

Figure 6. Central Control Station

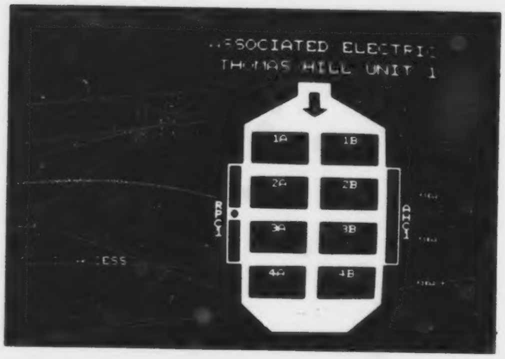

Figure 7. Menu Screen

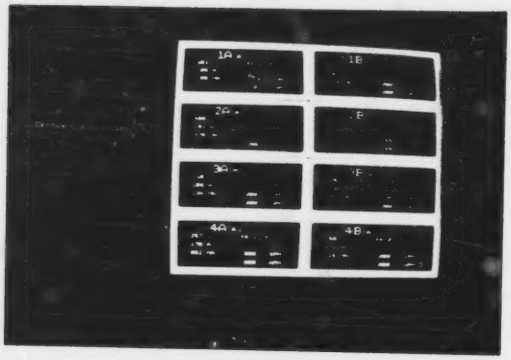

Figure 8. T-R Readings Screen

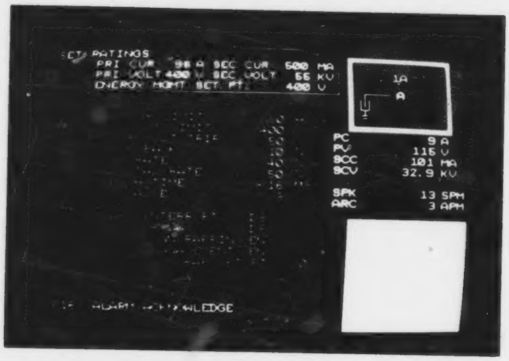

RATINGS
PRI CUR 98 A SEC CUR 500 MA
PRI VOLT 400 V SEC VOLT 55 KV
ENERGY MGMT SET PT 400 V

PC 9 A
PV 115 V
SCC 101 MA
SCV 32.9 KV
SPK 13 SPM
ARC 3 APM

ALARM ACKNOWLEDGE

Figure 9. T-R Control Screen

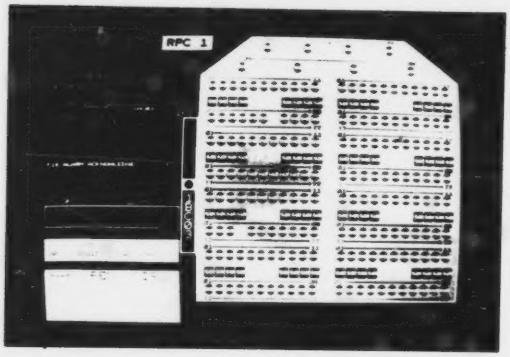

Figure 10. Rapper Control Screen

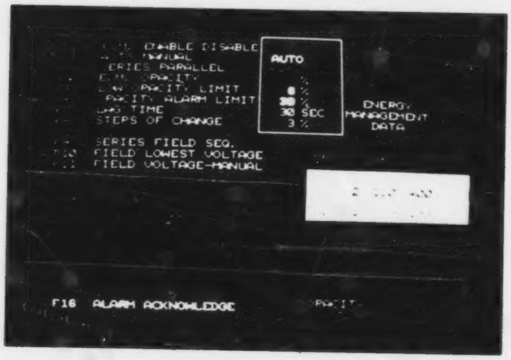

ENABLE DISABLE
MANUAL
SERIES PARALLEL
OPACITY
LOW OPACITY LIMIT
OPACITY ALARM LIMIT
LAG TIME
STEPS OF CHANGE
SERIES FIELD SEQ.
FIELD LOWEST VOLTAGE
FIELD VOLTAGE-MANUAL

0 %
30 %
30 SEC
3 %

F16 ALARM ACKNOWLEDGE

Figure 11. Energy Management Screen

POWER CONSUMPTION OF OPACITY FEEDBACK CONTROLLED ELECTROSTATIC PRECIPITATOR TRANSFORMER-RECTIFIERS

JENTJE J. ROOSMA
SENIOR ELECTRICAL ENGINEER
GENERAL ELECTRIC ENVIRONMENTAL SERVICES, INC.
LEBANON, PENNSYLVANIA

JOHN B. HOWARD
MANAGER, POWER PRODUCTION
ALABAMA ELECTRIC COOPERATIVE, INC.
TOMBIGBEE POWER PLANT
LEROY, ALABAMA

ABSTRACT

A series of comparison tests were performed from September 1984 through January 1985 on Unit #2 at the Alabama Electric Cooperative, Inc., Tombigbee Power Plant in Leroy, Alabama. The purpose of these tests was to evaluate the performance of an Opacity Feedback Controller (OFCON) which was interfaced with the electrostatic precipitator's transformer-rectifier control cabinets. Under varying load conditions, power levels of the transformer-rectifier (T-R) sets were automatically controlled based on the outlet opacity readings. Overall power consumption of the T-R sets was monitored with and alternatively without the opacity feedback control system in operation. The results of the tests clearly demonstrated that significant energy savings may be realized by automatically controlling power as a function of opacity levels during varying operating conditions.

INTRODUCTION

Electrostatic precipitators are normally equipped with transformer-rectifiers capable of supplying corona power for normal operation as well as increased levels for operation under variable conditions such as soot blowing or fuel changes. In order to accommodate these situations, supplying modestly oversized T-Rs is the conventional procedure since the expense for a higher KVA rated T-R is considerably less than the proportional KVA increase. Therefore, T-R sets may be able to operate at reduced power levels for significant periods of time.

The potential energy savings is site specific and related to various operating parameters. Assessment as to whether to use an opacity feedback control is a function of actual precipitator performance vis-a-vis required precipitator performance, installed T-R power capability and the boiler's operating load profile.

FUNCTION

The opacity feedback controller, developed by General Electric Environmental Services, Inc. under the trade name "OFCON" is designed to minimize T-R power consumption. Basically, OFCON controls the opacity level by altering transformer-rectifier output. It does this by modulating T-R power output to maintain opacity levels within operator pre-set limits.

The OFCON performs this function when it receives a signal from the opacity monitor, compares it with two preset opacity levels, and decides what action should be taken. The preset opacity levels represent "high" and "low" limits. The "high" limit is set well below regulatory requirements. The "low" limit, determined by the utility, is set at two to four points below the high preset opacity level. When opacity exceeds the "high" limit, the T-R power is automatically increased at a fast rate to decrease the opacity. When opacity levels drop below the "low" limit, the T-R power decreases at a slow rate and the opacity begins to increase. (See Figures 1 and 2)

Normally opacity will remain within a "dead band region"; i.e., between the "high" and "low" preset opacity levels. When operating in the "dead band region" the optimized opacity level demands no modification of T-R set output by OFCON. Occasionally, opacity will momentarily go slightly outside of the deadband, especially during periods of unstable boiler operation. However, power corrections for increasing power in response to opacity above the "high" limits are electronically set to react faster than for readings resulting in decreasing power. (See Figure 3)

CAPABILITY

OFCON is capable of controlling up to twenty-four T-R sets arranged as four independent electric fields, each with up to six transformers. (See Figure 4) Each of the four electrical fields can be manually set to a minimum level of transformer-rectifier power. The proportional power setpoint for each of the four fields is operator adjusted by means of a potentiometer. The setting determines the lowest power the T-R will supply during low opacity conditions. The level of the setting represents a percentage of the load as compared to air load test conditions. During high opacity conditions, maximum power is generally below the air load power levels, but will be as high as the automatic voltage control will permit for normal operation.

Generally, the recommended adjustment is to set the outlet fields at a lower power level than the inlet fields. After adjustment, the OFCON will automatically select the corona power level which achieves the most economical operating mode between the pre-selected high and low opacity levels.

Another capability provided by OFCON is the handling of periodic span/calibration cycles which are inherent to opacity monitors. During these cycles, the OFCON locks its output and momentarily ignores the signal from the monitor. The lockout eliminates false interpretation of the span/calibration cycles and thereby prevents unwarranted power reductions with their resultant high opacity conditions. Added to this circuit is an adjustable timer which forces the transformers to full power if the cycle is not complete within eight minutes (setting availability in one minute increments up to eight). The over-riding adjustment of maximum allowable cycle time is accomplished by an eight-position jumper arrangement designated on the board as "SPAN/CAL TIME OUT".

In these unusual situations or when OFCON control is not desired and power to the precipitator needs to be at a maximum level, a single remote contact closure is provided to over-ride the power-saving mode of the OFCON control. An alarm relay is also incorporated in the event of opacity monitor failure to supply a 4-20 mA signal to the OFCON control.

FEATURES

The OFCON has been engineered for durability and reliability, utilizing high-reliability, standard integrated circuits, designed to operate in the temperature range of 10°C to 50°C. The integrated circuits are designed to withstand shock, vibration, high humidity and temperature. Dependable performance is further ensured by manufacture according to strict quality assurance procedures which include functional testing.

The OFCON control has also been designed for easy access and maintainability. A self-test mode is included which allows the OFCON control to be functionally checked end-to-end. Light-emitting diodes (LEDs) provide guidance to the operator in servicing alarms and indicate the status of T-R set automatic voltage control (AVC) operating conditions.

Other features are a local control panel opacity meter to monitor performance, easy input accessibility for pre-setting opacity limits and AVC operating conditions for each of the four electrical fields, and availability of remote alarm indicators.

BENEFITS

To summarize benefits, the OFCON precipitator power controller provides minimum corona power usage to meet required performance levels. Modern design and QA-controlled construction, using highly reliable components, produce a dependable, easily maintained control device. The OFCON has the capacity to control up to twenty four transformers. The OFCON allows flexible control strategy by permitting the operator to preset the range of acceptable opacity levels as well as desired automatic voltage control.

In addition to its use on new equipment, OFCON is suitable for retrofitting, regardless of precipitator type or manufacturer. A prerequisite is that the automatic control interface with OFCON needs to be the General Electric AVCON 2000 or the Digital AVC automatic voltage controls. If not currently installed, AVCON 2000 or the Digital AVC controls can also be retrofitted with the OFCON control.

TEST RESULTS

Controlled opacity tests were performed on Boiler #2 at the Alabama Electric Cooperative, Inc., Tombigbee Power Plant, located in Leroy, Alabama using GE's OFCON control. The No. 2 Boiler is a balanced draft system rated at 1,755,000 lbs/hr. steam flow and operates at 1,980 PSIG steam pressure with superheat temperatures of 1,005°F. Total boiler gas flow rate at full load is 2,575,000 lbs/hr. Nominal generator rating is 250 MW. The electrostatic precipitator operates on the hot side of the air heater treating a flue gas flow rate of 840,000 ACFM at 710°F.

Coal samples collected during the tests indicated the following analysis (ultimate):

12.00%	Ash	61.60%	Carbon
9.97%	Moisture	1.17%	Nitrogen
1.52%	Sulfur	8.24%	Oxygen
4.48%	Hydrogen	H.H.V.	11,650 BTU/Lb.

The electrical arrangement of the T-R sets is illustrated in Figure 5. For OFCON control purposes, the T-Rs were arranged electrically as shown in Table 1.

TABLE 1. T-R CONTROL ARRANGEMENT

OFCON Field No.	T-R Identification
1	C, D, E, F
2	G, H, I, J, K, L
3	M, N, P, R
4	S, T, U, V

Note that T-R sets connected to the inlet (A, B) and outlet (W, X, Y, Z) fields were not connected to the OFCON system.

Three kWh meters were connected to the inputs of all T-R control cabinets for the purpose of monitoring the power consumption of the T-R sets. A summary of the test readings is shown in Table 2.

TABLE 2. SUMMARY OF TEST READINGS

Date	MW Output	Normal Control KW	% Opacity	OFCON Control KW	% Opacity	kW Reduction
10/01/84	200	376	2	140	10-12	235
10/16/84	250	312	3	274	12-14	38
11/07/84	150*	220	8	128	10-12	92
11/14/84	110	231	0	87	8-10	144
01/17/85	150*	578	4	197	9-11	381

*Averaged: Normal control 399 KW, OFCON control 162 KW.

The foregoing data is graphically illustrated in Figure 6. Note that the top line in the graph depicts T-R power consumption with normal control; the bottom line shows consumption with the OFCON in operation. The difference in kW between each testpoint is the energy savings at that particular load during that particular test. In order to assess power consumption more completely a one year load profile was also generated.

MW output data, primarily during 1983 with two months of 1982, was tabulated and is shown in Table 4. This data represents the frequency of hourly occurrences of the noted MW output over a 24 hour period and was recorded at two week intervals. A histogram of the data shown in Table 4 was utilized to produce a curve (Figure 7) which may be considered the load profile. Power consumption data was not measured below 110 MW. Therefore, power savings for that segment of the graph shown in Figure 6 are estimated. Projected power savings relative to the frequency distribution of occurrences for various MW output levels are shown in Table 3.

TABLE 3. PROJECTED POWER SAVINGS

From MW	To MW	Average kW Savings	Occurrences	kWh Savings
50	60	175	5	875 Est.
60	70	167	7	1,169 Est.
70	80	158	10	1,580 Est.
80	90	150	13	1,950 Est.
90	100	142	17	2,414 Est.
100	110	140	22	3,080 Est.
110	120	170	27	4,590
120	130	220	33	7,260
130	140	230	42	9,660
140	150	240	52	12,480
150	160	250	58	14,500
160	170	240	59	14,160
170	180	237	55	13,035
180	190	233	48	11,184
190	200	230	34	7,820
200	210	220	27	5,940
210	220	170	23	3,910
220	230	150	11	1,650
230	240	110	6	660
240	250	40	3	120
		TOTALS	552	118,037 kWh

CONCLUSION

Since each occurrence represents an increment of one hour and assuming a total operating time per year of 7,534 hours (86% capacity factor), estimated annual kWh savings would be:

$$\frac{7{,}534 \text{ Hours}}{552 \text{ Hours}} \times 118{,}037 \text{ kWh} = 1{,}610{,}950 \text{ kWh}$$

Based on a utility cost per kWh of $0.025 kWh, projected annual dollar savings are:

$$1{,}610{,}950 \times \$0.025 = \$40{,}274$$

This annual savings potential is available while maintaining electrostatic precipitator performance well within regulatory requirements.

Table 4. FREQUENCY DISTRIBUTION OF OCCURENCES OF MW OUTPUTS
(SAMPLE SIZE 552)

DATE	GENERATOR OUTPUT IN MW																				
	50	60	70	80	90	100	110	120	130	140	150	160	170	180	190	200	210	220	230	240	250
1-11-83		4	1	1	1		5	6	4	2											
1-26-83		1	1			3					3	3	5	4	3	1					
2-11-83								4	1	1	1	6	4	2	2	3					
2-26-83									1	3	1	3	2	2	2	1	2	3	2	2	
3-11-83													4	1	4	3	2	6	4		
3-26-83												1	4	4	1		5	2	4	2	1
4-7-83			1	1				1	2	3	2	2	1	2	1	4	3	1			
4-26-83									2	4		2	3	3	5	4	1				
	N.A.																				
5-26-82				2	3	2		1		1	8	2	3	2							
6-9-82				1	3	2	1		2	5	3	3	4								
6-26-82					2	6	5	5	3	3											
7-9-83			1	4	2	1	2	1		1	7	3	2								
7-26-83									5	5	5		3	1	1	1	2	1			
8-9-83	1					3	2	3	3	2		3	2		1		3	1			
8-26-83							2	3	1	4	2	5	6	1							
9-9-83						5	1	2	1	1	3	1	5	3	2						
9-26-83						4	1		1	1	1	4	4	7	1						
10-9-83							4	2	1	2	1	2	4	5	3						
10-24-83						2	2	1	1	1	1	1	9	4	2						
11-9-82	4	5	2	1	2	2	3	4	1												
11-26-82						2	2	3	2		1	3	2	3	4	2					
12-9-82						2	2	2	3	3	3	2	6	1							
12-30-83							1	1	1	1	3	2	4	5		1	1	3	1		
	5	10	6	10	13	34	33	39	35	43	45	48	77	50	32	20	19	17	11	4	1

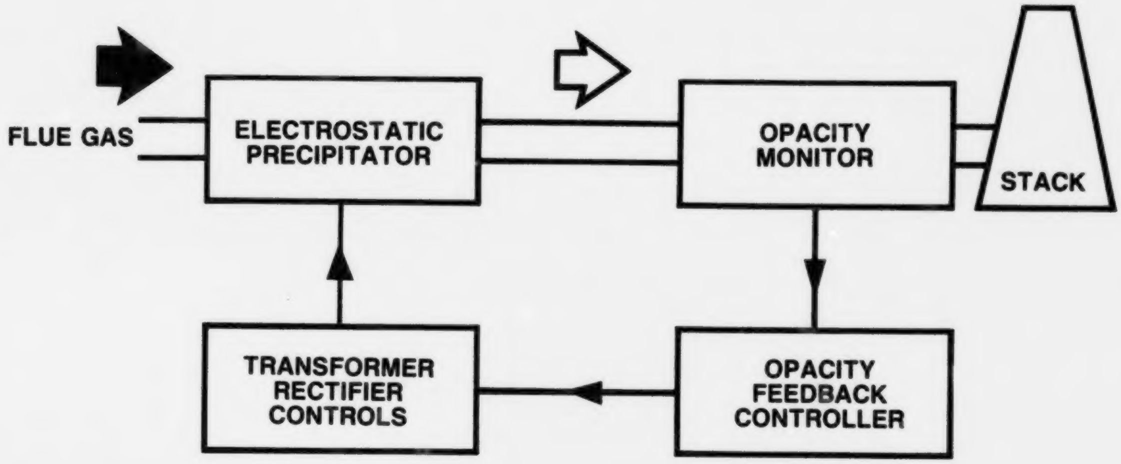
FLUE GAS
ELECTROSTATIC PRECIPITATOR
OPACITY MONITOR
STACK
TRANSFORMER RECTIFIER CONTROLS
OPACITY FEEDBACK CONTROLLER

Figure 1. Opacity Feedback Controller

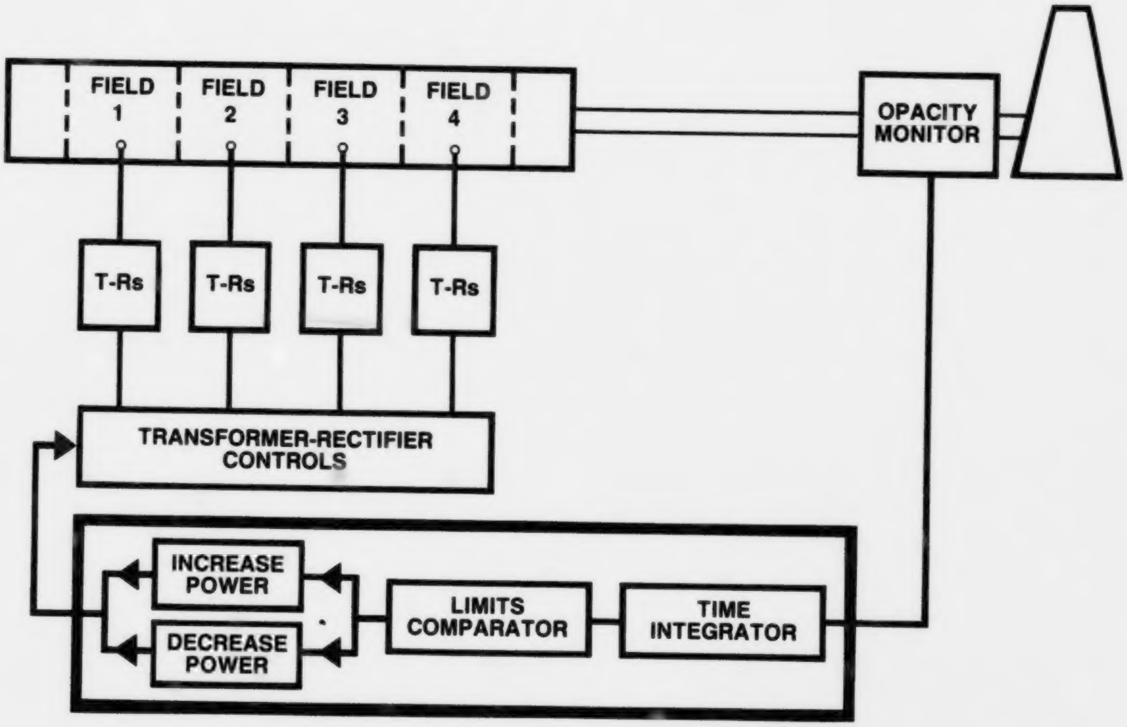

Figure 2. OFCON Control

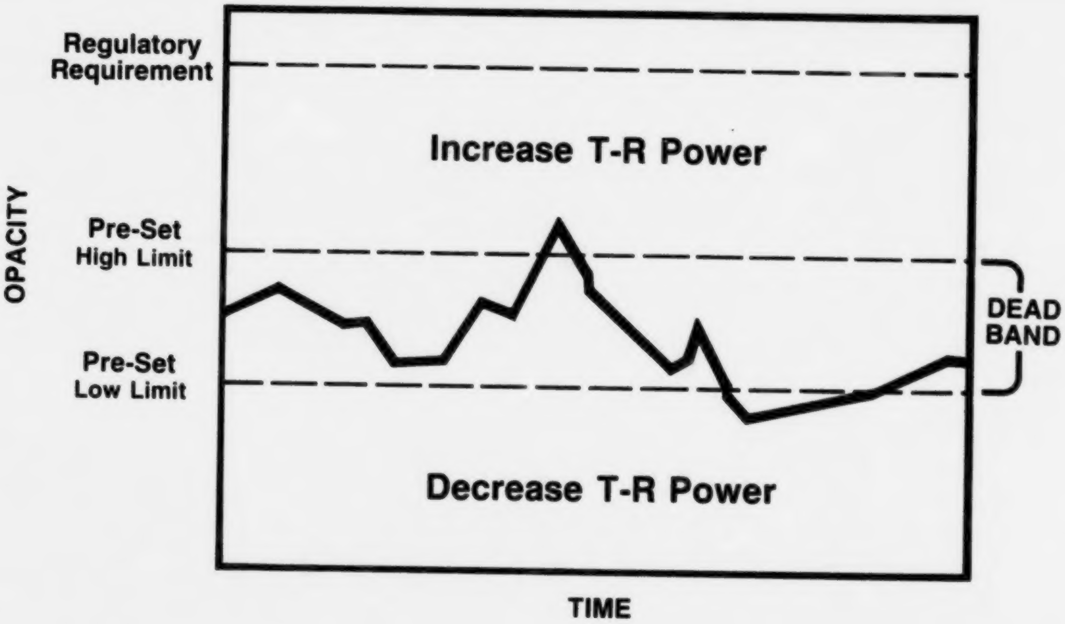

Figure 3. T-R Control versus Opacity Level

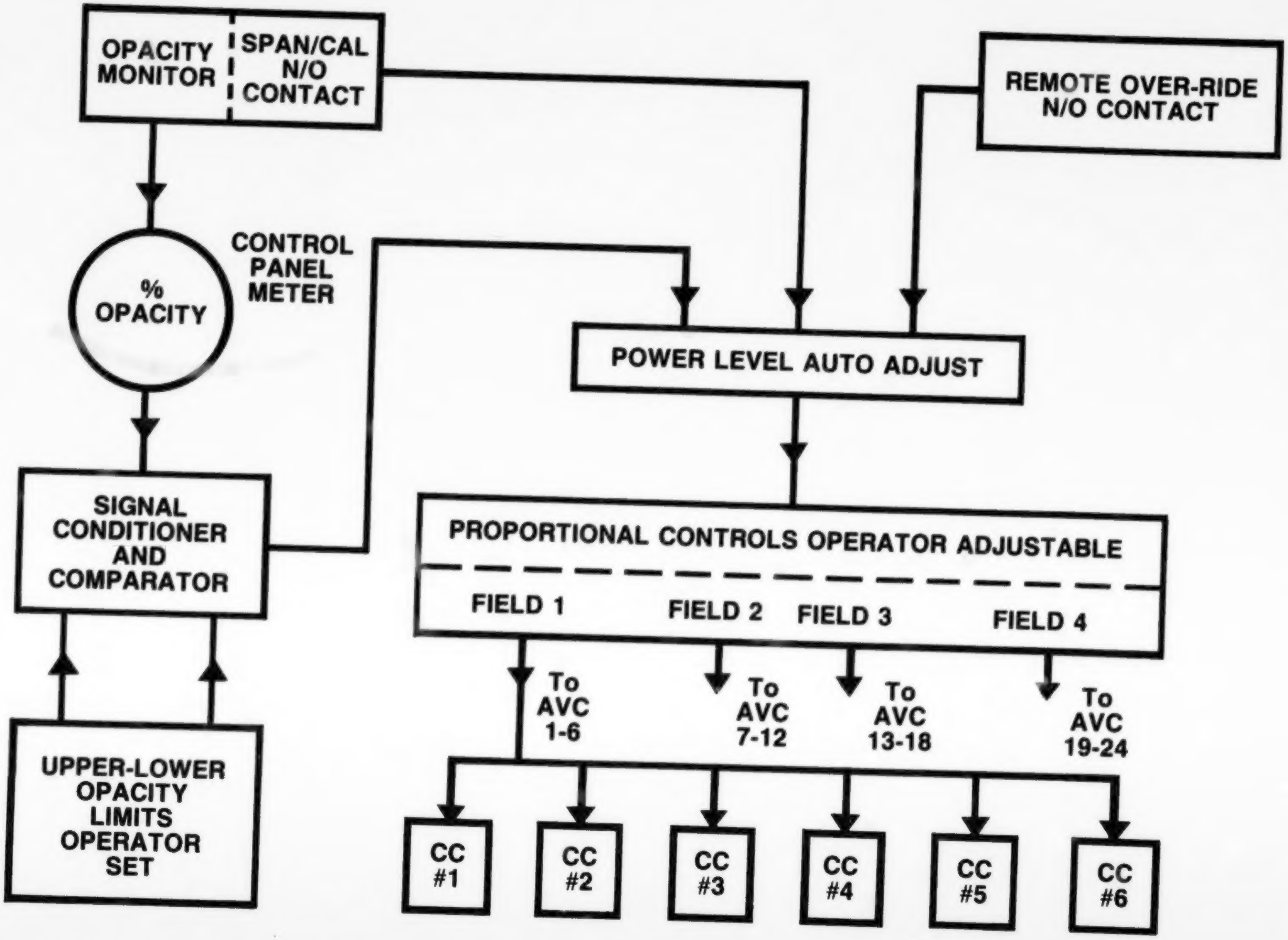

Figure 4. Typical OFCON System Block Diagram

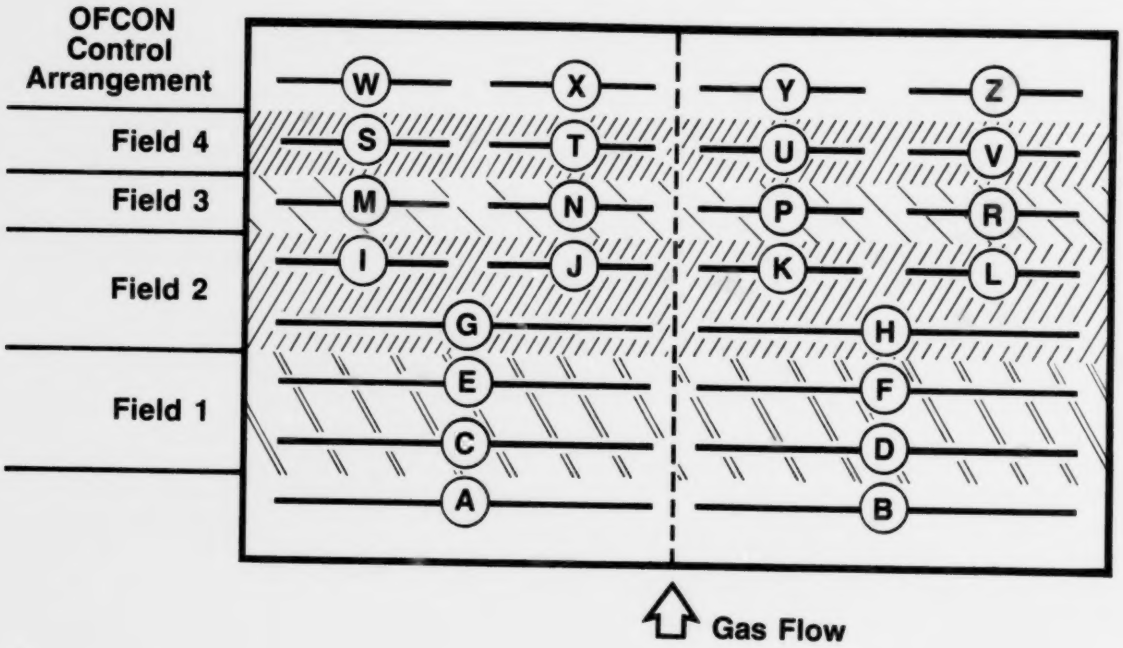

Figure 5. Transformer-Rectifier Electrical Arrangement

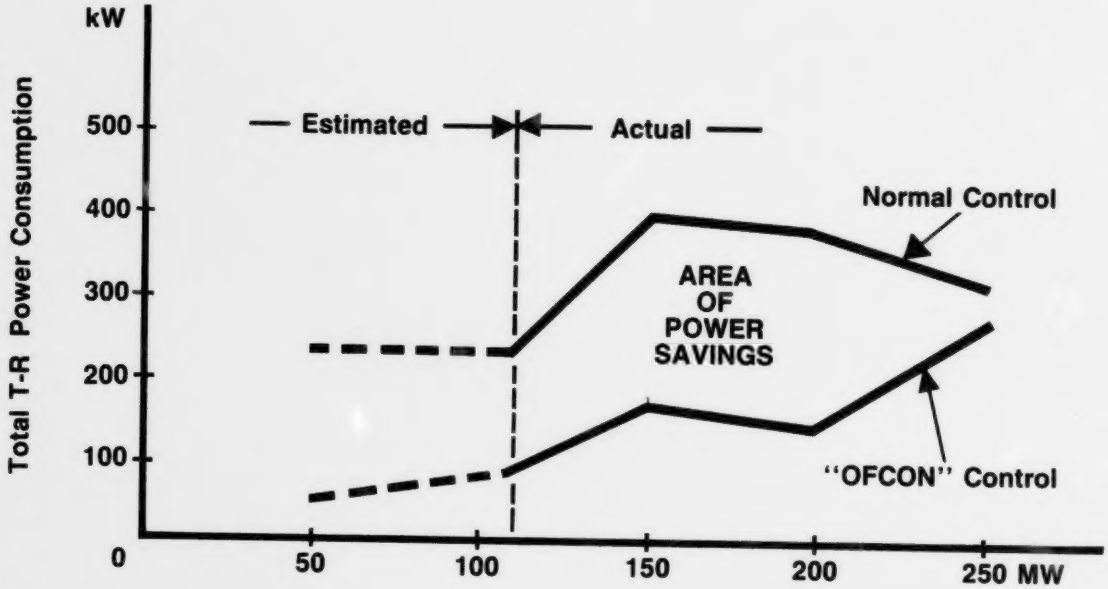

Figure 6. Measured Power Savings

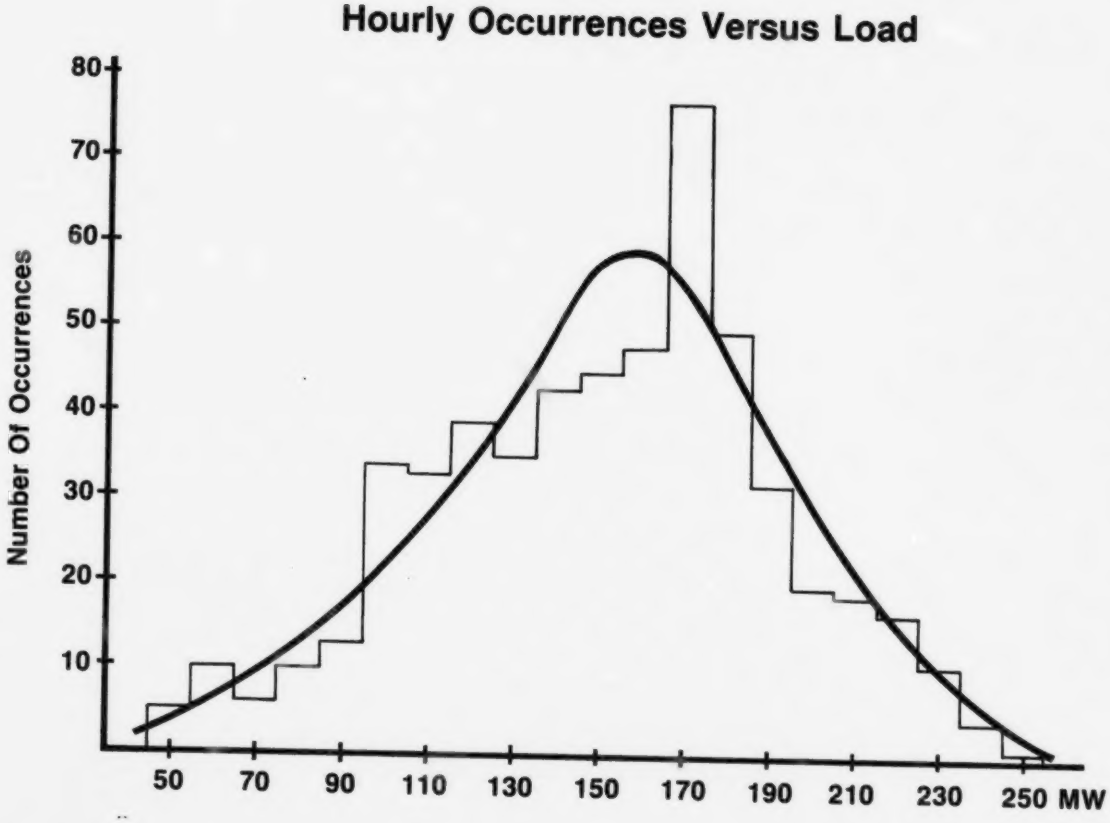

Figure 7. 1983 Operating Load Profile

Session A-7: FUNDAMENTALS II

Owen J. Tassicker, Chairman
Electric Power Research Institute
Palo Alto, CA

ELECTRIC FIELD MEASUREMENTS IN AN OPERATING PRECIPITATOR

by: J. L. DuBard
E. C. Landham, Jr.
Southern Research Institute
Birmingham, AL 35255-5305

R. F. Altman
Electric Power Research Institute
Palo Alto, CA 94303

ABSTRACT

A dynamic potential probe has been used to measure the interelectrode electric field in the hot, dirty flue gas of a fly ash precipitator. The probe was installed in the outlet field of a 1 MW pilot ESP at the EPRI Arapahoe Test Facility. Measurements were conducted at four different plate spacings in the range of 230 mm (9 inches) to 560 mm (22 inches) with low-resistivity fly ash. Comparisons of probe data under different precipitator operating conditions show the relative contributions to the local electric field from the applied high voltage, 30 kV to 70 kV, the molecular ions from the corona discharge, and the charged fly ash particles entrained in the gas stream.

INTRODUCTION

The Electric Power Research Institute has sponsored an evaluation of wide plate spacing in utility fly ash precipitators (ESP) based on pilot ESP performance tests at the Arapahoe Test Facility. The performance test results are discussed in another paper given at this Symposium. This paper describes auxiliary experiments designed to assist in the interpretation of the ESP performance test data. Novel instrumentation was used to measure variations in local values of interelectrode electric potential inside the ESP, during normal operation. The effort to develop and employ this novel instrumentation was based on two considerations:

1) Two fundamental physical parameters of electrostatic precipitation are the electric charge acquired by individual dust particles and the interelectrode electric field near the collecting plate. The two numerical values appear as a product in the Deutsch migration velocity of each dust particle and together specify the collection probability of that dust particle. A method of measuring the charge on fine dust particles has been developed at Southern Research Institute (1,2). Prior to this project, however, no direct measurement of the collecting electric field had been achieved.

2) One goal in the design and implementation of this project was to determine the physical basis of the wide plate spacing effect -- that is, the apparent increase in dust particle migration velocity with increasing plate spacing. The effect was thought to result primarily from an increase in the collecting electric field due to the greater quantity of ionic and particulate space charge contained within the wider interelectrode space. Therefore, it was desirable to measure directly the interelectrode electric potential and its gradient, the electric field.

POTENTIAL PROBE

The potential probe was invented several years ago by Professor Masuda of the Department of Electrical Engineering, University of Tokyo. This instrument was called the "bipolar current probe" because it was originally developed for the purpose of diagnosing back corona (3,4). This instrument has been used extensively at the University of Tokyo, under highly-controlled research conditions in a laboratory precipitator. A similar probe was custom fabricated by Kanomax (Nihon Kagaku Kogyo Co., Ltd) for use at Arapahoe. A spark protection circuit was included in the instrument, and a mechanism for periodically cleaning the probe tip, in situ.

A schematic drawing of the probe tip is shown in Figure 1. All three electrodes and the support rod have the same bias voltage. The three currents (I_+, I_c, I_-) are amplified and optically coupled to a low voltage measurement and control circuit. The basic principle of probing the interelectrode electric field is that the field is undisturbed, beyond a couple of probe diameters, when the probe bias voltage is adjusted to the undisturbed space potential. The value of that potential can be determined from the variations in ionic currents received by the three electrodes as the probe bias voltage is varied.

At Arapahoe, the probe was mounted in an enclosure on the roof of the pilot ESP. Figure 2 shows a schematic drawing of the probe extending down into the electrified field. Along the length of the precipitator, the probe was located just beyond the midpoint of the outlet field, C-Field. The probe could be manually moved on its base plate about 30 cm (roughly two discharge electrode spacings) along the gas passage. The vertical range of movement of the probe was about 60 cm. At the midpoint of this range, the probe was located about halfway down in the electrified field. The position of the probe was measured relative to fiducial marks on its support frame. These marks were established by measurements made inside the precipitator.

An ordinary high voltage power supply was used to bias the probe, as shown in Figure 3, and all probe data were obtained with an x-y recorder. The measurement technique consisted of recording voltage-current characteristic curves of the probe, as the probe bias voltage was varied. Each set of three V-I characteristic curves (for the three separate electrodes of the probe) was recorded on a separate piece of graph paper, along with voltage and current calibration marks.

TEST PROGRAM

The pilot ESP was installed on a flue gas sidestream from Arapahoe Unit 4. The nominal gas flow was 3500 ACFM (1.65 m^3/s) at 300°F (150°C) with average gas velocity 2.5 ft/s (0.765 m/s) through the precipitator. Potential probe tests were conducted with four different ESP plate spacings, in the range of 9 inches (230 mm) to 22 inches (560 mm). At 9-inch plate spacing, there were four parallel gas passages in the ESP and a nominal SCA of 400 ft^2/kACFM (78.4 $m^2/m^3/s$) divided among three identical electrical fields.

The operation of the probe required a substantial corona current (the order of a few hundred nanoamps) from a steady corona discharge. When the high voltage discharge electrodes (round wires) had become coated with fly ash, negative corona tuffs were well stabilized by irregularities in the fly ash deposit. It was always possible to find several strong corona discharges, with long-term stability, within the range of movement of the probe. All of the potential probe data reported here were obtained when the probe was positioned directly opposite a strong, steady corona discharge.

POTENTIAL PROBE DATA

An example set of raw data is shown in Figure 4. This first series of V-I curves for the data set 18-3 gives the first data point in Figure 8 below. The potential probe measurements were conducted with low-resistivity fly ash and without back corona. All current to the probe consisted of negative molecular ions from the high voltage corona discharge. The curve I_+ (the smallest curve in Figure 4) resulted from the motion of negative ions along electric field lines terminating on the back side of the probe, in an unbalanced condition.

When the probe bias voltage equals the undisturbed space potential, there are equal numbers of electric field lines terminating and originating on the narrow central electrode. The probe balance condition is indicated by an extrapolation of the linear portion of the I_c curve (the middle curve in Figure 4) to zero current, indicated as 6.3 kV on Figure 4. The negative ion current received by the balanced probe can be read from the I_- curve, at the probe balance potential. This current can be related to the local current density in the undisturbed interelectrode space by a geometrical formula:

$$I_- = 2\ell D J_- \cos(d/D)$$

where I_- = probe current,
J_- = current density at the probe position,
ℓ = length of electrodes, 10 mm,
d = width of center electrode, 1 mm, and
D = probe diameter, 6.2 mm.

Three sets of electric potential data obtained in the pilot ESP are shown in Figure 5. The corresponding data for local values of ionic current density experienced by the balanced probe are shown in Figure 6. These data were obtained when the plate spacing in the precipitator was set at 230 mm (9 inches) with four parallel gas passages. The discharge electrode spacing was fixed at 150 mm (6 inches) even though the plate spacing was increased in subsequent experiments. For six data sets discussed in this paper, the ESP secondary voltage and average current density data are summarized in Table 1.

The balanced probe potential was determined at each probe position, as the probe was moved in steps away from the grounded collecting plate and then back again. Figure 5 shows that the data were highly reproducible within each data set. The smallest possible separation between the probe assembly and the plate was 20 mm. The largest separation was limited by a maximum probe bias voltage of 20 kV.

TABLE 1. ELECTRICAL OPERATING PARAMETERS DURING POTENTIAL PROBE TESTS WITH 230 mm (9 INCH) AND 460 mm (18 INCH) PLATE SPACINGS IN THE PILOT ESP

Data Set	A-Field kV	B-Field kV	C-Field kV	C-Field nA/cm^2	Probe nA/cm^2
9-1	34	36	43	103	20-50
9-4	36	38	43	99	70-160
9-6	35	33	31	13	30-60
18-3	66	65	70	41	80-100
18-5	68	64	64	41	40-60
18-6	0	62	67	23	50-100

The electric potential values in data set 9-4 of Figure 5 (square symbols) extrapolate almost linearly to the origin of coordinates at the grounded collecting plate. That is, the electric field (3.4 kV/cm) is nearly constant in this region of the interelectrode space. However, the electric potential values in data set 9-1 (round symbols) must extrapolate to the origin with increasing slope. Table 1 shows that the spark-limited ESP operating voltages were 2 kV lower in A-Field and B-Field during test 9-1. Therefore, the upstream collection of fly ash was reduced, and the particulate space charge density in C-Field was increased. (Figure 10 below shows a comparison of two tests in which this effect was deliberately demonstrated.) The potential probe was located opposite different corona discharge points with greatly different corona intensity in tests 9-1 and 9-4. However, the increase in particulate space charge density in test 9-1 affected the local values of electric potential more strongly than the decrease in ionic space charge density.

Comparing data sets 9-1 and 9-6, Table 1 indicates that the ionic and particulate space charge experienced by the probe should have been comparable. However, the much lower operating voltage in C-Field during test 9-6 caused a much lower slope (2.1 kV/cm) of the measured electric potential values, shown by triangular symbols in Figure 5.

Three different contributors to local values of interelectrode electric potential in an ESP are illustrated in the computed curves of Figure 7 for 9-inch and 18-inch plate spacings. These curves do not correlate with any particular set of potential probe data, but rather illustrate general trends in the variations of electric potential and electric field opposite a discharge electrode. (In comparing the curves for 9-inch and 18-inch plate spacings, it should be noted that the wire spacing was fixed at 6 inches.) The curves were computed for typical values of applied voltage, ionic current density, and particulate mass loading following the rapid removal of large particles at the front end of an ESP. The purpose of Figure 7 is to illustrate how the interelectrode ionic and particulate space charge make substantial contributions to the electric field near the collecting plate.

Figures 8 and 9 show the potential probe data set 18-3, obtained with 460 mm (18-inch) plate spacing in the ESP and two parallel gas passages. The data in Figure 8 are compared with computed curves of the interelectrode electric potential at the position of the probe. The computation was performed for the entire ESP, using the inlet particle size distribution and the ESP secondary electrical operating points measured during test 18-3. In each ESP length increment, the computation obtained a self-consistent solution of Poisson's equation and the current continuity equation on a 12 mm rectangular coordinate grid in the interelectrode space (5). The lower curve in Figure 8 shows the normal computation using the average C-Field plate current density, 41 nA/cm^2. This curve does not reproduce the potential probe data. If the current density value used in the computation is increased in order to simulate the higher local current density experienced by the probe (Figure 9) good agreement can be obtained between theory and experiment.

Figure 10 compares the potential probe measurements during tests 18-5 and 18-6. The inlet electrical field of the precipitator was deliberately turned off during test 18-6 (as shown in Table 1) in order to measure the effect of increased particulate space charge at the position of the potential probe.

Although the two sets of electric potential data have nearly the same fitted slope (2.8 kV/cm) data set 18-6 must extrapolate to the origin of coordinates with greatly increased slope. These data illustrate how the electric field near the collecting plate is enhanced by charged particles suspended in the gas stream.

The performance of the pilot ESP was markedly different with 560 mm (22-inch) plate spacing. It was noted from the record of hopper ash catch weights (and later confirmed by inspection of the electrode deposits when the precipitator was off line) that particulate collection moved toward the back end of the precipitator. This resulted in an increased particulate space charge density in C-Field, similar to the effect of turning off A-Field during test 18-6 at 18-inch plate spacing. Figure 11 shows the higher values of local electric potential recorded at 22-inch plate spacing and the apparent increase in the slope of the electric potential curve as it extrapolates to the origin of coordinates. The effect of increased particulate space charge density at the position of the probe is evident in these data.

SUMMARY

- A dynamic method of probing the interelectrode space in an operating precipitator was effective for determining local values of electric potential and electric field, under two qualifying conditions:

a) The probe was used only with low-resistivity fly ash, with no disturbing effects of back corona on the probe voltage-current curves.

b) The probe was used only in the vicinity of strong localized corona tufts whose emission was unrelated to the average plate current density.

- The probe worked effectively in the hot, dirty flue gas in a fly ash precipitator installed at a coal-fired electric generating plant. The probe operation and the data acquisition were simple and dependable.

- The measurements of local electric potential were highly reproducible and did not require any complicated data reduction routine. The measurements were also accurate, as judged by comparison with electric potential maps computed from basic physical principles.

- The probe was sensitive to variations in local values of electric potential caused by variations either in the ionic space charge or in the particulate space charge. The probe clearly indicated a substantial increase in electric field near the collecting plate caused by charged particles in the gas stream at 18-inch and 22-inch plate spacings. Increasing collecting electric field is consistent with increasing particle migration velocity at increasing plate spacing, as demonstrated by the precipitator performance tests.

REFERENCES

1. M. H. Anderson, J. R. McDonald, and R. B. Mosley. Particle Charge Measurements. Int. Conf. on Electrostatic Precipitation, Monterey, October 1981.

2. J. L. DuBard and W. Piulle. Aerosol Particle Charging in a Pulsed Corona Discharge. EPA/EPRI Fifth Symposium on the Transfer and Utilization of Particulate Control Technology, Kansas City, August 1984.

3. S. Masuda and Y. Nonogaki. Bi-Ionized Structure of Back Discharge Field in an Electrostatic Precipitator. IEEE/IAS Annual Meeting, Philadelphia, October 1981.

4. S. Masuda and Y. Nonogaki. Sensing of Back Discharge and Bipolar Ionic Current. J. Electrostatics 10, 73-80 (1981).

5. Faulkner, M. G., and J. L. DuBard. A Mathematical Model of Electrostatic Precipitation (Revision 3): Volumes I, II, and Source Code Tape. EPA-600/7-84-069a,b,c. (NTIS PB84-212-679, PB84-212-687, PB84-232-990). U.S. EPA, AEERL, Research Triangle Park, NC, 1982.

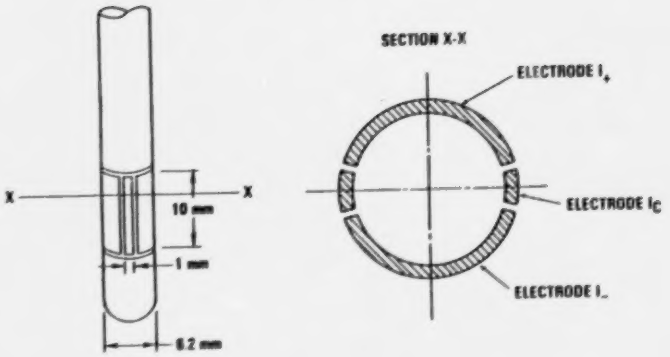

Figure 1. Schematic drawing of the potential probe tip.

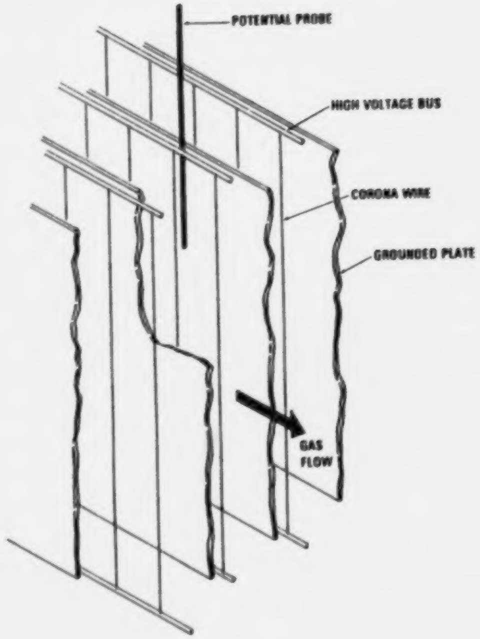

Figure 2. The potential probe inserted in a precipitator.

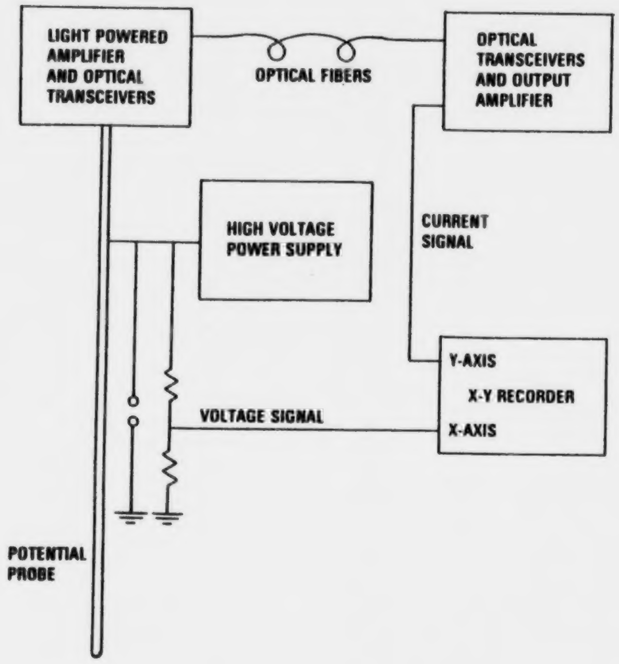
LIGHT POWERED AMPLIFIER AND OPTICAL TRANSCEIVERS
OPTICAL FIBERS
OPTICAL TRANSCEIVERS AND OUTPUT AMPLIFIER
HIGH VOLTAGE POWER SUPPLY
CURRENT SIGNAL
Y-AXIS
X-Y RECORDER
X-AXIS
VOLTAGE SIGNAL
POTENTIAL PROBE

Figure 3. Potential probe system used at Arapahoe.

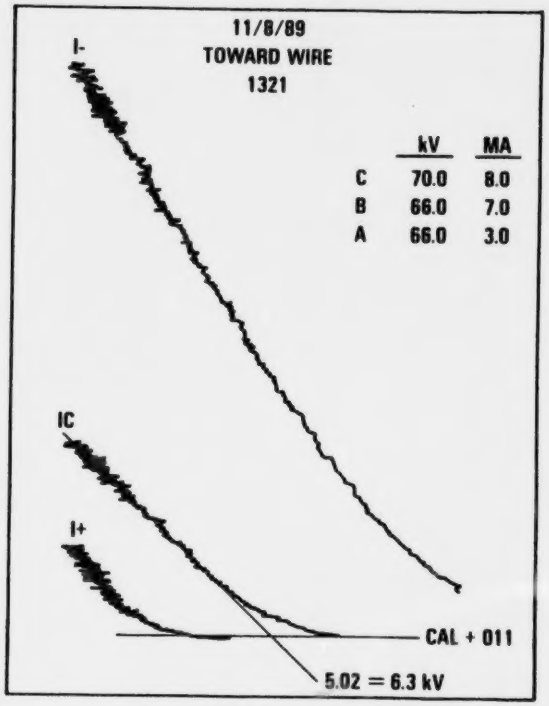

Figure 4. Raw potential probe data from test 18-3.

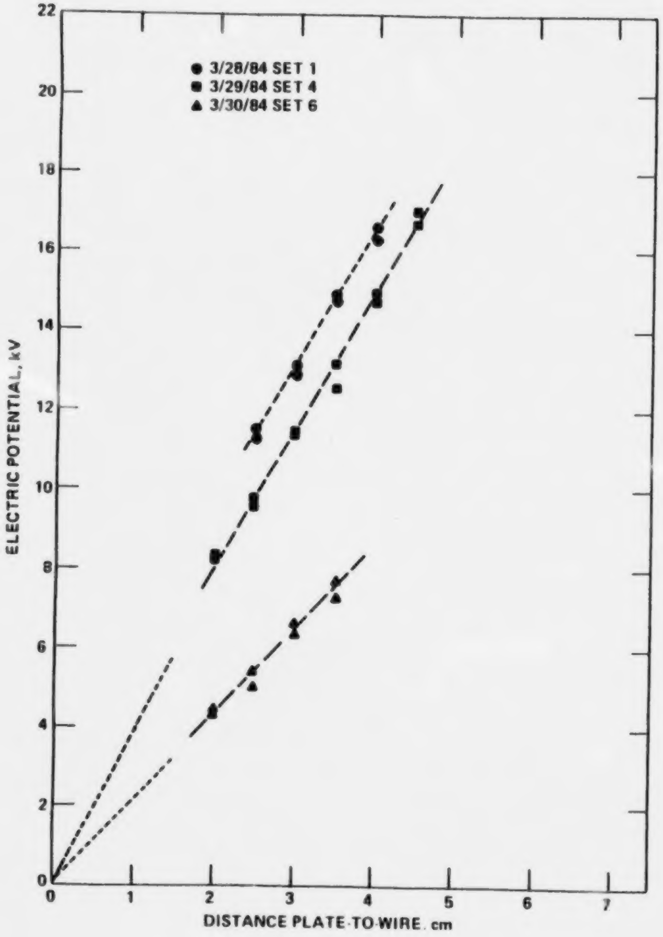

Figure 5. Electric potential data obtained in tests 9-1,4,6.

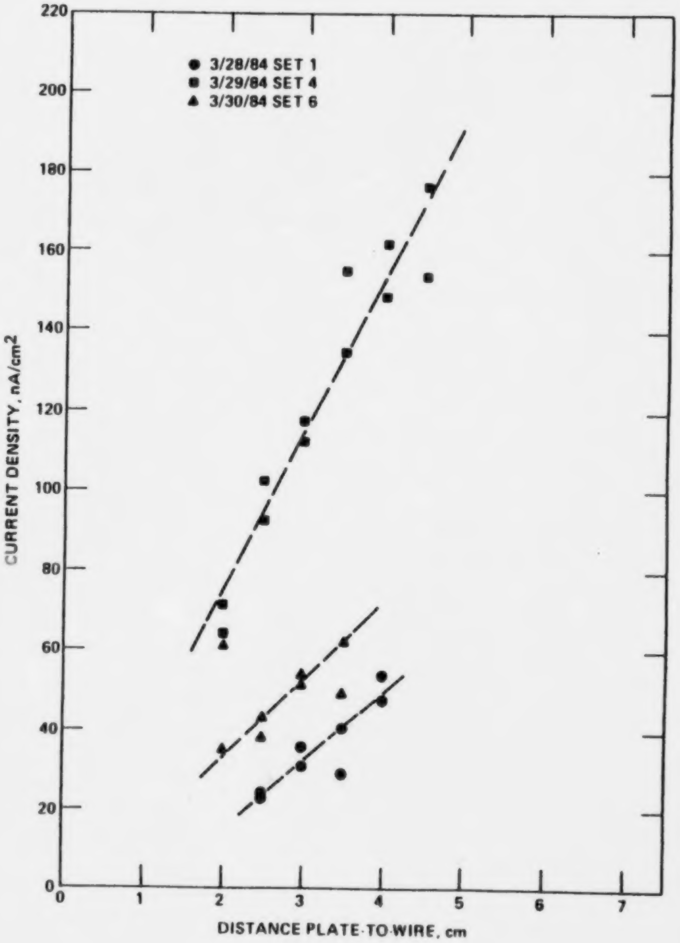

Figure 6. Current density data obtained in tests 9-1,4,6.

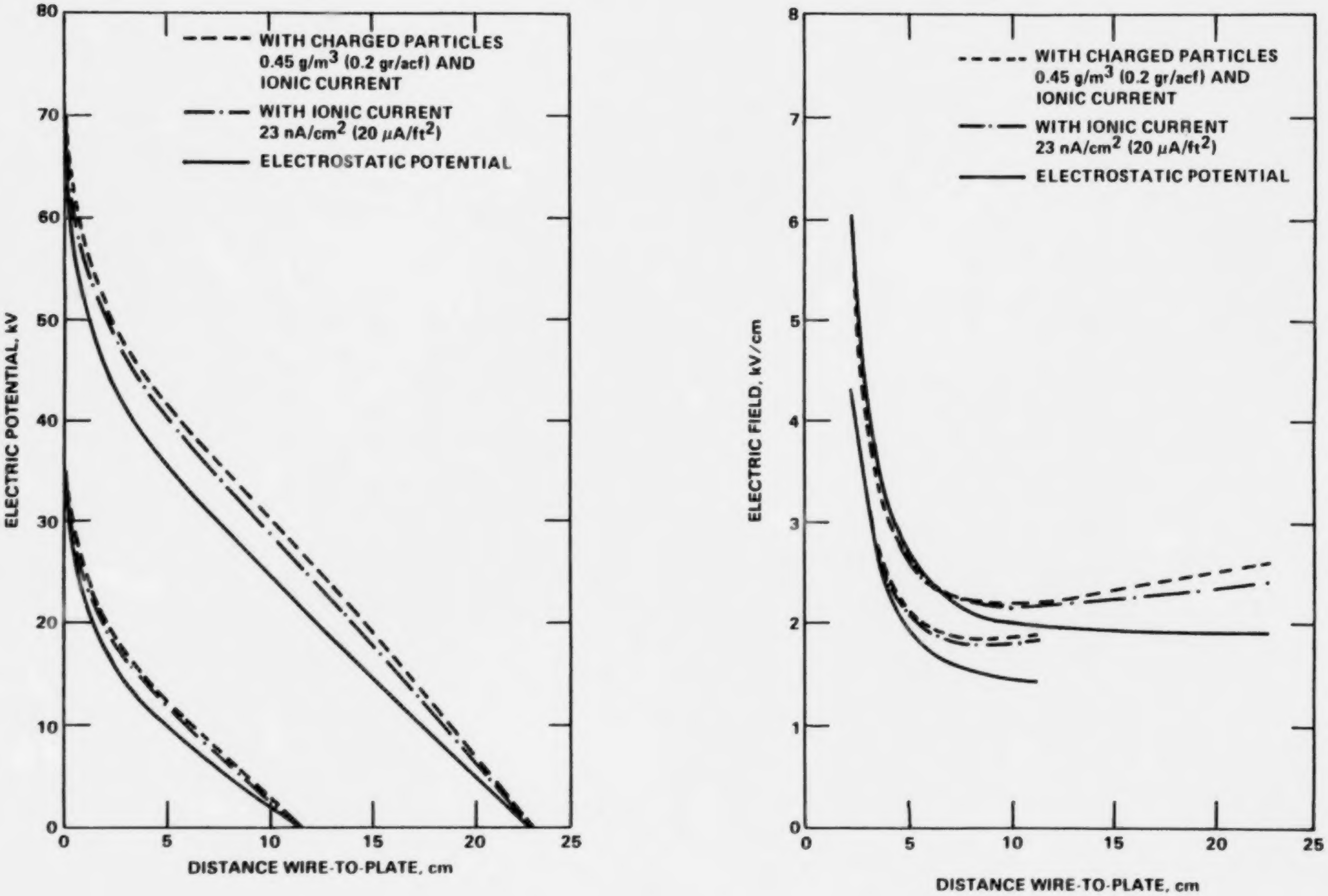

Figure 7. Computed curves of a) electric potential and b) electric field in the pilot ESP, along a line from wire to plate, for 230 mm and 460 mm plate spacings and 150 mm wire spacing.

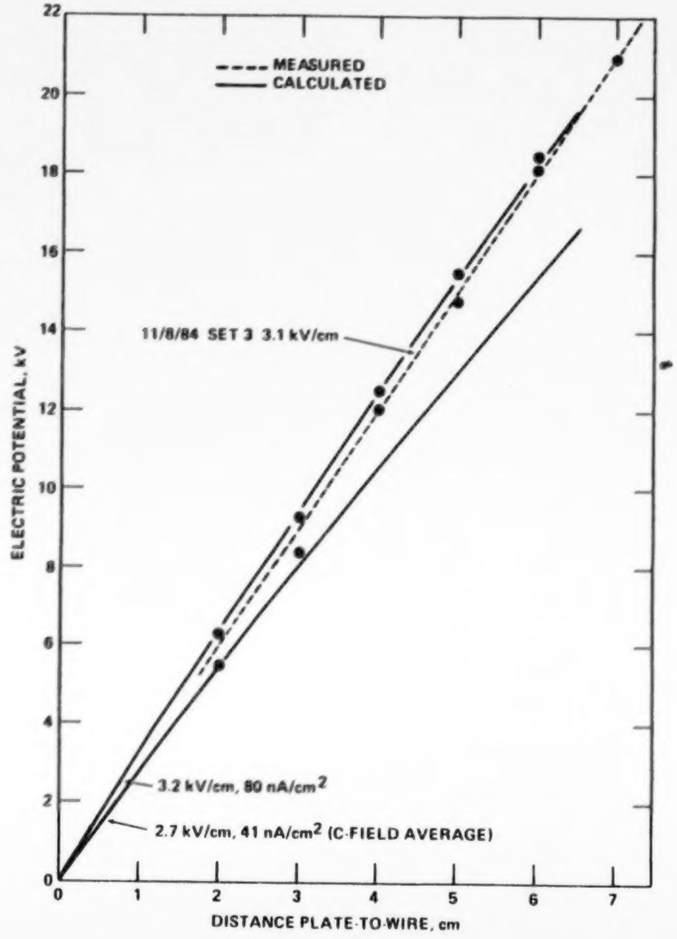

Figure 8. Electric potential data obtained in test 18-3 and compared with computed curves.

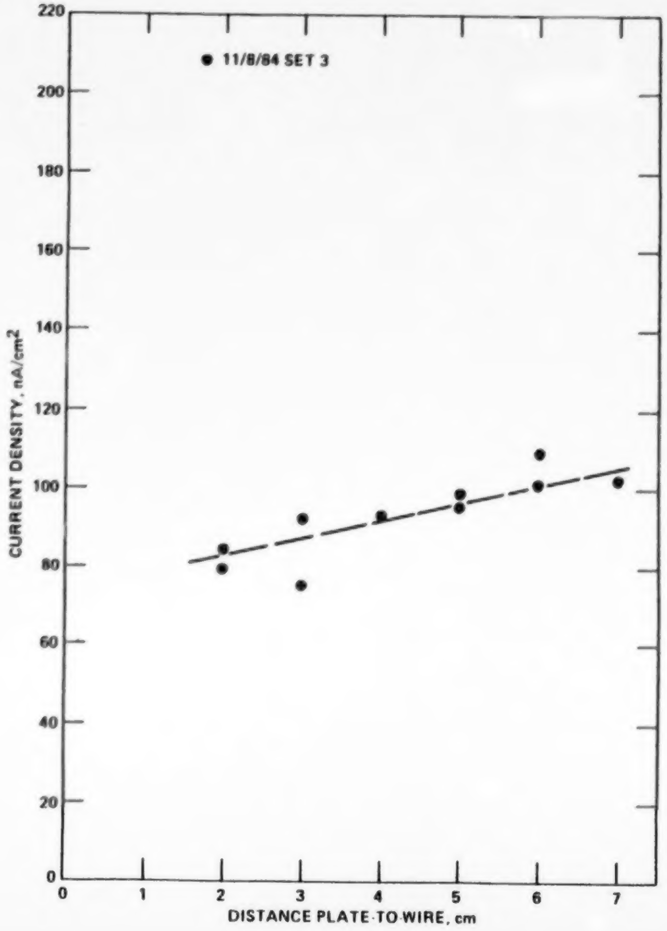

Figure 9. Current density data obtained in test 18-3.

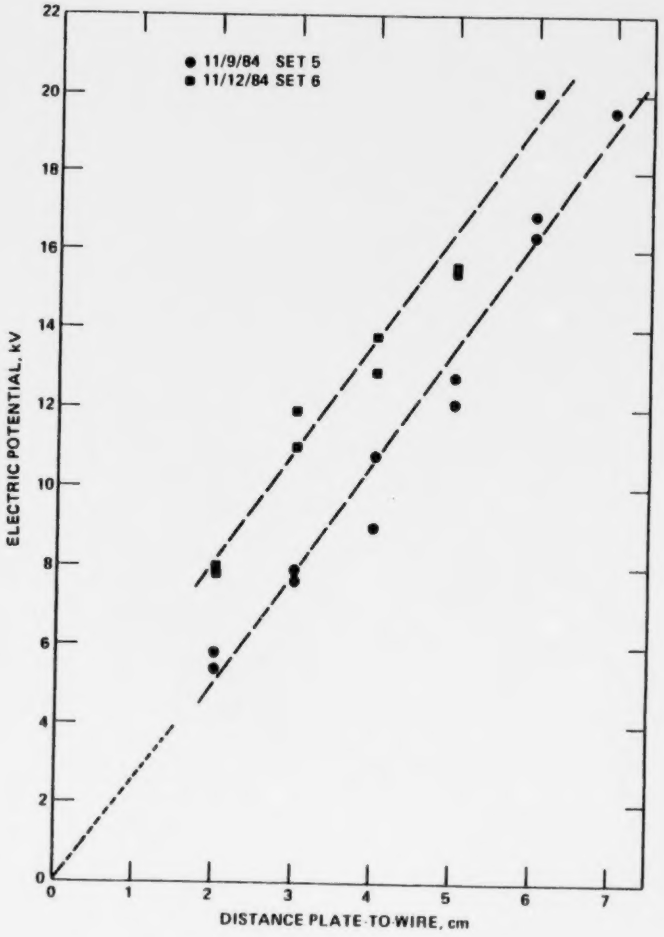

Figure 10. Electric potential data obtained in tests 18-5 and 18-6.

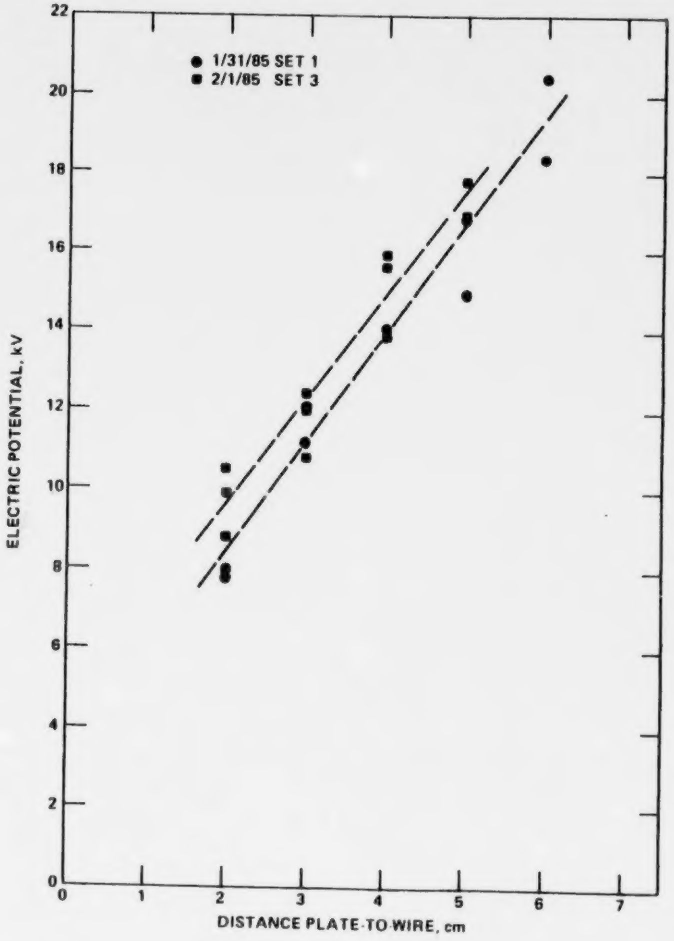

Figure 11. Electric potential data obtained in tests 22-1 and 22-3.

FINITE-DIFFUSIVITY EFFECTS IN SINGLE-STAGE PRECIPITATORS - THEORY AND EXPERIMENT

by: S.A. Self, M. Mitchner, D-H. Choi, K-D. Kihm and R. Leach
Mechanical Engineering Stanford University
Stanford, California 94305

ABSTRACT

Evidence is presented for the necessity of replacing the infinite-diffusivity Deutsch model for particle transport by a finite-diffusivity model in theoretical descriptions or computational codes for evaluating and predicting precipitator performance.

Measurements of fractional efficiency in a single-stage laboratory-scale precipitator, as a function of particle diameter, flow velocity and electrical conditions, are reported. These measurements are reduced and interpreted in terms of a uniform, finite-diffusivity model. Effective values of migration velocity and turbulent diffusivity, as a function of flow velocity and electrical conditions are inferred.

The implications for the design of higher performance precipitators are discussed.

INTRODUCTION

The most fundamental process in electrostatic precipitation is the transport of charged particles in the nonuniform electric field and the turbulent flowfield, particularly in single-stage wire-duct precipitators. For some time our research has focused on this aspect, with the aim of obtaining a more detailed understanding which can be incorporated into models for evaluating and predicting the performance of precipitators and to indicate approaches by which the performance may be improved, or the size and cost reduced.

It is clear that the traditional Deutsch model, which assumes uniform "effective" fields for particle charging and migration, and also assumes complete turbulent mixing transverse to the flow (and hence a uniform particle concentration profile at each streamwise location) is a gross simplification. In particular, the latter assumption yields a pessimistic result for the predicted performance, since it is clear that a laminar flow precipitator should ideally yield perfect collection efficiency in a finite length.

The flowfields in industrial-scale, single-stage precipitators are undoubtedly complex and poorly understood, yet are unlikely to be so turbulent that the assumption of perfect mixing (or, equivalently, infinite turbulent diffusivity) is inevitably satisfied. It appears that by paying closer attention to flow quality control, significant gains in performance (or size reduction) may be achieved.

FINITE DIFFUSIVITY MODELS AND THEIR TESTING IN A BENCH-SCALE PRECIPITATOR

The foregoing view is supported by the results of a theoretical model of precipitation from turbulent flows, based on solution of the convective-diffusion equation for particle transport developed several years ago (1,2)

IDEAL FINITE DIFFUSIVITY MODEL

This model considers precipitation in a uniform transverse electric field, E_y, of monodisperse, pre-charged particles, uniformly dispersed at the entrance of a uniform channel flow between parallel plate electrodes. The effect of turbulence is represented by a uniform eddy diffusivity D and, like the Deutsch model, the effect of diffusion in the axial (x) direction is neglected (this neglect is justified except for extremely high values of D).

For this model, the collection efficiency is shown to be a function of two dimensionless parameters, namely (i) the Deutsch number, which is a dimensionless measure of precipitator length:

$$De \equiv \frac{wL}{\bar{u}d} \qquad (1)$$

and (ii) the Peclet number, which is a measure of the relative strengths of migration and diffusion on particle transport:

$$Pe \equiv \frac{wd}{D} \qquad (2)$$

Here d is the plate spacing, L is the precipitator length in the flow direction and $\bar{u}$ is the uniform, time-average gas velocity along the channel axis.

The quantity w is the (theoretical) migration velocity, relative to a quiescent, stationary gas, of spherical particles of charge q, diameter 2a, in a uniform electric field E. This is given by equating the Coulomb force to the Stokes' drag, including the Cunningham correction factor C, as

$$w = \frac{CqE}{6\pi a\mu} \qquad (3)$$

Here μ is the gas viscosity and the Cunningham factor is given by (3)

$$C = 1 + \frac{\lambda}{2a} \left[A_1 + A_2 \exp\left(- 2 \frac{A_3 a}{\lambda}\right)\right] \tag{4}$$

where $A_1 = 1.257$, $A_2 = 0.400$ and $A_3 = 0.55$.

The penetration P and the fractional efficiency $\eta \equiv (1-P)$, calculated from this ideal finite diffusivity model, are shown as a function of Deutsch number, with Peclet number as a parameter, in Figure 1. In this plot of log P versus De, the Deutsch limit of infinite mixing, $D \to \infty$, $Pe \to 0$, plots as a straight line given by the Deutsch-Anderson formula

$$P = \exp(- De) \tag{5}$$

In this limit it is evident, for instance, that a Deutsch number of 6 is required to yield a penetration 0.25% corresponding to an efficiency of 99.75%.

The laminar limit $D \to 0$, $Pe \to \infty$ shows, as expected from simple considerations, that the penetration tends to zero, and the efficiency to 100% for De = 1, i.e. in a finite length $L = (\bar{u}d/w)$.

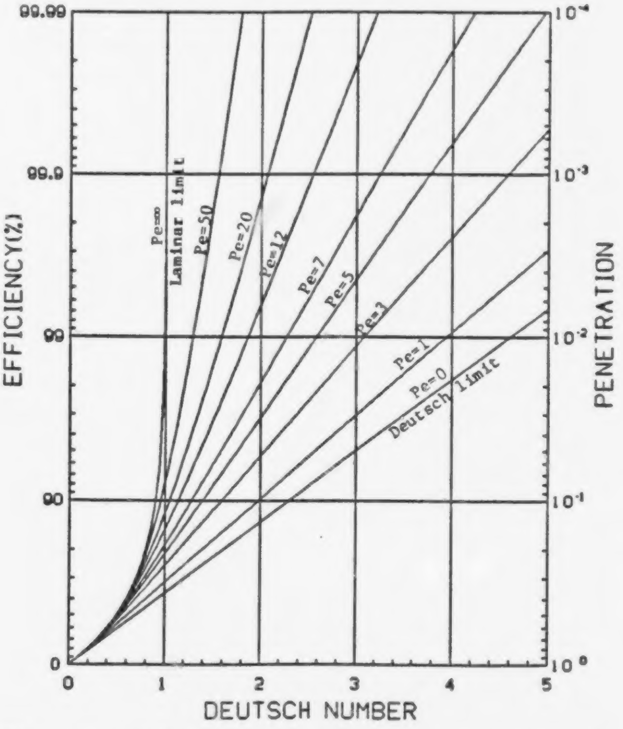

Fig. 1. Universal plot of penetration and efficiency versus Deutsch No. with Peclet No. as parameter.

In Figure 1, the various curves for finite D (and hence Pe) lie between these two limiting curves. They are all asymptotic to the Deutsch line (Eq. 5) for small De, because in the entrance region the particle concentration profile is uniform, as assumed by the Deutsch model. For larger De, i.e. further into the precipitator, the constant Pe curves become asymptotic to straight lines having greater slope than the Deutsch line, indicating an exponential decay of penetration with length, but at a faster rate than predicted by the Deutsch model. Concomitantly, the particle concentration profile develops into a self-similar (or dominant mode) profile for which the concentration increases monotonically towards the collecting plate. This profile is determined by a balance between particle transport towards the collector due to migration, and transport away from the collector due to (back) diffusion. This profile is flat in the Deutsch limit $Pe = 0$, becomes more pronounced as Pe increases, and tends to a step function in the laminar limit $Pe \to \infty$.

EXPERIMENTAL TEST OF IDEAL MODEL

This ideal, finite-diffusivity model was experimentally tested (2,4) in a bench-scale, parallel plate precipitator using monodisperse, precharged oil droplets dispersed into a well-characterized duct flow. The particle mobility $(w/E) = (Cq/6\pi a\mu)$ was determined by measuring the velocity by laser anemometry in a known field, and was found to be quite monodisperse.

Low levels of turbulence were generated by rectangular wire mesh grids placed across the duct just upstream of the precipitation section. It is difficult to determine the eddy diffusivity either by fluid-mechanical calculations or directly by measurements. For grid-generated turbulence, it is generally accepted that the diffusivity is given approximately by

$$D \approx 0.2\, u'\ell \qquad (6)$$

where u' is the rms fluctuation of the axial component of velocity about the mean value $\overline{u}$, and ℓ is the characteristic eddy size, which is on the order of the mesh opening size. The velocity fluctuation was measured and this indicated a value of $D \sim 1\ cm^2/s$. According to studies of grid-generated turbulence, downstream of the grid u' decays and ℓ increases so as to maintain a fairly constant value of D.

Measurements of the particle concentration profiles were made by a laser light scattering counter for both a fine grid and a coarse grid, and for various combinations of values of $\overline{u}$ and w, and at several stations in the flow direction x. By integrating the area under these profiles the penetration and efficiency were determined as a function of x.

The profiles (see Figure 2a for an example) and efficiencies were found to fit the theoretical predictions very well under all conditions if values of $D = 0.6\ cm^2/s$ and $1.2\ cm^2/s$ were taken for the fine and coarse grids respectively. The range of Peclet numbers covered in this experiment was $Pe = 30$ to 350, corresponding to relatively low diffusion coefficients.

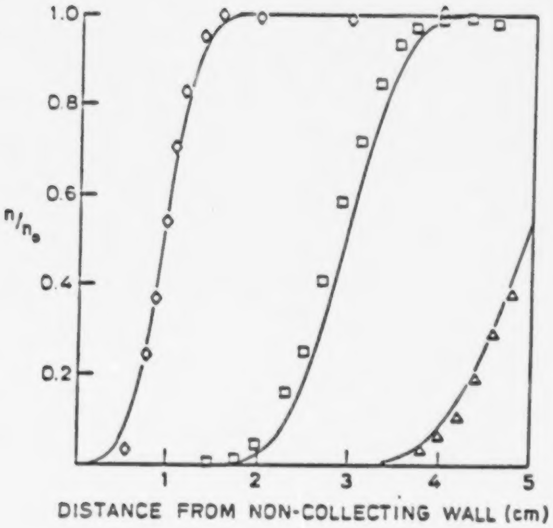

Fig. 2a. Particle concentration profiles: grid; u=3m/s, w=0.3m/s; ◇, x=5cm; □, x=25cm; △, x=45cm. Solid line-theory for $D=1.2cm^2/s$.

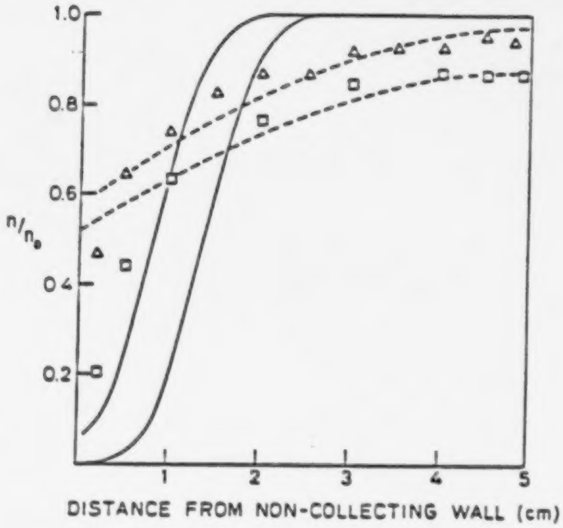

Fig. 2b. Particle concentration profiles: baffles; u=3m/s, w=0.7m/s; △, x=25cm; □, x=45cm. Solid line-theory for $D=1.2cm^2/s$. Broken line-theory for $D=30cm^2/s$.

For this range the experiments give excellent confirmation of the validity of the ideal finite diffusivity model for uniform electric field and uniform diffusivity.

In order to extend the range to higher diffusivities (i.e. lower Pe), in a few experiments the grid was replaced by a pair of baffles just upstream of the precipitator entrance. These baffles extended 1 cm in from each sidewall of the duct whose width was 5 cm. The effect of the baffles was to produce a marked flattening of the concentration profile and a corresponding marked drop in efficiency, as shown in Figure 2b. The value of D to produce the fit to theory was $D = 30\ cm^2/s$, corresponding to a value of Pe = 5.

EFFECT OF NONUNIFORM FIELDS

The effect of nonuniform electric fields in a typical wire-duct precipitator has been studied by numerical solution of the governing equations for the case of non-discharging electrodes and entering pre-charged particles (but retaining the uniform diffusivity assumption). Two cases were studied; (i) laminar flow D=0; and (ii) various values of uniform diffusivity, and are reported in (5) and (6) respectively.

The principal conclusion from these numerical studies, for all cases, is that although the concentration profiles are quite different from the case of uniform field, the efficiencies agree very closely with those calculated for the uniform field model (for the same values of De and Pe) provided that the equivalent uniform field is taken as the space-averaged field along the collector plate. This agrees with the long-established rule, in applying the Deutsch model, of taking the effective value of the precipitating field E_p as being given by the space-averaged value of the field at the collecting plate surface. It is fortunate that this rule still applies in the case of finite diffusivity, because the simpler results of the uniform field, finite diffusivity model can be used for wire-duct precipitators, provided the average value of the field at the plate is used as the effective precipitating field in the theory.

EFFECT OF NONUNIFORM DIFFUSIVITY

It is clear that the ideal, uniform, finite diffusivity model represents the mechanics of particle transport more correctly than the crude Deutsch model, and it would be convenient (and fortunate) if it proved to be adequate as a replacement for the Deutsch model in existing codes (7) for predicting and evaluating the performance of large, single-stage, wire-duct precipitators.

The flowfield in such units is likely to be very complex, being dependent on both the particular geometry of the ductwork and electrodes, and on the electrical conditions (via corona wind effects). Since it is impractical to adequately characterize the details of the turbulent flowfield, it is to be hoped that the effects of the turbulent flowfield can be represented, as far as particle transport and efficiency is concerned, in terms of an effective uniform diffusivity averaged over the whole precipitator (or possibly separate such values for separate sections).

However, from the point of view of understanding, at a fundamental level, the effects of nonuniform diffusivity on particle transport, it is desirable to study these effects under simple, well-controlled conditions. To this end we are currently studying the effect of nonuniform diffusivity for the canonical case of a parallel plate precipitator with developing boundary layers, in which the turbulent core flow is determined by upstream conditions. Thus the diffusivity profile is represented as decreasing from a uniform core value, through a boundary layer of specified width, to a very low value (the Brownian diffusivity) in the laminar sublayer.

This work, which will be reported in future, includes analytical, computational and experimental components. In the theory it is especially important to establish appropriate boundary conditions on the particle number density in the convective-diffusion equation. Experimentally we are using the bench-scale parallel-plate precipitator rig with pre-charged particles, employed for the earlier reported measurements. We are examining particularly the case of high levels of core turbulence produced by upstream baffle structures, corresponding to lower Pe values in the range 2-20.

Present indications are that with the new theory for nonuniform diffusivity, we can obtain a good fit to the experimental concentration profiles such as shown in Figure 2b (with baffles), for which the uniform diffusivity theory does not exactly fit the data near the non-collecting wall. However it should be noted that for the rest of the profile (for moderate levels of core turbulence $D \sim 10\ \text{cm}^2/\text{s}$) the uniform diffusivity model gives a very adequate fit up to the collecting wall.

THE FLOWFIELD IN SINGLE-STAGE WIRE-DUCT PRECIPITATORS

The flowfield in a single-stage, wire-duct precipitator can best be discussed as consisting of the basic fluid-mechanical flowfield, determined by the duct geometry, including the entrance conditions and obstacles immersed in the flow, modified by corona wind effects. However, it should be noted that for high currents and low flow velocities, when corona wind effects are strong, the character of the flowfield may be largely determined by the latter effects.

BASIC FLUID MECHANICAL CHARACTERISTICS

The basic fluid mechanical description is that each flow passage is a developing turbulent two-dimensional channel flow betwen parallel plates. The Reynolds' number based on duct width (2d) is

$$Re = \bar{u}\ (2d)/\nu \tag{7}$$

where $\bar{u}$, is the space-averaged flow velocity, and $\nu = \mu/\rho$ is the kinematic viscosity where ρ is the gas density. For typical conditions ($\bar{u} \sim 1.5$ m/s, (2d) ~ 0.3m, $\nu \sim 2.10^{-5} m^2/s$, we find $Re \sim 2.10^4$, which is well above the accepted critical value (~ 2.10^3) for laminar to turbulent transition.

For smooth walls, the developing (entrance) region consists of a core flow, whose turbulence character is determined by upstream conditions (with the turbulence level decaying with distance x from the entrance) together with developing boundary layers (of thickness δ) on each wall, which grow according to (8)

$$\delta\ (x) \simeq 0.37\ x\ (\ \bar{u}\ x/\nu)^{-\ 1/5}. \tag{8}$$

According to Eq. (8), the boundary layers merge (δ=d) in a distance x_m given by

$$x_m \simeq 1.75\ (Re)^{1/4}(2d) \tag{9}$$

For the typical conditions quoted, $x_m \sim 7m$, so that for most commercial precipitators the flow approaches the fully-developed condition towards the exit. For wide-spaced units, x_m may be larger than the precipitator length L, so the flow is entirely a developing one.

For a developing turbulent flow, when the turbulence intensity $(u'/\bar{u})$ in the core is low, $(u'/\bar{u})$ rises to a maximum value ~ 10-15% in the boundary layer and decreases to zero in the thin viscous sublayer next to the wall. For fully-developed flow, an estimate of the eddy diffusivity can be obtained from the correlation formula of Becker et al. (9) for a smooth round pipe.

$$D \simeq (1.10^{-3})\ \bar{u}\ d' \tag{10}$$

If we identify the pipe diameter d' with the duct width 2d, then for $\overline{u} \sim$ 1m/s and 2d ~ 0.3m, we have $D \sim 3.10^{-4} m^2/s$ (= 3 cm^2/s), quite a low value.

In commercial precipitators, turbulence is generated in the core flow by the high voltage electrodes and their supporting structure, and in the near wall region by eddies shed from stiffening baffles projecting from the collection plates transverse to the flow. As a result, significantly higher values of eddy diffusivity must be expected than in smooth channel flow.

A knowledge of the character of the turbulent flowfield in unenergized precipitators can be obtained from hot-wire (or laser) anemometer measurements of the mean ($\overline{u}$) and rms fluctuation (u') about the mean of the axial velocity component, as a function of position throughout the duct. However, to infer the eddy diffusivity D, it is also necessary to determine the eddy size distribution from correlations of the velocity measured at two positions as their separation is varied. It is difficult and laborious to measure the eddy size distribution.

Measurements of the flowfield in the Stanford laboratory precipitator tunnel, with and without energization, and with and without corona wires and wall baffles have been documented in (10). However these were restricted to measurements of the profiles of $\overline{u}$ and u' downstream of the final high voltage wire because it is impractical to measure the gas velocity inside an energized precipitator by either hot-wire or laser anemometry. Recently, in a cooperative effort, hot-wire measurements of $\overline{u}$ and u' have been made in an unenergized (1/8)th scale model of a commercial precipitator at Lodge-Cottrell's flow testing facility at Woodlands, Texas. The results have, however, not yet been reduced; they will be reported in a future publication. Generally, one can say from the measurements in the Stanford tunnel that, with simple wire electrodes and no wall baffles, the turbulence intensity ($u'/\overline{u}$) is generally low, but that the addition of substantial electrode supports or wall baffles increases the turbulence intensity markedly.

EFFECT OF CORONA WIND ON FLOWFIELD

It is well known that the streaming of high velocity ions through a stationary gas can set it into motion. In the case of a flowing gas, the flow structure is modified by the creation of secondary flows which may be either stable (laminar) or unstable, giving rise to turbulence. The nature of the flow perturbations produced by the corona wind are diverse and very sensitive to the geometry and polarity of the discharge electrode. For instance, it is much easier to characterize the perturbation produced by a uniform positive corona than from a negative corona on a smooth wire, which consists of randomly located discharge tufts. However, despite the diversity of the corona wind effect, certain general statements can be made regarding its form and magnitude.

First, for constant geometry, one can state on dimensional grounds that the appropriate measure of the relative effect of the corona wind is the electrohydrodynamic number N_{EHD}, defined as the ratio of the electric body force per unit volume to the inertial force per unit volume acting on the gas. For a wire-duct precipitator we have (2,11)

$$N_{EHD} = \frac{i}{\mu_i \rho \bar{u}^2} \qquad (11)$$

where i is the current per unit length of discharge wire, and μ_i is the ion mobility.

In general, when N_{EHD} is small, one expects corona wind perturbations to be minimal, while when it is large the corona wind effects should dominate the fluid mechanical ones.

For a uniform (positive) discharge in a wire-duct precipitator, it has been shown both theoretically (12) and experimentally (11) that a steady recirculation eddy is produced adjacent to the collectors opposite each discharge wire as shown in Figure 3. Moreover the size of this secondary flow eddy increases with N_{EHD}. In addition it was found (11) that at the ends of the wire, where the current density is nonuniform, unstable secondary flows are generated. The resulting turbulence propagates towards the center of the duct with increasing x. However, this effect may be less important in full scale precipitators, where the wire extends above and below the plates, and the aspect ratio is large.

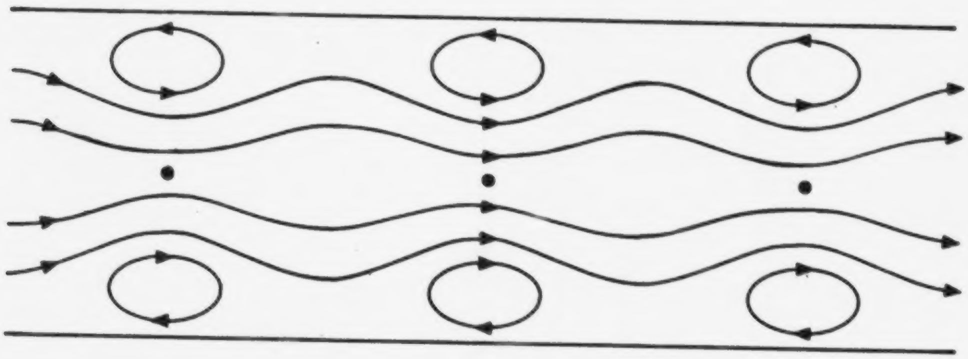

Fig. 3. Secondary flow in (x-y) plane for uniform positive corona: schematic.

For regularly barbed electrodes of either polarity, especially when the barbs are widely spaced and aligned from one electrode to the next, it has been shown that strong axially-aligned secondary flow vortices are generated which are very deleterious to precipitator performance since they induce strong mixing across the half-width of the duct (13).

For the important case of negative polarity in a smooth wire-duct precipitator, it appears that the random distribution and orientation of the discharge tufts inhibits the formation of regular secondary flow structures; rather, the corona wind redistributes the existing turbulence and enhances it (10,14). However, because, with increasing current, the tufts become more closely spaced, it is probable that the eddy size decreases, and the corona generated diffusivity may not increase indefinitely with N_{EHD} (15).

The general dependence of the turbulence intensity on current and mean flow velocity for negative polarity and smooth wires is summarized in Figure 4. These results are from measurements made downstream of the last wire in the Stanford laboratory tunnel with smooth walls.

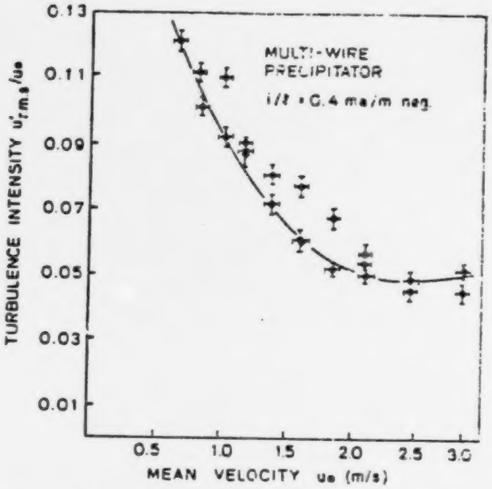

Fig. 4a. Laboratory precipitator; negative corona, i=0.4mA/m; centerline turbulence intensity, downstream of seventh wire, vs. flow velocity.

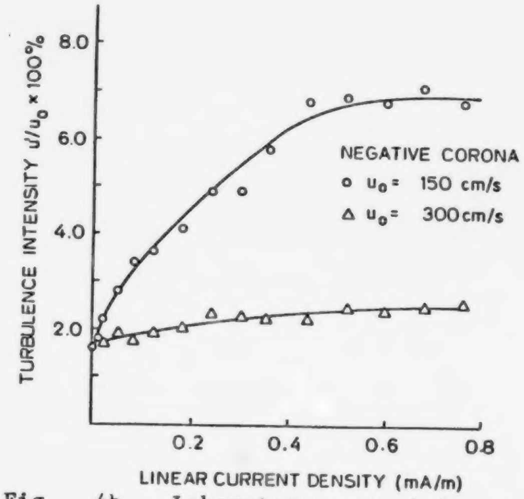

Fig. 4b. Laboratory precipitator; negative corona, turbulence intensity midway between center and wall, downstream of seventh wire, versus linear current density.

In Figure 4a, the centerline turbulence intensity as a function of mean flow velocity (at a constant linear current density of i=0.4 mA/m) is seen to decrease to a minimum at $\overline{u} \sim 2.5$ m/s. In Figure 4b the turbulence intensity roughly midway between the collector and the centerline (0.07m from the collector) is seen to increase with increasing current for both mean velocities shown. However the increase is relatively large (from 2% to 6%) for the lower velocity $\overline{u} = 1.5$ m/s), but is quite small for the higher velocity ($\overline{u} = 3$ m/s). All these results are consistent with the notion that the relative effect of the corona wind depends on the EHD number N_{EHD}. In fact it is clear that the increase in turbulence level due to the corona wind is negligible for $N_{EHD} \lesssim 0.5$.

When baffles were fitted to the collectors midway between wires, and projecting 2.5 cm into the flow, no increase in turbulence was seen on energization, because the level was already high in the unenergized case.

In summary, for the negative discharge wire-duct precipitator with smooth wires and plates, one can say that for gas speeds greater than about 2 to 3 m/s, and for currents of practical interest, corona-induced turbulence has little influence on the background fluid mechanical turbulence generated in the boundary layer and by the wire wakes. For gas speeds of about 1.5 m/s, the corona-induced turbulence is of the same magnitude as the background turbulence, while for lower gas speeds the corona-induced turbulence becomes increasingly intense for decreasing gas speeds and is likely to dominate the background fluid mechanical turbulence level if this is already low (i.e. in the absence of flow obstructions due to support structure or baffles). When the turbulence intensity is already high, due to the presence of flow obstructions, the effect of corona-induced turbulence is likely to be negligible at all currents and flow velocities of interest.

Thus it is clear that corona-induced turbulence is not, per se, a barrier to the achievement of relatively low turbulence flows in duct-type precipitators. Moreover substantial reductions in turbulence and eddy diffusivity should be possible by proper aerodynamic design, minimizing flow disturbances produced by electrode structures and wall baffles.

PERFORMANCE MEASUREMENTS ON THE STANFORD LABORATORY PRECIPITATOR

An extensive series of fractional efficiency measurements have been made on the Stanford laboratory precipitator, under well-controlled conditions, with the aim of correlating the results with the theoretical model which incorporates finite eddy diffusivity rather than the Deutsch model for particle transport. Measurements have been made for both re-dispersed flyash and oil droplets over a wide range of flow velocity and electrical conditions.

PRECIPITATOR FACILITY

The Stanford laboratory precipitator is a versatile facility capable of simulating the conditions of full-scale precipitators in most respects, but having certain features which allow better controlled conditions and the isolation of certain non-ideal loss mechanisms.

It consists of a moderately low turbulence wind tunnel with a long working section, 0.25m (10") wide by 0.74m (30") high, into which various modular test sections can be inserted. One such section (Figure 5) consists of a 1.8m (6') long wire-duct precipitator having seven wire electrodes 2.77mm (0.109") diameter spaced every 0.25m (10") along the vertical midplane of the duct. This section is fitted with a glass top, a teflon bottom and a removable side door which facilitates observations and measurements. A pair of wet-wall plates, which reduce the width to 0.2m (8"), can be inserted for use in reentrainment studies.

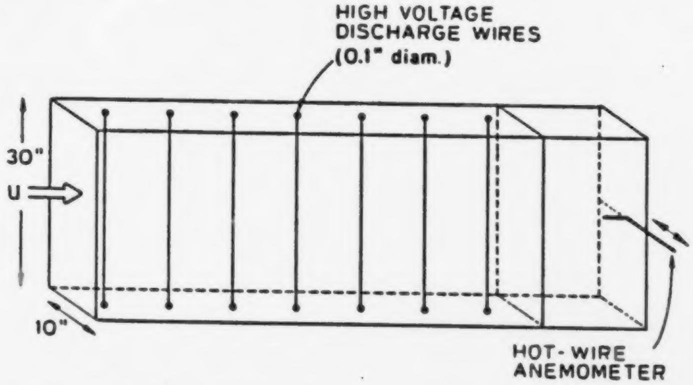

Fig. 5. Stanford laboratory precipitator: schematic.

The flow velocity can be varied up to 8 m/s, corresponding to a throughput of $1.5m^3/s$ (3,200 acfm). However at a velocity of 2 m/s, more typical of modern precipitators the throughput is $0.38m^3/s$ (825 acfm) and the specific collector area (SCA) is $7.2m^2/m^3/s$ (= 36 ft^2/1000 cfm). The air stream can be heated and humidified to simulate cold-side operation but, for convenience, the tunnel is usually operated with ambient outside air which is humidified with a swamp cooler to inhibit back-discharge when using flyash.

Flyash is fed from a heated screw feeder into a sonic nozzle driven by compressed air, and dispersed via a set of tubes counter to the main flow in a downflow section well upstream of the precipitator section, so as to produce a spatially uniform aerosol. Usually, a fine ash, of mean diameter by mass of 4-5μm, from EPRI's Arapahoe test facility is used and with ambient air, no back-discharge is observed provided the relative humidity is greater than 50%.

Alternatively, an aerosol of corn oil droplets is used. This is produced by a set of four medical nebulizers connected to a common reservoir and driven by compressed nitrogen (16). This unit is mounted in the downflow section leading to the precipitator tunnel and provides a very stable aerosol which is uniformly dispersed across the tunnel cross section. The size distribution is relatively fine, extending from below 0.1μm to about 4 μm diameter (16). The loading is much lower than for flyash and no appreciable corona quenching is observed, as is the case for flyash.

The precipitator is energized to either polarity in the range 30 kV to 55 kV (pos) or 60 kV (neg), these being respectively the corona onset and sparkover limits. At 50 kV, the linear current densities are ~ 0.85mA/m (neg) and ~ 0.38 mA/m (pos). The corresponding average collector plate current densities are $1.68mA/m^2$ (neg) and $0.75mA/m^2$ (pos).

From the above description it is clear that the laboratory precipitator closely simulates the conditions of one channel of a full scale unit except that the aspect ratio (3:1) is much smaller. It does not have any flow space above the collector plates for high voltage clearance, nor any hoppers or facility for rapping. Thus the loss mechanisms associated with sneakage and rapping reentrainment are effectively eliminated, allowing one to isolate and study the basic precipitation process, which determines the ultimate performance.

MEASUREMENT TECHNIQUES

The mean flow velocity is measured with a pitot tube and sensitive manometer, which can be used in particle laden flows. For more detailed measurements of the flowfield, a hot wire anemometer has been used in clean flows, as described in Reference (10).

To test the theoretical model which takes account of finite diffusivity it was judged necessary to make fractional efficiency measurements (as a function of particle size) and also to measure the profiles of the particle concentration (by size class) at the exit of the precipitator section. These profiles should provide a sensitive test of the theory; for the Deutsch model they are flat, whereas for the finite diffusivity model the profiles should have a central minimum and maxima at the collector walls. Moreover, the profile should be more pronounced for large particles which have a higher Peclet number, because they have a higher migration velocity.

All the efficiency measurements (for both ash and oil droplets) were made by measuring the particle flux at the precipitator exit (~ 0.5m downstream of the last wire) and taking the ratio of the fluxes with the precipitator energized and unenergized as the penetration. This avoids the perturbation produced by an upstream probe measurement of inlet flux and moreover, yields a conservative result for efficiencies since it does not include purely mechanical collection.

For flyash two measurement techniques were employed. The first used a rake of ten isokinetic sampling filter probes, having a common pumping manifold, disposed across the width of the tunnel. The ash samples collected in measured exposure times were weighed and also size analyzed by Coulter counter. The second method employed a cascade impactor, fitted with isokinetic entrance cones, positioned on the tunnel axis to determine the fractional penetration (uncorrected for nonuniform profiles).

For the oil droplet aerosol, an isokinetic sampling probe was connected (via short, 1/4" diameter tubulation) to a 100:1 diluter and Climet optical sizing-counter. To measure the concentration profile, the probe was traversed across the width of the tunnel. This technique gave more consistent results, more quickly and with much less effort than the techniques used for flyash. The Climet counter has 8 channels covering the range 0.3 μm to 10 μm.

RESULTS WITH REDISPERSED FLYASH

Measurements of fractional efficiency using the sampling probe and Coulter counter technique, some of which were reported in (17), showed anomalous behavior. When reduced to plots of effective migration velocity versus particle diameter via the Deutsch equation, they did not show the linear behavior $w_{eff} \propto a$ to be expected for fixed flow velocity and electrical conditions in the range where field charging is applicable. The dependence was highly nonlinear, with the small particles having too high a value and the large particles too small a value of w_{eff}. A second anomalous feature was that, for constant electrical conditions, w_{eff} increased with flow velocity $\bar{u}$, whereas simple theory indicates it should be independent of $\bar{u}$.

After considerable study and further experimentation to uncover the cause of the anomalous behavior, it was traced to the fact that, despite our best efforts, we were not able to adequately deagglomerate the ash fed to the tunnel. This was confirmed by measurements with the cascade impactor and electron micrographs of the material collected on the various stages.

These electron micrographs revealed a significant fraction of agglomerates collected in the top stages, with the system unenergized, and an even larger proportion of agglomerates on the same stages with the precipitator energized. This indicated the presence of a significant fraction of large agglomerates which are detected as large particles by the impactor, but which do not have the high migration velocity to be expected from large single particles of that size. This lower migration velocity can be attributed to a combination of smaller charge and higher drag coefficient than single spheres of equivalent size.

The anomalously high migration velocity of small particles observed with the Coulter counter can be explained as follows. Small particles existing in agglomerates enjoy the higher effective migration velocity of large particles, but the Coulter counter technique, which effects good deagglomeration in solution, detects them as small particles.

For these reasons it was concluded that because we are unable to achieve adequate deagglomeration, re-dispersed flyash is unsuitable as an aerosol for measuring the basic collection performance of a laboratory precipitator. Measurements on agglomerates cannot be satisfactorily related to theory, because we have no adequate way to model the charging theory or drag coefficient of agglomerates of arbitrary shape. This conclusion does not apply, of course, to coal-fired facilities, either at full scale or in laboratory models, because the agglomeration only occurs on collection, and is a problem only when using re-dispersed ash.

Our experience calls into question the validity of all test data obtained on laboratory facilities using re-dispersed ash, and for this reason we turned to the use of oil droplets.

RESULTS WITH OIL DROPLETS

In the past two months, an extensive set of fractional efficiency measurements employing an aerosol of corn oil droplets has been made using the sampling probe-diluter-optical counter technique described above. These have been made for $\overline{u}$ = 1,2 and 4m/s and for applied voltages of both polarities at intervals of 5 kV from just above corona onset (± 30 kV) to close to sparkover (+ 55 kV, -60 kV).

Only the data for negative polarity and $\overline{u}$ = 1 and 2m/s will be reported here because we have not had sufficient time to reduce and interpret the data from all of the test conditions. Also, the range of particle diameters provided by the present nebulizer system is rather limited at the large end and, in future, an attempt will be made to extend the range to larger sizes of interest for precipitation of flyash. Thus the results reported below, and their interpretation should be regarded as provisional.

Initially, for each test condition, the fractional penetration was measured by taking the ratio of the particle fluxes in the energized and unenergized conditions, with the probe positioned on the tunnel axis. This is designated the uncorrected penetration P and $\eta \equiv (1-P)$ is the uncorrected efficiency. By traversing the probe in steps, the flux profile (by size class) for the energized condition was measured, and a correction factor found by taking the ratio of the area under the profile to the product of the centerline value and the duct width. The true (or corrected) penetration P_c was then found by multiplying P by the correction factor, and the corrected efficiency taken as $\eta_c \equiv (1-P_c)$. Of course, if the profile is flat then the correction factor is unity, but for a profile having a central minimum, the factor is greater than unity, and the corrected efficiency is less than the uncorrected value.

Figure 6 shows the flux profiles by size class for the test condition $\bar{u}$ = 2m/s, V = - 45kV. It is evident that the profiles have a central minimum and maxima at the collector plates, and that these are more pronounced the larger the particle. This is exactly what is predicted by the finite diffusivity theory and is incompatible with the flat profile assumption of the Deutsch model. The reason for the slight asymmetry is presently unknown.

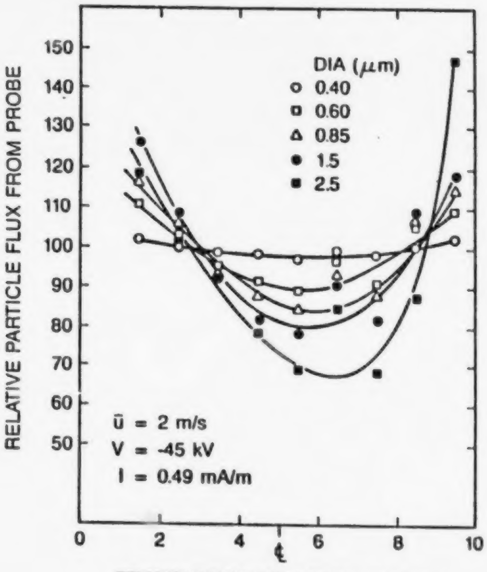

Fig. 6. Particle concentration profiles downstream of seventh wire.

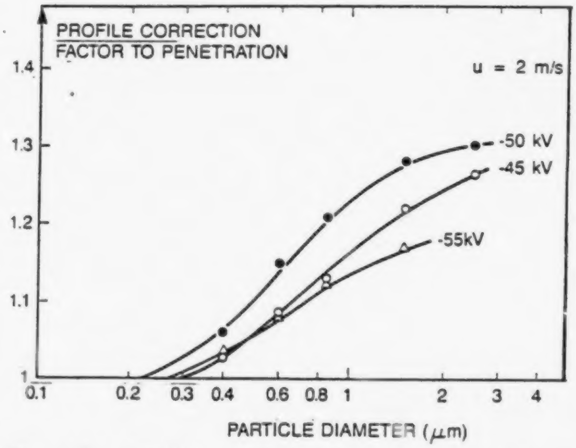

Fig. 7. Profile correction factors to penetration.

Several other points should be noted. First, the particle concentration profiles will be more pronounced than the flux profiles because u is lower in the boundary layers adjoining the collector plates. Second, the profiles would be more pronounced if we were able to measure them at the plane of the last wire, because as the electric field decays downstream of the last wire, the profile relaxes towards a flat one, due to back-diffusion. Third, the profiles may not have reached their self-similar shapes because the precipitator is not long enough (i.e. the Deutsch number is not large enough).

The profile correction factors as a function of particle diameter are shown for several test conditions in Figure 7. It is seen that they increase with particle diameter as expected. Unfortunately we have not had time to make profile measurements for all the test conditions reported below, so that corrected values of efficiency are not available for all cases at the time of writing.

Figure 8 shows measurements of penetration and efficiency as a function of particle diameter for V = - 50 kV, i = 0.85 mA/m, and $\bar{u}$ = 1,2 and 4m/s. The diameters are plotted as the mean of the nominal ranges of the eight channels of the Climet counter. The solid lines show the uncorrected values and the broken lines the corrected values (where available).

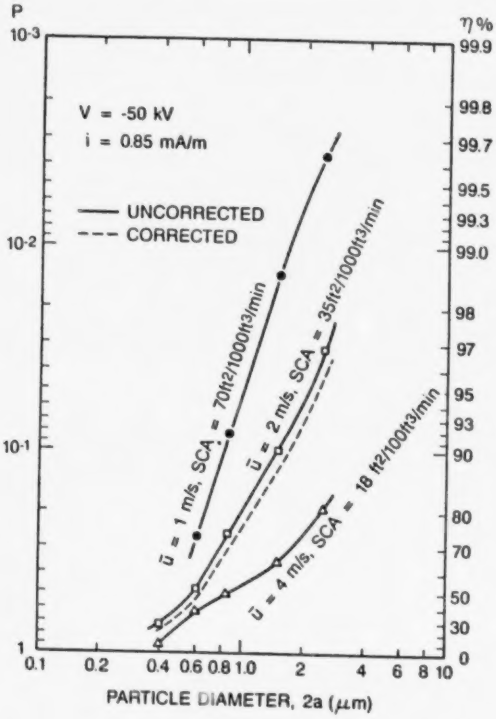

Fig. 8. Fractional efficiency at three gas velocities.

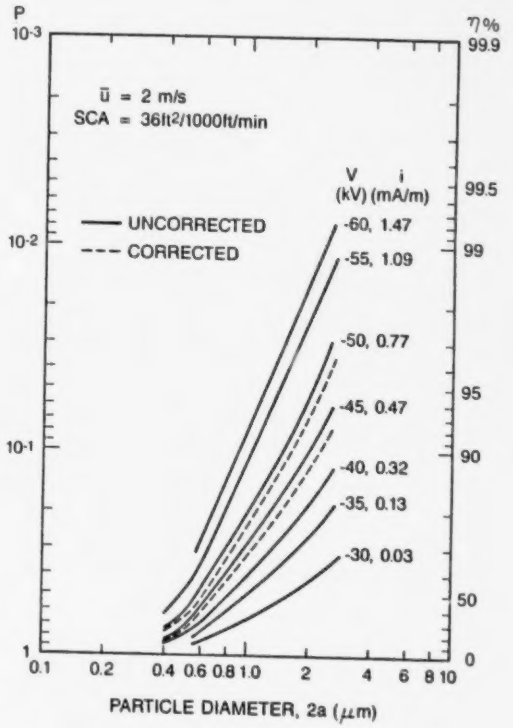

Fig. 9. Fractional efficiency at various voltages.

Figure 9 shows experimental measurements of penetration and efficiency as a function of particle diameter for $\bar{u}$ = 2m/s and V = − 30 kV (in 5 kV increments) to − 60 kV. Again, solid lines are uncorrected values and broken lines are corrected ones.

It should be noted that, generally, the efficiencies are remarkably high for such small particles and small specific collection areas. Also, there is no minimum and associated increase in efficiency for submicron particles which is commonly seen in field measurements on flyash precipitators. However the latter relatively large efficiency for submicron particles may well be due to agglomeration at the high loadings of fine particles present in such precipitators. Such agglomeration would not be expected for the extremely low loadings existing in these oil droplet dispersions.

INTERPRETATION OF RESULTS

In the following we analyze and interpret the measurements of fractional efficiency, first by comparison with computations using the EPA/SoRI code (7) which uses the Deutsch model for particle transport, and second, in terms of the finite, uniform diffusivity model (1).

COMPARISON WITH COMPUTATIONS FROM EPA/SoRI CODE

Before discussing the results, a brief description of the salient features of the latest version of this code is in order.

For specified geometry, the first subroutine computes the distributions of potential, electric field components, ion current density and ionic space charge from a 2-D Poisson solver. Unlike earlier versions, the current version utilizes experimental data on the linear current density i for given applied voltage V without having to assume a value for the ionic mobility μ_i. As a result the computed electrical conditions are much more in accord with the experimental conditions than were given by earlier versions of the code which computed the currents for an assumed mobility.

A second subroutine computes, for specified particle diameters, the average particle charge $\overline{q}(t)$ and hence $\overline{q}(x)$ where $x = \overline{u}t$ is the average position in the streamwise direction measured from the leading edge of the (first) collector plate. The charge calculation is based on an approximate theory which includes both field and diffusion charging (18). In the field charging component the field E_c is taken as the average field $E_{av} \equiv (V/d)$ in the transverse plane of the high voltage wires, and the charging rate is based on a space-averaged value of the ion number density $\overline{n}_i$. A value for the relative permittivity ε_r of the particle material has to be specified in the field charging algorithm.

A third subroutine then calculates, for each particle diameter (2a) the average migration velocity $\overline{w}_y$ (a,x) from the formula

$$\overline{w}_y(a, x) = \frac{C(a)\ \overline{q}\ (a, x)}{6\pi a\mu}\ \overline{E}_p \tag{12}$$

where $\overline{E}_p$, the average precipitating field, is taken as the spatial average of the field at the collector plate $\langle E_y \rangle_{pl}$. The viscosity μ appropriate to the gas composition, temperature and pressure is used in Eq. (12).

Assuming a uniform profile is maintained in each transverse plane (the Deutsch assumption), a fourth subroutine then calculates, for each particle diameter, and for a given precipitator length L, the penetration from the formula

$$\overline{P}(a) = \exp\left[-\frac{1}{\overline{u}d}\int_o^L \overline{w}(a, x)\ dx\right] \tag{13}$$

The mean fractional efficiency is then given by

$$\overline{\eta}(a) = \left[1 - \overline{P}(a)\right] \tag{14}$$

An average migration velocity (averaged over the length L) is then defined by and computed from

$$\langle \overline{w}(a)\rangle \equiv \frac{1}{L}\int_{o}^{L} \overline{w}(a,\ x)\ dx \tag{15}$$

This average migration velocity allows for the time development of particle charge through the precipitator and clearly satisfies the simple Deutsch formula

$$\overline{P}(a) = \exp\left[-\ \langle\overline{w}(a)\rangle\ L/\overline{u}d\right] \tag{16}$$

Thus $\langle\overline{w}(a)\rangle$ should correspond to the effective migration velocity, as a function of particle diameter, inferred from fractional efficiency measurements by use of the Deutsch formula, if the Deutsch assumption is valid.

The code has many other features which allow for a spread of mean velocities $\overline{u}$ among the many parallel channels of industrial precipitators, and, by empirical formulae, allow for sneakage and rapping reentrainment, but these are not needed for the present purpose.

Figure 10 compares the measured fractional efficiency and that computed by the code for the case $\overline{u}$ = 2 m/s, V = - 45 kV, $\overline{I}$ = 0.57 mA/m. Both the uncorrected and corrected experimental results are shown.

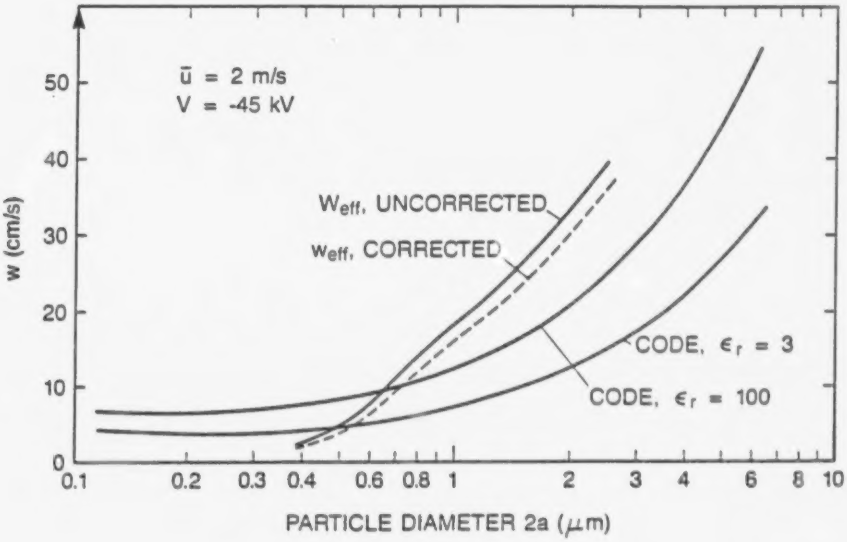

Fig. 10. Measured fractional efficiency compared with those computed from EPA/SoRI code.

It is important to note that the code computations were made for a particle dielectric constant of ε_r = 100. This effectively assumes the particle is conducting, and is the value usually employed for flyash in combustion gases on the grounds that the surface resistivity is low because of the high humidity. However, for oil droplets the Pauthenier factor

$\varepsilon_r/(\varepsilon_r + 2)$ should multiply the expression for the saturation charge (for field charging). Inclusion of this factor significantly reduces the computed migration velocity and efficiency.

We have not been able to find literature values of ε_r for corn oil, but that for linseed oil is quoted as 3.3. In Figure 10 we show an approximate curve for the computed fractional efficiency allowing for $\varepsilon_r = 3$ which reduces the saturation charge to 60% of its value for $\varepsilon_r = 100$. The electrical resistivity of such vegetable oils is quoted as being very high ($\gtrsim 10^{12}$ ohm-cm) so that the assumption of a dielectric particle is justified.

Examination of Figure 10 reveals a marked discrepancy between the measured fractional efficiency and that computed from the code and an even more marked discrepancy when the computed values are corrected for the lower dielectric constant. We believe that the higher experimental values are a clear indication of the fact that the relatively low turbulent diffusivity in our laboratory precipitator leads to much higher efficiencies than are predicted on the basis of the Deutsch model for particle transport. For small enough particles, for which w and hence P_e is small ($Pe \sim 1$) one would expect the experimental and Deutsch code efficiencies to agree, because the profiles become flat. However, if the trend of the experimental efficiency for small particles is to be believed, it would appear that the approximate algorithm in the code for particle charging overestimates the contribution of diffusion charging. This point needs further investigation.

Figure 11 shows the same data as Figure 10, presented in the form of effective migration velocity $w_{eff}(a)$ from experiment and $\langle \overline{w}\ (a)\rangle$ from code computation. For the theoretical curve, corrected for $\varepsilon_r = 3$, $\langle \overline{w}\ (a)\rangle$ is taken as 60% of the computed values for $\varepsilon_r = 100$. This should be a good approximation for all but the smallest particle diameters, when diffusion charging (which is not dependent on ε_r) is significant.

Unfortunately a similar comparison at higher voltages and currents could not be made because the Poisson solver in the code, as currently configured, would not converge for $V > 45$ kV, apparently because our experimental currents were higher than those for which the code has been used hitherto. It appears that the negative ion mobility under our conditions (ambient air) is significantly higher than is appropriate to combustion gases.

COMPARISON WITH UNIFORM, FINITE-DIFFUSIVITY MODEL

From the foregoing comparison it is clear that the experimental results cannot be explained by the Deutsch model. The next logical choice is then to compare the results with the uniform, finite diffusivity model (1).

In the case of the Deutsch model the comparison is easily effected, because the fractional penetration is a simple function of only one dimensionless parameter, i.e. $P(a) = \exp - De(a)$ where $De \equiv w(a)\ L/\overline{u}d$. Since d, L and $\overline{u}$ are known, or easily measured, the measured fractional penetrations are easily converted to give effective values of migration velocity as a function of particle size, $w_{eff}(a)$. Then, depending on the model used for

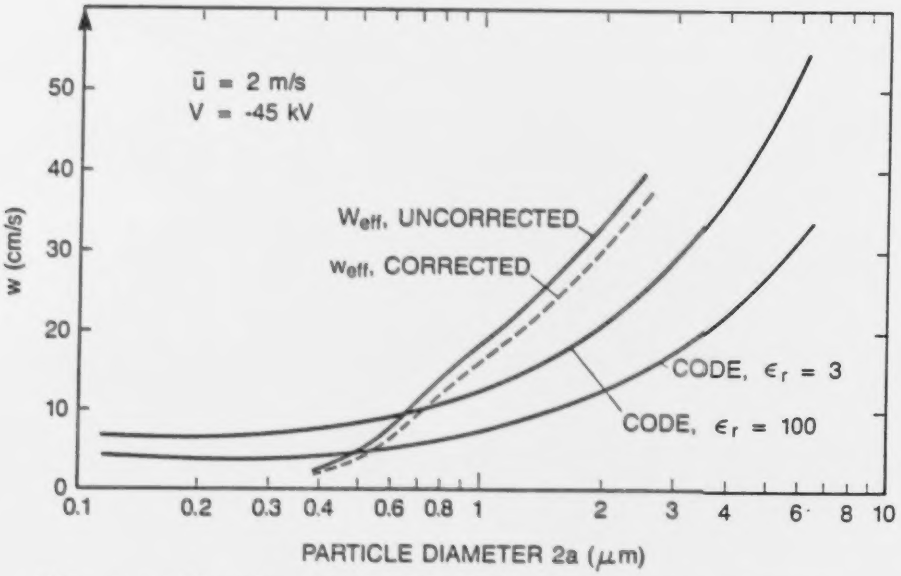

Fig. 11. Effective (Deutsch) migration velocity compared with computations from EPA/SoRI code.

charging, $w_{eff}(a)$ can be compared with $w(a)$ calculated for the fields (and currents) computed for the known electrical conditions.

For instance, if one neglects diffusion charging, and assumes particles rapidly acquire their saturation charge $q_s(a)$, then

$$w(a) = \frac{q_s(a)\ E_p\ C(a)}{6\pi a\mu} = \frac{2a\ C(a)}{\mu}\ \frac{\varepsilon_o\ \varepsilon_r}{(\varepsilon_r + 2)}\ E_c\ E_p \tag{17}$$

where $C(a)$ is the Cunningham factor, and E_c and E_p are the effective (uniform) fields for charging and precipitation respectively. Moreover if one takes

$$E_c = k_c\ E_{av} \tag{18a}$$

and

$$E_p = k_p\ E_{av} \tag{18b}$$

where $E_{av} \equiv (V/d)$ is known, E_{pl} is the average field at the collector plate, which is a function of E_{av} (and i), and k_c, k_p are numerical coefficients, then on equating $w_{eff}(a)$ and $w(a)$ one can deduce a value for the product $(k_c\ k_p)$. Traditionally it is assumed that $k_c = 1$ and in that case the value of k_p deduced from the experiments, via Eqs. (17) and (18) should agree with the value $k_p = (E_{pl}/E_{av})$ computed from a 2-D Poisson code for the known electrical conditions.

Thus, as a measure of the fit to the theory, one can either (i) compare $w_{eff}(a)$ and $w(a)$, calculated assuming $k_c = 1$ and k_p as given by the Poisson code, or (ii) assuming $k_c = 1$ and equating $w_{eff}(a)$ to $w(a)$, one can compare the effective value $k_{p(eff)}$ deduced from the experiments with k_p computed from the Poisson solver. The comparison shown in Figure 11 utilized the former comparison.

In the case of the finite diffusivity model the comparison between theory and experiment is more complex because the fractional penetration is a function of two dimensionless parameters, De $\equiv (wL/\overline{u}d)$ and Pe $\equiv (wd/D)$. For given operating conditions $(\overline{u}, V)$ and particle radius a, one wishes to locate the operating point in the P (De, Pe) plane of Figure 1. The measured penetration determines on what horizontal line (parallel to the abscissa) the operating point lies, but there is an infinite set of (De, Pe) pair values which satisfy this condition. Equivalently, one can say that one wishes to use the experimental data to back out, for each operating point, the values of both w(a) and the diffusivity D (which is itself a function of both $\overline{u}$ and the electrical conditions).

In the following we describe an approximate procedure for determining the w(a) and D values, and hence the operating parameters De and Pe from the experimental data.

First, it should be noted with regard to the dimensionless parameters that De $\equiv (w(a)L/\overline{u}d)$ involves the unknown w(a), while Pe $\equiv w(a)d/D$ involves both of the unknowns w and D. This is inconvenient and we therefore use for a second dimensionless parameter, in place of Pe, the quantity

$$\mathrm{Sc} \equiv \frac{\mathrm{Pe}}{\mathrm{De}} \equiv \frac{ud^2}{DL} \qquad (19)$$

This is a type of turbulent Schmidt number and is a measure of the ratio of the axial particle flux (due to convection) to the transverse flux (due to diffusion). It has the advantage of involving only the single unknown D, (and not also w, as does the Peclet number).

The solution of the problem of precipitation in a uniform field for finite, uniform diffusivity, P(De, Pe) shown in Figure 1 is readily converted to an equivalent plot of P(De, Sc) as shown in Figure 12, which shows contours of constant Sc analogous to those of constant Pe in Figure 1. Note that with increasing De, the constant Sc contours do not become straight and they cross the constant Pe contours upwards to higher efficiency.

Analytically, this numerical solution can be regarded as an expression of the fact that the penetration P is a function only of the two dimensionless parameters De and Sc; thus

$$P = P\,(\mathrm{De}, \mathrm{Sc}) \qquad (20)$$

In principle, this functional relation can be inverted (or solved) to yield

$$\mathrm{De} = \mathrm{De}\,(P, \mathrm{Sc}) \qquad (21)$$

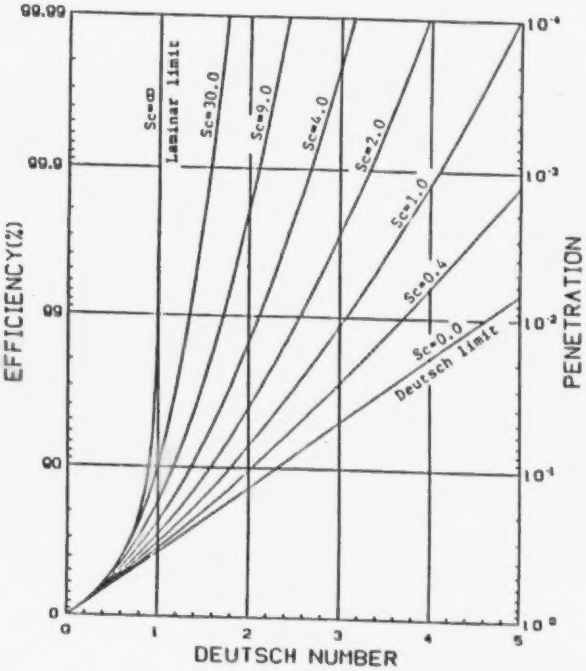

Fig. 12. Universal plot of penetration and efficiency versus Deutsch No. with Schmidt No. as parameter.

or, using the definition of Deutsch number

$$w(a) = \left(\frac{\overline{u}d}{L}\right) \mathrm{De}\ (P(a),\ Sc) \tag{22}$$

Note that Sc is not a function of particle radius a. Also, for fixed $\overline{u}$, d and L, Eq. (22) is equivalent to the functional relation

$$w(a) = w\ (P(a),\ D) \tag{23}$$

which can be regarded as a known function.

Experimentally we measure $P_{exp}(a,V)$ so we can use Eq. (23) to back out an effective value of w from

$$w_{eff}(a) = w(P_{exp}(a,\ V),\ D) \tag{24}$$

but only provided we assign (or guess) a value of diffusivity D, which, of course, is a function of $\overline{u}$ and electrical conditions, but not of the particle radius a.

If we equate this value $w_{eff}(a)$ (backed out of the theory using the experimental penetration and some assumed value of D) to w(a) based on the simple field charging theory (Eq. 17), we have

$$\frac{w\left(P_{exp}(a,\ V),\ D\right)}{2a\ C(a)} = \frac{\varepsilon_o}{\mu}\ \frac{\varepsilon_r}{(\varepsilon_r + 2)}\ (k_c\ k_p)\ \left(\frac{V}{d}\right)^2 \qquad (25)$$

Here, since the rhs is independent of particle radius a, so also must be the lhs.

Now, suppose we have available a set of values of measured penetrations $P_{exp}(a,\ V)$ over a set of particle sizes for a number of different applied voltages V, for some gas velocity $\bar{u}$. Then for some chosen value of D we can evaluate the left hand side of Eq. 25 for each particle radius a and voltage V. The right hand side of Eq. 25 is known, apart from the factor $(k_c\ k_p)$. Then we can plot, for the chosen D, a set of points in the $(V/d)^2$, $(w/2a\ C(a))$ plane corresponding to the set of measured penetrations $P_{exp}(a,\ V)$.

Two such plots are shown in Figures 13(a) and (b) for $\bar{u}$ = 2m/s and D equal to 10 cm^2/s and 40 cm^2/s respectively. The points for each particle size in the set are joined to form a piecewise linear curve.

Now notice that because the lhs of Eq. (25) is independent of a, then if we have chosen the correct value of D for a given voltage V, the points on the graph for that value of V should collapse to a single point. Because it is anticipated that D is a function of electrical conditions (on account of corona wind effect), we expect that the correct value of D (i.e. which collapses the points on the graph to a single point) will vary with V.

To determine the correct value of D for each V we have adopted the following stratagem. On Figures 13(a) and (b) we have plotted (as a thick solid line) the mean value of the values of w/2a C(a) for different a's at each V. We have also evaluated the standard deviation about this mean of the separate values composing the mean, and this is plotted as a thick shaded line (at the bottom). Then among a set of graphs such as Figures 13, spanning a wide range of D, we should find that for each V, there is a graph which makes the standard deviation go to zero for the appropriate $(V/d)^2$ abscissa.

Of course, in practice, because of inherent tolerances in the experimental data one should not expect the standard deviation to go to zero, but to a minimum at the correct value of D for each V. Also the process described was in fact carried out on a personal computer.

Figure 14 shows a set of curves of the standard deviation of the values of w/2a C(a) versus D (actually 1 + log D, for convenience of plotting) for the various voltages between V = - 30kV and - 60 kV. With the exception of the curve for V = - 30kV, which is very close to the threshold voltage and gave unreliable data, each curve has a minimum which is marked by an arrow. The D value of the minimum D_{min} is then the appropriate value of diffusivity $D(\bar{u},\ V)$ corresponding to the experimental conditions $\bar{u}$, V.

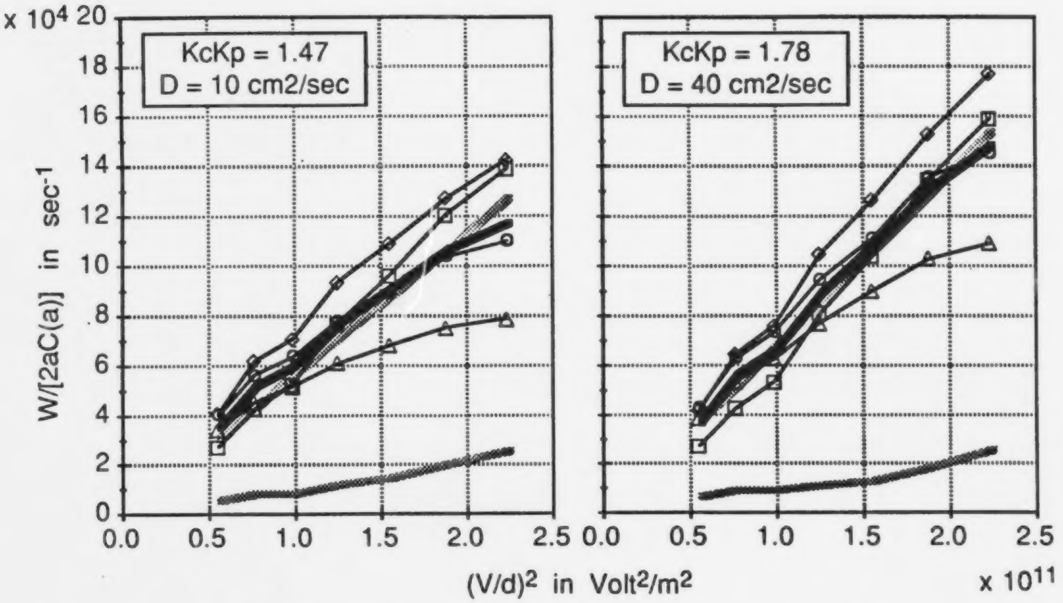

Fig. 13. Plot of $w/[2aC(a))]$ versus $(V/d)^2$ for u_g=2.0 m/sec, negative corona and two chosen values of D: a) D=10cm^2/sec and b) D=40cm^2/sec. Symbols correspond to different particle diameters:

▣ (2a) = 0.6 μm ◈ (2a) = 0.8 μm ⊙ (2a) = 1.5 μm △ (2a) = 2.5 μm

Returning to Figures 13, also plotted are the best straight lines (by minimum least squares fit) through the origin and the data points, shown as a thick shaded line. According to Eq. 25, the slope of this line is $(\varepsilon_o/\mu)(\varepsilon_r/\varepsilon_r+2)$ $(k_c\ k_p)$, so that for known values of gas viscosity μ, and dielectric constant ε_r, the value of $(k_c\ k_p)$ can be determined. The latter values for $\mu=1.82\times10^{-5}$ Kg/m.s and $\varepsilon_r=3$ are shown on Figures 13a and 13b, and these values of $(k_c\ k_p)$ as a function of D are plotted in Figure 14 as a broad solid line. For each voltage, the value of D_{min} and the corresponding value of $(k_c\ k_p)$ is tabulated at the side of the graph. It will be seen that generally the values of $(k_c\ k_p)$ deduced in this way from the experimental data are somewhat greater than unity and increase with increasing voltage.

If, as is usually assumed, the effective charging field E_c is taken as equal to the average applied field $E_{av} \equiv (V/d)$, then $k_c = 1$, and the $(k_c\ k_p)$ values then correspond to $k_p(V)$. Now, according to the assumption that the effective precipitating field E_p is equal to the average value of the field at the collector $E_{pl} \equiv \langle E_y(d)\rangle$, k_p is given by $E_{pl}/(V/d)$. Thus the values of $k_p(V)$ inferred from the experimental data by the procedure described above, should agree with the values of $k_p = E_{pl}/(V/d)$ given by the solution of Poisson code for the given geometry and electrical conditions.

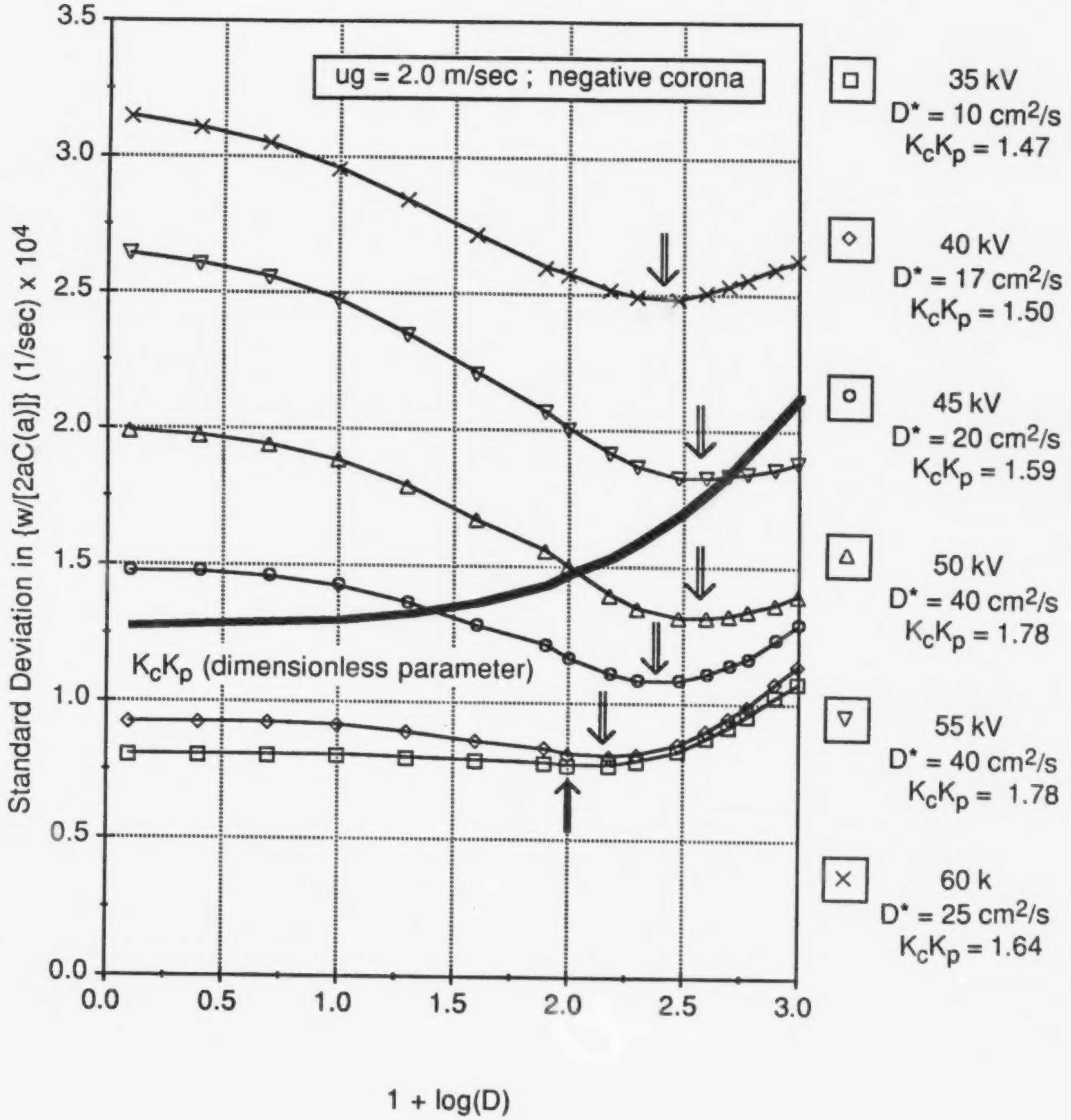

Fig. 14. Standard deviation in w/(2aC) versus chosen D value, showing minima at correct D value. Also plotted is k_ck_p value versus D. Inferred values of D and k_ck_p for each voltage shown in legend.

The theoretical values of $k_p(V)$ have been determined by running the EPA/SoRI code. As noted earlier, this code would not converge for our experimental currents $i(V)$ for voltages greater than 45kV. Consequently an extrapolation scheme, based on a dimensional argument, has been used to generate theoretical k_p values for $V > 45$ kV.

Table 1 shows for each voltage these theoretical values of k_p from the Poisson code and its extrapolation, and also, for both $\bar{u}$ = 1m/s and $\bar{u}$ = 2m/s the values of D and k_p backed out from the fractional penetration measurements by the data reduction scheme described above.

TABLE 1. VALUES OF DIFFUSIVITY D AND $k_p = \langle E_{p1} \rangle /(V/d)$ INFERRED FROM MEASUREMENTS AND FINITE-DIFFUSIVITY THEORY. ALSO SHOWN ARE k_p VALUES CALCULATED BY EPA/SoRI CODE.

		V (negative) (kV)						
		30	35	40	45	50	55	60
k_p	(code)	0.69	0.90	1.08	1.22	1.37	1.45	1.51
$\bar{u}$ 1 m/s	D(cm^2/s)	-	-	3.5	6	8	6	3.5
	k_p (expt)	-	-	0.90	0.97	1.03	0.97	0.90
$\bar{u}$ 2 m/s	D(cm^2/s)	-	10	17	20	40	40	25
	k_p (expt)		1.47	1.50	1.59	1.78	1.78	1.64

The fact that the values inferred for D are of the expected order of magnitude and show the expected increasing trends with $\bar{u}$ and V is encouraging. Also, the fact that the values of k_p inferred from the data are relatively close to the values calculated from the EPA/SoRI Poisson code, and show the correct, increasing trend with increasing V is likewise encouraging.

Several comments should be made concerning the lack of more exact agreement in the k_p values. First, it should be noted that the reduction scheme employed the uncorrected penetration values (because all the necessary profile measurements were not available at the time the data was reduced). Second, the value of k_p inferred from the data depends on the value of the dielectric constant ε_r, which has been taken as $\varepsilon_r = 3$. A different choice of ε_r will scale the inferred k_p values by the factor $(\varepsilon_r + 2)/\varepsilon_r$ irrespective of the value of $\bar{u}$, though it is clear that a different choice of ε_r cannot bring the inferred values of k_p into better agreement with those calculated from the Poisson solver for both $\bar{u}$ = 1 m/s and $\bar{u}$ = 2 m/s. Third, the data reduction scheme is inherently more accurate for higher Deutsch numbers, so that the inferred value k_p is in closer agreement with theory for u=1m/s than for 2m/s. It seems likely, therefore, that the inferred values of D and k_p for u=2m/s are both too high. Finally, of course, it should be recognized that the assumption that the charging and precipitation processes can be adequately represented in terms of effective uniform values of E_c, E_p and D may not be adequately satisfied. However, a more detailed treatment which treats these processes more realistically is likely to be too complicated for practical engineering use. In particular, however, it may well be that the assumption that the effective collecting field $E_c = (V/d)$, i.e. $k_c = 1$ is not good enough, and this point needs further investigation. Also, it should be noted that our charging model neglects diffusion charging so that the data reduction procedure is inaccurate for small particles.

Nevertheless, it is remarkable that the fit of the experimental data to the uniform, finite diffusivity model is as good as it is. It allows one to infer an effective uniform, global value of the turbulent diffusivity as a function of $\bar{u}$ and electrical conditions, and also allows one to check the validity of the use of the notion of effective average fields for charging and precipitation. The inferred values of D and k_p are of the expected magnitudes and show the correct trends. It should be particularly noted that if much larger values of D were assumed to apply, then the (k_c k_p) values would come out much too large to be credible.

With the inferred values of $D(\bar{u}, V)$ one can then determine for each particle diameter and run condition ($\bar{u}$, V), the appropriate values of the dimensionless parameters (De, Pe) or (De, Sc), and so a curve representing the operating points as a function of diameter (2a) can be plotted for each test condition ($\bar{u}$, V) on a dimensionless plot such as Figure 1 or Figure 12.

Some of these operating lines are shown in Figures 15(a) and (b) for $\bar{u}$ = 1m/s and $\bar{u}$ = 2m/s respectively. For 1m/s, it is seen that the operating lines lie well above the Deutsch line, and increasingly so for higher voltages. For V = - 50kV, the Peclet number is approximately 20 for 2.5μm diameter particles, and about 10 for 0.6μm particles. The corresponding Deutsch numbers and efficiencies are respectively De ~ 1.8 and 0.8, and $\eta \sim$ 99.6% and 75%.

It should be noted that these results (for $\bar{u}$ = 1 m/s) are for a specific collection area of only 14.4 $m^2/m^3/s$ (= 72 ft^2/1000 acfm). With increasing length (and SCA), the operating lines move up (higher Pe) and to the right (higher De). Moreover, the efficiency increase is relatively larger for the smaller particles because, for the present operating line, the operating point for small particles still lies in the region where the constant Pe curves have not reached their maximum slope. Physically, this means that the precipitator is not long enough for the concentration profile for small particles to have evolved to its self-similar shape. Depending on the particle size distribution and efficiency required, these results show that performance equivalent to that of a modern commercial precipitator, that is performing at the Deutsch level, could be built with perhaps one-third of the SCA, and hence at approximately one-third of the cost.

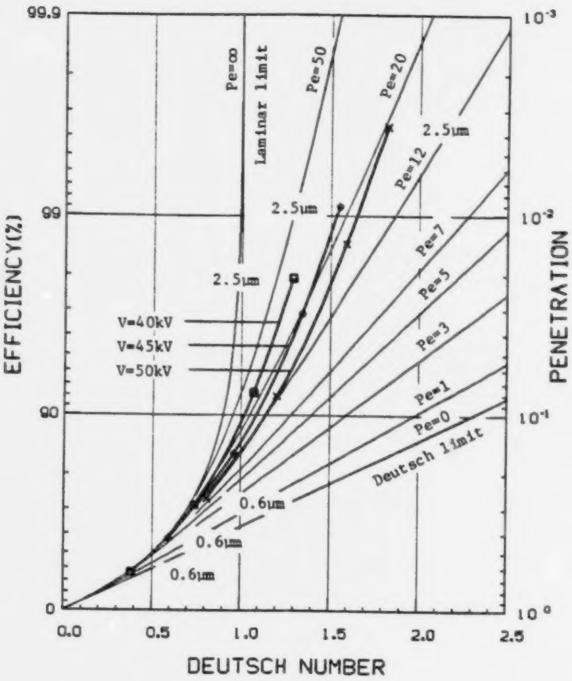

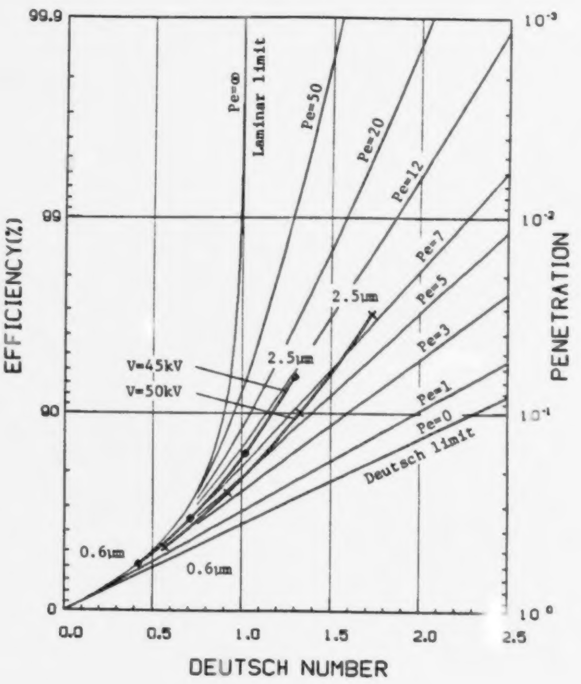

Fig. 15a. Operating line as a function of particle diameter for u=1m/s, V=40, 45, 50kV (negative corona).

Fig. 15b. Operating line as a function of particle diameter for u=2m/s, V=45, 50kV (negative).

SUMMARY AND CONCLUSION

The work presented, both theoretical and experimental, has emphasized that to understand and model precipitator performance more accurately, the long standing Deutsch model which assumes infinite turbulent diffusivity must be replaced by one which allows for finite diffusivity. Performance markedly superior to that predicted by the Deutsch model is to be expected on theoretical grounds if excessively high values of diffusivity can be avoided.

The experimental results for the laboratory tunnel using oil droplets confirm this, and allow one to infer volume-averaged values of effective diffusivity, as a function of flow velocity and electrical conditions. For the conditions of the laboratory precipitator (smooth wires, smooth collector walls, and no non-ideal effects) the values of diffusivity are quite moderate. It is also clear that corona wind induced turbulence for negative corona is not a hindrance, per se, to the realization of moderately low values of diffusivity.

This focuses attention on the need, in commercial precipitators, to minimize the diffusivity due to fluid-mechanical turbulence by reducing, as far as possible, flow disturbances produced by poor entrance conditions, high voltage electrode supports and stiffening baffles on the collectors.

It seems likely that in many modern commercial precipitators the performance is, in fact, limited by non-ideal effects. Rapping losses from the downstream collectors appear to be the most likely cause of performance loss on precipitators which are otherwise performing well (e.g. no back-discharge). However this "fact", if true, is no justification for not taking steps to improve the basic performance by streamlining the flow system. Rather, it indicates that a concerted effort should be made to ameliorate, by appropriate steps (e.g. by the use of wet wall final collectors, or valving off the flow while rapping) the cause of the non-ideal performance).

ACKNOWLEDGEMENTS

This work was supported by the Electric Power Research Institute (Contract No. RP-533-1) and by the National Science Foundation (Grant No. CPE 82-17719-A1). We are grateful to Dr. J. Maulbetsch, Mr. W. Piulle and Mr. R. Altman for continued support and encouragement; also to Mr. C. Leivo for cooperation in making measurements on the flow model at Lodge-Cottrell. We are particularly indebted to Dr. B. Nichols of Southern Research Institute for facilitating at short notice the computations using the EPA/SoRI code and to Dr. M.G. Faulkner for performing the computations and for illuminating discussions.

The work described in this paper was not funded by the U.S. Environmental Protection Agency and therefore the contents do not necessarily reflect the views of the Agency, and no official endorsement should be inferred.

REFERENCES

1. Leonard, G.L., Mitchner, M. and Self, S.A., Particles Transport in Electrostatic Precipitators, Atmospheric Environment 14, 1980, pp. 1289-1299.

2. Leonard, G.L., Effect of Turbulence on Electrostatic Precipitator Performance, Ph.D. Dissertation, HTGL Report No. 196, Department of Mechanical Engineering, Stanford University, 1982.

3. Friedlander, S.K., Smoke, Dust and Haze, Wiley 1977, p. 32.

4. Leonard, G.L., Mitchner, M. and Self, S.A., Experimental Study of the Effect of Turbulent Diffusion on Precipitator Efficiency, J. Aerosol Science 13, 1981, pp. 271-284.

5. Kihm, K.D., Mitchner, M. and Self, S.A., Comparison of Wire-Plate and Plate-Plate Electrostatic Precipitators in Laminar Flow, J. Electrostatics.

6. Kihm, K.D., Mitchner, M. and Self, S.A., Comparison of Wire-Plate and Plate-Plate Precipitators in Turbulent Flow, J. Electrostatics (in press).

7. EPA/SoRI Code, A Mathematical Model of Electrostatic Precipitation, Revision 3, Vol. I, PB 84/212/679; Vol. II, PB 84/212/680, 1984.

8. Schlichting, H. Boundary Layer Theory, McGraw Hill 1979, 7th Edition, Ch. 21.

9. Becker, H.A., Rosensweig, R.E. and Gwodz, J.R., Turbulent Dispersion in a Pipe Flow, AIChE Jour. 12, 1966, pp. 964-972.

10. Kumaran, A.R., Aspects of the Fluid Mechanics of Electrostatic Precipitators, Engineers Thesis, HTGL Report No. 15-83-TR, Stanford University, May 1983.

11. Leonard, G.L., Mitchner, M. and Self, S.A., Experimental Study of the Electrohydrodynamic Flow in Electrostatic Precipitators, J. Fluid Mech. 127, 1983, pp. 123-140.

12. Yamamoto, T. and Velkoff, H.R., Electrohydrodynamics in an Electrostatic Precipitator, J. Fluid Mech. 108, 1981, pp. 1-18.

13. Larsen, P.S. and Sorensen, S.K., "Effect of Secondary Flows and Turbulence on Electrostatic Precipitation Efficiency," Atmospheric Environment, 18, 1963-1967, 1984.

14. Mitchner, M., Leonard, G.L. and Self, S.A., Corona-Induced Turbulence, Fourth Symposium on the Transfer and Utilization of Particulate Control Technology, Houston, Texas, October 1982.

15. Shaughnessy, E.J., Davidson, J.H. and Hay, J.C., The Fluid Dynamics of Electrostatic Precipitators: Effects of Electrode Geometry, 5th EPA/EPRI Symposium on Transfer and Utilization of Particle Control Technology, August 1984.

16. Agarwal, J.K., Sen, G.J. and Remiarz, R.J., Filter Testing with the Continuous Flow, Single Particle Counting Condensation Nucleus Counter, TSI Quarterly, Vol. XI, 1, 1985, pp. 3-12.

17. Self, S.A., Mitchner, M., Kihm, K.D., Choi, D.H. and Leach, R., Effect of Turbulence on Precipitator Performance, Second International Conference on Electrostatic Precipitation, Kyoto, Japan, November 1984.

18. Smith, W.B. and McDonald, J.R., "Development of a Theory for the Charging of Particles by Unipolar Ions," J. Aerosol Science 7, 151-156, 1976.

THREE-DIMENSIONAL CALCULATIONS OF NEGATIVE TUFT CORONA

M.K. Owen, T. Yamamoto, and P.A. Lawless

Research Triangle Institute
P.O. Box 12194
Research Triangle Park, NC 27709

and

L.E. Sparks

Air and Energy Engineering Research Laboratory
U. S. Environmental Protection Agency
Research Triangle Park, NC 27711

ABSTRACT

Numerical simulation of the voltage, current density, and electric field distributions associated with negative tuft corona on smooth wires has been performed. Although precise boundary conditions for describing the tuft are not available, realistic values for voltage and current from a single tuft are used. The calculated results agree well with the experimental measurements, giving confidence in the predicted values for ionic density and electric field, which are otherwise difficult to obtain. A visual presentation of the results shows some striking features of the structure surrounding the negative tuft.

This paper has been reviewed in accordance with the U.S. Environmental Protection Agency's peer and administrative review policies and is approved for presentation and publication.

INTRODUCTION

The uneven and tuft-like local corona discharge occurs on smooth wire discharge electrodes. Existing analytical techniques have ignored these tufts and assumed that the discharge is evenly distributed. The tuft corona is known to produce a strong uneven current distribution on the plate electrode with the regions of very high current density immediately under each individual tuft discharge. This is important in studies seeking to quantify the conditions of back corona formation. Another feature is that the tufts form at voltages well below the Peak corona onset value, Vc, possibly as low as 0.6 Vc (1,2). In this voltage range, $0.6\ Vc < V < Vc$, the tufts are produced randomly along the discharge wire, and when the voltage is Vc, the tufts become reasonably uniform along the full range of the wire.

Existing three-dimensional calculations of negative corona (3) have been modified in such a way that the nomenclature and coordinate system are similar to those used by McDonald et al. (4). The model incorporates the effects of geometrical configurations (wire-to-wire spacing, wire-to-plate spacing, tuft spacing, and discharge wire radius), operating conditions (applied voltage, current density, gas temperature, and pressure), and the effects of both ionic and particulate space charge. The program is menu driven so that the user can control the parameters of the model. The geometrical configurations and operating conditions mentioned above can be varied easily. Graphical presentation of the results shows some striking structural features surrounding the negative tuft and also provides insight into the detailed electrical characteristics of the tuft corona.

Numerical simulations of the voltage, current density, and electric field distributions have been performed using a microcomputer. This paper discusses the results of two simulations: one for a wide tuft spacing, and the other for a narrow spacing.

FUNDAMENTAL EQUATIONS FOR THREE-DIMENSIONAL TUFT CORONA

Figure 1 shows the physical arrangement of a mathematical model used to describe the three-dimensional tuft corona. By using a set of Maxwell equations and current continuity equations, the governing equations can be written as:

$$\text{div grad } V = -(\rho_i + \rho_p)/\epsilon_o \qquad (1)$$

$$\vec{J} = (\rho_i b_i + \rho_p b_p)\vec{E} \qquad (2)$$

$$\text{div } \vec{J} = 0 \qquad (3)$$

$$\vec{E} = - \text{grad } V \tag{4}$$

where V = voltage, ρ_i = ionic space charge, ρ_p = particulate space charge, ϵ_o = permittivity of vacuum, $\vec{J}$ = current density, b_i = mobility of ions, b_p = mobility of particulate, and $\vec{E}$ = electric field.

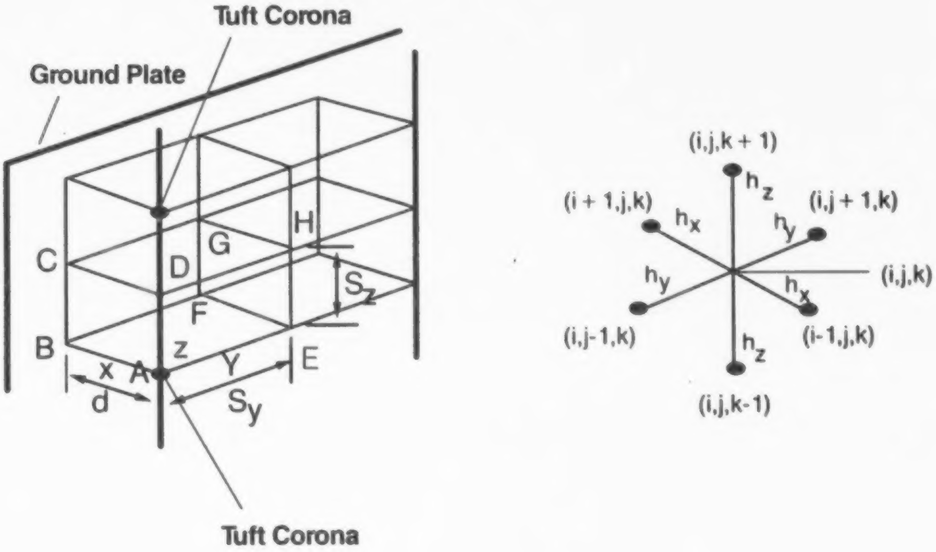

Figure 1. Working domain and grid points.

Current continuity Equation (2) can be modified by using Equations (1), (3), and (4) and assuming $b_i \gg b_p$:

$$\rho_i^2 = \epsilon_o \text{ grad } \rho_i \bullet \text{grad } V \quad . \tag{5}$$

Mathematical modeling of the tuft corona has evolved from Cooperman's two-dimensional analytical solutions (5):

$$V(x,y) = V_o \frac{\displaystyle\sum_{m=-\infty}^{\infty} \ln\left[\frac{\cosh[\pi(y - 2mS_y)/2d] - \cos(\pi x/2d)}{\cosh[\pi(y - 2mS_y)/2d] + \cos(\pi x/2d)}\right]}{\displaystyle\sum_{m=-\infty}^{\infty} \ln\left[\frac{\cosh(\pi m S_y/d) - \cosh(\pi a/2d)}{\cosh(\pi m S_y/d) + \cosh(\pi a/2d)}\right]} \tag{6}$$

where V_o = applied voltage, m = integer, S_y = half the distance between the wires, a = radius of the electrode, and d = wire-to-plate distance.

In addition, Figure 1 illustrates the working domain in the wire-plate precipitator. A series of inner grid points for the numerical simulation of the given differential equations and the coordinates (x,y,z) are shown. The origin of these coordinates is selected at the tuft on the wire. The finite difference approximation using the successive-over-relaxation (SOR) method becomes:

$$
\begin{aligned}
V^{(t)}(i,j,k) = \frac{\omega}{2(1+\alpha^2+\beta^2)} & \left[V^{(t-1)}(i+1,j,k) + V^{(t)}(i-1,j,k)\right] d^2 \\
& + V^{(t-1)}(i,j+1,k) + V^{(t)}(i,j-1,k) \\
& + [V^{(t+1)}(i,j,k+1) + V^{(t)}(i,j,k-1] \beta^2 \\
& + \frac{\left[P_i{}^{(t)}{}_{(i,j,k)} + P_p\right](i,j,k)}{\epsilon_o} \left.h_x{}^2\right\} + (1-\omega)V^{(t-1)}(i,j,k)
\end{aligned}
\tag{7}
$$

where superscript (t) denotes the updated values, ω = extrapolation factor, $\alpha = hy/hx$, and $\beta = hy/hz$.

Analogously, the finite difference approximation for current continuity Equation (5) becomes:

$$
\rho_i^{(t)}(i,j,k) = \frac{1}{2}\left(= \gamma + \sqrt{\gamma^2 + \sigma^2}\right) \tag{8}
$$

where

$$
\gamma = \frac{\epsilon_o}{h_x}\left[\alpha E_x^{(t)}(i,j,k) + E_y^{(t)}(i,j,k) + \beta E_z^{(t)}(i,j,k)\right]
$$

$$
\begin{aligned}
\sigma = \frac{\epsilon_o}{h_x} \Big[& \alpha E_x^{(t)}(i,j,k)\rho^{(t)}(i-1,j,k) \\
& + E_y^{(t)}(i,j,k)\, \rho^{(t)}(i,j-1,k) \\
& + \beta E_z^{(t)}(i,j,k)\rho^{(t)}(i,j,k-1) \Big] .
\end{aligned}
\tag{9}
$$

The solutions to Equations (7) and (8) are obtained subject to the following boundary conditions:

$V = V_o$ (applied voltage) along the wire
$\vec{J}$ = measured average current density at the plate (BCGF)
$V = 0$ on the plate (BCGF)
$\vec{E}_x = 0$ on the plane (AEHD) except along the wire (AD)
$\vec{E}_y = 0$ on the planes (ABCD and EFGH) except along the wire (AD)
$\vec{E}_z = 0$ on the planes (ABFE and DCGH).

The tufts are assumed to be stationary and considered to be the only source of negative ions along the smooth wire without regard to the details of corona generation.

DESCRIPTION OF THE NUMERICAL CALCULATION METHOD

The calculation method is the same as that reported earlier by Yamamoto and Sparks (3). It starts with the ionic space-charge-free and two-dimensional electrostatic potential distribution for the wire-duct geometry given by Equation (6). This potential expression is differentiated to give initial values of E_x and E_y as a function of position. Using these initial values and the desired current density, an initial estimate of space-charge density near the tuft is estimated using Equation (2).

The space-charge densities on lines (AB), (AE), and (AD) are first determined; for instance, the space-charge densities along the line (AB) can be obtained by sweeping j in the increasing order, because E_y and E_z in Equation (9) are zero along the line (AB). Their distributions on the planes (ABCD), (ABFE), and (ADHE) are next calculated, and, finally, the entire volume domain (ABCDEFGH) is preceded by Equations (8) and (9), using the initial values for the electric fields. Next, the voltage is recomputed from Equation (7) using the values of space-charge density just obtained. This procedure is repeated until the fractional difference between the new and previous voltages at each point becomes less than 0.002; i.e., until convergence occurs. The best convergence rate was obtained for the value $\omega = 1.70$.

The current density obtained by Equation (2) is compared with the measured current density. If the fractional difference between the computed and measured current densities is not less than 0.001, the space charge near the tuft is again estimated using the fractional difference of current densities, and the process starts again. The same procedures are repeated alternately until agreement is achieved. The final solution for the voltage distribution is obtained by the superposition of the space-charge-free analytical solution and the Poisson solution obtained by this iterative process.

NUMERICAL RESULTS AND DISCUSSION

Figure 2 shows experimental results for the number of tufts obtained for various voltages (2). This curve was used to determine the applied voltages necessary to produce specific tuft spacings. Hence, an applied voltage of 36,000 V was chosen to produce a wide tuft spacing of 0.152 m. Likewise, 53,000 V led to a narrow tuft spacing of 0.03 m. Next, the experimental relationship determined between voltage and measured current density, Figure 3, led to the choice of measured current densities of 50 μA/m/plate for the wide spacing and 220 μA/m/plate for the narrow spacing (2). Both cases were run for standard temperature and pressure. The electrode-to-plate distance was maintained at 0.114 m, corresponding to the experimental conditions. The x-y-z grids used for these computations were 15x15x5.

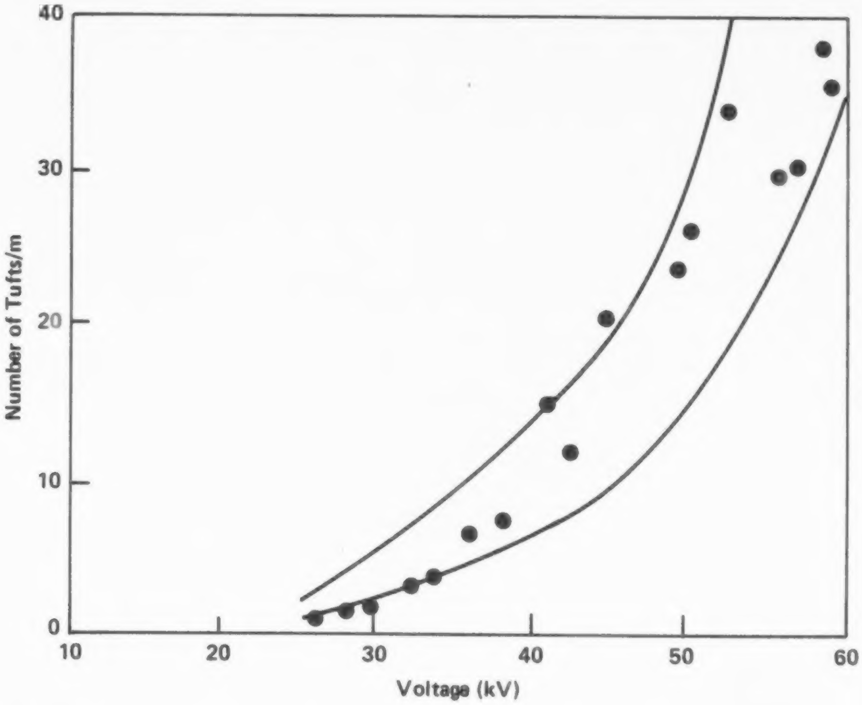

Figure 2. Experimental results for the number of tufts for various voltages.

The current-density distributions for both cases were calculated and their contours plotted. Figure 4 shows contours for the 15.2 cm tuft spacing case at the ground plate, Level 15 of the simulation. One tuft-to-tuft section is modeled. Because the tufts are symmetrical, the information presented is sufficient to describe the situation. The contours represent 10, 25, 50, and 75 percent of the peak value for this level. The highest

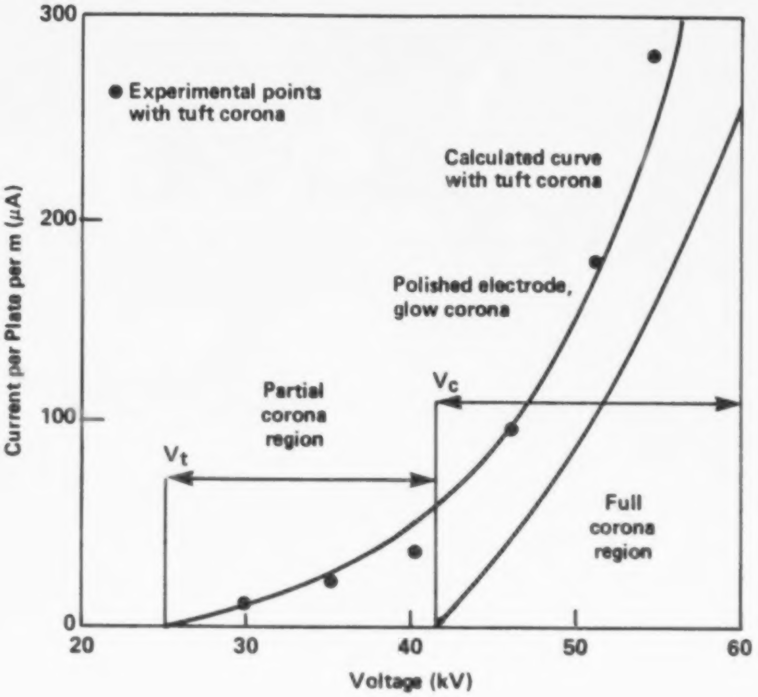

Figure 3. Glow and tuft V-I curves.

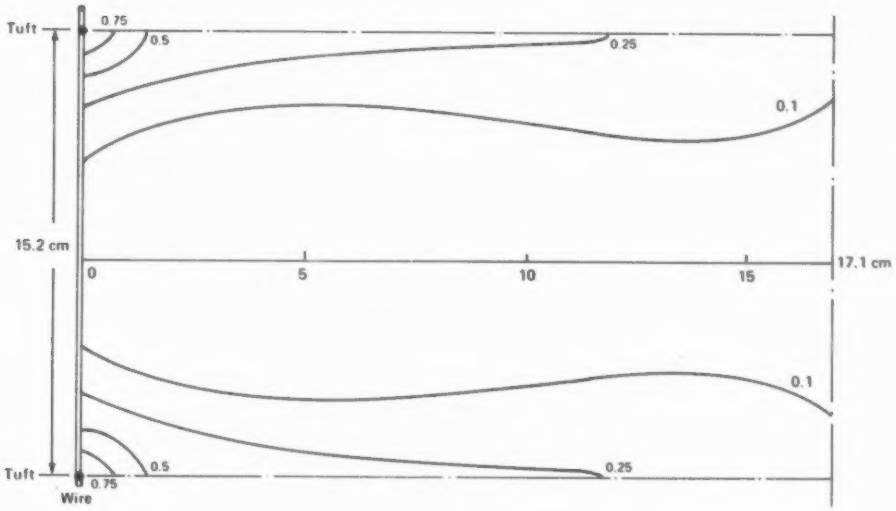

Figure 4. Current density distribution Level 15.

value occurs directly beneath the tuft. The 10-percent contour represents an absolute value of approximately 9.2×10^{-5} A/m^2 (9.2 nA/cm^2). Contours for this value are shown on all plots for the wide-spacing simulation in order to facilitate the visualization of the three-dimensional situation from the two-dimensional slices. Notice the regions of very low current density between the tufts, which are essentially dead space. This is the region where particles can escape charging and, consequently, reduce particle migration velocity.

Moving one-third of the distance toward the tuft to Level 10 gives the current-density distribution shown in Figure 5. Again, contours representing 10, 25, 50, and 75 percent of the peak value for this level are plotted. The outside contour is the 9.2×10^{-5} A/m^2 absolute value curve corresponding to that shown in Figure 4. Figure 6 is up another third of the distance toward the tuft. Integration of these three figures will give a three-dimensional view of the current-density distributions obtained when tufts are present at a 15.2 cm spacing.

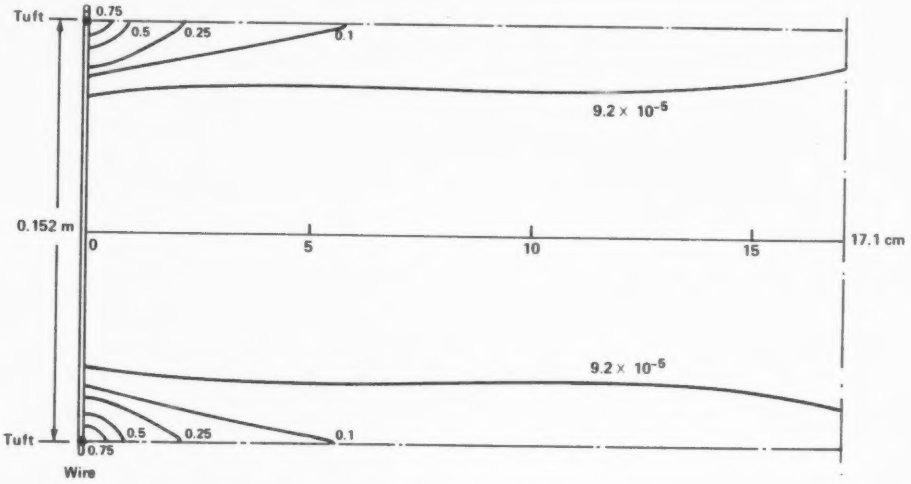

Figure 5. Current density distribution Level 10.

The 15.2 cm spacing, which defines dead space as regions where the current density is below 10 percent of the peak ground-plate value (9.2×10^{-5} A/m^2), yields a value of approximately 79 percent dead space. In other words, if the particle concentration is uniform, 79 percent of the particles gain a small amount of charge resulting in a reduction of the particle migration. If the cutoff value is reduced to 2 percent (1.84×10^{-5} A/m^2), the volume of dead space is 54 percent.

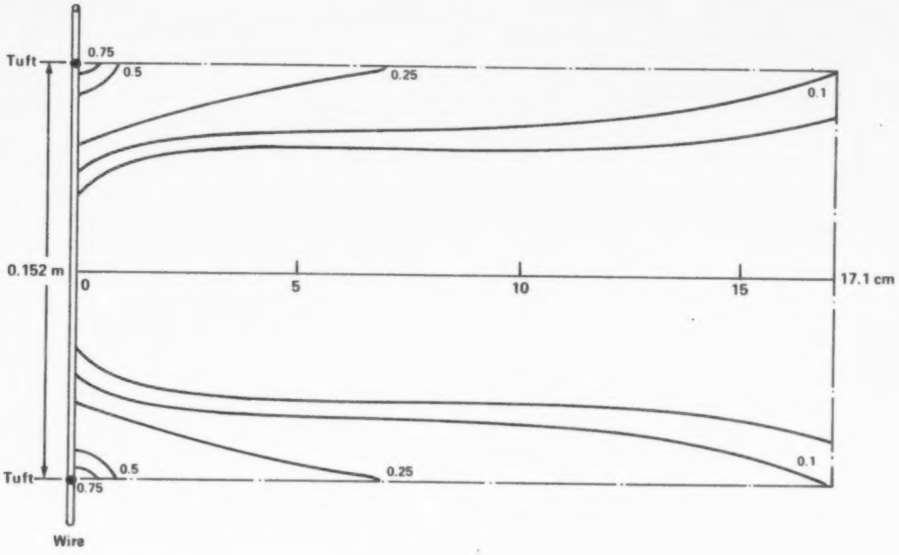

Figure 6. Current density distribution Level 5.

Narrow tuft spacing yielded curves of similar shape but with different absolute values. Figure 7 shows the model results for the 3 cm tuft spacing at the ground plate. The graph in this figure shows two complete sections scaled the same as that used for the wide spacing. The dotted lines are the lines of symmetry. For this case, the 10-percent contour represents approximately 3.8×10^{-4} A/m^2. Notice that, even with the tufts in close proximity to each other, there is still near-dead space.

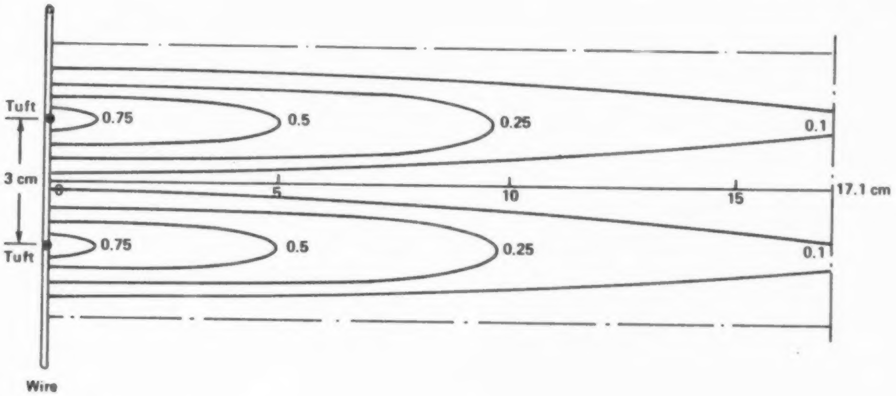

Figure 7. Current density distribution Level 15.

Level 10, one-third of the way up toward the tuft, is shown in Figure 8. The percentage of this level's peak value contours is given, along with the 3.8×10^{-4} A/m^2 curve. The current-density distribution shown in Figure 9 is that of Level 5. This level, near the tuft, completes

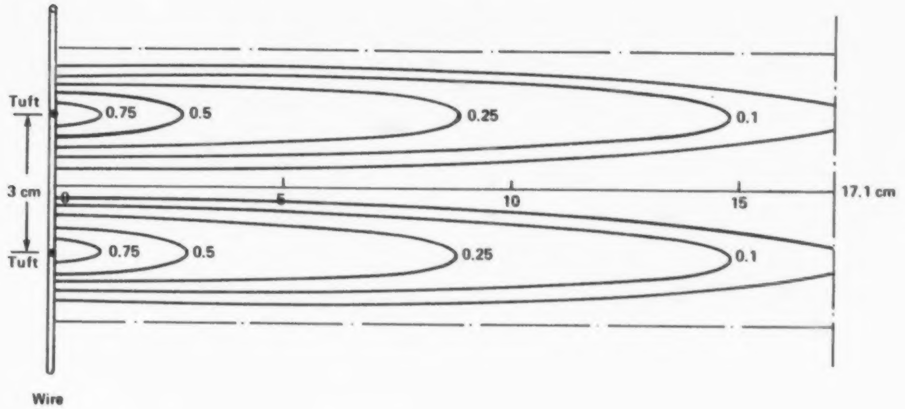

Figure 8. Current density distribution Level 10.

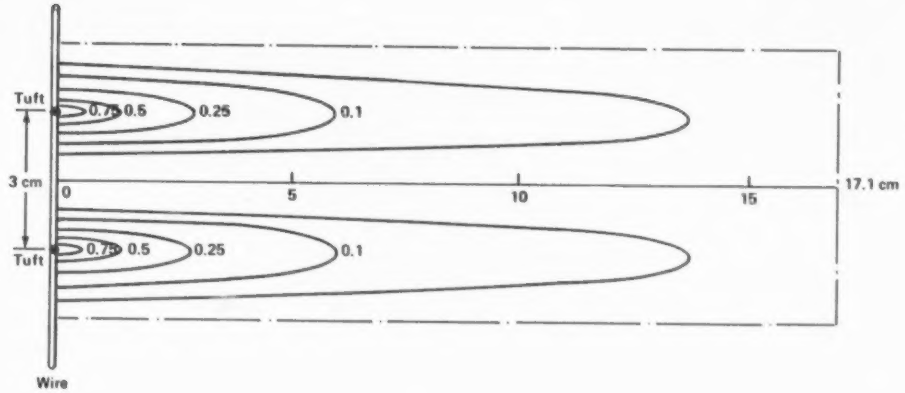

Figure 9. Current density distribution Level 5.

the representation of the three-dimensional distribution for the narrow, 3 cm, spacing. In this case, choosing the cutoff current-density value as 10 percent of the ground plate peak gives 59 percent dead space. The 2-percent value, 7.6×10^{-5} A/m^2, yields 40 percent dead space. Using the same absolute value as in the wide spacing (9.2×10^{-5} A/m^2) indicates that 37 percent of the volume is resulting in uncharged particles. This value, while much lower than the 79-percent value obtained for the wide spacing, shows that a substantial number of particles will still escape charging.

Figures 10-12 compare the current-density distributions for wide and narrow tuft spacing and the resulting regions of very low current density. The scale is the same on both sides of the dividing line. Figure 10 shows the relationship for the two cases at the ground-plate level; the sets of curves show distinct similarity even though there are differences in the absolute values. Figures 11 and 12 show the distributions for Levels 10 and 5, respectively. The contours of the computed current-density distributions show close agreement with those obtained in earlier experimental work (2).

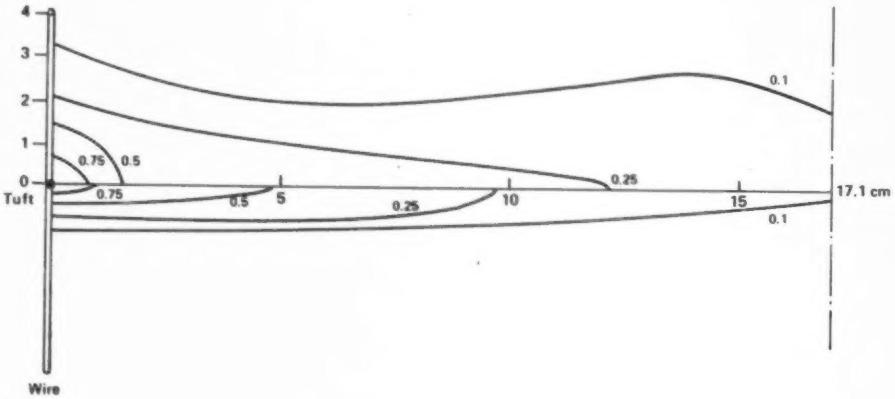

Figure 10. Comparison of current density distributions for wide and narrow tuft spacing Level 15.

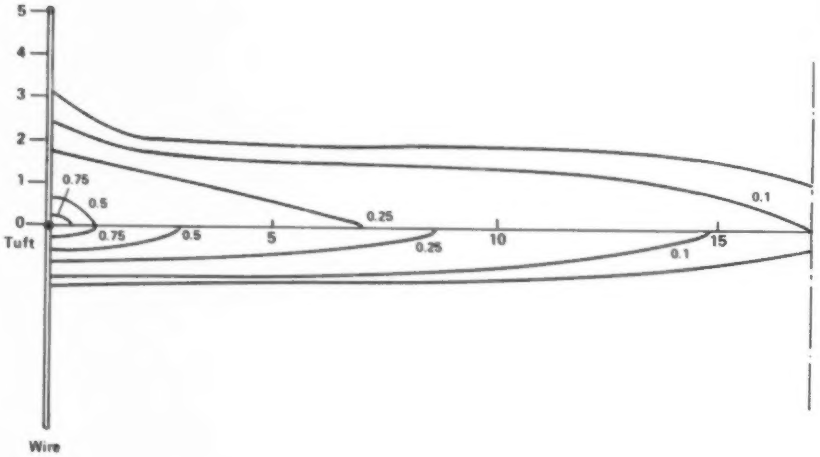

Figure 11. Comparison of current density distributions for wide and narrow tuft spacing Level 10.

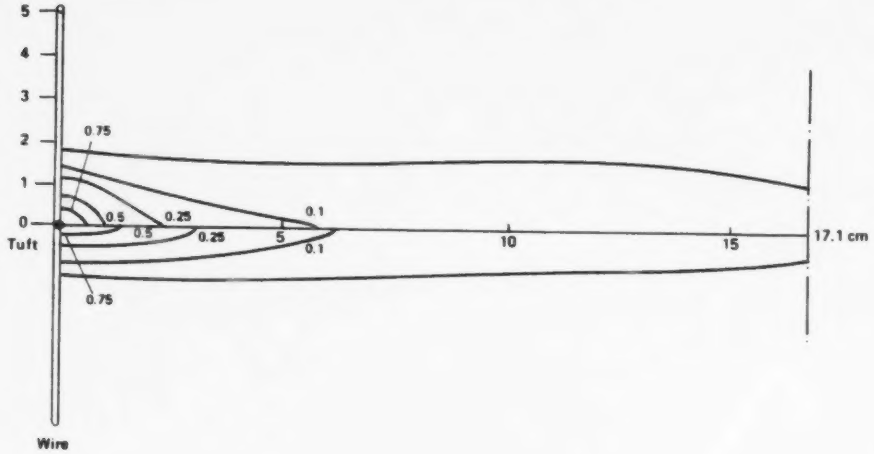

Figure 12. Comparison of current density distributions for wide and narrow tuft spacing Level 5.

This program also gives numerical and graphical results for the space-charge, voltage, and electric field distributions. Because the agreement between the calculated and experimental results for current density is good, confidence can be placed in the predicted values for ionic space-charge density and electric field, which are otherwise difficult to obtain.

SUMMARY AND CONCLUSION

The mathematical model for the three-dimensional tuft corona was successfully developed using a microcomputer. The model is easy to use and flexible, allowing a variety of simulations to be run. In addition, the user is able to gain insight into the detailed three-dimensional electrical characteristics associated with the negative tuft corona on a smooth wire-duct precipitator.

These two simulations show that, although the amount of near-dead space is decreased by decreasing the tuft spacing, there are still large low-charging regions for both wide and narrow tuft spacings.

ACKNOWLEDGMENTS

This work is supported by the U.S. Environmental Protection Agency under cooperative agreement CR-810152-02.

REFERENCES

1. Lawless, P. A., McLean, K. J., Sparks, L. E., and Ramsey, G. H. Negative corona in wire-plate electrostatic precipitators: Part I characteristics of individual tuft-corona discharges. Accepted for publication by J. Electrostatics, 1986.

2. McLean, K. J., Lawless, P. A., Sparks, L. E., and Ramsey, G. H. Negative corona in wire-plate electrostatic precipitators: Part II calculation of electrical characteristics of contaminated discharge electrodes. Accepted for publication by J. Electrostatics, 1986.

3. Yamamoto, T., and Sparks, L. E. Numerical Simulation of Three-Dimensional Tuft Corona and Electrohydrodynamics. Accepted for publication in Proceedings of IEEE-IAS Transactions, Toronto, Canada, October 1985. pp. 1359-1363.

4. McDonald, J. R., Smith, W. B., Spencer, H. W., III, and Sparks, L. E. A mathematical model for calculating electrical conditions in wire-duct electrostatic precipitation devices. J. Appl. Physics., Vol. 48, 1977. pp. 2231-2243.

5. Cooperman, P. A theory for space charging limited current with application to electrical precipitation. Am. Inst. Electr. Eng., Vol. 79, 1972. pp. 47-50.

THE SIMULATION OF CORONA DISCHARGES UNDER PRACTICAL PRECIPITATOR CONDITIONS

by : I. Gallimberti
Istituto di Elettrotecnica ed Elettronica,
Padova, Italy

SUMMARY

Important advancements in the simulation of positive corona discharges have been recently realized, in the studies of air and SF_6 spark breakdown. At Padova University a computer program has been developed for the simulation of filamentary streamer discharges, based on the iterative simultaneous solution of continuity equations for electrons and ions and of Poisson equation. This program has been adapted for the simulation of positive and negative pulse coronas, and used to a tentative modelling of streamers under precipitator practical conditions (taking into account non uniform field distribution, gas composition, temperature, etc.). The results of these simulations are discussed in comparison with other models which do not take into account the filamentary structure of the individual discharges and the particular composition of the ESP gas.

INTRODUCTION

The industrial application of pulse corona discharges to the treatment of exausted gases in electrical power plants became in recent years more and more attractive, because of its relatively simple technology and high efficiency. In electrostatic precipitators, the application of pulsed power supply instead of conventional DC energization, has been shown to increase the migration velocity, particularly in presence of high resistivity particulate. In the treatment with electron radiation of the contamination by Nitrogen and Sulfur oxides, corona discharges have been proposed and tested as efficient and economical sources.

In practical applications, the knowledge on the discharge characteristics is very poor and a direct similarity with atmospheric air discharges is assumed; the few theoretical simulations have generally assumed the electron transport coefficients of normal air, neglecting the influence of relatively high concentrations of H_2O and CO_2. Therefore, the control of the H.V. energization and of the corona discharge is realized on the basis of very empirical criteria, so that the optimum conditions for the process efficiency are rarely realized.

The present paper reports the first results of an experimental and theoretical investigation on impulse corona characteristics in practical ESP gas, whose final objective is to define the optimum energization conditions in applications to particulate and oxides abatement; the study will be carreid on in subsequent steps: the gas characteristics are first considered and the electron transport coefficients are calculated in comparison with those of normal air; then theoretical simulation models are applied to analyze the particularities of both positive and negative corona formation in practical ESP gas, and to check similarities and differences with air discharges; in the mean time an experimental cell will be prepared at a coal power plant by Enel, where the corona characteristics in air and in ESP gas will be experimentally compared.

In the present paper the computed swarm characteristics of the flue gas are discussed, and the expected differences between pulsed coronas in pure air and in flue gas are analyzed. A test experiment which confirms these differences is also reported. A model of the impulse corona is then described and applied to positive streamers in both air and flue gas. The simulation results are in excellent agreement with the experimental observations and put in evidence the peculiarities of the ESP gas; they indicate that in this case all assumptions of corona similarity are far to be acceptable.

SWARM CHARACTERISTICS OF THE ESP GAS

The composition of the exausted gases of a fuel fired power plant depends on a number of parameters (type of fuel, characteristics of burners, boiler load, air flow, etc.) which are variable in time and from plant to plant. In average, the basic components of the ESP gas, whose concentration can affect the transport characteristics of an electron swarm, are reported in Table I: the main difference with respect to atmospheric air is the presence of H_2O and CO_2 at the place of O_2 ; the percentage of H2O which is generally higher for oil than for coal fuels, is responsible for the major changes in the swarm characteristics, because of the high value of the attachment cross section. The following composition -70 % N_2, 12 % H_2O, 15 % CO_2, 2.5 % O_2 , 0.5 % CO - has been assumed as representative of the extreme conditions of the ESP gas.

The electron energy distribution and the transport coefficients in this gas mixture have been calculated by a Montecarlo simulation of the electron swarm [1]; the cross sections that have been used in this simulation are reported in reference [2,3]. As the total collision cross section of the ESP gas mixture is not very different from that of normal air, the calculated electron energy distributions in the two gases are very similar: they are both not maxwellian (due to the high contribution of inelastic collisions) and present a tail which decreases faster in the high energy region [2]. The electron characteristic energies (ratio D_T/μ of the transversal diffusion coefficient to mobility) are very similar, the values in the ESP gas beeing sligtly higher (fig. 1a). The electron drift velocities v_e result also very similar in the two gases (fig. 1b); the major differences beeing limited to less than 10 % in the low field region.

TABLE I

Average composition of the exhausted gases of a power plant depending on the type of fuel burned

FUEL	N_2	O_2	H_2O	CO_2	CO	SO_2	NO
OIL	72%	1%	12%	15%	100 ppm	1500 ppm	300 ppm
COAL	74%	5%	6%	15%	40 ppm	700 ppm	600 ppm

The most striking differences appear in the attachment coefficient: both H_2O and CO_2 molecules have relatively high cross sections for dissociative attachment, so that the reduced attachment coefficient η/p in the ESP gas, for the field range of interest in corona discharges, results almost 10 times larger than in normal air, and only 2-3 times smaller than in pure oxygen (fig. 1c). On the contrary the reduced ionization coefficient α/p in the ESP gas is only sligtly higher than in air and quite smaller than in pure oxygen (fig. 1d).

The above reported differences are more pronounced at relatively low E/N values, where the resonant structure of the various cross sections plays a major role.

In conclusion it can be stated that the swarm characteristics of the ESP gas are not significantly different from those of normal air except for the attachment coefficient, that is very much increased by the high attachment rate of H_2O and CO_2. This difference depends obviously on the ESP gas composition and is generally more important for oil fuels than for coal.

The first consequence of the change in the attachment coefficient is the change in the static breakdown field in uniform gaps (the so called "critical field" where ionization probability equals attachment probability): it results around 26 kV/cm.bar in air and increases to about 35 kV/cm.bar in the ESP gas. However, as it will be discussed in the next paragraph the increase of the attachment coefficient can drastically change also the corona characteristics in non-uniform fields (extention, current, charge, power input etc.), from

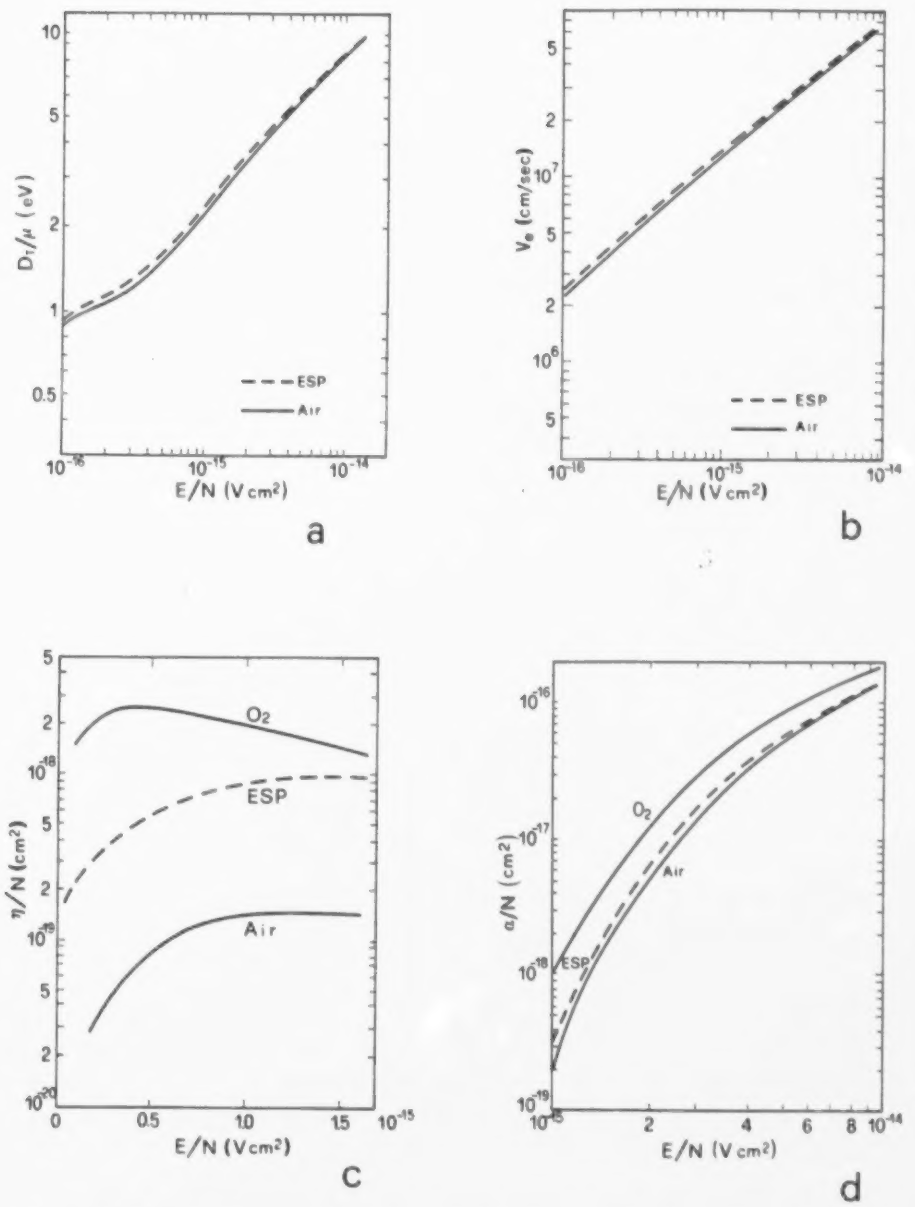

Fig. 1 - Comparison between the computed electron swarm characteristics in air and in ESP gas.
a) characteristics energy D_T/μ ;
b) drift velocity v_e;
c) reduced attachment coefficient η/N;
d) reduced ionization coefficient α/N.

those typical of non-electronegative or weakly-electronegative gases, to those of strongly-electronegative gases [4,5].

IMPULSE CORONA CHARACTERISTICS

Under impulse conditions, the structure and the formation mechanism of the positive corona are very different from those under DC conditions [6]; in the first case, the ionization grows from the highly stressed electrode into a background field which is purely geometric; the discharge assumes the form of a number of branched, tree-like streamers whose starting points are discrete and distributed over the highly stressed region with a specific density; in the second case, the continuously developing ionization creates space charge regions which affect the geometrical field distribution; if the voltage is not very near to the breakdown voltage the discharge assumes the form of a diffuse glow continuously covering the highly stressed region. If the pulsed discharges are repeated at relatively low frequency (with a period longer than the ion transit-time in between the electrodes), the space charge produced by any discharge is completely dissipated during the time interval between pulses, so that each discharge develops independently from the others. Under practical ESP applications the ion transit-time does not exceed the millisecond, so that the discharge mantains the typical impulse structure up to repetition frequencies of the order of 1 KHz, which are quite higher than those of practical application.

For this reason the form of corona discharge that has been considered for practical ESP simulations is the filamentary impulse streamer (of positive or negative polarity).

Streamer discharges are highly localized positive or negative space charge waves (fig. 2), which enhance the applied field in front of the wave (active region) and propagate because of electrons avalanching in this high field [7]: for positive streamers the electron avalanches are directed towards the positive space charge (streamer head), while for negative streamers they are directed outwards the negative space charge. Photoionization is generally assumed to be the mechanism that supplies secondary seed electrons and triggers the avalanches. Along the track of the wave remains a weakly ionized plasma filament (passive region), along which flows the conduction current to the high voltage electrode, that supplies the energy for the streamer advancement.

The high field created by the space charge wave makes possible its propagation also in relatively low applied field regions (much lower than the "critical field"). Experimental and theoretical studies [8,9] have made possible to define a "stability field", which is the externally applied field which makes the propagation of positive streamers energetically stable: in air it results around 5 kV/cm.bar. In higher externally applied fields, the streamer space charge wave increases in size and stores potential energy; in lower applied fields the propagation dissipates the stored potential energy until the propagation stops.

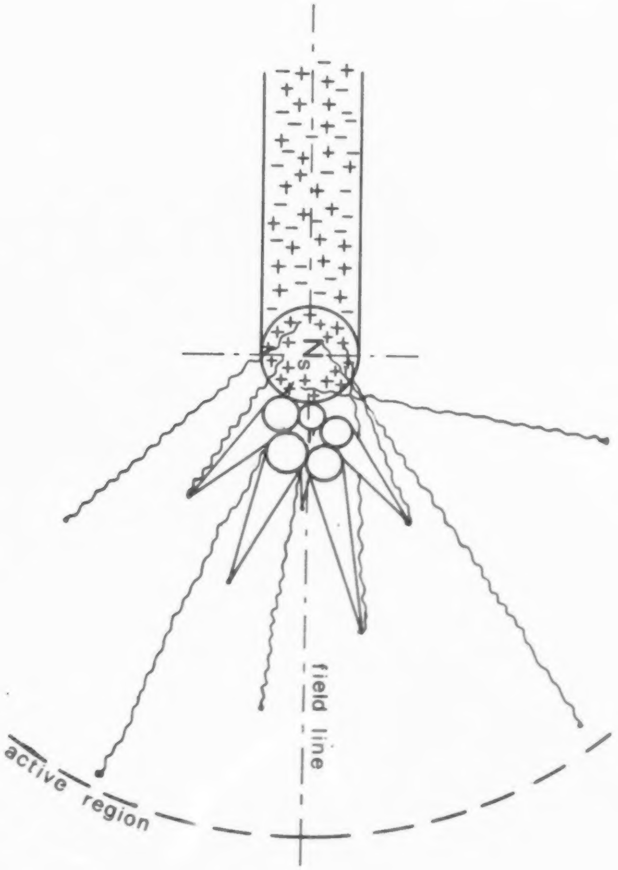

Fig. 2 - Schematic representation of the positive streamer development mechanism.

Recent experimental and theoretical studies [5,10] have shown that the propagation characteristics of positive streamers depend very much on the degree of electronegativity of the buffer gas. In weakly electronegative gases (like atmospheric air) the streamers appear much longer and more branched than in strongly electronegative gases (like SF_6): the corresponding currents and charges are also much higher, and the average field along the streamer track increases from the "stability value" to the "critical value".

The transition between the weakly-electronegative behaviour to the strongly-electronegative behaviour has been recently studied in air SF_6 mixtures, [4] and it has been shown to occur when the attachment mean free path $1/\lambda$ becomes of the same order of magnitude as the size of the streamer head. In weakly electronegative gases the attachment mean free path is quite long and the electrons produced by avalanche ionization in the active region can fly away from the head region leaving a net unipolar positive space charge. On the contrary in strongly electronegative gases the electrons are attached whithin a short path behind the space charge head, giving rise to a sort of dipolar space charge distribution which chockes the field in the active region, and makes streamer advancement more difficult. Furthermore, in order to ensure energy supply from the external circuit to the streamer front a certain level of conduction current has to flow along the streamer track, which is only possible if the field in the track itself sets to a value not far from the critical field where the disappearance of electrons by attachment is partly compensated by new production b[illegible]ization.

The degree of electronegativity of the ESP gas is just across the transition region: the extreme case that has been analyzed in Sec. 2 has characteristics very near to the strongly electronegative gases, while mixtures with lower contents in H_2O and CO_2 should be exactly in the transition region. For this reason a quite different behaviour of the positive corona has to be expercted with respect to normal air.

In order to check experimentally these differences in the positive corona, a comparative test has been realized in a 10 cm point-plane gap subjected to 75 kV lighting impulses of positive voltage. Atmospheric air and a 99 % Air - 1 % SF_6 mixture have been used as test gases: the latter has almost all the swarm coefficients unchanged with respect to air, except the attachement coefficient which results about 10 times larger; it is therefore a good substitute of the ESP gas for laboratory tests. The corona propagation curves have been measured with a 6 photomultiplier device [4], together with the current signals.

The comparison of the experimental observations is reported in fig. 3: the corona streamers in pure air cross the whole 10 cm gap, while in the mixture they extend not more than 2 cm; the peak current is reduced by a factor 3, while the total charge associated to the corona formation is reduced by about one order of magnitude.

Such a striking change in corona characteristics has to be expected also in the practical ESP gas.

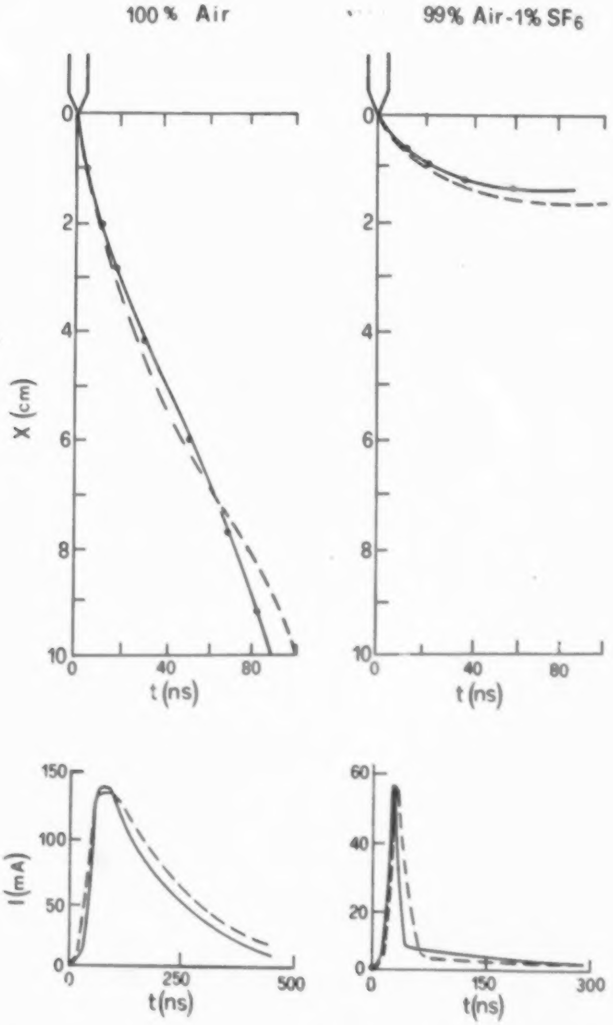

Fig. 3 - Comparison between the experimental characteristics of corona formation in air and in a mixture of 99% air - 1% SF_6.
10 cm point-plane gap; 5 mm point curvature radius; 75 kV applied voltage.
The voltage and field distributions are reported in fig. 7.
a) propagation curves
b) current oscillogram
The dashed lines represent computed values for air and ESP gas (see next section).

IMPULSE CORONA MODELLING

Different models have been proposed to simulate the formation of corona streamers in air [7]. Some of them introduce mathematical and physical simplifications which are adequate to the case of weakly-electronegative gases; however, it has been recently evidenced that these models cannot be applied to electronegative gases [10]. It is therefore necessary to start from the more general formulation.

The set of equations which can describe the behaviour of charged particles (electrons, positive ions and negative ions) in the streamer space charge wave are the continuity equations for each charged species, together with the Poisson's equation [11]:

$$\begin{aligned}
&\frac{\partial n_e}{\partial t} + \nabla\cdot(n_e \bar{v}_e) - D_e \nabla^2 n_e = (\alpha-\eta) n_e \, |v_e| - a_e n_+ n_e + \frac{n_-}{\tau} S_{ph} \\
&\frac{\partial n_+}{\partial t} + \nabla\cdot(n_+ \bar{v}_+) - D_+ \nabla^2 n_+ = \alpha n_e |v_e| - a_e n_+ n_e - a n_+ n_- \\
&\frac{\partial n_-}{\partial t} + \nabla\cdot(n_- \bar{v}_-) - D_- \nabla^2 n_- = \eta n_e |v_e| - a n_+ n_- - \frac{n_-}{\tau} \qquad (1) \\
&\nabla\cdot(\bar{E}) = \frac{(n_e + n_- - n_+)e}{\varepsilon_0}
\end{aligned}$$

where n_e, n_+ and n_- represent the electron, positive and negative ion densities, v_e, v_+ and v_- their drift velocities, D_e, D_+, D_- their diffusion coefficients, α and η the ionization and attachments coeficients, a_e and a the electron-ion and ion-ion recombination coefficients,   the detachment lifetime, E the local electric field and S_{ph} the source term due to photoionization. The latter can be calculated as [12]:

$$S_{ph} = \sum_i \iiint_V \eta_i \mu_i \delta_i \frac{n_e |v_e| e^{-\mu_i r}}{4\pi \, r^2} \, dV \qquad (2)$$

where the sum is extended over all the transitions of energy higher than the ionization thereshold; δ_i represents the excitation coefficient of the upper state, μ_i and η_i the absorption coefficient and the photoionization efficiency, and r the distance between the volume dV and the point where S_{ph} is calculated.

In the actual model the streamer filament is assumed to have a rotational simmetry with a constant radius R, equal to the diffusion radius of an avalanche producing the critical charge of 10^8 electrons (around 30-35 μm); all the particle densities on a transversal section are assumed to have a gaussian profile, which in fact derives from the radial diffusion of the avalanche head. Positive and negative ion drift and diffusion velocities are neglected, while recombination and detachment are considered, even if they play a minor role. Electron radial diffusion is also neglected because it occurs essentially at ambipolar rate.

The set of continuity equations (1) can be therefore rewritten in the form;

$$\begin{aligned}
&\frac{\partial n_e}{\partial t} + \frac{\partial}{\partial x}(n_e v_e) - D\frac{\partial^2 n_e}{\partial x^2} = (\alpha-\eta)n_e v_e - a_e n_e n_+ + \frac{n-}{\tau} + S_{ph} \\
&\frac{\partial n_+}{\partial t} = \alpha n_e v_e - a_e n_e n_+ - a n_+ n_- \\
&\frac{\partial n_-}{\partial t} = \eta n_e v_e - a n_+ n_- - \frac{n-}{\tau} \\
&S_{ph} = \sum_i \int \eta_i \, \mu_i \, \delta_i \, \frac{2\, n_e\, R^2 e^{-\mu_i x}}{(2x+R)^2}\, dx
\end{aligned} \tag{3}$$

The electron and ion densities in this case represent the values they assume on the streamer axis.

The Poisson's equation is solved in its integral form, by considering the streamer filament divided in to a number of thin disks over which the net space charge is distributed with a gaussian profile. An analytical espression is derived to calculate the field of these thin disks all along the discharge axis and then the effect is cumulated numerically for all the disks. [13]

The set of continuity equations (3) is solved with a flux-corrected finite difference technique, in a step by step procedure in the direction of time [14]. A spatial integration mesh is fixed along the discharge axis, and a temporal step Δt is selected. At time step j, from the knowledge of the electron and ion densities in all mesh points at step j-1, the Poisson's equation is solved and all the constants in the continuity equations which are field dependent are estimated. Then with these values assumed constant in Δt the new values of electron and ion densities at step j are estimated. The flux-correction in expressing the spatial derivatives to the finite difference ensure a very good numerical stability [14].

A typical example of the calculated results in air is reported in fig. 4 for the same conditions of the experimental results of fig. 3. In fig. 4a the advancing front of electron density is reported: the ionization growth in the active region is very rapid; then the electron density decreases in the streamer filament due to attachment. In the streamer track, a trail of positive (and negative) ion remains (fig. 4b).

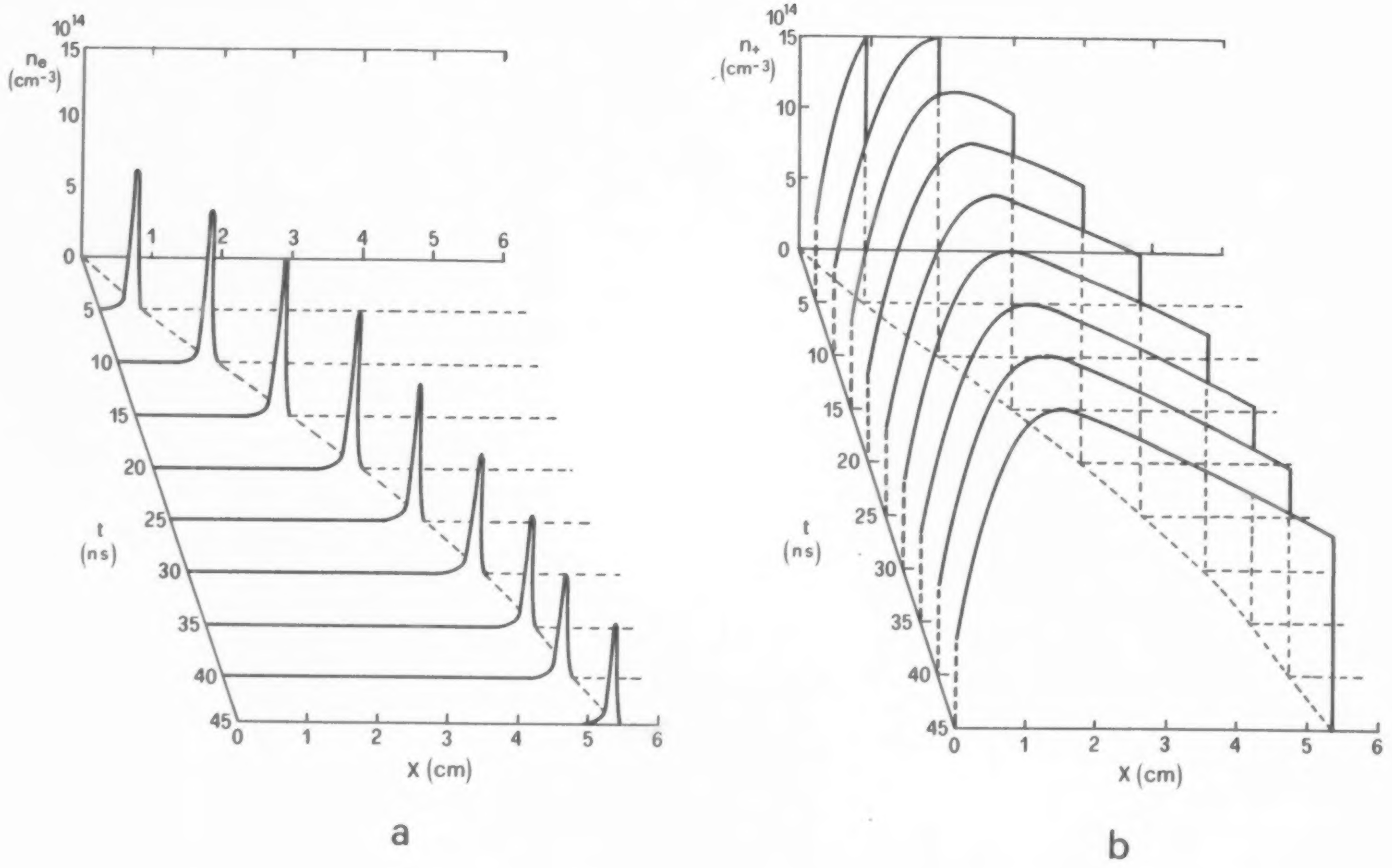

Fig. 4 - Computed propagation characteristics of positive streamers in air (point-plane gap, same conditions as in fig. 3).
a) electron density;
b) positive ion density.

The calculated propagation curves and currents for both air and ESP gas are very similar to the experimental measurements (see fig. 3).

The relatively long tail of the current in the ESP gas is not obtained in the simulation if the ion drift velocity is assumed zero: in the case of fig. 3 a non zero ion mobility has been introduced and consistent results have been obtained. The long tail is therefore thought to be associated to ion drift after corona has stopped its propagation.

Let's now analyse in more detail the streamer mechanism and the differences which appear in air and in ESP gas. In fig. 5 and 6 the characteristics of the streamer filament are reported respectively in air and in ESP gas, for a total length of 4.5 mm (which is reached after 4.0 ns in air and 8.8 ns in the ESP gas). In fig. 5a the electron and ion densities are reported: the electron density grows almost esponentially together with the positive ion density in the active region (from 5 to 4.5 mm) where the field (fig. 5c) is highly distorted by the net space charge (fig. 5b); this exponential growth is laumched by secondary electrons produced at the boundary of the active region by photoionization. Just behind the front position the field start to decrease, the electron and positive ion densities reach their maxima, while negative ions start to appear because of attachment prevailing on ionization: the electron decrease into the channel towards the anode corresponds to the negative ion density growth (fig. 5a).

The decrease of the net space charge density behind the front (fig. 5b) is not very sharp and defines a "field transition region" (down to 0.3 mm), where the field decreases and levels off to an almost constant value of 5 kV/cm, which corresponds to the "stability field".

The space charge then inverts itself and the field increases again in correspondence to the "anode-fall".

The behaviour in the active region of the ESP gas in very similar (from 5 to 4.5 mm in fig. 6). However, due to the higher attachment rate the electron density reaches a sharp maximum and then decreases rapidly, building up behind the front a quite high density of negative ions (fig. 6a). The net space charge results almost half than in air (fig. 6b), which leads to a lower field peak value and a thinner high field region (fig. 6c); as a consequence the peak electron and ion densities are reduced by a factor almost two.

The decrease of the net space charge behind the front is very sharp, and the "field transition region" is very thin: this produces the big drop in the field behind the front, where the electrons are a rapidly attached. Then the field in the filament restores to a value just below the critical value to ensure conduction current and potential rearrangement through the displacement of new free electrons produced by ionization.

One important consequence of the computed results is that the fields needed to sustain conduction in the streamer filament are quite

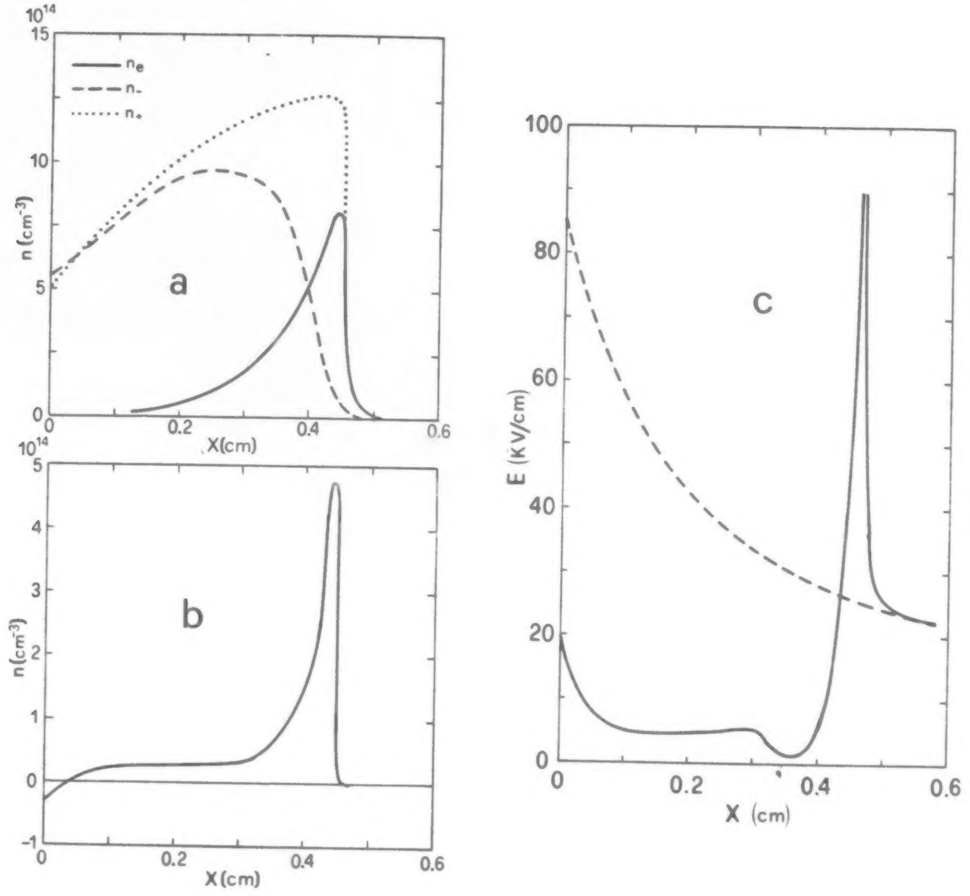

Fig. 5 - Streamer characteristics in air 4 ns after start (length = 4.5 mm).
a) electron, positive and negative ion densities;
b) net charge density;
c) applied geometric field and space charge distorted field.

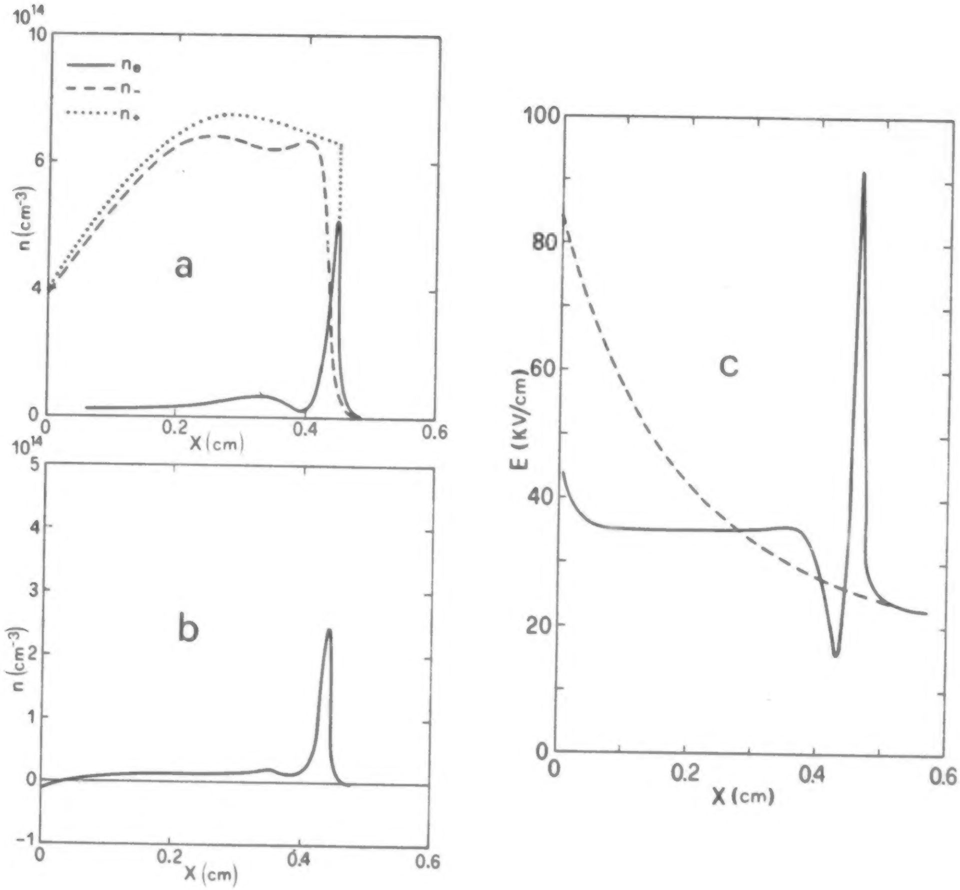

Fig. 6 - Streamer characteristics in ESP gas 8.8 ns after start (length = 4.5 mm).
a) electron, positive and negative ion densities;
b) net charge density;
c) applied geometric field and space charge distorted field.

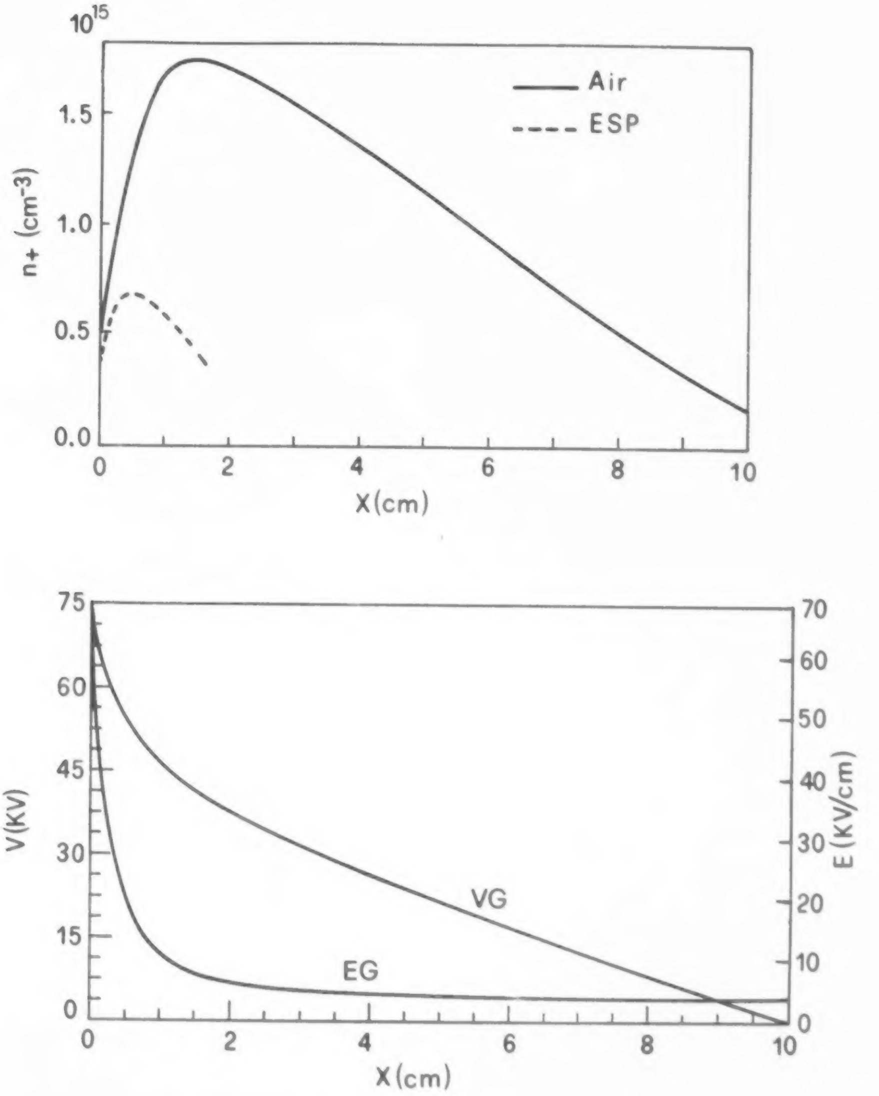

Fig. 7 - Positive ion density distributions along the streamer track for both air and ESP gas, together with applied voltage and field distributions.

different in air and ESP gas. This implies different propagation capabilities: in fig. 7 the positive ion densities along the streamer track are reported for both air and ESP gas, together with the externally applied voltage and field distributions. In air the ion density in the front increases until 15 mm, where a field around the stability value of 5 kV/cm is reached; then it decreases, but the net density is enough to ensure the propagation across the whole gap.

In the ESP gas, the ion density increases only in the first 4 mm where the field is higher than the critical value (~ 35 kV/cm), and then decreases until 17 mm, where the net charge becomes too low to sustain the propagation.

CONCLUSIONS

The presented results, even if limited to some preliminary calculations and tests, indicate that the gas composition in practical ESP configurations is a critical variable, upon which the characteristics of the impulse corona depend strongly. In particular, the content of H_2O and CO_2 determine the degree of electronegativity of the ESP gas: the average content is situated in the transition region between weakly and strongly electronegative behaviour, where the corona characteristics may be largly affected even by minor changes in the gas composition. A better knowledge of the impulse corona characteristics and of their dependence upon the content of the various gas components is therefore requested in order to optimize the design of pulsed electrostatic precipitators and of their control system. This knowledge may also be of interest for applications of corona discharges to the treatment of exausted gases against nitrogen and sulfur oxides.

REFERENCES

[1] J.P.Boef, E.Marode: "Montecarlo simulation of electron swarm motion of SF_6", J.Phys. D: Appl.Phys., 17, 1133, 1984

[2] I.Gallimberti, S.Stangherlin: "Electron swarm characteristics in exausted gases of power plants", Padova Univ. Report UPee/02

[3] P.Laborie, J.M.Rocard, J.A.Rees: "Section efficaces electroniques, coefficients macroscopies", Dunod, Paris 1971

[4] I.Gallimberti, G.Marchesi, R.Turri: "Corona formation and propagation in weakly or strongly attaching gases", 8th Int.Conf. on Gas Discharges, Oxford 1985

[5] I.Gallimberti, N.J.Wiegart: "Impulse corona and streamer to leader transition in SF_6", 8th Int.Conf. on Gas Discharges, Oxford 1985

[6] L.B.Loeb: "Elerctrical coronas", University of California Press, 1965

[7] I.Gallimberti: "The mechanism of the long spark formation", Jour. de Physique, 40, C7 193-250, 1979

[8] R.F.Griffiths, C.T.Phelps: "The effects of air pressure and water wapour content on the propagation of positive corona streamers", Quart. J.R.Mat.Soc. 102, 419-26, 1976

[9] I.Gallimberti: "A computer model for streamer propagation", J.Phys.D: Appl.Phys. 5, 2179-89, 1972

[10] I.Gallimberti, N.J.Wiegart: "Streamer formation and streamer-to-leader transition in SF_6 and SF_6-air mixtures: Part I Corona formation" to be published.

[11] I.Gallimberti: "Physical model of long air gap breakdown processes", Nato-ASI Series B - Physics, vol. 89A, 1983

[12] I.Gallimberti: "Mathematical models for streamer formation in non uniform gaps", Padova Univ.Report, UPee 72/04, 1972

[13] I.Gallimberti, B.Gle[illegible] "The field computation in filamentary gas discharges", Atti Ist. [illegible] LL.SS.AA., 136, 75-99, 1978

[14] R.Morrow, L.E.Cran: "Flux-corrected transport and diffusion on a non uniform mesh", J.Comp.Phys., 65, 111, 1984.

SOME ELECTRICAL CHARACTERISTICS OF BACK CORONA

Kenneth J. McLean
University of Wollongong
Wollongong, N.S.W., 2500, Australia

Leslie E. Sparks
Geddes H. Ramsey
Air and Energy Engineering Research Laboratory
U.S. Environmental Protection Agency
Research Triangle Park, N.C., 27711

ABSTRACT

Back corona in the laboratory is modelled using compacted layers of flyash, a matrix of holes in a non-porous insulating sheet, and a mini-needle projecting from the plate electrode. The voltage-current, current density distribution, voltage onset, and sparkover characteristics are measured for each of these models and compared with each other.

The formation of back corona is very dependent on the dust layer thickness. Thin layers produce a close matrix of back corona discharges generating a large positive ion current flow but not affecting the sparkover voltage. Thick layers produce a few back corona discharges which appear to form streamers that significantly reduce the sparkover voltage.

This paper has been reviewed in accordance with the U.S. Environmental Protection Agency's peer and administrative review policies and approved for presentation and publication.

INTRODUCTION

It is well established that electrostatic precipitators encounter special difficulties when collecting high resistivity particulate. The mechanism by which this reduces the precipitator's performance is known. The reduction results when the negative corona current flows through the high resistivity layer on the collecting plate, and generates a back discharge in the layer which behaves like a positive corona discharge. This has two obvious deleterious effects; first, it significantly reduces the sparkover voltage; and second; it injects a cloud of reverse charging positive ions into the gas space. Both the effects, and possibly others, significantly reduce the performance of an electrostatic precipitator collecting high resistivity particulate.

The importance of back corona has been recognized, and there exists a significant body of research aimed at understanding the mechanisms of back corona and of quantifying its effects (1)(2)(3)(4).

The purpose of the existing research program at the Air and Energy Engineering Research Laboratory is to identify and then quantify those characteristics of back corona that affect the electrical characteristics of electrostatic precipitators. The final objective is to develop a computer program that can confidently predict a precipitator's voltage-current characteristics from the electrode geometry and flyash resistivity. This paper records the first stage of this investigation.

MODELLING OF BACK CORONA

INTRODUCTION

The formation of back corona in industrial electrostatic precipitators takes place in a very dynamic environment in which many of the parameters that affect their characteristics are themselves changing with respect to time and location. The more important of these are:

(i) Time variation of the applied voltage waveshape.

(ii) Variation and unevenness of dust layer thickness, especially as the result of rapping.

(iii) Space charge variation through the precipitator.

(iv) Continuous deposition of dust during back corona development.

(v) Effects of electric wind and gas flow turbulence.

In order to systematically investigate the behavior of back corona, and especially to model it in the laboratory, it is necessary in the first instance to make a number of simplifications.

In these investigations it has been decided to ignore the effects of space charge and of simultaneous dust precipitation with the growth and development of back corona. These are difficult to simulate in the laboratory and can be taken into account at a later date once the fundamental processes are better understood.

The effect of rapping on dust layer thickness is modelled by considering the behavior of different thicknesses of dust layers, and the effect of the instantaneous voltage variation is modelled by measurements at different voltages. In the latter case, the method ignores any effects that may exist due to the rapid rate of change of voltage experienced in practice. With a suitable computer program, it is possible to calculate the average voltage and current values for a given instantaneous applied voltage waveshape.

MATHEMATICAL MODELS

The fundamental equation traditionally used to calculate the conditions for the onset of back corona is:

$$E_o = J\rho \qquad (1)$$

where J is the current density and ρ the flyash resistivity. Since it is known that the current density distribution is non-uniform on the collecting plate, and since most instrumentation can be used to measure the average current, J is usually related to the average current density through an arbitrary multiplying factor. This has not produced satisfactory results.

As a result of the development of the tuft-corona method of modelling negative corona (5)(6), it is now possible to use an explicit equation to calculate J. Hence, using the modified saturated current density equation together with the Warburg law (7), the current density is given by:

$$J = \frac{\epsilon o \mu [V - V_d - dE_o]^2 \cos^n \theta}{S^3} \qquad (2)$$

where ϵo = permittivity
μ = mobility
V = applied voltage
V_d = voltage drop across the discharge
d = dust layer thickness
E_o = breakdown electric field of layer
S = distance of maximum current density flux path (120 mm)
n = Warburg constant, 4.6
θ = angle.

Combining Equations (1) and (2), letting θ=0, and solving for the applied voltage V:

$$V = V_d + dE_o + \sqrt{\frac{S^3 E_o}{\rho \epsilon o \mu}} \qquad (3)$$

In order to solve this equation, it is necessary to use current values for E_o and ρ.

From our limited testing, E_o corresponds approximately to the breakdown value of dust layers placed between parallel plates and thus varies with the thickness of the layer. An approximate expression for d between 0.2 and 10 mm is given by:

$$E_o = (1.8 - 140d)10^6 \text{ V/m} \tag{4}$$

where d is expressed in meters.

The effective resitivity of a flyash layer varies with the magnitude of the applied electric field and reduces as the field increases. Most flyash resistivities are quoted at a low electric field (2 kV/cm) where, as the value of interest is at the breakdown value of between 8 and 20 kV/cm, the actual value depends on the dust layer thickness. Resistivity at breakdown can be up to one order of magnitude less than that at low electric fields (8).

Substituting Equation (4) in Equation (3), we obtain the onset voltage for back corona:

$$V_o = V_d + d(1.800 - 140d)10^6 \sqrt{\frac{S^3(1.800-140d)10^6}{\rho\epsilon o\mu}} \tag{5}$$

This relationship is shown plotted in Figure 1 for different dust layer thicknesses. It is of interest to note that the relationship is almost independent of dust layer thickness and that the critical resistance is in the range 10^{11}-10^{12} ohm-cm.

Once back corona is established, the voltage-current characteristic of each individual back corona discharge can be modelled by the equation:

$$I_{bc} = \frac{K_1V(V-V_o)}{(S)^m} \tag{6}$$

where V_o is the voltage at which back corona is formed, given by Equation (4), and m is a constant. It is more convenient at this preliminary stage to approximate this second order expression with a linear one: hence, for a given distance S:

$$I_{bc} = K_2\ (V - V_o) \tag{7}$$

The total back corona current is the summation of the individual back corona discharges and, as will be shown later, the number density is a function of dust layer thickness. K_2 is not always constant and may vary over a wide range of values.

The negative ion current that flows in the flux lines between the back-corona-produced positive ion current follows Equation (2) very closely.

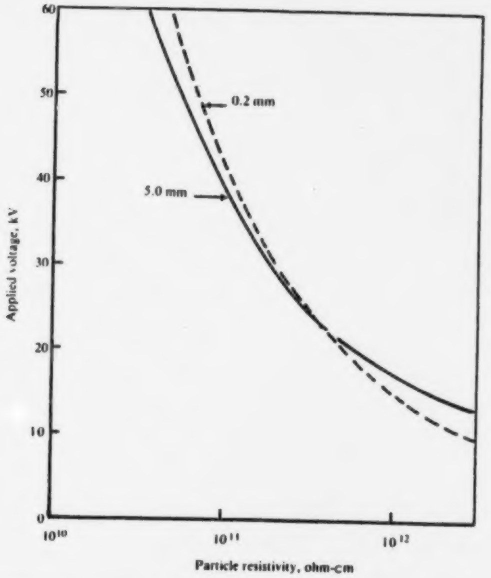

Figure 1 Corona onset voltage for different particulate resistivities and layer thicknesses

EXPERIMENTAL MODELS

It is important in setting up an experimental model to ensure that the electrical and field conditions are similar to those encountered in practice. In these experiments only a single negative corona tuft is produced on the discharge electrode (produced either by a long needle or by a micro-point on a rod electrode). The gap spacing is 120 mm.

Preliminary measurements were made in air at ambient temperatures, but the main tests were conducted at 150°C. This at least models the effect of temperature on gas ion mobility, although some additional numerical adjustment will be necessary to take into account differences in gas composition if the results are to be applied to industrial precipitators.

The back corona in an electrostatic precipitator can be reproduced, and hence modelled, in several different ways in the laboratory:

(i) Depositing flyash layers of different thickness on the passive plate.

(ii) Covering the passive electrode with a porous dielectric material.

(iii) Placing a mini-needle perpendicular to the surface of the passive plate.

Each of these models is useful and, in different ways, each contributes to a better understanding of back corona.

EXPERIMENTAL RESULTS

PROCEDURE

For all the experimental models used, the current density was measured by means of a matrix of 100 mm^2 squares built into the passive electrode. This enabled current density and voltage-current measurements to be made of individual back-corona discharges and in the regions of no back corona.

The optical behavior of back corona was observed with a Cohu High Performance Television camera, model 5860, which has a face plate illumination of 1.08×10^7 lux. This was of particular value in observing back corona on the dust layers, and it was possible to relate some of the electrical measurements to the optical observations.

Mini-Needle Projection

This consisted of a sharp needle projecting 3-10 mm perpendicularly from the flat passive electrode. The back discharge forms on this needle only if there is a flow of negative ions, and its onset voltage can be regulated by adjusting the length of the needle. Some of the more interesting characteristics are:

(i) The voltage-current characteristics are similar to those of back corona formed in a dust layer and porous dielectric sheet. If the linear approximation given by Equation (6) is used, K_2 has a value between 0.3 and 0.4 μA/kV.

(ii) The current distribution on either side of a discharge is not significantly affected by the strong back corona discharge as shown in Figure 2.

(iii) The current from a single mini-needle located in one of the 100mm^2 segments, is not greatly increased with the addition of other mini-needles. This is consistent with the truncation of one another's current field as has been discussed in the work on corona tufts (5)(6).

Porous Dielectric

This method of modelling back corona has been widely used. For the method to be successful, it is important that the dielectric sheet comprise a matrix of holes that can form back corona, otherwise there is a large build up of space charge on the surface which significantly distorts the electric field.

Several important features arose from these tests.

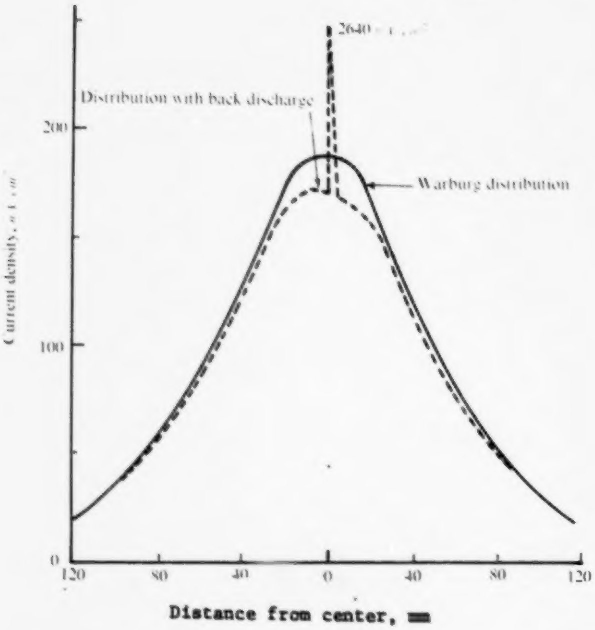

Figure 2 Current density distribution pattern with and without the back discharge produced by a mini-needle

(i) Typical voltage-current characteristics of the individual back corona are similar to those for the mini-needle and dust layer discharge, and have a $K_2 = 0.1$ μA/kV for ambient temperature and S = 120 mm.

(ii) When a micro-point is used on a 7.25 mm diam. wire, back corona formed only in the area of the clean-plate footprint (6). This implies that the back corona does not significantly distort the main negative ion current flow.

(iii) The intensity of the back corona decreases with distance from the discharge.

MECHANICALLY DEPOSITED DUST LAYER

The dust layer is placed on the passive plate and, using fixed-size spacers, it was spread out to a uniform thickness by rolling a heated metal cylinder across the layer. The characteristics of the dust were then measured for thicknesses from 0.2 to 6.4 mm. All of these measurements are made in air at 150°C.

Back Corona Intensity and Distribution

On thin layers, the back corona forms as a close matrix of very steady and stable discharges which cover the whole surface. It is not possible to measure the voltage-current characteristics of an individual discharge but they can be measured for a 100 mm^2 area. This contains about five discharges and a K_2 = 0.1 μA/kV.

As the thickness of the dust layer increases, the back corona points form farther apart and each becomes brighter and carries more current. There are now regions of relatively low current density between the stronger back corona discharges.

For layers 3 mm and greater, the back corona discharges become much more widely distributed (i.e., one per 800 mm^2) and the current density between the discharges stabilizes at the corona onset value, is very unstable because back corona forms, and then switches off. The discharges produce flares that reach into the gas space. The voltage-current characteristics of the individual discharges can have slopes of K_2 = 0.2 μA/kV. Since their number density is less than for thin layers, the total current from a larger area is less than from thin layers.

Sparkover Voltage

One of the unexpected characteristics of thin layers is that, even though large total back corona currents flow and the back discharge is uniformly distributed over the surface, the sparkover voltage is above 70 kV. However, as the layer thickness increases, the sparkover voltage decreases to a minimum of 38 kV with the 6.14 mm layer. This is shown in Figure 3.

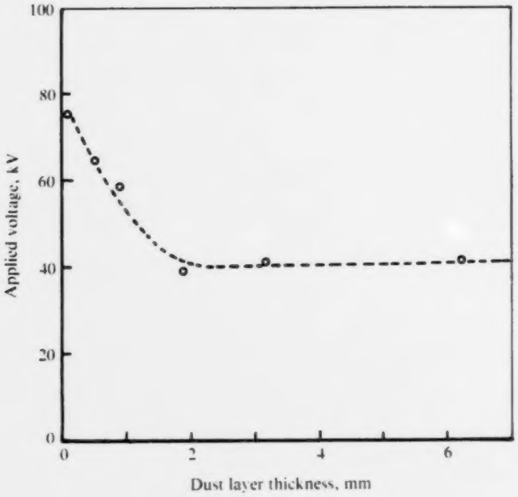

Figure 3 Variation of sparkover voltage with dust layer thickness S = 120 mm, temperature = 150°C, and resistivity = 3 x 10^{12}ohm-cm at 2 kV/cm

The reduced sparkover voltage is associated with the nature of the back corona discharge. As the dust layer thickens, the back corona forms at the bottom of the layer, and the channelling effect of the dust layer generates streamers that reach out into the gas space and initiate a spark.

Corona Onset Voltage

A typical voltage-current characteristic of a back corona discharge and an adjacent 100 mm^2 area not in back corona is shown in Figure 4.

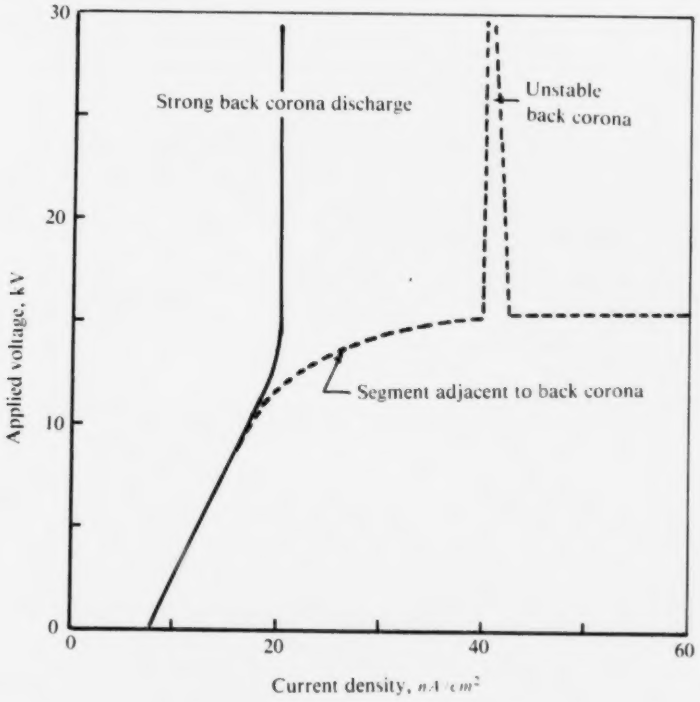

Figure 4 Voltage-current characteristic of a back corona discharge and of an adjacent 100 mm^2 segment

The current density at which breakdown occurs is easily measured and, for the flyash tested, occurs at $J = 14$ nA/cm^2. The resistivity of the flyash is 3×10^{12} ohm-cm at low electric fields but is measured as 6×10^{11} ohm-cm at breakdown fields for the thickness. Hence $E_0 = 7.2$ kV/cm which is the measured value for a thickness of 5 mm. The current density as measured at the bottom of the layer remains at 14-15 nA/cm^2 even for increased voltage.

DISCUSSION

It is not possible at this stage to develop a consistent model of back corona, but it is possible to make some positive statements about some of the possible features of the final model.

(i) It is possible to calculate the applied voltage for corona onset using Equation (5), providing the correct values are used for ρ and E_0. The value of resistivity needs to be that for the breakdown field for the dust layer thickness. Equation (4) is an approximate expression for the breakdown field, but a more accurate one will need to be developed.

(ii) The model must take into account that the number density of the back corona discharges reduces with dust layer thickness. A two dimensional representation of the current flow is shown in Figure 5. As the dust layer thickness, d, decreases, the spacing between adjacent back corona channels, L, also decreases.

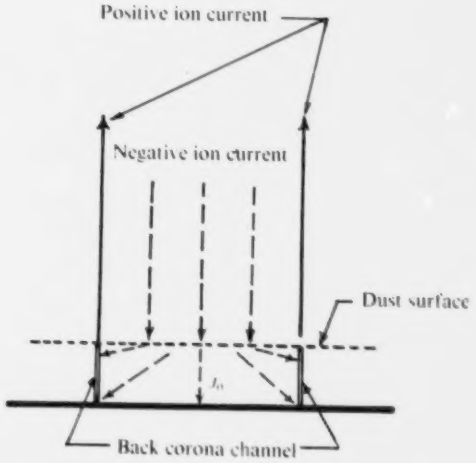

Figure 5 Diagrammatic representation of current flow in the presence of back corona

(iii) It is reasonable to assume that the positive ion flow from the back discharges follows very narrow channels in the gas space back to the discharge electrode. This will have characteristics given by Equation (6) or (7). The negative ion current flow in the inbetween regions is given by Equation (2). At the surface this current is diverted to the back corona channels where it is neutralized, and only a current just below breakdown value (i.e., J_0 = 15 nA/cm^2) reaches the metal surface at the bottom of the layer.

(iv) The sparkover voltage is not related to the intensity of the back corona current but to the thickness of the dust layer. In the thick layers, the back corona is formed at the bottom of the layer and the discharge is channelled by the layer so that it forms streamers that reach out into the gas space and initiate sparkover. The physics of this process needs to be more fully developed.

(v) Additional research would help to better understand the voltage-current characteristics of back corona and how they are related to spacing, S, and temperature variations.

From this preliminary investigation, it appears that the effect of back corona depends on the thickness of the dust layer. If the layer is thin, then large back corona currents can be expected to flow, producing significant distortion of the applied voltage waveshape; this will drive most power supplies into current limit. No sparking need occur. Presumably the air space is flooded with positive ions, and considerable reverse charging can be expected.

If the dust layer builds up to a reasonable thickness (i.e., greater than 3 mm), sparking will occur soon after back corona is formed. Since there will be many less back corona discharges, the current increase will not be as great as for the thin layers. Reduction in performance is most likely due to the reduced voltage level, and very little reverse charging is expected.

ACKNOWLEDGEMENTS

This work is supported under the U.S. Environmental Protection Agency Contract 68-02-3907 with the University of Wollongong.

REFERENCES

1. Masuda, S. and Mizuno, A. Initiation conditions and mode of back discharge. Jn. of Electrostatics 4, 1977/78, p.35.

2. Thanh, L.C. Back corona. Part 1 : its formation. Jn. of Electrostatics, 6, 1979, p.139.

3. Lawless, P.A. and Sparks, L.E. Factors leading to electrical breakdown of resistive dust layers and sustained back corona. In: Fourth Symposium on the Transfer and Utilization of Particulate Control Technology, Volume II, EPA-600/9-84-025b (NTIS PB85-161909), November 1984.

4. McLean, K.J. Back corona and voltage-current hysteresis in electrostatic precipitators. Proc. International Conference on Electrostatic Precipitation, Monterey, 1981, p.326.

5. Lawless, P.A., McLean, K.J., Sparks, L.E., and Ramsey, G.H. Negative corona in wire-plate electrostatic precipitators. Part I: Characteristics of individual tuft-corona discharges. Accepted for publication in J. of Electrostatics.

6. McLean, K.J., Sparks, L.E., and Ramsey, G.H. Approximate method to calculate characteristics of contaminated wire and strip discharge electrodes. Presented at the Sixth Symposium on the Transfer and Utilization of Particulate Control Technology, New Orleans, February 25-28, 1986.

7. Sigmond, R.S. Simple approximate treatment of unipolar space-charge-dominated coronas: The Warburg law and the saturated current. J.Appl. Phys 53, 1982, p.891.

8. McLean, K.J. Properties of the particulate dust layer that arise because of its particulate nature. In: Proceedings of the Second International Conference on Electrostatic Precipitation, Kyoto, November 1984.

Session B-7: DESIGN CONSIDERATIONS

Sidney R. Orem, Chairman
Industrial Gas Cleaning Institute
Alexandria, VA

LABORATORY MEASUREMENTS OF SOME ELECTRICAL PARAMETERS IN CONVENTIONAL AND WIDE DUCT PRECIPITATORS

A.A. Elmoursi** and G.S.P. Castle*

**General Motors Research
Laboratories
Warren, Michigan
U.S.A.

*Faculty of Engineering Science
The University of Western Ontario
London, Ontario, Canada

ABSTRACT

Experimental measurements were conducted in clean air on a laboratory scale electrostatic precipitator with variable duct spacing. Measurements of the current density and electric field distributions were performed at the collecting plate using a current probe similar to that of Tassicker. Two operating modes i.e. constant linear corona current density and constant wire potential were investigated for three different duct spacings and the results compared with those predicted by a charge simulation model. The work reported here attempts to elucidate the enhanced performance observed for electrostatic precipitators with wide duct spacing.

INTRODUCTION

In recent years there has been increased interest in the use of wide-duct precipitators, particularly in Japan and Europe. Some authors [1, 2] have shown that the precipitator efficiency may increase or remain unchanged as the duct spacing is increased for the same precipitator volume. This is on the condition that the applied voltage is correspondingly increased to maintain a constant average field, $E_{av} = V_c/h$. On first consideration this appears to be in contradiction to the Deutsch Equation (1).

$$\eta = 1 - \exp(-A\omega/v_g) \qquad (1)$$

Since the collection area is decreased with the increase of duct spacing, these results would seem to imply an increase in the magnitude of the particle migration velocity, ω.

In a recent paper Heinrich (3) has reviewed various proposed explanations for this so-called wide spacing effect. He suggests that the measured results of Misaka (1) demonstrate that the migration velocity is proportional to duct spacing through its dependency upon the collection electric field. This should not be unexpected for although it is known that the effective migration velocity is governed by a number of factors including electrical, mechanical and aerodynamic, the classical value for this term may be calculated using equation (2).

$$\omega = \frac{2P\varepsilon_o E_p E_c a}{3\mu} \qquad (2)$$

Furthermore, Matts has recently stated that his modified or "effective migration velocity", ω_k has been found to increase roughly in proportion to duct spacing. (6)

These observations have led to proposals to eliminate the concept of migration velocity and to rewrite the Deutsch equation in terms of a so called "performance factor" (Heinrich (3)), "migration time" (Darby (4)) or "dust constant" (Matts (6)). Although this offers some convenience for discussions centering on the overall performance of a precipitator it further disguises the parameters affecting the physics of operation of the precipitator. Furthermore, although many theories and experiments [2, 7, 8, 9, 10, 11] have been presented to explain the enhanced performance of wide plate precipitators, they have mainly emphasized the measured efficiencies. With the exception of the experimental work of Misaka [1] and the analytical work of Lindau [12], little attention has been given to the electrical conditions that exist in these precipitators.

It is proposed here that a comparative study of the electrical characteristics of wide duct precipitators, to those of conventional duct spacing, may give further insight to the so called wide-spacing effect.

In particular, equation (2) can be used to predict the dependency of migration velocity on field using either of two assumptions;

a) the charging field is equal to the average field,

$$\therefore \omega \propto E_{av} E_p \qquad (3)$$

b) the charging field is equal to the precipitating field

$$\therefore \omega \propto E_p^2 \qquad (4)$$

To check these dependencies and carry out this comparative study, experimental measurements were performed on a laboratory scale electrostatic precipitator in which the duct spacing could be varied. The study was supplemented by adapting the charge simulation model developed by the authors [13] for predicting the electrical conditions in duct type electrostatic precipitators and using the experimental measurements to confirm the accuracy of the model.

EXPERIMENTAL SET-UP

The experimental set-up is shown schematically in Figure 1. It consisted of a model section of a duct-type electrostatic precipitator, which had one fixed plate while the other could be adjusted to achieve plate to plate spacings (2h) of 0.2, 0.4 and 0.6 m. The corona wires used were 0.25 mm in diameter and made of Chromel-A. The wire to wire spacing (2s) could be varied in multiples of 0.05 m. The wires were energized from a common bus bar connected to a Universal Voltronics high voltage D.C. power supply, model BAL 100-18. The two plates were connected together and grounded either directly or through a digital ammeter. A current probe similar in concept to that of Tassicker's [14] was used for monitoring the current density distribution at the fixed plate along the length of the section (i.e. the x-direction). The ratio of the probe insulation thickness to the active diameter of the probe (inner diameter) was 0.04. This ratio is approximately equal to that of the smallest diameter probe used by Tassicker. Hence, according to Tassicker's analysis, the leakage flux for the probe used here is expected to be no more than 8%.

The probe current, in the order of nano amperes, was measured by a Keithley Instruments electrometer model 602. To evaluate the current density the value of the measured current was divided by the probe surface area which was equal to 1.28×10^{-6} m^2.

In addition to measuring local current density, the technique developed by Tassicker [14] was adopted here to evaluate the electric field at the fixed plate.

Prior to each set of experiments the corona wires and the probe plate were cleaned with petroleum solvent. Weights were used on the ends of the corona wires to ensure straightness and minimum vibration. All experiments were conducted at room temperature and pressure. The ambient relative humidity ranged from 40 to 65 percent.

All experiments were performed using positive corona in preference to negative. It was found that when measuring the probe currents under negative corona large fluctuations were observed and in some cases the current would drop to about 10% of its nominal expected value. This was because the current probe had a relatively small surface area and thus it was very sensitive to the localized corona glow points or tufts that appear on the wire surface in negative corona [15]. Positive corona was found to produce stable and reproducible readings from the current probe.

Initially only three corona wires were used. In this case it was observed that because of end effects the linear corona current emanating from the central wire was significantly less than that of the outer wires. This agrees with the observations of Lawless and Sparks [16].

To reduce the end effects, the number of corona wires was increased to five. As demonstrated in the appendix, this approach was most successful for the smallest duct spacing (0.2 m) and less successful for the widest duct spacing (0.6 m). To further reduce end effects, particularly for wider duct spacings (0.4 and 0.6 m), additional corona wires would have to be used. This was not feasible because of space limitations.

The linear corona current J_ℓ of the central wire was evaluated by integrating the measured current density distribution along the plate from a point below the central wire to the centre line between corona wires, as shown by equation (5).

$$J_\ell = 4\int_0^s J.dx \qquad (5)$$

Experimentally, it is difficult to achieve constant linear corona current density (as evaluated by Equation (5)), for different duct spacings. Thus for the case of constant linear corona current with variable duct spacings, a constant linear corona current J_ℓ^* was assumed. The actual experimental value of linear current density (which varied slightly for the three spacings) as well as the assumed constant value were applied independently, as input parameters, to the charge simulation model. This calculation was performed for the three duct spacings investigated.

CONSTANT LINEAR CORONA CURRENT DENSITY

In this mode of operation, the linear corona current (J_ℓ^*) was assumed constant at 0.1 mA/m. The wire to wire spacing was held constant at 0.1 m. Thus this case also represents the case of 0.5 mA/m^2 constant average surface current density at the collecting walls. The three wire to plate spacings investigated were 0.1, 0.2 and 0.3 m, the corona wire radius was equal to 0.127 mm and the ion mobility was assumed equal to 1.8×10^{-4} m^2/V.s corresponding to positive corona.

Figures 2 to 4 give the experimental and simulation results for the current density distribution at the collecting plate for the three duct spacings. The corresponding electric field distributions at the plate are given in figures 5 to 7.

For the smallest spacing both the assumed constant value (J_ℓ^*) and the experimental value calculated using Equation (5) were equal, as seen from Figures 2 and 5. For the larger spacings of 0.2 and 0.3 m, although the experimental values of J_ℓ differed from the assumed constant value of 0.1 mA/m, good agreement with the charge simulation model can be observed when the measured value of current was used in the calculations.

Since, in this section it is intended to investigate the operational mode of constant linear corona current, only the simulation results which used $J_\ell^* = 0.1$ mA/m will be considered in the following discussion when comparisons are made on the effect of changing plate spacing.

It can be seen from Figures 2 to 4, that the potential necessary for maintaining a current of 0.1 mA/m was 23.4, 53.5 and 92.2 kV for spacings of 0.1, 0.2 and 0.3 m respectively. This corresponds to an average field ($E_{av} = V_c/h$) of 2.3, 2.7 and 3.1 kV/cm. Thus an increase in the duct spacing by a factor of 3, requires an increase of potential by a factor of 4 to maintain the same current.

From Figure 2, it is seen that the current density distribution drops off in magnitude towards the center line between corona wires. This is in agreement to the experimental observations of Felici [17] and Tassicker [18]. Increasing the wire to plate spacing from 0.1 to 0.2 and 0.3 m, as in Figures 3 and 4 respectively, resulted in a more uniform current density distribution at the collecting walls. This is presumably due to the increased uniformity of space charge adjacent to the collecting walls, as indicated by the results of the corona model for the three duct spacings, at constant linear corona current.

Although the experimental results for the electric field distribution at the collecting plate vary within a relatively large range, (see Figures 5 to 7) the simulation results give a reasonably good fit when the value of J_ℓ as evaluated by Equation (5) is used. From these figures, it is seen that for a constant linear corona current of 0.1 mA/m the electric field at a point directly below the wire is 2.5, 3.5 and 4.3 kV/cm for the increasing order of duct spacing. Also for the wider duct spacing the electric field has a larger relative decrease near the center line between corona wires. The field drops to 2.4, 3.3 and 3.8 kV/cm at this center line for the same increasing order of duct spacing.

It was of interest to investigate the effect of increasing the duct spacing while maintaining the same value of linear current density as well as varying the wire to wire spacing so as to hold the ratio (h/2s) constant. Although this case was not performed experimentally, it was easily predicted with the charge simulation model.

Table 1 includes some of the significant data for the previously presented precipitator dimensions operated at a constant linear corona current of 0.1 mA/m. In the table, the ratio of the electric field at the plate (E_p) to the average electric field in the gap ($E_{av} = V_c/h$) is defined as the electric field enhancement factor. Also shown are the field products $E_{av}E_p$ (Equation 3) and E_p^2 (Equation 4) which describe the proposed dependencies of migration velocity.

From this table it can be seen that for a constant wire to wire spacing the field enhancement factor increases from 1.1 at h = 0.1 m to 1.4 at h = 0.3 m. Even more significant, for the case of h = 0.3 m, the absolute value of the average field (E_{av}) is increased by 35% and similarly the value of the field at the plate is increased by 72%. This implies better precipitator performance, since the particle charging and precipitating fields are both increased.

Figure 8 shows the results of graphing the field products defined by Equations 3 and 4. For the case of constant wire to wire spacing note that both equations predict a linear increase in migration velocity as the wire to plate spacing is increased. For this case in changing from a wire to plate spacing h = 0.1 m to h = 0.3 m, the applied potential is increased by a factor of four while the collecting area is reduced by a factor of three (assuming constant precipitator volume). Equation (3) predicts an increase in migration velocity of 2.32 whereas Equation (4) predicts an improvement of 2.96 a value almost equal to the reduction in collection area. Thus both cases suggest that migration velocity is a linear function of wire to plate spacing and in the case of Equation (4) one could predict little or no change in collection efficiency, an observation consistent with the experimental results reported earlier.

For a constant ratio of (h/2s), the field enhancement factor increased from 1.2 at h = 0.1 m to 1.4 at h = 0.3 m. However, this was not accompanied by an increase in the average field, but rather reduction was observed. Similarly, the magnitude of the field at the plate was essentially unchanged. The net result of this (see Figure 8) was to produce a slight decrease in the predicted value of migration velocity as given by both Equations (3) and (4). Thus compared to the case of constant wire to wire spacing, one would expect a decrease in the collection efficiency of the precipitator as the area is decreased by a factor of three.

From Table 1, it is also observed that reducing the wire to wire spacing to .05 m while keeping the duct spacing constant at 0.1 m would require an increase of voltage of about 30% to maintain the same current. This is accompanied by an increase of 30% and 44% in the average and plate fields respectively with the resulting improved performance predicted in Figure 8.

From the results shown in Table 1 and Figure 8 the following conclusions can be made for an operating mode of constant linear corona current.

i) For a given precipitator volume, increasing the duct spacing while keeping the wire to wire spacing constant, results in a predicted linear increase in migration velocity. Furthermore, the increase predicted by Equation (4) approximately compensates for the reduction in collection area.

ii) For a given precipitator volume, increasing the duct spacing while keeping (h/2s) constant, results in a predicted linear decrease in migration velocity. This slight decrease coupled with the reduction in collection area implies a reduction in collection efficiency.

CONSTANT WIRE POTENTIAL

For this mode of operation, the wire to wire spacing was held constant at 0.1 m, the corona wire radius was 0.127 mm and the potential was fixed at 35 kV. The three duct spacings investigated were 0.2 0.4 and 0.6 m.

The value of the linear current density J_ℓ at the central wire, corresponding to V_c = 35 kV, was evaluated using Equation (5). These values for J_ℓ were found to be equal to 320 +13/-10, 34 +2.4/-1.0 and 7 +0.9/-0.8 μA/m for the duct spacings of 0.2, 0.4 and 0.6 m respectively.

From the above experimental ranges, it can be concluded that for more stable corona, such as found with the smallest duct spacing, the experimental error is relatively less.

The above values of J_ℓ were applied (as input parameters) independently to the corona model along with their respective geometrical values. The value of ion mobility used was 1.8×10^{-4} $m^2/V.s$ corresponding to positive corona.

Results of the model indicated that the potential V_c necessary to maintain the above values of linear current densities was 36, 35 and 33 kV for the increasing order of duct spacing. The reason for the slight deviation of the calculated potentials from the experimental value of 35 kV, is probably due to the experimental error in measuring the current density.

The electric field distributions at the collecting plate for the three spacings, as evaluated by the model and measured experimentally, are shown in Figure 9.

Figures 10 to 12, give the current density distributions at the collecting plate for the three duct spacings.

It was of interest, in this case, to find that the average ionic charge density along a line extending from wire to plate was reduced to 50% and 7% for h = 0.2 and 0.3 m respectively, as compared to h = 0.1 m. The corresponding reductions in the average electric field (E_{av}) were 51% and 28%. The large difference between both percentage reductions for the largest duct spacing is probably because the electrostatic field (at 35 kV) is comparable in magnitude to the electric field due to ion space charge. This is more clearly understood by evaluating the ratio of the average electrostatic field (V_o/h) to the average ionic field (V_c/h) for the three duct spacings. When this was performed the results were: 31, 43 and 55% for the increasing order of duct spacing.

Table 2 includes some of the significant data for the previously presented precipitator dimensions operated at a constant potential of 35 kV.

It is clear from this table, that increasing the duct spacing while keeping the applied potential constant will result in the degradation of the precipitator performance. This is simply because of the reduction in both the average and the plate fields (E_{av} and E_p respectively), which leads to a reduction in the migration velocity as predicted both by Equations (3) and (4).

CONCLUSIONS

1) The experimental results reported here show generally good agreement with the results predicted by the charge simulation model previously presented (13), thus confirming the validity and accuracy of the model.

2) Increasing the duct spacing while maintaining the wire to wire spacing and the linear corona current constant (i.e. maintaining the average current density at the duct surface constant) leads to an enhanced collecting field at the duct surface. Under these conditions Equations (3) and (4) both show a linear increase of migration velocity with duct spacing. Furthermore, the increase in migration velocity predicted by Equation (4) is approximately equal to the reduction in collection area thus implying little or no change in collection efficiency.

3) Increasing the duct spacing while keeping the ratio (h/2s) and the linear corona current constant does not produce an enhanced collecting field at the duct surface. Under these conditions equations (3) and (4) both show a slight linear decrease of migration velocity with duct spacing. This implies a net reduction in collection efficiency as the surface area is reduced.

4) Increasing the duct spacing while keeping the wire to wire spacing and the applied potential constant leads to a considerable reduction in corona current and the collecting field strength at the duct surface. Under these conditions Equations (3) and (4) show a major reduction in migration velocity with duct spacing. This implies a major reduction in collection efficiency as the surface area is reduced.

5) These results along with the previous measured results of Misaka (1) support the contention of Heinrich (3) that Deutschian behavior does exist in wide duct precipitators. Under appropriate conditions, the enhanced electric fields can increase the effective migration velocity to compensate for the reduced collection area.

6) It was found that for an array of corona wires energized from the same bus bar, the corona onset potential for the outer wires is lower than that of the inner wires. Similarly, the linear corona current emanating from the outer wires is higher than that of the inner wires. This confirms the observations of Lawless and Sparks (16).

ACKNOWLEDGEMENTS

The authors acknowledge with thanks the Natural Science and Engineering Research Council of Canada for their financial support of this work.

TABLE 1. ELECTRIC FIELD STRENGTH FOR VARIABLE DUCT SPACINGS UNDER CONSTANT LINEAR CORONA CURRENT = $J_\ell^* = 0.1$ mA/m

	Wire to Wire Spacing (m)	Wire to Plate Spacing (m)	Voltage (kV)	E_{av} (kV/cm)	E_p (kV/cm)	Ratio E_p/E_{av}	$E_p E_{av}$ Eqn(3)	E_p^2 Eqn(4)
Constant	0.1	0.1	23.4	2.3	2.5	1.1	5.75	6.25
Wire to Wire	0.1	0.2	53.5	2.7	3.5	1.3	9.45	12.25
Spacing	0.1	0.3	92.9	3.1	4.3	1.4	13.33	18.5
Constant	0.05	0.1	30.4	3.0	3.6	1.2	10.8	12.9
Ratio of	0.10	0.2	53.5	2.7	3.5	1.3	9.45	12.25
(h/2s) = 2:1	0.15	0.3	76.6	2.6	3.5	1.4	9.1	12.25

TABLE 2. ELECTRIC FIELD STRENGTH FOR VARIABLE DUCT SPACINGS UNDER CONSTANT APPLIED VOLTAGE = 35 kV

Wire to Wire Spacing (m)	Wire to Plate Spacing (m)	Voltage (kV)	Linear Current Density, J_ℓ (mA/m)	E_{av} (kV/cm)	E_p (kV/cm)	Ratio E_p/E_{av}	$E_p E_{av}$ Eqn(3)	E_p^2 Eqn(4)
0.1	0.1	35	0.320	3.5	4.4	1.26	15.4	19.36
0.2	0.1	35	0.034	1.8	2.1	1.17	3.78	4.41
0.3	0.1	35	0.007	1.2	1.25	1.04	1.5	1.56

NOMENCLATURE

a	mean particle radius (m)
A	total collecting surface area (m^2)
E_{av}	average electric field in gap (V/m)
E_c	charging electric field (V/m)
E_p	plate (precipitating) electric field (V/m)
h	wire to plate spacing (m)
I_{tot}	experimental current from all corona wires (A)
J	current density (A/m^2)
J_ℓ	linear corona current density (A/m)
J_ℓ^*	assumed constant linear corona current density (A/m)
P	dimensionless parameter
s	half wire to wire spacing (m)
T	residence time (sec.)
v_g	gas flow rate (m/s)
V_c	corona wire potential (V)
V_o	corona onset potential (V)
ε_o	permittivity of free space, 8.86×10^{-12} (F/m)
η	precipitator fractional efficiency
μ	viscosity of air (dp)
ω	particle migration velocity (m/s)
ω_k	effective particle migration velocity (m/s)

REFERENCES

1. T. Misaka, K. Sugimoto, H. Yamada, "Electric Field Strength and Collection Efficiency of Electrostatic Precipitator Having Wide Collecting Plate Pitches", CSIRO Conference on Electrostatic Precipitation, Leura, August 23-24, 1978, paper No. 11.

2. D.O. Heinrich, "Review and Some Practical Aspects of Wide Duct Spacing", Proceedings of the First International Conference on Electrostatic Precipitation, Monterey, California, October 14-16, 1981, pp. 638-653.

3. D.O. Heinrich, "Are Non-Deutschian Phenomena Required to Explain Wide Spacing", Proceedings of the Second International Conference on Electrostatic Precipitation, Kyoto, Japan, November 12-15, 1984, pp. 865-870.

4. K. Darby, "Plate Spacing Effect on Precipitator Performance", Proceedings of the Second International Conference on Electrostatic Precipitation Kyoto, Japan, November 12-15, 1984, pp. 386-383.

5. W. Diener, "Operating Results of Commercial Precipitators with 400 mm Plate Spacing", Proceedings of the Second International Conference on Electrostatic Precipitation, Kyoto, Japan, November 12-15, 1984, pp. 384-386.

6. S. Matts, "Flakt Electrostatic Precipitator an Update on Sizing and Pulsing", Internal Publication, Flakt Industri AB, S-35187 Vaxjo, Sweden.

7. D.O. Heinrich, "Electrostatic Precipitator Collector Spacings", Atmospheric Environment, Vol. 13, 1979, pp. 1707-1711.

8. S. Noso, "Performance Characteristics of Electrostatic Precipitators with Wide Spacing", Proceedings of the First International Conference on Electrostatic Precipitation, Monterey, California, October 14-16, 1981, pp. 654-667.

9. S.A. Matts, "Some Experiences with Increased Electrode Spacing", CSIRO Conference on Electrostatic Precipitation, Leura, August 23-24, 1978, paper No. 13.

10. S. Masuda, "Present Status of Wide-Spacing Type Precipitator in Japan", EPA Symposium, Denver, 1979, pp. 483-501.

11. C. Golkowski and M. Chojnowski, "The Role of Electrode Spacing in the Performance of the Electrostatic Precipitator", Journal of Electrostatics, Vol. 14, 1983, pp. 339-348.

12. L. Lindau and S. Matts, "Some Space Charge Problems Encountered With Large Electrode Spacing", Proceedings of the Second International Conference on Electrostatic Precipitation, Kyoto, Japan, November 12-15, 1984 , pp. 911-916.

13. A.A. Elmoursi and G.S.P. Castle, "Modeling of Corona Characteristics in a Wide-Duct Precipitator Using the Charge Simulation Technique", Industry Applications Society Conference Record, 1984, pp. 1192-1200.

14. O.J. Tassicker, "Boundary Probe for Measurement of Current Density and Electric Field Strength - With Special Reference to Ionized Gases", Proc. IEEE, Vol. 121, No. 3, March 1974, pp. 213-220.

15. E. Nasser, Fundamentals of Gaseous Ionization and Plasma Electronics, Wiley Interscience, New York, 1971.

16. P.A. Lawless and L.E. Sparks, "Prediction of Voltage-Current Curves for Novel Electrodes, Part I. Wire Electrodes", presented at the Fifth Symposium on the Transfer and Utilization of Particulate Control Technology, Kansas City, Missouri, August 27-30, 1984.

17. N.J. Felici, "Recent Advances in the Analysis of D.C. Ionized Electric Fields", Direct Current, Vol. 8, No. 9, 1963.

18. O.J. Tassicker, "Aspects of Forces on Charged Particles in Electrostatic Precipitators", Ph.D. Thesis, Wollongong University College, University of New South Wales, July 1972, pp. 159-161.

APPENDIX

THE SIGNIFICANCE OF END EFFECTS

Initially only three corona wires were used. For the three duct spacings: 0.2, 0.4 and 0.6 m, the average linear corona current density was held constant at 0.1 mA/m. This was achieved by increasing the applied voltage until the total corona current measured from the two plates was equal in magnitude to the value calculated by Equation (A.1).

$$I_{tot} = J_{\ell} \text{ (No of wires x length of a single wire)} \qquad \text{(A.1)}$$

The three precipitator geometries were applied to the charge simulation model using a mobility value of 1.8×10^{-4} $m^2/V.s$, a wire to wire spacing of 0.1 m, while maintaining a value of 0.1 mA/m for the linear corona current. The output voltage V evaluated by the model showed very good agreement to the corresponding experimental value for the smallest duct spacing of 0.2 m. This was not the case for the larger spacings. It was found that the model gave values of V_c greater than the experimental values by 7% and 19% for the 0.4 and 0.6 m spacings respectively.

When the number of wires were increased to 5 while maintaining the same value of 0.1 mA/m for the average linear corona current, the above percentage differences dropped to 2% and 6.5% respectively.

From the above results and from theoretical expectations due to shielding effects, it is clear that if a finite array of corona wires is energized from one bus bar, each corona wire will produce a different value of corona per unit length. The outer wires, which are less shielded, will contribute the largest value of linear corona current, while the central wire will contribute the smallest value of linear corona current. This phenomenon has recently been observed and investigated by Lawless and Sparks [16]. In the case considered here the corona onset voltage V_o predicted by the model for the increasing order of duct spacing was 10.9, 15.1 and 19.3 kV. These values are slightly higher than the experimental values of 10.3, 14.5 and 18 kV. This is as expected, since the corona model assumes a constant onset potential for all corona wires, whereas for the experimental set-up the effect of end wires is to cause the outer wires to reach corona at a potential lower than that of the inner wires. Since the experimental onset potentials documented here correspond to those of the outer wire, thus it makes sense that their values should be lower than those predicted by the corona model.

To evaluate the corona onset potential for the central wire, the formula developed by Lawless and Sparks was used [16]. Applying this formula to the three duct spacings: h = 0.1, 0.2 and 0.3 m, it was found that the corona onset potential at the central wire was equal to 10.8, 16.1 and 22.4 kV, while the corona onset potential at the outer wires was equal to 9.9, 13 and 16.3 kV respectively. It is interesting to observe that the value of onset potential predicted by the corona model, lies in between the values of onset potential predicted for the central and outer wires using Lawless and Spark's relation. This was found to be the case for the three duct spacings investigated.

According to the preceeding description, it is clear that for an array of wires connected to the same bus bar, the onset potential for each wire is slightly different. This difference approaches zero for an infinite number of wires such as assumed in the charge simulation model and is approached in practice in real precipitators. This explains the better agreement observed between the corona model results and the experimental results for five wires as compared to three wires. Based on this, further agreement may be achieved by increasing the number of corona wires in the experimental set-up. This was not done because of space limitations.

Since the apparatus was constructed without the provision for measuring the corona current emanating from each wire independently. The linear corona current J_ℓ at the central wire was evaluated by integrating the measured current density distribution along the plate from a point below the central wire to the centre line between corona wires, as shown by Equation (A.2).

$$J = 4 \int_0^s J.dx \qquad (A.2)$$

Using the value of J_ℓ as evaluated by Equation (A.2) rather than Equation (A.1), as input parameter to the charge simulation model [13], gave good agreement to the experimental data for all the duct spacings investigated. This is clearly seen from Table A.1.

TABLE A.1 COMPARISON OF SIMULATION RESULTS TO THE EXPERIMENTAL DATA

Wire to Wire Spacing (2s) (m)	Wire to Plate Spacing (h) (m)	Experimental Applied Voltage (V_c(exp)) (kV)	Linear Corona Current (mA/m)		Wire Potential as Evaluated by Charge Simulation Model (kV)	
			J_ℓ* Assumed Const. Current	J_ℓ According to Equ(5)	V_c^*	V_c
0.1	0.1	22.5	0.1	0.1	23.4	23.4
0.1	0.2	49	0.1	0.082	53.5	49.2
0.1	0.3	77	0.1	0.066	92.2	76.7

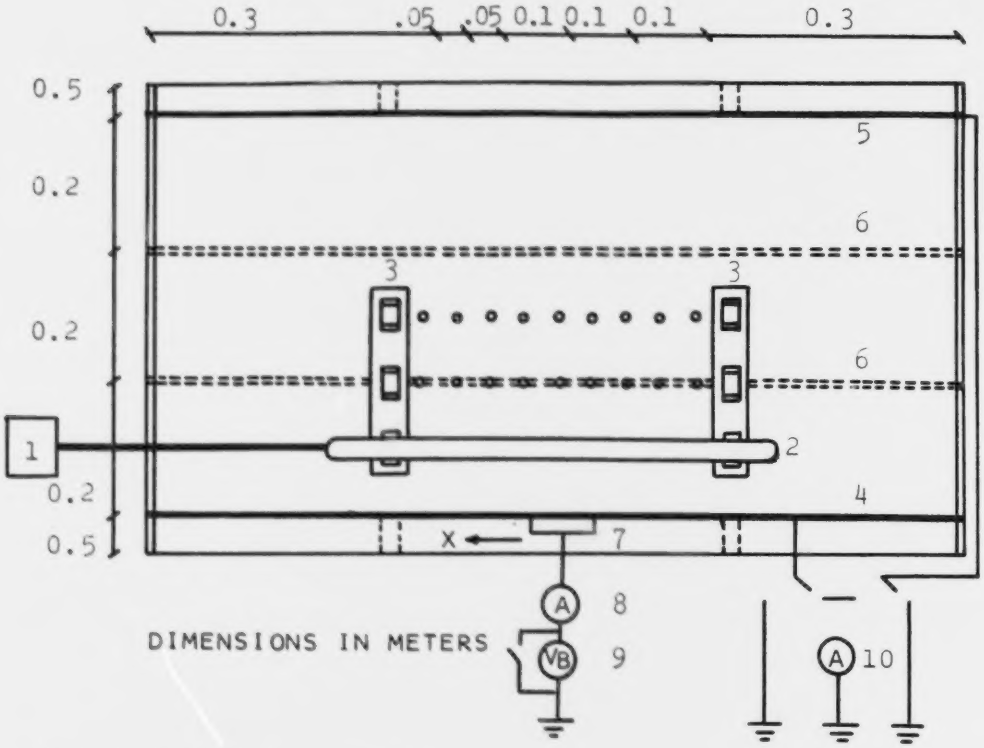

DIMENSIONS IN METERS

1. HIGH VOLTAGE D.C. SUPPLY
2. BUS BAR
3. BUS BAR SUPPORTS
4. FIXED PLATE
5. MOVABLE PLATE
6. SLOTS FOR MOVABLE PLATE
7. PROBE AND PROBE SUPPORT
8. ELECTROMETER
9. D.C. POWER SUPPLY
10. AMMETER

FIGURE 1. SCHEMATIC TOP VIEW OF THE EXPERIMENTAL SET-UP

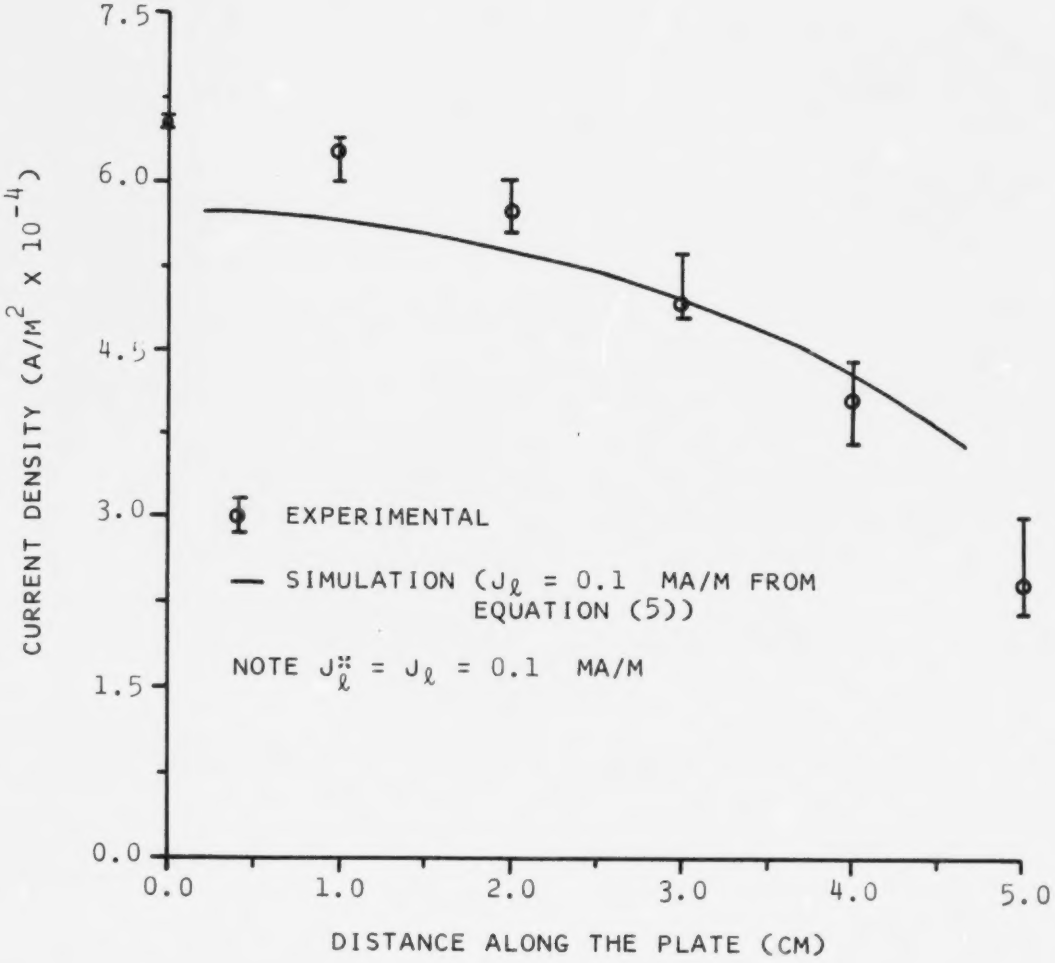

R_C = 0.127 MM

H = 0.1 M

S = 0.05 M

V_C = 23.4 KV

V_C^{*} = 23.4 KV

V_C(EXP) = 22.5 KV

FIGURE 2. EXPERIMENTAL AND SIMULATION CURRENT DENSITY DISTRIBUTIONS AT THE COLLECTING PLATE FOR H = 0.1 M

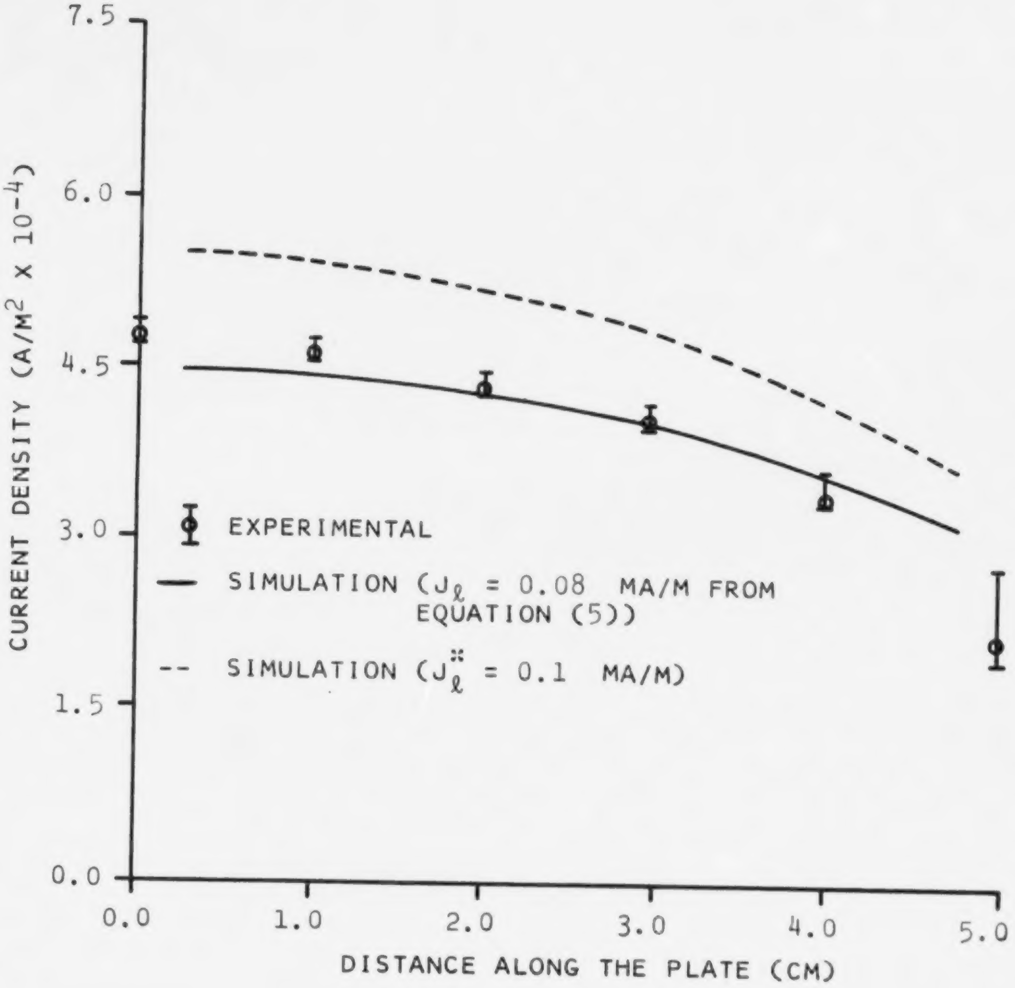

R_C = 0.127 MM

H = 0.2 M

S = 0.05 M

V_C = 49.2 KV

V_C^* = 53.5 KV

V_C(EXP)= 49.0 KV

FIGURE 3. EXPERIMENTAL AND SIMULATION CURRENT DENSITY DISTRIBUTION AT THE COLLECTING PLATE FOR H = 0.2 M

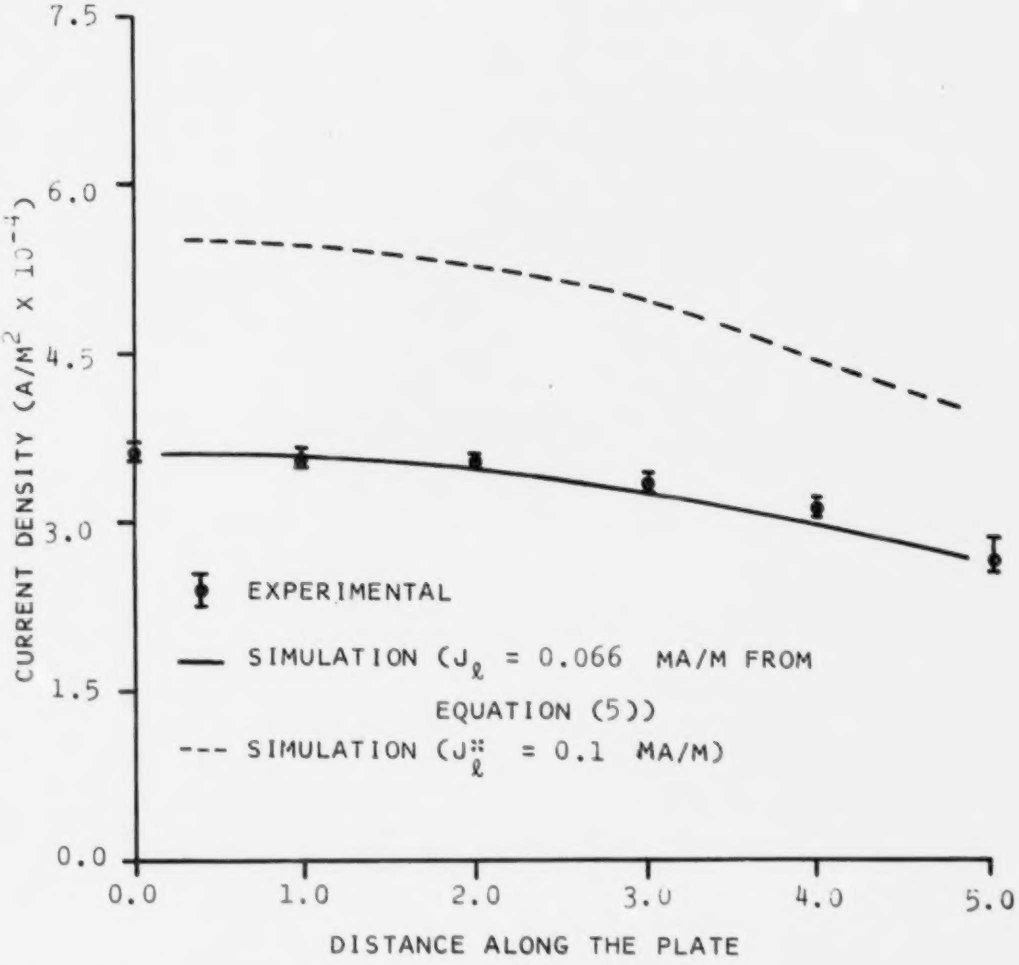

R_C = 0.127 MM

H = 0.3 M

S = 0.05 M

V_C = 76.7 KV

V_C^* = 92.2 KV

V_C(EXP) = 77.0 KV

FIGURE 4. EXPERIMENTAL AND SIMULATION CURRENT DENSITY DISTRIBUTIONS AT THE COLLECTING PLATE FOR H = 0.3 M.

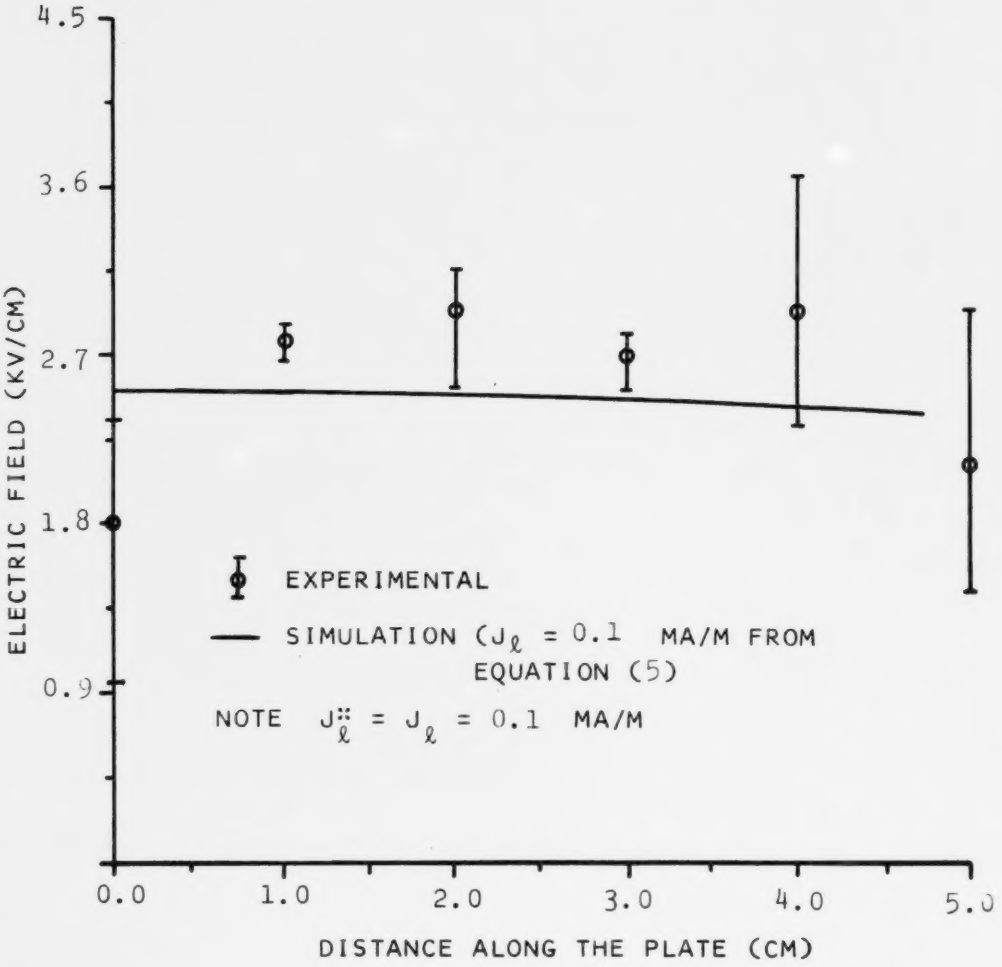

R_C = 0.127 MM

H = 0.1 M

S = 0.05 M

V_C = 23.4 KV

V_C^{*} = 23.4 KV

V_C(EXP) = 22.5 KV

FIGURE 5. EXPERIMENTAL AND SIMULATION ELECTRIC FIELD DISTRIBUTIONS AT THE COLLECTING PLATE FOR H = 0.1 M.

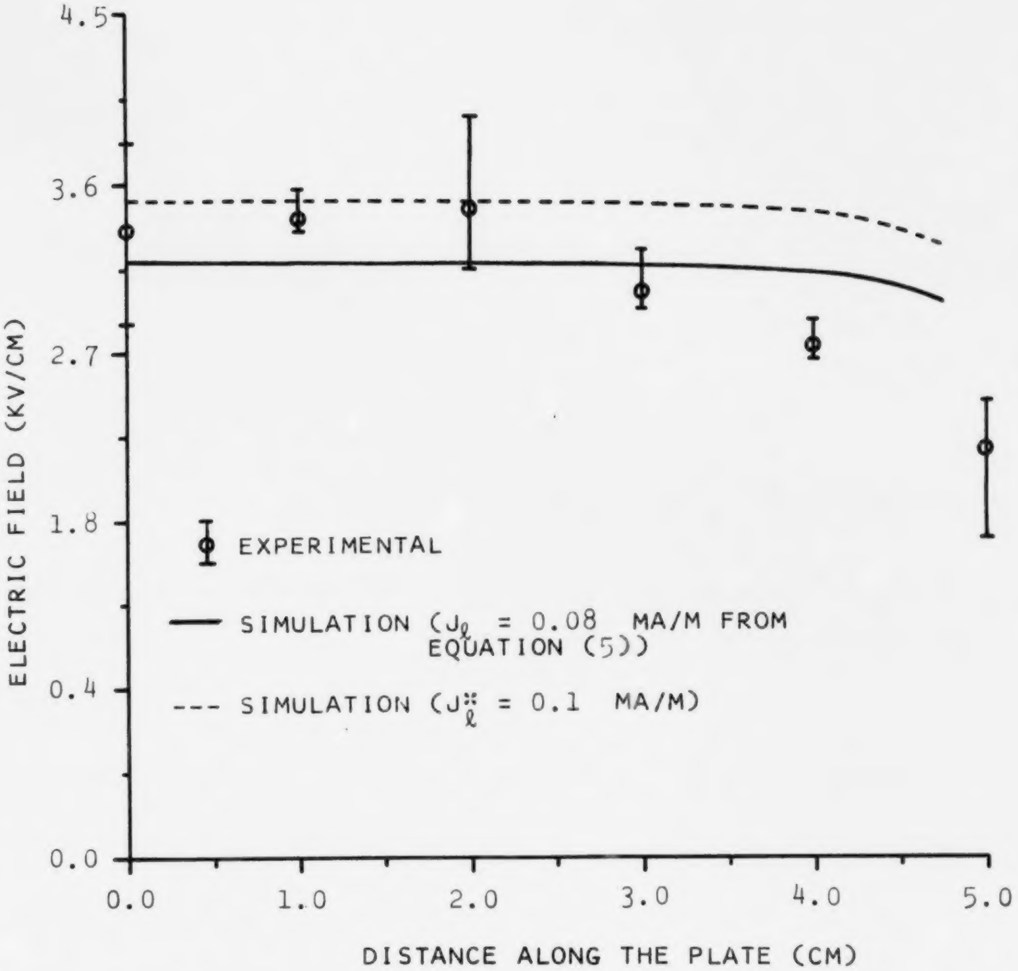

R_C = 0.127 MM

H = 0.2 M

S = 0.05 M

V_C = 49.2 KV

V_C^{*} = 53.5 KV

V_C(EXP) = 49.0 KV

FIGURE 6. EXPERIMENTAL AND SIMULATION ELECTRIC FIELD DISTRIBUTION AT THE COLLECTING PLATE FOR H = 0.2 M

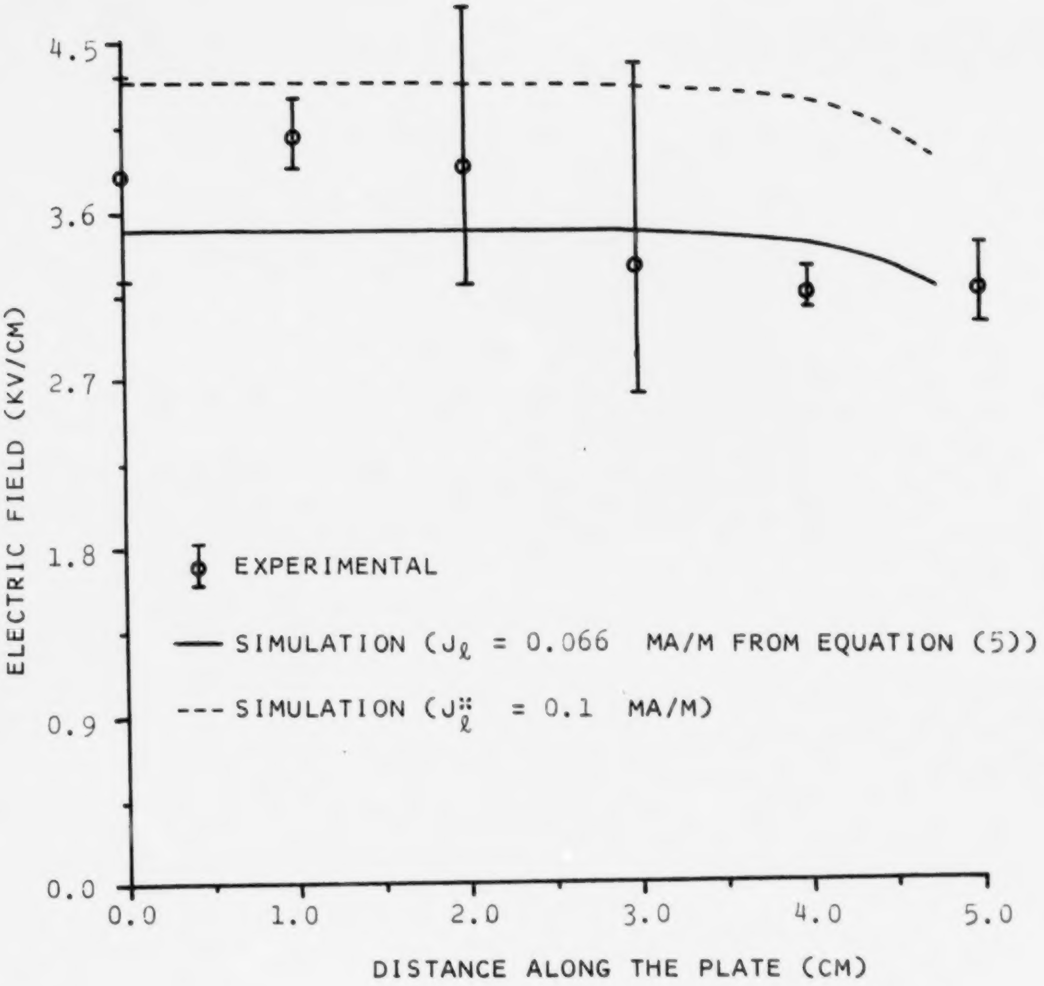

R_C = 0.127 MM

H = 0.3 M

S = 0.05 M

V_C = 76.7 KV

V_C^* = 92.2 KV

V_C(EXP) = 77 KV

FIGURE 7. EXPERIMENTAL AND SIMULATION ELECTRIC FIELD DISTRIBUTIONS AT THE COLLECTING PLATE FOR H = 0.3 M

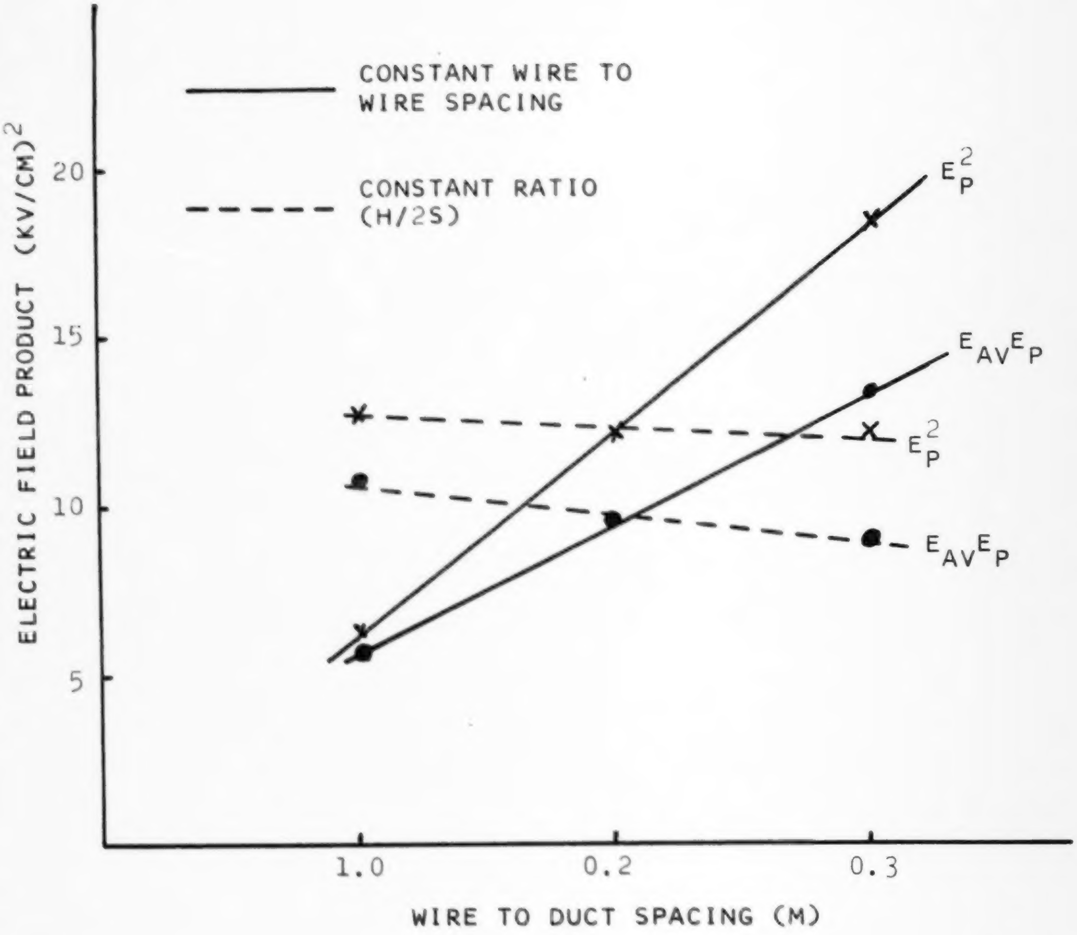

FIGURE 8. FIELD DEPENDENCIES DEFINED BY EQUATIONS (3) AND (4)

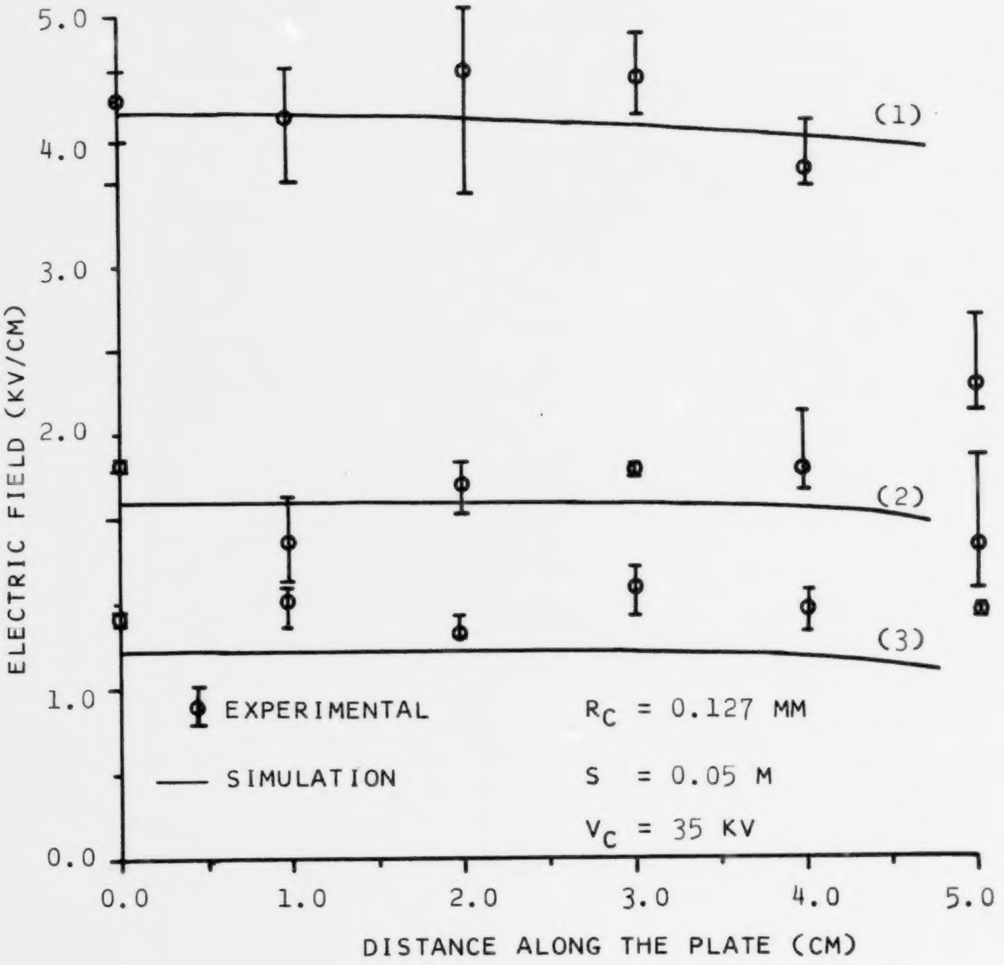

(1) H = 0.1 M	J_ℓ = 0.320 MA/M
(2) H = 0.2 M	J_ℓ = 0.034 MA/M
(3) H = 0.3 M	J_ℓ = 0.007 MA/M

FIGURE 9. EXPERIMENTAL AND SIMULATION ELECTRIC FIELD DISTRIBUTION ALONG THE COLLECTING PLATE AT CONSTANT OPERATING POTENTIAL

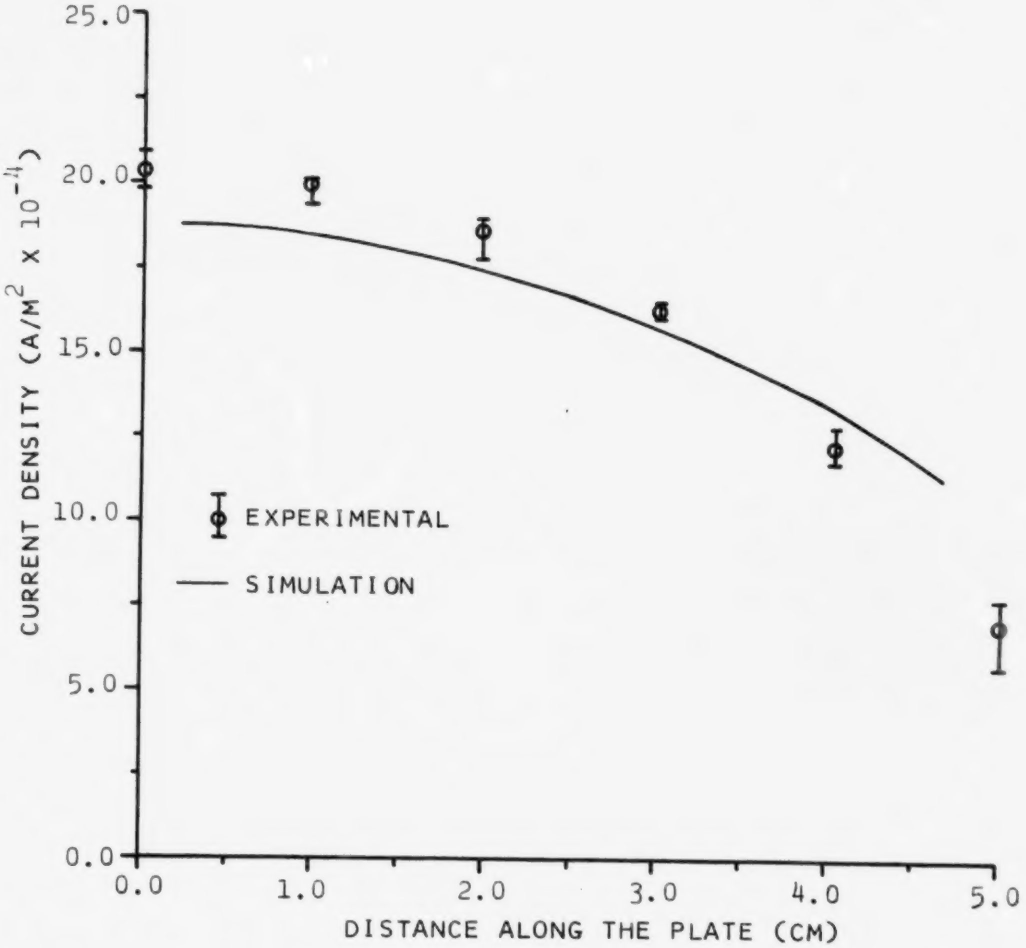

R_C = 0.127 MM

H = 0.1 M

S = 0.05 M

J_ℓ = 0.32 MA/M

V_C = 36 KV

V_C(EXP) = 35 KV

FIGURE 10. EXPERIMENTAL AND SIMULATION CURRENT DENSITY DISTRIBUTION AT THE COLLECTING PLATE FOR CONSTANT APPLIED POTENTIAL AND H = 0.1 M

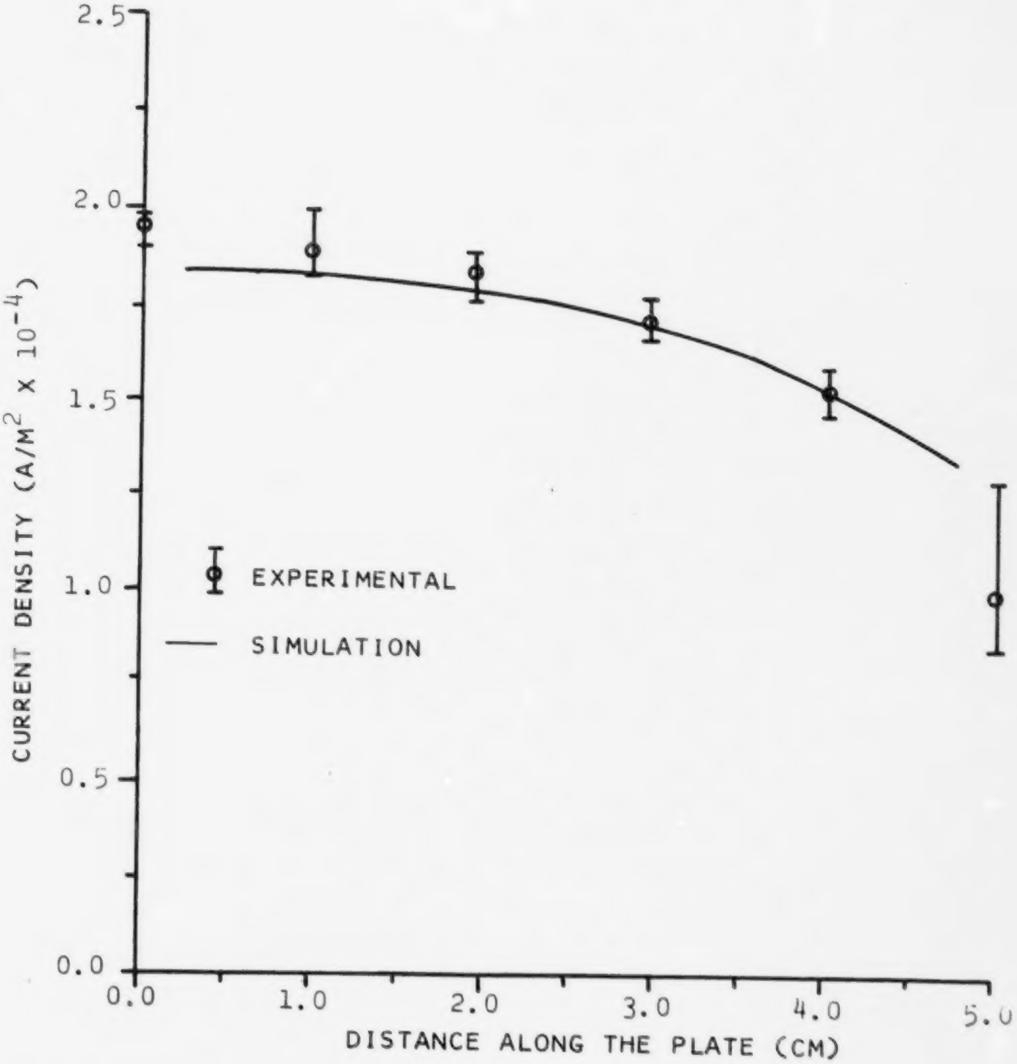

R_C = 0.127 MM

J_ℓ = 0.034 MA/M

H = 0.2 M

V_C = 35 KV

S = 0.05 M

V_C(EXP) = 35 KV

FIGURE 11. EXPERIMENTAL AND SIMULATION CURRENT DENSITY DISTRIBUTIONS AT THE COLLECTING PLATE FOR CONSTANT APPLIED VOLTAGE AND H = 0.2 M

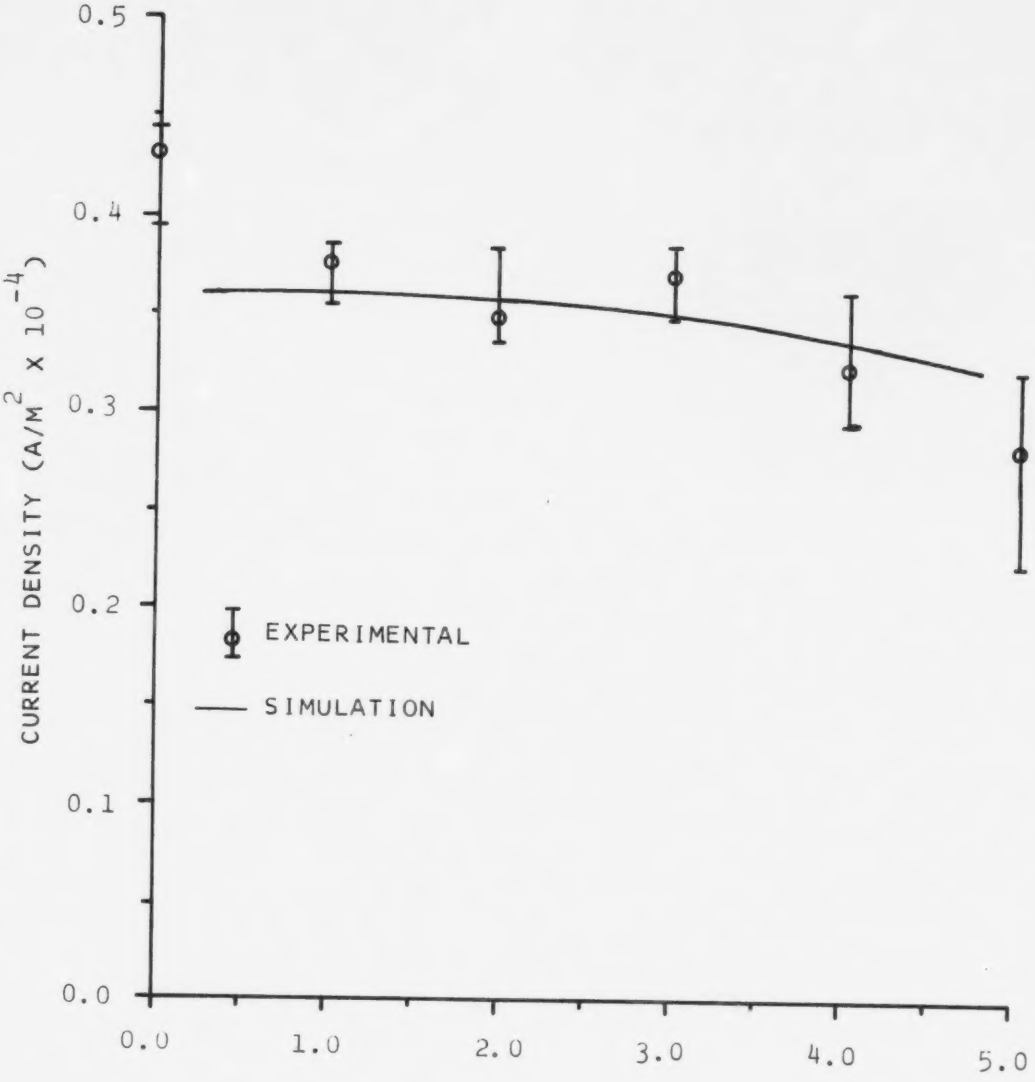

R_C = 0.127 MM

H = 0.3 M

S = 0.5 M

J_ℓ = 0.007 MA/M

V_C = 33 KV

V_C(EXP) = 35 KV

FIGURE 12. EXPERIMENTAL AND SIMULATION CURRENT DENSITY DISTRIBUTION AT THE COLLECTING PLATE FOR CONSTANT APPLIED VOLTAGE AND H = 0.3 M

INFLUENCE OF GAS DISTRIBUTION ON PRECIPITATOR PERFORMANCE

by: Leif Lind
F.L. Smidth & CO
Copenhagen, Denmark

ABSTRACT

The gas distribution in electrostatic precipitators is of major importance for precipitator performance, and in several cases specifications or standards of distribution must be met. Most of these specifications call for very uniform distribution although theoretical considerations and practical experience do not necessarily support the opinion that a unique relationship between perfect distribution and maximum precipitator performance does exist. This relationship will be discussed with reference to precipitator physics and fluid mechanics. The results, supported by practical examples, will contribute to existing knowledge concerning the influence of gas distribution on precipitator performance.

INTRODUCTION

It is generally accepted that the distribution of the gases over the cross section of the electrostatic precipitator must be uniform in order to obtain maximum efficiency. Contractors specify demands on the gas distribution indicating the accepted derivation from uniformity inherently based on theories correlating optimum efficiency to different statistical parameters of the velocity distribution.

This paper will describe the theories connecting the precipitator efficiency with the gas distribution quality and show some examples of practical experienced distribution and the corresponding performance. The most recent knowledge of the physics of the precipitation process will be referenced and will be used to stand for a more varied view on the gas distribution.

THE DEUTSCH EQUATION

About a decade after the introduction of the industrial electrostatic precipitator the so-called Deutsch-Anderson equation for precipitator efficiency was formulated.

$$\eta = 1 - \exp(-\frac{L \cdot w}{b \cdot v}) \qquad (1)$$

η is the precipitator efficiency, $0<\eta<1$, L the length of the collecting system, b half the duct width (plate spacing), w the so-called particle migration velocity and v the gas velocity equal to the axial particle velocity.

In the Deutsch equation it is assumed that turbulence and diffusion creates a uniform particle concentration across the duct, corresponding to infinite turbulence level, and that the migration velocity is independent of the gas flow pattern. Eqn.1 shows that the efficiency increases with the migration velocity and decreases with the duct width. Defining penetration $P = 1 - \eta$, the equation (1) yields the known expression:

$$P = 1 - \eta = \exp(-\frac{L \cdot w}{b \cdot v}) \qquad (1b)$$

THE MIGRATION VELOCITY

Eqn.(1) and Eqn.(1b) may be used to determine the particle migration velocity experimentally for specific processes. The most common expression for particle migration velocity based on the physical laws governing the motion of a single particle in a precipitator is derived on the condition that the gas is quiescent and that only the electrostatic force and the gas friction are acting on the particle. Then the stationary equilibrium gives the migration velocity (2):

$$w = \frac{q \cdot E_p}{6 \cdot \pi \cdot \mu \cdot a} \qquad (2)$$

q is the particle charge, E_p the precipitating electric field, μ the dynamic viscosity and a the particle radius.

Implicitly is assumed that the particle motion is creeping and the Stokes' formula is valid, that the particle is a sphere and the precipitating field and the charge are constant in time and space. The migration velocity in Eqn.2 has been connected with the Deutsch expression ever since the early twenties, despite the dubious assumption of infinite turbulence and quiescent gas.

REFINEMENT OF THE DEUTSCH EQUATION

Eqn.2 shows that w is inversely proportionel to particle radius a. However, also particle charge q is influenced by a. The simple expression for a conducting sphere charged by the electric field assuming field charging is:

$$q = 12 \cdot \varepsilon_o \cdot \pi \cdot E_o \cdot a^2 \qquad (3)$$

leading to the traditionally used expression for w:

$$w = 2\cdot\varepsilon_o\cdot E_o\cdot E_p\cdot a/\mu \qquad (4)$$

where ε_o is the gas permittivity and E_o the charging field strength. For practical purposes the expression for w in Eqn.4 is normally modified to account for the varying particle size always found in precipitators. In 1957 Matts and Allander (2) described a theory modifying the Deutsch equation and in 1963 White (1) introduced the log-normal particle size distribution often assumed in theoretical work today. Another important refinement is the introduction of a weight function for the velocity gas distribution in the equation. White (1) introduced the true gas velocities instead of the average velocity using a cross section distribution function. Thus the penetration can be expressed as:

$$P = \int_0^{v_{max}} \exp\left(-\frac{L\cdot w}{b\cdot v}\right)\cdot f(v)\cdot dv \qquad (5)$$

The distribution function f(v) is assumed to be a Gaussian distribution with average velocity $\bar{v}$ and standard deviation σ. In Figure 1 is shown a cumulative Gaussian distribution curve. The tangent at point ($\bar{v}$ | 50%) intersects the 100% line at the point ($\bar{v} + \sqrt{\pi/2}\cdot\sigma$|100%). If the point ($1.15\bar{v}$|85%) used in the IGCI rules is to fall on the curve, $0.15\bar{v}$ must equal $1.037\cdot\sigma$, meaning that $\sigma/\bar{v}$ = 14.5%. Although useful for theoretical considerations the normal distribution is seldom found in practice, where the distribution often has a peak at low velocity and at high velocity.

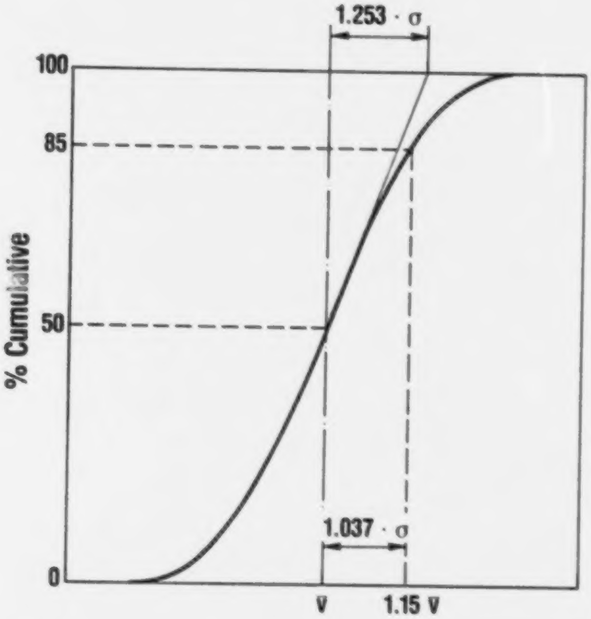

Figure 1. Gas velocity cumulative curve. Gauss distribution. Average velocity $\bar{v}$ and standard deviation σ.

Figure 2, upper part, shows an actual measured gas distribution frequency plot. The lower part of the figure is the cumulative distribution, which can be used for determining an approximate standard deviation, about 0.15 m/s or 17% normalized.

Idel'chik and Aleksandrov (3) adopt a different procedure claiming that a well suited modification is:

$$P = \exp\left(-\frac{L \cdot w}{b \cdot \bar{v} \cdot M}\right) \qquad (6)$$

with:

$$M = \frac{1}{A_c} \int_{A_c} (v/\bar{v})^2 \cdot dA_c \qquad (7)$$

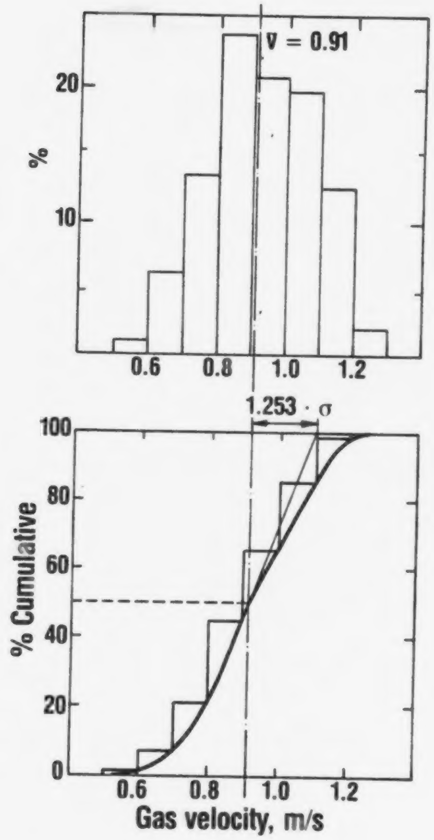

Figure 2. Actual velocity frequency distribution and cumulative distribution.

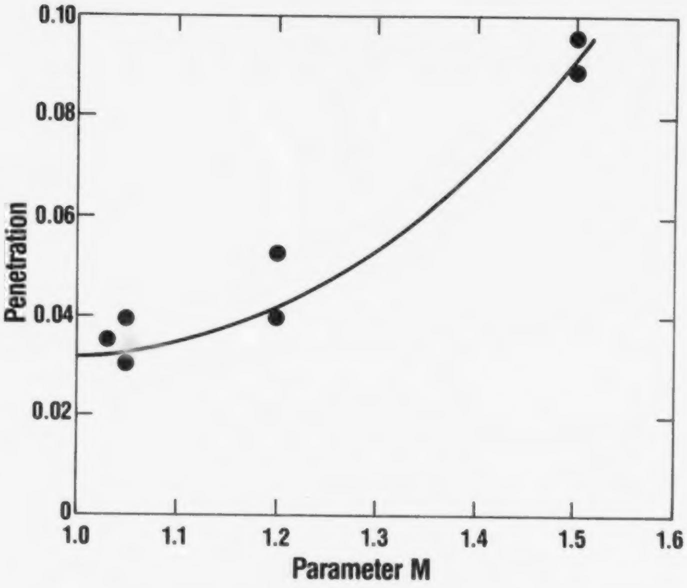

Figure 3. Penetration, P = exp(-Lw/bMv), in dependency of parameter M. From (3).

Figure 3 shows their results from measurements of the penetration and corresponding calculation in dependency of the parameter M. The agreement appears to be very good indeed.

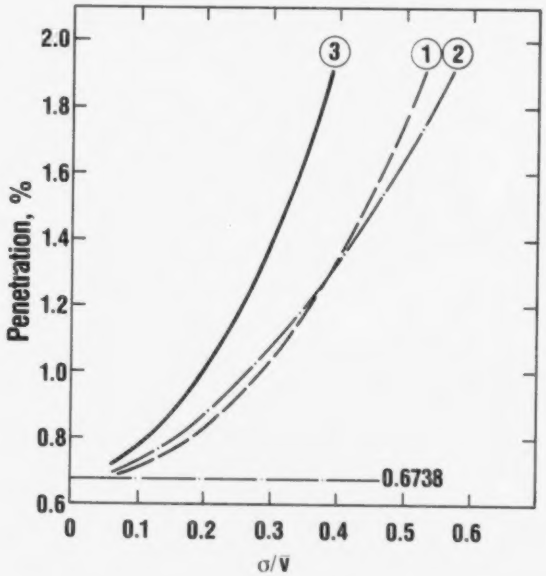

Figure 4. Penetration in dependency of normalized velocity standard deviation. ① Eqn.5, ② Eqn. 6, ③ Eqn. 8.

Gooch, McDonald and Oglesby in their "Mathematical Model of Electrostatic Precipitation" (4) use a velocity weighted version of Eqn.5:

$$P = \int_0^{v_{max}} \exp\left(-\frac{L \cdot w}{b \cdot v}\right) \cdot f(v) \cdot v/\bar{v} \cdot dv \qquad (8)$$

They also include measurement data to evaluate P in dependency of σ and $P(\sigma = 0)$. Figure 4 shows the relationship between P and $\sigma/\bar{v}$ for the three expressions, Eqn.5, 6 and 8, with $Lw/b = 5$ m/s. Although curve 3 may be more correct from a theoretical point of view, curve 1 agrees strikingly with curve 2 verified by practical measurements. This finding may indicate that use of too elaborate theoretical models may not be justified in practice.

PRACTICAL CONSIDERATIONS ON INFLUENCE OF GAS DISTRIBUTION ON EFFICIENCY

There may be much more important reasons for controlling the gas velocity profiles inside the precipitator compartment than the influence from residence time described theoretically in the preceeding section.

Sneakage of dust laden gases around the electrically energized electrode system must be kept at an absolute minimum, in particular at the bottom part of the precipitator. And large eddies in the bottom hoppers caused by the velocity "slip" at the bottom of the electrode system may aggravate the influence from sneakage because particles already picked up by the hopper are swept into the main flow again.

Reentrainment from the dust layer on the collecting surface can be caused by particles impacting on the surface and from back ionization blowing particles out in the gas stream. More serious is the redispersion and reentrainment of particles from tall collecting plates with loosely packed dust limiting the efficiency in particular due to rapping losses from the last field.

High local velocities may scour away already precipitated dust from the collecting plates. In this case a good gas distribution combined with high average velocity may not be superior to a bad gas distribution combined with low average velocity.

Finally gas distribution may influence the dust space charge distribution and thereby the current distribution in a separately energized precipitator field. In areas with low velocities or, in extreme situations, areas with recirculating flow, the particle concentration will be much lower than in corresponding areas with higher velocities. Consequently the power input will be limited in the high velocity areas causing a reduction in overall efficiency. In particular with high resistivity dust such uneven current distribution will cause back ionization and frequent sparking, resulting in lower average voltage and current and increased dust reentrainment. Due to the turbulence the gas distribution in each separate duct will tend to improve through the precipitator, thus smoothing the dust space charge. However, a skew cross distribution at the field inlet will not be smoothed to the same extent, and so the horizontal gas distribution should be fairly uniform in order to maintain a proper current distribution.

SOME PRACTICAL EXAMPLES DEMONSTRATING THE INFLUENCE OF GAS DISTRIBUTION

CASE NO.1

A three field precipitator after a 140 MW coal fired utility boiler was made with an inlet funnel comprising a central diffuser with three vertical distribution screens, and with an outlet funnel made as a contraction with a single vertical screen, with very little depth and a bottom exit due to space requirements. The contours of the outlet are seen in Figure 5. From the solid line of Figure 6 showing the vertical velocity profile measured at air load during commissioning, it is seen that too much gas flows in the bottom region. The volume flow rate of the lower half of the cross section area is about 15% above average and the peak velocity in this region is more than 1.2 times the overall average value.

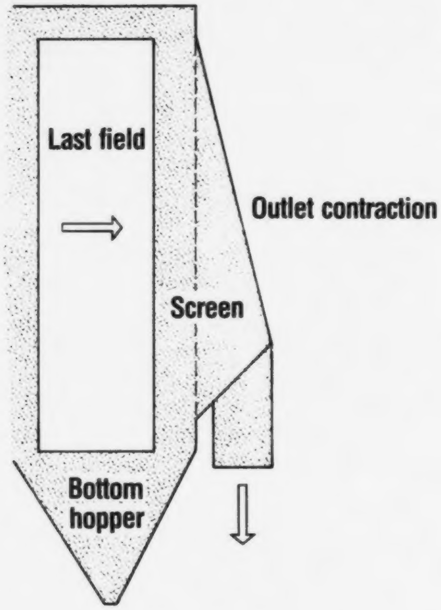

Figure 5. Outlet funnel with vertical screen and bottom exit.

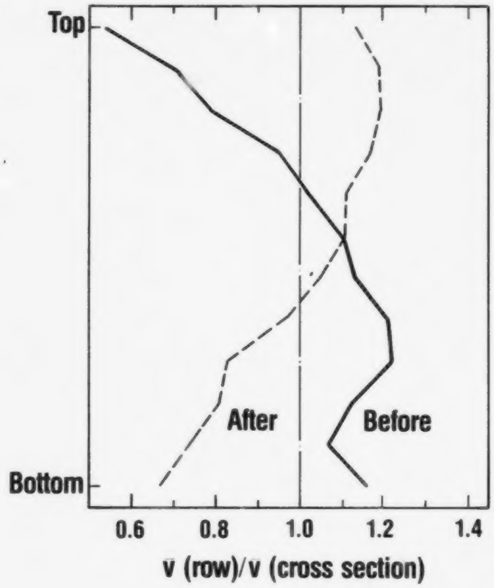

Figure 6. Outlet vertical velocity profiles corresponding to figure 5.

Although the precipitator was sized conservatively the guarantee limit of 150 mg/m^3 STP dry was exceeded admittedly at an excessive volume flow rate. From model testing it was decided to install a screen with half the open area at the lower 1/3 of the field height yielding a velocity profile as shown in Figure 6 as a dotted curve. After this modification gravimetrical measurements revealed an average emission of 50 mg/m^3 STP.

CASE NO.2

A three field precipitator after a four stage preheater cement kiln without conditioning tower was made with the inlet duct to the precipitator connected to the inlet funnel in the upper corner, see Figure 7. Only one horizontal grid and one vertical screen were fitted to the inlet and there were no guide vanes. At start-up the precipitator did not meet the guarantee and the VI-curves clearly indicated a skew gas distribution in the first field. Figure 8 shows the curve of field 1, marked 1b placed between 2b and 3b revealing an uneven current distribution. At a resistivity about $6 \cdot 10^{12}$ Ohm·cm and a temperature of 345°C current capsizing will cause severe sparking. After having corrected the distribution of the open area of the screen in order to achieve a better gas flow distribution, the VI-curves changed position. Now the curve of field 1, maked 1a, is placed at the higher voltage and the improved efficiency of field 1 has displaced the curves 2a and 3a towards lower voltage due to reduced particle concentration within these fields. All the VI-curves are displaced towards lower voltages because the dust layer thickness has changed.

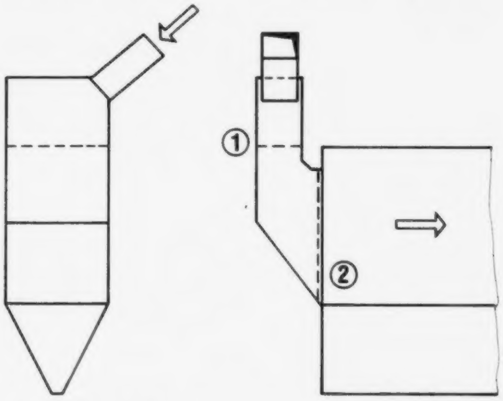

Figure 7. Inlet funnel with gas entry in the upper corner. ①is a horizontal grid, ②is the vertical inlet screen.

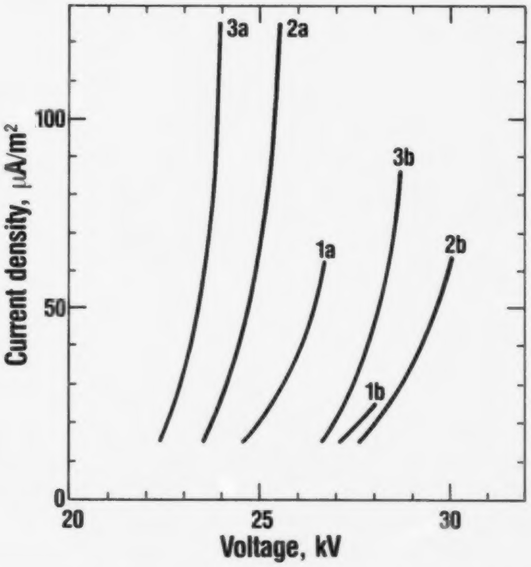

Figure 8. VI-curves from a three-field precipitator. b before modification of gas distribution, a after modification.

CASE NO.3

This example originates from a two field precipitator for a four stage preheater kiln with conditioning tower and illustrates that the traditional numbers used to correct the efficiency given by Deutsch's formula might lead to a pessimistic judgement of the precipitator capability. An elevation plan of the precipitator is seen in Figure 9 with the inlet and outlet funnel contours. Before start up the gas distribution was measured in the traverse planes at the inlet and outlet of each field.

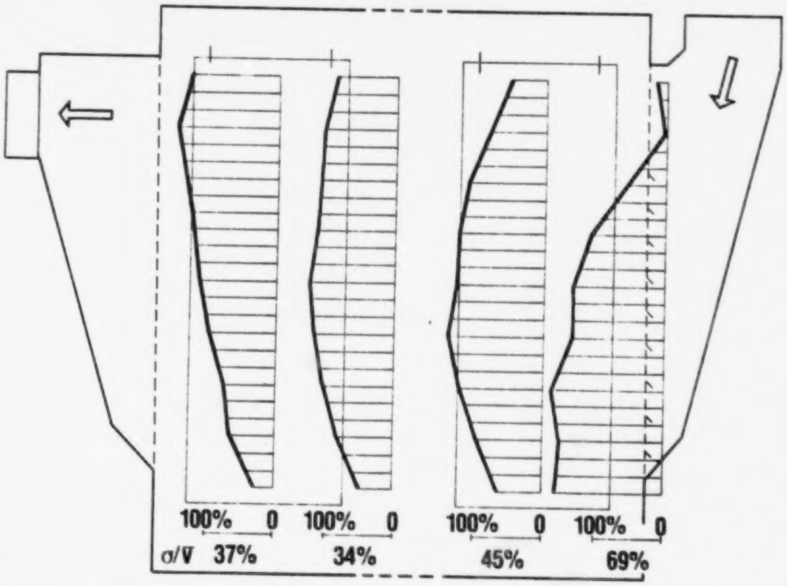

Figure 9. Contours of precipitator with four vertical velocity profiles and corresponding normalized standard deviations.

The measured vertical velocity profiles are shown in Figure 9 together with the calculated coefficients of variation, assuming that the data could be approximated by a Gauss distribution. The inlet profile reveals that the single vertical screen at the inlet cannot turn the flow at the top of the first field. However, as the screen is fitted with small turning vanes pointing upwards at an angle of 45°, the flow is in fact directed towards the upper part of the compartment, see the velocity profiles at the middle. Between and within field 1 and 2 turbulent diffusion tends to smooth the profile, but the exit opening placed on top of the outlet plenum creates a velocity profile at the outlet with low bottom velocities giving higher efficiency due to more effective migration and to less reentrainment. The precipitator efficiency was determined by measurement to 99.93% corresponding to a penetration of 0.00067 as compared to an expected penetration with a uniform gas distribution of 0.00056. The gas distribution data of the four traverse planes used to modify the Deutsch equation according to Eqn.5 yields the penetration listed in Table 1. Depending on the velocity used, the calculated penetration normalized with the design value using $v = \bar{v}$ varies from 2.6 to 9.1. However, it is hard to visualize that any improvement could be obtained by changing the gas velocity profiles towards increased uniformity.

TABLE 1. MEASURED TOTAL PENETRATION, DESIGN TOTAL PENETRATION AND TOTAL PENETRATION CALCULATED FROM EQU.5 USING ACTUAL GAS DISTRIBUTION DATA.

Traverse plane	P (Eqn.5)	P(calculated)/P(design)
inlet 1. field	0.00510	9.1
outlet 1. field	0.00178	3.2
inlet 2. field	0.00148	2.6
outlet 2. field	0.00153	2.7
Design	0.00056	
Measured	0.00067	1.2

At least it can be concluded that if the gas distribution influence is calculated using this traditional modification of the Deutsch equation, an average distribution of each individual field should be utilized to calculate the penetration fieldwise.

PERCEPTION OF THE INFLUENCE OF GAS VELOCITY AND TURBULENCE LEVEL

Recent investigations including the effect of flow turbulence does not support the common assumption of w being independent of the gas flow pattern and especially of the gas velocity. König (5), from experiments with a pilot precipitator, found the migration velocity to increase with gas velocity in the range from 0.5 to 1.0 m/s. Weber and Wiggers (6) published the graph reproduced in Figure 10 showing an almost linear relationship between migration velocity divided by duct width, w/2b, and gas velocity, v, up to 2 m/s with a slope close to 1 m^{-1}. This correlation was evaluated from measurements on a laboratory precipitator of the wind tunnel type.

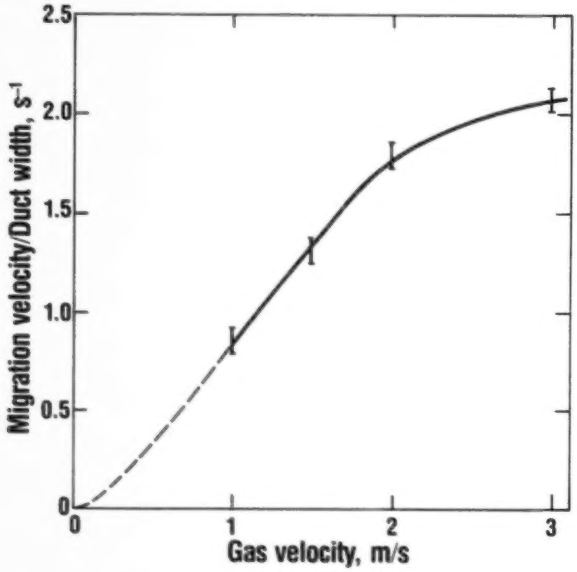

Figure 10. Migration velocity/duct width as a function of gas velocity. Reproduced from (6)

Leonard, Mitchener and Self (7) have put forward a theory including the influence of turbulent diffusion on the migration process. They demonstrated that infinite turbulence level assumed in Deutsch's equation did not represent an optium situation, but that the precipitator with a finite turbulent diffusivity would show a superior performance. Figure 11 from (7) shows penetration in dependency of a dimensionless precipitator lenght $L = x \cdot w_E / b \cdot v$.

The parameter P_E is a Péclet number:

$$P_E = w_E \, d/D \qquad d = 2 \cdot b \qquad (9)$$

expressing the balance between electrostatic migration and turbulent diffusion. w_E is the migration velocity taken from Eqn. 2 and D is the turbulent diffusivity.

As a consequence of this theory, the duct width, 2b, influences the efficiency. The greater the duct width the higher P_E and the lower the penetration.

The diffusivity D is proportional to $u'_{rms} \cdot l$. u' is the turbulent fluctuating component of the gas velocity and l is a measure of the size of the largest turbulence eddies.

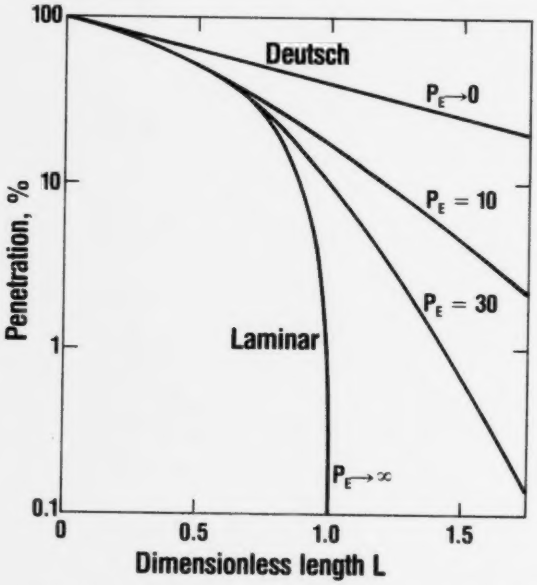

Figure 11. Penetration as a function of dimensionless precipitator length $L = x \cdot w_E / b \cdot v$. From (7).

From measurements on a laboratory precipitator Scheel Larsen and Sørensen (8) reported typical u'_{rms} values, Figure 12. Below 1 m/s the turbulent fluctuations increase drastically and the turbulent diffusivity coefficient increases. Even though the numerical numbers are specific to the experimental set up the work indicates that the P_E number decreases at low velocities causing increased penetration.

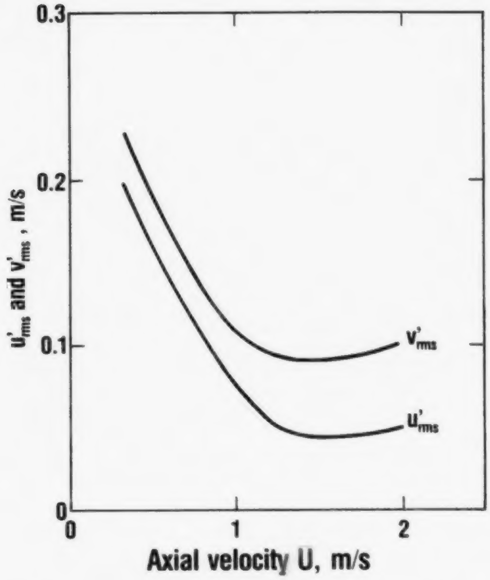

Figure 12. Turbulent fluctuating velocities in a precipitator model with varying gas velocity. u'_{rms} in axial direction, v'_{rms} in cross direction. From (8).

The implication of w being a function of v as reported in (6) may be illustrated by a calculation using the data of Figure 10. In the interval $0.5 \leqslant v \leqslant 2.0$ m/s the data may be approximated by a straight line $w = 0.25 \cdot v - 0.05$ m/s provided a duct width of 0.25 m. Figure 13 shows this line together with an actual velocity distribution.

Calculating the penetration by the simple Deutsch-Andersson equation using the expression, Eqn. 5, from a precipitator having $L/b = 25$ and $w = 0.20$ m/s yields:

$$P_1 = P(\text{Eqn.5}, w = 0.20) = 0.0104$$

Introducing the linear relationship for w from Figure 13 in Eqn.5 instead of $w = 0.20$ m/s results in the penetration:

$$P_2 = P(\text{Eqn.5}, w = 0.25 \cdot v - 0.05) = 0.0085$$

In comparison the Eqn.1b, assuming perfect even distribution predicts:

$$P_3 = P(\text{Eqn.1b}, w = 0.20) = 0.0067$$

The implication in precipitator size may be illustrated by comparing the relative increase of precipitator volume necessary to meet the penetration of 0.0067 utilizing the simple Deutsch-Andersson equation:

$$f\ (\text{Eqn.5}, w = 0.20) = \ln P_3 / \ln P_1 = 1.10$$

$$f\ (\text{Eqn.5},\ w = 0.25\cdot v - 0.05) = \ln P_3/\ln P_2 = 1.05$$

Replacing Eqn.5 by Eqn.8 in the calculation yields the corresponding figures:

$$f\ (\text{Eqn.8},\ w = 0.20) = 1.16$$

and

$$f\ (\text{Eqn.8},\ w = 0.25\cdot v - 0.05) = 1.02$$

These results indicate that the velocity shall be chosen as high as possible with due consideration to the negative effects such as gas sneakage and dust reentrainment inevitably present in a precipitator in practice and having increased influence with increasing gas velocity. Another negative effect may be caused by the organized secondary flow, socalled rolls, induced by the ionic wind, which decreases the efficiency at higher axial velocities because of particles trapped in the core of the rolls (8).

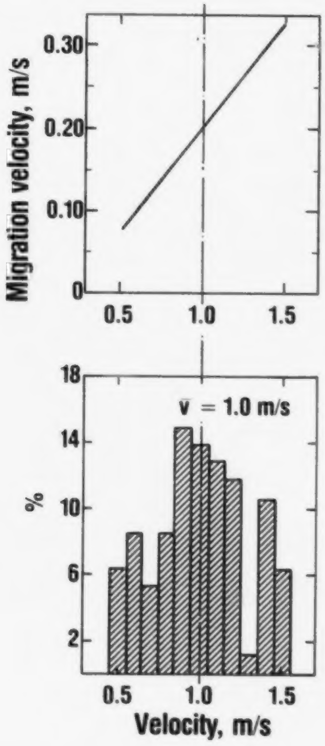

Figure 13. w = w(v)-dependency and an actual velocity frequency distribution used to predict the penetration from Eqn. 5 and Eqn. 8.

CONCLUSION

In general terms the ducting leading to the precipitator and the inlet and outlet funnels should be designed to ensure a proper gas velocity distribution in view of utilizing the whole collecting area and avoiding negative velocity effects. From a practical viewpoint this imply different requirements to the gas distribution in the different parts of the precipitator, and too strictly formulated numerical rules for deviation from uniformity may not be justified.

The inlet gas distribution must be sufficiently uniform to secure a reasonable uniform current distribution. This is especially important for precipitators for processes with high resistivity dust and fine particles.

At all places inside the precipitator compartment the gas distribution should be fairly uniform and special attention should be given to bottom peaks implying the risk of bottom sneakage and rapping reentrainment.

The velocity profile at the outlet should be specificly selected to reduce the risk of reentrainment in the bottom region.

Recent theories indicate that the gas velocity should be chosen higher than normally used today. However for precipitators specified for high efficiency the advantages of elevated velocity may be outbalanced by negative effects from the velocity such as increased gas sneakage around the electrically energized electrode systems and increased reentrainment in particular during electrode rapping.

Measurements reported in recent literature indicate an increase of migration velocity with gas velocity which may be introduced in the modification of the Deutsch equation, thus leading to a more moderate influence of gas distribution on precipitator performance.

REFERENCES

1. White, H.J., "Industrial Electrostatic Precipitation". Addison-Wesley Publ. Comp. 1963.

2. Allander, C. & Matts, S., "Einwirkung der Korngrössenverteilung auf den Abscheidungsgrad von Elektrofiltern". Staub (1957), Heft 52, pp738-745.

3. Idel'chik,I.E.& Aleksandrov, V.P., "The Effect of Nonuniformity of the Gas Flow on the Efficiency of Electrostatic Precipitators". Teploenergetika, 1974, 21, (8) 60-62, pp85-87.

4. Gooch, J.P., McDonald, J.R. & Oglesby Jr., S., "A Mathematical Model of Electrostatic Precipitation". EPA-650/2-75-037. April 1975.

5. König, W., "Zum Verhalten des Staubes im Elektrofilter". Dissertation, Technische Hochschule Stuttgart, 28.04.1965.

6. Weber, E. & Wiggers, H., "Untersuchungen an einem Laborelektrofilter über die Einflüsse der Gassenbreite und der Gasgeschwindigkeit auf das Abscheideverhalten und die Staubkonzentrationsverteilung". Staub-Reinhaltung der Luft, Bd.40 (1980), Nr.11 Nov., pp469-473.

7. Leonard, G., Mitchner, M. & Self, S.A., "Particle Transport in Electrostatic Precipitators". HTGL Report No.113. Dept. of Mech. Engineering. Stanford July 1979.

8. Larsen, P.S. & Sørensen, S.K., "Effect of Secondary Flows and Turbulence on Electrostatic Precipitator Efficiency". Atmospheric Environment, Vol.18, No.10, pp1963-1967, 1984.

DEVELOPMENT AND TESTING OF A COLLECTING CURTAIN FOR AN ELECTROSTATIC PRECIPITATOR

by: Heinz L. Engelbrecht and Robert J. McMullan
Wheelabrator Air Pollution Control
Technical Center
Coraopolis, PA 15108

ABSTRACT

Collecting curtains in an electrostatic precipitator (ESP) are part of the electrode system used to charge and precipitate particulates suspended in a gas stream. In addition to holding a layer of particulates for a predetermined time, the collecting curtain has to absorb and transmit rapping forces to release the precipitated particulates into the dust hopper.

Design criteria are outlined and the development of collecting curtains using electrical and mechanical performance evaluations is described. Electrical testing includes measurements of voltage gradients in a salt-water table, of current and voltage in a test stand with clean electrodes and under simulated high resistivity dust conditions, and of current density distribution. Mechanical testing includes measurements of rapping acceleration, rapping frequencies and stress levels. Development of the collecting curtain is completed by a comparative performance evaluation in a pilot ESP.

INTRODUCTION

Collecting curtains in an electrostatic precipitator (ESP) are part of the electrode system used to charge particulates suspended in the gas stream and are also the receptacle for these particulates once they are precipitated. This makes the collecting curtains unique as far as precipitator components are concerned. They come into the most direct contact with the particulates being precipitated and all particulates collected in any place of the ESP but on the collecting curtain have a harmful effect on the ESP performance and such collection has to be kept to a minimum if it can not be avoided at all. This statement obviously excludes direct fall-out of particulates into the ESP hopper while the ESP acts as a settling chamber.

To meet the requirements of collecting, holding, and intentionally releasing precipitated particulates, certain criteria have to be met by the collecting curtain. Some of these are contradicting, like having a smooth surface for equal current density levels and a baffled surface to prevent re-entrainment.

The designers of a collecting curtain usually start with developing several conceptual designs and select those which seem to be the most promising for future evaluation. This is an activity where everybody is interested in participating and even the most utopian ideas are actively pursued. This period of enthusiasm is followed by a period of serious evaluations and spending of substantial amounts of monies for prototypes and testing.

Today, we have the tools not to replace, but to back-up intuitive design selections with hard data. This paper is not a commercial presentation of a new product, but intended to outline the criteria and tests involved in the process of designing and optimizing a collecting curtain for an electrostatic precipitator.

DESIGN CRITERIA

To achieve the highest possible collecting efficiency requires that the collecting curtains meet the following criteria:

- An electrically smooth surface for a high breakdown voltage level
- Equal current density levels
- Holding capability to prevent precipitated dust from being re-entrained during normal operation and rapping periods
- Vibration characteristics that allows intentional removal of the precipitated dust layer with a minimum rapping impact
- Vibration characteristics which result in uniform rapping accelerations and minimize localized rapping stresses
- Physical strength and rigidity to prevent distortion during handling, shipping, and installing
- Suitability for maintaining straightness and alignment during precipitator operation
- Low weight per area

- Low fabrication and shipping cost

It should be noted that factory assembled curtains are also commonly used in electrostatic precipitators and offer adequate performance in many cases. This paper will concentrate on the development of a collecting strip, a multitude of which are field-assembled into collecting curtains.

Specific requirements for the new collecting curtain include:

- Produced by a roll-forming process
- Field heights up to 50 ft
- Field lengths up to 18 ft
- Useable with discharge systems having rigid frames or rigid electrodes
- Useable with bottom rapping systems with individual impact hammers striking each collecting curtain
- Stress levels below limits accepted as good engineering practice
- Minimum rapping acceleration levels of 100 g ($1g = 32.2$ ft/sec^{2})

A development program was started with the objectives listed above. The procedures employed and the results obtained are outlined in this paper.

DEVELOPMENT PROGRAM

A development program was set up to provide for an initial screening of various plate designs which included the following steps:

1) Electrical performance evaluation: a) simulation of iso-voltage lines in a salt-water bath, b) current/voltage data for "clean" and "dirty" electrodes, and c) current distribution mapping

2) Mechanical performance evaluation: a) plate rapping acceleration measurements, and b) measurements of rapping acceleration frequencies and stress levels

3) Flow model study

4) Comparative performance evaluations: a) pilot precipitator work using air/dust mixtures, and b) mobile precipitator work

using gas/dust mixtures

5) Use of new collecting curtains in a full-size installation

This program has led to the development of a collecting curtain which is intended for use in large industrial and utility electrostatic precipitators.

CONCEPTUAL DESIGNS

A collecting curtain is usually developed as an improvement over or a replacement of a previously used design. Based on the collecting curtain presently used for WAPC industrial and small utility precipitator applications, a systematic search for a new plate geometry was conducted. It is beyond the scope of this paper to list all alternative designs, but a selection of two, quite similar designs was made and prototype sections were obtained for future testing (Figure 1).

Considering the importance of electrical characteristics, these were tested first and the tests are described in the following section.

ELECTRICAL PERFORMANCE EVALUATION

The grounded collecting curtain is one of the electrodes in the precipitator and influences its current/voltage characteristics. The particulate collecting efficiency is a function of the specific electric power input (current times voltage divided by unit gas flow), thus it is imperative that the current (density) is uniformly high and the voltage is also at the highest suitable operating level.

SALT-WATER TABLE TEST

A salt-water table can be used to quickly and efficiently measure iso-voltage lines in a plate/wire geometry. The table itself consists of a stand with a deep basin of insulating material. The bottom plate is marked with a grid system to allow for positioning of the electrodes and location of the test points. The electrodes are made out of brass strips, approximately two-inches high and the basin is filled to 1.5 inches with an aqueous solution containing 0.1 N KCl. The "discharge electrodes" are located at the proper position between the "collecting electrodes" and a d.c. is applied to the electrodes, negative polarity to the "discharge electrodes", positive polarity to the "collecting electrodes" (Figure 2). The digital multi-meter was connected to the common ground or negative polarity of the power supply and the sensor connected to the positive lead of the multi-meter.

Testing is done by locating points with selected voltage levels, for example 4.5, 4.0, 3.5...0.5 in the salt-water bath representing the free space between the electrodes.

The following Figures are presented as examples of this work: a) collecting plates and wire discharge electrodes at twelve inches plate-to-plate spacing (Figure 3), b) collecting plates and rigid discharge electrodes (RDE) at twelve inches plate-to-plate spacing (Figure 4), and c) collecting plates and rigid discharge electrodes at fourteen inches plate-to-plate spacing (Figure 5).

The iso-voltage lines closest to the "collecting plates" hug the contour of the plates, whereas the lines closer to the "discharge wires" clearly show the influence of their location relative to the "collecting plates" and to the adjacent "discharge wires". Comparing the iso-voltage lines obtained in the tests using "rigid discharge electrodes", the decreasing influence of the shape of the "collecting plates" with increasing plate-to-plate spacing is clearly visible.

These tests allowed a cursory evaluation of various plate designs and completed the first step of the evaluation process.

CURRENT/VOLTAGE DATA

A high-voltage test stand is used for the evaluation of the current/voltage data. Plates for the test stand measure 6' x 6' for a total collecting plate area of 72 square feet for a single gas passage. The T/R and control set can supply 70,000 volts, 50 ma, d.c.

A prototype plate was used with different discharge electrodes. Wide body RDE's and rigid frame designs with spiked wires were evaluated. Two test conditions were used, clean plates and plates covered with polyethylene to simulate a high resistivity dust layer on the collecting plates. Modifications were made to the discharge electrodes during the project for the purpose of determining the best possible distribution of corona generating points. All tests were run using plate spacings of 10, 12 and 14 inches.

Digital voltage and milliamp meters along with a data terminal and computer were used for acquisition and processing of the current/voltage data. Analyzing data obtained for the rigid discharge electrodes show a shift in the I/V curves with the simulated dust layer. This indicates back corona was produced. However, the data show the back corona shift was not severe until about 3.0 KV/cm. This seems to indicate corona current is evenly distributed at the plate surface for both test conditions (Figure 6).

Comparison results of the RDE with six versus three inch spaced spikes shows the RDE with three inch spaced spikes providing a greater current density. However, the current density increase was less than 20% for a doubling of the spikes over that of the six inch spaced spike RDE (Figure 7).

Comparing the results at different plate spacings, the data show that for a given electrical field, E (kV/cm) a corresponding current density, J (na/cm^2) is produced (Figure 8).

Results of the tests with spiked wires mounted in a rigid frame at varied plate spacings show a similar consistency in the data with that of the RDE at varied plate spacing. However, comparing the spiked wires and the RDE, the data show the spiked wires generally produced a higher current density than the RDE.

CURRENT DISTRIBUTION MAPPING

Current density mapping is done on a test stand which holds the collecting plates and the discharge electrodes. One of the collecting plates is a normal plate segment, whereas the opposite plate is divided in a large number of current sensing coupons. The degree of resolution of the measured current levels increases with the number of coupons. Each coupon is electrically isolated and connected to ground in series with a 1000-OHM resistor. A digital voltmeter measures the potential across the resistors. The current density on each coupon can be calculated from the measured value and the known coupon area. The test stand is energized by a 150 KV, 10 ma power supply.

Using a standard plate/wire arrangement to which all other electrode performances are compared, the following parameters can be evaluated: a) corona onset voltage, b) sparkover voltage, c) current density pattern, and d) corona power characteristics (current versus voltage).

The test procedure has been standardized for each individual test. To map the corona current densities under stable conditions, the current is adjusted to approximately 1.5 ma for a current density of 0.25 ma/ft^2 (2.7 ma/m^2). Data is taken by stepping through each individual coupon.

A typical plate segment approximately twenty inches wide and twenty-four inches high contains 480 one square inch coupons some of which are again divided. It proved to be too time consuming to manually handle this test and the device is being modified for an automatic data acquisition system.

MECHANICAL PERFORMANCE EVALUATION

Mechanical performance evaluation of a candidate for a collecting curtain focuses on the following requirements: a) high physical strength to withstand rapping forces and also to remain properly aligned, and b) favorable acceleration characteristics to dislodge the accumulated dust when the plate is rapped.

High physical strength can be achieved by making the curtains out of single stiffened plates or individually roll formed strips. The collecting curtain being evaluated is a roll formed strip with three pockets per strip and C-shaped ends for added rigidity.

In order to evaluate the collecting plate for acceleration characteristics, a full scale plate was assembled in WAPC's test tower. The plate consisted of eight strips, 18 gage, 20" wide x 41'6" long. The curtain is supported at the top by two hangers per strip and connected at the bottom by a rapper bar.

Rapping force is applied to the anvil of the rapper bar by a single, rotating tumbling hammer. During operation, the hammer shaft rotates and after the hammer reaches a position with the hammer head vertically above the rotating support point, the hammer falls by gravity and strikes the anvil. Rapping accelerations are then transmitted through the rapper bar into the collecting curtain.

A rapping impact causes a compression-tension stress wave which propagates at the speed of sound in steel throughout the collecting plate. This wave generates an acceleration component in the plane of the plate. In response to the compression-tension wave, a flexural or bending stress wave is generated, which propagates at a slower speed than the compression-tension wave. The flexural wave produces acceleration normal or perpendicular to the surface of the plate. Although there are differences of opinion as to which acceleration (parallel or normal) is most effective in removing precipitated dust from the collecting plate, WAPC measures and reports peak acceleration normal to the surface of the collecting plate.

RAPPING ACCELERATION MEASUREMENTS

For a utility collecting plate, it is desirable to achieve a minimum acceleration of 100g (1g = 32.2 ft/sec^2) measured normal to the collecting surface. Measurements of the plate accelerations are made at a suitable number of test points on the collecting surface to determine if this requirement is met.

All acceleration measuring equipment presently being used has been supplied by Bruel and Kjaer (B&K). There are three major components in the acceleration measuring system: (1) accelerometers, (2) charge amplifiers, and (3) peak holding voltmeters (Figure 9). Most collecting plate acceleration measurements utilize the B&K Type 4344, piezoelectric accelerometer. This accelerometer weighs two grams bare, but has an effective weight of 2.3 grams with the cable attached. The frequency response extends to 21 KHz and the sensitivity is approximately 0.30 pc/ms^2. The B&K Type 2635 Charge Amplifier is used to amplify the signal generated by the piezoelectric accelerometer. The charge amplifier also eliminates the effect of cable capacitance so that different lengths of cable can be used. The output of the charge amplifier is input to a B&K Type 2427 Autoranging Digital Voltmeter.

This instrument measures and holds the peak positive or negative impulse signal. A B&K Type 4291 Calibrator is used to check the sensitivity factor of the accelerometers. For in-depth evaluations, the output of the charge amplifier can be input to an oscilloscope or spectrum analyzer for time/amplitude and frequency/amplitude analyses.

A fast curing adhesive is used to secure the accelerometers in place. The attached cable is also secured to the collecting plate. Accelerometers are generally mounted at various elevations in the center of each strip forming the collecting curtain assembly. The measured peak acceleration will vary for each impact. Therefore, the acceleration at any given point on a collecting plate is defined as an average of at least ten measurements. Where the standard deviation is large, more measurements may need to be averaged to produce acceptable data.

Even though the mass of the accelerometer is only about two grams, the weight of the accelerometer affects the measurement of the peak acceleration. A correction factor can be obtained to compensate and is determined by measuring the acceleration at a single point with the bare accelerometer and then with 1, 2, 4, and 8 gram weights added under the accelerometer. The added mass results in lower measured acceleration. A mathematical curve fit of the relative acceleration versus mass can be extrapolated to zero mass (Figure 10). The ratio of the "zero mass" acceleration to that with the mounted accelerometer and cable can be used to multiply the measured acceleration at any point to produce a "mass corrected" acceleration value.

For this testing, a total of forty-eight acceleration measurements were taken at selected heights on the eight strips to achieve an acceleration contour. Thirty-five data points at each accelerometer location were taken by a computerized data acquisition system which controls operation of the rapper and data gathering. Data is reported as follows: a) arithmetic average of each test point, b) standard deviation at each test point, c) arithmetic average of the acceleration in one collecting strip, and d) arithmetic average of the rapping acceleration in one collecting curtain.

Selected test data for rapping acceleration using a 20 pound hammer are shown on Figure 11, using a 12.4 pound hammer on Figure 12. Rapping acceleration contours are shown on Figures 13 and 14, respectively. As expected, high accelerations occur near the point of impact and decrease with increasing distance from this point.

Further test results showed that an adequate (greater than 100g) minimum rapping acceleration could be achieved throughout the collecting curtain even when using a 10.25 pound hammer.

STRESS MEASUREMENTS

The collecting plate, supports, and rapper assembly are designed to withstand the rapping forces applied to the assembly by the tumbling hammer. Determining if the stress values are acceptable is required and this involves installing strain gages to measure the dynamic stresses at selected areas. Output from the strain gages was sent through a conditioning amplifier to a Nicolet Oscilloscope which displayed: a) stress versus time and b) frequency (modal analysis) versus stress. The stress versus time display enables the maximum stress to be determined while the frequency versus stress display enables one to determine at what frequency (Hz) the maximum stress occurs. This is useful in analyzing how the rapping force is transmitted to the plates and how the components are coupled.

LIFE TIME TESTING

An important step in the design of a new collecting curtain is the evaluation of its expected lifetime under actual operating conditions. Since operating conditions, such as gas temperature, corrosion, erosion by dust particles cannot readily be simulated, one depends on lifetime testing of rapping effects on the collecting curtain and associated hardware at ambient conditions.

It is normally sufficient to test the end connections of the collecting curtain only, since failures occur predominantly in these areas. It is warranted that a full-scale collecting curtain is used for testing with the exception of plate height, which can be substituted by equivalent weights added to the collecting curtain.

Lifetime testing is done under an accelerated rapping schedule to compress as much lifetime as possible into the available test time. Accelerations of 1 to 20 are feasible considering a prototype rapping system operating at a frequency of thirty raps per hour.

FLOW MODEL STUDY

Electrostatic precipitation of particulates is also a function of the dispersion of particles generated by the turbulence of the gas flow and the influence of the electrical wind generated by the corona on the discharge wires. Influences of plate and wire geometry and of other obstacles located in the gas stream are obviously also important. The latter can readily be evaluated using a two dimensional flow model study using water flow instead of gas flow and visualizing the flow pattern by adding a dye or a powder (for example aluminum oxide) to the water and recording the pattern by photography or video recording to provide indications of the location of quiescent zones where dust particles can be collected and shielded from the main gas flow to prevent re-entrainment, particularly during plate rapping.

PILOT PREÇIPITATOR

WAPC's pilot precipitator is used to evaluate collecting and discharge electrodes for: a) current/voltage characteristics for various electrode combinations, and b) collecting efficiency for various electrode combinations.

The pilot ESP is a two field and two gas passage unit. Each field can accommodate collecting plates up to 24" high by 57" long with a maximum plate spacing of 20". Gas flow into the ESP is controlled by an induced draft fan. A set of heater banks up-stream of the ESP is used to vary gas and dust temperature. Power input to each ESP field is controlled by a variable power supply. Testing can be done at a specified power input by selecting current or voltage levels.

Efficiency is calculated from the amount of particulate entering and exiting the ESP. Inlet and outlet loadings are assessed by an optical particle counter (OPC). The OPC is a laser-based particle measuring scattering aerosol spectrometer with four 15-channel particle size ranges. Sampling is controlled by solenoid valves and the OPC counts particles of a 12:1 diluted sample for time intervals of 30-120 seconds. An HP-85 computer is used to control the solenoid valves and to compute the data.

Current/voltage data corresponded to the data obtained in the high voltage test stand and only ESP performance using the above electrodes will be reviewed. Each collecting plate/discharge electrode combination was tested under ambient or high air temperature and at constant current or constant voltage conditions.

The following graphs show the collecting efficiencies of particle sizes in channel No. 2 (0.50 to 2.75 m) as examples of this work: a) spiked wire electrode (Figure 15) and b) rigid discharge electrode (Figure 16). The higher voltage of the rigid discharge electrode (38 versus 30 KV) at 0.50 mA resulted in a higher average collecting efficiency (59.2 versus 46.1 percent) for this particle size range.

MOBILE ELECTROSTATIC PRECIPITATOR

The next step will be to test the new collecting curtain in a pilot precipitator in the field under actual operating conditions. The mobile electrostatic precipitator (MESP) used by WAPC is a three field trailer-mounted unit complete with automatic voltage controls, rappers, vibrators, hoppers and an induced draft fan capable of handling 9000 ACFM at 700°F. The collecting surface plates are 6'-6" high by 6'-3" long. The plate spacing can be 10", 12", 14", 16", 18" and 20". Discharge wires mounted in rigid frames or rigid discharge electrodes can be used. The plate rapping system uses rotating hammers. The discharge electrode rapping system uses externally mounted vibrators.

The automatic voltage controls are modified Allen-Bradley Bulletin 1082 AVCs. The transformer/rectifiers (T/Rs) have variable tap transformers rated at 45 KV, 60 KV, and 75 KV at secondary current of 50 ma.

CONCLUSION

The development of a collecting curtain for an electrostatic precipitator was traced through the initial design steps, electrical, mechanical and performance testing.

This developmental program is only one of the many programs conducted by manufacturers of electrostatic precipitators. They provide the improvements which keep the electrostatic precipitator a viable solution to many utility and industrial particulate emission problems, 101 years after Walker and Hutchings made the first attempt to apply electrostatic precipitation commercially.

The work described in this paper was not funded by the U.S. Environmental Protection Agency and therefore the contents do not necessarily reflect the views of the Agency and no official endorsement should be inferred.

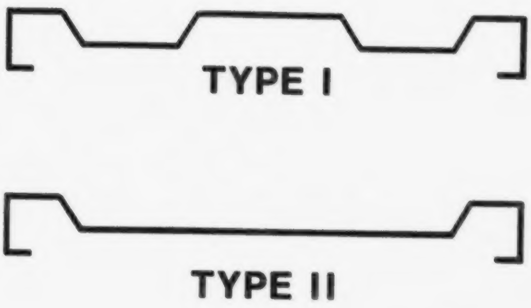

Figure 1. Conceptual designs of a collecting plate

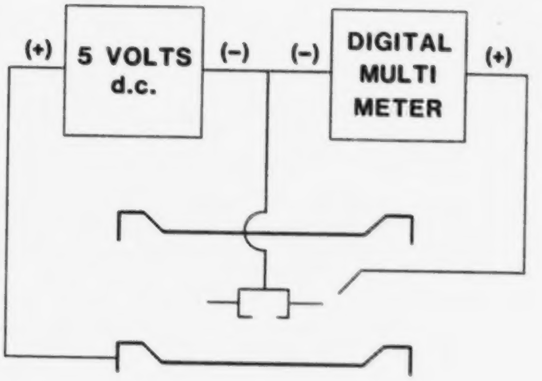

Figure 2. Salt-water test stand

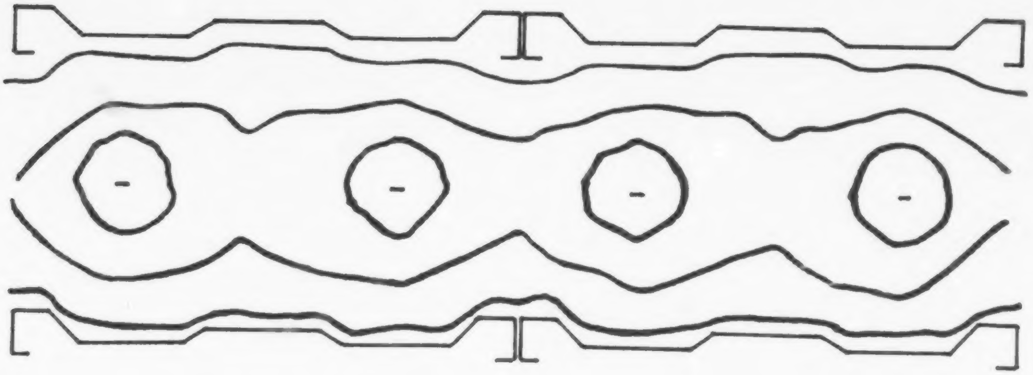

Figure 3. Wire electrode at 12" plate spacing

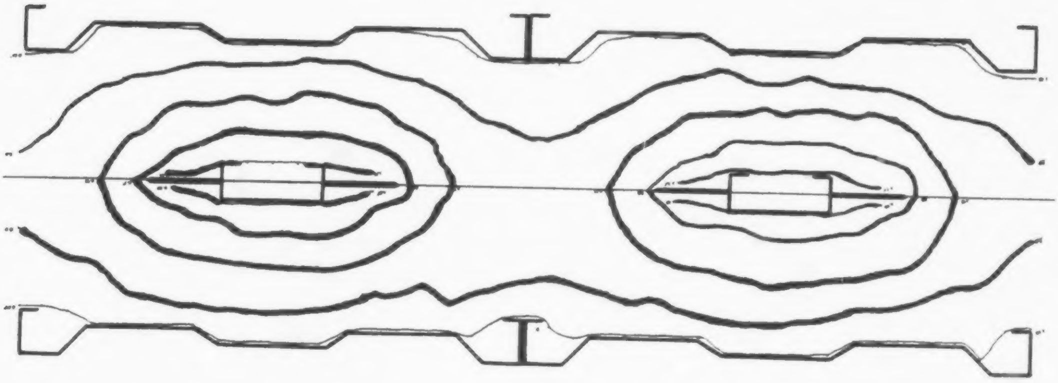

Figure 4. Rigid discharge electrode at 12" plate spacing

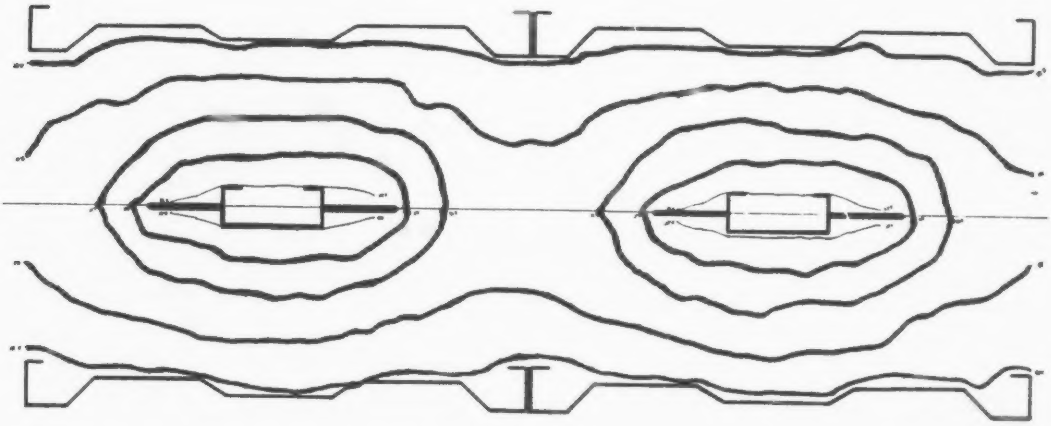

Figure 5. Rigid discharge electrode at 14" plate spacing

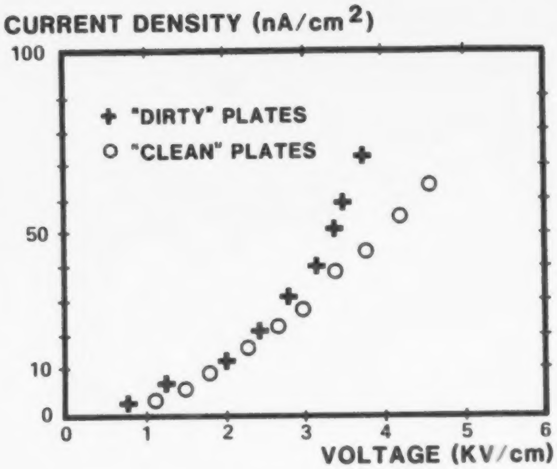

Figure 6.
I/V curve for rigid discharge electrode with "clean" and "dirty" collecting plates

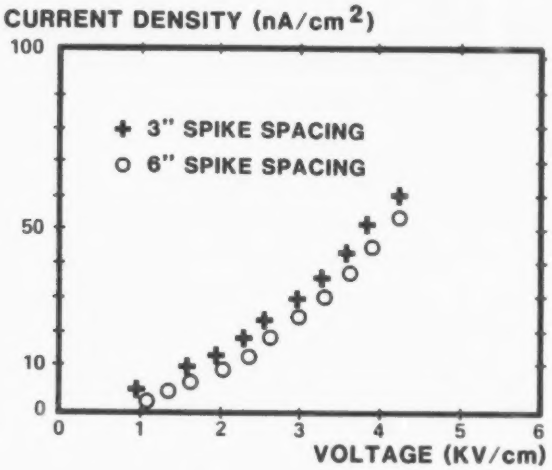

Figure 7.
I/V curve for rigid discharge electrode with 3" and 6" spike spacing

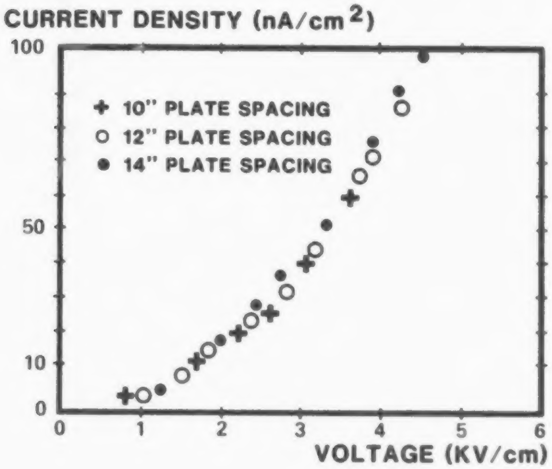

Figure 8
I/V curve for rigid discharge electrode with 10", 12" and 14" plate spacing

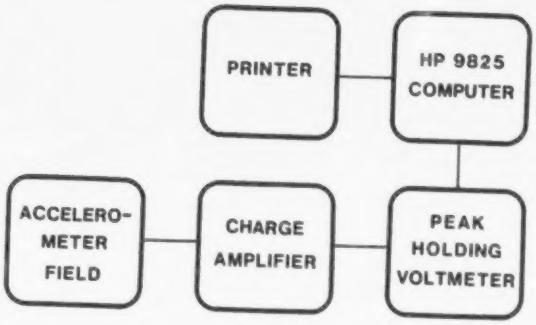

Figure 9. Rapping acceleration test equipment

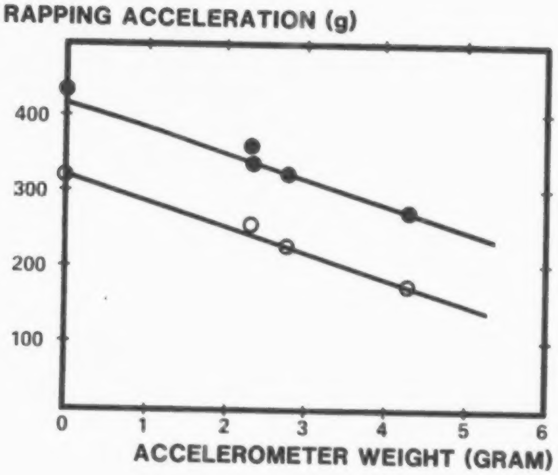

Figure 10. Relative rapping acceleration versus accelerometer weight

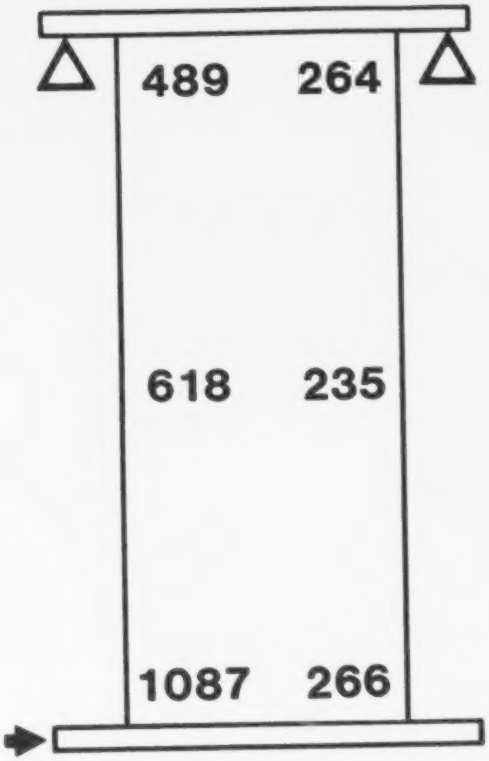

Figure 11.
Rapping acceleration test data using 20-pound hammer

Figure 12.
Rapping acceleration test data using 12.4-pound hammer

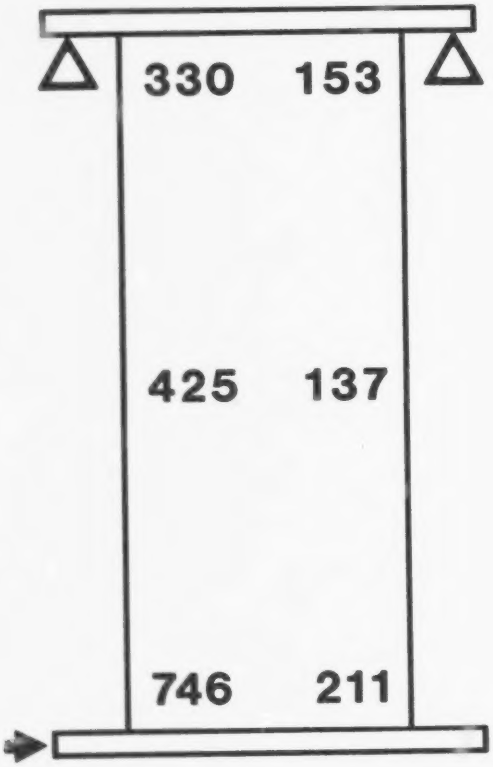

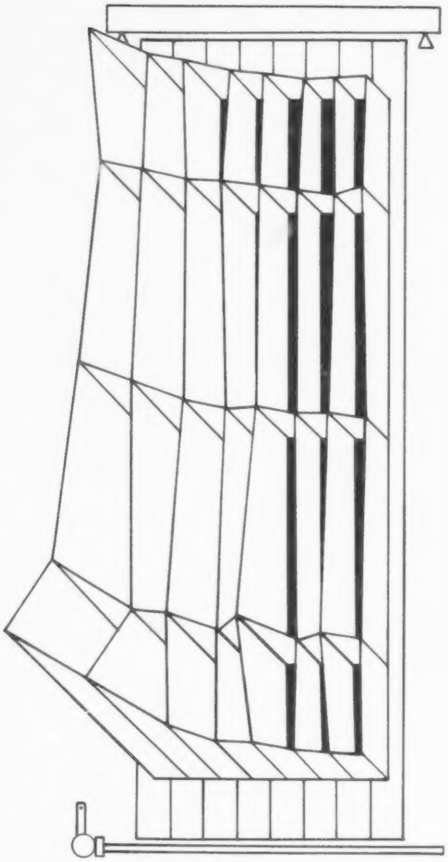

Figure 13.
Rapping acceleration pattern using
20-pound hammer

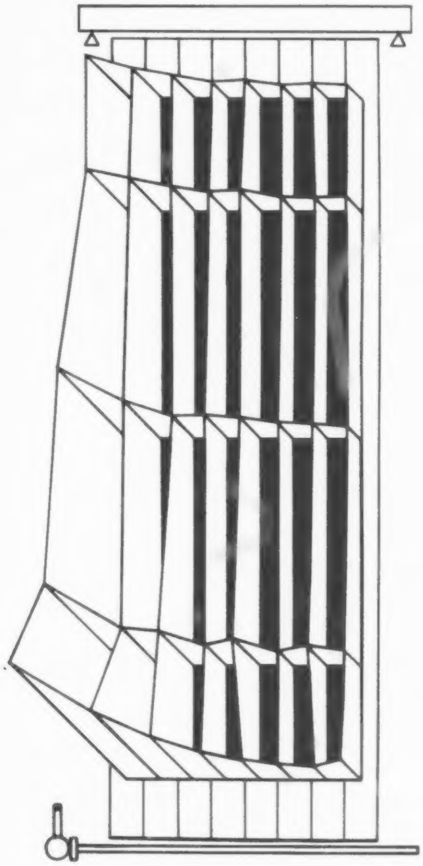

Figure 14.
Rapping acceleration pattern using
12.4-pound hammer

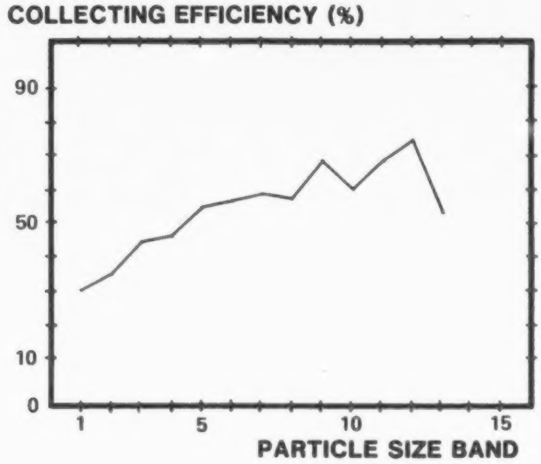

Figure 15. Pilot precipitator collecting efficiency using spiked electrodes

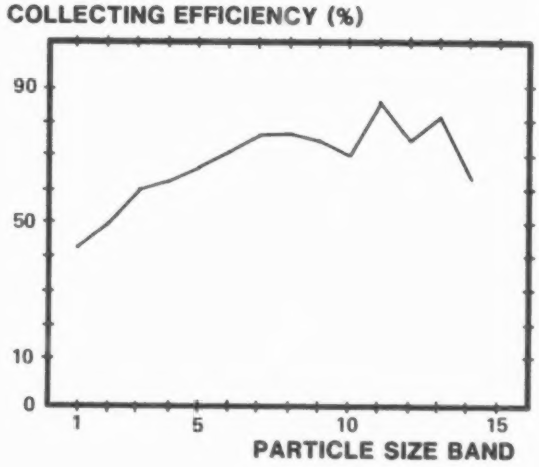

Figure 16. Pilot precipitator collecting efficiency using rigid discharge electrodes

CHARACTERIZATION OF DISCHARGE ELECTRODE PERFORMANCE: RESULTS OF LABORATORY AND PILOT PLANT EXPERIMENTS

by: L. A. Hawkins and H. L. Wheeler
Combustion Engineering, Inc.
Environmental Systems Division
P.O. Box 43030
Birmingham, Alabama 35243

INTRODUCTION

The Environmental Systems Division of Combustion Engineering, Inc. (C-E) has over ten years' experience designing and building electrostatic precipitators (ESPs) for industrial and utility markets. C-E's design has historically been a rigid-frame discharge electrode system with 11 or 12 inch plate spacing. As part of an extensive research and development program begun four years ago, several projects were initiated to further improve the design of the current ESP offering. Two of these projects recently came to fruition.

The first project was to develop a marketable rigid discharge electrode design. The new design would be cost efficient, reliable and capable of maintaining ESP performance with power consumption equivalent to electrodes currently in use. The project to develop the new electrode was divided into two phases - a screening process to select an electrode with desirable electrical characteristics and a pilot study to evaluate the selected electrode under operating conditions.

The barb electrode and the star electrode, shown in Figure 1, are C-E's traditional electrodes. The barb electrode is a high-power electrode, that is, it produces substantial corona current at a given voltage. The barb electrode was originally used in all fields of the ESP, but in most applications this electrode uses more power than necessary in the outlet fields. The star electrode, a low-power electrode, was introduced six years ago for use in the outlet fields of the ESP. The star electrode allows higher spark voltages and substantially reduced current levels. Using the barb electrode in the inlet field and the star electrode in the remaining fields results in substantial power savings. The combination of the barb and the star electrodes has produced excellent results. The rigid discharge electrode that was selected in this project is also shown in Figure 1. C-E's new patented electrode (U.S. Patent No. 4,521,229) is a studded tube electrode (STE).

The second project was a pilot test of C-E's electrode system with a plate spacing of 16 inches. C-E and the Electric Power Research Institute (EPRI) recently conducted a test program to evaluate the effects of increasing plate spacing and applied voltage on ESPs. Preliminary results have been reported (Ref. 1) and they indicate that performance of a precipitator can be maintained while plate spacing is increased providing secondary voltage is increased commensurately. This result was conclusive only for high resistivity applications (1×10^{12} ohm-cm). The test program was conducted at EPRI's Arapahoe Test Facility, and the pilot precipitator used round wire discharge electrodes and flat plate collecting electrodes. An economic analysis (Ref. 1) indicated that a cost savings of 10-15% could be realized if plate spacing is increased from 9 to 16 inches.

The C-E pilot precipitator was used to verify the results obtained in the Arapahoe study and to establish the operating parameters for C-E's standard discharge electrodes and collecting plates, Figure 1, when plate spacing is 16 inches. The results of this study are reported here.

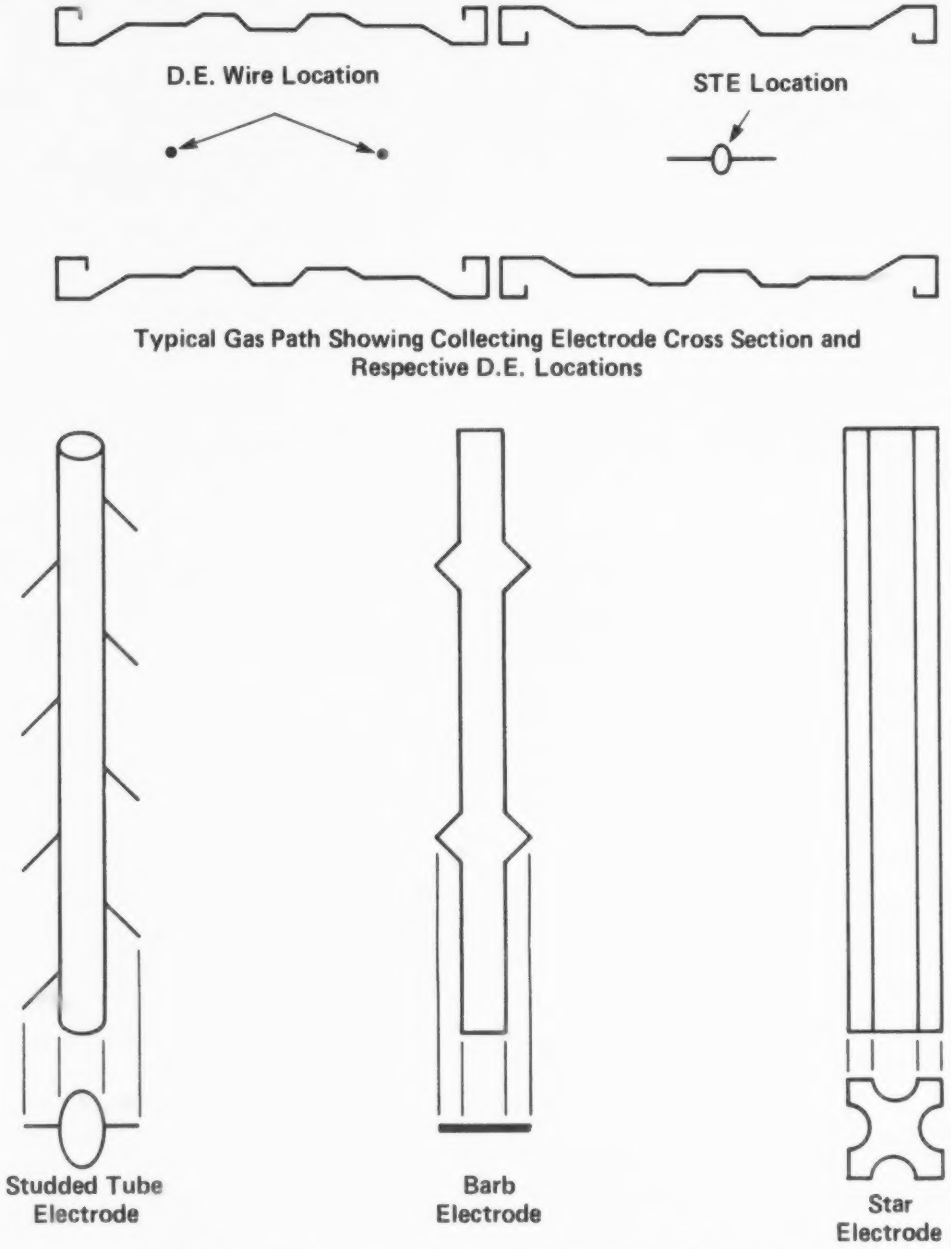
D.E. Wire Location
STE Location
Typical Gas Path Showing Collecting Electrode Cross Section and Respective D.E. Locations
Studded Tube Electrode
Barb Electrode
Star Electrode

Figure 1. Discharge and Collecting Electrode Configuration.

ELECTRICAL CHARACTERIZATION TESTS

A discharge electrode development program was initiated to evaluate various discharge electrode configurations and, from these evaluations, develop an efficient, marketable rigid discharge electrode. The first phase of the development program was a screening process - many different configurations were characterized electrically and those that met all the selection criteria were chosen for pilot testing. The selection criteria were as follows:

(a) Reliability - The new electrode must be of a rigid type that can be expected to be unbreakable.

(b) Cost Effectiveness - The new electrodes must be economical to fabricate and erect.

(c) Good Current Distribution - The new electrodes must have an ionic current distribution measured at the collecting electrode that is at least as uniform as the current distribution of the barb electrode.

(d) Desirable Voltage/Current Characteristics - The new electrodes must have a voltage/current characteristic curve that falls between the characteristic curves of the barb electrode and the star electrode.

The electrode types that were characterized electrically are shown in Figure 2. The rod type electrodes, which include the barb and star electrodes, are traditional electrodes and were included to provide a baseline for the electrical characterization. The plate and pipe/stud electrodes meet both the reliability and the cost effectiveness criteria.

The electrical characterization was conducted at C-E's High Voltage Test Facility (HVTF) located in Helena, Alabama. A test frame was erected which allowed electrical energization of a discharge electrode placed between two 19 inch wide collecting electrode panels. The panels were eight feet tall and the discharge electrodes were six feet long. Two rod type electrodes were used per 19 inch panel. When testing either the plate type or the pipe/stud type, only one electrode was used. Ascending and descending voltage/current characteristic curves were taken for each discharge electrode configuration tested.

Current distribution was measured for each discharge electrode using a segmented sensor panel attached to the collecting electrode panel. The arrangement is shown in Figure 3. The sensor panel was segmented to measure a horizontal distribution, and the entire panel could be moved vertically allowing a two dimensional current distribution measurement.

A total of 58 evaluations were made on 39 different discharge electrode configurations. The testing on each type of electrode followed the same procedure. The basic shape was tested and the results were evaluated to determine what modifications could be made to enhance the electrical characteristics. The modifications were implemented and evaluated. This procedures was repeated several times for each electrode type, until it was determined that further modifications would be pointless. The number of configurations of each electrode which were tested are listed below:

Basic D.E. Type	No. of Configurations Tested	Total No. of Tests
Rod	12	20
Plate	14	18
Studded Tube	13	21

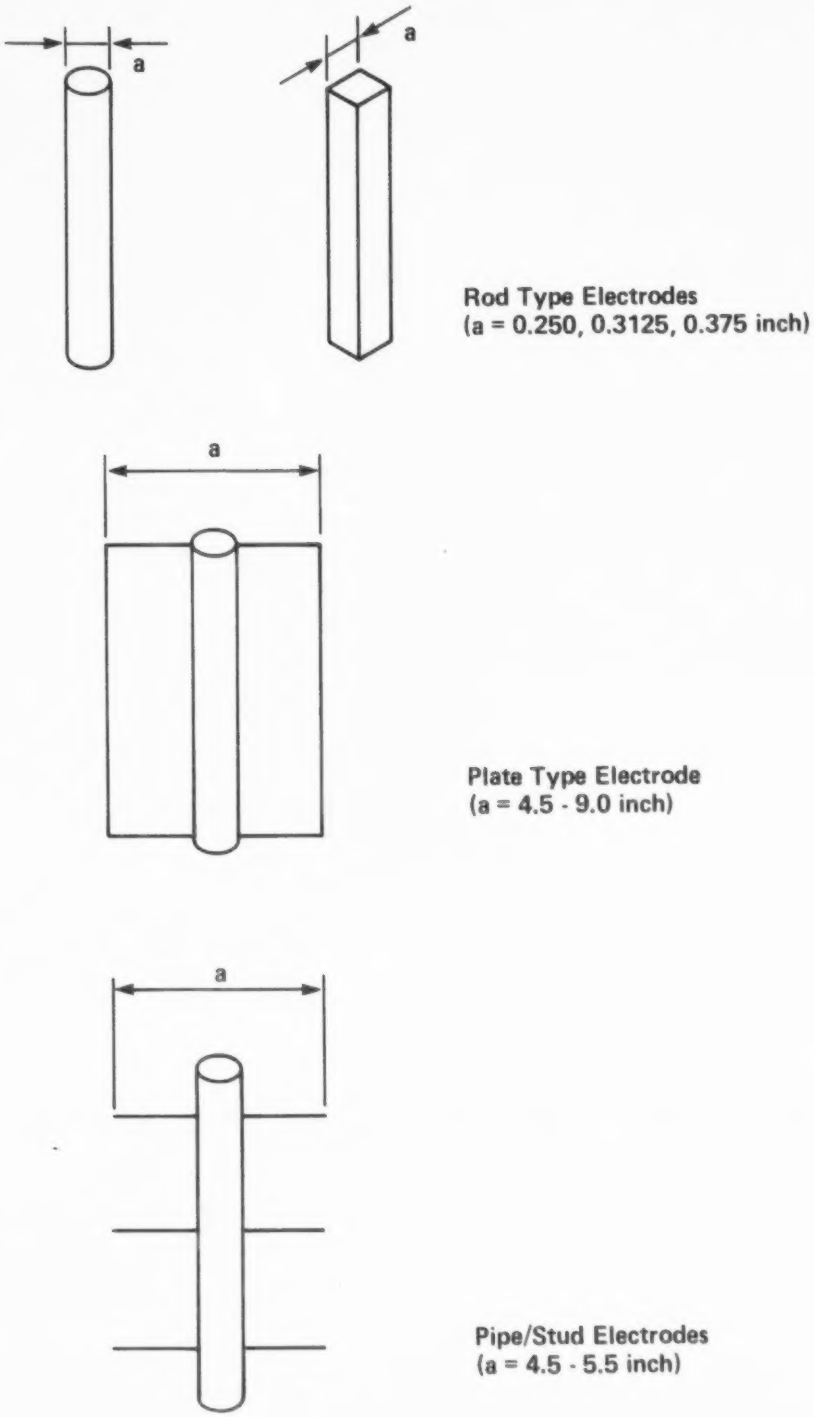

Figure 2. General Classification of Rigid Discharge Electrode Configurations Investigated

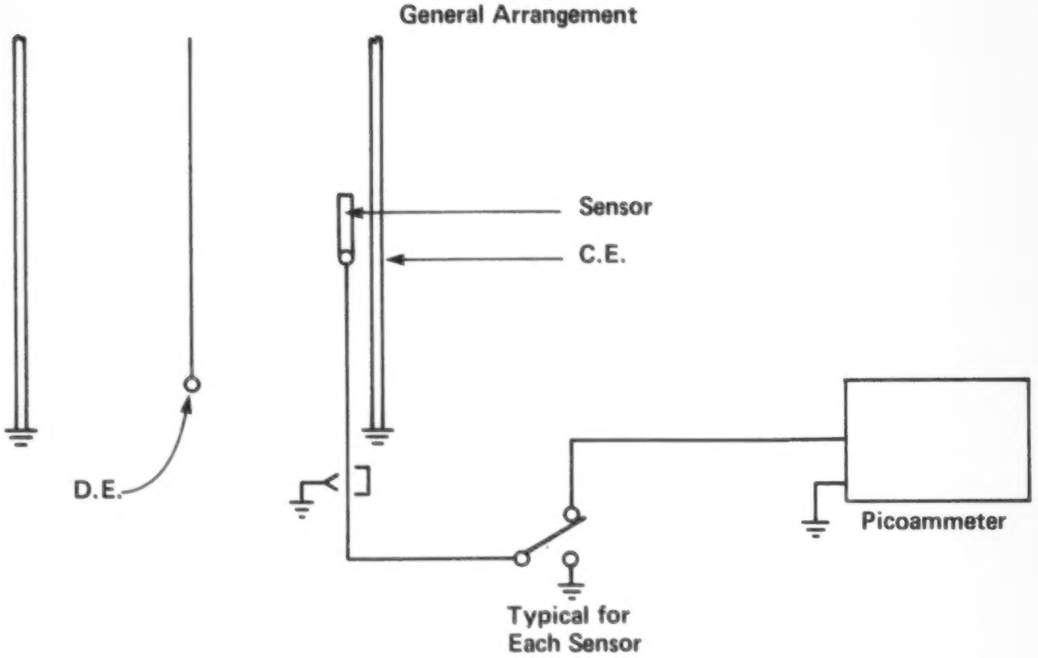

Figure 3. Current Density Distribution Measurement Apparatus

Each type of electrode tested could be modified to produce the desired voltage/current characteristic; therefore, the governing selection criteria became the uniformity of the current distribution. A uniform current distribution is important if maximum efficiency is to be achieved because it will allow the highest possible voltage and total current. Regions of the plate receiving higher than average current density will suffer electrical breakdown at a lower voltage than if current density was uniform. Also, regions of the plate receiving low current density will be subject to a low ash layer holding force and may experience excessive reentrainment if ash resistivity is low.

The barb electrode was used as a baseline to ensure that the efficiency of any discharge electrode selected would match, or exceed, that of the barb electrode. The current distribution produced by the barb electrode is shown in Figure 4. The current is high opposite the wire and falls off between the wires. All rod type electrodes tested produced a similar distribution. However, rods with no specific corona sites (barbs) produced more uniform distributions. The most uniform distributions measured were from 3/16 to 5/16 inch square rods. The star electrode is essentially a 3/16 inch square rod, and it produced the same current distribution.

The plate type electrodes produced the most non-uniform distribution. The area of the collecting electrode opposite the plate electrode receives little current. Very high current is received opposite the edges of the plate electrode and the current level falls off from that point to the edge of the collecting electrode. The uniformity of the current distribution can be improved by decreasing the width of the plate electrode. Plate electrodes that were tested ranged from 4.5 to 9 inches in width.

The current distribution produced by one of the studded tube electrodes is shown in Figure 4. The lowest current is opposite the tube and the highest current opposite the tips of the pins. Several studded tube configurations produced a current distribution better than the barb electrode. The best distribution was produced by a 1-1/2 inch tube with pins at a 45° angle to the tube. A sketch is shown in Figure 1. This configuration of the studded tube electrode (STE) was chosen for evaluation in the pilot plant.

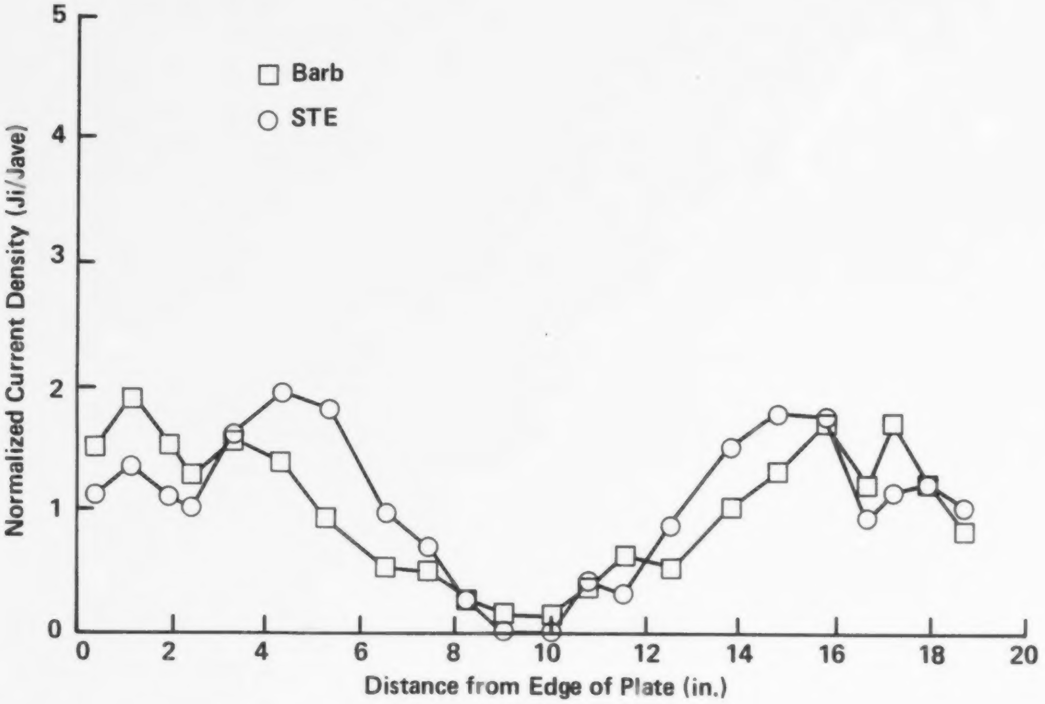

Figure 4. Discharge Electrode Evaluation, Current Density Distribution, Helena Test Facility, Air Load

PILOT TEST PROGRAM

The barb electrode, the STE and the star electrode were each tested separately in a pilot precipitator with 12 inch plate spacing. The testing was performed to compare the efficiency of the STE to the two standard electrodes, to obtain operating voltage/current characteristics for the STE, and to obtain operating current distribution data on the three electrodes. The results have been used as scale-up data for the STE and as an initial calibration point for the STE in C-E's computer design program (Ref. 2).

The barb electrode and the star electrode were also tested with 16 inch plate spacing. The data collected were used in conjunction with the 12 inch plate spacing data to verify the results of the Arapahoe study, and to establish the operating parameters for the barb electrode and the star electrode when plate spacing is 16 inches.

All pilot testing described herein was performed using a three-field pilot precipitator installed at a coal fired utility steam plant. The 3600 acfm pilot has a treatment length of 14.4 feet and a plate height of 5 feet. When plate spacing is 12 inches, the pilot has four gas ducts and an SCA of 160 ft^2/1000 acfm. The pilot has three gas ducts and an SCA of 120 ft^2/1000 acfm when plate spacing is 16 inches. Each TR set is controlled by a CE Model 80 AVC. The collecting plates and wire frames are rapped from the top using pneumatic rappers. Ash is moved from the hoppers into a vacuum removal system by air lock feeders.

Collection efficiency was measured by simultaneously measuring dust concentration at the inlet and the outlet of the precipitator using EPA Method 17. Four test runs were conducted for each electrode configuration. Electrical operating conditions were recorded several times during each test run and averaged to produce one set of readings for each field for each test series. Coal and ash samples were collected during each test series. Prior to each test run the outlet field collecting plates and discharge electrodes were rapped manually, and the outlet rappers were turned off until completion of the test run. Voltage/current data were taken under air load and under operating conditions.

Each time the electrode configuration was changed, the precipitator was washed down and then operated continuously on the gas stream for three to five days to allow it to reach stable operation. Throughout all the pilot testing, the coal burned at the host plant was quite consistent in composition. Coal sulfur content was 0.8-1.0%, flue gas moisture was 6-8% and ash sodium content was 0.15-0.40%. Resistivity varied in a narrow range around $1x10^{12}$ ohm-cm.

Summary efficiency test results are shown in Table 1. The efficiency with all three electrodes at 12 inch plate spacing was roughly the same, with the STE slightly better than the barb electrode and the star electrode slightly better than the STE. The differences in the efficiencies can probably be attributed directly to the differences in the operating voltages. These results indicate that an ESP using the STE can achieve the same collection efficiency as an ESP using the barb and star electrodes.

TABLE 1. PILOT PRECIPITATOR PERFORMANCE SUMMARY

INTERNAL CONFIGURATION (Plate Spacing/Discharge Electrode)	12/BARB	12/STE	12/STAR	16/BARB	16/STAR
SCA (ft^2/1000 acfm)	157	159	161	116	115
Efficiency (%)	93.81	94.20	94.52	95.1	96.6
Migration Velocity (cm/s)	9.0	9.1	9.2	13.4	15.0
Average Voltage (kv)	38	39	42	50	52
Average Current Density (nA/cm^2)	18	18	11	16	12

The STE was expected to produce less current under operating conditions than the barb electrode. The STE is a lower power electrode under air load conditions, Figure 5, but this is true only above 35 KV. The two electrodes are similar in the operating range of 25-40 KV, Figure 6, and similar power consumption should have been expected at these power levels. The voltage/current characteristics of the STE can be altered based on the electrical characterization tests by changing pin spacing, pin length and pin end treatment. A reduction in power consumption for the outlet fields might be desired on an ash of high resistivity like the one in this test. The STE as configured would use less power than the barb electrode when collecting a lower resistivity ash.

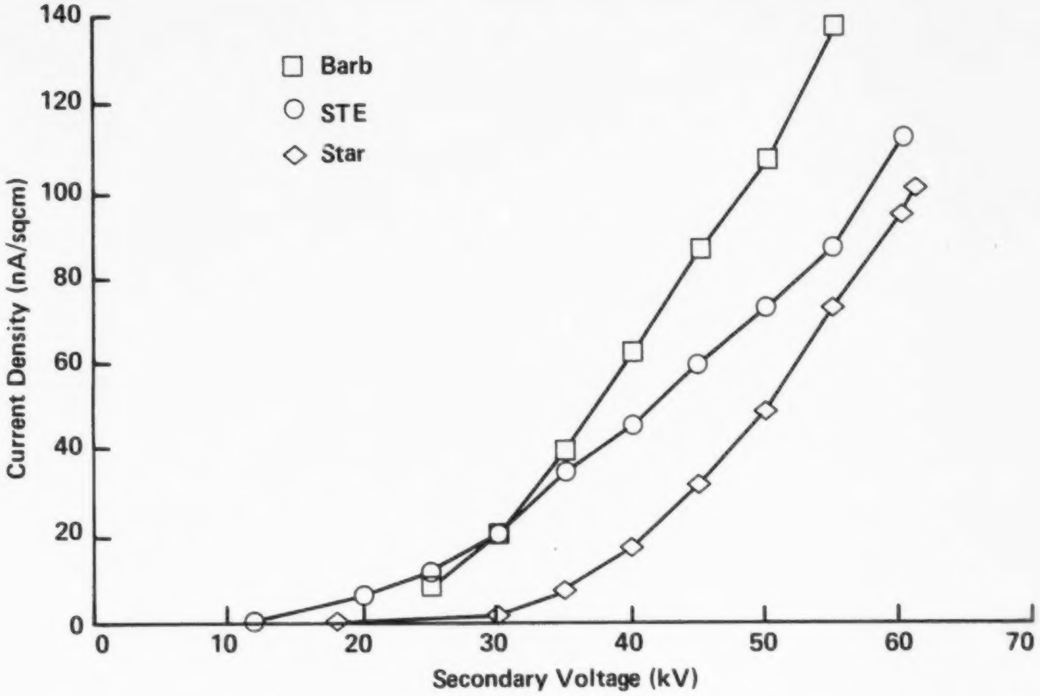

Figure 5. ESD Pilot Precipitator, Clean Plate, Air Load - V vs J, 12 in. Plate Spacing

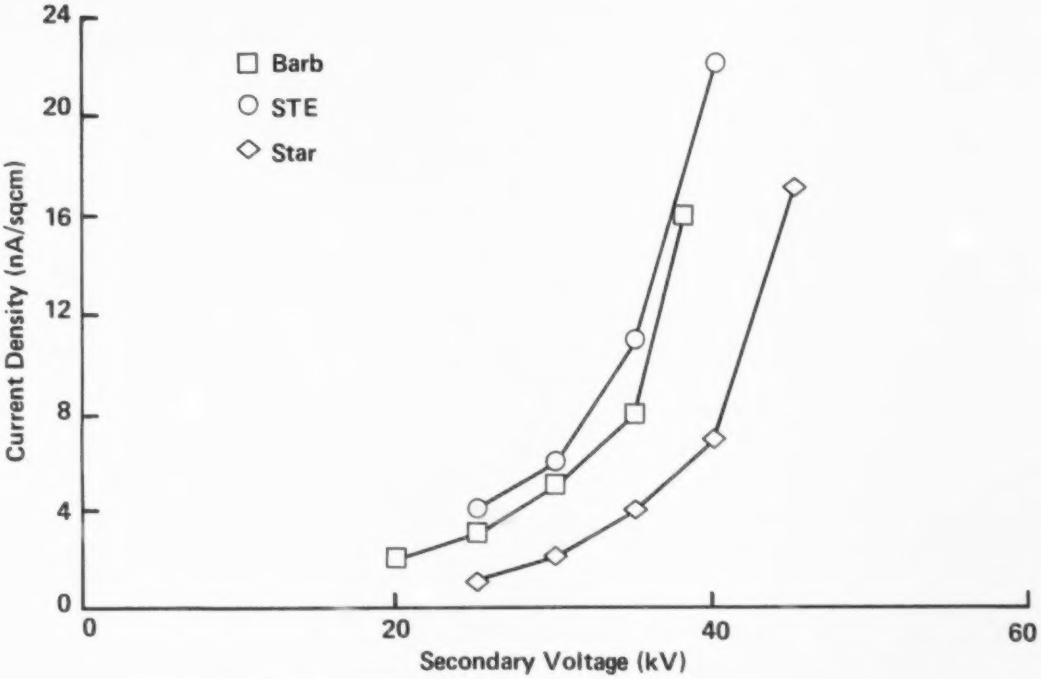

Figure 6. ESD Pilot Precipitator, Operating - V vs J, 12 in. Plate Spacing

The voltage/current characteristic curves for the barb and star electrodes have been compared to curves from a full-scale ESP that collects a similar ash. The comparison yields an adjustment for the STE curves to allow prediction of a full-scale voltage/current characteristic for the STE.

The efficiency data for the 16 inch plate spacing tests is also presented in Table 1. Collection efficiency increased as plate spacing increased - an unexpected result. Previous work (Ref. 1) indicates that the efficiency should stay about the same. As plate spacing is increased, operating voltage should increase commensurately. Migration velocity should increase with operating voltage, and since the SCA is decreasing at the same rate, the collection efficiency should remain constant. The results presented in Table 1 show that operating voltage did increase linearly with plate spacing. However, the measured efficiency data indicate that the migration velocity increased much more than expected.

The cause of this inconsistency is the operation of the host steam plant. The plant load and thus gas flow was 75% higher during the 16 inch plate spacing tests than during the 12 inch plate spacing tests. Because the slipstream bringing gas to the pilot plant has a constant area opening, higher gas flow from the boiler results in a higher ash particle size distribution in the slipstream duct. This is a familiar result when a gas stream is sampled at a velocity that is less than 100% isokinetic. The particle size distribution was higher during the 16 inch spacing tests, and a higher than expected migration velocity was the result.

The air load and operating voltage/current characteristic curves for the 16 inch plate spacing tests are shown in Figures 7 and 8. These curves can be adjusted to obtain full-scale characteristic curves for 16 inch operation. The procedure is similar to that used to predict full-scale for the STE V/I characteristics.

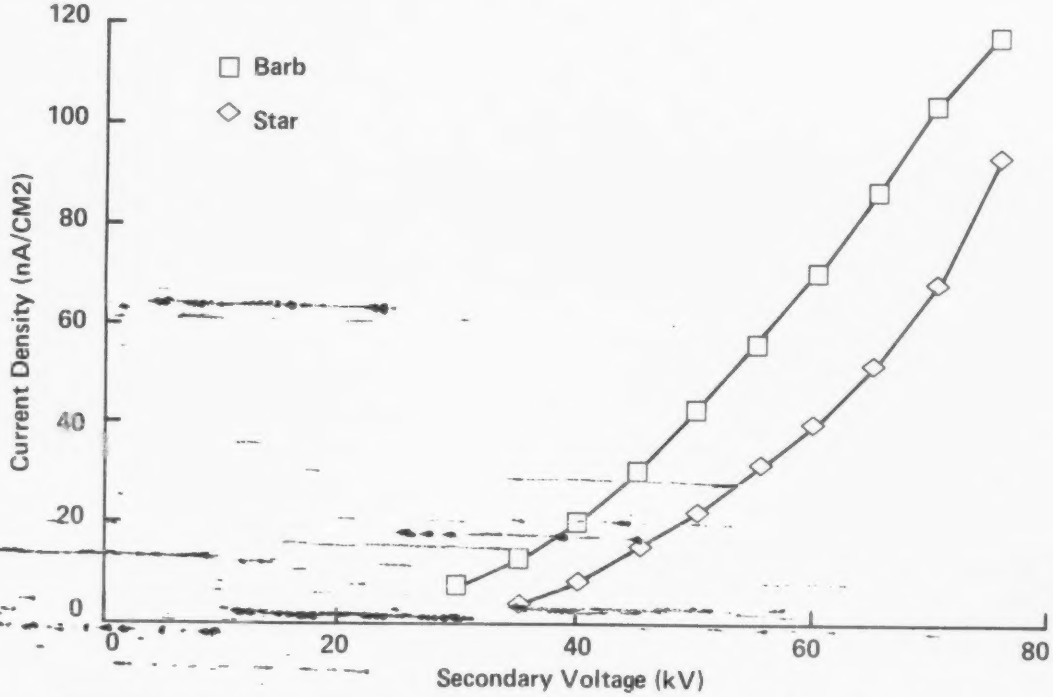

Figure 7. ESD Pilot Precipitator, Clean Plate, Air Load - V vs J, 16 in. Plate Spacing

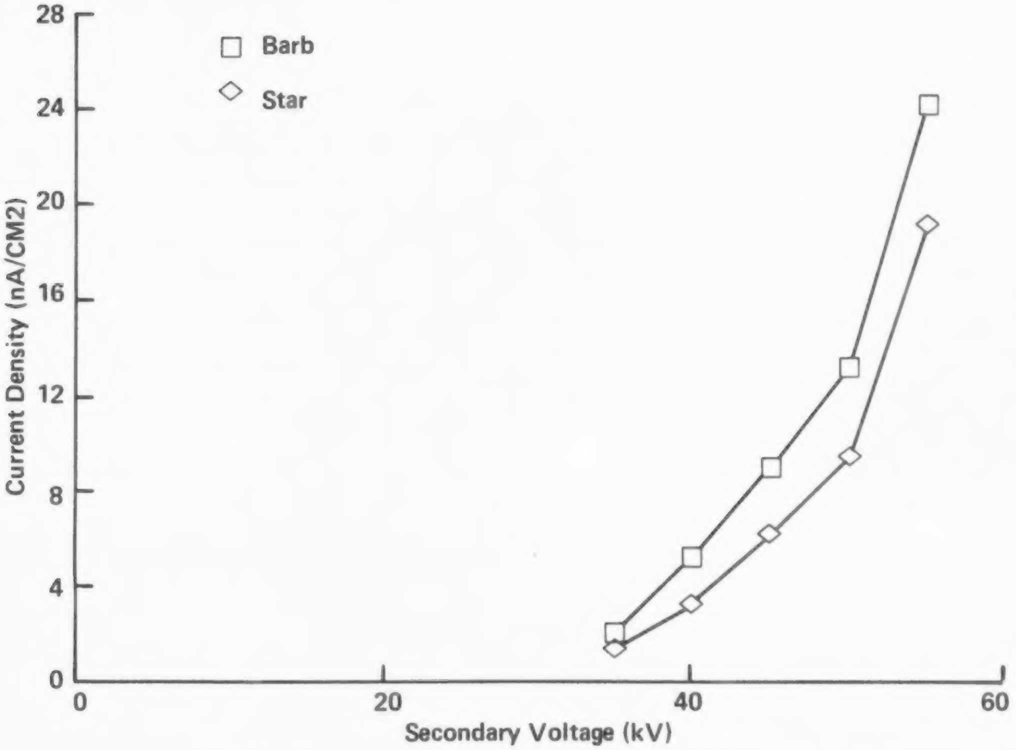

Figure 8. ESD Pilot Precipitator, Operating - V vs J, 16 in. Plate Spacing

Current distribution at the collecting panel was measured for each discharge electrode at the 12 inch plate spacing condition. The location of the sensors is shown in Figure 9. The sensors were bonded directly to the collecting panel; therefore, only the average distribution in the vertical plant could be obtained. Measurements were taken under three sets of test conditions: 1) ambient air load; 2) operating conditions with clean sensors; and 3) operating conditions with ash covered sensors.

The results for the air load current distribution tests are shown in Figure 10. These results closely approximate the results from the electrical characterization tests shown in Figure 4. A major difference is at the edge of the panel for each electrode where the existence of upstream and downstream electrodes in the pilot reduce the current. The results for the tests at operating conditions with clean sensors are shown in Figure 11. Each set of data was recorded approximately ten minutes after unit start-up. The results for both the barb and the STE indicate a greater concentration of current to the portions of the collecting panel opposite the corona discharge. This is indicated by curves with more pronounced peaks and valleys than were shown on their respective air load curves.

The results for the tests at operating conditions with ash covered sensors are not presented. The current measured at each sensor was very erratic over a broad range. When an ash layer forms on the collecting panel, the charges arriving at the surface of the layer are subjected to lateral as well as through-thickness electrical forces. Thus, the charges tend to spread in the ash layer, and by the time they reach the sensor panel they are distributed more evenly. As the charges drain to the plate, the sensor panel indicates changing values of current that stay within a range of numbers dictated by irregular local conditions. Since the current distribution on the ash layer, not in the ash layer, is pertinent to particle charging, space charge and the electrostatic holding force on the ash layer, the current distribution indicated under operating conditions with clean sensors should be more indicative of the operating conditions of interest.

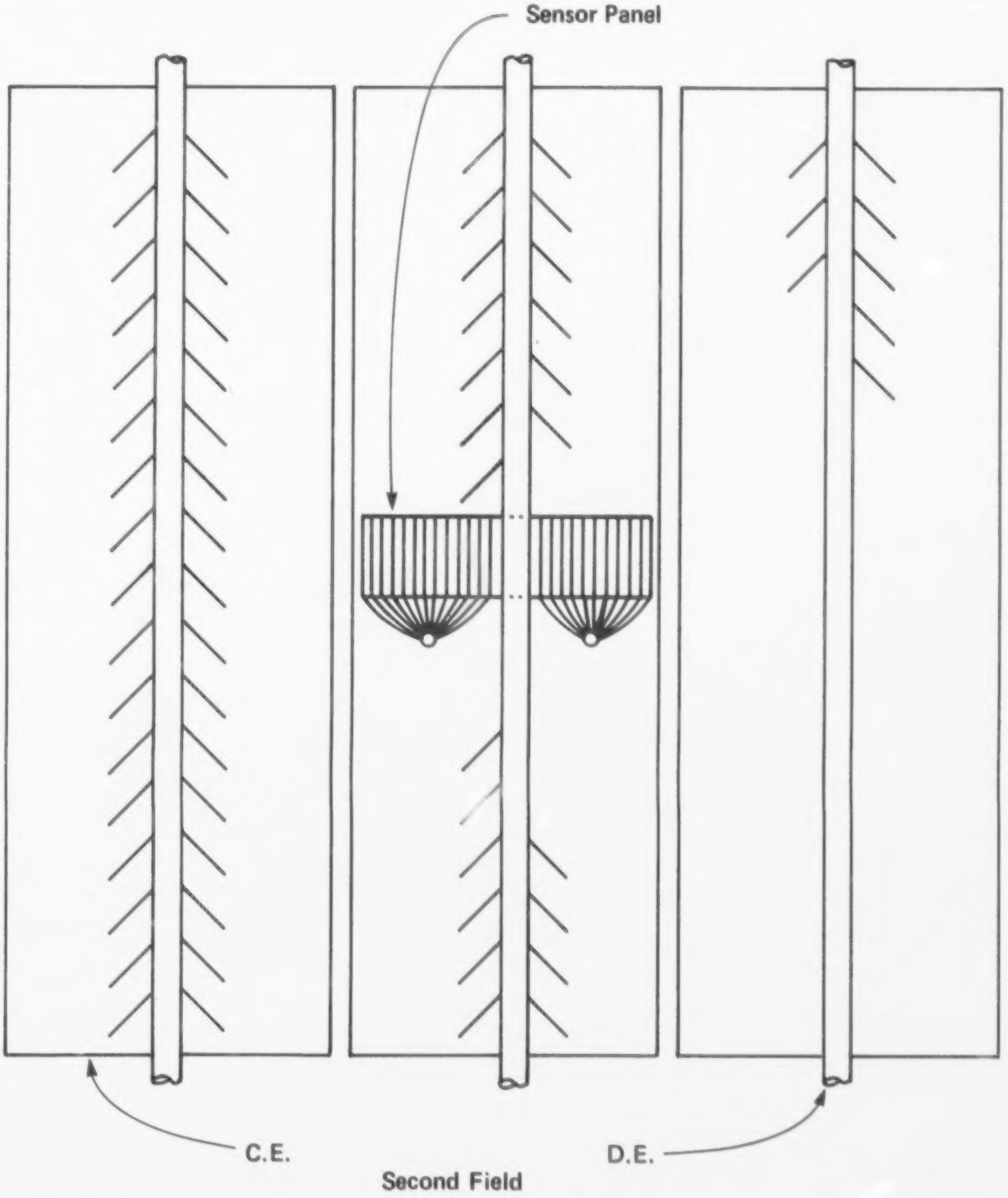

Figure 9. Location of Current Density Measurement Apparatus, ESD Pilot Precipitator

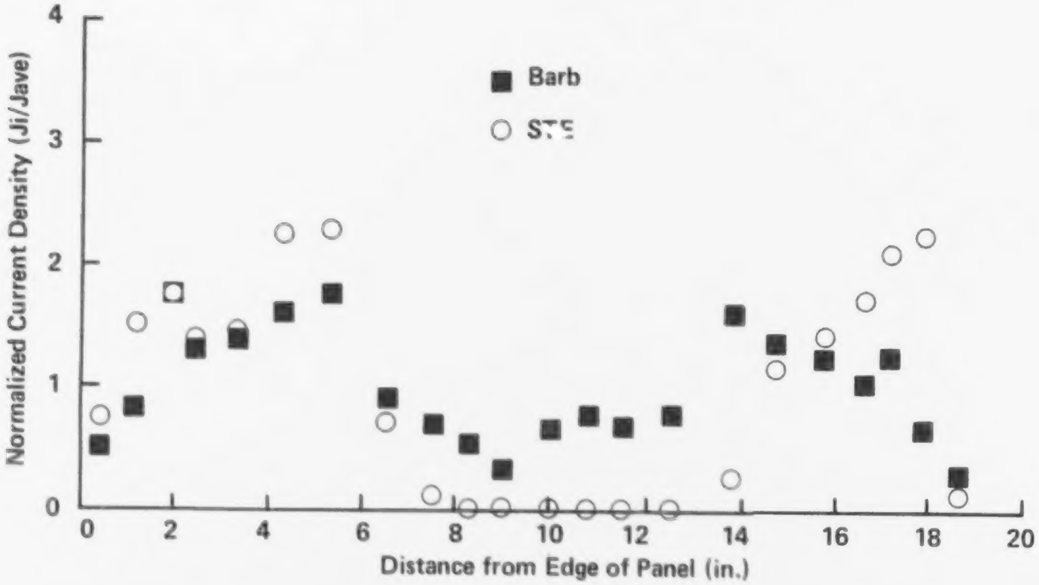

Figure 10. ESD Pilot Precipitator, Current Density Distribution, Air Load

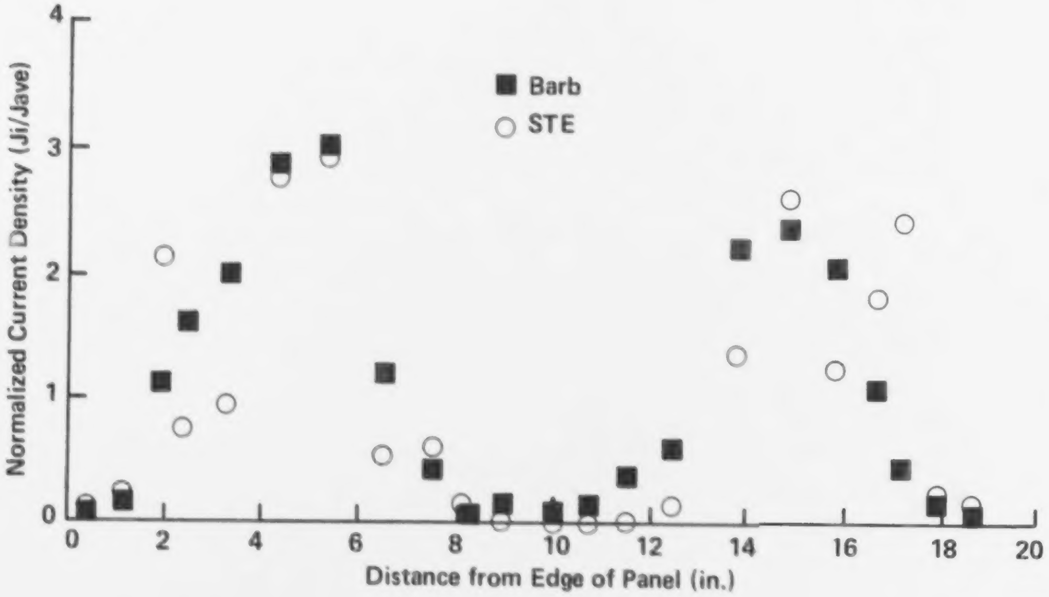

Figure 11. ESD Pilot Precipitator, Current Density Distribution, Operating

Visual observation of the collected ash layer after shutdown of the pilot following each test series was enlightening. The ash deposition patterns that remained on the collecting panels clearly indicated areas of high and low current. First, the ash collected by the barb electrode compacted tightly in closely spacing ovals on the collecting panels directly across from the barbs.

Elsewhere on the panel, the ash formed a thicker, less compact layer. Similarly for the STE, the ash layer directly across from the tube, where there is little or no current flow, was significantly less compact than the ash layer across from the ends of the studs and on the edge of the collecting panel. There were no obvious ash patterns on the panels after operation with the star electrode, indicating well distributed corona and the integrated effects of corona tufts in changing random locations. Similar ash patterns have been reported by others (Ref. 3).

C-E uses a modified version of the EPA/SoRI mathematical process model (Ref. 4) as a design model. The model has been calibrated previously to allow an accurate prediction of the performance of C-E's standard discharge and collecting electrode system (Ref. 2). The current distribution measurements from the pilot tests reported here have been used in a similar manner to calibrate the model for the STE.

The results of the computer modeling efforts are shown in Table 2. In each case the predicted migration velocity is within 5% of the measured migration velocity. Results of this quality are usually obtainable when the important input parameters have been measured or can be accurately predicted. The agreement of the predicted efficiency with the measured efficiency indicates that the model can be used to predict the performance of C-E precipitators using the STE with 12 inch spacing or the standard electrodes with 16 inch spacing. The model can also be used to predict the performance to the STE with 16 inch spacing.

TABLE 2. PILOT PRECIPITATOR COMPUTER MODELING RESULTS

INTERNAL CONFIGURATION (Plate Spacing/Discharge Electrode)	12/BARB	12/STE	12/STAR	16/BARB	16/STAR
Measure Efficiency (%)	93.81	94.02	94.52	95.1	96.6
Predicted Efficiency (%)	94.13	94.57	94.89	95.6	96.2
Percent Difference in Migration Velocity (%)	2.2	4.3	2.2	2.2	4.1

When predicting the performance of a new ESP using either the STE or 16 inch spacing, the procedure is the same as that used for a conventional design. The only complication is the accurate prediction of voltage/current characteristics. In both cases, operating voltage/current characteristics are first obtained for the barb electrode based on a knowledge of the fuel to be burned or the ash to be collected. These characteristics are then modified based on the pilot plant results.

SUMMARY

Two test programs designed to improve the design of electrostatic precipitators have been successfully completed. The first program, to develop a new rigid discharge electrode design, included electrical characterization tests to evaluate several electrode designs and pilot plant tests to obtain data necessary to scale-up the selected electrode. A studded tube electrode (STE) was selected as the optimum rigid discharge electrode design. Pilot testing indicated that the STE is capable of the same performance as C-E's standard electrodes. The second program was designed to verify previously published results on the benefits of plate spacings wider than 12 inches and to obtain design data for C-E precipitators using wider plate spacings. The results show that as plate spacing is increased to 16 inches, operating voltage increased proportionately, current density remains essentially constant, and collection efficiency is maintained. Compared to conventional precipitators, wide spaced precipitators offer equivalent performance at a reduced cost.

REFERENCES

1. Altman, Ralph A., et. al., Technical Evaluation of Plate Spacing Effects on Fly Ash Collection in Precipitators; presented at the Fifth Symposium on the Transfer and Utilization of Particulate Control Technology, August 1984.

2. Arstikaitis, A. A., Driggers, G. W., and Hawkins, L. A., Computer Model Use for Precipitator Sizing. In: Proceedings of the Fourth Symposium on the Transfer and Utilization of Particulate Control Technology, October, 1982.

3. Adams, R. and Gelfand, P., Development and Evaluation of a New Precipitator Emitter Electrode. In: Proceedings of the Fourth Symposium on the Transfer and Utilization of Particulate Control Technology, October, 1982.

4. McDonald, J. R., A Mathematical Model of Electrostatic Precipitation, EPA-600.7-78-111b, U.S. EPA, Washington, D.C., 1980.